

**Development of Semiconductor Nanomaterial
based Heterostructures for Photocatalytic
Applications**

Thesis

Submitted for the degree of

DOCTOR of PHILOSOPHY (Science)

Jadavpur University

Kolkata-700 032, India

By

Susmita Bera

Under the supervision of

Dr. Rajendra Nath Basu

Dr. Srabanti Ghosh

Energy Materials & Devices Division
(Former Fuel Cell & Battery Division)

CSIR-Central Glass & Ceramic Research Institute


196, Raja S.C. Mullick Road

Kolkata-700 032, India

May 2022

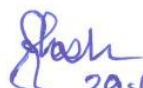
CERTIFICATE

This is to certify that the thesis entitled “*Development of Semiconductor Nanomaterial based Heterostructures for Photocatalytic Applications*” Submitted by **Ms. Susmita Bera** who got her name registered on 27th September, 2018 for the award of Ph. D. (Science) degree of Jadavpur University, is absolutely based upon her own work under the supervision of **Dr. Rajendra Nath Basu** and **Dr. Srabanti Ghosh** and that neither this thesis nor any part of it has been submitted for either any degree/diploma or any other academic award anywhere before.


20/05/2022

(Signature of the Supervisor date)

Dr. Rajendra Nath Basu
Chief Scientist & HOD (Retired)
Fuel Cell & Battery Division
CSIR-Central Glass & Ceramic Research Institute
Kolkata 700 032, India


20-05-2022

(Signature of the Supervisor date with official seal)

Dr. Srabanti Ghosh
Senior Scientist
Energy Materials & Devices Division
CSIR-Central Glass & Ceramic Research Institute
Kolkata 700 032, India

डॉ श्रावन्ती घोष
Dr. SRABANTI GHOSH
वरिष्ठ वैज्ञानिक / Senior Scientist
ऊर्जा सामग्री और उपकरण प्रभाग
Energy Materials & Devices Division
सीएसआईआर-केंद्रीय काँच एवं सिरामिक अनुसंधान संस्थान
CSIR - Central Glass and Ceramic Research Institute
११६, राजा एस. सी. मल्लिक रोड, कोलकाता-७०००३२, भारत
106, Raja S. C. Mullick Road, Kolkata - 700032, INDIA

DECLARATION

I hereby declare that the research work included in my thesis entitled “**Development of Semiconductor Nanomaterial based Heterostructures for Photocatalytic Applications**” is carried out by me in Energy Materials & Devices Division (Formerly known as Fuel Cell & Battery Division), CSIR-Central Glass & Ceramic Research Institute, Kolkata under the supervision of **Dr. Rajendra Nath Basu** and **Dr. Srabanti Ghosh** with the support of DST INSPIRE Fellowship. This work or any part of the work has not been submitted anywhere else for any other degree of diploma or any other academic award.

Date: 23.05.2022

Place: Kolkata

Susmita Bera

Susmita Bera
Senior Research Fellow
Energy Materials & Devices Division
(Former Fuel Cell & Battery Division)
CSIR-Central Glass & Ceramic Research Institute
Kolkata 700 032, India

*Dedicated to
My Parents, Brother
And Husband*

Acknowledgement

Firstly, I wish to express my deep sense of gratitude and regards towards my research supervisor **Dr. Rajendra Nath Basu** for his continuous support, encouragement and giving me the opportunity to work in his research group. I greatly respect his valuable, insightful guidance and suggestions. I am also extremely thankful to my research supervisor **Dr. Srabanti Ghosh**, who has allowed me to do mistakes so that I can enlighten my knowledge and develop my own research style. I am highly motivated by her scientific knowledge, personality, creative thinking, hardworking, perfection, punctuality, dedication and mostly the excellent approach towards solving research problems. Her guidance and valuable suggestions in the every stage of my research have made this work possible. They not only put in great efforts towards my PhD work but also taught me the basics of material science, basic chemistry behind the synthesis procedures and encouraged me to work on the global challenge of green H₂ generation through photocatalytic water splitting. Without their valuable and constructive suggestions my PhD would have been a distant dream. I always feel myself enough fortunate to work under their supervision.

I would like to thank **Dr. Abhijit Das Sharma**, Senior Principal Scientist & Head, Energy Materials & Devices Division, CSIR-CGCRI for his kind support and suggestions as my divisional HOD. My sincere thanks to all scientists of my division for their encouragement and suggestions.

My sincere acknowledgement to **Department of Science & Technology (DST)** for five years financial support through **DST INSPIRE** fellowship and **Newton Bhabha PhD Placement Award**.

My sincere thanks to **Dr. Suman Kumari Mishra**, Director, CSIR-CGCRI and **Dr. K. Muraleedhran**, Former Director, CSIR-CGCRI for their kind support and encouragement.

I would like to thank **Dr. Chinmoy Bhattacharya**, Associate professor, Department of Chemistry, Indian Institute of Engineering Science and Technology, Shibpur for providing the infrastructure and advanced facilities for measuring the photoelectrochemical properties at his lab, IEST and collaborative contribution in my thesis work.

I wish to thank **Dr. Thandavarayan Maiyalagan**, Associate professor, Department of Chemistry, SRM Institute of Science and Technology, Kattankulathur, India for collaborative contribution in my thesis.

I convey my sincere thanks to **Prof. Vinod R. Dhanak**, Professor, Stephenson Institute for Renewable Energy and Department of Physics, University of Liverpool, United Kingdom for giving me the opportunity to carry out Newton Bhabha PhD placement project work in his laboratory and his resourceful guidance, active supervision throughout the stay and collaborative contribution. Here, I must thank to **Prof. Dhanak** and his wife **Ketki Dhanak** for their help and support, Indian food during the stay in Liverpool and the kind gift 'Sapiens-A Brief History of Humankind'.

My sincere thanks to **Dr. Dipayan Sanyal**, Chief Scientist & Head, Advances Ceramics & Composite Division, CSIR-CGCRI, **Dr. Sunirmal Jana**, Senior Principal Scientist and his student **Dr. Hasmat Khan**, Specialty Glass Division, CSIR-CGCRI, and **Dr. Rajat Banerjee**, Senior

Technical Officer, Advances Ceramics & Composite Division for providing facility to measure the UV-Vis absorption of the materials.

*My special thanks to **Mr. Atanu Hota** for his supportive advices in professional and personal matters, visit to many restaurants in Kolkata and especially every year outing, where both of sir and ma'am have always been most generous. During these outing, discussion on many topics, such as physics, chemistry, history, and politics with full enjoyment gives fresh oxygen to my brain to work again. Moreover, my deep acknowledgement to their support during the stay of UK in covid pandemic situation.*

*I shall remain ever indebted to all the technical staff of our department, in particular **Mr. Debayan Gupta, Mrs. Nabanita Chakraborty, Mr. Sudip Kumar Ghosh, Mr. Suman Das, Mr. Satyendra Barik, Mr. Asian Hemron, Dr. Pradip Sekhar Das, Mr. Debabrata Biswas, Mr. Tapas Kumar Mishra, Mr. Debabrata Roy, Mr. Goutam Dey, Mr. Sunil Kumar Singh, Mr. Bimal Dey, Mr. Ratikanta Pal, Mr. Dibyendu Palit, Mr. Pratik Lal, Mr. Debasish Chokraborty.***

*I would also like to acknowledge the cooperation I get from the technical staffs of the **Central Characterization Unit** of our institute.*

*I deeply acknowledge the academic support from **Dr. Sanjib Shyamal** (IEST, Shibpur), **Dr. Soumyadipta Rakshit** (IIT Bombay) for the thesis work.*

*I deeply acknowledge the supports and warm friendship from my laboratory friends, seniors and juniors who make my days enjoyable. In particular, I would like to thank **Shoroshi Dey, Sayani Hui, Deepra Bhattacharya, Monojit Das Bairagya, Md. Rashid, Arpita Banerjee, Paramita Hajra, Shibnam Sahu, Kuntal Ghosh, Koyel Dey, Mononita Das, Indrajeet Mondal, Soumita Samajdar, Sourabh Pal.** We have shared many memorable moments during the period.*

*I would like to thank the M. Sc., M. Tech. and summer project students, in particular **Kuntal Jana, Divya Rashmi, Mampi Mondal, Shweta Rani Keshri, Ankita Kumari, Prama Adhya, Anuj Kumar, Santhosh Kumar, Tamal Ghosh, Aritra Banerjee, Maitrayee Biswas** for many memorable moments and help in my thesis work.*

*I would like to convey my heartiest thank to school and college friends, in particular **Aditi Sahoo, Dipanjan Maity, Dibyendu Rana, Chandan Samanta, Satabdi Samanta, Debjani Bera (Giri)** for their mental support, encouragement and academic support.*

*I have no words to express my feelings towards my parents and family whose support, blessings, love, sacrifice, care and constant encouragement throughout my life have made me what I am today. This thesis is also a dream of my father **Mr. Lakshmikanta Bera** and mother **Mrs. Suchitra Bera**. They don't have much knowledge of what I do, but I know they are proud and support me in any way they can. It is a great pleasure to deeply acknowledge the love of my beloved husband, and would like to thank for showing his absolute trust in my dreams and deeds. This journey could not have been possible without his love, support, understanding and patience throughout this time period. I wish to mention here the strong decision and support of my husband **Mr. Ritwik Maity** and brother **Mr. Swayangdipta Bera** to send me alone for Newton Bhabha Visit at University of Liverpool, UK, which helped me to enrich my self-confidence.*

PREFACE

As efficient, stable and economic photocatalyst development is the key challenge for large scale green H₂ generation, the present research work aims to develop stable, reusable, nontoxic, cost effective and visible light active semiconductor nanomaterial based heterostructures as photocatalysts for the environmental remediation and renewable energy H₂ generation through photocatalytic and photoelectrochemical water splitting. This work explores the band structure analysis and charge migration pathway of heterostructured materials under light illumination for water splitting reactions.

The chapters in this thesis covers the followings:

Chapter 1: This chapter provides the background of photocatalysis, basic of semiconductor, nanomaterial and heterostructures. The reactions involved in photocatalytic H₂ generation and photoelectrochemical water splitting are described in details along with the photon to current conversion efficiency measurement. The mechanism of co-catalyst, doping and various types of heterostructures (Type-I, Type-II, Z-Scheme, p-n heterojunction, Schottky junction) are discussed with examples. Finally, the advantages and limitations of Bi-based semiconductors towards water splitting and the challenges of water spitting are illustrated.

Chapter 2: This chapter covers the motivation and objectives of the thesis work with literature review on Bi-based semiconductor heterostructures used in various photocatalytic application, such as organic pollutant degradation, solar fuel H₂ and O₂ generation, CO₂ reduction to value added products etc. under solar light irradiation. The challenges in water splitting and the strategies to improve the catalytic activity are described with examples.

Chapter 3: The synthesis methods and the characterization techniques, including structural, morphology, optical and electrochemical property measurements. All the tools used in this thesis work has been described with operating principal, condition and the model number. The photocatalytic and photoelectro chemical water splitting set up, reactor and the reaction condition are also illustrated.

Chapter 4: A facile hydrothermal followed by in-situ deposition method described to synthesize a highly active Bi₂S₃/ZnO Type-II heterostructures for organic pollutant degradation and photocatalytic H₂ generation. The physical, chemical, and electrochemical techniques to characterize the Bi₂S₃/ZnO heterostructures are described and the Type-II charge transfer pathway

through the junction are proposed. The prepared Bi₂S₃/ZnO heterostructures shows 8.6 times higher H₂ generation compared to bare Bi₂S₃ under visible light illumination.

Chapter 5: A new strategy has been developed through two steps, comprising of hydrothermal method followed by radiolysis for an efficient Schottky junction between noble metal gold nanoparticles (Au NPs) and bismuth ferrite (BiFeO₃) fabrication. The catalytic activity of as developed metal-semiconductor Schottky junction was investigated by photocatalytic H₂ generation and PEC water splitting under visible light. The effect of pH, various sacrificial agent, catalyst loading have been tested in details to optimize the reaction parameters of photocatalytic H₂ generation. The hot electron generation by virtue of surface plasmonic effect and the transfer from Au surface to BiFeO₃ *via* Schottky junction has been described. The prepared Au/BiFeO₃ heterostructures shows two fold improved H₂ generation rate compared to bare BiFeO₃.

Chapter 6: An efficient *p-n* heterojunction between Bi-doped TiO₂ and MoS₂ has been developed for visible light active water splitting. The band gap reduction of TiO₂ by Bi doping and suppression of electron-hole recombination by developing *p-n* heterojunction has been described in this chapter. Further, an indirect Z-scheme charge transfer mechanism for MoS₂/Ag-AgVO₃ heterostructures are characterized and described. Finally, the effect of *p-n* heterojunction and indirect Z-scheme heterostructures towards photocatalytic H₂ generation and photo electrochemical water splitting are illustrated. The four times higher H₂ generation rate obtained for Bi-doped TiO₂/MoS₂ *p-n* heterojunction compared to bare MoS₂.

Chapter 7: We have enhanced the photocatalytic performance of bismuth oxyhalides (BiOX, X=Cl, Br, I) through the coupling with low bandgap spinel structure copper ferrite (CuFe₂O₄) *via* in-situ co-precipitation method. Three types of heterostructures (Type-I, Type-II and direct Z-scheme) have been formed between BiOX and CuFe₂O₄ depending on the position of their valence band, conduction band location and fermi level. The highest efficiency for BiOCl/CuFe₂O₄ direct Z-scheme heterostructures towards H₂ generation are described on the basis of bandgap engineering, carrier concentration, charge transfer pathway and redox capability. The highest efficiency towards H₂ generation was achieved for BiOCl/CuFe₂O₄ direct Z-scheme heterostructures (~22.2 mmol h⁻¹), which is two times than BiOI/CuFe₂O₄ and BiOBr/CuFe₂O₄ heterostructures, highlighting the intense promoting effect of direct Z-scheme charge transfer mechanism.

Chapter 8: A summary of the most important findings from the previous chapters and future research directions are discussed.

Contents

| | |
|-----------------------|---------|
| Abstract | i |
| List of Figures | ii-xiii |
| List of Tables | xiv |
| List of Abbreviations | xv-xvii |

Chapter 1: General Introduction

| | |
|--|-------|
| 1.1 Background | 1-2 |
| 1.2 Semiconductor | 3-5 |
| 1.3 Nanomaterial | 5-7 |
| 1.4 Photocatalysis | 8-11 |
| 1.5 Photocatalytic H ₂ Generation | 11-13 |
| 1.6 Photoelectrochemical (PEC) Water Splitting | 13-15 |
| 1.7 Photocatalytic Efficiency Measurement | 15-19 |
| 1.8 Co-catalyst | 19-20 |
| 1.9 Heterostructures | 21-28 |
| (i) Type-I Heterostructures | 21-22 |
| (ii) Type-II Heterostructures | 22-23 |
| (iii) Type-III or Z-scheme Heterostructures | 23-24 |
| (iv) p-n Heterojunction | 24-25 |
| (v) Schottky Junction | 25-27 |
| 1.10 Main Challenges in Photocatalysis | 27-28 |
| 1.11 Bismuth based Materials as Photocatalysts | 28-37 |
| 1.11.1 Bi-based Oxide | 29-31 |
| 1.11.2 Bi-based Vanadate | 32 |
| 1.11.3 Bi-based Chalcogenide | 32-33 |
| 1.11.4 Bi-based Halide | 33-34 |
| References | 38-49 |

Chapter 2: Genesis of the thesis

| | |
|--|-------|
| 2.1 Motivation | 50-65 |
| 2.1.1 Type-II Heterostructures using Bi-based Semiconductors | 55-56 |
| 2.1.2 Bi-based p-n Heterojunctions | 56-57 |
| 2.1.3 Bi-based Z-Scheme Heterojunctions | 57 |
| 2.2 Scope of the Thesis | 65 |
| 2.3 Objectives | 66 |
| 2.4 The Main Features of the Thesis | 67-68 |
| 2.5 Research Focus | 68-70 |
| References | 71-91 |

Chapter 3: Experimental

| | |
|---|---------|
| 3.1 Introduction | 92 |
| 3.2 Synthesis Methods | 92-95 |
| 3.2.1 Hydrothermal and Solvothermal Method | 92-93 |
| 3.2.2 Co-Precipitation Method | 93-94 |
| 3.2.3 Gamma Radiolysis | 94-95 |
| 3.3 Characterization Techniques | 95-125 |
| 3.3.1 Structural Characterization | 95-106 |
| 3.3.1.1 Powder X-Ray Diffraction (XRD) | 95-97 |
| 3.3.1.2 X-Ray Photoelectron Spectroscopy (XPS) | 98-100 |
| 3.3.1.3 Raman Spectroscopy | 100-101 |
| 3.3.1.4 Brunauer–Emmett–Teller (BET) Surface Area | 102-104 |
| 3.3.1.5 Fourier Transform Infrared Spectroscopy (FTIR) | 104-105 |
| 3.3.1.6 Thermogravimetry-Differential Thermal Analysis (TG-DTA) | 105-106 |
| 3.3.2 Morphology and Elemental Analysis | 106-109 |
| 3.3.2.1 Field Emission Scanning Electron Microscope (FESEM) | 106-107 |
| 3.3.2.2 Transmission Electron Microscopy (TEM) | 107-108 |
| 3.3.2.3 Energy Dispersive X-Ray Spectroscopy (EDX) | 108 |

| | |
|---|---------|
| 3.3.2.4 ICP-MS and Atomic Absorption Spectroscopy (AAS) | 108-109 |
| 3.3.3 Optical Properties Measurement | 109-114 |
| 3.3.3.1 UV-Vis Absorption Spectroscopy | 109-111 |
| 3.3.3.2 Photoluminescence (PL) Spectroscopy | 111-113 |
| 3.3.3.3 Time-Correlated Single Photon Counting (TCSPC) | 113-114 |
| 3.3.4 Electrochemical Properties Measurement | 114-123 |
| 3.3.4.1 Cyclic and Linear Sweep Voltammetry and Chronoamperometry | 116-119 |
| 3.3.4.2 Electrochemical Impedance Spectroscopy (EIS) | 119-121 |
| 3.3.4.3 Mott-Schottky | 122-123 |
| 3.3.5 Vibrating Sample Magnetometer (VSM) | 124 |
| 3.3.6 Gas Chromatography (GC) | 124-125 |
| 3.4 Organic Pollutant Degradation | 125-126 |
| 3.5 Photocatalytic H ₂ Generation Method | 126-127 |
| 3.6 Photoelectrochemical Measurements | 127-128 |
| References | 129-137 |

Chapter 4:
Fabrication of Bi₂S₃/ZnO Heterostructures: An Excellent Photocatalyst for Visible-Light-Driven Hydrogen Generation and Photoelectrochemical Properties

| | |
|--|---------|
| 4.1 Introduction | 138-140 |
| 4.2 Experimental | 140-142 |
| 4.3 Results and Discussion | 142-163 |
| 4.3.1 Structural Characterization | 142-143 |
| 4.3.2 Morphology | 143-148 |
| 4.3.3 Growth Mechanism | 149-150 |
| 4.3.4 XPS Analysis | 150-151 |
| 4.3.5 TG and BET Surface Area Analysis | 151-152 |
| 4.3.6 Optical Characterization | 152-153 |
| 4.3.7 Photocatalytic MO Degradation | 153-155 |
| 4.3.8 Photocatalytic H ₂ Generation | 155-157 |

| | |
|--|---------|
| 4.3.9 Photoelectrochemical Performance | 157-161 |
| 4.3.10 Mechanism | 162-163 |
| 4.4 Summary | 163 |
| References | 164-170 |

**Chapter 5:
Photocatalytic Hydrogen Generation using Gold Decorated BiFeO₃
Heterostructures as an Efficient Catalyst under Visible Light Irradiation**

| | |
|---|---------|
| 5.1 Introduction | 171-173 |
| 5.2 Experimental | 173-175 |
| 5.3 Results and Discussion | 176-196 |
| 5.3.1 Phase Purity and Crystal Structure | 176-177 |
| 5.3.2 Microstructures | 177-178 |
| 5.3.3 X-Ray Photoelectron Spectroscopy and Bet Surface Area | 178-180 |
| 5.3.4 UV-Vis Spectroscopy | 180-181 |
| 5.3.5 Photocatalytic H ₂ Production | 181-186 |
| 5.3.6 Photoelectrochemical Activity | 186-189 |
| 5.3.7 Mechanism | 189-196 |
| 5.4 Summary | 196 |
| References | 197-203 |

**Chapter 6:
Assemble Of Bi-Doped TiO₂ and Ag-AgVO₃ onto 2D MoS₂: Efficient p-n
Heterojunction and All Solid State Z-Scheme for Photocatalytic H₂ Generation
under Visible Light**

| | |
|----------------------------|---------|
| 6.1 Introduction | 204-207 |
| 6.2 Experimental | 207-209 |
| 6.3 Results and Discussion | 209-237 |

| | |
|--|---------|
| 6.3.1 Morphology | 209-213 |
| 6.3.2 Structural Analysis | 213-217 |
| 6.3.3 XPS Analysis | 217-221 |
| 6.3.4 Optical Properties | 221-223 |
| 6.3.5 Photocatalytic H ₂ Generation | 223-227 |
| 6.3.6 Photoelectrochemical Properties | 227-232 |
| 6.3.7 Photocatalytic Mechanism | 232-237 |
| 6.4 Summary | 238 |
| References | 239-247 |

**Chapter 7:
Band Edge Engineering of BiOX/CuFe₂O₄ Heterostructures for Efficient Water Splitting**

| | |
|--|---------|
| 7.1.1 Introduction | 248-250 |
| 7.2 Experimental | 251-252 |
| 7.3 Results and Discussion | 253-281 |
| 7.3.1 Structural Analysis | 253-258 |
| 7.3.2 Morphology | 258-261 |
| 7.3.3 Photoelectrochemical Properties | 261-271 |
| 7.3.4 UV-Vis Absorption and Bandgap Calculation | 271-273 |
| 7.3.5 Photocatalytic H ₂ Generation | 273-278 |
| 7.3.6 Proposed Mechanism for H ₂ Generation | 278-281 |
| 7.4 Summary | 281-282 |
| References | 283-291 |

**Chapter 8:
Conclusion and Future Scope**

| | |
|--------------------|---------|
| 8.1 Conclusions | 292-296 |
| 8.2 Future Aspects | 296-297 |

ABSTRACT

Design and fabrication of artificial catalytic systems to mimic natural photosynthesis which can harvest solar energy and directly convert into usable or storable energy resources may resolve the global energy and environment crisis. Remarkably, photocatalysis is an efficient approach to utilize solar photons in order to drive the thermodynamic uphill reaction to generate chemical fuels H_2 and O_2 by water splitting in presence of efficient photocatalyst. In this regards, Bi-based semiconductors are focused as photocatalyst due to low cost, nontoxic, facile synthesis, interesting optoelectronic and physicochemical properties. As single semiconductor could not meet all the stringent requirements for water splitting under visible light, development of new functional semiconductor based hybrid materials and understanding of interfacial band edge energetics have been studied in this thesis work, which are useful for photocatalytic and photoelectrochemical solar fuel H_2 generation. The coupling of two materials as a semiconductor heterostructures is an effective strategy to increase charge separation efficiency and lowering the fast electron-hole recombination by allowing multiple active sites and thereby improve their solar light harvesting efficiency. The conventional heterostructures of Type-II, Schottky junction, p-n junction and advanced type direct and indirect Z-scheme heterostructures have been developed by facile methods and studied their physical, morphological, optical and electrochemical properties and finally the charge transfer mechanisms through the junction interfaces are proposed. Therefore, the present work will be focused to introduce a stable, reusable, nontoxic, cost effective and visible light active Bi-based heterostructures as photocatalysts for the environmental remediation and renewable energy production.

List of Figures

| | |
|--|----|
| Figure 1.1 Standard solar light spectra as a function of wavelength on the earth's surface | 2 |
| Figure 1.2 Schematic presentation of band structures for metal, semiconductor and insulator. | 3 |
| Figure 1.3 (a) Schematic presentation of fermi level position for n-type and p-type semiconductors. (b) Electron and hole generation and separation within a semiconductor. | 4 |
| Figure 1.4 Electron and hole generation and separation within a semiconductor. | 5 |
| Figure 1.5 Schematic presentation of the energy level and the confined direction for 0D, 1D, 2D and 3D confined nanomaterials. | 7 |
| Figure 1.6 Schematic diagram of the basic steps of photocatalysis. | 9 |
| Figure 1.7 Electron and hole generation and separation within a semiconductor during overall water splitting and organic pollutant degradation under light irradiation. | 10 |
| Figure 1.8 Types of electron-hole recombination in a photocatalyst. | 12 |
| Figure 1.9 (a) Schematic presentation and (b) image of photocatalytic H ₂ generation reactor. | 13 |
| Figure 1.10 Energy diagrams of PEC water oxidation and reduction on an n-type semiconductor photoanode and Pt counter electrode (one-step excitation). | 14 |
| Figure 1.11 Schematic energy band diagram of a n-type semiconductor-electrolyte interfaces (a) before equilibration, (b) after equilibration (without light) and (c) in quasi-static equilibrium under steady state light illumination. | 15 |
| Figure 1.12 The number of photons for AM 1.5G and theoretical solar-to-hydrogen efficiency as a function of wavelength. | 17 |
| Figure 1.13 Band-edge positions and the band gaps of some typical semiconductor photocatalysts. Dotted lines indicates the relative energy levels of redox reactions for organic pollutant degradation and water splitting. | 18 |
| Figure 1.14 Schematic diagram of (a) donor level, (b) acceptor level and (c) intermediate energy level generation due to doping of anions or cations. | 19 |
| Figure 1.15 Schematic diagram of photogenerated electron-hole migration mechanism of co-catalyst modified semiconductor and the widely used co-catalysts for H ₂ and O ₂ generation through water splitting. | 20 |

| | |
|--|----|
| Figure 1.16 Schematic energy band diagram and the photogenerated electron-hole separation on Type-I heterostructures. | 22 |
| Figure 1.17 Schematic energy band diagram and the photogenerated electron-hole separation on Type-II heterostructures. | 23 |
| Figure 1.18 Schematic energy band diagram and the photogenerated electron-hole separation on Type-III or Z-scheme heterostructures. | 23 |
| Figure 1.19 Schematic energy band diagram and the photogenerated electron-hole separation on a p-n junction. | 25 |
| Figure 1.20 Schematic diagram of Schottky junction between a metal and an n-type semiconductor (a) before contact, (b) electron flow after contact and (c) band bending of semiconductor interface at equilibrium. | 26 |
| Figure 1.21 Schematic diagram of depletion region formation at a metal-semiconductor interface under light illumination. | 27 |
| Figure 1.22 The crystal structure of the (a) α - Bi_2O_3 (monoclinic, P21/c), (b) β - Bi_2O_3 (tetragonal, P-421c), (c) γ - Bi_2O_3 (cubic, 123), (d) δ - Bi_2O_3 (cubic, Fm3m). | 29 |
| Figure 1.23 The crystal structure of rhombohedral (R3c) BiFeO_3 . | 31 |
| Figure 1.24 The crystal structure of orthorhombic (Pca2) Bi_2WO_6 . | 31 |
| Figure 1.25 The crystal structure of monoclinic phase (15, C2h) BiVO_4 . | 32 |
| Figure 1.26 The crystal structure of orthorhombic structure (Pnma) Bi_2S_3 . | 33 |
| Figure 1.27 The crystal structure of tetragonal structure (PbFCl-type) BiOX (X= Cl, Br, I). | 34 |
| Figure 1.28 Band-edge positions and the band gaps of commonly used Bi-based photocatalysts. Dotted lines indicate the relative energy levels of redox reactions for water splitting and organic pollutant degradation. | 35 |
| Figure 2.1 Various strategies for improvement of the photocatalytic activity of semiconductor nanomaterials. | 51 |
| Figure 2.2 The schematic presentation of various TiO_2 nanostructures according to the structural dimensionality. | 52 |
| Figure 2.3 The number of publications reported on Bismuth based semiconductor materials as photocatalyst during the last decade | 54 |
| Figure 3.1 Schematic presentation of hydrothermal synthesis of assembled flower nanostructures. | 93 |

| | |
|--|-----|
| Figure 3.2 Schematic presentation of co-precipitation method to prepare nanoparticle decorated flower like nanostructures. | 94 |
| Figure 3.3 Schematic Au/BiFeO ₃ heterostructures synthesis by gamma radiolysis. | 95 |
| Figure 3.4 Schematic representations of diffracted beams in crystal lattice. | 96 |
| Figure 3.5 (a) The XRD instrumental set up and (b) schematic presentation of working principal. | 97 |
| Figure 3.6 Schematic illumination of (a) photoelectron emission by absorption of a photon, (b) a core electron is expelled leaving a hole to fill the vacancy at valence level by releasing energy as fluorescence, (c) or an Auger electron from the same valence level. | 98 |
| Figure 3.7 Electronic energy level determination from a combination of valence band XPS and secondary electron cutoff (SEC) spectra. | 99 |
| Figure 3.8 (a) The XPS instrumental set up and (b) schematic presentation of working principal. | 99 |
| Figure 3.9 (a) The Raman instrumental setup and (b) schematic of Rayleigh, Stokes and Anti-Stokes lines formation at Raman Scattering. | 100 |
| Figure 3.10 Schematic presentation of the working principal of Raman spectroscopy. | 101 |
| Figure 3.11 (a) Schematic of N ₂ multilayers formation to fill the pores during adsorption. (b) Six types of isotherms. | 103 |
| Figure 3.12 (a) BET instrument and (b) schematically present the working principal of BET surface area. | 104 |
| Figure 3.13 Schematic presentation of the operational principal of FTIR. | 105 |
| Figure 3.14 (a) TG-DTA instrumental setup and (b) schematic presentation of the working principal. | 106 |
| Figure 3.15 (a) The FESEM instrument available and (b) schematic set up of FESEM column. | 107 |
| Figure 3.16 (a) Schematic set up of TEM column and (b) TEM instrumental setup. | 107 |
| Figure 3.17 Schematic presentation of the working principal of inductively coupled plasma mass spectrometry (ICP-MS). | 108 |
| Figure 3.18 Schematic presentation of the working principal of atomic absorption spectroscopy (AAS). | 109 |

| | |
|--|-----|
| Figure 3.19 (a) Schematic presentation of Beer-Lambert law and (b) UV-Vis absorption spectrophotometer. | 110 |
| Figure 3.20 Working principal of UV-Vis absorption spectrophotometer. | 111 |
| Figure 3.21 The schematic presentation of photoluminescence (PL) working principle. | 112 |
| Figure 3.22 The schematic presentation of Time-correlated single photon counting (TCSPC) working principle. | 114 |
| Figure 3.23 (a) Schematic presentation of double-layer created at an interface of n-type semiconductor electrode and electrolyte at equilibrium. The blue line indicates the potential (ϕ) across the double-layer. The potential drop at space charge layer (I), Helmholtz layer (II) and Gouy layer (III) are represented by $\Delta\phi_{SC}$, $\Delta\phi_H$, and $\Delta\phi_G$, respectively. (b) Schematic of energy bands of an redox states and n-type semiconductor in electrolyte (Red and Ox), Fermi level ($E_{f(\text{redox})}$) and re-organization energy of solvent (λ). | 115 |
| Figure 3.24 Schematic presentation of built-in potential (E) of an n-type electrode - electrolyte interface under dark and light during equilibrium condition. R_{ss} , R_{sc} and R_{bulk} are resistance due to the surface state, space charge layer and bulk recombination. Here, J_{redox} represents the charge transfer from VB to redox reagent. | 116 |
| Figure 3.25 (a) A triangular potential waveform applied for CV measurement. (b) Concentration of CP (blue) and CQ (red) versus distance from the electrode at various points during a reversible CV at scan rate of 100 mV s^{-1} . | 117 |
| Figure 3.26 A linear potential waveform and the corresponding Linear Sweep Voltammetry (LSV) curve. | 119 |
| Figure 3.27 (a) The representation of impedance (Z) <i>via</i> planar vector and (b) the corresponding Nyquist plot. | 120 |
| Figure 3.28 (a) RC circuit and the (b) corresponding Nyquist plot for single semiconductor. (c) RC equivalent circuit and (d) corresponding Nyquist plot for heterogeneous electrode. | 121 |
| Figure 3.29 The schematic representation of electrode-electrolyte interface. | 123 |
| Figure 3.30 Schematic diagram of (a) part of the VSM setup and (b) types of sample holder used in VSM. | 124 |
| Figure 3.31 (a) Schematic presentation of the working principle of Gas Chromatography (GC) and (b) On-line GC setup. | 125 |
| Figure 3.32 (a) Schematic presentation of quartz cell reactor for organic pollutant degradation. (b) Image of quartz cell reactor with light illumination. | 126 |

| | |
|--|-----|
| Figure 3.33 Online photocatalytic H ₂ generation set up. | 127 |
| Figure 3.34 Three electrode photoelectrochemical cell (a) without light and (b) under light irradiation. | 127 |
| Figure 3.35 Prepared working electrode by doctor-blade method on FTO glass (a) Bi ₂ S ₃ , ZnO, Bi ₂ S ₃ /ZnO, (b) BiFeO ₃ , Au/BiFeO ₃ , (c) BiOCl, BiOCl/CuFe ₂ O ₄ . | 128 |
| Figure 4.1 XRD patterns of as prepared (a) pure L-Bi ₂ S ₃ and L-Bi ₂ S ₃ decorated with ZnO NPs. Inset: XRD pattern of ZnO nanoparticles. (b) Pure M-Bi ₂ S ₃ rod shaped structures and M-Bi ₂ S ₃ decorated with ZnO NPs. The samples have been synthesized at 16 h and metal salt to surfactant ratio 1: 3. (c) XRD patterns of M-Bi ₂ S ₃ at three different reaction times as 10 hours, 16 hours and 24 hours. | 143 |
| Figure 4.2 FESEM images of Bi ₂ S ₃ using L-cysteine as structure controlling agent at three different reaction time (a) 10 h, (b) 16 h, (c) 24 h (metal: L-cysteine of 1:1.5). Effect of surfactant concentrations during the formation of Bi ₂ S ₃ at three different metal/surfactant ratio of (d) 1:1.5, (e) 1:3 and (f) 1:6 at 16 h under similar condition. | 144 |
| Figure 4.3 FESEM images of (a) – (c) flower like assembled structures of Bi ₂ S ₃ using mercaptosuccinic acid as structure controlling agent at three different magnifications and (d) EDS spectrum of Bi ₂ S ₃ synthesized at 16 h and metal salt to surfactant ratio 1 : 3. | 145 |
| Figure 4.4 TEM images of (a) pure L-Bi ₂ S ₃ nanostructures (b) HRTEM of L-Bi ₂ S ₃ inset: SEAD pattern, (c) pure M-Bi ₂ S ₃ nanostructures and (d) HRTEM image of M-Bi ₂ S ₃ at metal: surfactant of 1:3 in reaction time 16 h. | 146 |
| Figure 4.5 (a-b) FESEM images of L-Bi ₂ S ₃ /ZnO heterostructures at two different magnifications. TEM image of (c) ZnO nanoparticles decorated on rod shaped Bi ₂ S ₃ structures, (d) HRTEM, (e) SAED and (f) EDX spectrum of L-Bi ₂ S ₃ /ZnO heterostructures. | 147 |
| Figure 4.6 FESEM images of M-Bi ₂ S ₃ /ZnO heterostructures at (a) low magnification, (b) high magnification. TEM image of (c) ZnO nanoparticle decorated on rod shaped Bi ₂ S ₃ structures, (d) HRTEM of M-Bi ₂ S ₃ /ZnO heterostructures. | 148 |
| Scheme 4.1 Schematic illustration of ZnO nanoparticles decorated Bi ₂ S ₃ assemblies structure synthesized by simple hydrothermal method using L-Cysteine hydrochloride as structure controlling agent. | 149 |
| Scheme 4.2 Schematic illustration of ZnO nanoparticles decorated Bi ₂ S ₃ rods synthesized by simple hydrothermal method using mercaptosuccinic acid as structure controlling agent. | 150 |
| Figure 4.7 XPS spectra of as-prepared heterostructures. (a) The overall spectra of M-Bi ₂ S ₃ and M-Bi ₂ S ₃ /ZnO. (b) The Bi 4f and S 2p spectra, (c) Zn 2p spectra and (d) O 1s | 151 |

spectra of M-Bi₂S₃/ZnO. Here the scatter and solid lines indicate the experimental and fitted data.

Figure 4.8 TG curves of (a) pure L-Bi₂S₃ and L-Bi₂S₃/ZnO, (b) pure M-Bi₂S₃ and M-Bi₂S₃/ZnO. (c) N₂ adsorption-desorption isotherm of bare M-Bi₂S₃ and M-Bi₂S₃/ZnO heterostructures. 152

Figure 4.9 (a) Diffuse reflectance spectra of L-Bi₂S₃ (Pink line), L-Bi₂S₃/ZnO (Blue line), M-Bi₂S₃ (Black line) and M-Bi₂S₃/ZnO (red line) respectively. Inset: absorption spectra of ZnO nanoparticles (5 nm). (b) Photoluminescence spectra of ZnO (5 nm), L-Bi₂S₃/ZnO and M-Bi₂S₃/ZnO. (c) Photocatalytic degradation of methyl orange in presence of catalyst, bare semiconductors L-Bi₂S₃, M-Bi₂S₃ and heterostructures L-Bi₂S₃/ZnO, M-Bi₂S₃/ZnO under visible light irradiation. (d) Effect of argon, isopropanol, Cu²⁺ on the photocatalytic activity of M-Bi₂S₃/ZnO for methyl orange degradation. 154

Figure 4.10 (a) Photocatalytic hydrogen generation in presence of catalyst L-Bi₂S₃, M-Bi₂S₃, L-Bi₂S₃/ZnO, M-Bi₂S₃/ZnO for 3h under visible light from an aqueous solution containing 25 volume % methanol at pH 7. (b) Effect of pH on hydrogen evolution from aqueous solution after 1h and 3h irradiation. 156

Figure 4.11 Recycling test of (a) M-Bi₂S₃/ZnO during MO degradation and (b) L-Bi₂S₃/ZnO during hydrogen generation. (c) The XRD pattern and (d) FESEM image of L-Bi₂S₃/ZnO after and before catalytic reaction of MO degradation and H₂ generation at pH 7. 157

Figure 4.12 Photoelectrochemical current density vs potential plot of (a) M-Bi₂S₃, (b) ZnO (5 nm) and (c) M-Bi₂S₃/ZnO *via* LSV method without light (dark) and light illuminating condition at a scan rate of 20 mV sec⁻¹ using 0.1 M KOH solution as electrolyte, Pt wire as counter electrode and Ag/AgCl as reference electrode and (d) time dependence of photocurrent density at external bias 0.26V vs Ag/AgCl with illumination, at scan rate of 20 mV sec⁻¹ for bare M-Bi₂S₃ and heterojunction M-Bi₂S₃/ZnO. 158

Figure 4.13. (a) Comparative time dependent photocurrent density response of the (i) heterostructures M-Bi₂S₃/ZnO and (ii) pure M-Bi₂S₃ with illumination (switched on) and off in air at a bias of 500 mV and (b) the picosecond-resolved PL spectra of ZnO (5 nm), M-Bi₂S₃ and M-Bi₂S₃/ZnO heterostructures. 161

Scheme 4.3 Proposed diagram for the possible band edge energy for charge separation and migration in the Bi₂S₃/ZnO heterostructures. 162

Figure 5.1 X-ray powder diffraction pattern of (a) pure BiFeO₃-Ns (BFO-Ns) and Au/BiFeO₃-Ns (Au/BFO-Ns) heterostructures, (b) BFO-Ns, Bi₂S₃/BFO-Ns, CdS/BFO-Ns, ZnS/BFO-Ns and Ag/BFO-Ns heterostructures. 176

Figure 5.2 (a) FESEM image, (b, c) low and high magnification TEM images and (d) HETEM of BiFeO₃ Nanosheets (BFO -Ns). Inset d: SAED pattern of BiFeO₃ nanosheets. 177

(e, f) Low and high magnification TEM images of Au/BiFeO₃-Ns heterostructures. Inset f: HRTEM image of Au/BiFeO₃-Ns heterostructures. All the samples are prepared at NaOH concentration of 5M.

Figure 5.3 (a) Energy-dispersive X-ray spectra (EDX) of Au/BiFeO₃-Ns (Au/BFO-Ns) heterostructures. X-ray photon spectroscopy (XPS) of (b) pure BiFeO₃-Ns (BFO-Ns) and Au/BFO-Ns heterostructures, (c) Au and (d) Bi of Au/BFO-Ns heterostructures. 179

Figure 5.4 (a) X-ray photon spectroscopy of (a) Bi, (b) Fe and (c) O for pure BFO-Ns and Au/BFO-Ns heterostructures. (d) Isothermal N₂ gas adsorption–desorption curves of the pure BFO-Ns and Au/BFO-Ns heterostructures. 180

Figure 5.5 (a) Diffuse reflectance spectra of pure BiFeO₃ nanosheets (BFO-Ns) and Au/BFO-Ns heterostructures. (b) Kubelka–Munk [$(\alpha h\nu)^2$ vs photonenergy (h ν)] plot of pure semiconductor BFO-Ns and Au/BFO-Ns heterostructures. 181

Figure 5.6 (a) Photocatalytic hydrogen generation and (b) H₂ evolution rate in presence of BiFeO₃ nanosheet (BFO-Ns, black line) and Au/BFO-Ns heterostructures (red line). (c) FESEM images of cylindrical shaped BiFeO₃ (BFO -Cyl) nanostructures using 2M NaOH, (d) octahedral shaped BiFeO₃ (BFO-Oct) nanostructures using 12M NaOH. 183

Figure 5.7 (a) Comparative H₂ generation data after 2 h visible light irradiation using the catalysts of BiFeO₃ nanosheet (BFO-Ns), BiFeO₃ octahedral (BFO-Oct), cylindrical shaped BiFeO₃ (BFO-Cyl) and their heterostructures as Au/BFO-Ns, Au/BFO-Oct, Au/BFO -Cyl from an aqueous solution containing 25 volume % methanol at pH 7. (b) Diffuse reflectance spectra of BiFeO₃ nanostructures with different morphologies. Effect of (c) pH and (d) sacrificial agents on hydrogen generation using Au/BFO-Ns as photocatalyst under visible light illumination. 185

Figure 5.8 (a) Photocatalytic H₂ generation using as developed heterostructures. (b) Recycling test of Au/BFO-Ns heterostructures during photocatalytic hydrogen generation and (c) TEM image of Au/BFO-Ns heterostructures after catalytic reaction of H₂ generation at pH 7. 186

Figure 5.9 Linear sweep voltammograms (LSV) curves of BiFeO₃ nanosheet (BFO-Ns), Au NPs and Au/BFO-Ns at (a) positive potential (b) negative potential range in presence of 0.1 M Na₂SO₄–phosphate buffer solution (pH 7), under continuous light illumination of 100 mW/cm². (b) Chopped LSV of BFO-Ns after three successive runs. (d) Chronoamperometry profile of the BFO-Ns and Au/BFO-Ns thin film semiconductor electrodes measured at 0.6 V vs Ag/AgCl under chopped illumination. 187

Figure 5.10 Calculated (a) IPCE (%) and corresponding integrated current density (product of the IPCE spectrum with the AM1.5G photon flux, blue stars) and (b) APCE (%) of BiFeO₃ nanosheet (BFO-Ns) and Au/BFO-Ns photoanodes using same electrolyte within the wavelength range 300 to 700 nm. 189

Figure 5.11 (a) Photoluminescence spectra of pure BiFeO₃ nanosheet (BFO-Ns) and Au/BFO-Ns heterostructures at an excitation of 380 nm. Mott–Schottky plots of (b) pure 192

BFO-Ns and Au/BFO-Ns heterostructures and in presence of 0.1 M Na₂SO₄ electrolytes (pH 7) using an AC frequency of 1000 Hz. The intercept of the plot (at $1/C^2 = 0$) has been used to determine the E_{fb} of the BFO-Ns and Au/BFO-Ns photoelectrodes. Effect of (c) frequency and (d) various morphology of BiFeO₃ (BFO nanosheet, octahedral shaped and cylindrical shaped nanostructures) on heterostructures in Mott-Schottky plot keeping other conditions same.

Figure 5.12 (a) Nyquist plot of BiFeO₃ nanosheet (BFO-Ns) and Au/BFO-Ns using same electrolyte under dark and light illumination of 100 mW/cm² at an applied potential 0.6V vs Ag/AgCl. Inset. Equivalent circuit model to analyze the Nyquist plot. (Nyquist plot under dark and light illumination. (b) Magnetic hysteresis loop for pure BiFeO₃ (BFO-Ns) and Au/BiFeO₃ heterostructures at room temperature. Inset: magnified views of the low field region. 193

Scheme 5.1 Schematic representations of the band edges of Au/BiFeO₃ heterostructures and proposed mechanism of photocatalytic H₂ generation (a) when the incident light wavelength < 420 nm, (b) when the incident light wavelength > 420 nm, hot electron injection from the surface plasmon state of Au NPs to CB of BiFeO₃ in Au/BiFeO₃ heterostructures and (c) photoelectrochemical water splitting under visible light irradiation. 194

Scheme 6.1 Schematic depiction of synthesis of MoS₂/Bi-TiO₂ and MoS₂/Ag-AgVO₃ heterostructures by chemical mixing and co-precipitation method, respectively. 209

Figure 6.1 FESEM images of (a) bulk MoS₂ powder, (b) MoS₂ nanosheets. TEM images of (c) MoS₂ nanosheets, (d) Bi modified TiO₂ (using 2 mM Bi), (e) high resolution (HRTEM) and (f) selected area electron diffraction pattern of Bi modified TiO₂ (using 2 mM Bi). 210

Figure 6.2 (a) TEM image, (b) HRTEM image, (c) SAED pattern and (d) EDX spectrum of MoS₂/Bi-TiO₂ (MBT-10) heterostructures. 211

Figure 6.3 FESEM images of (a) Ag-AgVO₃ and (b) MoS₂/Ag-AgVO₃ heterostructures. (c) HRTEM image and (d) SEAD pattern of Ag nanoparticle. 212

Figure 6.4 (a) TEM image, (b) HRTEM image and (c) SAED pattern of Ag-AgVO₃ synthesized at room temperature. (d) Low and (e) High magnification TEM images and (f) EDX spectrum of MoS₂/Ag-AgVO₃ heterostructures. 213

Figure 6.5 (a) XRD pattern of TiO₂, Bi-doped TiO₂ (using 2mM Bi), MoS₂ and MoS₂/Bi-TiO₂ (MBT-10) heterostructures. (b) XRD of Bi-modified TiO₂ materials synthesized using 1 mM, 2 mM, 3 mM, 5 mM and 10 mM Bi-salt. 214

Figure 6.6 TG analysis of Bi-doped TiO₂ as photocatalyst with various loading concentration. The Bi doping samples are marked as (i), (ii), (iii), (iv) according to the amount of Bi-salt used during the synthesis (1 mM, 2 mM, 3 mM and 5 mM) respectively. 214

| | |
|---|-----|
| Figure 6.7 (a) XRD patterns, (b) FTIR spectra and (c) Raman spectra of the synthesized Ag-AgVO ₃ , bare MoS ₂ and MoS ₂ /Ag-AgVO ₃ heterostructures. | 216 |
| Figure 6.8 (a) The surface survey XPS spectra of the MoS ₂ /Bi-TiO ₂ (MBT-10) heterostructures and the bare MoS ₂ . Magnified XPS spectra for (b) Mo 3d, (c) Bi 4f, S 2p, (d) Ti 2p and (e) O 1s of MoS ₂ /Bi-TiO ₂ (MBT-10) heterostructures. The scattered lines represent the experimental data and solid lines for fitted data. | 218 |
| Figure 6.9 (a) The XPS spectra of the Ag-AgVO ₃ , bare MoS ₂ and MoS ₂ /Ag-AgVO ₃ heterostructures. Magnified XPS spectra of (b) Ag 3d, (c) V 2p, (d) O 1s of MoS ₂ /Ag-AgVO ₃ heterostructures. The magnified XPS spectra of (e) Ag 3d of the bare Ag-AgVO ₃ and MoS ₂ /Ag-AgVO ₃ heterostructures. | 219 |
| Figure 6.10 Magnified XPS spectra of (a) Mo 3d, (b) S 2p of MoS ₂ /Ag-AgVO ₃ heterostructures. The magnified XPS spectra of (c) Mo 3d and (d) S 2p of the bare MoS ₂ and MoS ₂ /Ag-AgVO ₃ heterostructures. | 220 |
| Figure 6.11 UV-Vis absorption spectra of (a) bare MoS ₂ , MoS ₂ /TiO ₂ and MoS ₂ /Bi-TiO ₂ (MBT-10) heterostructures and (b) Ag-AgVO ₃ , MoS ₂ /Ag-AgVO ₃ heterostructures. | 221 |
| Figure 6.12 Kubelka–Munk [$(\alpha h\nu)^2$ vs photonenergy (hν)] plot of (a) bare MoS ₂ and (b) MoS ₂ /Bi-TiO ₂ . (c) UV-Vis spectra of TiO ₂ (Inset: Kubelka–Munk of TiO ₂) and (d) Bi-doped TiO ₂ , (Inset: Kubelka–Munk of Bi-doped TiO ₂). (e) Kubelka–Munk plot of Ag-AgVO ₃ . | 222 |
| Figure 6.13 (a) Photocatalytic H ₂ generation using Bi-doped TiO ₂ as photocatalyst with various loading concentration which are synthesized using (i) 1 mM, (ii) 2 mM, (iii) 3 mM and (iv) 5 mM Bi-salt. The H ₂ data of bare TiO ₂ has been incorporated to compare the doping effect. (b) Effect of Bi-TiO ₂ loading on MoS ₂ . (c) Photocatalytic H ₂ generation in presence of MoS ₂ , MoS ₂ /TiO ₂ -10 (MT-10) and MoS ₂ /Bi-TiO ₂ heterostructures (MBT-10) after 240 mins of visible light irradiation. (d) Photocatalytic H ₂ generation rate of MBT-10 with linear fitting. | 224 |
| Figure 6.14 (a) Effect of pH for photocatalytic H ₂ generation under visible light. (b) Recycling test of MoS ₂ /Bi-TiO ₂ during H ₂ generation. (c) The XRD pattern and (d-e) FESEM image of MoS ₂ /Bi-TiO ₂ after and before catalytic reaction for H ₂ generation. | 225 |
| Figure 6.15 (a) Photocatalytic hydrogen generation in presence of Ag-AgVO ₃ (black line), bare MoS ₂ (red line) and MoS ₂ /Ag-AgVO ₃ heterostructures (blue line) after 120 mins of visible light irradiation. (b) Photocatalytic H ₂ generation of MoS ₂ /Ag-AgVO ₃ heterostructures at different volume % of methanol and (c) apparent quantum yield (AQY %) of Ag-AgVO ₃ , bare MoS ₂ and MoS ₂ /Ag-AgVO ₃ heterostructures. | 226 |
| Figure 6.16 (a) Transient photocurrent spectra of MoS ₂ , MoS ₂ /TiO ₂ and MoS ₂ /Bi-TiO ₂ heterostructure-modified ITO electrodes at a bias of 0.26 V versus Ag/AgCl reference electrode in presence of 0.1M Na ₂ SO ₄ buffer solution (suppress photogenerated holes and drive photogenerated electrons to reduce protons to H ₂). Nyquist plots of the | 228 |

electrodes (b) MoS₂, MoS₂/TiO₂ and MoS₂/Bi-TiO₂ heterostructure, (c) MoS₂/Bi-TiO₂ heterostructures with various Bi-TiO₂ loading concentration at potential 0.1 V vs Ag/AgCl under continuous light illumination. (d) Linear sweep voltammetry curves of MoS₂/Bi-TiO₂ samples at various loading of Bi-doped TiO₂.

Figure 6.17 Mott–Schottky plots of (a) bare MoS₂, (b) MoS₂/TiO₂ (MT-10), (c) Bi-doped TiO₂ and (d) MoS₂/Bi-TiO₂ (MBT-10) heterostructures. The experiment was carried out in Na₂SO₄ solution (0.1 M) under 1000 Hz AC frequency. E_{fb} of photoelectrodes have been calculated from the intercept of the plots at $1/C^2 = 0$. 229

Figure 6.18 (a) Cyclic voltammogram of prepared electrodes in presence of 0.1M Na₂SO₄-phosphate buffer solution (pH 7) as electrolyte at a scan rate of 10 mV s⁻¹. (b) Linear sweep voltammetry and (c) chronoamperometry under chopped light illumination of 100 mW cm⁻² of as prepared electrodes in presence of 0.1M Na₂SO₄-phosphate buffer solution at a scan rate of 10 mV s⁻¹. (d) Nyquist plots of Ag-AgVO₃, bare MoS₂ and MoS₂/Ag-AgVO₃ heterostructures recorded at 0.1 V vs Ag/AgCl under light illumination. 231

Figure 6.19 (a) Calculated incident photon to current conversion efficiency (IPCE %) and (b) Absorbed photon to current conversion efficiency (APCE %) of MoS₂/Ag-AgVO₃ photoanode within the wavelength range 350–700 nm. 232

Scheme 6.1 Schematic illustration of the charge transfer in MoS₂/Bi-TiO₂ p-n heterojunction. 233

Figure 6.20 (a) Photoluminescence (PL) spectra of Ag-AgVO₃ and MoS₂/Ag-AgVO₃ heterostructures upon excitation at 340 nm. (b) The picosecond-resolved TCSPC spectra of as prepared materials upon excitation at 375 nm. Mott–Schottky plots of (c) Ag-AgVO₃, bare MoS₂ and the MoS₂/Ag-AgVO₃ heterostructures in the presence of 0.1 M Na₂SO₄ electrolytes (pH 7) using an AC frequency of 1000 Hz. The intercept of the plot (at $1/C^2 = 0$) has been used to determine the flat band potential (E_{fb}) of the photoelectrodes. 235

Scheme 6.2 Proposed (a) Type II heterostructures and (b) Z-scheme mechanism of MoS₂/Ag-AgVO₃ heterostructures for photocatalytic H₂ generation under visible light irradiation. 237

Figure 7.1 XRD pattern of (a) bare semiconductors BiOI, BiOCl, BiOBr with the standard XRD patterns, (b) CuFe₂O₄ (CFO) nanoparticles with standard XRD patterns, BiOI/CFO, BiOCl/CFO and BiOBr/CFO heterostructures. 253

Figure 7.2 (a) Surface survey XPS spectra of BiOCl/CFO heterostructures. High resolution XPS spectra of (b) Bi 4f, (c) Cl 2p, (d) O 1s, (e) Cu 2p and (f) Fe 2p of BiOCl/CFO heterostructures. 254

Figure 7.3 (a) Surface survey XPS spectra of BiOBr/CFO heterostructures. High resolution XPS spectra of (b) Bi 4f, (c) Br 3d, (d) O 1s, (e) Cu 2p and (f) Fe 2p. 255

| | |
|--|-----|
| Figure 7.4 (a) Surface survey XPS spectra of BiOI/CFO heterostructures. High resolution XPS spectra of (b) Bi 4f, (c) I 3d, (d) Fe 2p, (e) Cu 2p and (f) O 1s. | 256 |
| Figure 7.5 Core level Bi 4f XPS spectra of (a) BiOCl and BiOCl/CFO (b) BiOBr and BiOBr/CFO and (c) BiOI and BiOI/CFO heterostructures. | 257 |
| Figure 7.6 TG curves of (a) BiOI, CuFe ₂ O ₄ (CFO), BiOI/CFO, (c) BiOCl, CFO, BiOCl/CFO and (c) BiOBr, CFO, BiOBr/CFO under Argon atmosphere. | 257 |
| Figure 7.7 (a) Raman spectra and (b) FTIR spectra of bare semiconductors BiOCl, CFO and BiOCl/CFO heterostructures. | 258 |
| Figure 7.8 TEM image of (a) BiOI/CFO, (b) BiOCl/CFO and (c) BiOBr/CFO. HRTEM images of (d) BiOI/CFO, (e) BiOCl/CFO and (f) BiOBr/CFO heterostructures. Insets: corresponding SAED pattern. FESEM images of bare semiconductors (g) BiOI, (h) BiOCl and (i) BiOBr. | 259 |
| Figure 7.9 TEM image of CuFe ₂ O ₄ (CFO) nanoparticles. | 260 |
| Figure 7.10 TEM-EDX (a) BiOCl, (b) BiOBr (c) BiOI and (d) BiOCl/CFO heterostructures. | 260 |
| Figure 7.11 Mott-Schottky plots of pure semiconductors (a) BiOI, (b) BiOCl, (c) BiOBr and (d) CuFe ₂ O ₄ . | 262 |
| Figure 7.12 Mott-Schottky plots of (a) BiOI, (b) BiOCl and (c) BiOBr at three different frequencies. | 262 |
| Scheme 7.1 Band alignments of (a) BiOI/CFO, (b) BiOBr/CFO and (c) BiOCl/CFO heterostructures. | 264 |
| Figure 7.13 Mott-Schottky plots of (a) BiOI/CFO, (b) BiOCl/CFO and (c) BiOBr/CFO heterostructures. | 264 |
| Figure 7.14 Space charge layer width vs applied potential plots of bare semiconductors (a) BiOI, (b) BiOCl, (c) BiOBr, and (d) BiOI/CFO, (e) BiOCl/CFO and (f) BiOBr/CFO heterostructures. | 266 |
| Figure 7.15 Impedance spectra of (a) bare BiOI, BiOCl, BiOBr, Inset: bare CuFe ₂ O ₄ (CFO), (b) BiOI/CFO, BiOCl/CFO, BiOBr/CFO heterostructures. The equivalent circuit parameters are shown in the inset of (a) and (b). Linear sweep voltammetry (LSV) curves of (c) bare semiconductors BiOI, BiOCl, BiOBr, CFO and (d) BiOI/CFO, BiOCl/CFO, BiOBr/CFO heterostructures under continuous light illumination (35W Xenon lamp) in 0.1 M Na ₂ SO ₄ electrolyte. | 267 |
| Figure 7.16 Fitted Nyquist plots of (a) BiOI, (b) BiOCl, (c) BiOBr, (d) BiOI/CFO, (e) BiOCl/CFO, (f) BiOBr/CFO and (g) bare CuFe ₂ O ₄ (CFO) under light illumination. | 268 |

| | |
|--|-----|
| Figure 7.17 Linear sweep voltammetry curves of (a) BiOCl/CFO, (b) BiOI/CFO and (c) BiOBr/CFO heterostructures under dark and continuous light illumination (35W Xenon lamp) in 0.1 M Na ₂ SO ₄ electrolyte. | 269 |
| Figure 7.18 Transient photocurrent spectra of (a) bare semiconductors CuFe ₂ O ₄ (CFO), BiOI, BiOCl, BiOBr and (b) the BiOI/CFO, BiOCl/CFO, BiOBr/CFO heterostructures under chopped light condition, measured by chronoamperometry at a fixed potential of 0.6V vs Ag/AgCl. | 269 |
| Figure 7.19 Chopped chronoamperometry spectra and calculated PEC H ₂ spectra of BiOCl/CFO Z-scheme heterostructures. | 270 |
| Figure 7.20 Incident Photon to Current Conversion Efficiency (IPCE %) spectra of BiOCl/CFO heterostructures using 0.1 M Na ₂ SO ₄ electrolyte within the wavelength range 400–750 nm. | 271 |
| Figure 7.21 Diffuse reflectance spectra of BiOCl, BiOCl/CFO, and bare CuFe ₂ O ₄ (CFO). Inset: Kubelka–Munk [$(\alpha hv)^2$ vs photon energy (hv)] plots of CFO, BiOCl and BiOCl/CFO. | 272 |
| Figure 7.22 UV-Vis absorption spectra of BiOI, BiOBr, BiOI/CFO and BiOBr/CFO heterostructures. | 272 |
| Figure 7.23 Kubelka–Munk [$(\alpha hv)^2$ vs photon energy (hv)] plots of (a) BiOI, (b) BiOBr, (c) BiOI/CFO, (d) BiOBr/CFO. | 273 |
| Figure 7.24 Photocatalytic hydrogen generation in the presence of (a) bare BiOX (X= Cl, Br, I) and CFO, (b) BiOX/CFO (X= Cl, Br, I) heterostructures for 2 h under visible light from an aqueous solution containing 25 volume % methanol as sacrificial agent at pH 7, (c) Recycling test of BiOCl/CFO heterostructures for H ₂ generation, (d) FESEM image of BiOCl/CFO after the catalytic reaction of H ₂ generation under visible light. | 274 |
| Figure 7.25 Linearly fitted H ₂ generation of (a) bare BiOX and CuFe ₂ O ₄ (CFO), (b) BiOX/CFO heterostructures. | 275 |
| Figure 7.26 Apparent quantum yield (AQY %) of the as developed bare semiconductors and heterostructures. | 276 |
| Figure 7.27 Effect of (a) different sacrificial hole scavengers and (b) sacrificial donor/solvent ratio in photocatalytic H ₂ generation for BiOCl/CFO heterostructures. | 277 |
| Scheme 7.2 Schematic illustration of the charge transfer process and the photocatalytic H ₂ generation of the novel Z-scheme BiOCl/CFO heterostructures under visible light irradiation. | 279 |

List of Tables

| | |
|---|-----|
| Table 1.1 The bandgap, advantages and the limitations of commonly used Bi-based photocatalysts. | 35 |
| Table 2.1 Bi-based conventional and Z-scheme heterostructures, their synthesis methods and the photocatalytic applications. | 58 |
| Table 4.1 Comparative study of current density measured from photoelectrochemical studies performed in 0.1 M KOH solution as electrolyte, Pt wire as counter electrode and saturated Ag/AgCl as reference electrode within the voltage range -0.4V to 0.8V under dark and light condition. | 159 |
| Table 4.2 Dynamics of picosecond-resolved luminescence transients and decay parameters of ZnO (5 nm) and $\text{Bi}_2\text{S}_3/\text{ZnO}$. | 161 |
| Table 5.1 Permittivity and oxidation potential of the sacrificial agents. | 184 |
| Table 5.2 Electrochemical parameters calculated from Mott-Schottky plot for BiFeO_3 -Ns and Au/ BiFeO_3 -Ns catalysts. | 190 |
| Table 5.3 Electrochemical parameters calculated from Mott-Schottky plot of the Au/BFO heterostructures for three different morphologies of BiFeO_3 . | 191 |
| Table 5.4 The Randles equivalent circuit fitting parameters of Nyquist plots for BiFeO_3 and Au/ BiFeO_3 heterostructures. | 193 |
| Table 5.5 Comparative study of photocatalytic performance of BiFeO_3 based heterostructures for photocatalytic H_2 generation. | 195 |
| Table 6.1 Bi loading (wt %) calculated from the TGA and ICP-AES. | 215 |
| Table 6.2 Decay parameters of Ag-AgVO ₃ , MoS ₂ and MoS ₂ /Ag-AgVO ₃ heterostructures. | 234 |
| Table 6.3 Electrochemical parameters calculated from Mott-Schottky plots for prepared electrodes. | 236 |
| Table 7.1 Calculated flat band potentials (E_{fb}), position of the VB and CB potentials and bandgaps the as synthesized materials. | 263 |
| Table 7.2 Calculated charge carrier concentrations from the Mott-Schottky measurements. | 265 |
| Table 7.3 Fitting parameters of linearly fitted photocatalytic H_2 generation. | 267 |
| Table 7.4 Fitting parameters of Nyquist plots. | 275 |
| Table 7.5 Permittivity and oxidation potential of the sacrificial agents. | 277 |
| Table 7.6 Comparison table of photocatalytic applications of CuFe_2O_4 (CFO) and BiOX based materials. | 279 |

List of Abbreviation

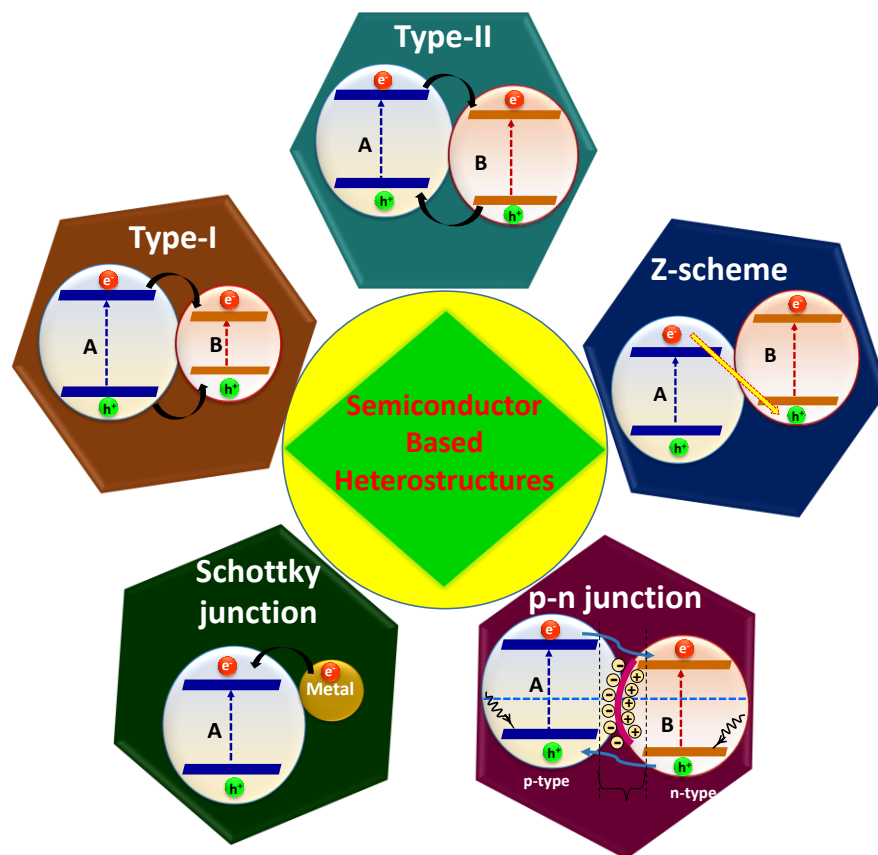
| | | | |
|-----------------|-----------------------------|-------------------|---|
| H ₂ | Hydrogen | STH | Solar-to-hydrogen conversion efficiency |
| O ₂ | Oxygen | AQE | Apparent quantum efficiency |
| N ₂ | Nitrogen | APCE | Absorbed photon-to-current efficiency |
| CO ₂ | Carbon Di-oxide | IPCE | Incident photon-to-current efficiency |
| e ⁻ | Electrons | A _λ | Absorbance |
| h ⁺ | Holes | α(λ) | Absorption co-efficient |
| λ | Wavelength | SPR | Surface plasmon resonance |
| E _g | Bandgap | hν | Photon energy |
| VB | Valence band | eV ₀ | Contact potential |
| CB | Conduction band | φ _B | Schottky barrier |
| E _f | Fermi level | φ _M | Work function energy of the metal |
| UV | Ultraviolet | φ _{Semi} | Work function energy of semiconductor |
| Vis | Visible | RHE | Reversible Hydrogen Electrode |
| NIR | Near infrared | NHE | Normal Hydrogen Electrode |
| IR | Infrared | MOF | Metal–organic framework |
| K | Boltzmann constant | COF | Covalent Organic Framework |
| T | Temperature in kelvin | RhB | Rhodamine B |
| E | Applied field | QDs | Quantum dots |
| V _e | Drift velocity for electron | MO | Methyl orange |
| V _h | Drift velocity for hole | MB | Methylene Blue |
| μ _e | Mobility of electron | XRD | X-Ray Diffraction |

| | | | |
|------------------------|---------------------------------------|-----------|---|
| μ_h | Mobility of hole | XPS | X-ray photoelectron spectroscopy |
| As | Arsenic | E_k | Kinetic energy |
| In | Indium | E_B | Binding energy |
| Ge | Germanium | VBO | Valence band offset |
| 1D | One dimension | CBO | Conduction band offset |
| 2D | Two dimension | IP | Ionization potential |
| 3D | Three dimension | SEC | Secondary electron cutoff |
| 0D | Quantum dot | EA | Electron affinity |
| J | Current density | FTIR | Fourier Transform Infrared Spectroscopy |
| $J_{\text{diffusion}}$ | Current density by diffusion | TG | Thermogravimetry |
| J_{drift} | Current density by drift | DTA | Differential Thermal Analysis |
| D | Diffusion coefficient | FESEM | Field Emission Scanning Electron Microscope |
| Δn | Electron gradient | TEM | Transmission electron microscopy |
| Δp | Hole gradient | EDX | Energy Dispersive X-ray Spectroscopy |
| m^* | Effective mass | AAS | Atomic Absorption Spectroscopy |
| τ_c | Collision time of electrons and holes | PL | Photoluminescence spectroscopy |
| ΔG_0 | Gibbs free energy change | TCSPC | Time-correlated single photon counting |
| $O_2^{\bullet-}$ | Superoxide radicals | GPD | Geiger Photo Diodes |
| OH^{\bullet} | Hydroxyl radicals | TAC | Time-to-analog converter |
| HER | H ₂ evolution reaction | $E_{f,n}$ | Quasi-fermi levels correspond to electrons |
| H^+ | Protons | $E_{f,p}$ | Quasi-fermi levels correspond to holes |
| δ | Diffusion layer | V_{ph} | Open-circuit-photovoltage |
| ω | Frequency | CV | Cyclic Voltammetry |

| | | | |
|----------|------------------------------------|--------------|---|
| ρ | Charge density | LSV | Linear Sweep Voltammetry |
| FTO | Fluorine-doped Tin Oxide | CA | Chronoamperometry |
| MSA | Mercaptosuccinic acid | EIS | Electrochemical Impedance Spectroscopy |
| SAED | Selected area electron diffraction | VSM | Vibrating Sample Magnetometer |
| O_L | Lattice oxygen | GC | Gas Chromatography |
| PEC | Photoelectrochemical | TCD | Thermal conductivity detector |
| W_{sc} | Space charge layer width | DRS | Diffuse reflectance spectroscopy |
| L_D | Debye length | CBM | Conduction band minima |
| R_s | Ohmic resistance | VBM | Valence band maxima |
| R_{ct} | Charge transfer resistance | ϵ | Dielectric constant of the semiconductors |
| F | Faraday constant | ϵ_0 | Permittivity of free space |

CHAPTER 1

General Introduction



1.1 Background

Environmental remediation and generation of renewable energy source would be highly desirable and become a major challenge for the 21st century. In 2012 the world's energy consumption was 5.79×10^{20} J, which increased by more than 50% until 2030 due to the world population growth [1]. The future energy demand is predicted to reach 8.60×10^{20} J in 2040, which causes the higher rate of fossil fuels consumption, as it accounts for more than 80% of this energy. As a result, the emission of green-house gas and other environmental pollutions will also increase over the next several decades. Therefore, development of green and renewable energy source, alternative to fossil fuels is strongly required to address the energy shortage in near future. A number of approaches have been pursued to tackle these global challenges. Among which, hydrogen and electricity generation using sunlight and water, could be an effective approach because the solar energy reaching on the Earth's surface is 1.3×10^5 TW, larger than the human energy consumption by more than three orders of magnitude [2-5]. Owing to its potential environmental and economic benefits, solar energy conversion can be a fruitful approach to compensate recent increasing global energy demand. Large-scale energy harvesting can possible only through huge collection of solar spectrums. In this regard, water splitting in presence of solar energy and photocatalyst, analogous to natural photosynthesis occurred in green plants, is a promising method for solar fuel H₂ generation. There has been a global interest to make hydrogen as alternative fuel owing to the wide variety of sources, no emission of carbon, high energy content (120–142 MJ kg⁻¹) which is about three times higher than that of gasoline [6]. Therefore, research is going on over the last few years on production of H₂ in a sustainable manner so that it could be the first step towards a hydrogen economy [7, 8]. The Conventional methods of hydrogen production are steam-methane reforming, electrolysis, radiolysis, photobiological water splitting, photoelectrochemical water splitting and photocatalytic water splitting [9]. H₂ is generally labeled as green, gray, and blue based on the production source [10]. The most common H₂ production method, steam reforming of natural gas is termed as gray H₂. Hydrogen is labelled as blue when the steam reforming is captured and stored through industrial carbon capture and storage method. When H₂ is generated from renewable sources like solar, water, wind, biomass, waste i.e. climate-natural manner, known as green H₂. Among the green H₂ sources, solar to H₂ generation method has the potential to meet the global energy demand in a sustainable pathway [11]. For example, H₂ can be used as fuel in transportation sector, fertilizer sector to produce intermediate energy sources, such as ammonia, methanol,

natural gas, formaldehyde. Being a tropical country, India has the opportunity to harness abundant solar energy and notably the solar capacity rose from 6.8 GW to 34.6 GW during 2016-2020. On 15th August 2021, the Prime Minister of India launched the ‘**National Hydrogen Mission**’ to transform India into a global hub for green hydrogen production. Therefore, a target of 75% fossil fuel replacement with green H₂ to produce H₂ has been set by 2050 [12-15].

Since the discovery of electrochemical water oxidation by Honda and Fujishima on a TiO₂ single-crystal photoanode in 1972, photocatalytic and photoelectrochemical (PEC) water splitting have been studied widely using semiconductor based materials as catalyst [16]. Although, TiO₂ has been serve as the benchmark photocatalysts, but catalytic performance is limited due to the wide bandgap which allow to absorb only UV light and low-efficiency in charge separation [17]. The light response of a photocatalyst mainly depends on the bandgap. The threshold wavelength and bandgap of a semiconductor is inversely proportional to each other ($\lambda = 1240/E_g$), clearly reveals that wide bandgap photocatalyst (> 3.0 eV) can absorb UV light ($\lambda < 413$ nm) only. On the other hand, narrow bandgap photocatalysts (< 3.0 eV) have the potential towards partial absorption of visible light (415 nm to 700 nm). As shown in Figure 1.1, proportions of the UV, visible and IR light in solar spectrum are 4%, 43% and 53%, respectively [18]. Therefore, development of visible and IR light active low bandgap semiconductors is the special interest.

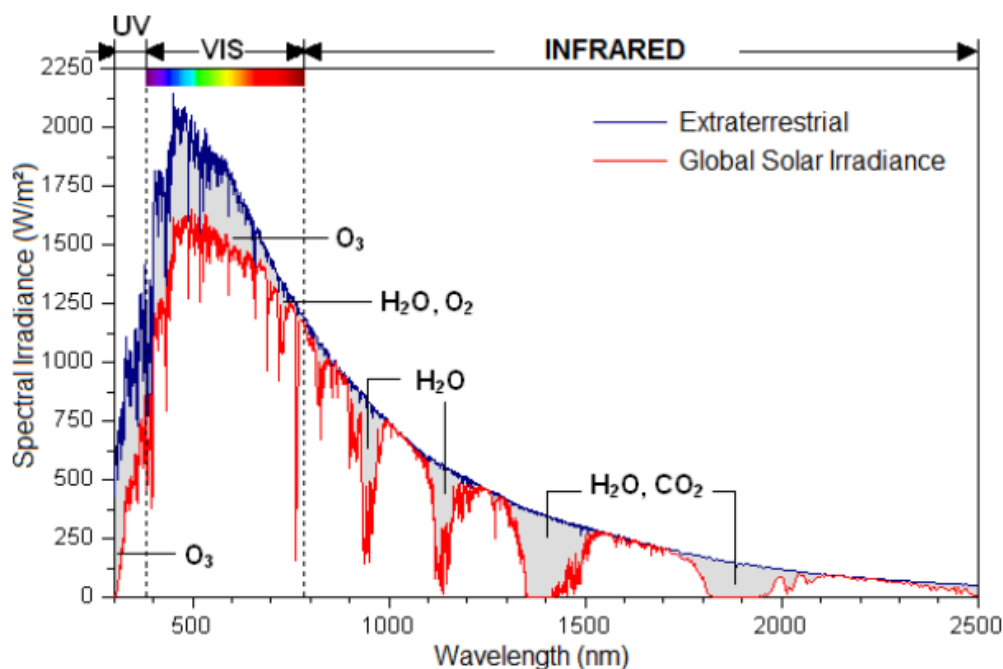


Figure 1.1 Standard solar light spectra as a function of wavelength on the earth’s surface [19].

1.2 Semiconductor

When atoms brought together, electrons interact with each other and energy levels split. In case of molecules, having large numbers of atoms, the energy levels become very closely and termed as energy bands [20]. Now for a material, a series of energy bands will be created which are separated by a certain distance. These energy bands and their accompanying difference, defined as band structure. Depending on the band structure, materials can be classified as conductor, semiconductor and insulator. Conductors have high electrical conductivity in the order of $10^7 \Omega\text{m}^{-1}$ whereas insulators have no electrical conductivity. The conductivity of semiconductors lie between insulators and conductors and their conductivities are generally between 10^3 to $10^5 \Omega\text{m}^{-1}$. According to the electronic band structure, lower energy position called valence band (VB), which is occupied by valence electrons and higher energy position as conduction band (CB), empty at ground state. The energy difference between VB and CB is termed as bandgap (E_g) (Figure 1.2). As the VB and CB are overlapped with each other, thus the Fermi level (E_f) will lie at middle, overlapping region of two bands and for insulators and semiconductors it lies between VB and CB [21]. Semiconductors are mainly two types; one is intrinsic and another is extrinsic. Intrinsic semiconductors are those having an energy gap in the order of 1 eV. In case of intrinsic semiconductor, room temperature thermal energy (KT) is sufficient to excite the VB electrons to the CB. However, when electric field is applied the electrons drift towards the +ve electrode and holes to the -ve electrode, constitute a current. Thus, the drift velocity under the applied field E is,

$$V_e = \mu_e E \quad (1.1)$$

$$V_h = \mu_h E \quad (1.2)$$

Where, μ_e and μ_h are the mobility of electrons and holes. The intrinsic charge density of n_i^2 , which is in the order of $\sim 10^{19} \text{m}^{-3}$.

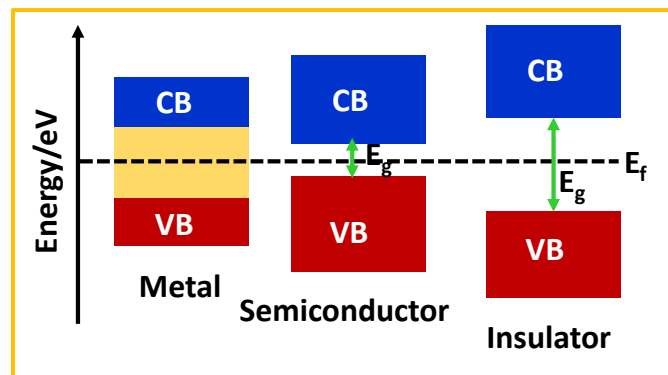


Figure 1.2 Schematic presentation of band structures for metal, semiconductor and insulator.

Extrinsic semiconductor is generated by doping of some impurities and its property depends on the type of the impurity induced. The impurity which supplies free electrons without simultaneously creating holes are termed as donors and those trap electrons add holes in the VB without adding conduction electrons are termed as acceptor. For example, when pentavalent arsenic (As) and trivalent indium (In) are doped in germanium (Ge), n-type and p-type conductivity would be created due to the extra electrons and holes within the system (Figure 1.3a and 1.3b). The position of the fermi level (E_f) generally controls by the conductive nature of the semiconductors (p-type or n-type). In case of n-type semiconductor, E_f lies near the CB and for p-type it prefers to lie close to VB (Figure 1.3c). When VB electrons get excited by thermal, light or other energy greater than the bandgap, then they jump into the CB by creating a positive charge, named as hole at the VB. The conductivity of semiconductors occurs because of excited electrons and holes movement. When a semiconductor is irradiated with photons with energy equal or greater than the bandgap of the semiconductor, photogenerated electrons and photoinduced holes will be created and separated at the VB and CB (Figure 1.4).

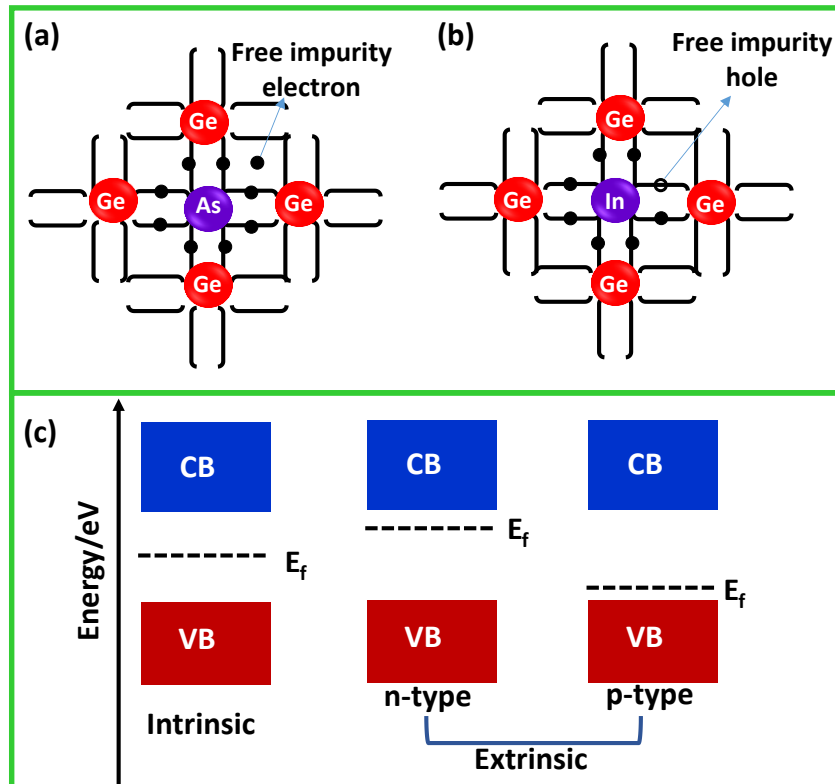


Figure 1.3 (a) Schematic presentation of fermi level position for n-type and p-type semiconductors. (b) Electron and hole generation and separation within a semiconductor.

Some of the excited electrons will try to come back to the VB to get kinetically and thermodynamically stable by dissipate the input energy in heat or light form [22, 23]. Some electrons will migrate to the semiconductor's surface without recombination and they further involve in catalytic reactions with the adsorbed species. Semiconductors are extensively used in environmental and energy applications, for example air purification, organic pollutant degradation, heavy and toxic metal decomposition, renewable fuel generation (H_2 and O_2), CO_2 reduction and valuable product generation, N_2 fixation etc. [24]. The efficiency of the semiconductor photocatalyst determines by the redox ability of photogenerated charge carriers.

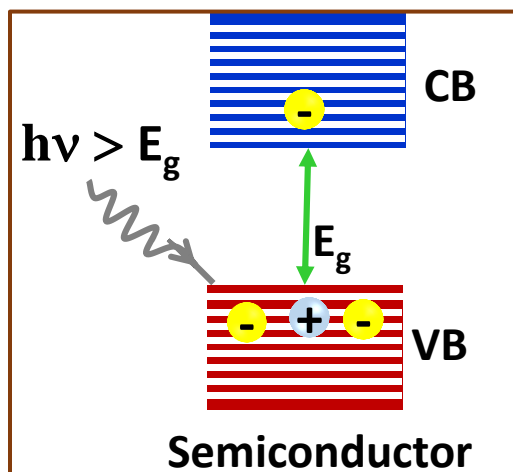


Figure 1.4 Electron and hole generation and separation within a semiconductor.

1.3 Nanomaterials

Nanomaterials possess size in the range of 1 to 100 nm have emerged as exciting and high demanding material for a range of practical applications. The history of utilization of nanomaterial is ancient, and human beings used nanomaterials a long time ago for various kinds of applications unknowingly. The ancient Egyptians used PbS nanoparticles in hair-dyeing formula about 4000 years ago [25]. About 4500 years ago, asbestos nanofibers were used to reinforce ceramic mixtures [26]. The Romans used Lycurgus Cup from 4th century A.D. which changes the colour depending on the incident light due to presence of Ag and Au nanoparticles [27]. However, Richard Feynman [28] first introduced nanomaterials as “There’s Plenty of Room at the Bottom” and the specific concept of nanotechnology in 1959. Norio Taniguchi first gives the definition of nanotechnology in 1974 as “nano-technology mainly consists of the processing of, separation, consolidation, and deformation of materials by one atom or one molecule.” [29]. Before 1980s, nanotechnology was

a discussion but now it becomes a developing area of research and almost covers all area of research field, including material chemistry, bio-medicine, optoelectronics, sensors, energy and environmental protection, water purification, aerospace and many more because of superior physicochemical properties which are completely different from their bulk counterparts [24, 30, 31] The unique properties of the nanomaterials mainly depend on size confinement, atomic and micro structure, compositions, defects, electronic states and interfaces, which can be tailored through synthesis. Therefore, synthesis of nanomaterials plays crucial role for the cutting-edge applications [24, 32]. Most of the solid materials possess ionic, covalent or metallic bond with periodic order. The exact arrangement of atoms in a particular lattice mainly determines both the chemical and physical properties of a bulk crystalline material. If a crystal broke into two, then the exposed surface area will be enhanced. At the same time, the ratio of strained surface bonds to the bulk bonds will be slightly increased. If the breaking of crystal will be continued then after a certain time the surface bonds will dominate over the bulk bonds. Theoretical calculations and experimental result confirmed that the cross-over of surface to bulk ratio occurs when dimensions of a material go down than 100 nanometers and this is called ‘nano-size’ effect [33]. The strained bonds of surface atoms are mainly responsible for determining new properties of nano-sized material [34]. For example, the ability to share or exchange electrons largely improved for a nanomaterial compared to their bulk counterparts, thereby boosts the chemical reactivity. In addition, the quantum mechanical states of the electrons will be changed due to nano-scale effect. From Bohr’s postulate it is well known that electrons in an atom can absorb or loose discrete quanta of energies to move from its one energy state to the next allowed energy state [35]. Now, the availability of allowed states for an excited electron in per unit volume is called the ‘density of states’ [35]. For bulk material, plenty of available states create a continuum energy level, called conduction band (CB) and the corresponding ground states form valence band (VB). Therefore, the density of states is continuous and smooth for bulk crystals, however it become discreet and far apart for nanomaterials because of a smaller number of atoms, thereby lack of available energy states. Such nanocrystals with size less than exciton Bohr radius are called as quantum confined systems [36-38]. The excited electron of a quantum confined system is physically constrained by the dimension of the nanocrystal and can only be confined in one dimension (1D), two dimensions (2D) or three dimensions (3D). Therefore, size and the direction of confinement have significant role in controlling the density of energy states and bandgap. Depending on the density of states

and degrees of confinement, quantum confined nanocrystals have been marked as 0D, 1D and 2D nanomaterials (Figure 1.5). In case of 0D nanomaterials, confinement of excited electrons may be possible in all three dimensions with well separated discrete energy states [24]. For 1D nanomaterials, the excited electrons are confined only in two directions and generally experience no confinement along c-axis, i.e. length of the material. The density of states for 1D nanomaterials are quasi-discrete with respect to increase of excitation energy. The density of states is quasi-continuous for the 2D nanomaterials. In case of larger nanocrystals (size > 100 nm) surface to volume ratio is very important which strongly affects the surface properties [39, 40]. For a given mass, 0D nanomaterials possess maximum exposed surface area, followed by 1D, and 2D.

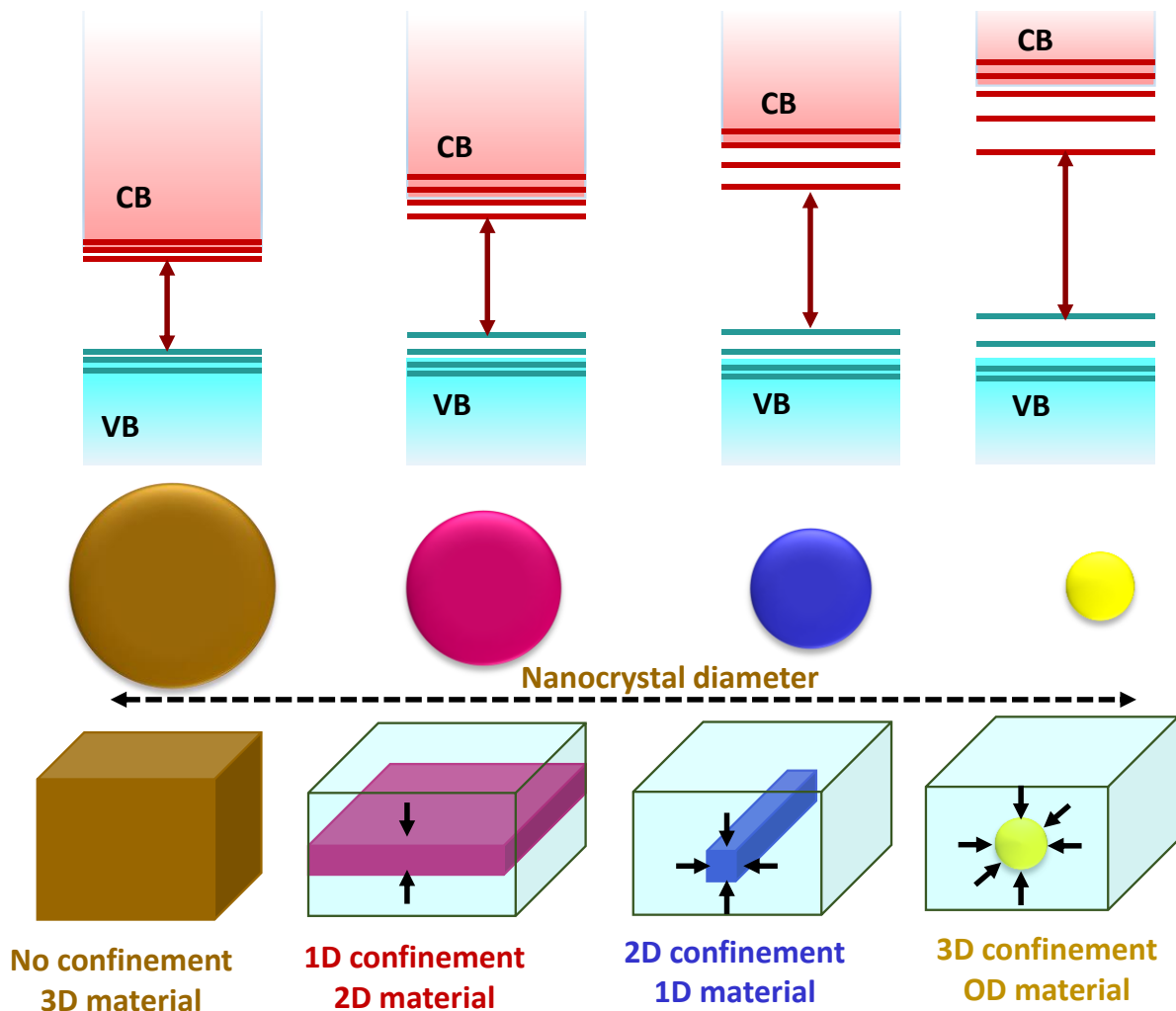


Figure 1.5 Schematic presentation of the energy level and the confined direction for 0D, 1D, 2D and 3D confined nanomaterials.

1.4 Photocatalysis

Photocatalysis is a chemical reaction that involves absorption of light by one or more reacting species and results excited electron-hole pairs, which further helps in free radical generation to undergo the secondary reactions without being consumed photocatalyst itself [4]. The sufficient light energy can activate the photocatalyst and stimulate chemical reactions on the surface, for example water reduction and oxidation, hydrogen and oxygen generation, organic compound degradation etc. The overall photocatalysis process can be classified into five basic steps [41, 42]. The steps are as follows and schematically shown in the Figure 1.6.

- Photon absorption by the catalyst
- Generation and separation of excited electrons (e^-) and holes (h^+)
- Photo-generated charge carrier diffusion from the bulk to the catalyst surface
- Photo-generated charge carrier transport
- Catalytic reaction (oxidation/reduction) with the absorbed species

When photons (with higher or equal energy than the work function energy of semiconducting material) interact with VB electrons, an exciton will be created and jumped to the CB. This picosecond process is followed by relaxation of excitons to the ground state, called recombination. The probability of electron-hole separation predominantly controlled by the electronic structure of semiconductor, mainly local displacement of atoms [43]. When the excitons (electron-hole pair) overcome the exciton binding energy, they can move independently within the semiconductor by the influence of their effective masses, termed as polaron. Carrier diffusion and transport occur simultaneously however they are independent to each other and strongly related to the physical properties of catalyst. The charge carrier separation and transfer are two most important events in photocatalysis, which primarily depend on the electronic structure of photocatalyst and free charge carrier concentration. After polaron generation, they must travel to the surface from the bulk to undergo the redox reactions [44]. Such phenomena of free charge carrier flow within the excited semiconductor can be described as current flow. Further the excited carrier must transport to the redox sites *via* two driving forces, one is for electron (n) movement and another for hole (p) movement. The electron movement is happened through diffusion, directed by charge carrier concentration gradient and hole movement by drift, guided by potential gradient at interfaces [45]. Total current density can be written as,

$$J = J_{\text{diffusion}} + J_{\text{drift}} \quad (1.3)$$

$$\text{The current density for the free electrons, } J_e = eD_e\Delta n + ne\mu_e E \quad (1.4)$$

$$\text{The current density for the free holes, } J_h = -eD_h\Delta p + pe\mu_h E \quad (1.5)$$

Here, e is electronic charge, μ is mobility of charge carrier, D is diffusion coefficient, Δn and Δp are electron and hole gradients, E is induced electric field, n and p denote electron and hole concentration. Now, the diffusion part is strongly associated with D and μ by the relation of,

$$D = \frac{k_B T}{e} \mu \quad (1.6)$$

$$\mu = e \frac{\tau_c}{m^*} \quad (1.7)$$

Where, k_B is Boltzmann constant, m^* is effective mass and τ_c is collision time of the electrons and holes. On the other hand, a drift current will be generated when the free charge carriers experience potential gradients. Such gradients mainly generated at semiconductor-electrolyte, semiconductor-semiconductor or metal-semiconductor interfaces [44]. After being transferred to the catalyst surface, electrons and holes involve in redox reaction according to their reduction/oxidation potential. The photo absorption depends on the size, absorption co-efficient, optical penetration depth, refractive index, scattering of light (UV>VIS>NIR), bandgap (direct/indirect) and band edge position of the catalyst material [46, 47]. The work function energy and the dielectric constant of the material have crucial role in excited electron-hole (exciton) generation and separation. Next, the carrier diffusion is related to the effective mass, charge carrier lifetime, mobility and the diffusion length. Finally, the carrier transport depends on the surface state of the catalyst, i.e. space charge layer, depletion width etc.

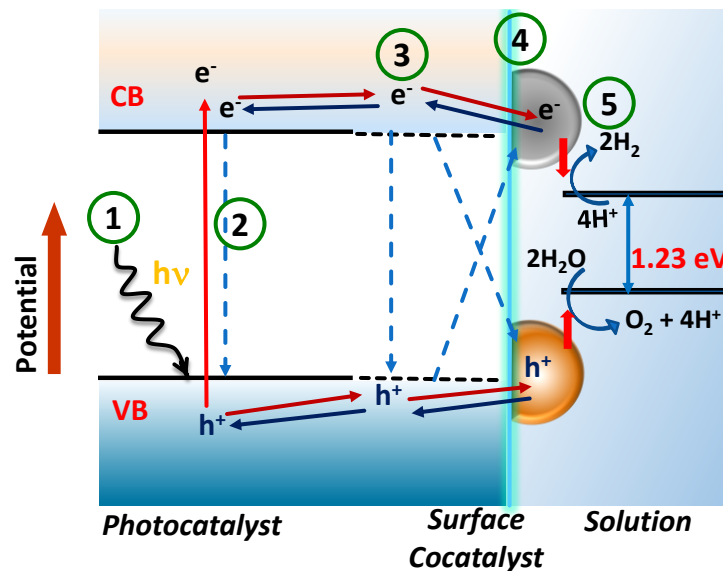
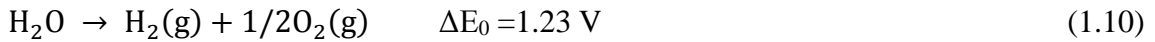
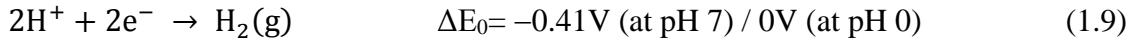
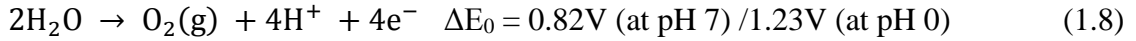


Figure 1.6 Schematic diagrams of the basic steps of photocatalysis.

Overall water splitting is a process that enables to generate H₂ and O₂ simultaneously by the decomposition of water molecules in presence of external energy, which may be in the form of electrical (current), thermal (heat) and light (photon or electromagnetic radiation). Two half reactions, proton reduction and water oxidation in a single material is called overall water splitting, which are shown in Eq. 1.8 and 1.9. Based on the thermodynamics, water-splitting is an endothermic and energetically uphill reaction with Gibbs free energy change (ΔG_0) of 237 kJ/mol [16].



Essentially, water oxidation by the photoinduced holes is the first step which involves four electrons transfer and reaction, generated protons and O₂. Further, the protons are consumed by the photogenerated electrons to generate H₂ (Figure 1.7) [48, 49].

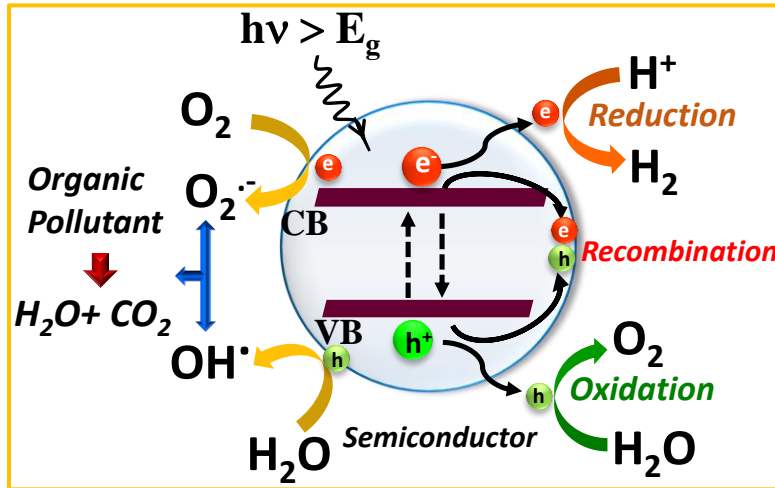
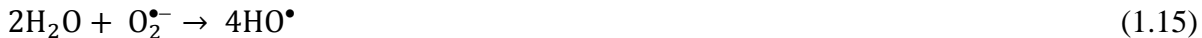


Figure 1.7 Electron and hole generation and separation within a semiconductor during overall water splitting and organic pollutant degradation under light irradiation.

In case of photocatalytic decomposition, photogenerated charge carriers participate in several oxidation and reduction reactions with the adsorbed species at the surface of the catalyst (Figure 1.7) [50]. The reaction steps are as follows:





The photogenerated electrons react with the surface absorbed oxygen to balance the charge neutrality at the catalyst surface. Therefore, excess oxygen has been employed during experiment which may serve as electron scavenger to enhance the oxidation of organic pollutants under light illumination. When excited electron interacts with surface absorbed O_2 , various free radicals may be generated, among which superoxide radicals ($\text{O}_2^{\bullet-}$) are the main oxidizing product having very short lifetime (E^0 , $\text{O}_2/\text{O}_2^{\bullet-} = -0.33 \text{ V}_{\text{NHE}}$) [51]. These $\text{O}_2^{\bullet-}$ further react with water molecule, leads to production of hydroperoxyl (HO_2^{\bullet}) and hydroxyl radicals (OH^{\bullet} , E^0 of $\text{OH}^{\bullet}/\text{HO}^- = +2.80 \text{ V}_{\text{NHE}}$) which finally react with dye molecules very rapidly degrade it [52]. Owing to strong oxidation power of photoinduced holes, oxidation can take place *via* reaction with the surface-bound hydroxyl radical ($\bullet\text{OH}$). These $\bullet\text{OH}$ radicals contain enormous potential to react with the pollutants and break their bonding. The holes can also diffuse to the surface and they may directly oxidize the pollutant molecules or drive oxygen-evolution half-reaction at pH 7 [53].

1.5 Photocatalytic H_2 Generation

The photocatalytic production of hydrogen represents a fascinating way to convert and store solar energy as chemical energy, in the form of renewable hydrogen. Photocatalytic process involves three important steps i.e. light absorption, excited electron hole generation and separation and catalytic redox reactions. In presence of light, photo-generated charge carriers are generated upon light irradiation by absorbing photons and their behavior, transfer, migration, lifetime have been focused further. The photogenerated electrons at the VB of photocatalyst further promoted to the CB by leaving holes, thereby charge separation happened within the semiconductor. Furthermore, the charge carriers should have sufficient transfer efficiency to undergo the catalytic redox reactions. The electron survival is also an important parameter as most of the photogenerated charge carriers, i.e. electrons and holes undergo recombination after being transferred to the surface by emitting thermal and optical radiations. The recombination may be occurred directly or at the surface and bulk, resulted a smaller number of charge carriers for catalytic reactions (Figure

1.8). This electron-hole recombination may be suppressed by spatial separation of electrons and holes, which is still bottleneck of the photocatalytic technology [54-56]. Therefore, sufficient charge separation is necessary. The last step is the utilization of photogenerated electrons and holes. After transfer of holes at the surface, they are consumed by scavengers used during photocatalysis. Alcohols, such as ethanol, methanol, glycerol, ethylene glycol, acids like lactic acid, ascorbic acid, disodium ethylenediamine tetra acetic acid, acetic acid and other reducing agents including glucose, triethanolamine are generally used as scavenger. The remaining electrons at the surface drive the H₂ evolution reaction (HER) to reduce H⁺ to H₂. Thermodynamically the potential of the electrons should be sufficiently negative than the water reduction potential (0V, H⁺/H₂). In addition, some parameters including number of active sites, adsorption efficiency of water molecule at the catalyst surface, H₂ evolution pathway, and transport impedance at the catalyst-water interface are very important to determine the H₂ generation efficiency [57-60]. Therefore from the viewpoint of thermodynamics, semiconductors having more negative CB potential with respect to water reduction potential are acceptable for photocatalytic H₂ evolution. The minimum bandgap of a H₂ generation photocatalyst should be 1.23 eV. However, practically bandgap of a single semiconductor photocatalyst material should lie in the range of 1.5 eV to 2.5 eV because of the extra energy to overcome the overpotentials.

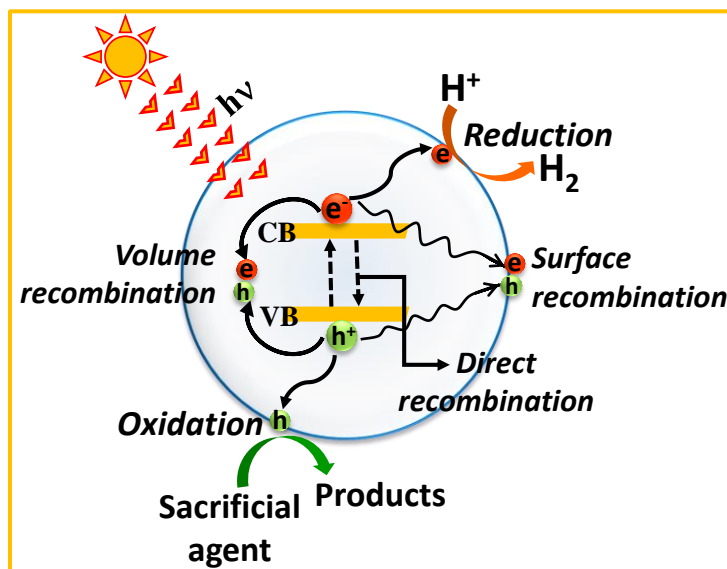


Figure 1.8 Types of electron-hole recombination in a photocatalyst.

The overpotential can be defined as difference between the Fermi level of catalyst and electrolyte in photocatalytic system. On the other hand, it can be defined as an additional voltage required to

drive the oxidation or reduction reactions which is associated to the thermodynamic potential [61]. Therefore, low overpotential photocatalysts is suitable for efficient water splitting. In this regard, nickel-iron oxides, perovskites, and spinel ferrites have reported as low overpotential electrocatalysts for O_2 evolution reaction [62, 63]. In case of photocatalytic H_2 generation, powder semiconductors are dispersed within the solution, containing water and hole scavenger and irradiated by visible light (Figure 1.9). To minimize the overpotential in photocatalytic H_2 generation, solution pH may be changed. Low pH i.e acidic medium is suitable for H_2 evolution whereas high pH (alkaline) is advantageous for O_2 evolution.

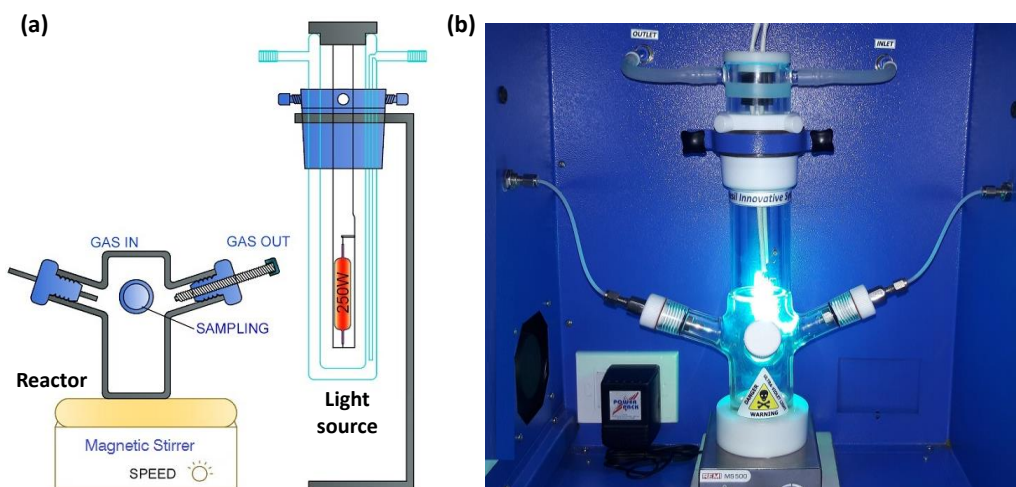


Figure 1.9 (a) Schematic presentation and (b) image of photocatalytic H_2 generation reactor.

1.6 Photoelectrochemical (PEC) Water Splitting

Photoelectrochemical water splitting has been considered as one of the most attractive approaches which can also convert solar energy into H_2 and O_2 efficiently. There are also three important steps for overall PEC water splitting which have been shown in Figure 1.10. First one is the light absorption and generation of photogenerated electrons and holes which are further spatially separated by the influence of external electric field, applied at the semiconductor and electrolyte junction. In second step, the photoinduced holes with sufficient positive potential will drift to the surface of semiconductor and involve in water oxidation to generate O_2 . On the other hand, the majority carrier electrons will be conducted *via* external potential toward the counter electrode. These excited electrons further reduce the protons (H^+) and generate H_2 . The Gibbs free energy required for this reaction is +237 kJ/mol, which corresponds to the energy difference of 1.23 V. However, there are some losses of energy during charge carrier transfer processes at the electrode-

electrolyte interface due to back reactions [64]. Thus, overpotential is required to drive the H₂ and O₂ evolution reactions. The electron-hole transfer to electrolyte from the surface of electrode must be selective for redox reactions than that of corrosion on semiconductor's surface.

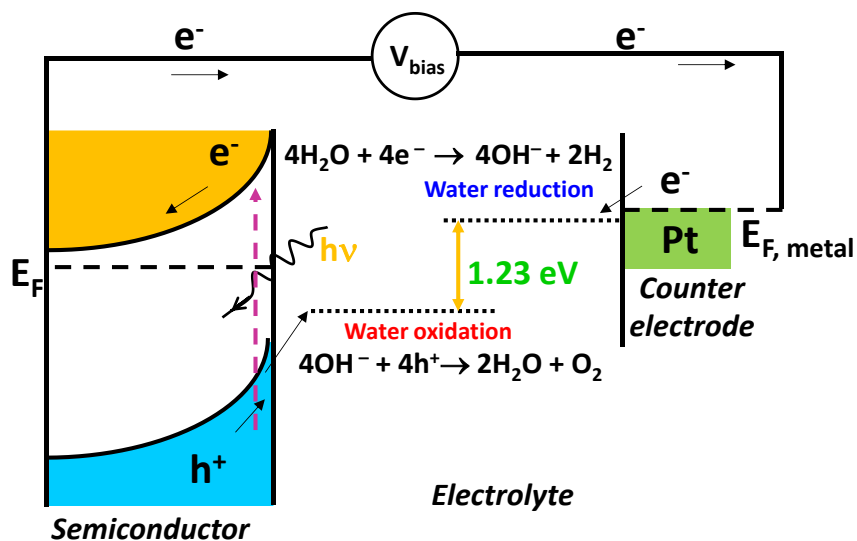


Figure 1.10 Energy diagrams of PEC water oxidation and reduction on an n-type semiconductor photoanode and Pt counter electrode (one-step excitation).

Now, to design an efficient photoanode/photocathode, position of the band edges and nature of the band bending should be studied in details. Figure 1.11 demonstrates the interfacial energy diagrams of an n-type semiconductor-electrolyte interface before equilibrium, after equilibrium and under light illumination. When an n-type semiconductor has been immersed within an electrolyte, the position of the Fermi level (E_f) for semiconductor must be located at a higher potential compared to the redox potential of electrolyte. The difference between E_f of semiconductor and electrolyte is called the barrier height (Figure 1.11a). It is well known that electrons will try to move higher potential to the lower potential to achieve equilibrium. Thus, electron transfer takes place from semiconductor to electrolyte to line up the E_f . Now, the electron transfer from semiconductor to electrolyte results positive charge at the semiconductor surface and negative charge at the electrolyte surface, leads to formation of space charge layer or depletion layer (Figure 1.11b). The space charge layer formation further results upward band bending as the majority charge carrier electrons are removed from this region [65]. The band bending resulted a built in electric field which further oppose the electron flow from semiconductor to electrolyte. The electric field in turns boosts the electron-hole separation through the electrode-electrolyte interface [66]. When the system is irradiated by light, excited electrons and holes would be created,

leads to increase of E_f with an electron quasi-Fermi level and hole quasi-Fermi level. An internal photovoltage or open circuit voltage V_{oc} will be formed by the free energy difference between majority carrier electrons and the photoexcited minority carriers, which further determines the PEC reactions (Figure 1.11c). In case of photoelectrochemical water splitting, external bias is required so that the V_{oc} exceeds 1.23V, otherwise the photoanode/photocathode remains inactive even the semiconductor has appropriate band-edge positions for water splitting. Therefore, the kinetics of excited charge carrier transfer through electrode-electrolyte interface is important to achieve efficient PEC performances of a photoanode/photocathode. At the same time, the charge carrier concentration at the electrode surface is also an important parameter which greatly influences the catalytic activity.

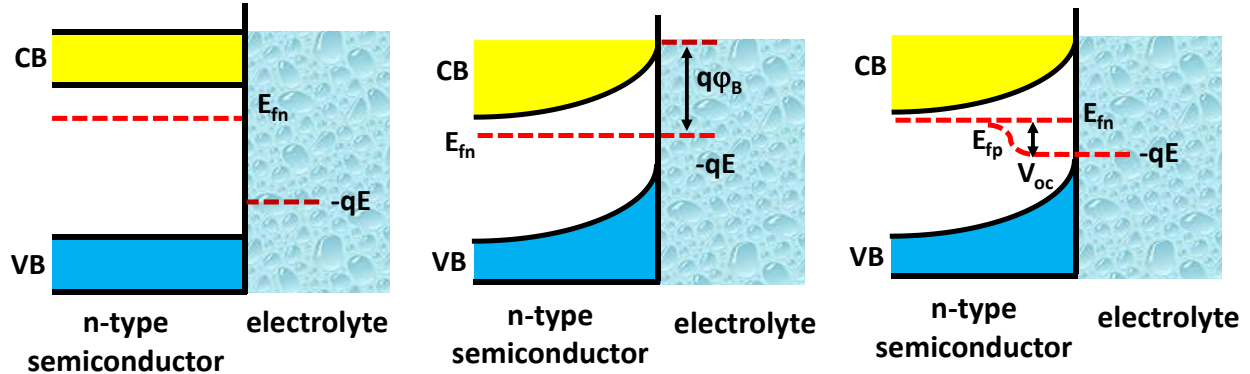


Figure 1.11 Schematic energy band diagram of a n-type semiconductor-electrolyte interfaces (a) before equilibration, (b) after equilibration (without light) and (c) in quasi-static equilibrium under steady state light illumination.

1.7 Photocatalytic Efficiency Measurement

The efficiency for photochemical and PEC water splitting can be defined as follows:

- Solar-to-hydrogen conversion efficiency (STH)
- Apparent quantum efficiency (AQE)
- Absorbed photon-to-current efficiency (APCE)
- Incident photon-to-current efficiency (IPCE)

As the solar energy conversion is main step in photocatalysis, solar-to hydrogen (STH) conversion efficiency may provide theoretical maximum efficiency. It is defined as:

$$STH = \frac{\text{Output Energy}}{\text{Energy of Incident solar light}} \quad (1.20)$$

$$STH = \frac{R_{H_2} (\text{mmol/s}) \times \Delta G (237000 \text{ J/mol})}{P_{\text{sun}} (\text{mW/cm}^2) \times A_{\text{geometric area of reactor}} (\text{cm}^2)} \quad (1.21)$$

Here, P_{Sun} is energy flux of sunlight, ΔG is change of Gibbs free energy per mole of H_2 , R_{H_2} is rate of H_2 generation. The solar energy spectrum, i.e. $P_{\text{Sun}} = 1003 \text{ W/m}^2$ has almost 93 W/m^2 energy in UV region ($\lambda < 400 \text{ nm}$), $\sim 543 \text{ W/m}^2$ energy in the visible range ($400 \text{ nm} < \lambda < 800 \text{ nm}$) and $\sim 367 \text{ W/m}^2$ energy in IR region ($\lambda > 800 \text{ nm}$) [64]. The STH efficiency for PEC water splitting can alternatively express as:

$$\text{STH} = \frac{J_{\text{sc}}(\text{mA/cm}^2) \times 1.23 \text{ (V)} \times \eta_{\text{F}}}{P_{\text{total}}(\text{mW/cm}^2)} \quad (1.22)$$

According to STH efficiency for PEC water splitting, the excess energy of photons, i.e. the energy greater than 1.23 eV, must be dissipated as heat energy. For UV photons more than half photonic energy would be dissipated as heat, thus the theoretical maximum STH efficiency for UV light is 3.3% using standard AM 1.5G spectrum [66]. Whereas, the visible ($< 600 \text{ nm}$) and near IR ($< 800 \text{ nm}$) photons result 17.8% and 35% maximum theoretical STH efficiency, respectively [67]. Therefore, visible and IR responsive photocatalyst development is important to achieve maximum STH efficiency (Figure 1.12). Now, the benchmark for STH efficiency is set to 10% for hydrogen market, which corresponds to H_2 generation rate of $\sim 154 \mu\text{mol/cm}^2/\text{h}$ and photocurrent density of $\sim 8.3 \text{ mA/cm}^2$. To achieve such amount of H_2 , photon consumption rate would be $\sim 260 \text{ photon/nm}^2/\text{s}$ on a flat surface which requires semiconductor having strong light absorption capability within the wavelengths range 600–700 nm, i.e. bandgap $\sim 1.8 \text{ eV}$ to 2.0 eV . At the same time suitable band edge potentials also essential to drive the water splitting reactions.

The apparent quantum yield (AQY) of photocatalytic H_2 generation is defined as:

$$\text{AQY}\% = \frac{2 \times \text{moles of } \text{H}_2 \text{ produced}}{\text{no. of incident photons}} \times 100 \quad (1.23)$$

Here no external bias has been applied and the photon generation fully depends on the power of light illumination. The Incident Photon-to-Current conversion Efficiency (IPCE) is also important for PEC devices and it gives insight into the cathode/anode properties. It is defined as follows:

$$\text{IPCE} (\%) = \frac{I_{\text{ph}}}{P_{\text{in}}} \times \frac{1240}{\lambda} \times 100 \quad (1.24)$$

Generally, IPCE has been measured from chronoamperometry measurement, which describes the photocurrent collected per incident photon flux as a function of illumination wavelength. Therefore, it gives an estimation of maximum possible efficiency of H_2 generation, assuming all electrons used for the H_2 generation and holes for O_2 generation.

Furthermore, to understand the inherent light absorption efficiency and catalytic efficiency, measurement of absorbed photon to current conversion efficiency (APCE) is important. It describes the photocurrent collected per incident photon absorbed per unit area.

$$\text{APCE (\%)} = \frac{\text{IPCE}}{(1 - 10^{-A_\lambda})} \times 100 \quad (1.25)$$

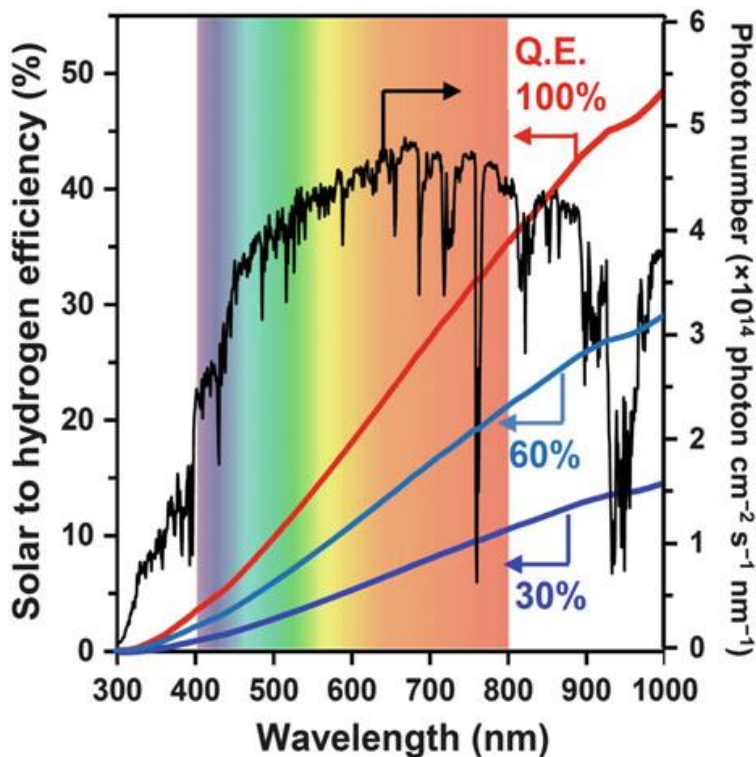


Figure 1.12 The number of photons for AM 1.5G and theoretical solar-to-hydrogen efficiency as a function of wavelength. [46]

In this regard, analysis of band structure of the semiconductors is key thermodynamic requirement to understand the catalytic efficiency. The incident photon absorption by the catalyst and exciton generation are mainly determine by bandgap of the semiconductor and absorption co-efficient $[\alpha(\lambda)]$, which can be defined as how far a particular wavelength photon can penetrate before it's absorption within the semiconductor. The bandgap and the corresponding band edge potentials of commonly used semiconductor photocatalysts have been shown in Figure 1.13. The materials with highly negative CB are more efficient for H_2 evolution reaction and the materials having VB potential more than 1.23V can effectively oxidize the water molecule and generate O_2 .

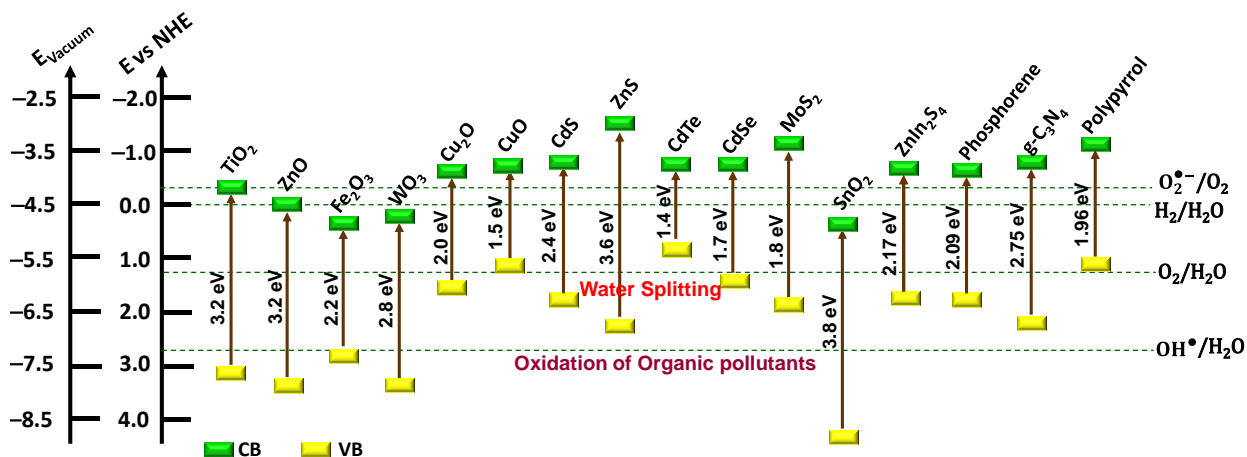


Figure 1.13 Band-edge positions and the bandgaps of some typical semiconductor photocatalysts. Dotted lines indicates the relative energy levels of redox reactions for organic pollutant degradation and water splitting.

Single semiconductors could not meet all the synergetic requirement for water splitting under visible light either due to insufficient bandgap energy or band edge potentials. Significant efforts have been made to design and develop efficient visible light active photocatalysts through doping, surface modification, photosensitization, crystal faces design, defect engineering, bandgap engineering etc. [68]. Bandgap engineering has recently attracted enormous attention as an efficient approach to tune the electronic band structure as well as charge carrier separation and transfer which in turn influences the catalytic activity for water splitting. In general, substitution with less electronegative anions add donor states to the top of the valence band (Figure 1.14a) and more electronegative cations add acceptor states below the conduction band (Figure 1.14b) [69]. The net result is a decrease in the bandgap. For example, Asahi et al. [70] narrowed the bandgap of TiO₂ to 2.5 eV from 3.2 eV by introducing donor level on the top of VB through N-doping and enhances the absorption up to 500 nm. Furthermore, it has been reported that metal-ion doping results enhancement in exposed catalytic sites, thus improves photocatalytic activity towards H₂ and O₂ generation [71]. On the other hand, an intermediate band or mid-gap states can be generated when sufficiently high dopant content would be used (Figure 1.14c). For example, Yang et al. [72] observed that Sn doping in CuGaS₂ and CuInS₂ introduces a partially filled intermediate band state. The Sn-doped CuInS₂ exhibited a photocurrent density of 3.52 mA/cm² at 0V vs Ag/AgCl with improved PEC activity than that of undoped CuInS₂ (2.83 mA/cm²) because of bandgap reduction and enhance light absorption, achieved *via* intermediate state generation.

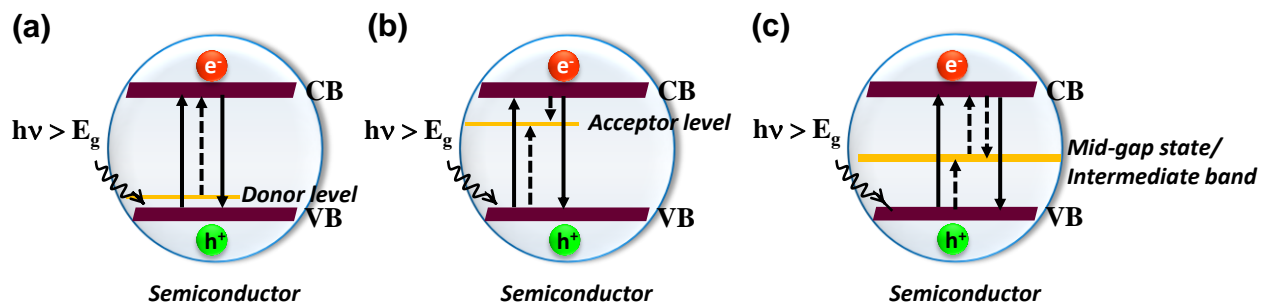


Figure 1.14 Schematic diagram of (a) donor level, (b) acceptor level and (c) intermediate energy level generation due to doping of anions or cations.

1.8 Co-catalyst

Co-catalyst is a material that may be attached at the catalyst's surface and help in improve the catalytic reaction kinetics. As the electron-hole recombination is the bottleneck issue which lower the number of active species during photocatalysis, addition of co-catalyst attracted intense research interest. In this regard, the platinum-group elements, such as Pd, Pt, Os, Ru, Rh, Ir, Ag, Au are very promising co-catalyst for H₂ and O₂ evolution (Figure 1.15). Notably, noble metal Au and Ag attracted intense attention due to additional effect of surface plasmon resonance (SPR), which may be defined as the collective oscillations of conduction band electrons under visible light which results upshifted energy levels and enhances the H₂ generation rate [73]. The transition metals, such as Cu, Cr, Ni, Fe, Mn, Co) and their oxides were reported as efficient earth-abundant co-catalysts for photocatalytic H₂ production [74]. Due to low Fermi levels than the commonly used semiconductor photocatalysts, Pt and Pd have recognized as best co-catalyst for H₂ generation as they can trap photogenerated electrons from the adjacent semiconductor. On the other hand, RuO₂ and IrO₂ have reported as two best co-catalysts for O₂-evolution as they have strong hole capturing properties. However, all these efficient co-catalysts composed of precious metal elements which prohibit the wide-scale energy production. Therefore, research interest directed to develop low cost, non-toxic, highly efficient earth-abundant co-catalysts for water splitting. Recent study on co-catalyst demonstrated that metal oxides [75] and hydroxides [76] have potential for both H₂ and O₂ evolution. In spite of these, metal carbides [77], sulphides [78], phosphides [79, 80] and alloys [81] are promising for H₂ generation, whereas, metal phosphates [82], borates [83] are found to be good for O₂ evolution. For example, metal sulfide MoS₂ has been widely used as H₂-evolution co-catalyst because of active S atoms on the exposed edges of MoS₂ which can be easily reduced by excited electrons to generate H₂ [84]. Recently, Shao et al. [85] reported carbonized MoS₂ as

efficient H₂ evolution co-catalyst on CdS photocatalyst, which displayed ~112 times higher H₂ generation rate (34 mmol h⁻¹g⁻¹) compared to bare CdS along with excellent AQE of 41.4% under visible light. The carbonized MoS₂ able to provide suitable Gibbs free energy, exposed catalytic active sites and electron-hole separation for redox reactions. Due to the metallic nature, 1T-MoS₂ quantum dots is also a good co-catalysts which may facilitate the conductivity and boost the density of active sites for photocatalytic H₂ and O₂ generation [86]. The use of Co-Pi as co-catalyst for water oxidation first demonstrated by Kanan et al. [87]. Further it has been widely used for PEC water splitting as it leads to cathodic shift in onset potential and high capability for charge carrier separation [88]. Recently, Gao et al. [89] developed Co-Pi modified polymer/BiVO₄ heterostructures which showed ~7 times greater photocurrent density (2.47 mA/cm² at 1.23 V vs RHE) than bare BiVO₄ along with IPCE value of 27% (400 nm). Thus, existence of co-catalysts not only boosts the electron-hole pair separation but also provides extra electronic state for proton reductions, accelerating redox reactions with the advantage of prolonged lifetime of electrons and holes. At this point, density-functional theory calculations and combinatorial approaches may provide potential opportunities to understand the electron-hole migration pathway through photocatalysts and co-catalysts interfaces.

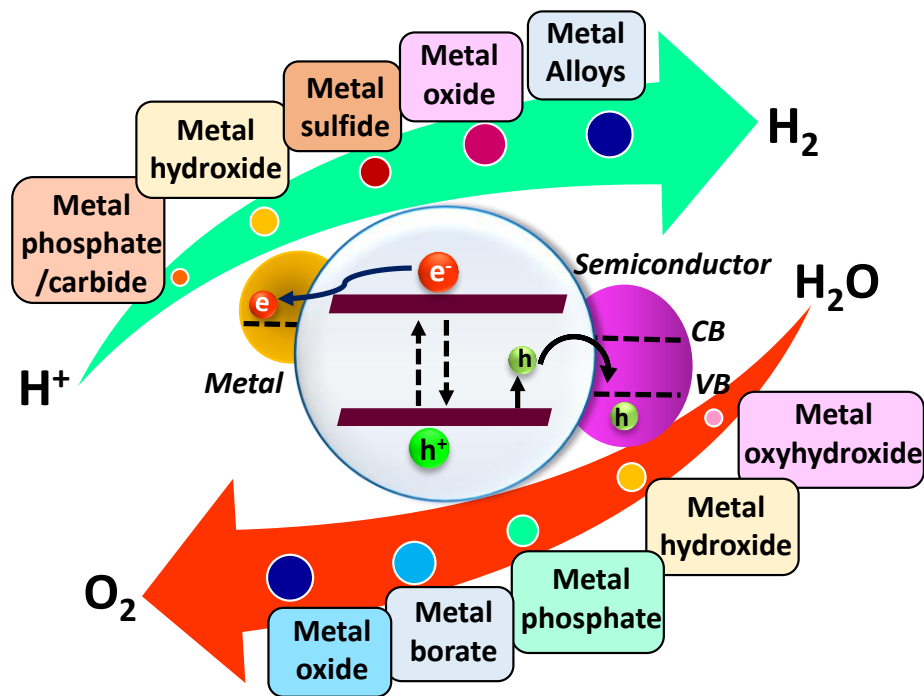


Figure 1.15 Schematic diagram of photogenerated electron-hole migration mechanism of co-catalyst modified semiconductor and the widely used co-catalysts for H₂ and O₂ generation through water splitting.

1.9 Heterostructures

Heterostructures, an integrated structure composed of two or more semiconductors, in which the free charge carriers are migrated from one material to the other depending on their position of the fermi level and thereby prolong the lifetime of electron-hole pairs. Development of heterostructures facilitate effective charge separation and hinder the fast recombination rate which is very crucial to design an efficient photocatalyst [90, 91]. More importantly, heterostructure offers more number of catalytic active sites and availability of the excited charge carriers for the redox reactions. Some important parameters, such as position of the fermi level, diffusion length, carrier mobility etc. strongly related to the overall catalytic activity of a heterostructures photocatalyst. The advantages of heterostructures formation are as follows:

- Charge carrier recombination rate may be suppressed as the electrons and holes can vectorially transfer to the neighboring semiconductor, therefore the life time of the carriers would be enhanced.
- The presence of multiple active sites within the heterostructures may be advantageous to provide large active surface area for the redox reactions.
- Heterostructures can promote spatial charge separation at the interface which may effectively enhance photocatalytic activity of the material.

Based upon the nature of the charge transfer through the junction interface, there are five types of heterostructures:

- i) Type-I heterostructures
- ii) Type-II heterostructures
- iii) Type-III heterostructures/Z-scheme heterostructures
- iv) p-n heterojunction
- v) Schottky junction

(i) Type-I Heterostructures

Type-I heterostructures formed when two semiconductors, leveled as A and B with specific band alignments came contact. The CB of 'A' semiconductor should be located at more negative potential compared to the CB of 'B' semiconductor. At the same time, the VB potential of 'A' semiconductor should be more positive than the VB of 'B' semiconductor. Under this circumstances, when light illuminated, photogenerated electrons and holes will be created on the

both semiconductors, and the CB electrons of ‘A’ tried to transfer to the CB of ‘B’ because of lower energy. Simultaneously, the photoinduced holes at ‘A’ semiconductor will transfer to the ‘B’ due to low VB potential than that of ‘A’ semiconductor. Therefore electrons and holes would be accumulated at the CB and VB of ‘B’ semiconductor, respectively, which may further resulted fast electron–hole recombination (Figure 1.16).

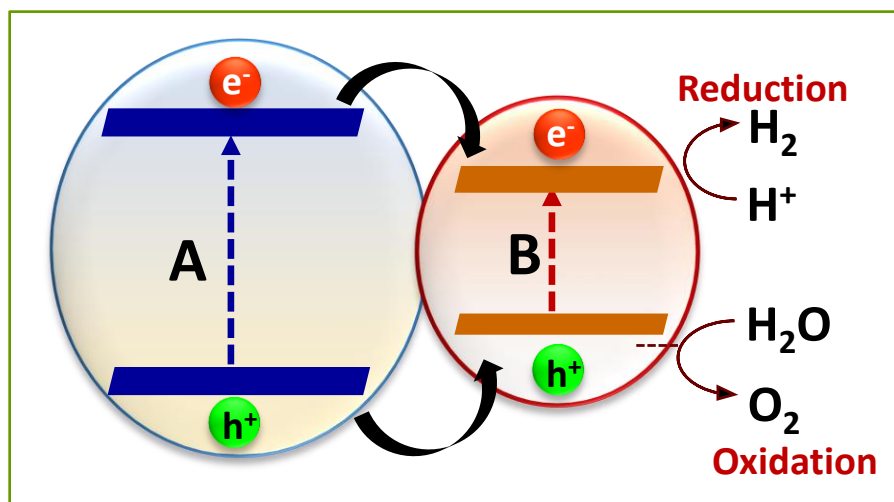


Figure 1.16 Schematic energy band diagram and the photogenerated electron-hole separation on Type-I heterostructures.

(ii) Type-II Heterostructures

In case of Type-II heterojunction, the CB potential of ‘A’ semiconductor should be located at more negative potential compared to the B semiconductor. In addition, the VB potential of ‘A’ must be less positive than the VB of ‘B’ semiconductor. Therefore, under light illumination, photogenerated electrons of ‘A’ tried to migrate to the CB of ‘B’, while the photoinduced holes of ‘B’ semiconductor transfer to the VB of ‘A’, as excited charge carriers always move to the lower potential for getting the stable state. Thus, electrons and holes are separated in two different semiconductors, resulted low recombination rate. From this energy band configuration and the charge transfer pathway, it can be concluded that Type-II heterostructures is more efficient for spatial separation. However, the redox ability of this system is not satisfactory because some energy loss may happen during the charge transfer and redox reactions occur at the lower potentials (Figure 1.17).

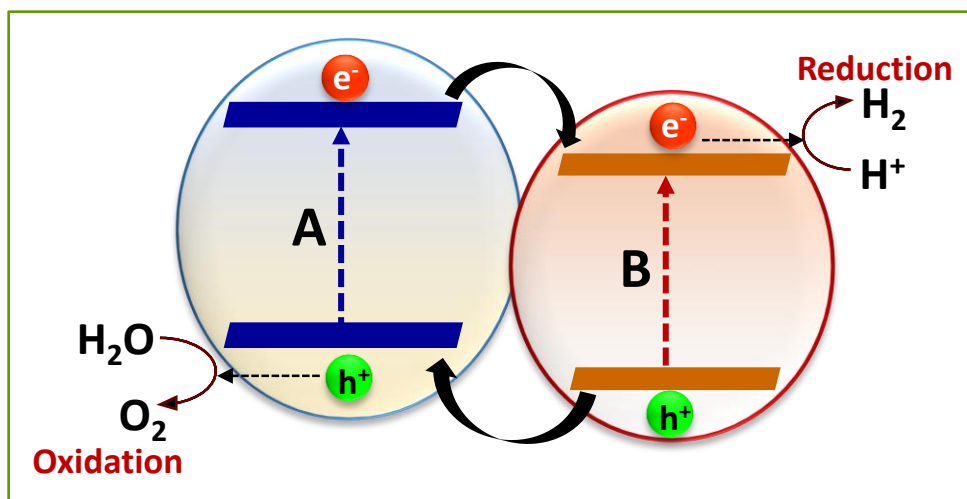


Figure 1.17 Schematic energy band diagram and the photogenerated electron-hole separation on Type-II heterostructures.

(iii) Type-III or Z-scheme Heterostructures

To overcome the aforesaid issue, Bard et al. [92] proposed an idea of developing Z-scheme photocatalytic system, where photogenerated CB electrons of ‘A’ semiconductor may directly recombine with the photoinduced VB holes of ‘B’ semiconductor. An ionic or solid conductor or Ohmic contact may be happened for this direct electron-hole recombination (Figure 1.18). As a result, excited electrons of ‘B’ semiconductor, having more negative potential and holes of ‘A’ semiconductor with more positive potential become free for catalytic reduction and oxidation reactions, respectively.

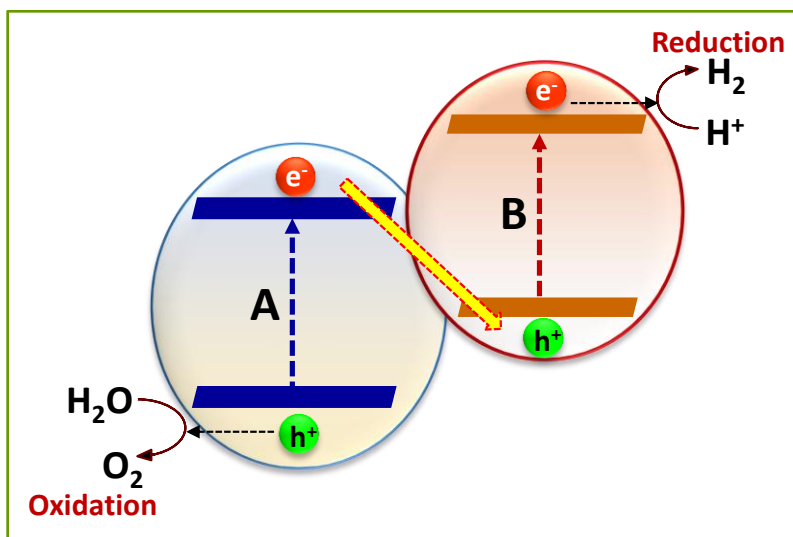


Figure 1.18 Schematic energy band diagram and the photogenerated electron-hole separation on Type-III or Z-scheme heterostructures.

Therefore, both the requirements of spatial charge separation as well as sufficient potentials for photocatalytic reactions may be achieved by developing this Z-scheme heterostructures. Depending on the conductor used between two semiconductors, Z-scheme photocatalytic systems are of three types, solid-state Z-scheme system, ionic liquid Z-scheme system and direct Z-scheme system. Recently, development of direct Z-scheme has been attracted research focus as it is mediator free and the backward reaction rate also low.

(iv) p-n Heterojunction

The p-n heterojunction is similar to Type-II heterojunction, where ideal separation of the photogenerated electrons and holes with high migration rate can be achieved by development of internal field gradient. Basically, the selective combination of one n-type and one p-type semiconductors can effectively form p-n heterojunction. Figure 1.19 shows the schematic energy diagram and charge separation of a p-n junction photocatalytic system. Before light illumination, as the fermi level of n-type semiconductor lies higher potential than the fermi level of p-type semiconductor, thus electrons of n-type semiconductor would be tried to diffuse into p-type semiconductor near the junction, resulted accumulation of positive charges near the junction. Similarly, holes of p-type semiconductor would be tended to diffuse into n-type semiconductor and resulted gathering of negatively charged electrons near the surface. Until the Fermi level lines up, i.e. achieve equilibrium, the charge carrier diffusion would be continued. Therefore, a space charge region at the both sides of the junction interface (positively charges at n-side and negatively charged at p-side) would be created, which further resulted an internal electric field. This electric field further oppose further charge diffusion so that the equilibrium condition would be continued. Now, under light illumination when energy of light ($h\nu$) is equal or greater than bandgap energy of the constituent semiconductors, then excited charge carriers, i.e. electrons and holes would be created. The excited electrons tried to transfer from the CB of p-type semiconductor to CB of the n-type semiconductor to get lower energy. At the same time, photoinduced holes will migrate from the n-type semiconductor to the VB of p-type semiconductor directed by internal electric field. Thus, a special separation of photogenerated charge carriers may possible by the p-n junction which further reduce the fast electron-hole recombination. Notably, the CB of p-type semiconductor should be more negative than the n-type semiconductor and VB should lie at lower potential than n-type semiconductor to make the charge separation thermodynamically feasible.

Due to the presence of internal electric, the charge separation and transfer efficiency of a p–n junction photocatalysts is faster compared to conventional type-II heterojunction. For example, Chen et al. [93] prepared a series of TiO₂ based p–n heterojunction and Type-II heterostructures for organic pollutant degradation and demonstrated that p–n heterojunction is more effective than Type-II heterostructures towards charge separation.

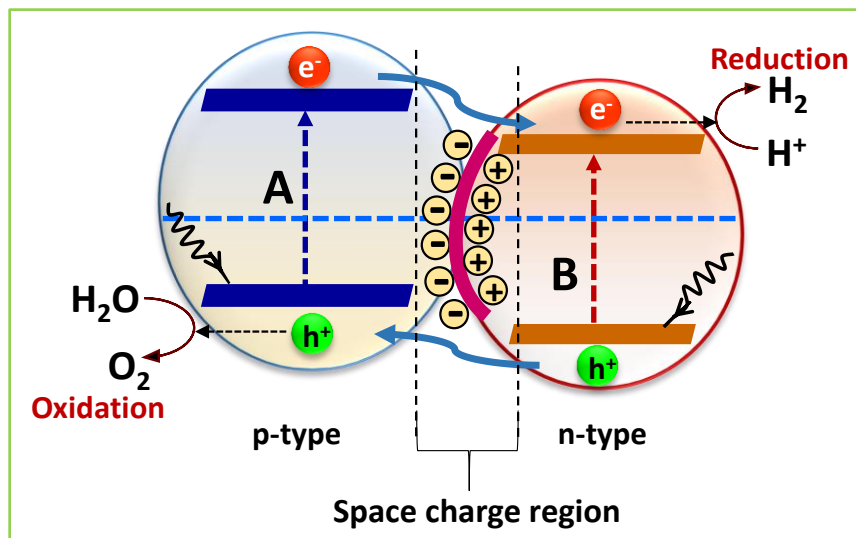


Figure 1.19 Schematic energy band diagram and the photogenerated electron-hole separation on a p-n heterojunction.

(v) Schottky Junction

When one metal and one semiconductor attached with each other, depending on their work function energies Schottky junction and Ohmic junction will be created. If work function energy of the metal (ϕ_M) is greater than the work function energy of semiconductor (ϕ_{semi}), then Schottky junction formed at the metal-semiconductor interface and in reverse case ($\phi_M < \phi_{\text{semi}}$) Ohmic junction formed. Figure 20a shows the condition of Schottky junction formation before contact between an n-type semiconductor and a metal. It is well known that when two materials came in contact, an equilibrium will be formed to line up the E_f of adjacent materials. Here, CB electrons of semiconductor will flow to the metal and tried to lineup the E_f (Figure 1.20b). As electrons are ejected from the semiconductor so it becomes positive and metal acts as sink, i.e. getting negative. A contact potential (eV_0) will be formed at the metal-semiconductor interface which oppose the further motion of electrons [20, 64]. Therefore, an internal electric field (E) may create at the junction that resulted upward band bending at the semiconductor in the direction of electric field (Figure 1.20c). The band bending further helps in movement of electrons both in surface and bulk.

Notably, the electrons are not only move on the surface but they also move from a certain region within the bulk. This distance where electrons move from semiconductor to metal is called ‘**Depletion region**’ or **Space Charge region**’, marked in the Figure 1.20c. On the other hand, there is a barrier for the electrons to transfer at the semiconductor from metal, called Schottky barrier (ϕ_B) [64].

$$\phi_B = (\phi_M - \phi_{\text{semi}}) + (E_C - E_{fn}) \quad (1.26)$$

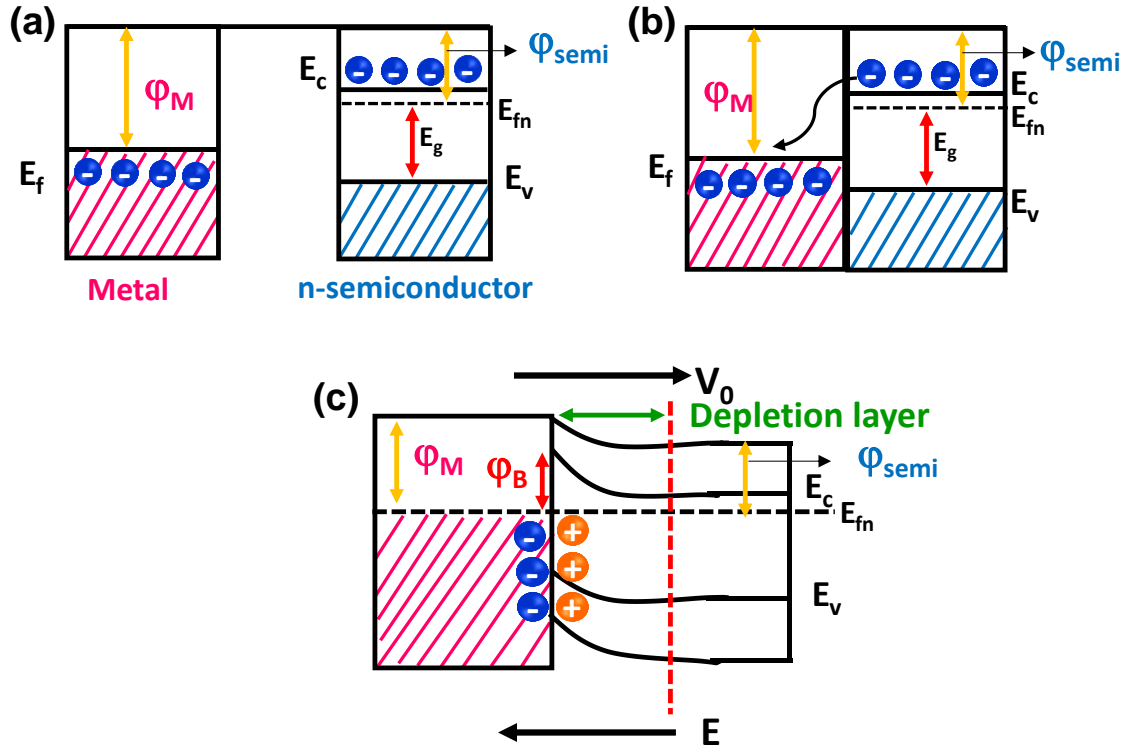


Figure 1.20 Schematic diagram of Schottky junction between a metal and an n-type semiconductor (a) before contact, (b) electron flow after contact and (c) band bending of semiconductor interface at equilibrium.

When this Schottky junction is irradiated by light with the equal or greater energy compared to the work function energy of semiconductor, excited electrons-holes are generated at the CB and VB of semiconductor, respectively. Due to the upward band bending, excited electrons may not transfer to metal from the semiconductor, thereby tried to move away from the junction and result a self-powered photocurrent. On the other hand, photoinduced holes move towards the metal side by the influence of built-in-electric field E . During the hole migration, some of these may be trapped at the junction and decreased the electric field E , reveals decrease in Schottky barrier width

and enhances the photocurrent. In this way spatial separation of photogenerated charge carriers occur at the metal-semiconductor Schottky junction in presence of light illumination (Figure 1.21).

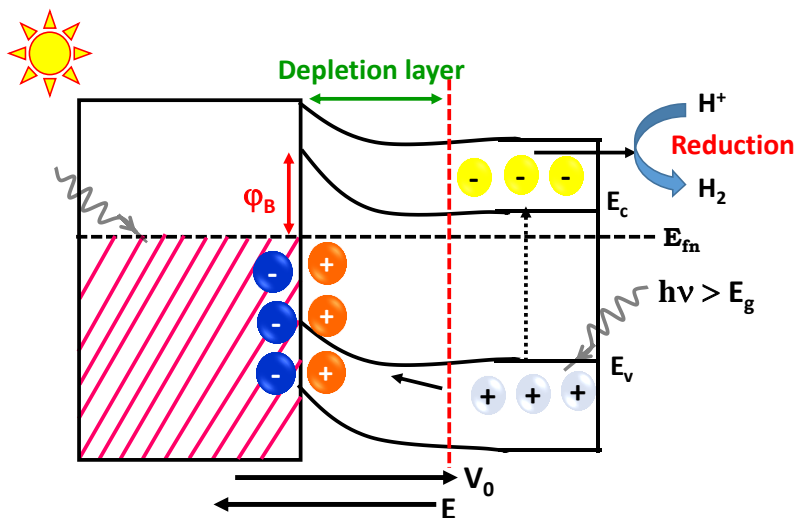


Figure 1.21 Schematic diagram of depletion region formation at a metal-semiconductor interface under light illumination.

1.10 Main Challenges in Photocatalysis

Two physical parameters of a semiconductor catalyst play crucial role during the photocatalytic reactions, one is the bandgap and the other is band edge potentials. According to theoretical calculation, bandgap (E_g) of a visible light active photocatalyst should be equal or greater than 1.23 eV, however experimentally higher bandgap (> 2.0 eV) is required to overcome the overpotentials related to the catalytic reactions. At the same time, a narrow bandgap is also required to absorb longer wavelength lights of the solar spectrum. The charge separation and transfer kinetics should be faster to efficiently drive the photocatalytic reactions. More importantly, the position of the CB and VB of semiconductor photocatalyst should be closely located to the desired oxidation and reduction, so that excited charge carriers may easily engage into water splitting reactions. Hence, the overall mechanistic approach should favor the desired conditions of low recombination rate, fast charge separation and stability under long time light illumination. Therefore, it is very challenging for a single semiconductor to meet all these requirements at a time. A large number of semiconductors based photocatalysts have been examined for energy and environmental application for the last few decades. Metal oxides, like TiO_2 , ZnO , $SrTiO_3$, Fe_2O_3 , $BiFeO_3$, $BiVO_4$, Bi_2WO_6 etc., have been extensively tested for H_2 generation through water splitting [94]. Further, metal chalcogenides including CdS , ZnS , MoS_2 ,

MoSe₂, WS₂, Bi₂S₃, layer double hydroxide, graphene, g-C₃N₄, conjugated polymers have been reported for photocatalytic and PEC water splitting to generate H₂ [95]. However, the wide bandgap of metal oxides catalyst restricts the catalytic activity only under UV light, which accounts 4% of total solar spectrum. In addition, the CB potential of most of metal oxides located at positive potential which resists the water reduction capability [94]. In case of transition-metal semiconductors, either empty d orbitals (d⁰) or filled d orbitals (d¹⁰) are present, results improved photo-response compared to other semiconductors [96]. However, stability and durability of these semiconductors under long light illumination remains an issue. Therefore, development of stable and efficient visible light active photocatalysts, which can absorb natural sunlight is now the research goal.

1.11 Bismuth based Materials as Photocatalysts

Bismuth (Bi) is a pentavalent transition metal and its oxides, sulfides and halides represent semiconducting properties at room temperature. Kudo et al. [97, 98] first reported photocatalytic O₂ evolution using Bi₂WO₆ and BiVO₄ as catalyst under visible light irradiation, which triggered research focus to develop Bi-based semiconductor photocatalyst. Further, Bi-based oxides such as, Bi₂O₃, (BiO)₂CO₃, BiFeO₃, BiMO₄ (M = V, P, Nb, Ta), Bi₄Ti₃O₁₂, Bi₂MO₆ (M = Mo, W, Cr), Bi-based chalcogenides such as, Bi₂S₃, Bi₂Se₃, Bi₂Te₃ etc. and Bi-based halides BiOX (X = Cl, Br, I) have been studied and found to be potential for photocatalysis owing to tunable bandgap, suitable band edge potentials, light sensitivity, structure-dependent optical property and photostability [99–107]. Considering the layered structure, stability of Bi³⁺ and tendency to form nanosheet like structure, Bi³⁺-containing compounds (Bi₂O₃, BiPO₄, BiVO₄, BiFeO₃, Bi₂WO₆, Bi₁₂TiO₂₀, Bi₄Ti₃O₁₂, Bi₃TiNbO₉, Bi₂O₂CO₃, BiOX (X = Cl, Br, I)) are focused for solar light driven photocatalysis. On the other hand, Bi⁵⁺ containing semiconductors, including KBiO₃, LiBiO₃ and NaBiO₃ have less reports as photocatalyst due to instability of Bi⁵⁺ ions [108, 109]. Most of the Bi³⁺-containing semiconductors have hybridized VB (O 2p and Bi 6s² orbitals) which helps to narrow the bandgap by upshifting the VB potential. In addition, they possess sufficient positive potential which introduce strong oxidizing capability, makes materials preferable for organic pollutant degradation and photocatalytic O₂ evolution. However, these are not suitable for photocatalytic H₂ generation, CO₂ reduction because of the less negative CB potential. Therefore, a series of strategies like doping, coupling with others have been adopted to shift the CB at negative

potentials than water reduction potential (0V vs RHE) [103–106]. Heterostructures formation between Bi-based semiconductors and other photocatalyst (such as semiconductors, conjugated polymers, carbon-based nanostructures, graphene etc.) has been founded as an efficient approach which can fulfill the requirements of water splitting and H₂ generation [99]. In addition, Bi nanoparticles can exhibit SPR effect under visible light illumination, which upshifted the energy levels and improve the light absorption capability.

1.11.1 Bi-based Oxide

In solar light driven water splitting Bi₂O₃, Bi₂WO₆, Bi₂MoO₆ are widely used due to hybridized VB containing overlap of Bi 6s² and O 2p orbitals, which offers a moderate bandgap (< 3 eV). Bismuth oxide (Bi₂O₃) is a p-type semiconductor and has six crystallographic polymorphs, denoted as α-Bi₂O₃, β-Bi₂O₃, γ-Bi₂O₃, ω-Bi₂O₃, ε-Bi₂O₃ and δ-Bi₂O₃. Among these, monoclinic α-Bi₂O₃ is only stable phase and rest of the phases are metastable at room temperature. Due to suitable bandgap (~2.5 eV to ~2.8 eV), α-, β-, γ-phases have application in photocatalytic water splitting, organic pollutant degradation under UV and visible light [107]. However, rapid recombination of charge carriers frequently leads to poor catalytic activity under light irradiation. Additionally, it is incapable of water reduction due to less negative CB potential. The application of δ-Bi₂O₃ is limited in photocatalysis because of large bandgap (3.01 eV to 3.5 eV), however some research group tuned its bandgap through metal ion doping. The crystal structure of α-, β-, γ-, δ-Bi₂O₃ are presented in Figure 1.22, where monoclinic (P21/c), tetragonal (P-421c), cubic (123) and cubic (Fm3m) phases are obtained. It has been reported that photocatalytic activity of the aforementioned phases mainly depends on the band structures and density of states. In this regard, Wang et al. [110] found the order of increasing photocatalytic efficiency γ>β>α-Bi₂O₃ through both experimentally and theoretical calculation.

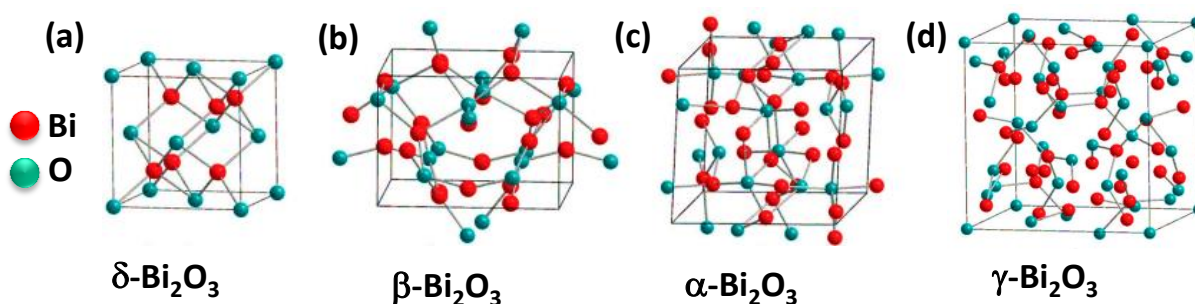


Figure 1.22 The crystal structure of the (a) α-Bi₂O₃ (monoclinic, P21/c), (b) β-Bi₂O₃ (tetragonal, P-421c), (c) γ-Bi₂O₃ (cubic, 123), (d) δ-Bi₂O₃ (cubic, Fm3m) [107].

Bismuth ferrite (BiFeO_3) is a single perovskite having ABO_3 structure, where A-site is responsible to generate ferroelectricity and B-site for magnetism [112]. The active lone pair of Bi^{3+} ions generate polarization whereas Fe^{3+} ions result magnetization. Interestingly, it has room temperature multiferroic nature. Generally, tetragonal, orthorhombic and rhombohedral structure of BiFeO_3 are observed due to rotation and tilting of the $[\text{BO}_6]$ octahedral. The crystal structure of rhombohedral ($\text{R}\bar{3}\text{c}$) BiFeO_3 has been shown in Figure 1.23. Due to spontaneous switching of the polarization, an electric field will be induced within the lattice, thereby applications focused on spintronics and memory devices [111]. Because of the moderate bandgap, in the range of ~ 2.1 eV to 2.7 eV with allowed transition, BiFeO_3 has attracted instance research interest for solar induced photocatalysis. Primarily, BiFeO_3 was used for photocatalytic organic pollutants degradation, however, the rate kinetics was sluggish. Therefore, many strategies including nanostructure formation, doping, coupling with other semiconductors etc. have been carried out to improve the photocatalytic activity. In 2007, Gao et al. [113] prepared BiFeO_3 nanoparticles of size range 80–120 nm by a facile sol–gel method which showed a significantly improved photocatalytic activity towards MO degradation compared to bulk BiFeO_3 under UV-Vis light. They demonstrated that large surface to volume ratio and the greater number of catalytic active sites for nanosized BiFeO_3 improve the redox reactions, thereby photocatalytic efficiency. In addition, a weak ferromagnetism has been governed by the BiFeO_3 nanoparticles, which boosts the charge separation efficiency. Further, Guo et al. [114] developed Gd Doped BiFeO_3 which demonstrated distorted spin cycloid and magnetically active properties of Gd^{3+} ions in magnetization hysteresis loops, resulted increased activity for RhB degradation under visible light. Consequently, Ba-doped BiFeO_3 also synthesized which showed significant visible light absorption due to the reduction of bandgap to 1.79 eV from 2.3 eV and enhanced magnetic saturation value, leading to three times higher photocatalytic activity for benzene removal from water under visible light [115]. BiFeO_3 also reported as efficient photocathode and photoanode for PEC water splitting because of structural stability, suitable band edge potentials and low photo-bleaching [116, 117]. On the other hand, heterostructures formation leads to high rate of charge carrier separation, mobility of excitons and a greater number of exposed surfaces [110, 118]. As another important Bi-based semiconductor oxide, $\text{Bi}_2\text{Fe}_4\text{O}_9$ and $\text{Bi}_4\text{Ti}_3\text{O}_{12}$ have been widely used as a visible light driven catalyst for organic pollutant degradation and water splitting.

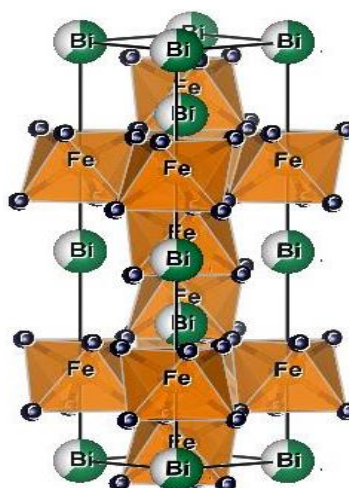


Figure 1.23 The crystal structure of rhombohedral (R3c) BiFeO₃.

Bismuth molybdate oxide (Bi₂MoO₆, E_g= ~2.6 eV) and bismuth tungsten oxide (Bi₂WO₆, E_g= ~2.6 eV) are two simplest Aurivillius oxides. These attracted research focus owing to extraordinary layered structure which are constructed by the alternating fluorine-like layers (Bi₂O₂)²⁺ and perovskite layers (WO₄/MoO₄)²⁻ (Figure 1.24). These materials possess open crystalline structure, excellent electrochemical and physicochemical properties and high structural and thermal stability. In addition, highly exposed active sites and the large surface area can be achieved by tuning the morphology. Besides, Bi₂WO₆ have been chosen as model photocatalyst in various oxidation reactions, as example, O₂ evolution, water purification owing to highly positive VB. The light absorption of bare Bi₂WO₆ is limited in visible region and suffers undesirable photo generated electron-hole recombination. Thus, research focus aimed to tune the bandgap of Bi₂WO₆ so that it can absorb visible light effectively.

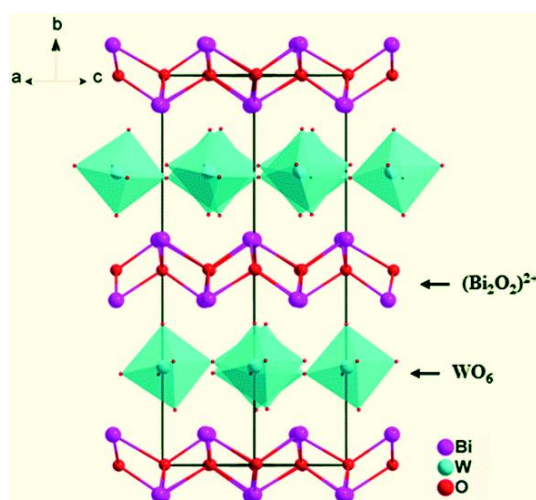


Figure 1.24 The crystal structure of orthorhombic (Pca2) Bi₂WO₆ [137].

1.11.2 Bi-based Vanadate

Bismuth vanadate (BiVO_4) is most promising catalyst for photoelectrochemical water splitting under visible light. BiVO_4 exists in the form of orthorhombic, tetragonal and monoclinic, where monoclinic phase (space group 15, $C2h$) is only thermodynamically stable. The crystal structure of monoclinic BiVO_4 has been presented in Figure 1.25. Kudo et al. [119] first reported water oxidation using monoclinic BiVO_4 in presence of electron scavengers Ag^+ ions under visible light. The narrow bandgap, suitable band edge potentials, facile synthesis, low cost make it very attractive for organic pollutant degradation [120, 121]. Due to positive CB potential, BiVO_4 is incapable for water reduction. However, some research group reported photocatalytic H_2 generation using nanostructured BiVO_4 [122]. Theoretically, η_{STH} of BiVO_4 photoanode is around 9.2% with the maximum photocurrent density of $\sim 7.5 \text{ mA/cm}^2$ under standard AM 1.5G solar light illumination. Although, the efficiency experimentally achieved using BiVO_4 as photoanode is far low from the theoretical result. The possibility of self-trapping of photogenerated charge species and fast recombination hinder the charge separation as well as transfer through the electrode-electrolyte interface during photocatalysis experiments. As a result, BiVO_4 exhibits very slow kinetics for O_2 evolution.

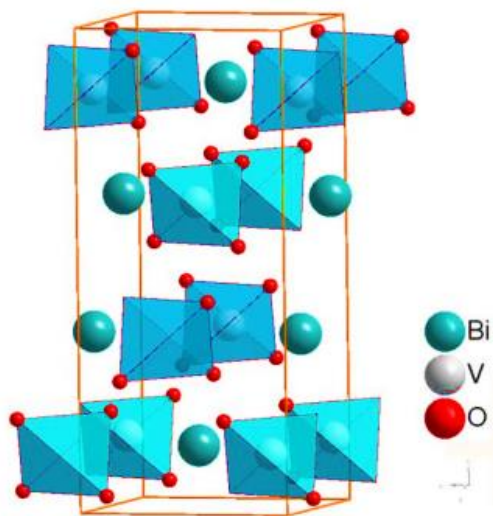


Figure 1.25 The crystal structure of monoclinic phase (15, $C2h$) BiVO_4 [122].

1.11.3 Bi-based Chalcogenide

Bi-based chalcogenides, as example Bi_2S_3 , Bi_2Te_3 , Bi_2Se_3 are very promising materials for photocatalysis because of size dependent physical and chemical properties. Most of the Bi-based

chalcogenides have narrow bandgap, thereby suitable for visible light absorption. For example, Bi_2S_3 has bandgap in the range of 1.3 eV – 1.5 eV, size dependent quantum confinement effect and thereby widely used in photocatalytic applications. The crystal structure of Bi_2S_3 has been shown in Figure 1.26. An anisotropic orthorhombic structure with Pnma space group where four molecular chains (Bi–S–S) are present in per unit cell along the crystallographic c-axis. As a result, one-dimensional nanostructures, for example nanowires, nanorods, nanotubes are preferably formed for Bi_2S_3 [123]. On the other hand, Bi_2Se_3 possess layered structure having a weak forces between the interlayers. Thus, 2D nanosheets of Bi_2Se_3 have been preferably formed and possess high exposed surface area. In addition, being topological insulators Bi-based chalcogenides have minimum scattering effect because of opposite spin polarization which facilitates the electron transfer, thereby improve the conductivity of the materials during catalytic reactions [124]. On the other hand, Bismuth telluride (Bi_2Te_3) extensively used in the refrigeration and thermoelectric power generation owing to high melting point (585°C). Recently, it has been attracted interest in photocatalysis because of narrow bandgap (~ 1.32 eV). The electrochemical and thermocatalytic properties make Bi_2Te_3 potential catalyst for water splitting [125].

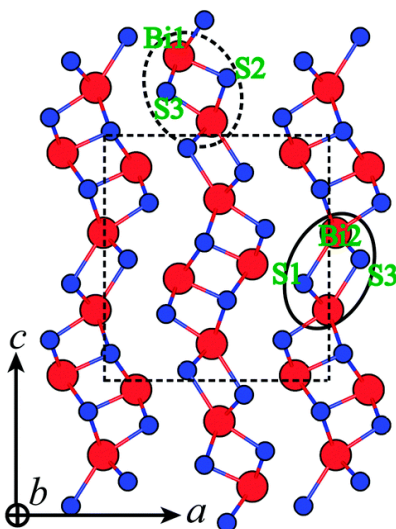


Figure 1.26 The crystal structure of orthorhombic structure (Pnma) Bi_2S_3 [123].

1.11.4 Bi-based Halide

Bismuth oxyhalides (BiOX , $\text{X} = \text{Cl}, \text{Br}, \text{I}$), a new class of promising materials have attracted recent interest in photocatalysis due to layered structure, composed of $[\text{Bi}_2\text{O}_2]^+$ slabs interleaved by double halogen atoms $[\text{X}]^-$ with open crystalline nature [126-128]. A tetragonal matlockite

(PbFCl-type) structure, Van der Waals force within the halide layers and covalent bond between $[\text{Bi}_2\text{O}_2]^+$ and $[\text{X}]^-$ make BiOX chemically stable (Figure 1.27) [129, 130]. Additionally, the open crystalline structure of BiOX benefits a large space for polarization of atoms and orbitals, results a static internal electric field perpendicular to the $[\text{Bi}_2\text{O}_2]^+$ slabs, which further boosts the electron-hole separation along the (001) direction [130, 131]. Besides, BiOX generate facile O-vacancy during photocatalysis under UV light due to low energy Bi–O bonds at the surface. The bandgaps of BiOCl, BiOBr and BiOI are ~ 3.3 eV, ~ 2.7 eV and ~ 1.8 eV.

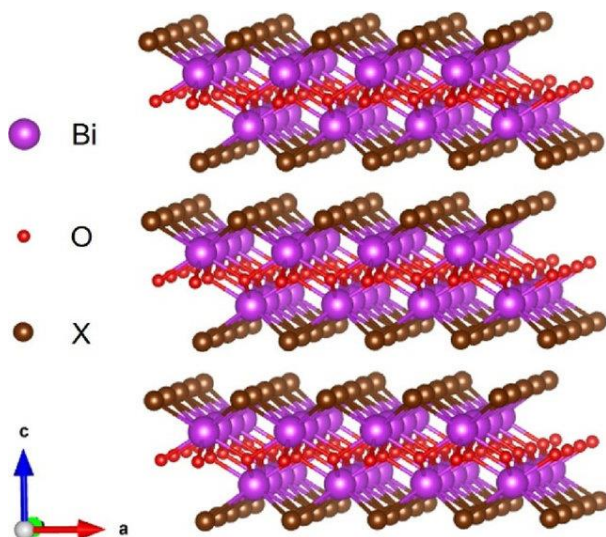


Figure 1.27 The crystal structure of tetragonal structure (PbFCl-type) BiOX (X= Cl, Br, I) [129].

Thus, BiOCl is a wide bandgap semiconductor and its activity is limited in the UV region. Although, BiOBr has moderate bandgap and could absorb visible light, however the band edge potentials restrict its performance for hydrogen generation. On the other hand, BiOI is a narrow bandgap semiconductor and efficient for visible light absorption, however suffers from fast charge carrier recombination. Owing to suitable VB potential, BiOI also reported as efficient O_2 evolving catalyst under visible light. Thus, coupling of secondary semiconductors with BiOBr and BiOI may improve the photocatalytic performance under visible light. The bandgap, band edge potentials with respect to vacuum energy scale and normal hydrogen electrode (NHE) scale of commonly used Bi-based photocatalysts are presented in Figure 1.28. Furthermore, the advantages and the limitations of these photocatalysts for water splitting are summarized in brief (Table 1.1).

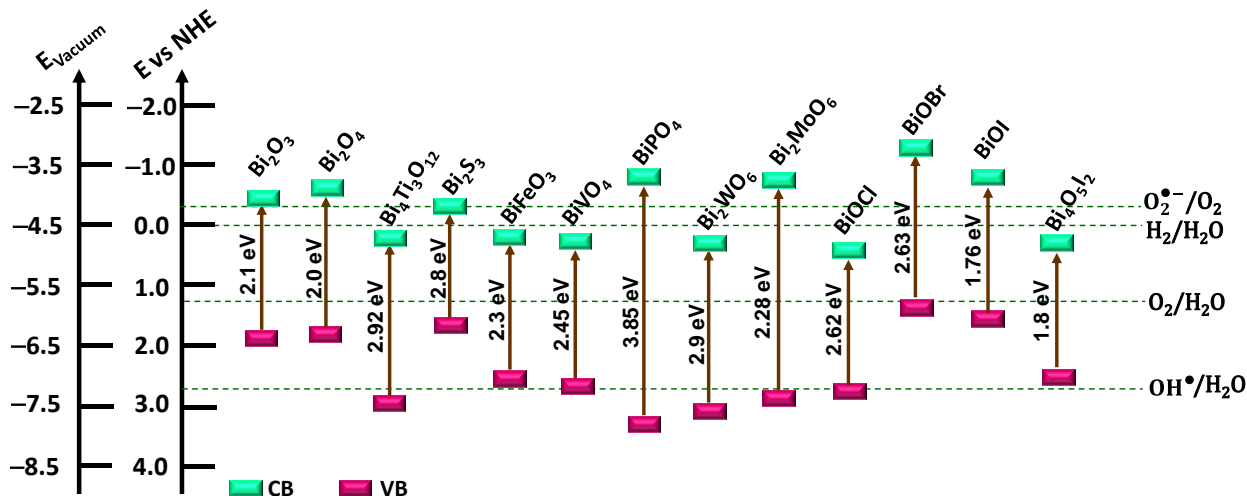


Figure 1.28 Band-edge positions and the bandgaps of commonly used Bi-based photocatalysts. Dotted lines indicate the relative energy levels of redox reactions for water splitting and organic pollutant degradation.

Table 1.1 The bandgap, advantages and the limitations of commonly used Bi-based photocatalysts.

| Materials | Bandgap | Advantages | Limitations | Reference |
|---|-------------------------------------|---|--|-----------|
| Bi₂O₃ | Direct: 3.5 eV Indirect: 2.85 eV | <ul style="list-style-type: none"> • p-type semiconductor • High ion conductivity • Remarkable photo-conductivity | <ul style="list-style-type: none"> • High density of oxygen vacancy at the surface boosts electron-hole recombination | 132 |
| Bi₂O₄ | ~ 2.0 eV | <ul style="list-style-type: none"> • Generally rod like structure formed • n-type semiconductor • CB (−0.39V vs NHE) suitable for H₂ generation • VB (1.61 vs NHE) close to water oxidation potential (1.23 V vs NHE) • Mixed valence state present (Bi³⁺ and Bi⁵⁺) | <ul style="list-style-type: none"> • Fast electron-hole recombination • Formation of defects, promote recombination of photoinduced electron-hole pairs. | 133, 134 |
| Bi₄Ti₃O₁₂ | ~ 2.4 – 2.9 eV | <ul style="list-style-type: none"> • Layered Aurivillius ferroelectric material • n-type semiconductor • 1D and 2D nanostructures are reported • Highly positive VB (2.92 V vs NHE), suitable for water oxidation, organic pollutant degradation | <ul style="list-style-type: none"> • Fast electron-hole recombination • CB (0.05 V vs NHE) not-suitable for H₂ generation | 135 |
| Bi₂S₃ | ~ 1.3 eV – 1.4 eV | <ul style="list-style-type: none"> • CB (−0.33V vs NHE) suitable for water reduction, H₂ generation • n-type semiconductor • Generally 1D nanostructure formed • Strong visible light absorption | <ul style="list-style-type: none"> • VB (1.05 V vs NHE) is low enough for water oxidation • Fast electron-hole recombination | 123 |

| Materials | Bandgap | Advantages | Limitations | Reference |
|--------------------------------------|-------------------|--|---|-----------|
| BiFeO₃ | ~ 2.3 eV | <ul style="list-style-type: none"> • VB (2.4 V vs NHE) is suitable for water oxidation • n-type semiconductor • Visible light active catalyst • Internal electric field exists due to multiferroic nature • Chemically stable perovskite | <ul style="list-style-type: none"> • CB is positive (0.14 V vs NHE), not suitable for water reduction | 110 |
| BiVO₄ | ~ 2.45 eV | <ul style="list-style-type: none"> • VB (2.4 V vs NHE) is suitable for water oxidation • n-type semiconductor • Visible light active catalyst • Morphology dependent photocatalytic activity | <ul style="list-style-type: none"> • CB is positive (0.14 V vs NHE), not suitable for water reduction | 119 |
| BiPO₄ | Indirect: 3.85 eV | <ul style="list-style-type: none"> • High photocatalytic oxidative ability for organic dye decomposition • n-type semiconductor • Highly negative CB (-0.56 V vs NHE) suitable for H₂ generation | <ul style="list-style-type: none"> • Mainly UV active due to large bandgap | 136 |
| Bi₂WO₆ | ~ 2.6 eV – 2.8 eV | <ul style="list-style-type: none"> • Generally n-type semiconductor but it shows p-type conductivity in presence of O-vacancy • VB (2.9 V vs NHE) is suitable for water oxidation, • Visible light active catalyst • Size dependent optical properties • Chemically stable • Layered structure provides large surface area | <ul style="list-style-type: none"> • CB is positive (0.24 V vs NHE), not suitable for water reduction | 137 |
| Bi₂MoO₆ | ~ 2.5 eV – 2.8 eV | <ul style="list-style-type: none"> • n-type semiconductor • CB= -0.46 V, VB= +2.28 V vs NHE suitable for water splitting • Visible light active | <ul style="list-style-type: none"> • Fast electron-hole recombination | 138 |
| BiOCl | ~ 3.3 eV | <ul style="list-style-type: none"> • Layer structure endows internal static electric field which boosts charge separation • Depending on the synthesis method it shows both n-type and p-type conductivity • Facile generation of O-vacancies • Highly positive VB potential | <ul style="list-style-type: none"> • Low visible light absorption • Not suitable for H₂ generation | 129 |
| BiOBr | ~ 2.7 eV | <ul style="list-style-type: none"> • Highly positive VB (2.76 V vs NHE) suitable for water oxidation, O₂ generation • n-type semiconductor • Visible light active • Layered structure • High chemical stability | <ul style="list-style-type: none"> • Lower redox activity • Rapid recombination of the photo induced charge carrier • Less photo sensitive | 130 |

| Materials | Bandgap | Advantages | Limitations | Reference |
|---|-------------------|--|--|-----------|
| BiOI | ~ 1.8 eV – 2.0 eV | <ul style="list-style-type: none"> • Narrow bandgap facilitates the visible light absorption • Depending on the synthesis method it shows both n-type and p-type conductivity • Band edge potentials are suitable for water splitting • 2D nanostructure | <ul style="list-style-type: none"> • Unstable under long time light irradiation • Fast electron hole recombination | 130 |
| Bi₄O₅I₂ | ~ 1.8 eV | <ul style="list-style-type: none"> • Highly positive VB (2.35 V <i>vs</i> NHE) suitable for water oxidation, O₂ generation • n-type semiconductor • Visible light active | <ul style="list-style-type: none"> • Not suitable for H₂ generation, CB (0.51 V <i>vs</i> NHE) | 139 |

References

- [1] B. Looney, S. Dale, BP Statistical Review of World Energy 2021. 70th Edition (2021) 1–72.
- [2] K. S. Joya, Y. F. Joya, K. Ocakoglu, R. Kro, Water-Splitting Catalysis and Solar Fuel Devices: Artificial Leaves on the Move. *Angew. Chem. Int. Ed.* **52** (2013) 10426 – 10437.
- [3] C. Bozal-Ginesta, J. R. Durrant, Artificial photosynthesis – concluding remarks. *Faraday Discuss.* **215** (2019) 439–451.
- [4] A. Kudo, Y. Miseki, Heterogeneous photocatalyst materials for water splitting. *Chem. Soc. Rev.* **38** (2009) 253–278.
- [5] T. Hisatomi, K. Domen, Introductory lecture: sunlight-driven water splitting and carbon dioxide reduction by heterogeneous semiconductor systems as key processes in artificial photosynthesis. *Faraday Discuss.* **198** (2017) 11–35.
- [6] U.S. Energy Information Administration. (2019, September 24). International Energy Outlook 2019. www.eia.gov/ieo.
- [7] B. Zhang, L. Sun, Artificial photosynthesis: opportunities and challenges of molecular catalysts. *Chem. Soc. Rev.* **48** (2019) 2216–2264.
- [8] D. A. J. Rand, R. M. Dell, Hydrogen Energy: Challenges and Prospects. Print publication date 14 Dec 2007, Print ISBN 978-0-85404-597-6, PDF eISBN 978-1-84755-802-2, RSC Energy Series.
- [9] C. J. Quarton, O. Tlili, L. Welder, C. Mansill, H. Blanco, H. Heinrichs, J. Leaver, N. J. Samsatli, P. Lucchese, M. Robinius, S. Samsatli, The curious case of the conflicting roles of hydrogen in global energy scenarios. *Sustainable Energy Fuels* **4** (2020) 80–95.
- [10] O. P. Agarwal, P. Mulukutla, K. Malladi, Basics of Hydrogen Technology. Nel ASA, Green Hydrogen: Insights & Outlook (2021).
- [11] International Renewable Energy Agency. (2020). Renewable Capacity Statistics 2020. https://www.irena.org//media/Files/IRENA/Agency/Publication/2020/Mar/IRENA_RE_Capacity_Statistics_2020.pdf
- [12] A projects nearly 50% increase in world energy usage by 2050, led by growth in Asia. (2019, September 24).
- [13] Today in Energy. U.S. Energy Information Administration. <https://www.eia.gov/todayinenergy/detail.php?id=41433>.

- [14] Hydrogen production and consumption worldwide in 2019, by sector. (n.d). Statista. <https://www.statista.com/statistics/1199339/globalhydrogen-production-and-consumption-by-sector/>.
- [15] Combustion of fuels–Carbon dioxide. (n.d). The Engineering Toolbox. https://www.engineeringtoolbox.com/co2-emission-fuels-d_1085.html.
- [16] A. Fujishima, K. Honda, Electrochemical Photolysis of Water at a Semiconductor Electrode. *Nature* **238** (1972) 37–37.
- [17] M. D. Hernández-Alonso, F. Fresno, S. Suárez, J. M. Coronado, Development of alternative photocatalysts to TiO₂: Challenges and opportunities. *Energy Environ. Sci.* **2** (2009) 1231–1257.
- [18] J. Liu, N. Ma, W. Wu, Q. He, Recent progress on photocatalytic heterostructures with full solar spectral Responses. *Chem. Eng. J.* **393** (2020) 124719.
- [19] The American Society for Testing and Materials (ASTM, 2003).
- [20] M. A. Wahab, Solid State Physics: Structure and Properties of Materials. Narosa Publishing House (2001), ISBN-10: 8173192669.
- [21] C. Kittel, Introduction to solid state Physics, Wiley (2004), ISBN: 978-0-471-41526-8.
- [22] A. J. Dekker, Solid State physics. Springer (1981).
- [23] R. K. Puri, V. K. Babbar, Solid State Physics. Springer (1990).
- [24] H. Gleiter, Nanostructured materials: state of the art and perspectives, *Nanostructured Mater.* **6** (1995) 3–14.
- [25] P. Walter, E. Welcomme, P. Halle´got, N. J. Zaluzec, C. Deeb, J. Castaing, P. Veyssie`re, R. Bre´niaux, J.-L. Le´ve`que, G. Tsoucaris, Early Use of PbS Nanotechnology for an Ancient Hair Dyeing Formula. *Nano Lett.* **6** (2006) 2215–2219.
- [26] F. J. Heiligtag, M. Niederberger, The fascinating world of nanoparticle research. *Mater. Today* **16** (2013) 262–271.
- [27] I. Freestone, N. Meeks, M. Sax, C. Higgitt, The Lycurgus Cup — A Roman nanotechnology. *Gold Bull.* **40** (2007) 270–277.
- [28] R. P. Feynman, There’s Plenty of Room at the Bottom. *Eng. Sci.* **23** (1960) 22–36.
- [29] N. Taniguchi, Proc. Int. Conf. Prod. Eng. Issue PART II (1974) 18–23.
- [30] S. Hu, X. Wang, Ultrathin nanostructures: smaller size with new phenomena. *Chem. Soc. Rev.* **42** (2013) 5577–5594.

- [31] J. Baxter, Z. Bian, G. Chen, D. Danielson, M. S. Dresselhaus, A. G. Fedorov, T. S. Fisher, C. W. Jones, E. Maginn, U. Kortshagen, A. Manthiram, A. Nozik, D. R. Rolison, T. Sands, L. Shi, D. Sholl, Y. Wu, Nanoscale design to enable the revolution in renewable energy. *Energy Environ. Sci.* **2** (2009) 559–588.
- [32] N. Baig, I. Kammakakam, W. Falath, Nanomaterials: a review of synthesis methods, properties, recent progress, and challenges. *Mater. Adv.* **2** (2021) 1821–1871.
- [33] R. Viswanatha, H. Amenitsch, D. D. Sarma, Growth Kinetics of ZnO Nanocrystals: A Few Surprises. *J. Am. Chem. Soc.* **129** (2007) 4470–4475.
- [34] X. Chen, C. Li, M. Grätzel, Robert Kosteci, Samuel S. Mao, Nanomaterials for renewable energy production and storage. *Chem. Soc. Rev.* **41** (2012) 7909–7937.
- [35] N. BOHR, The Quantum Postulate and the Recent Development of Atomic Theory. *Nature* **1** (1928) 580.
- [36] T. Edvinsson, Optical quantum confinement and photocatalytic properties in two-, one- and zero-dimensional nanostructures. *R. Soc. Open Sci.* **5** (2018) 180387–180394.
- [37] X.-B. Li, C.-H. Tung, L.-Z. Wu, Semiconducting quantum dots for artificial photosynthesis. *Nat. Rev. Chem.* **2** (2018) 160–173.
- [38] C. Katan, N. Mercier, J. Even, Quantum and Dielectric Confinement Effects in Lower-Dimensional Hybrid Perovskite Semiconductors. *Chem. Rev.* **119** (2019) 3140–3192.
- [39] S. Sapra, D. D. Sarma, Evolution of the electronic structure with size in II-VI semiconductor nanocrystals. *Phys. Rev. B* **69** (2004) 125304–125311.
- [40] R. Viswanatha, D. D. Sarma, Study of the Growth of Capped ZnO Nanocrystals: A Route to Rational Synthesis. *Chem. Eur. J.* **12** (2006) 180–186.
- [41] J. M. Herrmann, Heterogeneous photocatalysis: fundamentals and applications to the removal of various types of aqueous pollutants. *Catal. Today* **53** (1999) 115–129.
- [42] J. M. Herrmann, Heterogeneous photocatalysis: State of the art and present applications. *Top. Catal.* **34** (2005) 49–65.
- [43] N. Sato, *Electrochemistry at Metal and Semiconductor Electrodes*. Elsevier, Amsterdam, (1998) 1–396.
- [44] H. J. Gerischer, A mechanism of electron hole pair separation in illuminated semiconductor particles. *Phys. Chem.* **88** (1984) 6096–6097.

- [45] C. Kittel (Ed.), Introduction to Solid State Physics, 8th Ed.; Wiley, Weinheim; 2005: pp 1-704.
- [46] Z. Chen, T. F. Jaramillo, T. G. Deutsch, A. Kleiman-Shwarsctein, A. J. Forman, N. Gaillard, R. Garland, K. Takanabe, C. Heske, M. Sunkara, E. W. McFarland, K. Domen, E. L. Miller, J. A. Turner, H. N. Dinh, Accelerating materials development for photoelectrochemical hydrogen production: Standards for methods, definitions, and reporting protocols. *J. Mater. Res.* **25** (2010) 3–16.
- [47] K. Takanabe, Photocatalytic Water Splitting: Quantitative Approaches toward Photocatalyst by Design. *ACS Catal.* **7** (2017) 8006–8022.
- [48] K. Maeda, K. Domen, New Non-Oxide Photocatalysts Designed for Overall Water Splitting under Visible Light. *J. Phys. Chem. C* **111** (2007) 7851–7861.
- [49] K. Villa, J. R. Galán-Mascarós, N. López, E. Palomares, Photocatalytic water splitting: advantages and challenges. *Sustainable Energy Fuels* **5** (2021) 4560–4569.
- [50] S. Ghosh, N. A. Kouame, L. Ramos, S. Remita, A. Dazzi, A. Deniset-Besseau, P. Beaunier, F. Goubard, P.-H. Aubert, H. Remita, Conducting polymer nanostructures for photocatalysis under visible light. *Nat. Mater.* **14** (2015) 505–511.
- [51] V. S. Kirankumar, S. Sumathi, A review on photodegradation of organic pollutants using spinel oxide. *Mater. Today Chem.* **18** (2020) 100355.
- [52] V. Diesen, M. Jonsson, Tris(hydroxymethyl)aminomethane as a probe in heterogeneous TiO₂ photocatalysis. *J. Adv. Oxid. Technol.* **15** (2012) 392–398.
- [53] K. J. Young, L. A. Martini, R. L. Milot, R. C. Snoeberger, V. S. Batista, C. A. Schmuttenmaer, R. H. Crabtree, G. W. Brudvig, Light-driven water oxidation for solar fuels. *Coord. Chem. Rev.* **256** (2012) 2503–2520.
- [54] K. Maeda, K. Domen, Photocatalytic Water Splitting: Recent Progress and Future Challenges. *J. Phys. Chem. Lett.* **1** (2010) 2655–2661.
- [55] T. Takata, J. Jiang, Y. Sakata, M. Nakabayashi, N. Shibata, V. Nandal, K. Seki, T. Hisatomi, K. Domen, Photocatalytic water splitting with a quantum efficiency of almost unity. *Nature* **581** (2020) 411–414.
- [56] P. Moroz, A. Boddy, M. Zamkov, Challenges and Prospects of Photocatalytic Applications Utilizing Semiconductor Nanocrystals. *Front. Chem.* **6** (2018) 353–360.

- [57] M. R. Hoffmann, S. T. Martin, W. Y. Choi, D. W. Bahnemann, Environmental Applications of Semiconductor Photocatalysis. *Chem. Rev.* **95** (1995) 69–96.
- [58] N. Serpone, Relative photonic efficiencies and quantum yields in heterogeneous photocatalysis, *J. Photochem. Photobio. A* **104** (1997) 1–12.
- [59] H. Kim, S. Lee, Y. Han, J. Park, Preparation of dip-coated TiO₂ photocatalyst on ceramic foam pellets, *J. Mater. Sci.* **40** (2005) 5295–5298.
- [60] U. I. Gaya, A. H. Abdullah, Heterogeneous photocatalytic degradation of organic contaminants over titanium dioxide: A review of fundamentals, progress and problems. *J. Photochem. Photobiol. C* **9** (2008) 1–12.
- [61] T. Shinagawa, A. T. Garcia-Esparza, K. Takanabe, Insight on Tafel slopes from a microkinetic analysis of aqueous electrocatalysis for energy conversion. *Sci. Rep.* **5** (2015) 13801–13822.
- [62] M. Gong, W. Zhou, M. C. Tsai, J. Zhou, M. Guan, M. C. Lin, B. Zhang, Y. Hu, D. Y. Wang, J. Yang, S. J. Pennycook, B. J. Hwang, H. Dai, Nanoscale nickel oxide/nickel heterostructures for active hydrogen evolution electrocatalysis. *Nat. Commun.* **5** (2014) 5695–5701.
- [63] M. Gong, Y. Li, H. Wang, Y. Liang, J. Z. Wu, J. Zhou, J. Wang, T. Regier, F. Wei, H. J. Dai, An Advanced Ni–Fe Layered Double Hydroxide Electrocatalyst for Water Oxidation. *Am. Chem. Soc.* **135** (2013) 8452–8455.
- [64] Z. Chen, H. N. Dinh, E. Miller, Photoelectrochemical Water Splitting Standards, Experimental Methods, and Protocols. Springer (2013) ISBN 978-1-4614-8297-0.
- [65] Z. Zhang, J. T. Yates, Jr. Band Bending in Semiconductors: Chemical and Physical Consequences at Surfaces and Interfaces. *Chem. Rev.* **112** (2012) 5520–5551.
- [66] C. F. Bohren, D. R. Huffman, Absorption and scattering of light by small particles. Wiley-VCH, Weinheim (2004) 1–476.
- [67] H. Tüysüz, C. K. Chan (Eds.) Solar Energy for Fuels, Springer (2016) ISBN 3319230980 9783319230986.
- [68] S. Bera, S. Ghosh, Bandgap Engineering of Heterostructures for Visible Light-Driven Water Splitting. Chapter 8, Green Photocatalytic Semiconductors, Springer, Cham (2022) 701–722.

- [69] X. Chen, S. Shen, L. Guo, S. S. Mao, Semiconductor-based Photocatalytic Hydrogen Generation. *Chem. Rev.* **110** (2010) 6503–6570.
- [70] R. Asahi, T. Morikawa, T. Ohwaki, K. Aoki, Y. Taga, Visible-Light Photocatalysis in Nitrogen-Doped Titanium Oxides. *Science* **294** (2001) 269–271.
- [71] C. Wang, Q. Hu, J. Huang, C. Zhu, Z. Deng, H. Shi, L. Wu, Z. Liu, Y. Cao, Enhanced hydrogen production by water splitting using Cu-doped TiO₂ film with preferred (0 0 1) orientation. *Appl. Surf. Sci.* **292** (2014) 161–164.
- [72] C. Yang, M. Qin, Y. Wang, D. Wan, F. Huang, J. Lin, Observation of an Intermediate Band in Sn-doped Chalcopyrites with Wide-spectrum Solar Response. *Sci. Rep.* **3** (2013) 1286–1293.
- [73] S. Linic, P. Christopher, D. B. Ingram, Plasmonic-metal nanostructures for efficient conversion of solar to chemical energy. *Nat. Mater.* **10** (2011) 911–921.
- [74] P. Du, R. Eisenberg, Catalysts made of earth-abundant elements (Co, Ni, Fe) for water splitting: Recent progress and future challenges. *Energy Environ. Sci.* **5** (2012) 6012–6021.
- [75] R. D. L. Smith, M. S. Prévot, R. D. Fagan, Z. Zhang, P. A. Sedach, M. K. J. Siu, S. Trudel, C. P. Berlinguette, Photochemical route for accessing amorphous metal oxide materials for water oxidation catalysis. *Science* **340** (2013) 60–63.
- [76] R. Subbaraman, D. Tripkovic, K.-C. Chang, D. Strmcnik, A. P. Paulikas, P. Hirunsit, M. Chan, J. Greeley, V. Stamenkovic, N. M. Markovic, Trends in activity for the water electrolyser reactions on 3d M(Ni, Co, Fe, Mn) hydr(oxy)oxide catalysts. *Nat. Mater.* **11** (2012) 550–557.
- [77] H. Vrubel, X. Hu, Molybdenum Boride and Carbide Catalyze Hydrogen Evolution in both Acidic and Basic Solutions. *Angew. Chem., Int. Ed.* **51** (2012) 12703–12706.
- [78] X. Zong, H. Yan, G. Wu, G. Ma, F. Wen, L. Wang, C. Li, Enhancement of Photocatalytic H₂ Evolution on CdS by Loading MoS₂ as Cocatalyst under Visible Light Irradiation. *J. Am. Chem. Soc.* **130** (2008) 7176–7177.
- [79] E. J. Popczun, J. R. McKone, C. G. Read, A. J. Biacchi, A. M. Wiltrot, N. S. Lewis, R. E. Schaak, Nanostructured Nickel Phosphide as an Electrocatalyst for the Hydrogen Evolution Reaction. *J. Am. Chem. Soc.* **135** (2013) 9267–9270.

- [80] E. J. Popczun, C. G. Read, C. W. Roske, N. S. Lewis, R. E. Schaak, Highly active electrocatalysis of the hydrogen evolution reaction by cobalt phosphide nanoparticles. *Angew. Chem., Int. Ed.* **53** (2014) 5427–5430.
- [81] J. R. McKone, E. L. Warren, M. J. Bierman, S. W. Boettcher, B. S. Brunschwig, N. S. Lewis, H. B. Gray, Evaluation of Pt, Ni, and Ni–Mo electrocatalysts for hydrogen evolution on crystalline Si electrodes. *Energy Environ. Sci.* **4** (2011) 3573–3583.
- [82] M. W. Kanan, D. G. Nocera, In situ formation of an oxygen-evolving catalyst in neutral water containing phosphate and Co^{2+} . *Science* **321** (2008) 1072–1075.
- [83] D. K. Bediako, Y. Surendranath, D. G. Nocera, Mechanistic Studies of the Oxygen Evolution Reaction Mediated by a Nickel–Borate Thin Film Electrocatalyst. *J. Am. Chem. Soc.* **135** (2013) 3662–3674.
- [84] B. Hinnemann, P. G. Moses, J. Bonde, K. P. Jorgensen, J. H. Nielsen, S. Horch, I. Chorkendorff, J. K. Nørskov, Biomimetic Hydrogen Evolution: MoS_2 Nanoparticles as Catalyst for Hydrogen Evolution. *J. Am. Chem. Soc.* **127** (2005) 5308–5309.
- [85] M. Shao, Y. Shao, S. Ding, R. Tong, X. Zhong, L. Yao, W. F. Ip, B. Xu, X.-Q. Shi, Y.-Y. Sun, X. Wang, H. Pan, Carbonized MoS_2 : Super-Active Co-Catalyst for Highly Efficient Water Splitting on CdS. *ACS Sustainable Chem. Eng.* **7** (2019) 4220–4229.
- [86] Z. Liang, Y. Guo, Y. Xue, H. Cui, J. Tian, 1T-phase MoS_2 quantum dots as a superior co-catalyst to Pt decorated on carbon nitride nanorods for photocatalytic hydrogen evolution from water. *Mater. Chem. Front.* **3** (2019) 2032–2040.
- [87] M. W. Kanan, D. G. Nocera. In situ formation of an oxygen evolving catalyst in neutral water containing phosphate and Co^{2+} . *Science* **321** (2008) 1072–1075.
- [88] X. Shi, K. Zhang, J. H. Park, Understanding the positive effects of (Co-ePi) co-catalyst modification in inverse-opal structured $\alpha\text{-Fe}_2\text{O}_3$ -based photoelectrochemical cells. *Int. J. Hydrogen Energy* **38** (2013) 12725–12732.
- [89] Y. Gao, W. Fan, K. Qu, F. Wang, P. Guan, D. Xu, H. Bai, W. Shi, Confined growth of Co–Pi co-catalyst by organic semiconductor polymer for boosting the photoelectrochemical performance of BiVO_4 . *New J. Chem.* **43** (2019) 8160–8167.
- [90] S. Ghosh (Ed), Heterostructured photocatalysts for solar energy conversion, Elsevier Inc., 2020, ISBN: 9780128200735.

- [91] S. J. A. Moniz, S. Ghosh (Ed), Visible-Light-Active Photocatalysis: Nanostructured Catalyst Design, Mechanisms and Applications, Wiley-VCH VerlagGmbH& Co. KGaA, Germany, Chapter 8, 2018, ISBN: 978-3-527-34293-8.
- [92] A. J. Bard, photoelectrochemistry and heterogeneous photocatalysis at semiconductors, *J. Photochem. Photobio. A* **10** (1979) 59–75.
- [93] Y. Chen, J. C. Crittenden, S. Hackney, L. Sutter, D. W. Hand, Preparation of a Novel TiO₂-Based p-n Junction Nanotube Photocatalyst. *Environ. Sci. Technol.* **39** (2005) 1201–1209.
- [94] S. Martha, P. C. Sahoo, K. M. Parida, An overview on visible light responsive metal oxide based photocatalysts for hydrogen energy production. *RSC Adv.* **5** (2015) 61535–61553.
- [95] L. R. MacFarlane, H. Shaikh, J. D. Garcia-Hernandez, M. Vespa, T. Fukui, I. Manners, Functional nanoparticles through π -conjugated polymer self-assembly. *Nat. Rev. Mater.* **6** (2021) 7–26.
- [96] A. Rahmana, M. M. Khan, Chalcogenides as photocatalysts. *New J. Chem.* **45** (2021) 19622–19635.
- [97] A. Kudo, S. Hijii, H₂ or O₂ evolution from aqueous solutions on layered oxide photocatalysts consisting of Bi³⁺ with 6s² configuration and d⁰ transition metal ions. *Chem. Lett.* **28** (1999) 1103–1104.
- [98] S. Tokunaga, H. Kato, A. Kudo, Selective preparation of monoclinic and tetragonal BiVO₄ with scheelite structure and their photocatalytic properties. *Chem. Mater.* **13** (2001) 4624–4632.
- [99] R. He, D. Xu, B. Cheng, J. Yu, W. Ho, Review on nanoscale Bi-based photocatalysts, *Nanoscale Horiz.* **3** (2018) 464–504.
- [100] H. He, J. Yin, Y. P. Li, Y. Zhang, H. Qiu, J. Xu, T. Xu, C. Wang, Size controllable synthesis of single-crystal ferroelectric Bi₄Ti₃O₁₂ nanosheet dominated with {001} facets toward enhanced visible-light-driven photocatalytic activities. *Appl. Catal. B.* **156** (2014) 35–43.
- [101] Z. Ni, Y. Sun, Y. Zhang, F. Dong, Fabrication, modification and application of (BiO)₂CO₃-based photocatalysts: A review. *Appl. Surf. Sci.* **365** (2016) 314–335.
- [102] N. Zhang, R. Ciriminna, M. Pagliaro, Y.-J. Xu, Nanochemistry-derived Bi₂WO₆ nanostructures: towards production of sustainable chemicals and fuels induced by visible light. *Chem. Soc. Rev.* **43** (2014) 5276–5287.

- [103] J. Zai, F. Cao, N. Liang, K. Yu, Y. Tian, H. Sun, X. Qian, Rose-like I-doped $\text{Bi}_2\text{O}_2\text{CO}_3$ microspheres with enhanced visible light response: DFT calculation, synthesis and photocatalytic performance, *J. Hazard. Mater.* **321** (2017) 464–472.
- [104] H. L. Tan, R. Amal, Y. H. Ng, Alternative strategies in improving the photocatalytic and photoelectrochemical activities of visible light-driven BiVO_4 : a review, *J. Mater. Chem. A* **5** (2017) 16498–16521.
- [105] S. Chandrasekaran, L. Yao, L. Deng, C. Bowen, Y. Zhang, S. Chen, Z. Lin, F. Peng, P. Zhang, Recent advances in metal sulfides: from controlled fabrication to electrocatalytic, photocatalytic and photoelectrochemical water splitting and beyond. *Chem. Soc. Rev.* **48** (2019) 4178–4280.
- [106] H. Cheng, B. Huang, Y. Dai, Engineering BiOX ($X = \text{Cl}, \text{Br}, \text{I}$) nanostructures for highly efficient photocatalytic applications. *Nanoscale* **6** (2014) 2009–2026.
- [107] A. P. Reverberi, P. S. Varbanov, M. Vocciante, B. Fabiano, Bismuth oxide-related photocatalysts in green nanotechnology: A critical analysis. *Front. Chem. Sci. Eng.* **12** (2018) 878–892.
- [108] M. Saiduzzaman, S. Yanagida, T. Takei, N. Kumada, K. Ogawa, C. Moriyoshi, Y. Kuroiwa, S. Kawaguchi, Crystal Structure, Thermal Behavior, and Photocatalytic Activity of $\text{NaBiO}_3 \cdot n\text{H}_2\text{O}$. *Inorg. Chem.* **57** (2018) 8903–8908.
- [109] X. Chang, G. Yu, J. Huang, Z. Li, S. Zhu, P. Yu, C. Cheng, S. Deng, G. Ji, Enhancement of photocatalytic activity over $\text{NaBiO}_3/\text{BiOCl}$ composite prepared by an in situ formation strategy. *Catal. Today* **153** (2010) 193–199.
- [110] S. Wang, L. Wang, W. Huang, Bismuth-based photocatalysts for solar energy conversion. *J. Mater. Chem. A.* **8** (2020) 24307–24352.
- [111] T. Zhao, A. Scholl, F. Zavaliche, K. Lee, M. Barry, A. Doran, M. P. Cruz, Y. H. Chu, C. Ederer, N. A. Spaldin, R. R. Das, D. M. Kim, S. H. Baek, C. B. Eom, R. Ramesh, Electrical control of antiferromagnetic domains in multiferroic BiFeO_3 films at room temperature. *Nat. Mater.* **5** (2006) 823–829.
- [112] S.-M. Lam, J.-C. Sin, A. R. Mohamed, A newly emerging visible light-responsive BiFeO_3 perovskite for photocatalytic applications: a mini review. *Mater. Res. Bull.* **90** (2017) 15–30.

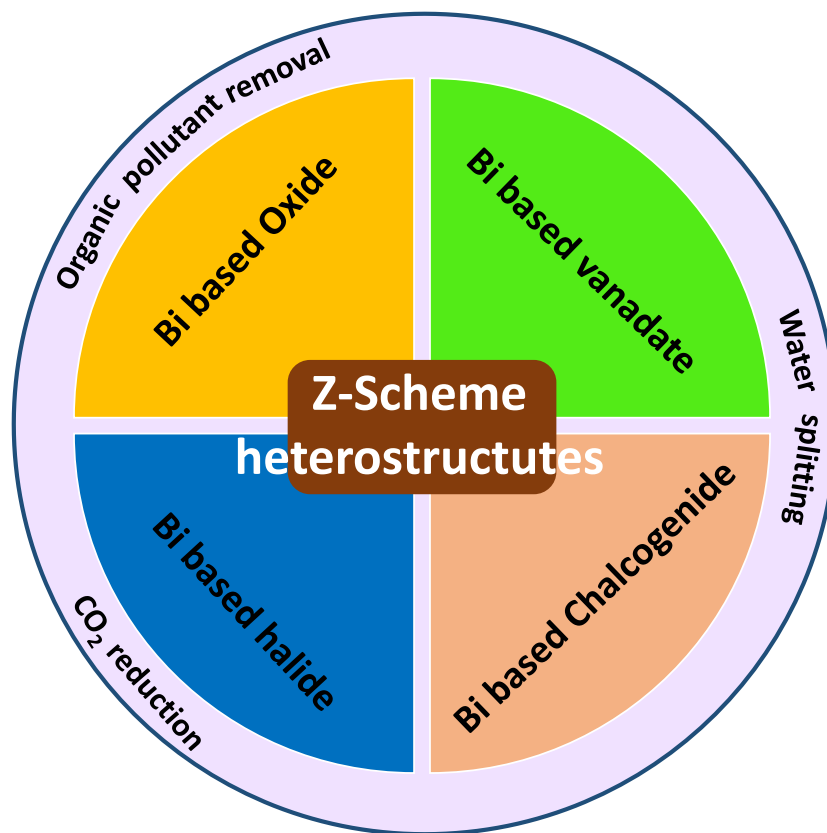
- [113] F. Gao, X. Y. Chen, K. B. Yin, S. Dong, Z. F. Ren, F. Yuan, T. Yu, Z. G. Zou, J.-M. Liu, Visible-Light Photocatalytic Properties of Weak Magnetic BiFeO₃ Nanoparticles. *Adv. Mater.* **19** (2007) 2889–2892.
- [114] R. Guo, L. Fang, W. Dong, F. Zheng, M. Shen, Enhanced Photocatalytic Activity and Ferromagnetism in Gd Doped BiFeO₃ Nanoparticles. *J. Phys. Chem. C* **114** (2010) 21390–21396.
- [115] T. Soltani, B.-K. Lee, Novel and facile synthesis of Ba-doped BiFeO₃ nanoparticles and enhancement of their magnetic and photocatalytic activities for complete degradation of benzene in aqueous solution. *J. Hazard. Mater.* **316** (2016) 122–133.
- [116] Y.-L. Huang, W. S. Chang, C. N. Van, H.-J. Liu, K.-A. Tsai, J.-W. Chen, H.-H. Kuo, W.-Y. Tzeng, Y.-C. Chen, C.-L. Wu, C.-W. Luo, Y.-J. Hsu, Y.-H. Chu, Tunable photoelectrochemical performance of Au/BiFeO₃ heterostructure. *Nanoscale* **8** (2016) 15795–15801.
- [117] S. J. A. Moniz, R. Quesada-Cabrera, C. S. Blackman, J. Tang, P. Southern, P. M. Weaver, C. J. Carmalt, A simple, low-cost CVD route to thin films of BiFeO₃ for efficient water photo-oxidation. *J. Mater. Chem. A* **2** (2014) 2922–2927.
- [118] J. H. Kim, H. E. Kim, J. H. Kim, J. S. Lee, Ferrites: emerging light absorbers for solar water splitting. *J. Mater. Chem. A* **8** (2020) 9447–9482.
- [119] A. Kudo, K. Ueda, H. Kato, I. Mikami, Photocatalytic O₂ evolution under visible light irradiation on BiVO₄ in aqueous AgNO₃ solution. *Catal. Letters* **53** (1998) 229–230.
- [120] H. L. Tan, R. Amal, Y. H. Ng, Alternative strategies in improving the photocatalytic and photoelectrochemical activities of visible light-driven BiVO₄: A review. *J. Mater. Chem. A* **5** (2017) 16498–16521.
- [121] Y. Park, K. J. McDonal, K.-S. Choi, Progress in bismuth vanadate photoanodes for use in solar water oxidation. *Chem. Soc. Rev.* **42** (2013) 2321–2337.
- [122] G. P. Nagabhushana, G. Nagaraju, G. T. Chandrappa, Synthesis of bismuth vanadate: its application in H₂ evolution and sunlight-driven photodegradation. *J. Mater. Chem. A* **1** (2013) 388–394.
- [123] T. Pandey, A. K. Singh, Simultaneous enhancement of electrical conductivity and thermopower in Bi₂S₃ under hydrostatic pressure. *J. Mater. Chem. C* **4** (2016) 1979–1987.

- [124] C. R. Rajamathi, U. Gupta, K. Pal, N. Kumar, H. Yang, Y. Sun, C. Shekhar, B. Yan, S. Parkin, U. V. Waghmare, C. Felser, C. N. R. Rao, Photochemical Water Splitting by Bismuth Chalcogenide Topological Insulators. *Chem. Phys. Chem.* **18** (2017) 2322–2327.
- [125] Y.-J. Lin, I. Khan, S. Saha, C.-C. Wu, S. R. Barman, F.-C. Kao, Z.-H. Lin, Thermocatalytic hydrogen peroxide generation and environmental disinfection by Bi₂Te₃ nanoplates. *Nat. Commun.* **12** (2021) 180–191.
- [126] D. S. Bhachu, S. J. A. Moniz, S. Sathasivam, D. O. Scanlon, A. Walsh, S. M. Bawaked, M. Mokhtar, A. Y. Obaid, I. P. Parkin, J. W. Tang, C. J. Carmalt, Bismuth oxyhalides: synthesis, structure and photoelectrochemical activity. *Chem. Sci.* **7** (2016) 4832–4841.
- [127] J. Jiang, K. Zhao, X. Y. Xiao, L. Z. Zhang, Synthesis and Facet-Dependent Photoreactivity of BiOCl Single-Crystalline Nanosheets. *J. Am. Chem. Soc.* **134** (2012) 4473–4476.
- [128] M. L. Guan, C. Xiao, J. Zhang, S. J. Fan, R. An, Q. M. Cheng, J. F. Xie, M. Zhou, B. J. Ye, Y. Xie, Vacancy Associates Promoting Solar-Driven Photocatalytic Activity of Ultrathin Bismuth Oxychloride Nanosheets. *J. Am. Chem. Soc.* **135** (2013) 10411–10417.
- [129] J. Di, J. Xia, H. Li, S. Guo, S. Dai, Bismuth oxyhalide layered materials for energy and environmental applications. *Nano Energy* **41** (2017) 172–192.
- [130] J. Li, Y. Yu, L. Z. Zhang, Bismuth oxyhalide nanomaterials: layered structures meet photocatalysis. *Nanoscale* **6** (2014) 8473–8488.
- [131] A. H. Zahid, Q. Han, A review on the preparation, microstructure, and photocatalytic performance of Bi₂O₃ in polymorphs. *Nanoscale* **13** (2021) 17687–17724.
- [132] Y. Wu, G. Lu, The roles of density-tunable surface oxygen vacancy over bouquet-like Bi₂O₃ in enhancing photocatalytic activity. *Phys. Chem. Chem. Phys.* **16** (2014) 4165–4175.
- [133] J. Yang, Z. Liu, Y. Wang, X. Tang, Construction of a rod-like Bi₂O₄ modified porous g-C₃N₄ nanosheets heterojunction photocatalyst for the degradation of tetracycline. *New J. Chem.* **44** (2020) 9725–9735.
- [134] X. Cao, X. Zhao, J. Hu, Z. Chen, First-principles investigation of the electronic properties of the Bi₂O₄(101)/BiVO₄(010) heterojunction towards more efficient solar water splitting. *Phys. Chem. Chem. Phys.* **22** (2020) 2449–2456.

- [135] D. Hou, X. Hu, P. Hu, W. Zhang, M. Zhang, Y. Huang, Bi₄Ti₃O₁₂ nanofibers/BiOI nanosheets p-n junction: facile synthesis and enhanced visible-light photocatalytic activity. *Nanoscale* **5** (2013) 9764–9772.
- [136] B. Li, Z. Cao, S. Wang, Q. Wei, Z. Shen, BiVO₄ quantum dot-decorated BiPO₄ nanorods 0D/1D heterojunction for enhanced visible-light-driven photocatalysis. *Dalton Trans.* **47** (2018) 10288–10298.
- [137] P. Longchin, S. Sakulsermsuk, K. Wetchakun, P. Kidkhunthod, N. Wetchakun, Roles of Mo dopant in Bi₂WO₆ for enhancing photocatalytic activities. *Dalton Trans.* **50** (2021) 12619–12629.
- [138] P. Zhu, Y. Chen, M. Duan, Z. Rena, M. Hu, Construction and mechanism of a highly efficient and stable Z-scheme Ag₃PO₄/reduced graphene oxide/Bi₂MoO₆ visible-light photocatalyst. *Catal. Sci. Technol.* **8** (2018) 3818–3832.
- [139] H. Zhang, X. Zhang, Z. Zhang, X. Ma, Y. Zhu, M. Ren, Y. Cao, P. Yang, Ultrahigh Charge Separation Achieved by Selective Growth of Bi₄O₅I₂ Nanoplates on Electron-Accumulating Facets of Bi₅O₇I Nanobelts. *ACS Appl. Mater. Interfaces* **13** (2021) 39985–40001.

CHAPTER 2

Genesis of the Thesis



2.1 Motivation

The motivation and objectives of this thesis can be described on the basis of literature survey on surface modification of semiconductor-based nanomaterials used for visible-light-active photocatalysis. A wide variety of semiconductors such as TiO_2 , ZnO , CdS , Fe_2O_3 , BiVO_4 , SrTiO_3 , WO_3 etc. have been reported as solar light harvesting photocatalysts [1-3]. Recently, Ag_3PO_4 , $\text{g-C}_3\text{N}_4$, conducting polymers, metal-organic framework (MOF) and Covalent Organic Framework (COF) based materials are used as photocatalyst [4-6]. However, TiO_2 has been considered as benchmark photocatalyst because of the advantages of low cost, high photoreactivity, environmentally friendly and good stability with time [7, 8]. Since the late 1990s, TiO_2 has been used for self-cleaning windows and roads, air purifiers in Japan, Spain, USA [7-10]. However, its application was restricted as it only responds to the UV light because of large bandgap (~ 3.2 eV). Therefore, much efforts have been devoted to make TiO_2 colorful through doping of metal and non-metal so that it can absorb longer wavelength lights of solar spectrum. Since the early 1990s, various metal ions incorporated in the TiO_2 lattice to replace the Ti^{4+} ions. At the same time, a series of nonmetal elements were used for replacing the O^{2-} ions of TiO_2 to make it capable for the absorption of visible-light [11, 12]. As mentioned in *chapter 1*, the thermodynamic water splitting potential is 1.23 eV, so in ideal case photocatalyst should absorb 1000 nm wavelength of solar spectrum, for which TiO_2 should be tuned to black ideally. In 2011, Chen et al. [13] demonstrated the hydrogenation method as a potential way to develop black colour TiO_2 and also lower the bandgap in the range of ~ 1.5 eV. This discovery of black colour TiO_2 was stimulated global attention on visible light driven photocatalysis. The existence of Ti^{3+} ions, structural disorder, oxygen vacancies, Ti-OH and Ti-H groups in black TiO_2 make it potential for H_2 generation. Black TiO_2 nanomaterials have unfolded new applications of fuel cells, Li-ion batteries, supercapacitor, photoelectrochemical sensors and microwave absorbers with promising prospect [13-17]. However, the efficiency for photocatalysis under visible light is still far from satisfactory. Further, Liu et al. [18] prepared red TiO_2 through B-N co-doping at high concentration within anatase TiO_2 microspheres. Consequently, red TiO_2 extended the light absorption edge up to ~ 700 nm and showed $\sim 0.8\%$ IPCE for photoelectrochemical water splitting. Further, a variety of approaches has been proposed to assist the photogenerated charge carrier separation and migration efficiency of TiO_2 by reducing electron-hole recombination rate. The mostly used strategies are (i) surface modification by depositing redox couple, (ii) use of co-

catalyst, (iii) coupling with other materials, (iv) formation of heterostructures, which are schematically presented in Figure 2.1.

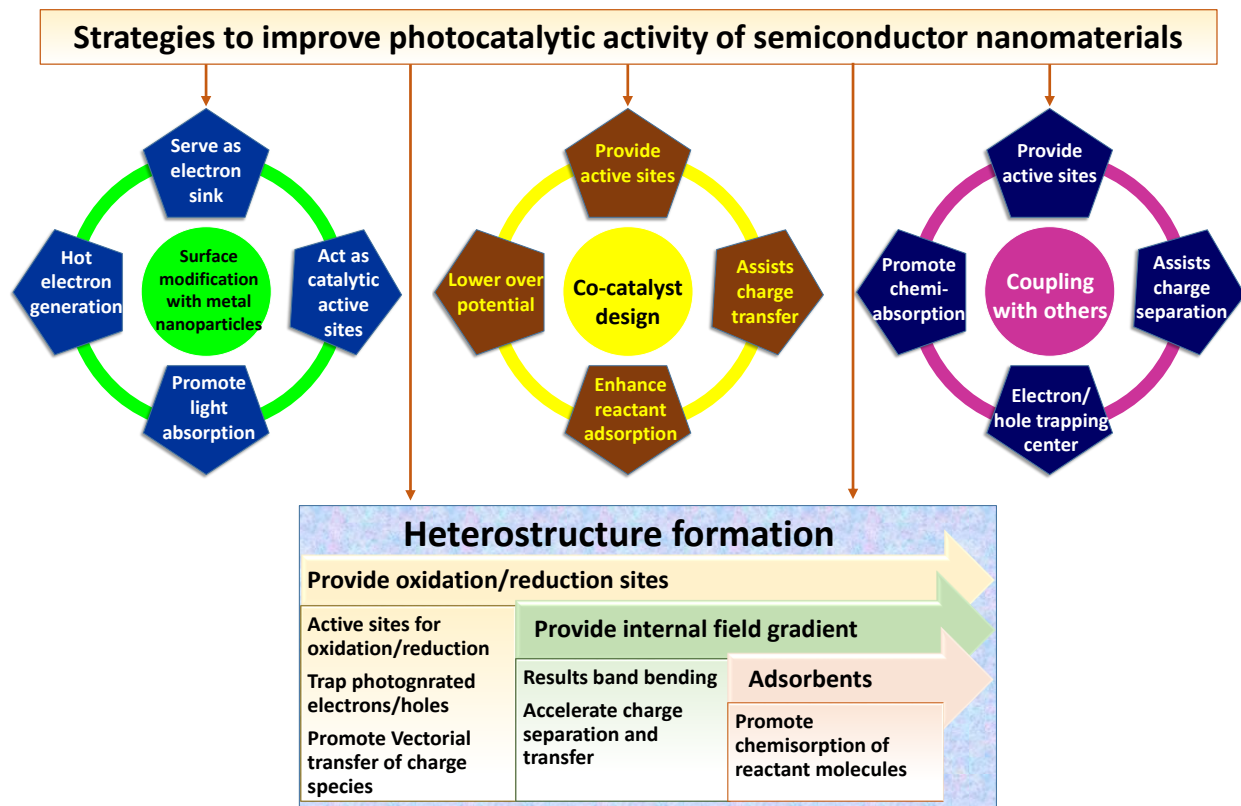


Figure 2.1 Various strategies for improvement of the photocatalytic activity of semiconductor nanomaterials.

Deposition of noble metal nanoparticles (Au Pt, Pd, Ag etc.) on the surface of semiconductor nanostructure showed a beneficial effect in the photocatalytic process due to hot electron generation by surface plasmon resonance effect (SPR) which provide high resistance to photo-corrosion and oxidation in moist air [19-21]. In addition, presence of a noble metal offers active catalytic sites to boosts the H₂ generation rate. For example, Zhang et al. [21] developed 5-12 nm Au and Pt nanomaterials decorated TiO₂ nanofibers which showed enhanced H₂ generation (12 μmol/g/h) and CO₂ reduction compared to bare TiO₂ (2.1 μmol/g/h). Co-catalyst modified TiO₂ have also reported as photocatalytic H₂ generation due to additional catalytic active sites [22, 23]. Coupling of TiO₂ with others semiconductor was also designed to extend the absorption range as well as electron-hole separation [24, 25]. On the other hand, the photocatalytic activity of semiconductor-based nanostructures is strongly related to their sizes and morphologies. The high specific surface area, hierarchical structure, hollow structures, low thickness may enhance the light

absorption capability of photocatalyst materials [26]. Optimizing the size of TiO₂ nanostructures, maximum efficiency may be achieved for photocatalysis due to high specific surface area [27]. Reported literatures showed that, various morphologies including nanotubes [28-30], nanofibers [31], nanorods [32, 33], foams [34] and mesoporous structures [35, 36] have larger surface area compared to the commercial TiO₂ nanoparticles (P25) (Figure 2.2).

On the other hand, two-dimensional (2D) TiO₂ nanostructures, such as nanoplates, nanosheets were explored to improve the specific surface area of TiO₂ photocatalyst. Based on the reported theoretical and experimental studies it has been proved that {001} face of anatase TiO₂ is more reactive compared to thermodynamically stable {101} facet [37]. For example, hierarchical sphere shaped TiO₂ with the 90% exposed {001} facets have been developed by Yang et al. [38] by solvothermal method which exhibited 7.51% energy conversion efficiency for dye-sensitized solar cells. Further, Hu et al. [39] prepared {001} facet exposed anatase TiO₂ nanosheets in large scale having high specific surface area (162.4 m² g⁻¹), exhibits two fold improved photodegradation activity for organic pollutant Rhodamine B (RhB) degradation than that of commercial TiO₂ (P25). Therefore, the available number of reaction sites and specific surface area both are crucial to optimize the photocatalytic activity.

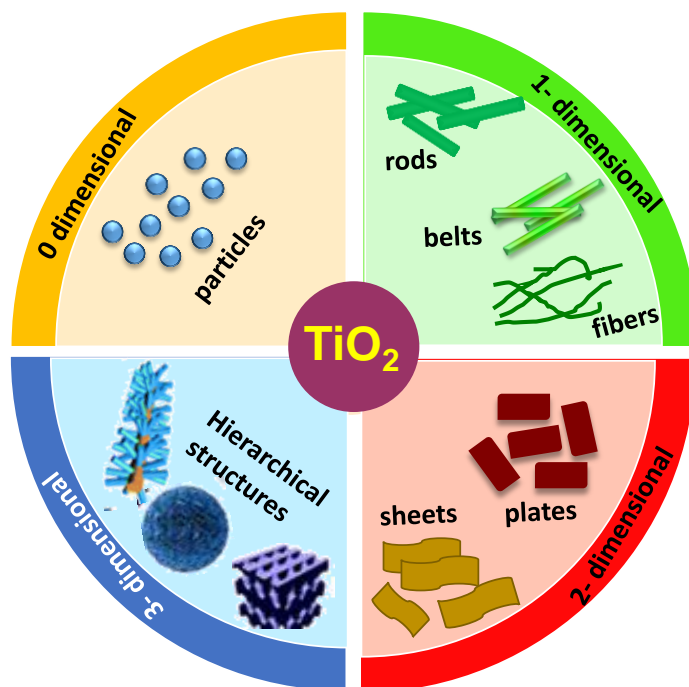


Figure 2.2 The schematic presentation of various TiO₂ nanostructures according to the structural dimensionality.

Three-dimensional (3D) TiO₂ structures have also reported as efficient catalyst for photocatalytic applications. For example, Zhang et al. [40] developed self-assembled TiO₂-ZrO₂ hollow spheres which exhibited significant catalytic activity both in organic pollutant removal and photocatalytic H₂ generation (23.7 μmol) because of prolonged lifetime of the electrons and improved light absorption. Recently, Rahman et al. [41] synthesized TiO₂ hollow spheres and modified the surface with Au nanoparticles and RuO₂ as co-catalyst to efficiently separate the excited electrons and holes. The dual co-catalyst modified TiO₂ showed two times and three higher H₂ generation rate (3165 μmol g⁻¹) compared to single co-catalyst loaded TiO₂ and bare TiO₂ (935 μmol g⁻¹). An interesting Au loaded hierarchical TiO₂ micro-flower was prepared by Duan et al. [42] *via* one-pot hydrothermal method which showed 1.3 folds enhanced photocurrent density than bare TiO₂ with ~25% IPCE efficiency at visible region. Therefore, morphology of a photocatalyst provides high surface to volume ratio with unique optical and carrier transfer properties [43, 44]. Core-shell structuring of TiO₂ is a potential approach for enhancing structural stability, unique optical properties, and high charge transfer efficiency of multi-functional photocatalysts [45]. The development of heterostructures between TiO₂ and other semiconductor have been attracted much attention as they can extend the absorption edge to the longer wavelengths. For example, heterostructures between TiO₂ nanofiber and SrTiO₃ nanocube resulted five times higher activity in photocatalytic H₂ generation (~1200 μmol) compare to bare TiO₂ nanofibers (~ 550 μmol) because of intimate contact and fast charge separation [46]. Further, Zhou et al. [47] reported high H₂ generation rate of 1.6 mmol/g/h using TiO₂/MoS₂ heterostructures as catalyst owing to strong adsorption capacity and high surface area. Up to now series of TiO₂-based binary, ternary, p-n junction, Schottky junction etc. have been developed and showed improved catalytic activity for organic pollutant removal from waste water, water splitting to generate renewable fuels, CO₂ reduction etc. due to combined advantages of excellent light trapping, large surface area for more reaction sites and rapid charge transfer [25, 48-50].

Recently, Z-scheme heterostructures based on TiO₂ have attracted research focus due to high photocatalytic efficiency and low recombination rate. In 2013, Yu et al. [51] first time demonstrated a direct Z-scheme charge transfer concept for TiO₂/g-C₃N₄ composites towards formaldehyde degradation under visible light illumination. Further, research has been explored on TiO₂-based Z-scheme photocatalysts for organic pollutant degradation [52], water oxidation and reduction [53], CO₂ capture and reduction [54], harmful gases decomposition [55] etc. As no redox

medium is required in direct Z-scheme system, it will be cost effective [56]. Despite these remarkable improvement of TiO₂-based heterostructures in photocatalytic activity, there are some significant limitations. For example, moderate reaction rate during decontamination of heavily polluted industrial elements [57, 58], limited light absorption and photon flux (< 6% of impinged solar energy on Earth's surface) restrict its prospective to develop a sustainable technology [59, 60]. This fact has triggered the research interest to develop narrow bandgap semiconductor nanostructures which are alternatives to TiO₂. These materials are not derived from TiO₂ and completely different materials with distinct composition. In this context, various novel photoactive semiconductors, such as transition metal (Nb, V, Ta) based mixed oxides, or main group elements of Ga, In, Sb or Bi-based oxides have been prepared as the substitutes of TiO₂ in the last few years [61]. In addition, metal nitrides and sulfides are synthesized to obtain photocatalytic activity under visible light.

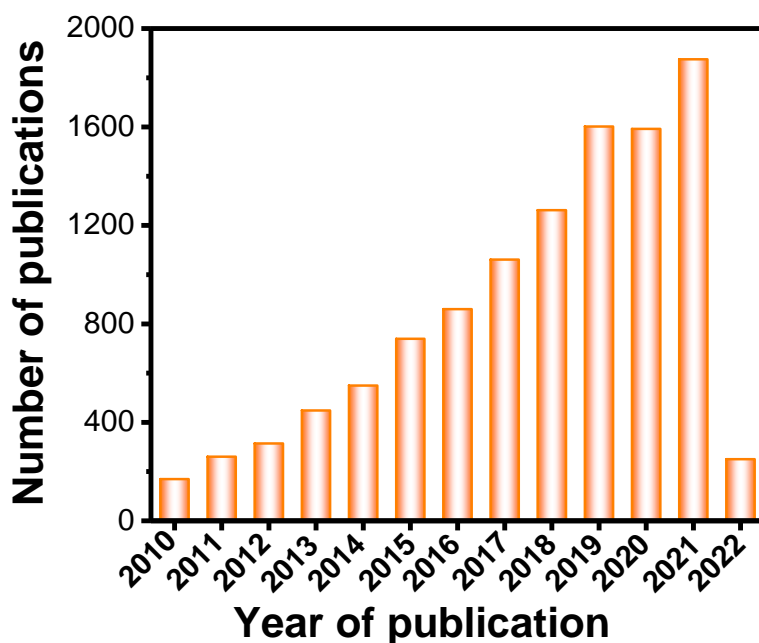


Figure 2.3 The number of publications reported on Bismuth based semiconductor materials as photocatalyst during the last decade [source: web of science; date: 5th April 2022; key word: Bi-based photocatalysis].

In this thesis, development of visible light active Bi-based semiconductor heterostructures are focused for organic pollutant degradation and H₂ generation through water spitting. Owing to many interesting physicochemical and electrochemical properties Bi-Based semiconductors are gaining research interest in photocatalysis and rapidly increasing publications (Figure 2.3). As most of the

Bi-based semiconductors are narrow bandgap, thus development of heterostructures is an effective way to hinder the fast electron-hole recombination rate. In the following section, Bi-based Type II, p-n heterojunction and Z-scheme heterostructures are summarized.

2.1.1 Type-II heterostructures using Bi-based semiconductors

The Type-II heterostructures has been considered as conventional heterojunction as both of excited electrons and holes are transferred in two different semiconductors and reduce the electron-hole recombination rate. For example, Zhu et al. [62] reported $\text{Bi}_4\text{Ti}_3\text{O}_{12}/\text{CeO}_2$ composite for the degradation of organic pollutant BPA, where enhanced catalytic activity towards reaction rate achieved than bare $\text{Bi}_4\text{Ti}_3\text{O}_{12}$. Fan and his co-workers [63] constructed $\text{Bi}_2\text{MoO}_6/\text{BiOI}$ heterojunction using an anion exchange method where 50% ratio of Mo/I exhibited best performance for organic pollutant rhodamine B (RhB) degradation upon visible light illumination due to development of type II heterojunction. The Type-II charge transfer mechanism has also been reported for ZnO/BiOI [64], ZnO/BiVO_4 [65], $\text{CuS}/\text{BiFeO}_3$ [66], $\text{Bi}_2\text{S}_3/\text{BiFeO}_3$ [67], $\text{BiVO}_4/\text{Bi}_2\text{S}_3$ [68], $\text{In}_2\text{S}_3/\text{Bi}_2\text{MoO}_6$ [69], $\text{Bi}_2\text{MoO}_6/\text{BiOBr}$ [70], $\text{NaNbO}_3/\text{Bi}_2\text{MoO}_6$ [71], $\text{BiOCl}/\text{BiOBr}$ [72] heterostructures for various photocatalytic applications. Zhu et al. [73] fabricated $\text{BiFeO}_3/\text{TiO}_2$ nanotube arrays and showed 100% photoelectrocatalytic degradation of RhB at 150 min because of the synergistic effects of applied bias, wider spectral response and reduced recombination rate. An effective Type-II charge separation between Bi_2WO_6 QDs (quantum dots) and reduced graphene oxide resulted eight times higher photodegradation efficiency than that of pure Bi_2WO_6 QDs [74]. Interestingly, Type-II $\text{Bi}_2\text{WO}_6/\text{TiO}_2$ heterostructures showed 100% methyl orange (MO) degradation within 25 min and 40 min under UV and Vis light, respectively. In addition, 74.3% degradation efficiency at 120 min under NIR irradiation. The superior catalytic activity of $\text{Bi}_2\text{WO}_6/\text{TiO}_2$ heterostructures achieved due to large number of catalytic active sites and specific surface area [75]. Bi-based Type-II heterostructures are also showed promising performance for photoelectrochemical water splitting and H_2 generation. For example, Liu et al. [76] prepared Bi_2S_3 sensitized WO_3 nanoplate array which showed eight fold enhanced photocurrent density ($\sim 12 \text{ mA}/\text{cm}^2$) than single semiconductor WO_3 along with 70% IPCE (incident photon to current conversion efficiency). The enhanced activity resulted due to intimate interfacial contact, facile electron-hole separation and migration to the surface. Shi et al. [77] fabricated BiVO_4 -decorated WO_3 helix nanostructures which showed

maximum photocurrent density of $\sim 35 \text{ mA/cm}^2$ at 1.23V vs RHE with H_2 and O_2 generation of $180 \text{ }\mu\text{mol/cm}^2$ and $85 \text{ }\mu\text{mol/cm}^2$, respectively under simulated solar light illumination. Further, an efficient and stable photoanode of $\text{Bi}_2\text{S}_3/\text{WO}_3$ heterojunction was prepared by He et al. [78], which resulted 40% higher photocurrent density (1.33 mA/cm^2) compared to bare WO_3 film in 0.1 M Na_2SO_4 electrolyte. On the other hand, $\text{Bi}_2\text{WO}_6/\text{BiVO}_4$ composite displayed 99.99% photocatalytic activity towards *Pseudomonas aeruginosa*, *Escherichia coli* and *Staphylococcus aureus* bacteria killing within 30 min [79]. Moreover, Bi-based ternary heterojunctions have been developed where double Type-II charge transfer mechanism are reported [80]. For example, Huang et al. [81] prepared a tri-junction of $\text{Bi}_2\text{S}_3/\text{Bi}_2\text{O}_3/\text{Bi}_2\text{O}_2\text{CO}_3$ photocatalyst which showed improved catalytic activity due to formation of double Type-II interface. Up to now numerous combinations of Bi-based conventional Type II heterostructures have been reported for organic pollutant degradation, solar fuel generation, CO_2 reduction etc. which are shown in Table 2.1. However, Type-II heterostructures have some limitation in redox capacity as the photogenerated charge carriers are migrated from higher potential to lower potential.

2.1.2 Bi-based p-n heterojunctions

Bismuth based p-n heterojunctions have attracted attention in photocatalysis owing to internal field gradient that may generate at the junction interface of two semiconductor and facilitate the electron-hole separation [82]. For example, Wang et al. [83] prepared a p-n heterojunction between AgBr and Bi_2WO_6 which showed 99% photodegradation efficiency for organic pollutant MB at 60 min under visible light irradiation because of the efficient electron-hole separation by the influence of internal potential gradient. Further, Ag_3PO_4 nanoparticle decorated rose like Bi_2WO_6 p-n heterojunction exhibited ten times increased activity for the removal of RhB than pure Bi_2WO_6 under simulated sunlight irradiation. The enhanced photocatalytic activity achieved due to efficient separation and migration of excited charge carriers [84]. Similarly, p-n heterojunction of $\text{BiOCl}/\text{BiVO}_4$ exhibited improved MO degradation rate compared to pure BiOCl , BiVO_4 and P25 because of improved charge transfer and strong oxidative ability [85]. Very recently, Parida et al. [86] developed an efficient p-n heterojunction between BiVO_4 and B- doped g- C_3N_4 which showed 4.2 times higher photocatalytic O_2 generation rate ($\sim 1350 \text{ }\mu\text{mol/g/h}$) compared to bare BiVO_4 due to the built in electrostatic field at the junction of two semiconductors. An n-n

heterojunction of $\text{Bi}_{3.64}\text{Mo}_{0.36}\text{O}_{6.55}/\text{Bi}_2\text{MoO}_6$ was reported for efficient organic pollutant degradation because of superior hole migration through the junction interface [87].

2.1.3 Bi-base Z-scheme heterojunctions

Recently, Z-scheme charge transfer mechanism is gaining much research interest as it can hold the redox capacity of excited electrons and holes [88, 89]. For example, $\text{BiFeO}_3/\text{Bi}_2\text{Fe}_4\text{O}_9$ heterojunctions exhibited improved photocatalytic H_2 generation ($\sim 800 \mu\text{mol/g}$), which is 2.0 fold and 2.7 fold higher than $\text{Bi}_2\text{Fe}_4\text{O}_9$ and BiFeO_3 . The enhanced activity achieved due to highly negative redox potential of excited electrons w.r.t. water reduction potential and low recombination of photogenerated charge carriers. [90]. Very recently, Mansour et al. [91] fabricated a Z-scheme heterojunction of $\text{Pt-BiVO}_4/\text{TiO}_2$ which showed highest H_2 generation of $\sim 160 \mu\text{mol}$, almost 100 times higher than pristine $\text{BiVO}_4/\text{TiO}_2$ composite. The Pt acted as migration-bridge between BiVO_4 and TiO_2 and the excited CB electrons of TiO_2 involved in H^+ reduction to form H_2 . Similarly, an all-solid-state Z-scheme of $\text{AgBr-Ag-Bi}_2\text{WO}_6$ was developed by Zhang et al. [92] for azo dye degradation, where Ag nanoparticles acted as charge migration-bridge for better electron-hole separation. Chen et al. [93] studied the effect of mass ratio in Z-scheme Bi_2WO_6 QDs/g- C_3N_4 system for the photodegradation of RhB and reported that higher amounts of g- C_3N_4 loading lower the photocatalytic activity. Further, an organic-inorganic hybrid photocatalytic system of $\text{BiVO}_4/\text{g-C}_3\text{N}_4$ exhibited significantly enhanced photocatalytic activity for RhB degradation and photocurrent generation due to the direct Z-scheme electron-hole transfer pathway, which provides much more powerful oxidation potential and reduction capability [94]. Recently, Z-scheme $\text{Bi}_2\text{WO}_6\text{-Cu}_3\text{P}$ photocatalytic system showed efficient H_2 ($\sim 10 \mu\text{mol/gcatalyst}$) and O_2 ($\sim 5 \mu\text{mol/gcatalyst}$) generation through water splitting under visible light irradiation without using any co-catalyst [95]. All solid-state Z-scheme heterostructures of Bi- BiOCl/AgCl showed both photocatalytic H_2 generation ($\sim 198.2 \mu\text{mol/h}$) and photoelectrochemical water splitting (photocurrent density $45 \mu\text{A/cm}^2$) due to the enhanced optical absorption, low recombination rate and suitable oxidation and reduction potential of holes and electrons, respectively [96]. A maximum $\sim 323 \mu\text{mol/h}$ O_2 evolution rate was reported for Z-scheme CeO_2/BiOI heterostructures because of excess oxygen vacancy and advanced charge transfer pathway [97].

Table 2.1 Reported Bi-based conventional and Z-scheme heterostructures, their synthesis methods and the photocatalytic applications.

| Bi-based semiconductor | Coupled material | Synthesis method | Application | Reference |
|---|---------------------------------|--|--|-----------|
| <i>Conventional Type II heterostructures</i> | | | | |
| Bi ₂ O ₃ | TiO ₂ | Hydrothermal followed by calcination | Methylene Blue (MB) degradation | 98 |
| Bi ₂ O ₃ | FeVO ₄ | Grinding followed by calcination | Malachite green decomposition | 99 |
| Bi ₂ O ₃ | g-C ₃ N ₄ | Solid state mixing followed by calcination | Rhodamine B (RhB) degradation | 100 |
| Bi ₂ O ₃ | g-C ₃ N ₄ | In-situ method | RhB degradation | 101 |
| Bi ₂ S ₃ | Pd ₄ S | Thermal reduction followed by exchange of cation | Atrazine degradation | 102 |
| Bi ₂ S ₃ | ZnS | Solvothermal | Photocatalytic H ₂ generation | 103 |
| Bi ₂ S ₃ | ZnS | Cation exchange | MB degradation | 104 |
| Bi ₂ Ti ₂ O ₇ | TiO ₂ | Hydrothermal | RhB degradation | 105 |
| Bi ₄ Ti ₃ O ₁₂ | g-C ₃ N ₄ | Ball milling method | Acid orange II degradation | 106 |
| Bi ₄ Ti ₃ O ₁₂ | CeO ₂ | Molten salt and ion impregnation | Bisphenol-A degradation | 62 |
| Bi ₁₂ TiO ₂₀ | g-C ₃ N ₄ | Hydrothermal | Gaseous HCHO decomposition | 107 |
| Bi ₂ O ₂ CO ₃ | CdS | Reflux | MB degradation | 109 |
| Bi ₂ O ₂ CO ₃ | g-C ₃ N ₄ | Solid state mixing and calcination | Methyl Orange (MO) and Dibutyl phthalate degradation | 108 |

| Bi-based semiconductor | Coupled material | Synthesis method | Application | Reference |
|--|---------------------------------|---|---|------------------|
| Bi ₂ O ₂ CO ₃ | Ag ₃ PO ₄ | Hydrothermal followed by precipitation | RhB degradation | 110 |
| BiFeO ₃ | CuO | Hydrothermal followed by impregnation | MO degradation | 111 |
| BiFeO ₃ | g-C ₃ N ₄ | Hydrothermal | Organic compound guaiacol decomposition | 112 |
| Bi ₂ Sn ₂ O ₇ | In ₂ O ₃ | Method of impregnation | RhB degradation | 113 |
| BiOCCOOH | Ag ₂ O | Solvothermal followed by co-precipitation | p-chlorophenol and RhB degradation | 114 |
| BiVO ₄ | TiO ₂ | Hydrothermal | Removal of brilliant red X-3B | 115 |
| BiVO ₄ | ZnO | Mixing and annealing | RhB degradation | 116 |
| BiVO ₄ | SnO ₂ | Hydrothermal | MB degradation | 117 |
| BiVO ₄ | CeO ₂ | Co-precipitation and subsequent annealing | RhB degradation | 118 |
| BiVO ₄ | Ag ₂ O | Impregnation and evaporation | MO degradation | 119 |
| BiVO ₄ | Co ₃ O ₄ | Drop-casting followed by calcination | Water oxidation | 120 |
| BiVO ₄ | g-C ₃ N ₄ | Ultrasonication | CO ₂ reduction | 121 |
| BiVO ₄ | PEDOT | Electrodeposition | PEC water splitting | 122 |

| Bi-based semiconductor | Coupled material | Synthesis method | Application | Reference |
|--|----------------------------------|---|--|------------------|
| Bi ₂ WO ₆ | TiO ₂ | Hydrothermal | Phenol and RhB degradation | 123 |
| Bi ₂ WO ₆ | TiO ₂ | Hydrothermal | MO and RhB degradation | 124 |
| (01) plane Bi ₂ WO ₆ | (01) plane TiO ₂ | Hydrothermal | MB degradation | 125 |
| Bi ₂ WO ₆ | α-Fe ₂ O ₃ | Electrospinning followed by sintering | RhB degradation | 126 |
| Bi ₂ WO ₆ | WO ₃ | Hydrothermal | RhB degradation | 127 |
| Bi ₂ WO ₆ | Ag ₂ O | Chemical precipitation | RhB degradation | 128 |
| Bi ₂ WO ₆ | AgCl | Hydrothermal | RhB degradation | 129 |
| Bi ₂ WO ₆ | CeO ₂ | Hydrothermal | RhB degradation | 130 |
| Bi ₂ WO ₆ | ZnS and CdS | Method of surface functionalization | RhB degradation | 131 |
| Bi ₂ MoO ₆ | TiO ₂ | Solvothermal | Nitrobenzene and phenol degradation | 132 |
| Bi ₂ MoO ₆ | Ag ₃ VO ₄ | Hydrothermal followed by precipitation | RhB degradation | 133 |
| Bi ₂ MoO ₆ | MoO ₃ | Hydrothermal | Photoanode in PEC water splitting | 134 |
| Bi ₂ MoO ₆ | MoO ₃ | Chemical vapor deposition | Glycerol oxidation and photocatalytic O ₂ evolution | 135 |
| Bi ₂ MoO ₆ | g-C ₃ N ₄ | Chemisorption followed by thermal treatment | RhB degradation | 136 |

| Bi-based semiconductor | Coupled material | Synthesis method | Application | Reference |
|----------------------------------|--|--|---|------------------|
| Bi ₂ MoO ₆ | AgI | Co-precipitation | BPA and RhB degradation | 137 |
| Bi ₂ MoO ₆ | AgBr | Co-precipitation | RhB degradation | 138 |
| Bi ₂ SiO ₅ | AgI | Co-precipitation | Gaseous HCHO and Acid red G decomposition | 139 |
| BiOCl | TiO ₂ | Solvothermal | Benzene degradation | 140 |
| BiOCl | CuS | Hydrothermal | RhB degradation | 141 |
| BiOCl | g-C ₃ N ₄ | Solvothermal | RhB degradation | 142 |
| BiOBr | La ₂ Ti ₂ O ₇ | Refluxed in oil bath | RhB degradation | 143 |
| BiOBr | CeO ₂ | Co-precipitation | RhB degradation | 144 |
| BiOBr | CoFe ₂ O ₄ | Solvothermal | Congo red degradation | 145 |
| BiOBr | CdWO ₄ | Hydrothermal followed by precipitation | RhB degradation | 146 |
| BiOBr | Ag ₃ PO ₄ | Co-precipitation | RhB degradation | 147 |
| BiOBr | N doped graphene | Wet chemical method | Chlorpyrifos detection | 148 |
| BiOI | TiO ₂ | Successive ionic layer adsorption and reaction | MO degradation | 149 |
| BiOI | TiO ₂ nanotube | Impregnating-hydroxylation | MO degradation | 150 |
| BiOI | La(OH) ₃ | Chemical impregnation | NO removal | 151 |

| Bi-based semiconductor | Coupled material | Synthesis method | Application | Reference |
|---|---|---|------------------------------------|------------------|
| BiOI | Fe ₂ O ₃ | In situ hydrolysis | RhB degradation | 152 |
| BiOX (X = Cl, Br, I) | AgX (X = Cl, Br and I) | Co-precipitation | RhB degradation | 153 |
| Bi ₄ O ₅ I ₂ | g-C ₃ N ₄ | Solvothermal | RhB and endocrine degradation | 154 |
| <i>Heterostructures between two Bi-based semiconductors</i> | | | | |
| α -Bi ₂ O ₃ | β -Bi ₂ O ₃ | In situ phase transformation by calcination | RhB degradation | 155 |
| α -Bi ₂ O ₃ | β -Bi ₂ O ₃ | Solid-state reaction | RhB and indigo carmine degradation | 156 |
| Bi ₂ O ₃ | Bi ₂ S ₃ | Hydrothermal | RhB degradation | 157 |
| Bi ₂ O ₃ QDs | BiVO ₄ | Heat treatment | RhB degradation | 158 |
| Bi ₂ O ₃ | BiVO ₄ | Hydrothermal | RhB degradation | 159 |
| Bi ₂ O ₃ | BiOCl | Alkaline treatment | MO degradation | 160 |
| β -Bi ₂ O ₃ | BiOI | In situ reaction | MO degradation | 161 |
| Bi ₂ O ₃ | Bi ₂ WO ₆ | Solid-state reaction | RhB degradation | 162 |
| Bi ₂ O ₃ | Bi ₅ O ₇ I | Chemical etching | Malachite green degradation | 163 |
| Bi ₂ O ₄ | BiOBr | Alkali posttreatment assisted light irradiation | MO degradation | 164 |
| Bi ₂ S ₃ | Bi ₄ Ti ₃ O ₁₂ | nanofibers In situ ion exchange | RhB degradation | 165 |
| Bi ₂ S ₃ | Bi ₂ WO ₆ | Hydrothermal | Cr(VI) reduction | 166 |
| Bi ₂ S ₃ | Bi ₂ WO ₆ | Anion exchange | RhB degradation | 167 |

| Bi-based semiconductor | Coupled material | Synthesis method | Application | Reference |
|---|---|--------------------------------|---------------------------------------|------------------|
| Bi ₂ S ₃ | Bi ₂ O ₂ CO ₃ | One-pot room temperature route | RhB degradation | 168 |
| Bi ₂ S ₃ | Bi ₂ O ₂ CO ₃ | Anion exchange | Gaseous NO removal | 169 |
| Bi ₂ S ₃ | BiOCl | Solvothermal | Salicylic acid, RhB degradation | 170 |
| Bi ₁₂ TiO ₂₀ | Bi ₂ WO ₆ | Hydrothermal | RhB degradation | 171 |
| Bi ₂ Ti ₂ O ₇ | Bi ₄ Ti ₃ O ₁₂ | One-step molten salt method | RhB and MO degradation | 172 |
| Bi ₂ O ₂ CO ₃ | BiVO ₄ | Hydrothermal | RhB degradation | 173 |
| Bi ₂ O ₂ CO ₃ | BiOI | Pore impregnation | RhB degradation | 174 |
| Bi ₂ MoO ₆ | BiVO ₄ | Spin-coating | Photoelectrode in PEC water splitting | 175 |
| Bi ₂ MoO ₆ | BiPO ₄ | Hydrothermal | RhB degradation | 176 |
| Bi _{3.64} Mo _{0.36} O _{6.55} | Bi ₂ MoO ₆ | Hydrothermal | RhB degradation | 87 |
| Bi ₂ W _x Mo _{1-x} O ₆ | BiOCl | Solvothermal | RhB degradation | 177 |
| BiPO ₄ | BiOBr | Mixing method | Gaseous o-dichlorobenzene degradation | 179 |
| Monoclinic BiVO ₄ | Tetragonal BiVO ₄ | Hydrothermal | RhB degradation | 179 |
| Bi ₂ MoO ₆ | BiOI | Hydrothermal | RhB degradation | 63 |
| BiOI | BiVO ₄ | Co-precipitation | Pseudomonas aeruginosa degradation | 180 |

| Bi-based semiconductor | Coupled material | Synthesis method | Application | Reference |
|---|--|---|--|------------------|
| BiOI | BiVO ₄ | Co-precipitation | MO degradation | 181 |
| BiOI | Bi ₂ MoO ₆ | Co-precipitation | BPA degradation | 182 |
| Bi ₂₄ O ₃₁ Cl ₁₀ | BiOCl | Phase transformation by annealing | Benzyl alcohol conversion | 183 |
| BiOCl | Bi ₁₂ O ₁₇ C ₁₂ | Hydrothermal | MO degradation | 184 |
| BiOCl | BiVO ₄ | Co-precipitation | RhB degradation | 185 |
| Bi ₄ O ₅ I ₂ | Bi ₅ O ₇ I | Hydrothermal | Propylparaben degradation | 186 |
| Bi ₄ O ₅ I ₂ | Bi ₅ O ₇ I | In situ phase transformation | RhB and BPA degradation | 187 |
| Ternary Heterostructure | | | | |
| Bi ₂ O ₃ /Bi ₂ S ₃ | MoS ₂ | Hydrothermal | MB degradation and photocatalytic O ₂ evolution | 80 |
| Bi ₇ O ₉ I ₃ | AgI/AgIO ₃ | Chemical deposition | MO and gaseous NO removal | 188 |
| BiOI–Bi ₂ O ₃ | AgI | Etching-deposition | Cr(VI) reduction | 189 |
| Bi ₂ S ₃ /Bi ₂ O ₃ | Bi ₂ O ₂ CO ₃ | Heat treatment followed by ion exchange | HCHO, MO, and phenol degradation | 81 |
| Bi ₇ O ₉ I ₃ /Bi ₅ O ₇ I | g-C ₃ N ₄ | Hydrothermal | Crystal violet | 190 |
| BiOCl _x /BiOBr _y | BiOI _z | Electrospinning followed by sol–gel | Trichloroethylene degradation | 191 |
| BiOBr/Co(OH) ₂ | PVP | Solvothermal | MO degradation | 192 |

| Bi-based semiconductor | Coupled material | Synthesis method | Application | Reference |
|--|---|--|---|-----------|
| Z-Scheme heterostructure | | | | |
| Bi ₂ O ₃ | g-C ₃ N ₄ | Ball milling and heat treatment | MB degradation | 193 |
| Bi ₂ O ₃ | NaNbO ₃ | Ball milling method | RhB degradation | 194 |
| BiVO ₄ | SiC | Co-precipitation followed by calcination | Photocatalytic O ₂ evolution | 295 |
| BiVO ₄ | Se film | Chemical vapor deposition | PEC water splitting | 196 |
| BiPO ₄ | Bi ₂ O ₂ | Hydrothermal | Dichlorophenol degradation | 197 |
| Bi ₂ WO ₆ | MoS ₂ | Hydrothermal method | RhB degradation | 198 |
| Bi ₂ MoO ₆ | Co ₃ O ₄ , CuO, NiO | Co-precipitation | RhB degradation | 199 |
| Bi ₂ MoO ₆ | g-C ₃ N ₄ | Hydrothermal | MB degradation | 200 |
| Bi ₂ Sn ₂ O ₇ | g-C ₃ N ₄ | High-temperature solid-state reaction | MB and acid red 18 degradation | 201 |
| BiOI | CdS | Hydrothermal | RhB degradation | 202 |
| BiOIO ₃ | g-C ₃ N ₄ | Hydrothermal | MO, RhB, and dichlorophenol degradation | 203 |
| BiOBr | g-C ₃ N ₄ | Reflux process | RhB and BPA degradation | 204 |
| BiOBr | Bi ₂ MoO ₆ | Two-step co-precipitation | RhB and CIP degradation | 205 |
| BiO _{1-x} Br | Bi ₂ O ₂ CO ₃ | Solvothermal | CIP degradation | 206 |
| BiVO ₄ | ZnIn ₂ S ₄ /g-C ₃ N ₄ | Impregnation and calcination | Congo red and metronidazole degradation | 207 |
| BiOI | MoS ₂ /AgI | Co-precipitation | RhB degradation | 208 |

2.2 Scope of the Thesis

There are many research challenges that remain to be addressed in the field of photocatalytic H₂ generation and PEC water splitting. For practical implementation, efficient, durable, economic and scalable photocatalytic system need to develop. The development of visible light active, efficient, non-toxic, low cost photocatalyst remains a significant challenge. Highly active photocatalyst is required to achieve the maximum solar to fuel conversion efficiency. The bandgap and band edge potentials should be tunable to design flexible devices. In case of PEC water splitting, Pt and Ir have been considered as best HER and OER catalyst, respectively, both of which are expensive, thus many efforts have been required to replace them with earth abundant materials. In this thesis work, low cost Bi-based materials would be developed as efficient photoanode material for PEC water splitting and catalyst for photocatalytic H₂ generation.

To design a stable and efficient photocatalyst for solar energy harvest, conversion and storage, first of all, the semiconductor must have a bandgap (E_g) > 1.23 eV to provide energetic electrons. At the same time, the semiconductor must have the potential to absorb visible light, for which E_g should be less than 3.0 eV. Furthermore, there must be a potential to efficiently drive electron-hole pair separation and the migration process. As single material cannot fulfill all these stringent requirements as ideal solar energy converters, coupling of two or more than two materials as heterostructures is an effective strategy to increase charge separation efficiency and lowering the fast recombination rate by allowing multiple active sites and thereby improve their solar light harvesting efficiency [209, 210]. In a heterostructures, lower bandgap semiconductor can be combined with high bandgap semiconductors (conventional Type-II, Z-scheme etc.), p-n heterojunction or the Schottky junction between metal-semiconductor interface with inbuilt potential gradient can be created or co-catalysts may present, which effectively direct excited electrons and photoinduced holes separation and migration through the junction interface [216].

The corrosion protection or the lowering of photobleaching effect of semiconductor photocatalyst is another critical challenge. Metal chalcogenides are generally suffer from the photobleaching effect under long time light irradiation [211, 212]. The development of heterostructures by in-situ methods may improve the inherent stability against photobleaching effect which are described in chapter 4 to 7.

2.3 Objectives

The overall objective of thesis is to prepare visible light active photocatalysts with enhanced quantum efficiency, toward the generation of clean and renewable solar fuels such as H₂. A facile hydrothermal method would be developed to synthesize Bi-based semiconductors and different strategies for the fabrication of semiconductor-based heterostructures. The photocatalytic activity would be examined through water splitting with the optimization of reaction parameters. The overall objective of this research work is to design, synthesize, and characterize visible light-active heterostructured photocatalysts to maximize the use of solar irradiation. The scope of this work can be summarized as follows:

- Synthesis of Bismuth based stable, low bandgap semiconductors through facile hydrothermal method.
- Design and synthesize different semiconductor-based heterostructures, for example conventional Type-II, p-n heterojunction, Schottky junction, direct and indirect Z-scheme heterostructures by in-situ method.
- Characterize the semiconductor nanostructure and the heterostructures by various structural, microscopic, optical and electrochemical techniques.
- Determination of photocatalytic performance of the heterostructured photocatalysts by organic pollutant degradation, photocatalytic H₂ generation and PEC water splitting.
- Propose possible mechanisms for the observed enhanced activity of different heterostructures and experimentally demonstrate their validity.

2.4 The Main Features of the Thesis

- Development of low cost, visible light active photocatalysts.
- Introduction of perovskite semiconductors as catalyst for solar water splitting.
- Formation of heterostructures to get better catalytic efficiency in dye degradation, H₂ generation and PEC water splitting.
- Synthesis of various kind of heterostructures and understanding their mechanism for photocatalytic activity
- Introduction of Z-scheme heterostructures, a new kind of concept for photocatalytic applications.
- Study of photochemical and photoelectrochemical properties of heterostructures.

- Mechanism developed for effective control over:
 - Particle size
 - Morphology
 - Porosity
 - Tunability of bandgap
 - Charge separation ability

2.5 Research Focus

Primarily, the focused of this work was to develop bismuth based low bandgap semiconductors and use it in organic pollutant degradation under visible light. Therefore, the simplest candidate of bismuth family, bismuth sulfide (Bi_2S_3) was focused as its bandgap is very low, nearly 1.3 eV. One dimensional rod like morphology of Bi_2S_3 has been prepared by hydrothermal method. However, it showed photocatalytic activity in organic pollutant degradation under visible light irradiation, catalytic efficiency is not high enough (only 26 %) because of rapid electron-hole pair recombination. To overcome this problem, Bi_2S_3 has been integrated with large bandgap semiconductor zinc oxide (ZnO) to fabricate heterostructures and successfully, 82% photocatalytic activity has been achieved. Furthermore, the $\text{Bi}_2\text{S}_3/\text{ZnO}$ heterostructures has been used in photocatalytic hydrogen generation using methanol as sacrificial agent under visible light. This Type-II heterojunction exhibits 2.7 fold enhancement in hydrogen generation compared to rod-shaped bare Bi_2S_3 . Therefore, heterostructures strategy can offers several potential benefits in photocatalysis like, charge carrier generation, separation and transportation through the junction. This approach may also be applicable for other semiconductor heterostructures.

Next, we focused to introduce bismuth based perovskite oxide materials in photocatalytic water splitting process for renewable fuel H_2 generation. In this contest, perovskite semiconductor, bismuth ferrite (BiFeO_3) would be an interesting material as its bandgap is narrow (~ 2.3 eV) which is very relevant to visible light induced photocatalysis. Moreover, BiFeO_3 is a potential multiferroic semiconductor in which ferroelectric and antiferromagnetic properties coexist at room temperature which can generates internal electric field by switching the spontaneous polarization. However, the low charge separation efficiency and fast recombination rate lower its catalytic efficiency. Therefore, integration of BiFeO_3 with noble metal NPs to develop metal-semiconductor Schottky junction can offer an effective way to improve their photocatalytic activities under visible

region. However, Noble metal nanoparticles are very promising for longer wavelength light absorption, as they exhibit plasmonic effect under visible light. Hexagonal 2D morphology of BiFeO₃ has been prepared by facile hydrothermal method and Au NPs have been formed on the surface of the BiFeO₃ by radiolysis. After radiolytic construction of the Au/BiFeO₃ Schottky junction, two times enhanced activity achieved for photocatalytic H₂ generation because of hot electron generation and transfer from Au to BiFeO₃ surface. The light response of Au/BiFeO₃ Schottky junction was assessed in terms of photocurrent density *via* PEC measurements, where ~3.8 times higher photocurrent density achieved after Schottky junction formation compared to pure BiFeO₃. Therefore, this study would be effective to design and develop plasmonic metal modified perovskites based heterostructures as photocatalyst for water oxidation and reduction.

In photocatalysis, TiO₂ has been considered as benchmark photocatalyst however the wide bandgap (3.2 eV) limits its catalytic activity in visible region. Therefore, in the next work we focused to reduce the bandgap of TiO₂ by Bi-metal doping. The bandgap of TiO₂ has been reduced to 2.5 eV from 3.2 eV after successful Bi doping (3.5 wt. %). Further, to hinder the fast electron-hole recombination and prolong the lifetime of excited charges, an efficient p-n junction was planned between p-type Bi-doped TiO₂ and n-type molybdenum disulfide (MoS₂). MoS₂ is an interesting 2D material owing to specific d-electronic configuration, large specific surface area and active surface site, probability of van der Waal heterostructures, which facilitate the reactivity for photocatalysis. Additionally, the unsaturated coordination at edges and dangling bonds between the layers boost the surface adsorption and reaction rate. The development of p-n junction resulted nine times higher H₂ generation rate than that of bare TiO₂ due to developed potential gradient at the junction interface which may improve electron-hole separation efficiency. Thus, this study would be effective to design a stable and efficient p–n heterojunction for green fuel H₂ generation through water reduction under visible light illumination.

Bismuth oxyhalides would be effective for photocatalytic H₂ generation because of their open crystalline structures and the indirect optical transition which can reduce the electron-hole recombination. Moreover, the layered structure, composed of [Bi₂O₂]⁺ slabs interleaved with double halogen atoms [X]⁻ with the interlayer van der Waals force make the intrinsic structure of BiOX very stable. Moreover, the open crystalline structure of BiOX may offer a large space for the polarization of atoms and create a static electric field which would be perpendicular to the [Bi₂O₂]⁺ slabs. The induced field gradient further accelerates the photogenerated electron-hole

separation along (001) direction. However, the large bandgaps for BiOCl and BiOBr still restrict the effective performance under visible light and BiOI suffers from fast electron-hole recombination. Bandgap engineering of BiOX would be an effective way to overcome the foresaid limitations and prolong the lifetime of excited charge carriers. Therefore, we are focused to develop heterostructures with low bandgap CuFe_2O_4 by co-precipitation method. Depending on the location of valence and conduction band of BiOX, three types of heterostructures (type-I, type-II, and Z-scheme) are formed. Among these, Z-scheme heterostructures ($\text{BiOCl}/\text{CuFe}_2\text{O}_4$) showed two times higher catalytic activity towards H_2 generation compared to Type-I ($\text{BiOBr}/\text{CuFe}_2\text{O}_4$) and Type-II ($\text{BiOI}/\text{CuFe}_2\text{O}_4$) heterostructures because of the synergetic effects of low charge transfer resistance, high carrier concentration at the junction interface, sufficient reduction and oxidation potentials. Therefore, this study would be significant for extensive and fine regulation of band edge energies to control the photocatalytic activity.

References

- [1] S. Martha, P. C. Sahoo, K. M. Parida, An overview on visible light responsive metal oxide based photocatalysts for hydrogen energy production. *RSC Adv.* **5** (2015) 61535–61553.
- [2] H. L. Tan, R. Amal, Y. H. Ng, Alternative strategies in improving the photocatalytic and photoelectrochemical activities of visible light-driven BiVO₄: a review. *J. Mater. Chem. A* **5** (2017) 16498–16521.
- [3] S. G. Kumar, K. S. R. K. Rao, Zinc oxide based photocatalysis: tailoring surface-bulk structure and related interfacial charge carrier dynamics for better environmental applications. *RSC Adv.* **5** (2015) 3306–3351.
- [4] S. Ghosh, N. A. Kouame, L. Ramos, S. Remita, A. Dazzi, A. Deniset-Besseau, P. Beaunier, F. Goubard, P.-H. Aubert, H. Remita, Conducting polymer nanostructures for photocatalysis under visible light. *Nat. Mater.* **14** (2015) 505–511.
- [5] Y. Bai, L. Wilbraham, H. Gao, R. Clowes, H. Yang, M. A. Zwijnenburg, A. I. Cooper, R. S. Sprick, Photocatalytic polymers of intrinsic microporosity for hydrogen production from water. *J. Mater. Chem. A* **9** (2021) 19958–19964.
- [6] L. Liu, M.-Y. Gao, H. Yang, X. Wang, X. Li, A. I. Cooper, Linear Conjugated Polymers for Solar-Driven Hydrogen Peroxide Production: The Importance of Catalyst Stability. *J. Am. Chem. Soc.* **143** (2021) 19287–19293.
- [7] G. Liao, Y. Gong, L. Zhang, H. Gao, G.-J. Yang, B. Fang, Semiconductor polymeric graphitic carbon nitride photocatalysts: the “holy grail” for the photocatalytic hydrogen evolution reaction under visible light. *Energy Environ. Sci.* **12** (2019) 2080–2147.
- [8] A. Fujishima, X. T. Zhang, Titanium dioxide photocatalysis: present situation and future approaches. *C. R. Chim.* **9** (2006) 750–760.
- [9] A. A. Adesina, Industrial exploitation of photocatalysis: progress, perspectives and prospects. *Catal. Surv. Asia* **8** (2004) 265–273.
- [10] A. Mills, S.-K. Lee, A web-based overview of semiconductor photochemistry-based current commercial applications. *J. Photochem. Photobiol., A* **152** (2002) 233–247.
- [11] P. S. Basavarajappa, S. B. Patil, N. Ganganagappa, K. Raghava Reddy, A. V. Raghu, Ch. V. Reddy, Recent progress in metal-doped TiO₂, non-metal doped/codoped TiO₂ and TiO₂ nanostructured hybrids for enhanced photocatalysis. *Int. J. Hydrogen Energy* **45** (2020) 7764–7778.

- [12] G. Liu, L. Wang, H. G. Yang, H.-M. Cheng, G. Q. (Max) Lu, Titania-based photocatalysts—crystal growth, doping and heterostructuring. *J. Mater. Chem.* **20** (2010) 831–843.
- [13] X. Chen, L. Liu, P. Y. Yu, S. S. Mao, Increasing solar absorption for photocatalysis with black hydrogenated titanium dioxide nanocrystals. *Science* **331** (2011) 746–750.
- [14] C. Xu, Y. Song, L. Lu, C. Cheng, D. Liu, X. Fang, X. Chen, X. Zhu, D. Li, Electrochemically hydrogenated TiO₂ nanotubes with improved photoelectrochemical water splitting performance. *Nanoscale Res. Lett.* **8** (2013) 391.
- [15] Z. Zhang, M. N. Hedhili, H. Zhu, P. Wang, Electrochemical reduction induced self-doping of Ti³⁺ for efficient water splitting performance on TiO₂ based photoelectrodes. *Phys. Chem. Chem. Phys.* **15** (2013) 15637–15644.
- [16] G. Wang, H. Wang, Y. Ling, Y. Tang, X. Yang, R. C. Fitzmorris, C. Wang, J. Z. Zhang, Y. Li, Hydrogen-Treated TiO₂ Nanowire Arrays for Photoelectrochemical Water Splitting. *Nano Lett.* **11** (2011) 3026–3033.
- [17] T. Xia, Y. Zhang, J. Murowchick, X. Chen, Vacuum-treated titanium dioxide nanocrystals: Optical properties, surface disorder, oxygen vacancy, and photocatalytic activities. *Catal. Today* **225** (2014) 2–9.
- [18] G. Liu, L.-C. Yin, J. Wang, P. Niu, C. Zhen, Y. Xie, H.-M. Cheng, A red anatase TiO₂ photocatalyst for solar energy conversion. *Energy Environ. Sci.* **5** (2012) 9603–9610.
- [19] F. Wang, R. J. Wong, J. H. Ho, Y. Jiang, R. Amal, Sensitization of Pt/TiO₂ Using Plasmonic Au Nanoparticles for Hydrogen Evolution under Visible-Light Irradiation. *ACS Appl. Mater. Interfaces* **9** (2017) 30575–30582.
- [20] T. Yui, A. Kan, C. Saitoh, K. Koike, T. Ibusuki, O. Ishitani, Photochemical Reduction of CO₂ Using TiO₂: Effects of Organic Adsorbates on TiO₂ and Deposition of Pd onto TiO₂. *ACS Appl. Mater. Interfaces* **3** (2011) 2594–2600.
- [21] Z. Zhang, Z. Wang, S.-W. Cao, C. Xue, Au/Pt Nanoparticle-Decorated TiO₂ Nanofibers with Plasmon-Enhanced Photocatalytic Activities for Solar-to-Fuel Conversion. *J. Phys. Chem. C* **117** (2013) 25939–25947.
- [22] Y. Xu, Y. Li, P. Wang, X. Wang, H. Yu, Highly efficient dual cocatalyst-modified TiO₂ photocatalyst: RGO as electron-transfer mediator and MoS_x as H₂-evolution active site. *Appl. Surface Sci.* **430** (2018) 176–183.

- [23] H. Song, X. Meng, S. Wang, W. Zhou, S. Song, T. Kako, J. Ye, Selective Photo-oxidation of Methane to Methanol with Oxygen over Dual-Cocatalyst-Modified Titanium Dioxide. *ACS Catal.* **10** (2020) 14318–14326.
- [24] L. Wei, C. Yu, Q. Zhang, H. Liu, Y. Wang, TiO₂-based heterojunction photocatalysts for photocatalytic reduction of CO₂ into solar fuels. *J. Mater. Chem. A* **6** (2018) 22411–22436.
- [25] J. Zhang, G. Xiao, F.-X. Xiao, B. Liu, Revisiting one-dimensional TiO₂ based hybrid heterostructures for heterogeneous photocatalysis: a critical review. *Mater. Chem. Front.* **1** (2017) 231–250.
- [26] M. Gao, L. Zhu, W. Ong, J. Wang, G. W. Ho, Structural Design of TiO₂-based Photocatalyst for H₂ Production and Degradation Applications. *Catal. Sci. Technol.* **5** (2015) 4703–4726.
- [27] S. Y. Chae, M. K. Park, S. K. Lee, T. Y. Kim, S. K. Kim, W. I. Lee, Preparation of Size-Controlled TiO₂ Nanoparticles and Derivation of Optically Transparent Photocatalytic Films. *Chem. Mater.* **15** (2003) 3326–3331.
- [28] J. Fan, L. Zhao, J. Yu, G. Liu, The effect of calcination temperature on the microstructure and photocatalytic activity of TiO₂-based composite nanotubes prepared by an in situ template dissolution method. *Nanoscale* **4** (2012) 6597–6603.
- [29] J. Yu, G. Dai, B. Cheng, Effect of Crystallization Methods on Morphology and Photocatalytic Activity of Anodized TiO₂ Nanotube Array Films. *J. Phys. Chem. C* **114** (2010) 19378–19385.
- [30] T. J. Wong, F. J. Lim, M. Gao, G. H. Lee, G. W. Ho, Photocatalytic H₂ production of composite one-dimensional TiO₂ nanostructures of different morphological structures and crystal phases with graphene. *Catal. Sci. Technol.* **3** (2013) 1086–1093.
- [31] X. Zhang, T. Zhang, J. Ng, D. D. Sun, High- Performance Multifunctional TiO₂ Nanowire Ultrafiltration Membrane with a Hierarchical Layer Structure for Water Treatment. *Adv. Funct. Mater.* **19** (2009) 3731–3736.
- [32] H. Xu, F. Jia, Z. Ai, L. Zhang, A General Soft Interface Platform for the Growth and Assembly of Hierarchical Rutile TiO₂ Nanorods Spheres. *Cryst. Growth Des.* **7** (2007) 1216–1219.
- [33] J. Yu, Q. Xiang, M. Zhou, Preparation, characterization and visible-light-driven photocatalytic activity of Fe-doped titania nanorods and first-principles study for electronic structures. *Appl. Catal. B.* **90** (2009) 595–602.

- [34] A. Yamamoto, H. Imai, Preparation of titania foams having an open cellular structure and their application to photocatalysis. *J. Catal.* **226** (2004) 462–465.
- [35] W. Zhou, W. Li, J.-Q. Wang, Y. Qu, Y. Yang, Y. Xie, K. Zhang, L. Wang, H. Fu, D. Zhao, Ordered mesoporous black TiO₂ as highly efficient hydrogen evolution photocatalyst. *J. Am. Chem. Soc.* **136** (2014) 9280–9283.
- [36] J. B. Joo, M. Dahl, N. Li, F. Zaera, Y. Yin, Tailored synthesis of mesoporous TiO₂ hollow nanostructures for catalytic applications. *Energy Environ. Sci.* **6** (2013) 2082–2092.
- [37] X. Q. Gong, A. Selloni, Reactivity of Anatase TiO₂ Nanoparticles: The Role of the Minority (001) Surface. *J. Phys. Chem. B.* **109** (2005) 19560–19652.
- [38] W. Yang, J. Li, Y. Wang, F. Zhu, W. Shi, F. Wan, D. Xu, A facile synthesis of anatase TiO₂ nanosheets-based hierarchical spheres with over 90% {001} facets for dye-sensitized solar cells. *Chem. Commun.* **47** (2011) 1809–1811.
- [39] C. Hu, X. Zhang, W. Li, Y. Yan, G. Xi, H. Yang, J. Li, H. Bai, Large-scale, ultrathin and (001) facet exposed TiO₂ nanosheet superstructures and their applications in photocatalysis. *J. Mater. Chem. A* **2** (2014) 2040–2043.
- [40] J. Zhang, L. Li, Z. Xiao, D. Liu, S. Wang, J. Zhang, Y. Hao, W. Zhang, Hollow Sphere TiO₂-ZrO₂ Prepared by Self-Assembly with Polystyrene Colloidal Template for Both Photocatalytic Degradation and H₂ Evolution from Water Splitting. *ACS Sustainable Chem. Eng.* **4** (2016) 2037–2046.
- [41] Z. U. Rahman, N. Wei, M. Feng, D. Wang, TiO₂ hollow spheres with separated Au and RuO₂ co-catalysts for efficient photocatalytic water splitting. *Int. J. Hydrogen Energy.* **44** (2019) 13221–13231.
- [42] Y. Duan, S. Zhou, Z. Chen, J. Luo, M. Zhang, F. Wang, T. Xu, C. Wang, Hierarchical TiO₂ nanowires/microflowers photoanode modified with Au nanoparticles for efficient photoelectrochemical water splitting. *Catal. Sci. Technol.* **8** (2018) 1395–1403.
- [43] L. Qin, G. Wang, Y. Tan, Plasmonic Pt nanoparticles-TiO₂ hierarchical nano-architecture as a visible light photocatalyst for water splitting. *Sci. Rep.* **8** (2018) 16198–16207.
- [44] Z. Haider, Y. S. Kang, Facile Preparation of Hierarchical TiO₂ Nano Structures: Growth Mechanism and Enhanced Photocatalytic H₂ Production from Water Splitting Using Methanol as a Sacrificial Reagent. *ACS Appl. Mater. Interfaces* **6** (2014) 10342–10352.

- [45] W. Li, A. Elzatahry, D. Aldhayan, D. Zhao, Core-shell structured titanium dioxide nanomaterials for solar energy utilization. *Chem. Soc. Rev.* **47** (2018) 8203–8237.
- [46] H. Bai, J. Juay, Z. Liu, X. Song, S. S. Lee, D. D. Sun, Hierarchical SrTiO₃/TiO₂ nanofibers heterostructures with high efficiency in photocatalytic H₂ generation. *Appl. Catal. B.* **125** (2012) 367–374.
- [47] W. Zhou, Z. Yin, Y. Du, X. Huang, Z. Zeng, Z. Fan, H. Liu, J. Wang, H. Zhang, Synthesis of Few-Layer MoS₂ Nanosheet-Coated TiO₂ Nanobelt Heterostructures for Enhanced Photocatalytic Activities. *Small* **9** (2013) 140–147.
- [48] Y. Chen, J. C. Crittenden, S. Hackney, L. Sutter, D. W. Hand, Preparation of a Novel TiO₂-Based p-n Junction Nanotube Photocatalyst. *Environ. Sci. Technol.* **39** (2005) 1201–1209.
- [49] L. Wei, C. Yu, Q. Zhang, H. Liu, Y. Wang, TiO₂-based heterojunction photocatalysts for photocatalytic reduction of CO₂ into solar fuels. *J. Mater. Chem. A* **6** (2018) 22411–22436.
- [50] A. Ajmal, I. Majeed, R. N. Malik, H. Idriss, M. A. Nadeem, Principles and mechanisms of photocatalytic dye degradation on TiO₂ based photocatalysts: a comparative overview. *RSC Adv.* **4** (2014) 37003–37026.
- [51] J. G. Yu, S. H. Wang, J. X. Low, W. Xiao, Enhanced photocatalytic performance of direct Z-scheme g-C₃N₄-TiO₂ photocatalysts for the decomposition of formaldehyde in air. *Phys. Chem. Chem. Phys.* **15** (2013) 16883–16890.
- [52] A. A. Essawy, S. M. Sayyah, A. M. El-Nggar, Wastewater remediation by TiO₂-impregnated chitosan nano-grafts exhibited dual functionality: High adsorptivity and solar-assisted self-cleaning. *J. Photochem. Photobio. B* **173** (2017) 170–180.
- [53] H. Zhao, M. Wu, J. Liu, Z. Deng, Y. Li, B. L. Su, CdS modified one-dimensional g-C₃N₄ porous nanotubes for efficient visible light photocatalytic conversion. *Appl. Catal. B.* **184** (2016) 182–190.
- [54] Y. C. Wei, J. Q. Jiao, Z. Zhao, J. Liu, J. M. Li, G. Y. Jiang, Y. J. Wang, A. J. Duan, Fabrication of inverse opal TiO₂-supported Au@CdS core-shell nanoparticles for efficient photocatalytic CO₂ conversion. *Appl. Catal. B.* **179** (2015) 422–432.
- [55] J. G. Yu, S. H. Wang, J. X. Low, W. Xiao, Enhanced photocatalytic performance of direct Z-scheme g-C₃N₄-TiO₂ photocatalysts for the decomposition of formaldehyde in air. *Phys. Chem. Chem. Phys.* **15** (2013) 16883–16890.

- [56] W. Fang, M. Xing, J. Zhang, Modifications on reduced titanium dioxide photocatalysts: A review. *J Photochem. Photobiol. C* **32** (2017) 21–39.
- [57] M. R. Hoffmann, S. T. Martin, W. Choi, D. W. Bahnemann, Environmental Applications of Semiconductor Photocatalysis. *Chem. Rev.* **95** (1995) 69–96.
- [58] S. Malato, J. Blanco, A. Vidal, D. Alarcon, M. I. Maldonado, J. Caceres, W. Gernjak, Applied studies in solar photocatalytic detoxification: an overview. *Sol. Energy* **75** (2003) 329–336.
- [59] A. Fujishima, T. N. Rao, D. A. Tryk, Titanium dioxide photocatalysis. *J. Photochem. Photobiol. C* **1** (2000) 1–21.
- [60] M. Romero, J. Blanco, B. Sanchez, A. Vidal, S. Malato, A. Cardona, E. Garcí'a, Solar Photocatalytic Degradation of Water and Air Pollutants: Challenges and Perspectives. *Sol. Energy* **66** (1999) 169–182.
- [61] F. E. Osterloh, Inorganic Materials as Catalysts for Photochemical Splitting of Water. *Chem. Mater.* **20** (2008) 35–54.
- [62] Y. Liu, G. Zhu, J. Gao, M. Hojamberdiev, H. Lu, R. Zhu, X. Wei, P. Liu, A novel CeO₂/Bi₄Ti₃O₁₂ composite heterojunction structure with an enhanced photocatalytic activity for bisphenol A. *J. Alloys Compd.* **688** (2016) 487–496.
- [63] L. Fan, B. Wei, L. Xu, Y. Liu, W. Cao, N. Ma, H. Gao, Ion Exchange Synthesis of Bi₂MoO₆/BiOI Heterojunctions for Photocatalytic Degradation and Photoelectrochemical Water Splitting. *Nano* **11** (2016) 1650095–1650105.
- [64] M. Yan, Y. Hua, F. Zhu, W. Gu, J. Jiang, H. Shen, W. Shi, Fabrication of nitrogen doped graphene quantum dots-BiOI/MnNb₂O₆ p-n junction photocatalysts with enhanced visible light efficiency in photocatalytic degradation of antibiotics. *Appl. Catal. B* **202** (2017) 518–527.
- [65] J. S. Chang, Y. W. Phuan, M. N. Chong, J. D. Ocon, Exploration of a novel Type II 1D-ZnO nanorods/BiVO₄ heterojunction photocatalyst for water depollution. *J. Ind. Eng. Chem.* **83** (2020) 303–314.
- [66] Y. P. Bhoi, B. G. Mishra, Photocatalytic degradation of alachlor using type-II CuS/BiFeO₃ heterojunctions as novel photocatalyst under visible light irradiation. *Chem. Eng. J.* **344** (2018) 391–401.

- [67] Y. P. Bhoi, A. K. Nayak, S. K. Gouda, B. G. Mishra, Photocatalytic mineralization of carbendazim pesticide by a visible light active novel type-II $\text{Bi}_2\text{S}_3/\text{BiFeO}_3$ heterojunction photocatalyst. *Catal. Commun.* **114** (2018) 114–119.
- [68] H.-Q. Chen, L.-Y. Lin, S.-L. Chen, Direct Growth of $\text{BiVO}_4/\text{Bi}_2\text{S}_3$ Nanorod Array on Conductive Glass as Photocatalyst for Enhancing the Photoelectrochemical Performance. *ACS Appl. Energy Mater.* **1** (2018) 6089–6100.
- [69] H. Cui, S. Dong, K. Wang, M. Luan, T. Huang, Synthesis of a novel Type-II $\text{In}_2\text{S}_3/\text{Bi}_2\text{MoO}_6$ heterojunction photocatalyst: Excellent photocatalytic performance and degradation mechanism for Rhodamine B. *Sep. Purif. Technol.* **255** (2021) 117758.
- [70] X. Ren, K. Wu, Z. Qin, X. Zhao, H. Yang, The construction of type II heterojunction of $\text{Bi}_2\text{WO}_6/\text{BiOBr}$ photocatalyst with improved photocatalytic performance. *J. Alloys Compd.* **788** (2019) 102–109.
- [71] Y. Qiao, X. Meng, Z. Zhang, A new insight into the enhanced visible light-induced photocatalytic activity of $\text{NaNbO}_3/\text{Bi}_2\text{WO}_6$ type-II heterostructure photocatalysts. *Appl. Surf. Sci.* **470** (2019) 645–657.
- [72] X. Jia, J. Cao, H. Lin, M. Zhang, X. Guo, S. Chen, Transforming type-I to type-II heterostructure photocatalyst via energy band engineering: A case study of I- $\text{BiOCl}/\text{I-BiOBr}$. *Appl. Catal. B* **204** (2017) 505–514.
- [73] A. Zhu, Q. Zhao, X. Li, Y. Shi, $\text{BiFeO}_3/\text{TiO}_2$ Nanotube Arrays Composite Electrode: Construction, Characterization, and Enhanced Photoelectrochemical Properties. *ACS Appl. Mater. Interfaces* **6** (2014) 671–679.
- [74] S. Sun, W. Wang, L. Zhang, Bi_2WO_6 Quantum Dots Decorated Reduced Graphene Oxide: Improved Charge Separation and Enhanced Photoconversion Efficiency. *J. Phys. Chem. C* **117** (2013) 9113–9120.
- [75] J. Tian, Y. Sang, G. Yu, H. Jiang, X. Mu, H. Liu, A Bi_2WO_6 -Based Hybrid Photocatalyst with Broad Spectrum Photocatalytic Properties under UV, Visible, and Near-Infrared Irradiation. *Adv. Mater.* **25** (2013) 5075–5080.
- [76] C. Liu, Y. Yang, W. Li, J. Li, Y. Li, Q. Chen, In situ synthesis of Bi_2S_3 sensitized WO_3 nanoplate arrays with less interfacial defects and enhanced photoelectrochemical performance. *Sci. Rep.* **6** (2016) 23451–23463.

- [77] X. Shi, Y. Choi, K. Zhang, J. Kwon, D. Y. Kim, J. K. Lee, S. H. Oh, J. K. Kim, J. H. Park, Efficient photoelectrochemical hydrogen production from bismuth vanadate-decorated tungsten trioxide helix nanostructures. *Nat. Commun.* **5** (2014) 4775–4783.
- [78] H. He, S. P. Berglund, P. Xiao, W. D. Chemelewski, Y. Zhang, C. B. Mullins, Nanostructured Bi₂S₃/WO₃ heterojunction films exhibiting enhanced photoelectrochemical performance. *J. Mater. Chem. A* **1** (2013) 12826–12834.
- [79] P. Ju, Y. Wang, Y. Suna, D. Zhang, Controllable one-pot synthesis of a nest-like Bi₂WO₆/BiVO₄ composite with enhanced photocatalytic antifouling performance under visible light irradiation. *Dalton Trans.* **45** (2016) 4588–4602.
- [80] J. Ke, J. Liu, H. Sun, H. Zhang, X. Duan, P. Liang, X. Li, M. O. Tade, S. Liu, S. Wang, Facile assembly of Bi₂O₃/Bi₂S₃/MoS₂ n-p heterojunction with layered n-Bi₂O₃ and p-MoS₂ for enhanced photocatalytic water oxidation and pollutant degradation. *Appl. Catal. B* **200** (2017) 47–55.
- [81] Y. Huang, W. Fan, B. Long, H. Li, F. Zhao, Z. Liu, Y. Tong, H. Ji, Visible light Bi₂S₃/Bi₂O₃/Bi₂O₂CO₃ photocatalyst for effective degradation of organic pollutions. *Appl. Catal., B* **185** (2016) 68–76.
- [82] C. Chang, H. C. Yang, N. Gao, S. Y. Lu, Core/shell p-BiOI/n-beta-Bi₂O₃ heterojunction array with significantly enhanced photoelectrochemical water splitting efficiency. *J. Alloys Compd.* **738** (2017) 138–144.
- [83] D. Wang, L. Guo, Y. Zhen, L. Yue, G. Xue, F. Fu, AgBr quantum dots decorated mesoporous Bi₂WO₆ architectures with enhanced photocatalytic activities for methylene blue. *J. Mater. Chem. A* **2** (2014) 11716–11727.
- [84] C. Zheng, H. Yang, Assembly of Ag₃PO₄ nanoparticles on rose flower-like Bi₂WO₆ hierarchical architectures for achieving high photocatalytic performance. *J. Mater. Sci. Mater. Electronics* **29** (2018) 9291–9300.
- [85] Z. He, Y. Shi, C. Gao, L. Wen, J. Chen, S. Song, BiOCl/BiVO₄ p-n Heterojunction with Enhanced Photocatalytic Activity under Visible-Light Irradiation. *J. Phys. Chem. C* **118** (2014) 389–398.
- [86] P. Babu, S. Mohanty, B. Naik, K. Parida, Serendipitous Assembly of Mixed Phase BiVO₄ on B- Doped g- C₃N₄: An Appropriate p-n Heterojunction for Photocatalytic O₂ evolution and Cr(VI) reduction. *Inorg. Chem.* **58** (2019) 12480–12491.

- [87] Z. Dai, F. Qin, H. Zhao, F. Tian, Y. Liu, R. Chen, Time-dependent Evolution of $\text{Bi}_{3.64}\text{Mo}_{0.36}\text{O}_{6.55}/\text{Bi}_2\text{MoO}_6$ Heterostructure for Enhanced Photocatalytic Activity via the Interfacial Hole Migration. *Nanoscale* **7** (2015) 11991–11999.
- [88] B. P. Mishra, K. Parida, Orienting Z scheme charge transfer in graphitic carbon nitride-based systems for photocatalytic energy and environmental applications. *J. Mater. Chem. A* **9** (2021) 10039–10080.
- [89] F. Wang, W. Li, S. Gu, H. Li, X. Wu, C. Ren, X. Liu, Facile fabrication of direct Z-scheme $\text{MoS}_2/\text{Bi}_2\text{WO}_6$ heterojunction photocatalyst with superior photocatalytic performance under visible light irradiation. *J. Photochem. Photobiol. A Chem.* **335** (2017) 140–148.
- [90] T. Zhang, Y. Shen, Y. Qiu, Y. Liu, R. Xiong, J. Shi, J. Wei, Facial Synthesis and Photoreaction Mechanism of $\text{BiFeO}_3/\text{Bi}_2\text{Fe}_4\text{O}_9$ Heterojunction Nanofibers. *ACS Sustainable Chem. Eng.* **5** (2017) 4630–4636.
- [91] S. Mansour, R. Akkari, E. Soto, S. B. Chaabene, N. Mota, R. M. N. Yerga, J. L. Garcí'a Fierro, M. Saïd Zina, Pt– $\text{BiVO}_4/\text{TiO}_2$ composites as Z-scheme photocatalysts for hydrogen production from ethanol: the effect of BiVO_4 and Pt on the photocatalytic efficiency. *New J. Chem.* **45** (2021) 4481–4495.
- [92] L. Zhang, K.-H. Wong, Z. Chen, J. C. Yu, J. Zhao, C. Hu, C.-Y. Chan, P.-K. Wong, AgBr–Ag– Bi_2WO_6 nanojunction system: A novel and efficient photocatalyst with double visible-light active components. *Appl. Catal. A* **363** (2009) 221–229.
- [93] W. Chen, T.-Y. Liu, T. Huang, X.-H. Liu, J.-W. Zhu, G.-R. Duan, X.-J. Yang, In-situ fabrication of a novel Z-scheme Bi_2WO_6 quantum dots/g- C_3N_4 ultrathin nanosheets heterostructures with improved photocatalytic activity. *Appl. Surf. Sci.* **355** (2015) 379–387.
- [94] N. Tian, H. Huang, Y. He, Y. Guo, T. Zhang, Y. Zhang, Mediator-free direct Z-scheme photocatalytic system: $\text{BiVO}_4/\text{g-C}_3\text{N}_4$ organic–inorganic hybrid photocatalyst with highly efficient visible-light-induced photocatalytic activity. *Dalton Trans.* **44** (2015) 4297–4307.
- [95] A. Rauf, M. Ming, S. Kim, M. S. A. S. Shah, C.-H. Chung, J. H. Park, P. J. Yoo, Mediator and Co-Catalysts-Free Direct Z-Scheme Composites of $\text{Bi}_2\text{WO}_6\text{-Cu}_3\text{P}$ for Solar-Water Splitting. *Nanoscale* **10** (2018) 3026–3036.
- [96] M. Du, S. Zhang, Z. Xing, Z. Li, J. Yin, J. Zou, Q. Zhu, W. Zhou, All-Solid Z-Scheme Bi– BiOCl/AgCl Heterojunction Microspheres for Improved Electron-Hole Separation and

- Enhanced Visible Light-Driven Photocatalytic Performance. *Langmuir* **35** (2019) 7887–7895.
- [97] S. Sultana, S. Mansingh, K. M. Parida, Facile Synthesis of CeO₂ Nanosheets Decorated upon BiOI Microplate: A Surface Oxygen Vacancy Promoted Z-Scheme-Based 2D-2D Nanocomposite Photocatalyst with Enhanced Photocatalytic Activity. *J. Phys. Chem. C* **122** (2018) 808–819.
- [98] Y. Huang, Y. Wei, J. Wang, D. Luo, L. Fan, J. Wu, Controllable fabrication of Bi₂O₃/TiO₂ heterojunction with excellent visible-light responsive photocatalytic performance. *Appl. Surf. Sci.* **423** (2017) 119–130.
- [99] X. Liu, Y. Kang, Synthesis and high visible-light activity of novel Bi₂O₃/FeVO₄ heterojunction photocatalyst. *Mater. Lett.* **164** (2016) 229–231.
- [100] Y. Li, S. Wu, L. Huang, H. Xu, R. Zhang, M. Qu, Q. Gao, H. Li, g-C₃N₄ modified Bi₂O₃ composites with enhanced visible-light photocatalytic activity. *J. Phys. Chem. Solids* **76** (2015) 112–119.
- [101] X. Dang, X. Zhang, Y. Chen, X. Dong, G. Wang, C. Ma, X. Zhang, H. Ma, M. Xue, Preparation of β-Bi₂O₃/g-C₃N₄ nanosheet p–n junction for enhanced photocatalytic ability under visible light illumination. *J. Nanopart. Res.* **17** (2015) 93–101.
- [102] L.-L. Long, A. Zhang, Y. Huang, X. Zhang, H. Yu, A robust cocatalyst Pd₄S uniformly anchored onto Bi₂S₃ nanorods for enhanced visible light photocatalysis. *J. Mater. Chem. A* **3** (2015) 4301–4306.
- [103] M. Nawaz, Morphology-controlled preparation of Bi₂S₃-ZnS chloroplast-like structures, formation mechanism and photocatalytic activity for hydrogen production. *J. Photochem. Photobiol. A* **332** (2017) 326–330.
- [104] D. Xiong, G. Huang, B. Zhou, Q. Yan, A. Pan, W. Huang, Facile ion-exchange synthesis of mesoporous Bi₂S₃/ZnS nanoplate with high adsorption capability and photocatalytic activity. *J. Colloid Interface Sci.* **464** (2016) 103–109.
- [105] D. Zhou, H. Yang, Y. Tu, Y. Tian, Y. Cai, Z. Hu, X. Zhu, In Situ Fabrication of Bi₂Ti₂O₇/TiO₂ Heterostructure Submicron Fibers for Enhanced Photocatalytic Activity. *Nanoscale Res. Lett.* **11** (2016) 193–201.

- [106] Y. Guo, J. Li, Z. Gao, X. Zhu, Y. Liu, Z. Wei, W. Zhao, C. Sun, A simple and effective method for fabricating novel p–n heterojunction photocatalyst g-C₃N₄/Bi₄Ti₃O₁₂ and its photocatalytic performances. *Appl. Catal. B* **192** (2016) 57–71.
- [107] H. Sun, J. Li, G. Zhang, N. Li, Microtetrahedral Bi₁₂TiO₂₀/g-C₃N₄ composite with enhanced visible light photocatalytic activity toward gaseous formaldehyde degradation: Facet coupling effect and mechanism study. *J. Mol. Catal. A Chem.* **424** (2016) 311–322.
- [108] W. Shan, Y. Hu, Z. Bai, M. Zheng, C. Wei, In situ preparation of g-C₃N₄/bismuth-based oxide nanocomposites with enhanced photocatalytic activity. *Appl. Catal. B* **188** (2016) 1–12.
- [109] Y. Ao, L. Xu, P. Wang, C. Wang, J. Hou, J. Qian, Preparation of CdS nanoparticle loaded flower-like Bi₂O₂CO₃ heterojunction photocatalysts with enhanced visible light photocatalytic activity. *Dalton Trans.* **44** (2015) 11321–11330.
- [110] Y. Hu, C. Dong, K. Wu, S. Xia, X. Li, X. Wei, Synthesis of Ag₃PO₄–Bi₂O₂CO₃ composites with high visible-light photocatalytic activity. *Mater. Lett.* **147** (2015) 69–71.
- [111] F. Niu, D. Chen, L. Qin, N. Zhang, J. Wang, Z. Chen, Y. Huang, Facile Synthesis of Highly Efficient p–n Heterojunction CuO/BiFeO₃ Composite Photocatalysts with Enhanced Visible-Light Photocatalytic Activity. *Chem. Cat. Chem.* **7** (2015) 3279–3289.
- [112] J. An, G. Zhang, R. Zheng, P. Wang, Removing lignin model pollutants with BiFeO₃–g-C₃N₄ compound as an efficient visible-light-heterogeneous Fenton-like catalyst. *J. Environ. Sci.* **48** (2016) 218–229.
- [113] Y. Xing, W. Que, X. Yin, Z. He, X. Liu, Y. Yang, J. Shao, L. B. Kong, In₂O₃/Bi₂Sn₂O₇ heterostructured nanoparticles with enhanced photocatalytic activity. *Appl. Surf. Sci.* **387** (2016) 36–44.
- [114] S. Li, K. Xu, S. Hu, W. Jiang, J. Zhang, J. Liu, L. Zhang, Synthesis of flower-like Ag₂O/BiOCCOOH p-n heterojunction with enhanced visible light photocatalytic activity. *Appl. Surf. Sci.* **397** (2017) 95–103.
- [115] N. Bao, Z. Yin, Q. Zhang, S. He, X. Hu, X. Miao, Synthesis of flower-like monoclinic BiVO₄/surface rough TiO₂ ceramic fiber with heterostructures and its photocatalytic property. *Ceram. Int.* **42** (2016) 1791–1800.

- [116] G. Joshi, J. K. Pandey, S. Singh, R. Sharma, Formation of intermediate band and low recombination rate in ZnO-BiVO₄ heterostructured photocatalyst: Investigation based on experimental and theoretical studies. *Korean J. Chem. Eng.* **34** (2017) 500–510.
- [117] J. Yin, S. Huang, Z. Jian, Z. Wang, Y. Zhang, Fabrication of heterojunction SnO₂/BiVO₄ composites having enhanced visible light photocatalytic activity. *Mater. Sci. Semicond. Process.* **34** (2015) 198–204.
- [118] J. Xu, W. Wang, J. Wang, Y. Liang, Controlled fabrication and enhanced photocatalytic performance of BiVO₄@CeO₂ hollow microspheres for the visible-light-driven degradation of rhodamine B. *Appl. Surf. Sci.* **349** (2015) 529–537.
- [119] J. Li, M. Cui, Z. Guo, Z. Liu, Z. Zhu, Preparation of p–n junction BiVO₄/Ag₂O heterogeneous nanostructures with enhanced visible-light photocatalytic activity. *Mater. Lett.* **151** (2015) 75–78.
- [120] X. Chang, T. Wang, P. Zhang, J. Zhang, A. Li, J. Gong, Enhanced Surface Reaction Kinetics and Charge Separation of p–n Heterojunction Co₃O₄/BiVO₄ Photoanodes. *J. Am. Chem. Soc.* **137** (2015) 8356–8359.
- [121] Y. Huang, M. Fu, T. He, Synthesis of g-C₃N₄/BiVO₄ Nanocomposite Photocatalyst and Its Application in Photocatalytic Reduction of CO₂. *Acta. Phys.-Chim. Sin.* **31** (2015) 1145–1152.
- [122] K. Trzcinski, M. Szkoda, K. Siuzdak, M. Sawczak, A. Lisowska-Oleksiak, Enhanced photoelectrochemical performance of inorganic–organic hybrid consisting of BiVO₄ and PEDOT:PSS. *Appl. Surf. Sci.* **388** (2016) 753–761.
- [123] X. Sun, H. Zhang, J. Wei, Q. Yu, P. Yang, F. Zhang, Preparation of point-line Bi₂WO₆@TiO₂ nanowires composite photocatalysts with enhanced UV/visible-light-driven photocatalytic activity. *Mater. Sci. Semicond. Process.* **45** (2016) 51–56.
- [124] C. Yang, Y. Huang, F. Li, T. Li, One-step synthesis of Bi₂WO₆/TiO₂ heterojunctions with enhanced photocatalytic and superhydrophobic property via hydrothermal method. *J. Mater. Sci.* **51** (2016) 1032–1042.
- [125] J. Zhang, L. Huang, L. Yang, Z. Lu, X. Wang, G. Xu, E. Zhang, H. Wang, Z. Kong, J. Xi, Z. Ji, Controllable synthesis of Bi₂WO₆(001)/TiO₂(001) heterostructure with enhanced photocatalytic activity. *J. Alloys Compd.* **676** (2016) 37–45.

- [126] X. Liu, Q. Lu, C. Wang, Direct electrospinning of α -Fe₂O₃/Bi₂WO₆ heterostructured nanotubes with enhanced visible light photocatalytic performance. *Mater. Lett.* **154** (2015) 81–84.
- [127] Z. Zhu, Y. Yan, J. Li, One-step synthesis of flower-like WO₃/Bi₂WO₆ heterojunction with enhanced visible light photocatalytic activity. *J. Mater. Sci.* **51** (2016) 2112–2120.
- [128] L. Chen, H. Hua, Q. Yang, C. Hu, Visible-light photocatalytic activity of Ag₂O coated Bi₂WO₆ hierarchical microspheres assembled by nanosheets. *Appl. Surf. Sci.* **327** (2015) 62–67.
- [129] J. Li, C. Yu, W. Fang, L. Zhu, W. Zhou, Q. Fan, Preparation, characterization and photocatalytic performance of heterostructured AgCl/Bi₂WO₆ microspheres. *Chin. J. Catal.* **36** (2015) 987–993.
- [130] S. Issarapanacheewin, K. Wetchakun, S. Phanichphant, W. Kangwansupamonkon, N. Wetchakun, A novel CeO₂/Bi₂WO₆ composite with highly enhanced photocatalytic activity. *Mater. Lett.* **156** (2015) 28–31.
- [131] R. Tang, H. Su, S. Duan, Y. Sun, L. Li, X. Zhang, S. Zeng, D. Sun, Enhanced visible-light-driven photocatalytic performances using Bi₂WO₆/MS (M = Cd, Zn) heterostructures: facile synthesis and photocatalytic mechanisms. *RSC Adv.* **5** (2015) 41949–41960.
- [132] J. Li, X. Liu, Z. Sun, L. Pan, Novel Bi₂MoO₆/TiO₂ heterostructure microspheres for degradation of benzene series compound under visible light irradiation. *J. Colloid Interface Sci.* **463** (2016) 145–153.
- [133] S. Jonjana, A. Phuruangrat, S. Thongtem, O. Wiranwetchayan, T. Thongtem, Preparation and characterization of Ag₃VO₄/Bi₂MoO₆ nanocomposites with highly visible-light-induced photocatalytic properties. *Mater. Lett.* **180** (2016) 93–96.
- [134] S. N. Lou, J. Scott, A. Iwase, R. Amal, Y. H. Ng, Photoelectrochemical water oxidation using a Bi₂MoO₆/MoO₃ heterojunction photoanode synthesised by hydrothermal treatment of an anodised MoO₃ thin film. *J. Mater. Chem. A* **4** (2016) 6964–6971.
- [135] A. Dittmer, J. Menze, B. Mei, J. Strunk, H. S. Luftman, R. Gutkowski, I. E. Wachs, W. Schuhmann, M. Muhler, Surface Structure and Photocatalytic Properties of Bi₂WO₆ Nanoplatelets Modified by Molybdena Islands from Chemical Vapor Deposition. *J. Phys. Chem. C* **120** (2016) 18191–18200.

- [136] W. Chen, G. Duan, T. Liu, S. Chen, X. Liu, Fabrication of Bi_2MoO_6 nanoplates hybridized with g- C_3N_4 nanosheets as highly efficient visible light responsive heterojunction photocatalysts for Rhodamine B degradation. *Mater. Sci. Semicond. Process.* **35** (2015) 45–54.
- [137] M. Xu, W. Zhang, Facile Preparation of $\text{AgI}/\text{Bi}_2\text{MoO}_6$ Heterostructured Photocatalysts with Enhanced Photocatalytic Activity. *Eur. J. Inorg. Chem.* **2016** (2016) 826–831.
- [138] S. Jonjana, A. Phuruangrat, T. Thongtem, S. Thongtem, Synthesis, analysis and photocatalysis of $\text{AgBr}/\text{Bi}_2\text{MoO}_6$ nanocomposites. *Mater. Lett.* **172** (2016) 11–14.
- [139] Z. Wan, G. Zhang, Synthesis and facet-dependent enhanced photocatalytic activity of $\text{Bi}_2\text{SiO}_5/\text{AgI}$ nanoplate photocatalysts. *J. Mater. Chem. A* **3** (2015) 16737–16745.
- [140] X. Wang, Q. Ni, D. Zeng, G. Liao, Y. Wen, B. Shan, C. Xie, $\text{BiOCl}/\text{TiO}_2$ heterojunction network with high energy facet exposed for highly efficient photocatalytic degradation of benzene. *Appl. Surf. Sci.* **396** (2016) 590–598.
- [141] X. Wang, H. Hu, S. Chen, K. Zhang, J. Zhang, W. Zou, R. Wang, One-step fabrication of BiOCl/CuS heterojunction photocatalysts with enhanced visible-light responsive activity. *Mater. Chem. Phys.* **158** (2015) 67–73.
- [142] S. Yin, J. Di, M. Li, Y. Sun, J. Xia, H. Xu, W. Fan, H. Li, Ionic liquid-assisted synthesis and improved photocatalytic activity of p-n junction g- $\text{C}_3\text{N}_4/\text{BiOCl}$. *J. Mater. Sci.* **51** (2016) 4769–4777.
- [143] Y. Ao, K. Wang, P. Wang, C. Wang, J. Hou, Synthesis of novel 2D-2D p-n heterojunction $\text{BiOBr}/\text{La}_2\text{Ti}_2\text{O}_7$ composite photocatalyst with enhanced photocatalytic performance under both UV and visible light irradiation. *Appl. Catal., B* **194** (2016) 157–168.
- [144] X. Wen, C. Zhang, C. Niu, L. Zhang, G. Zeng, X. Zhang, Highly enhanced visible light photocatalytic activity of CeO_2 through fabricating a novel p–n junction $\text{BiOBr}/\text{CeO}_2$. *Catal. Commun.* **90** (2017) 51–55.
- [145] R. Jiang, H. Y. Zhu, J. B. Li, F. Q. Fu, J. Yao, S. T. Jiang, G. M. Zeng, Fabrication of novel magnetically separable $\text{BiOBr}/\text{CoFe}_2\text{O}_4$ microspheres and its application in the efficient removal of dye from aqueous phase by an environment-friendly and economical approach. *Appl. Surf. Sci.* **364** (2016) 604–612.

- [146] Y. Shen, X. Yu, W. Lin, Y. Zhu, Y. Zhang, A facile preparation of immobilized BiOCl nanosheets/TiO₂ arrays on FTO with enhanced photocatalytic activity and reusability. *Appl. Surf. Sci.* **399** (2017) 67–76.
- [147] O. Mehraj, N. A. Mir, B. M. Pirzada, S. Sabir, Fabrication of novel Ag₃PO₄/BiOBr heterojunction with high stability and enhanced visible-light-driven photocatalytic activity. *Appl. Surf. Sci.* **332** (2015) 419–429.
- [148] D. Jiang, X. Du, D. Chen, Y. Li, N. Hao, J. Qian, H. Zhong, T. You, K. Wang, Facile wet chemical method for fabricating p-type BiOBr/n-type nitrogen doped graphene composites: Efficient visible-excited charge separation, and high-performance photoelectrochemical sensing. *Carbon* **102** (2016) 10–17.
- [149] K. Wang, C. Shao, X. Li, F. Miao, N. Lu, Y. Liu, Heterojunctions of p-BiOI Nanosheets/n-TiO₂ Nanofibers: Preparation and Enhanced Visible-Light Photocatalytic Activity. *Materials* **9** (2016) 90–102.
- [150] G. Dai, J. Yu, G. Liu, Synthesis and Enhanced Visible-Light Photoelectrocatalytic Activity of p–n Junction BiOI/TiO₂ Nanotube Arrays. *J. Phys. Chem. C* **115** (2011) 7339–7346.
- [151] Y. Sun, X. Xiao, X. Dong, F. Dong, W. Zhang, Heterostructured BiOI@La(OH)₃ nanorods with enhanced visible light photocatalytic NO removal. *Chin. J. Catal.* **38** (2017) 217–226.
- [152] O. Mehraj, B. M. Pirzada, N. A. Mir, M. Z. Khan, S. Sabir, A highly efficient visible-light-driven novel p-n junction Fe₂O₃/BiOI photocatalyst: Surface decoration of BiOI nanosheets with Fe₂O₃ nanoparticles. *Appl. Surf. Sci.* **387** (2016) 642–651.
- [153] S. Lee, Y. Park, D. Pradhan, Y. Sohn, AgX (X = Cl, Br, I)/BiOX nanoplates and microspheres for pure and mixed (methyl orange, rhodamine B and methylene blue) dyes. *J. Ind. Eng. Chem.* **35** (2016) 231–252.
- [154] J. Xia, M. Ji, J. Di, B. Wang, S. Yin, Q. Zhang, M. He, H. Li, Construction of ultrathin C₃N₄/Bi₄O₅I₂ layered nanojunctions via ionic liquid with enhanced photocatalytic performance and mechanism insight. *Appl. Catal. B* **191** (2016) 235–245.
- [155] L. Shan, G. Wang, D. Li, X. San, L. Liu, L. Dong, Z. Wu, Band alignment and enhanced photocatalytic activation of α/β -Bi₂O₃ heterojunctions via in situ phase transformation. *Dalton Trans.* **44** (2015) 7835–7843.

- [156] T. A. Gadhi, A. Hernandez-Gordillo, M. Bizarro, P. Jagdale, A. Tagliaferro, S. E. Rodil, Efficient α/β -Bi₂O₃ composite for the sequential photodegradation of two-dyes mixture. *Ceram. Int.* **42** (2016) 13065–13073.
- [157] L. Chen, J. He, Q. Yuan, Y. Liu, C. Au, S. Yin, Environmentally benign synthesis of branched Bi₂O₃–Bi₂S₃ photocatalysts by an etching and re-growth method. *J. Mater. Chem. A* **3** (2015) 1096–1102.
- [158] C. Lv, G. Chen, J. Sun, C. Yan, H. Dong, C. Li, One-dimensional Bi₂O₃ QD-decorated BiVO₄ nanofibers: electrospinning synthesis, phase separation mechanism and enhanced photocatalytic performance. *RSC Adv.* **5** (2015) 3767–3773.
- [159] Y. Cheng, H. Wang, Y. Zhu, F. Liao, Z. Li, J. Li, One-step hydrothermal synthesis of BiVO₄–Bi₂O₃ p–n heterojunction composites and their enhanced photocatalysis properties. *J. Mater. Sci.: Mater. Electron.* **26** (2015) 1268–1274.
- [160] Q. Zhao, X. Liu, Y. Xing, Z. Liu, C. Du, Synthesizing Bi₂O₃/BiOCl heterojunctions by partial conversion of BiOCl. *J. Mater. Sci.*, **52** (2017) 2117–2130.
- [161] S. Han, J. Li, K. Yang, J. Lin, Fabrication of a β -Bi₂O₃/BiOI heterojunction and its efficient photocatalysis for organic dye removal. *Chin. J. Catal.* **36** (2015) 2119–2126.
- [162] D. Peng, Z. Zou, F. Long, J. He, T. Zhang, Solid state synthesis of nonstoichiometric Bi₂WO₆/Bi₂O₃ composites as visible-light photocatalyst. *Ionics* **22** (2016) 2347–2353.
- [163] L. Cheng, Y. Kang, Bi₅O₇I/Bi₂O₃ composite photocatalyst with enhanced visible light photocatalytic activity. *Catal. Commun.* **72** (2015) 16–19.
- [164] D. Wu, L. Ye, S. Yue, B. Wang, W. Wang, H. Y. Yip, P. K. Wong, Alkali-Induced in Situ Fabrication of Bi₂O₄-Decorated BiOBr Nanosheets with Excellent Photocatalytic Performance. *J. Phys. Chem. C* **120** (2016) 7715–7727.
- [165] Y. Liu, M. Zhang, L. Li, X. Zhang, In situ ion exchange synthesis of the Bi₄Ti₃O₁₂/Bi₂S₃ heterostructure with enhanced photocatalytic activity. *Catal. Commun.* **60** (2015) 23–26.
- [166] A. Rauf, M. S. A. S. Shah, G. H. Choi, U. B. Humayoun, D. H. Yoon, J. W. Bae, J. Park, W. Kim, P. J. Yoo, Facile Synthesis of Hierarchically Structured Bi₂S₃/Bi₂WO₆ Photocatalysts for Highly Efficient Reduction of Cr(VI). *ACS Sustainable Chem. Eng.* **3** (2015) 2847–2855.
- [167] X. Li, Y. Li, J. Shen, M. Ye, A controlled anion exchange strategy to synthesize Bi₂S₃ nanoparticles/plate-like Bi₂WO₆ heterostructures with enhanced visible light photocatalytic activities for Rhodamine B. *Ceram. Int.* **42** (2016) 3154–3162.

- [168] Y. Wu, Q. Han, L. Wang, X. Wang, J. Zhu, One-pot synthesis of 3D hierarchical $\text{Bi}_2\text{S}_3/(\text{BiO})_2\text{CO}_3$ hollow microspheres at room temperature and their photocatalytic performance. *Mater. Chem. Phys.* **187** (2017) 72–82.
- [169] F. Dong, X. Feng, Y. Zhang, C. Gao, Z. Wu, An anion-exchange strategy for 3D hierarchical $(\text{BiO})_2\text{CO}_3/\text{amorphous Bi}_2\text{S}_3$ heterostructures with increased solar absorption and enhanced visible light photocatalysis. *RSC Adv.* **5** (2015) 11714–11723.
- [170] Y. Mi, H. Li, Y. Zhang, R. Zhang, W. Hou, One-pot synthesis of belt-like $\text{Bi}_2\text{S}_3/\text{BiOCl}$ hierarchical composites with enhanced visible light photocatalytic activity. *Appl. Surf. Sci.* **423** (2017) 1062–1071.
- [171] X. Zhang, L. Zhang, J. Hu, C. Pan, C. Hou, Facile hydrothermal synthesis of novel $\text{Bi}_{12}\text{TiO}_{20}\text{-Bi}_2\text{WO}_6$ heterostructure photocatalyst with enhanced photocatalytic activity. *Appl. Surf. Sci.* **346** (2015) 33–40.
- [172] Y. Liu, G. Zhu, J. Peng, J. Gao, C. Wang, P. Liu, One-step molten-salt method fabricated $\text{Bi}_2\text{Ti}_2\text{O}_7/\text{Bi}_4\text{Ti}_3\text{O}_{12}$ composites with enhanced photocatalytic activity. *J. Mater. Sci.: Mater. Electron.* **28** (2017) 2172–2182.
- [173] P. Madhusudan, J. Ran, J. Zhang, J. Yu, G. Liu, Novel urea assisted hydrothermal synthesis of hierarchical $\text{BiVO}_4/\text{Bi}_2\text{O}_2\text{CO}_3$ nanocomposites with enhanced visible-light photocatalytic activity. *Appl. Catal. B* **110** (2011) 286–295.
- [174] Y. Si, J. Li, J. Zhong, J. Zeng, S. Huang, W. Yuan, M. Li, J. Ding, Charge separation properties of $(\text{BiO})_2\text{CO}_3/\text{BiOI}$ heterostructures with enhanced solar-driven photocatalytic activity. *Curr. Appl. Phys.* **16** (2016) 240–244.
- [175] Y. Ma, Y. Jia, L. Wang, M. Yang, Y. Bi, Y. Qi, $\text{Bi}_2\text{MoO}_6/\text{BiVO}_4$ heterojunction electrode with enhanced photoelectrochemical properties. *Phys. Chem. Chem. Phys.* **18** (2016) 5091–5094.
- [176] X. Lin, D. Liu, X. Guo, N. Sun, S. Zhao, L. Chang, H. Zhai, Q. Wang, Fabrication and efficient visible light-induced photocatalytic activity of $\text{Bi}_2\text{MoO}_6/\text{BiPO}_4$ composite. *J. Phys. Chem. Solids* **76** (2015) 170–177.
- [177] Q. W. Cao, Y. F. Zheng, X. C. Song, The enhanced visible light photocatalytic activity of $\text{Bi}_2\text{W}_x\text{Mo}_{1-x}\text{O}_6\text{-BiOCl}$ heterojunctions with adjustable energy band. *Ceram. Int.* **42** (2016) 14533–14542.

- [178] X. Zou, Y. Dong, X. Zhang, Y. Cui, X. Ou, X. Qi, The highly enhanced visible light photocatalytic degradation of gaseous o-dichlorobenzene through fabricating like-flowers BiPO₄/BiOBr p-n heterojunction composites. *Appl. Surf. Sci.* **391** (2017) 525–534.
- [179] W. S. Dos Santos, M. Rodriguez, A. S. Afonso, J. P. Mesquita, L. L. Nascimento, A. O. T. Patrocinio, A. C. Silva, L. C. A. Oliveira, J. D. Fabris, M. C. Pereira, A hole inversion layer at the BiVO₄/Bi₄V₂O₁₁ interface produces a high tunable photovoltage for water splitting. *Sci. Rep.* **6** (2016) 31406–31415.
- [180] Z. Xiang, Y. Wang, D. Zhang, P. Ju, BiOI/BiVO₄ p-n heterojunction with enhanced photocatalytic activity under visible-light irradiation. *J. Ind. Eng. Chem.* **40** (2016) 83–92.
- [181] T. He, D. Wu, Y. Tan, Fabrication of BiOI/BiVO₄ heterojunction with efficient visible-light-induced photocatalytic activity. *Mater. Lett.* **165** (2016) 227–230.
- [182] T. Yan, M. Sun, H. Liu, T. Wu, X. Liu, Q. Yan, W. Xu, B. Du, Fabrication of hierarchical BiOI/Bi₂MoO₆ heterojunction for degradation of bisphenol A and dye under visible light irradiation. *J. Alloys Compd.* **634** (2015) 223–231.
- [183] X. Liu, Y. Su, Q. Zhao, C. Du, Z. Liu, Constructing Bi₂₄O₃₁C₁₁₀/BiOCl heterojunction via a simple thermal annealing route for achieving enhanced photocatalytic activity and selectivity. *Sci. Rep.* **6** (2016) 28689–28692.
- [184] L. Hao, H. Huang, Y. Guo, X. Du, Y. Zhang, Bismuth oxychloride homogeneous phasejunction BiOCl/Bi₁₂O₁₇Cl₂ with unselectively efficient photocatalytic activity and mechanism insight. *Appl. Surf. Sci.* **420** (2017) 303–312.
- [185] C. Feng, D. Wang, B. Jin, Z. Jiao, The enhanced photocatalytic properties of BiOCl/BiVO₄ p–n heterojunctions via plasmon resonance of metal Bi. *RSC Adv.* **5** (2015) 75947–75952.
- [186] S. Tu, M. Lu, X. Xiao, C. Zheng, H. Zhong, X. Zuo, J. Nan, Flower-like Bi₄O₅I₂/Bi₅O₇I nanocomposite: facile hydrothermal synthesis and efficient photocatalytic degradation of propylparaben under visible-light irradiation. *RSC Adv.* **6** (2016) 44552–44560.
- [187] H. Huang, K. Xiao, T. Zhang, F. Dong, Y. Zhang, Rational design on 3D hierarchical bismuth oxyiodides via in situ self-template phase transformation and phase-junction construction for optimizing photocatalysis against diverse contaminants. *Appl. Catal. B* **203** (2017) 879–888.

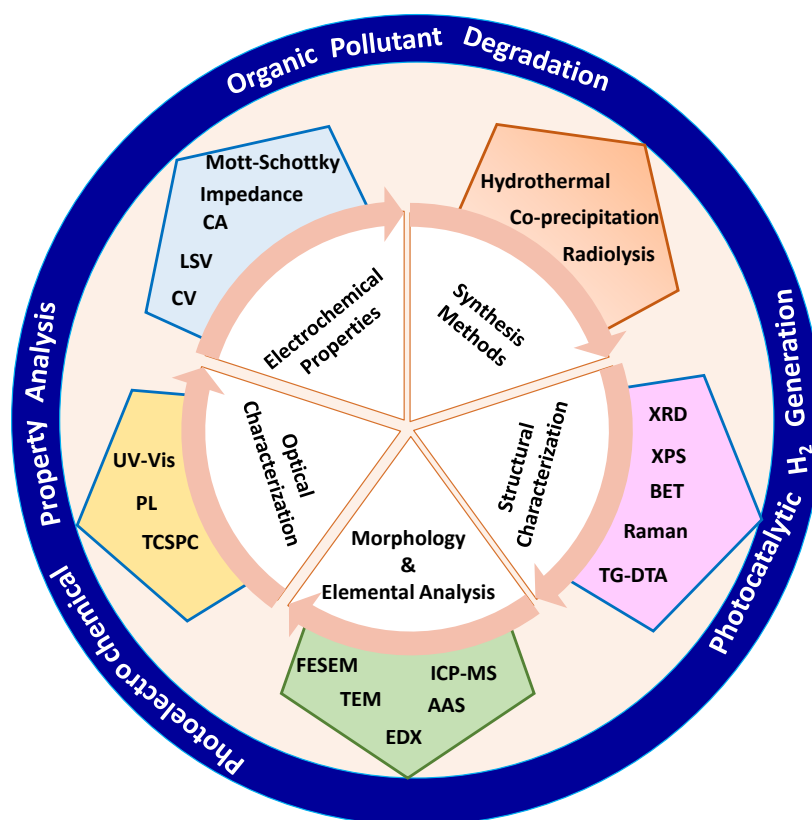
- [188] C. Zeng, Y. Hu, Y. Guo, T. Zhang, F. Dong, X. Du, Y. Zhang, H. Huang, Achieving tunable photocatalytic activity enhancement by elaborately engineering composition-adjustable polynary heterojunctions photocatalysts. *Appl. Catal. B* **194** (2016) 62–73.
- [189] Q. Wang, X. Shi, E. Liu, J. C. Crittenden, X. Ma, Y. Zhang, Y. Cong, Facile synthesis of AgI/BiOI-Bi₂O₃ multi-heterojunctions with high visible light activity for Cr(VI) reduction. *J. Hazard. Mater.* **317** (2016) 8–16.
- [190] S. Chou, C. Chen, Y. Dai, J. Lin, W. W. Lee, Novel synthesis of bismuth oxyiodide/graphitic carbon nitride nanocomposites with enhanced visible-light photocatalytic activity. *RSC Adv.* **6** (2016) 33478–33491.
- [191] Y. Zhang, M. Park, H. Y. Kim, B. Ding, S. Park, In-situ synthesis of nanofibers with various ratios of BiOCl_x/BiOBr_y/BiOI_z for effective trichloroethylene photocatalytic degradation. *Appl. Surf. Sci.* **384** (2016) 192–199.
- [192] W. Li, P. Li, Y. Liu, B. Zhang, H. Zhang, W. Geng, Q. Zhang, Efficient Photocatalytic Degradation of Dyes over Hierarchical BiOBr/β-Co(OH)₂/PVP Multicomponent Photocatalyst under Visible-Light Irradiation. *Chem. Cat. Chem.* **7** (2015) 4163–4172.
- [193] J. Zhang, Y. Hu, X. Jiang, S. Chen, S. Meng, X. Fu, Design of a direct Z-scheme photocatalyst: Preparation and characterization of Bi₂O₃/g-C₃N₄ with high visible light activity. *J. Hazard. Mater.* **280** (2014) 713–722.
- [194] S. Chen, Y. Hu, L. Ji, X. Jiang, X. Fu, Preparation and characterization of direct Z-scheme photocatalyst Bi₂O₃/NaNbO₃ and its reaction mechanism. *Appl. Surf. Sci.* **292** (2014) 357–366.
- [195] D. Wang, Z. Guo, Y. Peng, W. Yuan, A simple route to significant enhancement of photocatalytic water oxidation on BiVO₄ by heterojunction with SiC. *Chem. Eng. J.* **281** (2015) 102–108.
- [196] S. N. F. M. Nasir, H. Ullah, M. Ebadi, A. A. Tahir, J. S. Sagu, M. A. M. Teridi, New Insights into Se/BiVO₄ Heterostructure for Photoelectrochemical Water Splitting: A Combined Experimental and DFT Study. *J. Phys. Chem. C* **121** (2017) 6218–6228.
- [197] G. Liu, S. You, H. Huang, M. Ma, N. Ren, A novel Z-scheme BiPO₄-Bi₂O₂(OH)(NO₃) heterojunction structured hybrid for synergistic photocatalysis. *Chemosphere* **171** (2017) 702–709.

- [198] F. Wang, W. Li, S. Gu, H. Li, X. Wu, C. Ren, X. Liu, Facile fabrication of direct Z-scheme $\text{MoS}_2/\text{Bi}_2\text{WO}_6$ heterojunction photocatalyst with superior photocatalytic performance under visible light irradiation. *J. Photochem. Photobiol. A* **335** (2017) 140–148.
- [199] H. Li, T. Hu, R. Zhang, J. Liu, W. Hou, Preparation of solid-state Z-scheme $\text{Bi}_2\text{MoO}_6/\text{MO}$ (M double bond Cu, $\text{Co}_{3/4}$, or Ni) heterojunctions with internal electric field-improved performance in photocatalysis. *Appl. Catal. B* **188** (2016) 313–323.
- [200] J. Lv, K. Dai, J. Zhang, L. Geng, C. Liang, Q. Liu, G. Zhu, C. Chen, Facile synthesis of Z-scheme graphitic- $\text{C}_3\text{N}_4/\text{Bi}_2\text{MoO}_6$ nanocomposite for enhanced visible photocatalytic properties. *Appl. Surf. Sci.* **358** (2015) 377–384.
- [201] X. Zhao, J. Yu, H. Cui, T. Wang, Preparation of direct Z-scheme $\text{Bi}_2\text{Sn}_2\text{O}_7/\text{g-C}_3\text{N}_4$ composite with enhanced photocatalytic performance. *J. Photochem. Photobiol. A* **335** (2017) 130–139.
- [202] C. Song, Y. Feng, W. Shi, C. Liu, Fabrication and mechanism of a novel direct solid-state Z-scheme photocatalyst CdS/BiOI under visible light. *Cryst. Eng. Comm.* **18** (2016) 7796–7804.
- [203] W. Wang, H. Cheng, B. Huang, X. Liu, X. Qin, X. Zhang, Y. Dai, Hydrothermal synthesis of $\text{C}_3\text{N}_4/\text{BiOI/O}_3$ heterostructures with enhanced photocatalytic properties. *J. Colloid Interface Sci.* **442** (2015) 97–102.
- [204] C. Liu, Q. Wu, M. Ji, H. Zhu, H. Hou, Q. Yang, C. Jiang, J. Wang, L. Tian, J. Chen, W. Hou, Constructing Z-scheme charge separation in 2D layered porous $\text{BiOBr}/\text{graphitic C}_3\text{N}_4$ nanosheets nanojunction with enhanced photocatalytic activity. *J. Alloys Compd.* **723** (2017) 1121–1131.
- [205] S. Wang, X. Yang, X. Zhang, X. Ding, Z. Yang, K. Dai, H. Chen, A plate-on-plate sandwiched Z-scheme heterojunction photocatalyst: $\text{BiOBr}-\text{Bi}_2\text{MoO}_6$ with enhanced photocatalytic performance. *Appl. Surf. Sci.* **391** (2017) 194–201.
- [206] J. Ding, Z. Dai, F. Qin, H. Zhao, S. Zhao, R. Chen, Z-scheme $\text{BiO}_{1-x}\text{Br}/\text{Bi}_2\text{O}_2\text{CO}_3$ photocatalyst with rich oxygen vacancy as electron mediator for highly efficient degradation of antibiotics. *Appl. Catal., B* **205** (2017) 281–291.
- [207] W. Jo, T. S. Natarajan, Fabrication and efficient visible light photocatalytic properties of novel zinc indium sulfide (ZnIn_2S_4) – graphitic carbon nitride ($\text{g-C}_3\text{N}_4$)/bismuth vanadate

- (BiVO₄) nanorod-based ternary nanocomposites with enhanced charge separation via Z-scheme transfer. *J. Colloid Interface Sci.* **482** (2016) 58–72.
- [208] M. J. Islam, D. A. Reddy, N. S. Han, J. Choi, J. K. Song, T. K. Kim, An oxygen-vacancy rich 3D novel hierarchical MoS₂/BiOI/AgI ternary nanocomposite: enhanced photocatalytic activity through photogenerated electron shuttling in a Z-scheme manner. *Phys. Chem. Chem. Phys.* **18** (2016) 24984–24993.
- [209] S. J. A. Moniz, S. Ghosh (Ed), Visible-Light-Active Photocatalysis: Nanostructured Catalyst Design, Mechanisms and Applications, Wiley-VCH VerlagGmbH & Co. KGaA, Germany, Chapter 8, 2018, ISBN: 978-3-527-34293-8.
- [210] S. Ghosh (Ed), Heterostructured photocatalysts for solar energy conversion, Elsevier Inc., 2020, ISBN: 9780128200735.
- [211] M. D. Hernández-Alonso, F. Fresno, S. Suárez, J. M. Coronado, Development of alternative photocatalysts to TiO₂: Challenges and opportunities. *Energy Environ. Sci.* **2** (2009) 1231–1257.
- [212] Y. Xu, Y. Huang, B. Zhang, Rational design of semiconductor-based photocatalysts for advanced photocatalytic hydrogen production: the case of cadmium chalcogenides. *Inorg. Chem. Front.* **3** (2016) 591–615.

CHAPTER 3

Experimental



3.1 Introduction

Nanostructures have attracted huge interest as a rapidly growing class of materials due to superior properties including electronic, optical, magnetic catalytic compared to their bulk counterparts, because of surface defects, high surface to volume ratios and quantum confinement effects [1-3]. A Significant efforts have been made to develop efficient methods for nanomaterials synthesis with desired properties. In general, top-down and bottom-up methods have been reported for nanomaterials synthesis [4]. In case of top-down method, a large piece of material broken and turn into a nanosized material, which requires high energy, pressure and specialized setups to maintain the conditions [5, 6]. Thus, top-down method is expensive and not suitable for large scale applications. The sputtering, mechanical milling, electro-explosion, etching and laser ablation are the examples of Top-down methods. On the other hand, atoms or molecules are integrated to form nanomaterials in bottom-up methods, i.e. based on wet-chemical approaches, which is facile and scalable [7]. In addition, kinetic and thermodynamic parameters can be controlled to achieve uniform sizes and shapes, which further greatly influence the surface, optical and electronic properties [8, 9]. Bottom-up method includes chemical vapor deposition [10], solvothermal and hydrothermal [11], sol–gel method [12], soft and hard templating methods [13], reverse micelle methods [14] etc. A series of synthesis methods with controlled dimension, growth direction and the characterization techniques have been reported to use nanomaterials in diverse field of applications. The scalable synthesis of nanomaterials with desirable morphology, size and uniformity for photocatalytic application is the main aim of this doctoral work. Facile methods, including hydrothermal, solvothermal, co-precipitation, chemical exfoliation and gamma radiolysis etc. have been employed to prepare semiconductor nanomaterials and heterostructures.

3.2 Synthesis Methods

3.2.1 Hydrothermal and Solvothermal Method

Both the hydrothermal and solvothermal methods are potential way to synthesis semiconductor nanomaterials with high purity. In this method, a high temperature and vapor pressure have been employed to synthesis highly crystalline nanomaterials [15]. At first, the precursor materials are dissolved in the solvent and then transferred in a Teflon lined autoclave with steel jacket. The crystal growth is performed in the autoclave by the influence of temperature and pressure gradient generated in the oven (Figure 3.1). When water is used as solvent, then it called hydrothermal

method and while non-aqueous solvent like ethelene glycol, alcohol or any other organic or inorganic solvent acid etc. are used then termed as solvothermal method [16]. In this work, assembled flower like bismuth sulphide (Bi_2S_3), bismuth tungstate (Bi_2WO_6), hexagonal nanosheets of bismuth ferrite (BiFeO_3) and nanosheet like bismuth oxyhalides [BiOX ($\text{X}=\text{Cl}, \text{Br}, \text{I}$)] are synthesized through hydrothermal method. In addition, the growth control of Bi_2S_3 nanorods are studied in details.

The advantages of these methods:

The crystals with high melting points and high vapour pressure can be produced

Nanomaterials with uniform morphology can be produced

Morphology of nanomaterials can be tuned

Growth control of a nanomaterial can be investigated

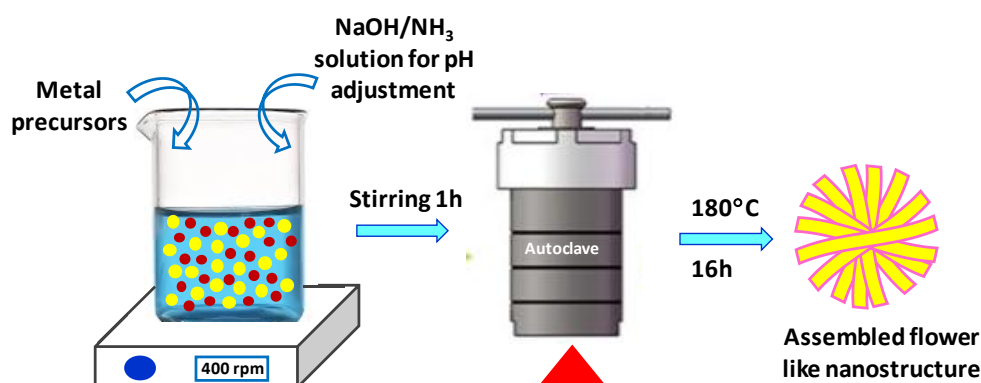


Figure 3.1 Schematic presentation of hydrothermal synthesis of assembled flower nanostructures.

3.2.2 Co-precipitation Method

Co-precipitation method is widely used to synthesis metal oxide nanoparticles. Different parameters, such as concentration of precursors, pH of the solvent, and temperature have important role in size and morphology controlling of developed nanomaterials [17, 18]. At first, raw materials, such as nitrate or chloride salts are dissolved in water or other non-aqueous solvent to prepare homogeneous solution. After that, pH of the solution has been controlled by adding $\text{NaOH}/\text{NH}_4\text{OH}$, which results formation of precipitates. The yield is very high which is advantageous for large scale application.

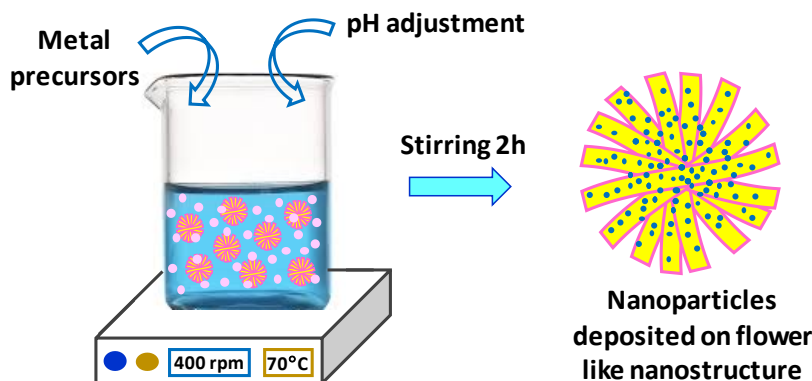
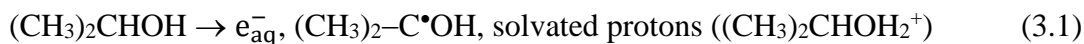


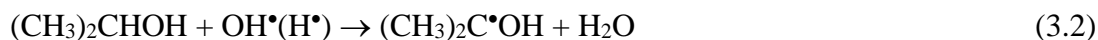
Figure 3.2 Schematic presentation of co-precipitation method to prepare nanoparticles decorated flower like nanostructures.

3.2.3 Gamma Radiolysis

Gamma radiolysis is a colloidal method to synthesis metal nanoparticles with controlled size and shape. The highly versatile and effective method of radiolysis for the synthesis of a wide range of nanomaterials including metals, metal alloys, semiconductors, polymers etc. [19-23] The radiation method requires aqueous solution of metal salts because hydrated electrons (e_{aq}^-) and various free radicles, for example OH^\bullet , H^\bullet , HO_2^\bullet , H_3O^+ , OH^- , H_2O_2 , H_2 are formed during radiolysis of water which further involved in reduction reaction (Figure 3.3) [24, 25]. The e_{aq}^- and H^\bullet are act as reducing agents, having the redox potentials of $E_0(H_2O/e_{aq}^-) = -2.87$ V vs NHE and $E_0(H^+/H^\bullet) = -2.3$ V vs NHE, respectively, suitable for monovalent or multivalent metal ions reduction [26-28]. In this thesis, Au nanoparticles have been synthesized using gamma radiation (^{60}Co gamma-facility) for 2h at dose rate of 5.5 kGy h^{-1} on the surface of $BiFeO_3$, in presence of water and 2-propanol mixture as solvent. Thus, 2-propanol produces free radicles during radiolysis [29].



The OH^\bullet and H^\bullet react with the 2-propanol to produce hydroxyalkyl radicals which further generate new radicals by reacting with solvent molecules for reduction of metal precursor into zero-valent state. Therefore, metal ions formation *via* radiolysis is a multistep process where unusual valence states are formed initially, after that reduction and agglomeration started to form stable nanoparticles [29]. The reactions are as follows.



For Au nanoparticle synthesis;

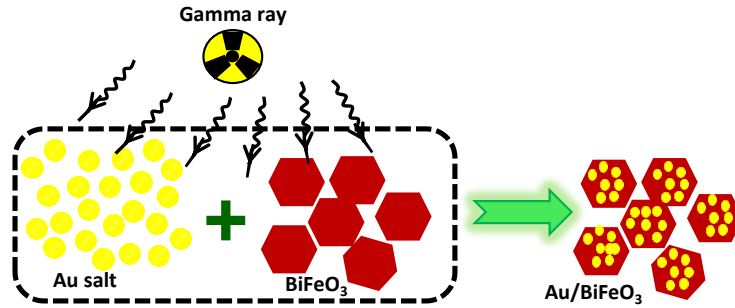


Figure 3.3 Schematic Au/BiFeO₃ heterostructures synthesis by gamma radiolysis.

3.3 Characterization Techniques

Several techniques have been used to characterize the size, crystal structure, elemental composition and a variety of other physical properties of nanoparticles can be evaluated by more than one technique. In this thesis work, the structural, morphological, optical, electrochemical and magnetic properties of the as prepared semiconductor nanostructures and heterostructures have been studied in details. The working principal, operational method and the application methods of each techniques have been described in brief.

3.3.1 Structural Characterization

The study of crystal structure, chemical composition, thermal stability, porosity, surface area etc. are the first step to characterize the semiconductor-based nanostructures after synthesis.

3.3.1.1 Powder X-Ray Diffraction (XRD)

XRD is a non-destructive powerful technique for characterizing the crystalline materials and has become defining way to understand the growth of semiconductors. It provides information on phases, structures, preferred crystal orientations, average grain size, unit cell dimension, crystallinity, strain and crystal defects [30, 31]. The basic principal can be explained through a classical treatment, scattering of electromagnetic waves. When X-rays travelled through a

crystalline material, an elastic (Rayleigh) scattering occurred due to the interaction between X-ray electrons and the atoms of material, which resulted a diffraction pattern. Consider a series of planes with interplanar spacing (d), and an electromagnetic wave of incident angle (θ). When the electromagnetic wave interacts with atoms, it will scatter in all possible directions, however, reflected from the atoms at the same angle of incident as the crystalline lattice has ordered and layered structure in a unit cell (Figure 3.4). Now for two reflected waves, ABC and A'B'C', the phase will be same and the phase difference between them is a multiple of 2π , which is equal to the path difference.

$$A'B'C' - ABC = n\lambda \quad (3.9)$$

$$(AB + BC + 2d\sin\theta) - (AB + BC) = n\lambda \quad (3.10)$$

$$2d\sin\theta = n\lambda \quad (3.11)$$

This equation is known as Bragg's law [32], where, n is an integer and λ is the wavelength.

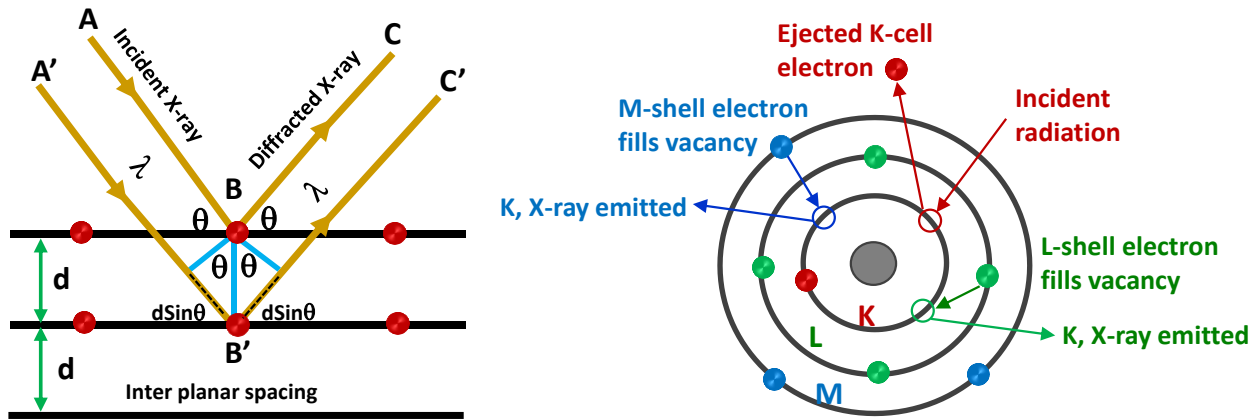


Figure 3.4 Schematic representations of diffracted beams in crystal lattice.

In case of powder material, different crystallites are arranged randomly which causes all planes to be perpendicular to the normal incident of the waves at some point within a sample. Therefore, a diffraction pattern can be generated by changing the incidence or detection angle, as a function of 2θ . The intensity of the diffracted peak (I_{hkl}) has been calculated from the square of structure factor [33].

$$I_{hkl} = |F_{hkl}|^2 \quad (3.12)$$

$$F_{hkl} = \sum_{n=0}^N f_n e^{2\pi i(hx_n + ky_n + lz_n)} \quad (3.13)$$

Where, hkl are the Miller indices of a certain series of planes, f_n is the atomic scattering factor. A relation between intensity and scattering angle can be obtained by varying the angles of both x-ray

source and detector (2θ). With the help of a database the elements can be identified according to their intensities. The crystallinity of the material can be determined from the peak intensity. The average particle size can be determined from the XRD diffraction using Scherrer's equation (Eq. 3.14):

$$\tau = K\lambda\beta\cos\theta \quad (3.14)$$

Where, $\tau \rightarrow$ average grain size, $K \rightarrow$ shape factor (~ 1), $\lambda \rightarrow$ x-ray wavelength, $\theta \rightarrow$ Bragg angle and $\beta \rightarrow$ line broadening at half the maximum intensity. However, Scherrer equation is not applicable for a grain size $> 0.1\mu\text{m}$. The X-ray are generated from a cathode ray tube then filtered and passed through the collimators to produce monochromatic ray. The monochromatic ray further directed towards sample and an interaction occurred between incident ray and electrons of the sample. A constructive interference would be happened which resulted diffracted rays that finally detected by the detector (Figure 3.5). In this thesis work, powder XRD has been performed using Rigaku XRD instrument for each of the synthesized semiconductor nanostructures and the heterostructures within the 2θ region, 10° to 80° at 1°min^{-1} scan rate. The Cu $K\alpha$ radiation has been used as X-ray radiation source at 40 kV, operate in 40 mA. The commonly used database for the identification of crystal structures is the Joint Committee on Powder Diffraction Standards–International Center for Diffraction Data (JCPDS-ICDD) system. This is a useful technique to determine impurities, phase and crystallinity of photocatalyst material and understand the effect of crystal structure in photocatalytic activity.

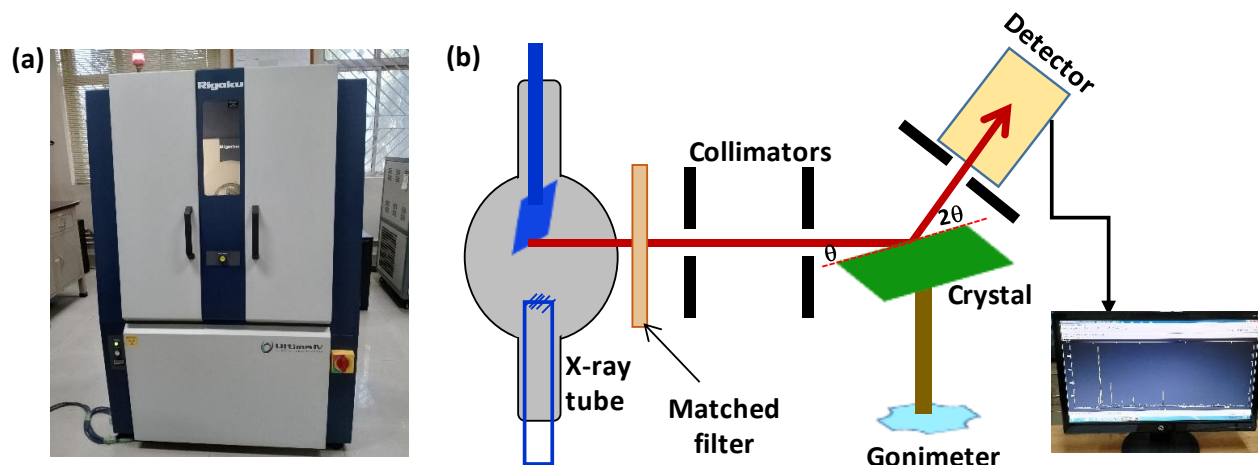


Figure 3.5 (a) The XRD instrumental setup and (b) the schematic presentation of working principal.

3.3.1.2 X-ray Photoelectron Spectroscopy (XPS)

XPS is a quantitative technique that measures the elemental composition, empirical formula, chemical state, and electronic state of the elements within a nanomaterial. The basic principle of XPS is based on photoelectric effect, where radiation beam of sufficient energy impacting on a material and causes the ejection of photoelectrons (Figure 3.6) [34].

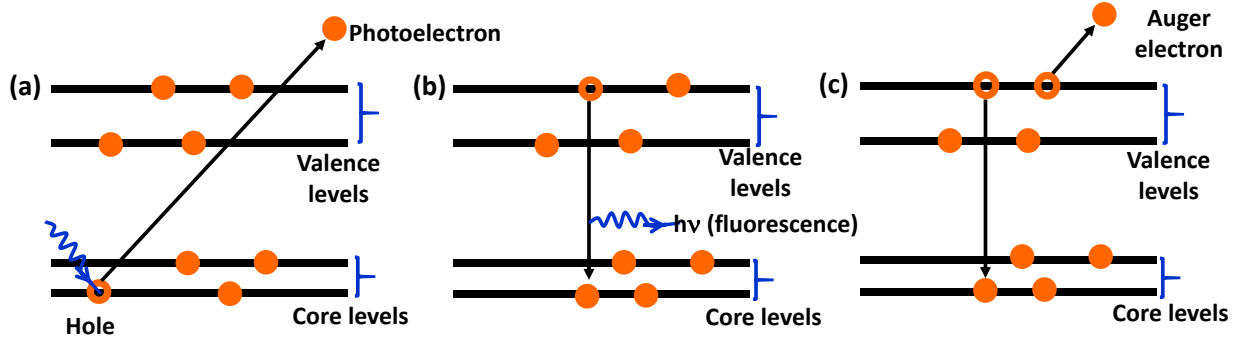


Figure 3.6 Schematic illumination of (a) photoelectron emission by absorption of a photon, (b) a core electron is expelled leaving a hole to fill the vacancy at valence level by releasing energy as fluorescence, (c) or an Auger electron from the same valence level.

These excited electrons then transfer to the material's surface through various scattering processes. After that, the electrons emitted into the vacuum by overcoming the work function energy (ϕ_s) of material. In these steps, there is no energy loss as electrons move through the sample. Therefore, the kinetic energy (E_k) of the electron is related to the work function energy, photon energy ($h\nu$) and binding energy (E_B) of material [35, 36]. Now, work function energy can be defined as the energy difference between vacuum level and Fermi-level, i.e. energy barrier for an electron to emit from the surface. The relation between the kinetic energy and binding energy is [37];

$$E_k = h\nu - E_B - \phi_s \quad (3.15)$$

In XPS study, the E_B of specific atomic orbitals are measured, which give the information about oxidation state, local electronic environment of the material. The change of electron density around the atom changes the amount of nuclear screening which causes binding energy shift [38-40]. The core levels analysis provide the information about elemental composition as well as oxidation states. Now, the electrons which are photo-emitted from VB create VB spectra from which band alignment of a semiconductor can be calculated. From the valence band offset (VBO), ionization potential (IP) of the material can be determined. On the other hand, secondary electrons are produced during photoemission, which have less kinetic energy compared to the photon energy as they have to overcome high threshold potential.

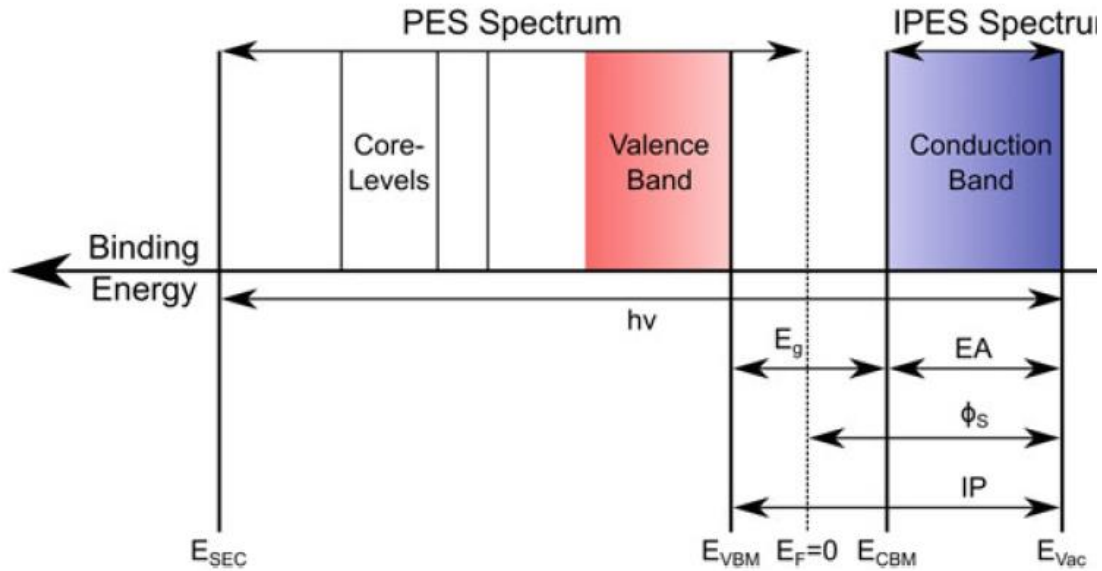


Figure 3.7 Electronic energy level determination from a combination of valence band XPS and secondary electron cutoff (SEC) spectra. [33]

As a result, a sharp, intense secondary electron cutoff (SEC) has been found where the kinetic energy becomes zero. From this SEC potential, work function energy can be calculated using the equation of [41, 42];

$$\phi_s = hv - E_{SEC} \quad (3.16)$$

Where, E_{SEC} is the potential of SEC. Now, the IP, electron affinity (EA) and bandgap (E_g) of the particular semiconductor can be calculated from the VBO and ϕ_s .

$$IP = \phi_s + E_{VBM} \quad (3.17)$$

$$EA = \phi_s + E_{SEC} \quad (3.18)$$

$$E_g = IP - EA \quad (3.19)$$

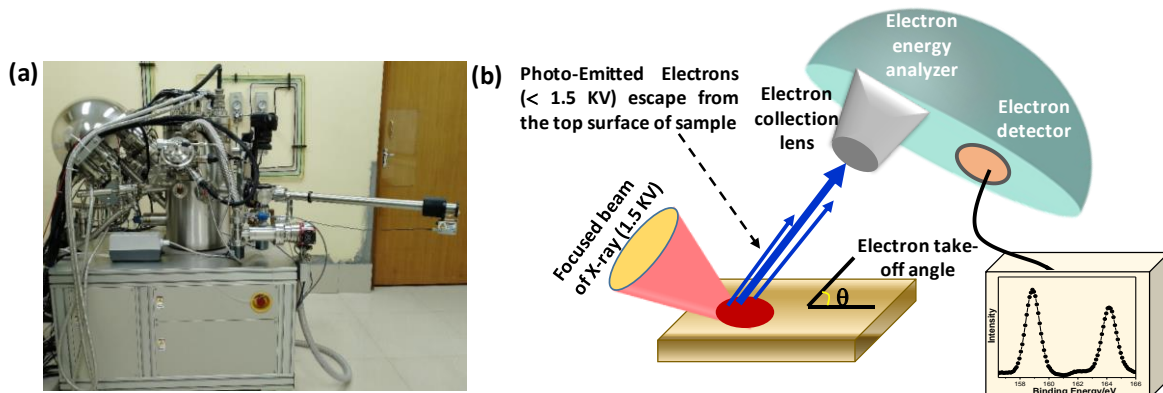


Figure 3.8 (a) XPS instrumental setup and (b) schematic presentation of the working principal of XPS.

In this thesis work, PHI 5000 Versa Probe II (Physical Electronics Inc., USA) spectrophotometer has been employed to study the core levels of the as developed materials under ultrahigh vacuum. A monochromatized X-ray beam (Al $K\alpha$, 1486.6 eV) of size 100 mm has been used.

3.3.1.3 Raman Spectroscopy

Raman spectroscopy is a convenient characterization tool used for structural identification, which can be treated as complement of XRD. Mainly rotational, vibrational and other low frequency modes are identified by this system. When a laser beam having a particular wavelength in the visible region irradiated on a material, an interaction occur between photons and the electrons, resulted electronic transitions in a “virtual” excited level (Figure 3.9) [39, 43]. As the virtual level is unstable thus excited electrons will quickly jump back to the ground level. Some electrons may come back to the original state and emit a photon of equal energy to the incident photon. This process is known as elastic scattering (Rayleigh scattering) [39]. In some cases, electrons can relax in a different rotational or vibrational energy state, emitting different energy photons due to inelastic scattering.

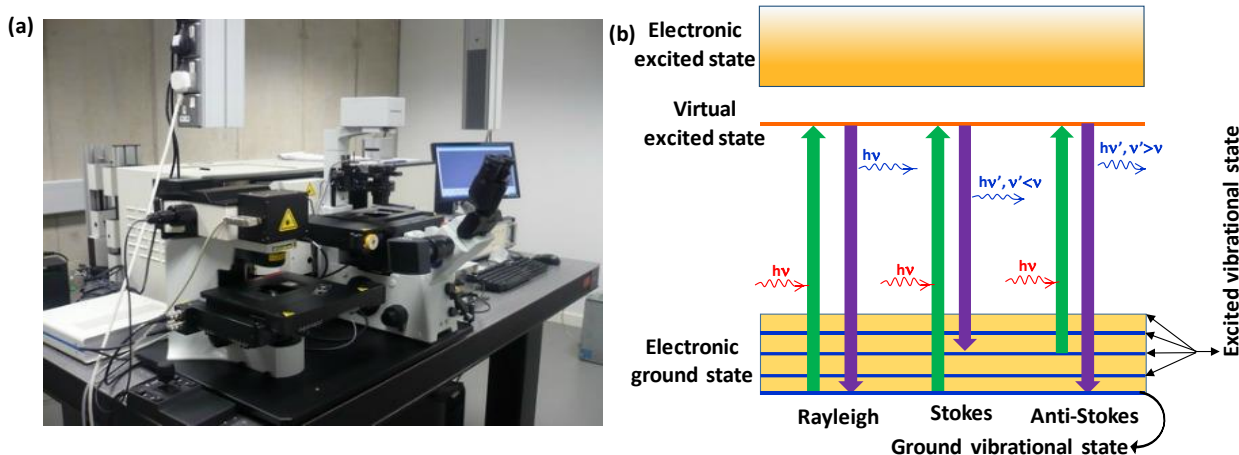


Figure 3.9 (a) The Raman instrumental setup and (b) schematic of Rayleigh, Stokes and Anti-Stokes lines formation at Raman Scattering.

If the final energy state has more energy than the initial one then low energy photons would be emitted compared to the incident photon, called Stokes lines. When the final energy state is less energetic than that of initial state, then high energy photons would be emitted, termed as anti-Stokes line [39, 44]. These Stokes and Anti-Stokes processes are known as Raman Effect. The Raman shift can be determined using the following equation.

$$\Delta\omega = \frac{1}{\lambda_1} - \frac{1}{\lambda_s} \quad (3.20)$$

Where, λ_1 and λ_2 are wavelengths of incident and scattered waves. Thus, a spectrum can be generated by measuring the energy difference as a function of Raman shift. The peaks appear in the spectrum is the same frequency of vibrational modes of the material. In general, a Raman spectrum plots the intensity of the inelastically scattered light as a function of shift of the radiation (in wave number). Each peak in the spectrum corresponds to one or more vibrational modes of the nanostructures. Jobin Yvon HR800 confocal Raman spectroscopy has been employed to identify the vibrational energy bands of the synthesized semiconductor nanostructures, where 540 nm laser beam used to excite the material. Figure 3.10 represents the schematic presentation of operational principal of Raman spectroscopy. The monochromatic laser beam is directed on the sample surface, which further undergo through different scattering. The backscattered light are identified as Rayleigh scattering which has much higher cross section. Then, the other ray passes through various types of filters and finally analyzed using a high-resolution dispersive spectrometer. The energy difference finally detected by the CCD (Charge Coupled Device) detector. Now, there are selection rules because some modes created from the phonon oscillation which are not Raman active. Therefore, by calculating the energies, predicting the phonon modes and applying the selection rules vibrational modes of the sample would be identified. Raman spectra provides a wide range of information about the strength of interatomic and intermolecular bonds within the material, mechanical strain, the material's degree of crystallinity, and the effects of pressure and temperature.

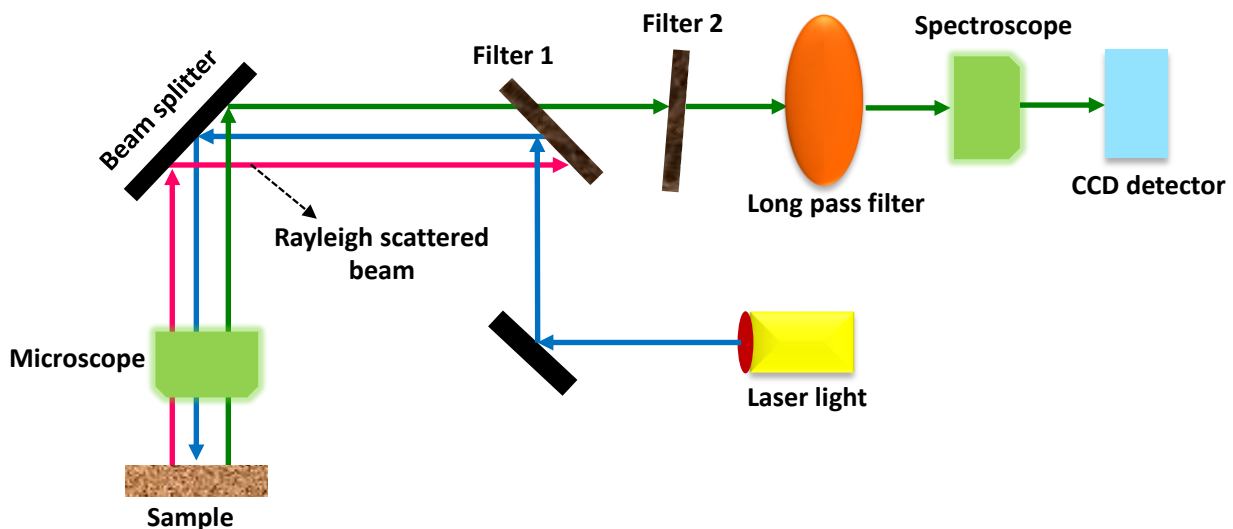


Figure 3.10 Schematic presentation of the working principal of Raman spectroscopy.

3.3.1.4 Brunauer–Emmett–Teller (BET) Surface Area

The BET surface area is a useful technique for calculating the pore volume, specific surface area, pore size and the pore size distribution of a material *via* nitrogen physisorption at a given temperature [45]. The material is exposed to N₂ gas for physical adsorption on the material surface, results weak van der Waals forces between adsorbent surface area and adsorbate gas molecules [46, 47]. Thus, an adsorption equilibrium would be established between gas and solid phase, which generated an adsorption isotherm between the relative vapour pressure and the adsorbed volume of gas. The N₂ gas molecules adsorb on the surface of the material at low pressure. With the increase of pressure, surface coverage enhances and forms a monolayer of N₂. After filling the smallest pores, multilayers formation starts to cover the large pores. Finally, the surface of the sample will be covered as the pressure rises (Figure 3.11a). The gas adsorbed is proportional to the total combined internal and external surface area of the material [48].

The assumptions in BET theory are, i) surface of the material should be homogeneous, ii) there are no lateral interactions between the molecules, iii) the uppermost layer of the surface considered as in equilibrium with vapor phase, iv) the number of the layers becomes infinite at the saturation pressure [49]. Then BET equation is as follows;

$$\frac{p}{v(p_0-p)} = \frac{1}{v_m C} + \frac{p(c-1)}{v_m c p_0} \quad (3.21)$$

Where, $p \rightarrow$ pressure, $v_m \rightarrow$ required volume of gas to form the first monolayer on the surface, $v \rightarrow$ total adsorbed volume, c is approximately equal to Eq. 3.22.

$$c \approx e^{\frac{E_1 - E_L}{RT}} \quad (3.22)$$

Here, $E_1 \rightarrow$ heat during adsorption of first layer, $E_L \rightarrow$ heat during liquefaction, $R \rightarrow$ universal gas constant, $T \rightarrow$ experiment temperature. An adsorption-desorption isotherm plot can be determined from the experimental data. There are six types of isotherms presented in Figure 3.11b. Type I isotherm suggests that pores are mainly microporous and can be fitted using Langmuir model. Initially, the isotherm curve increases rapidly with the increase of pressure and then almost saturated with the saturation in pressure [50].

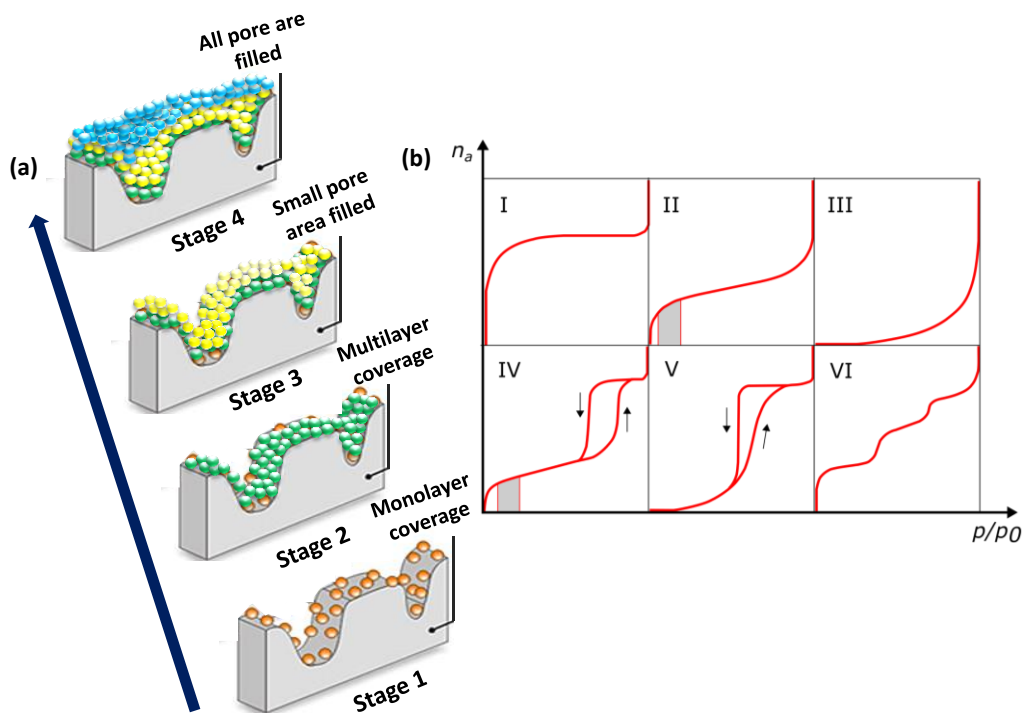


Figure 3.11 (a) Schematic of multilayers formation of N_2 to fill the pores during adsorption. (b) Six types of isotherms.

In case of nonporous materials or the powders having diameters exceeding micropores, Type II isotherm observed. The Type II, isotherm increases gradually with the pressure ratio and there is no plateau region. When complete monolayer of N_2 is not formed on the surface, then Type III isotherm may formed. It increases exponentially with the pressure ratio. It can be considered as the characteristics of Type I and Type II isotherms. At low pressure, a prominent saturation region of adsorption surface has been observed, which increases with the increase of pressure ratio and again resulted a saturation near the saturation pressure, confirms the formation of multilayer on the surface. Most commonly, Type IV isotherm obtained for porous adsorbents having pores size within the range of 1.5 – 100 nm [51]. Type V isotherm is nearly equal to the type III and obtained during adsorbate adsorbent interaction and associated with pore size range of 1.5 – 100 nm. Type VI isotherm is very complex and rarely founded for CH_4 adsorption on the MgO surface [52]. The schematic of the operational principal has been shown in Figure 3.12. The Quantachrome, FL-33426 instrument was used to determine the porosity and specific surface area of as synthesized semiconductor nanostructures and the heterostructures.

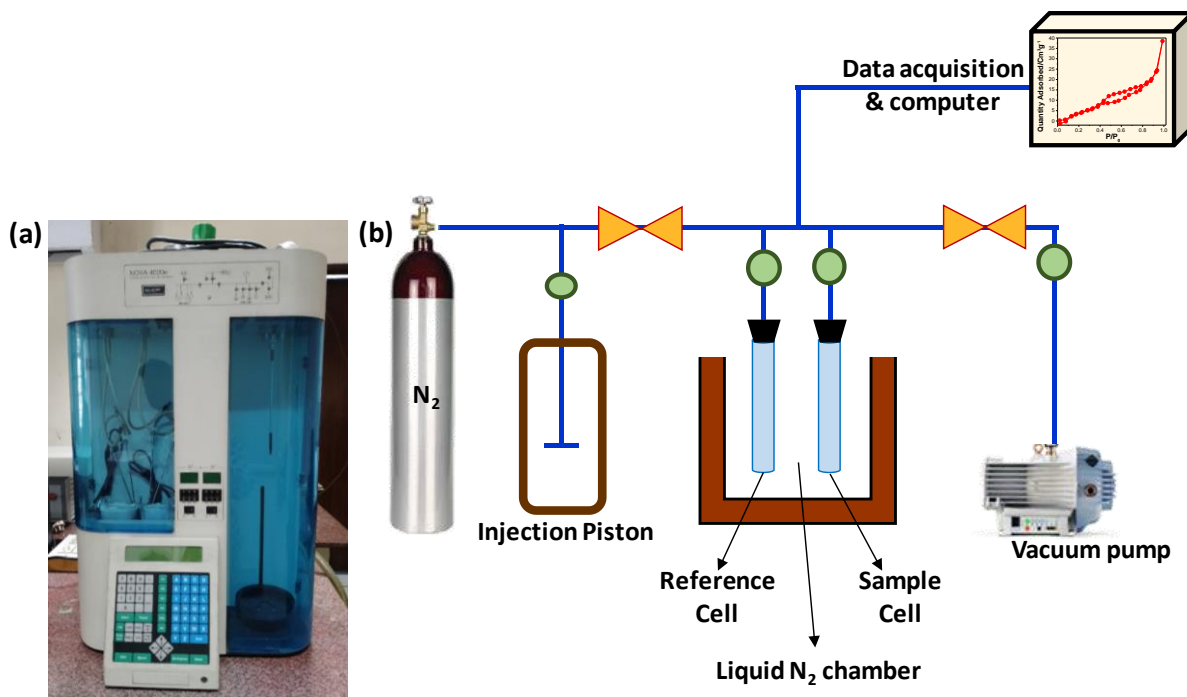


Figure 3.12 (a) BET instrumental setup and (b) schematically present the working principal of BET surface area.

3.3.1.5 Fourier Transform Infrared Spectroscopy (FTIR)

The FTIR is mainly employed to identify the chemical bonds in a molecule. Every material should have covalent bonds which absorb specific frequency of electromagnetic radiation [53]. The absorption is corresponding to energy change within the range of 8 – 40 kJ/mol. Notably, All the bonds of a molecule are not IR active, only those bonds having dipole moment can absorb IR light [54]. For example, heteronuclear diatomic molecules (CO, NO, HCl) and homonuclear diatomic molecules (H_2 , O_2 , Cl_2) do not have permanent dipole moment, thus inactive for IR spectrum. An infrared absorption spectra has been produced in FTIR by the Fourier-transformed of two beams separated by a beam splitter. Generally, monochromatic light is a superposition of same frequency waves. Thus, it shows maximum intensity when all the individual waves have same phase, and decreases when the phase difference becomes larger. This phase difference has been varied in FTIR using a moving mirror with constant speed, and a fixed mirror (Figure 3.13). A sinusoidal wave would be formed which gives single peak after Fourier transformation. For a constant light source, a destructive interference would be occurred and the resulted an interferogram. By taking a Fourier transform of the interferogram, the original frequency spectrum can be calculated. The

JASCO FTIR-6300 spectrometer was used to study chemical bonds of as prepared semiconductor nanostructures and heterostructures.

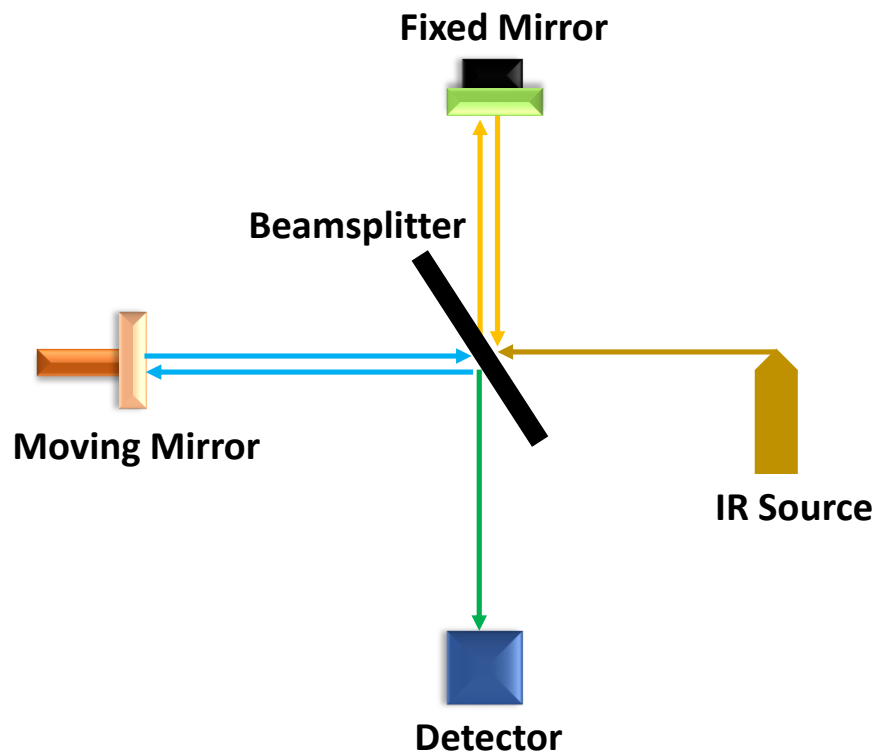


Figure 3.13 Schematic presentation of the operational principal of FTIR.

3.3.1.6 Thermogravimetry-Differential Thermal Analysis (TG-DTA)

TG-DTA is a useful measurement tool to study the thermal properties of a sample. The mass change due to evaporation, decomposition, oxidation etc. with the increase of temperature have been measured by TG [55, 56]. The DTA refers to differential thermal analysis, i.e. the exothermic or endothermic nature of decomposition processes. The temperature difference between the sample and reference has been measured by DTA, which showed step changes or a series of peaks over a programmed temperature range (Figure 3.14) [57]. The TG mainly used to analysis the thermal stability, oxidization, decomposition, heat resistance, dehydration and kinetics. In addition, loading of second material in a heterostructure can be calculated. Thermal properties of as synthesized semiconductor nanostructures and the heterostructures was studied by NETZSCH, STA 449 F3, Jupiter instrument in presence of argon medium at the flow rate of 10°C per minute within the temperature range of 30°C to 1200°C.

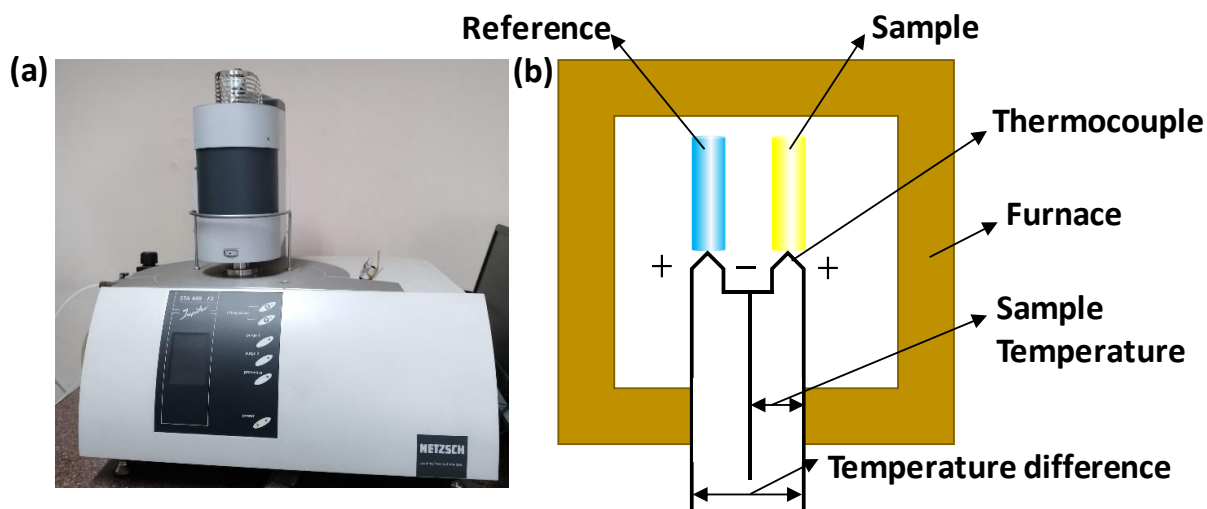


Figure 3.14 (a) TG-DTA instrumental setup and (b) schematic presentation of the working principal.

3.3.2 Morphology and Elemental Analysis

3.3.2.1 Field Emission Scanning Electron Microscope (FESEM)

In FESEM, a high energy electron beam are produced from a field emission source which further accelerated through high electrical field gradient and finally deflected by electronic lenses to generate a narrow and focused beam. The focused beam illuminates on the sample and interacts with the surface. The interaction results in emission of secondary electrons from each spot on the sample which finally capture by detectors and produce electronic signal [58]. An image can be generated by amplifying and transforming the electronic. The velocity and angle of the secondary electrons are strongly related to surface structure (Figure 3.15). Compared with conventional scanning electron microscope (SEM), FESEM produces high magnifications (10x to 300,000x) image with less electrostatically distorted and spatial resolution to 1-0.5 nanometers. The sample preparation for FESEM includes several steps, i) cleaning with ethanol or 2-propanol, ii) preparation dilute solution to avoid agglomeration, iii) make a thin film on the glass substrate by drop casting, iv) drying under IR lamp, v) coated with a conductive material. Notably, sample surface should be conductive as the non-conductive surface collects electrons and build up charge, which may artifacts the image. Therefore, a thin layer of carbon or gold coating has been applied on the surface of the sample to improve the surface conductivity and get the better quality image. Field Emission Scanning Electron Microscopy (LEO. 430i, Carl-Zeiss, Sigma) was employed to study the morphology of as prepared materials.

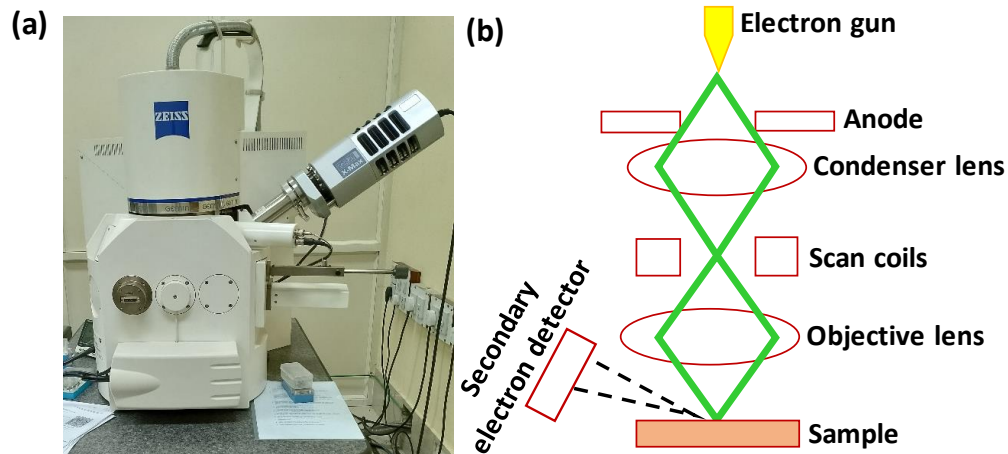


Figure 3.15 (a) The FESEM instrument and (b) schematic setup of FESEM column.

3.3.2.2 Transmission electron microscopy (TEM)

TEM is also a microscopy tool where nanoscale materials in atomic resolution have been allowed for imaging. The electrons are released from an electron gun under ultra-high vacuum *via* field emission or thermionic method and then transferred to the column by the influence of accelerating voltage (200 – 300 kV). After that, the electrons are directed through double and triple electromagnetic condenser lens and finally illuminated on the sample.

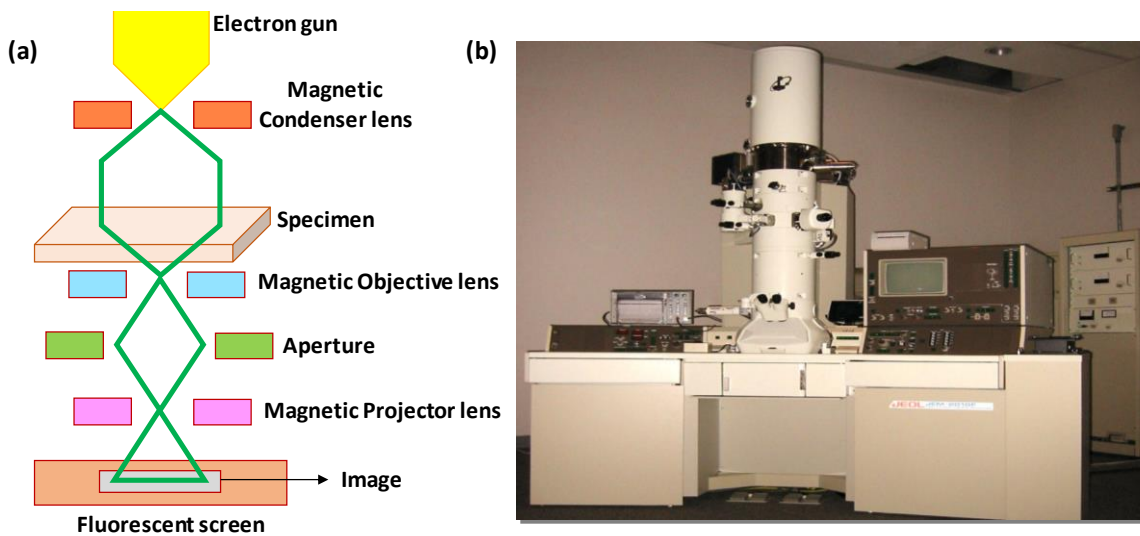


Figure 3.16 (a) Schematic setup of TEM column and (b) the image of TEM instrument.

During the transmission of electrons through the sample, interaction happened between electrons and atoms, resulted incoherent scattering and coherent diffraction which produces image contrast (Figure 3.16) [59]. In this thesis work, Tecnai G² 30ST (FEI), instrument at operating voltage 300 kV has been used to record the bright field images of the nanostructures and the heterostructures.

From the high-resolution TEM images, inter planar spacing (d) has been calculated which gives the idea about crystal plane, growth direction of the material, crystallinity (single crystal or polycrystal) and the formation of heterostructures.

3.3.2.3 Energy Dispersive X-ray Spectroscopy (EDX)

EDX is a useful method for elemental analysis and chemical characterization of a material. When the electron beam interacts with the surface atoms of a material, ground state electrons are stimulated and forced to be ejected. The higher energy electrons will fill the empty ground state and emit X-ray of energy equal to the difference between higher to ground state, which is the characteristic of individual elements [60]. The technique is based on the fact that every element has a unique atomic structure such that X-rays characteristic of different atomic structures are readily distinguishable. EDX systems are commonly used both with SEM and TEM.

3.3.2.4 ICP-MS and Atomic Absorption Spectroscopy (AAS)

Inductively coupled plasma mass spectrometry (ICP-MS) is a useful technique for determining the concentrations of elements in a materials. A plasma source has been used to ionize the atomic elements and excited them to a higher energy level so that a characteristic wavelength light can be emitted. The excited elements then expanded and cooled down in presence of Ar as carrier gas to form cations. The cations are then passed through mass analyzer and quadrupole or magnetic sector analyzer for separating them based on their atomic mass-to-charge ratio (Figure 3.17). The obtained mass spectra provide the quantification of present elements. The 8900 Triple Quadrupole ICP-MS, Agilent has been employed to study the materials.

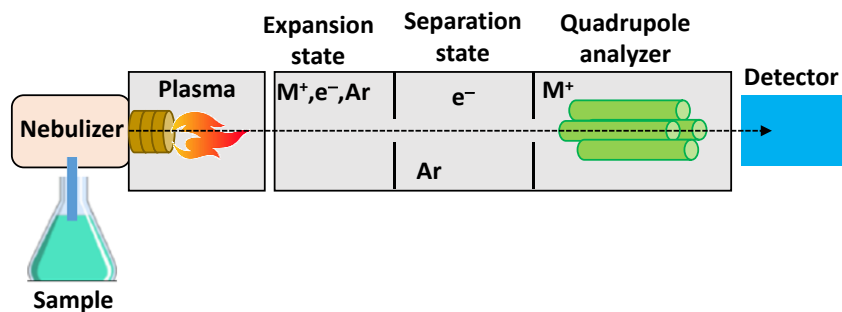


Figure 3.17 Schematic presentation of the working principal of inductively coupled plasma mass spectrometry (ICP-MS).

Atomic Absorption Spectroscopy (AAS) serves as fingerprint identification of elements in a sample. Each element in the periodic table has its own set of absorption lines which correspond to the most probable electronic transitions. Now, if the atomized sample irradiate with monochromatic light of same frequency with the specific element, then from the absorption spectra quantification of that element can possible (Figure 3.18). The concentration of that element present in the sample can be determined using the Beer's law [61]:

$$A = abc \quad (3.23)$$

where, $a \rightarrow$ absorption coefficient which is wavelength dependent, $b \rightarrow$ path length, $c \rightarrow$ concentration and $A \rightarrow$ absorbance.

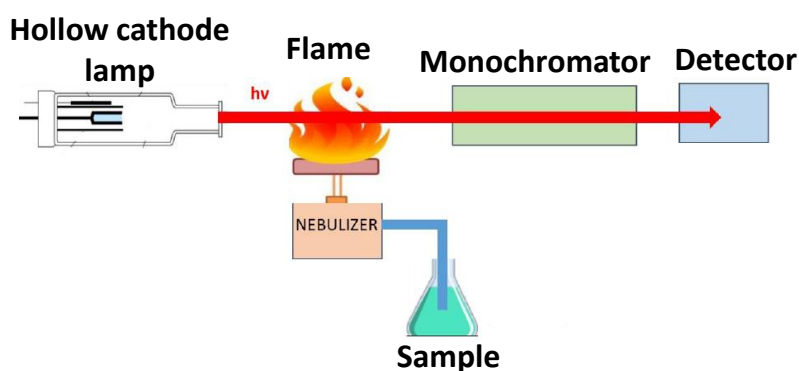


Figure 3.18 Schematic presentation of the working principal of atomic absorption spectroscopy (AAS).

3.3.3 Optical Properties Measurement

3.3.3.1 UV-Vis Absorption Spectroscopy

Ultraviolet-Visible spectroscopy is also an important tool for obtaining information about the electronic structure of semiconductor photocatalysts. When semiconductors are irradiated with higher energy photons (greater than the bandgap), absorption occurs which is corresponding to the excitation of valence electron and moving of electronic charges in a molecule. The change in the electronic dipole gives rise to an absorption spectrum. Let us consider, an incident light of intensity I_0 and wavelength λ is falling on a sample of path length d . Some of the light absorbed and some travelled through the sample and emerges with intensity I (Figure 3.19). Considering a thin layer of sample (dx) which is perpendicular to the direction of light, the $-dI/I$ (fraction of absorbed light) should be proportional to number of absorbed molecules.

$$-dI/I = C \epsilon' dx \quad (3.24)$$

Where, C is the concentration of absorbed molecules, $\epsilon' \rightarrow$ proportionality constant which is proportional to the probability photon absorbed by a molecule. By integrating the equation over the entire sample of length d ,

$$\ln(I_0/I) = C \epsilon' d \quad (3.25)$$

According to Johann Lambert, absorption is proportional to the thickness of a sample ($\propto d$). According to August Beer, absorption is proportional to the concentration of a sample ($\propto C$). Combining both, the well-known Beer-Lambert law has been found [61, 62].

$$\ln(I_0/I) = C \epsilon(\lambda) d \quad (3.26)$$

$$A(\lambda) = C \epsilon(\lambda) d \quad (3.27)$$

Where $A(\lambda)$ is absorbance and called as optical density OD, $\epsilon(\lambda) = \epsilon'/2.303$, molar absorption coefficient.

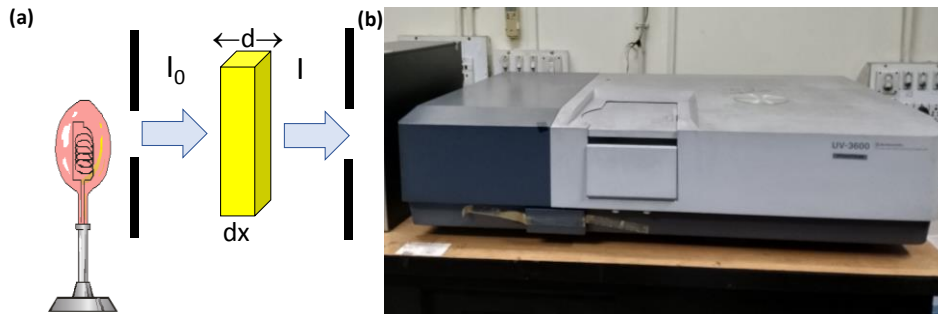


Figure 3.19 (a) Schematic presentation of Beer-Lambert law and (b) the UV-Vis absorption spectrophotometer.

In UV-Vis absorption spectroscopy, the light emitted from the source is first transmitted through a monochromator which further split into two equivalent beams by a chopper. One of them passes through the sample under study and another through the reference (Figure 3.20). Two detectors are placed to measure the sample beam and reference beam at a time. Generally, photodiodes are used as detector. For transmission measurements commercially available dual-beam spectrophotometers may be used in wavelengths ranging from 150 nm (ultraviolet) to 1200 nm (near-infrared). The absorption spectra are directly related to the bandgap of the semiconductor materials. A Shimadzu, UV-3600 spectrophotometer has been used to study the absorption range and bandgap of the semiconductor nanostructures and the heterostructures.

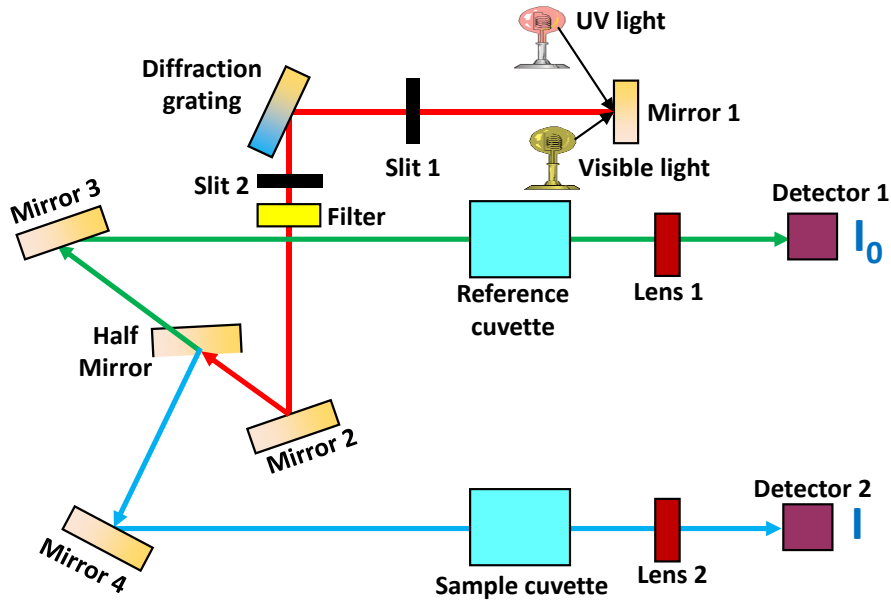


Figure 3.20 Working principal of UV-Vis absorption spectrophotometer.

The bandgap energy of a material and type of bandgap (direct or indirect) can be determined from the Kubelka–Munk (K–M) equation, which is given below.

$$F(R_\alpha) = \frac{(1-R_\alpha)^2}{2R_\alpha} = \frac{K}{S} \quad (3.28)$$

Where $F(R_\alpha) \rightarrow$ Kubelka-Munk function, $R_\alpha = R_{\text{sample}}/R_{\text{reference}}$, $k \rightarrow$ molar absorption co-efficient and $S \rightarrow$ scattering co-efficient. Now, optical bandgap and absorption coefficient can be determined from the Eq. 3.29 [63, 64]:

$$\alpha h\nu = c(h\nu - E_g)^n \quad (3.29)$$

where, $h\nu \rightarrow$ photon energy, $\alpha \rightarrow$ linear absorption coefficient, $C \rightarrow$ proportionality constant and n is a constant, which denotes different types of electronic transitions. For example, $n = 1/2, 3/2, 2$ and 3 implies direct allowed, direct forbidden, indirect allowed, and indirect forbidden transaction, respectively. When, $n = 1/2$ (for direct bandgap) then the Eq. 3.28 will be [65],

$$[F(R_\alpha)h\nu]^2 = c(h\nu - E_g) \quad (3.30)$$

3.3.3.2 Photoluminescence (PL) Spectroscopy

The PL is a nondestructive method to characterize the optoelectronic properties of semiconductors. When light energy is directed onto a sample, absorption and photo-excitation may occur. In case of photo-excitation, the electrons get excited by the higher energy photon

absorption ($h\nu > E_g$) and jump to a higher electronic state creating photo-excited electron-hole pairs, which further results recombination during return back from the excited state to ground state. The recombination causes transformation of energy partly into a radiative emission, i.e. emission of a photon and partly into a non-radiative emission, i.e. non-emission of a photon. The radiative relaxation gives the information about characteristics of the crystal matrix and also the defect site. The radiative luminescence may result from the band-to-band recombination, dopant impurities, intrinsic crystalline defects, or other extrinsic defects. Therefore, from the PL spectra specific defect present in semiconductor crystal and the rate of recombination can be obtained [66]. In case of indirect bandgap semiconductors, the photon emission process is phonon mediated in order to preserve the momentum of the lattice structure. The most common radiative and non-radiative transitions are band-to-band transitions, donor-acceptor pair transitions, free-to-bound transitions, excitonic transitions and Auger transitions. The introduction of impurities in a crystal create discrete energy levels which may form shallow donor and acceptor levels below and above the CB and VB, respectively. These donor or acceptor level may serve as recombination center to traps the excited electrons [67]. A complete PL spectrum can be characterized by an excitation spectrum and an emission spectrum which are characterized by the intensity as function of wavelength. Figure 3.21 shows the schematic diagram of PL spectrophotometer.

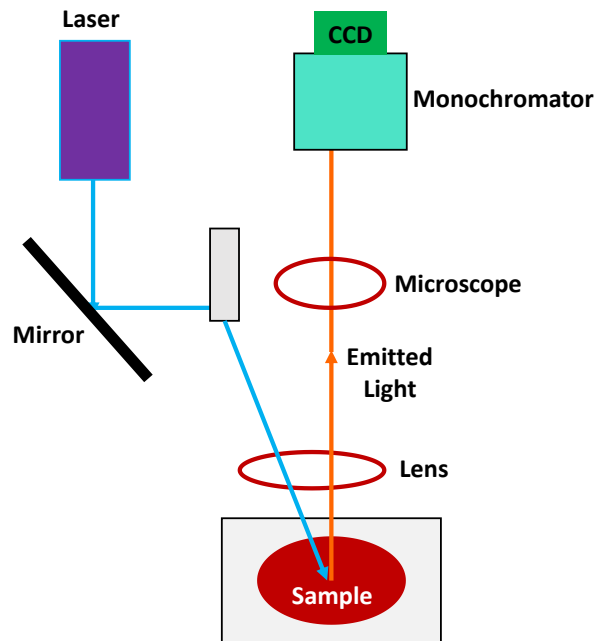


Figure 3.21 The schematic presentation of photoluminescence (PL) working principle.

At first the laser beam directed toward the optical mirror and then illuminated on the sample by passing through a lens. The illumination of laser beam excited the electrons which further transferred to the higher energy levels. During return back to the ground energy state, a radiation would be emitted. The emitted ray finally detected by the CCD detector after passing through lens, microscope and monochromator as a function of wavelength. Monochromator has been used to disperse white light into various colors to select single excitation during detection scans. Notably, the maximum emission wavelength has been selected to get the excitation spectrum. In this thesis work, the PL spectra of as developed semiconductors and the heterostructures have been taken at room temperature using FP-8500 JASCO fluorescence spectrofluorometer.

3.3.3.3 Time-correlated Single Photon Counting (TCSPC)

The TCSPC mainly used to measure the fluorescence decays of a material in a certain time domain, i.e. lifetime of an excited electron. The TCSPC works on the principal of detection of single photons and then measurement of arrival time with respect to a reference signal. A pulsed laser source with a high repetition rate has been employed to excite the sample. Similar to PL analysis, photons would be released during the relaxation of excited electrons, which are detected with a high-gain photomultiplier. A histogram of the photon distribution would be resulted by counting many events over time [68]. The schematic presentation of the working principle of TCSPC has been presented in Figure 3.22. A pulsed laser has been used to generate the fluorescence signal which is collected by a Geiger Photo Diodes (GPD) as detector after passing through the sample. Notably, one photon is collected during each of the laser pulse and the time duration between laser excitation (start) and detector output (stop) is recorded by a conventional time-to-analog converter (TAC). The accumulated charge has been measured by a charge sensitive amplifier, which further convert the charges into voltage. In this way, the time difference has been recorded for many laser pulses which gives rise to a histogram, containing the information about number of photons recorded at a given delay. Therefore, the probability of photon emission and fluorescent lifetime of a sample can be determined from the histogram. Notably, the probability of photon detection in a particular laser pulse should be less than one, otherwise the histogram distribution will be skewed to shorter times.

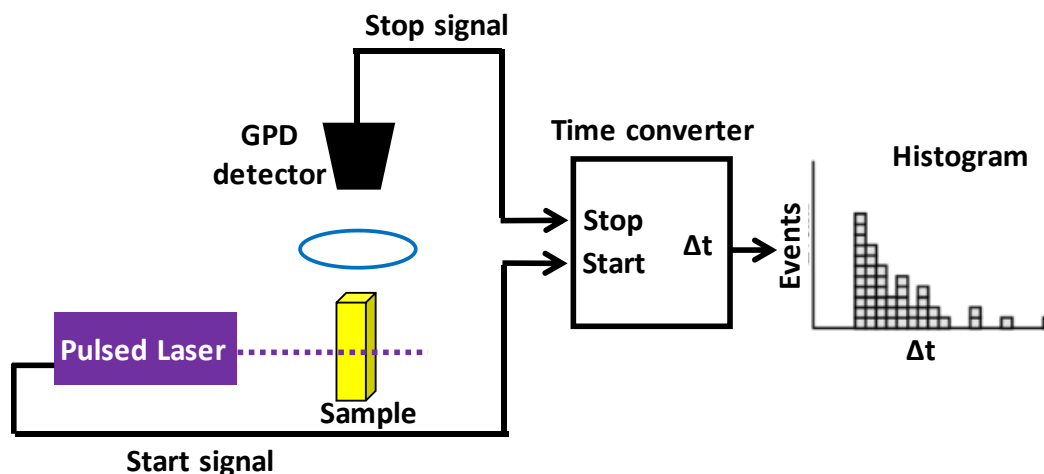


Figure 3.22 The schematic presentation of Time-correlated single photon counting (TCSPC) working principle.

3.3.4 Electrochemical Properties Measurement

Electrochemical study can be divided into four groups depending on the control parameters, which are potential, current, time and frequency. To investigate the electrochemical properties of an electrode material, the fundamental reactions of the PEC water splitting should be understood clearly as all the redox reaction take place at the interface of electrode and electrolyte. Figure 3.23a represents the semiconductor electrode-electrolyte double layer interface schematically. As the electrode is a semiconductor material, thus its potential has been identified by the location of Fermi level (E_f). On the other hand, the energy level of the electrolyte defines by the donors (Red) and acceptors (Ox) present. The density of the redox states for Ox and Red are described by the Gaussian distribution, shown in Figure 3.23b. If the electrode material is n-type semiconductor, then E_f should lie at the higher potential than $E_{f(\text{redox})}$. In this condition, a space charge layer (thickness 1–0.1 μm) would be formed at the electrode-electrolyte interface, near to electrode [69]. Now under slightly positive bias, depletion layer is formed where the number of majority carriers are less and density of ionized donors are excess [70]. When the bias is highly positive, then accumulation of minority carrier formed an inversion layer near the electrode. Therefore, depletion and inversion layer mainly contain positive charge carriers. At the same time, the electrolyte side of double layer is negatively charged, which consists of compact Helmholtz layer (thickness 3–5 \AA) and Gouy diffuse layer (negligible thickness for higher concentration of electrolyte) [71]. The solvent molecules, surface trapped electrons, ionized donors are accumulated in the Helmholtz layer. Thus, all these three layers contribute in potential drop at the double layer interface.

However, potential drop due to Helmholtz layer and Gouy diffuse layer are negligible when the electrolyte concentration is high. Thus effect of space charge layer through band bending mainly influences the potential drop and the density of charge carriers at interface. Now, surface states are mainly created by the adsorbed species and the defects in the crystal lattice which act as recombination center or electron mediator to accelerate the PEC activity. Notably, when the density of the surface state is high, then potential drop at Helmholtz layer becomes dominant and results ‘Fermi level pinning effect’ [72].

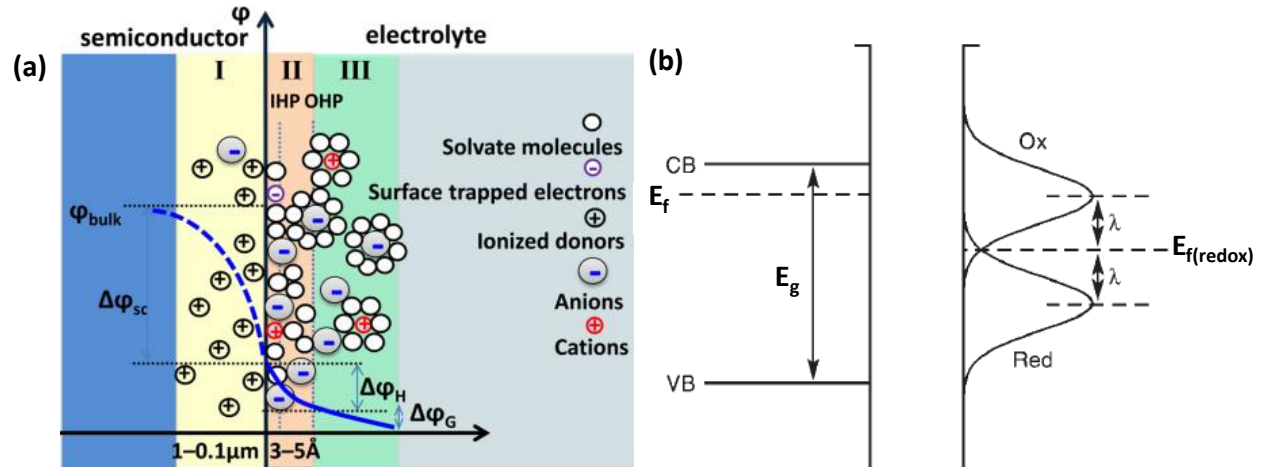


Figure 3.23 (a) Schematic presentation of double-layer created at an interface of n-type semiconductor electrode and electrolyte at equilibrium. The blue line indicates the potential (ϕ) across the double-layer. The potential drop at space charge layer (I), Helmholtz layer (II) and Gouy layer (III) are represented by $\Delta\phi_{sc}$, $\Delta\phi_H$, and $\Delta\phi_G$, respectively [95]. (b) Schematic of energy bands of a redox states and n-type semiconductor in electrolyte (Red and Ox), Fermi level ($E_{f(\text{redox})}$) and re-organization energy of solvent (λ) [93].

Now, under open-circuit condition and without light illumination, $E_{f(\text{redox})}$ and E_f will line up which resulted band bending in upward direction and built-in-field. Now, depending upon the upward bending, a barrier height (V_{barrier}) will be created which gives the idea about maximum energy at interface region (Figure 3.24). When light is illuminated, quasi-fermi levels correspond to electrons ($E_{f,n}$) and holes ($E_{f,p}$) are generated and resulted an open-circuit-photovoltage (V_{ph}). When, the electrode satisfy the condition of $V_{\text{ph}} > 1.23 \text{ V}$ (Figure 3.23), then water splitting is possible. Now, in this quasi-equilibrium condition there are several process of charge transfer and recombination, including electrode to electrolyte charge transfer, bulk recombination, surface state recombination, space charge layer recombination etc. which may influence the V_{ph} [73, 74].

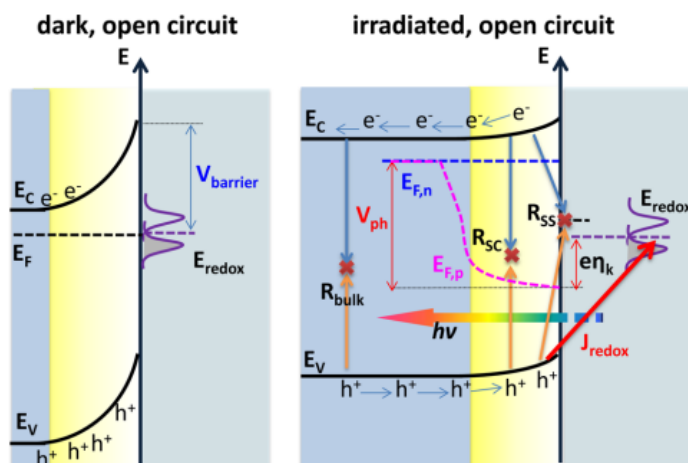


Figure 3.24 Schematic presentation of built-in potential (E) of an n-type electrode -electrolyte interface under dark and light during equilibrium condition. R_{ss} , R_{sc} and R_{bulk} are resistance due to the surface state, space charge layer and bulk recombination. Here, J_{redox} represents the charge transfer from VB to redox element [95].

3.3.4.1 Cyclic and Linear Sweep Voltammetry and Chronoamperometry

Cyclic Voltammetry (CV)

The CV is an electrochemical method which is mainly used to measure the current that generates in electrochemical cell between the working and counter electrode during the potential scan between working electrode and reference electrode. Thus, potential of a working electrode varied and the resulted current measured. The voltage range of the CV scan generally includes oxidation and reduction potentials of the working electrode material [75]. The reversibility of the reactions can also determine from CV. A CV system consists of potentiostat, current-to-voltage converter, electrolysis cell and data acquisition system. There are three electrodes in electrolysis cell: working, counter and reference electrode and electrolyte. The potential of the working electrode varies linearly with time and it acts as either cathode or anode. A constant potential has been maintained by the reference electrode throughout the measurement period. The counter electrode helps in conduct the electricity from signal source to working electrode. A dc power supply has been applied by using potentiostat which accurately determines the potential difference while allowing a small AC currents into the system. Moreover, resulting current signal and voltammogram measured by a current-to-voltage converter and data acquisition system. Now, a linear potential scan with a triangular waveform has been applied in CV, where the slope determines scan rate. Figure 3.25a shows a typical CV curve in solution-phase for sample P, which is undergoing through reversible one-electron reduction and generate Q. At the starting point, there

are no oxidation and reduction so no current created. When the potential scan is going on at negative site, a cathodic current flows as the reduction of P to Q (Figure 3.25b). The rate of electron transfer and mass-transport between electrode and analyte control the current response [76]. A rising cathodic current results when the electron transfer is much higher than the mass transport, explained by the Nernst equation [77],

$$E = E^\circ + \frac{RT}{nF} \ln \frac{C_P}{C_Q} \quad (3.31)$$

where E° is formal potential and C_P , C_Q are the concentrations of P and Q at the electrode surface, respectively, and. Notably, the ratio of C_P and C_Q chnges with the potential change. On the other hand, Butler–Volmer theory stated that the current increases exponentially at even more negative potentials [78].

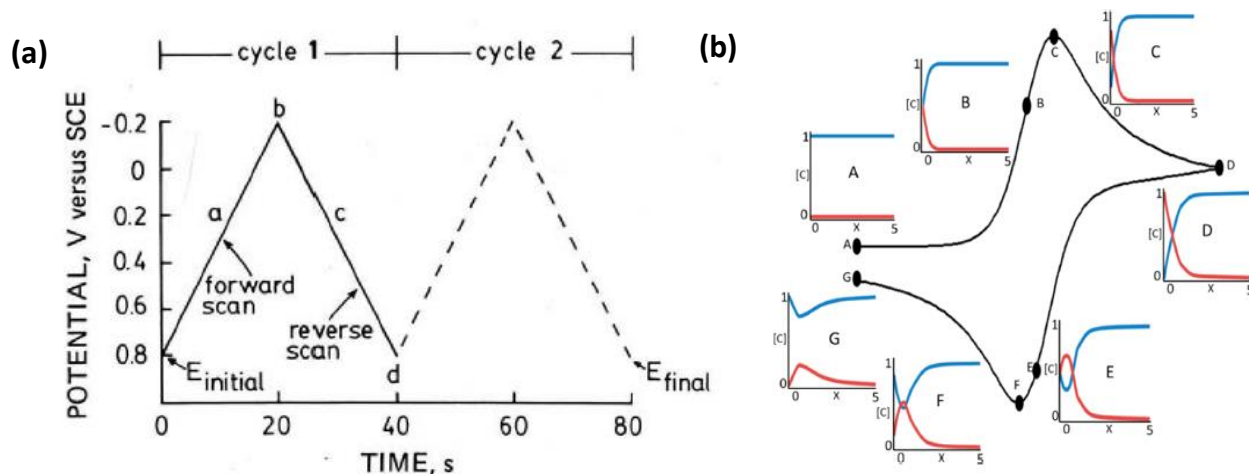


Figure 3.25 (a) A triangular potential waveform applied for CV measurement. (b) Concentration of C_P (blue) and C_Q (red) versus distance from the electrode at various points during a reversible CV at scan rate of 100 mV s^{-1} [70].

At sufficiently negative potentials, the C_P becomes very less near the electrode and resulted a peak (Figure 3.25b). At the electrode surface, concentration gradient is formed and the diffusion of oxidized species take place, where the thickness of diffusion layer (δ) depends on timescale (t) of voltammogram scan.

$$\delta \sim (Dt)^{1/2} \quad (3.32)$$

where, $D \rightarrow$ diffusion coefficient of P. The timescale is inversely proportional to scan rate (v).

$$(t \sim RT/Fv) \quad (3.33)$$

$$\delta \sim (DRT/Fv)^{1/2} \quad (3.34)$$

Therefore, diffusion layer thickens would be reduced with the increase of scan rate. At the switching potential, the diffusion layer thickness increases as no oxidation occurs. Now, with the increase of applied potential at positive site, an anodic current flow obtained, where the ratio of C_P/C_Q satisfies the Nernst equation (Figure 3.25b).

Linear Sweep Voltammetry (LSV)

LSV involves application of a linear potential sweep which results a current at the working electrode. A voltage sweep applies to the electrode as a wave form towards positive or negative direction from the lower to upper limit. The sweep rate can be represented as,

$$\text{Sweep rate} = dE/dt \quad (3.35)$$

Let us consider, material P oxidize and form Q and the formal potential of the reaction is E° . During the potential scan, initially a non-faradaic current flows and when the potential reaches to E° then reduction of P starts. As a result, a concentration gradient will be formed which led to increased flux, i.e. mass transfer to the surface of the electrode. During reduction, the rate of electron transfer is very high than that of voltage sweep rate which may generate a peak, can be described by Nernst equation (Figure 3.26). When the potential cross to E° , the mass transfer reaches maximum and diffusion layer has grown sufficiently, thereby Nernst equation is not satisfied. In this situation, the current drops again. The peak height can be calculated using the Randles–Ševčík equation of;

$$i_p = 0.4463FAC \left(\frac{nFvD}{RT} \right)^{1/2} \quad (3.36)$$

Where, $n \rightarrow$ number of electrons, $F \rightarrow$ Faraday constant, $A \rightarrow$ electrode area, $C \rightarrow$ concentration, $D \rightarrow$ diffusion co-efficient, $R \rightarrow$ gas constant (8.314 J/mol K), $v \rightarrow$ sweep rate and $T \rightarrow$ absolute temperature. The diffusion layer thickness depends on the voltage scan rate. At slow scan rate, the growth of diffusion layer is much, thus flux to the electrode surface is less which results less current. However the position of the peak for a fixed electrode will remain same with different scan rate. Notably, for samples having slow kinetics the peak position will be shifted with the scan rate variation as equilibrium is not reached properly. Therefore, the LSV for an electrode depends on (i) rate of electron transfer, (ii) chemical reactivity of electrode material and (iii) scan rate. LSV is mainly used to determine electroactive species concentration in solution quantitatively. Since the current density of LSV is proportional to the reaction rate over the working electrode, onset potential as well as electro-catalytic activity of the material can be determined [79-82].

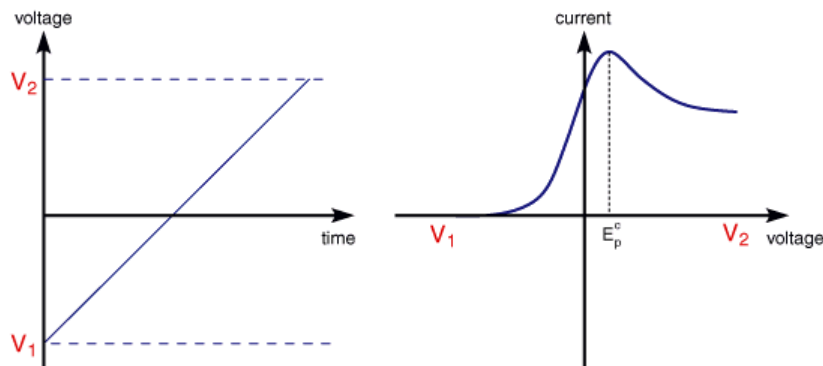


Figure 3.26 A linear potential waveform and the corresponding LSV curve [71].

Chronoamperometry (CA)

Chronoamperometry refers to the measurement of current generated at the electrode surface at fixed applied potential for a certain time period. The applied potential has been chosen from LSV curve at a point where no oxidation or reduction of material occurred and the current is totally diffusion-controlled [83-88].

3.3.4.2 Electrochemical Impedance Spectroscopy (EIS)

The EIS is a powerful and non-destructive methodology to measure the resistance, conductivity, dielectric properties and electric properties of a material. An AC potential has been applied to the electrochemical cell which measured the current generated at the cell. The steps include electron transport through conductors, transfer of electrons at the surface interfaces to form charged atoms and flow of the charged atoms in electrolyte. The rate of current in the cell depends on the ohmic resistance and reaction rates at the interface of electrode and electrolyte, assuming the interface is smooth and has simple crystallographic orientation. However, in reality the surface contains many defects which may influence the local electric field. The basis of an EIS experiment is the application of a small amplitude sinusoidal ac voltage, $V(t)$ [$V(t)=V_0$ for $t>0$, $V(t)=0$ for $t<0$], and then measure the amplitude and phase angle of resulted current, $I(t)$. The ratio of $V_0/i(t)$ is called time-varying resistance or impedance. A frequency-dependent impedance spectra can be obtained by applying Fourier or Laplace transformation of as obtained time-varying resistance [$V_0/i(t)$] at frequency domain. Let us consider, a monochromatic signal $V(t) = V_m \sin(\omega t)$ is applied to the cell which has frequency $\nu = \omega/2\pi$. The resulted current $I(t) = I_m \sin(\omega t + \theta)$, where θ is the phase difference between applied voltage and resultant current. When $\theta = 0$, electrode shows purely

resistive behavior. The impedance $Z(\omega)$ of the cell can be determined using Ohm's law *via* Fourier transformation:

$$V(t) = V_0 + V_m \sin(\omega t) \quad (3.37)$$

$$I(t) = I_0 + I_m \sin(\omega t + \theta) \quad (3.38)$$

$$Z(\omega) = V(t)/I(t) \quad (3.39)$$

Prof. Oliver Heaviside first introduced the concept of electrical impedance in 1880 and further A. E. Kennelly and especially C. P. Steinmetz represented it through a vector diagram. The magnitude and direction of a planar vector can be expressed by a complex number $Z = a + jb$, where $j = \sqrt{-1} = e^{j\pi/2}$ implies the anticlockwise rotation by $\pi/2$ relative to the X-axis. Thus, the impedance $Z(\omega)$ can be represented as,

$$Z(\omega) = Z' + jZ'' \quad (3.40)$$

And the two rectangular coordinate are

$$Z' = |Z(\omega)| \cos(\theta) \quad (3.41)$$

$$Z'' = |Z(\omega)| \sin(\theta) \quad (3.42)$$

$$\theta = \tan^{-1}\left(\frac{Z''}{Z'}\right) \quad (3.43)$$

$$|Z| = [(Z')^2 + (Z'')^2]^{1/2} \quad (3.44)$$

The expression for $Z(\omega)$ which is composed of a real and an imaginary part, is called Nyquist plot". (Figure 3.27).

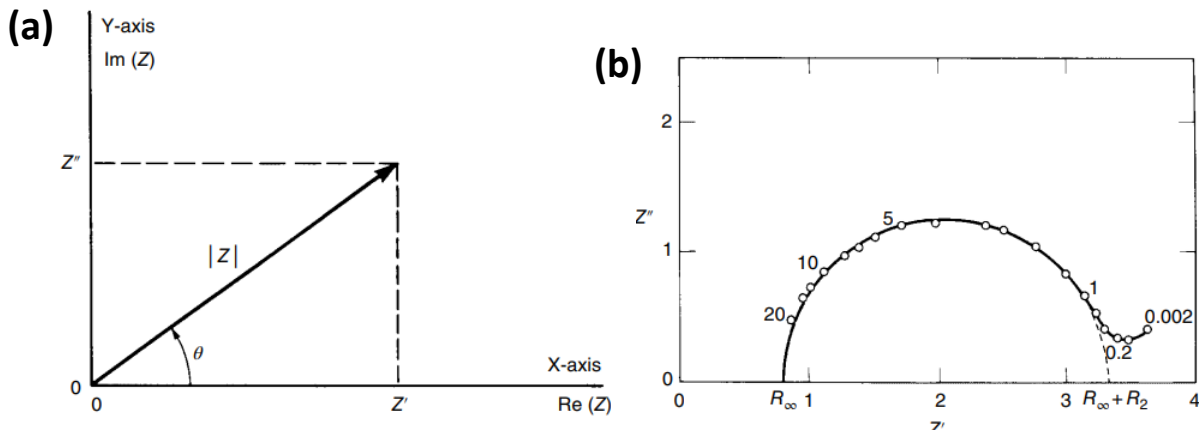


Figure 3.27 (a) The representation of impedance (Z) *via* planar vector and (b) the corresponding Nyquist plot [92].

The radius of the semicircular arc of EIS spectra can be used to quantify the impedance of the interface layer. The smaller diameter implies lower resistance at the surface of the electrode. To

get the idea about the resistance, capacitance and inductance formed at the electrode-electrolyte interfaces, the obtained spectra have been fitted with equivalent circuits. Resistance represents the conductivity of the electrode material. Sometimes, it represent the chemical steps associated with redox reaction happened at electrode surface [89, 90]. On the other hand, capacitance and inductance are associated with the space-charge polarization, specific adsorption and electrocrystallization at the electrode-electrolyte interface. Now, every material has geometric capacitance C_1 and bulk resistance R_1 , which are parallel to each other (Figure 3.28a,b) and led to time constant ($\tau_D = C_1 R_1$). In case of full semicircular curve, the peak frequency (ω_p) with satisfy $\omega_p \tau_D = 1$. In case of heterogeneous electrode, when two semicircular arc obtained (Figure 3.28c, d) then additional resistance and capacitance required to fit the circuit. Where, C_2 corresponds to the double-layer capacitance near the electrode and R_2 is the reaction resistance.

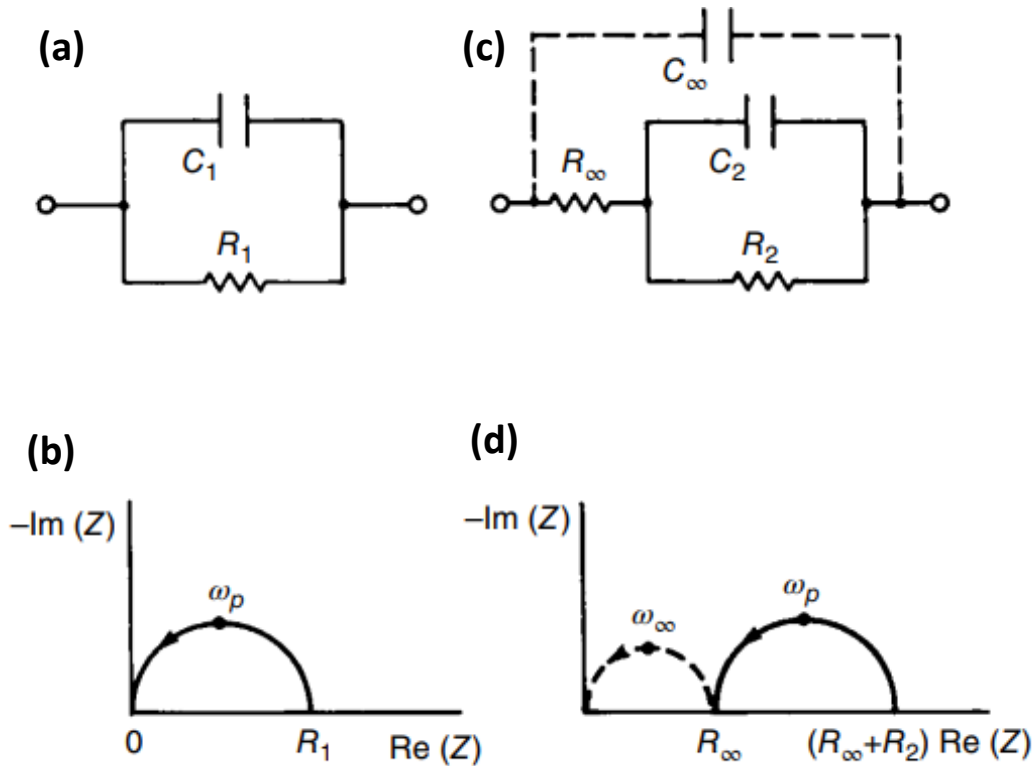


Figure 3.28 (a) RC circuit and the (b) corresponding Nyquist plot for single semiconductor. (c) RC equivalent circuit and (d) corresponding Nyquist plot for heterogeneous electrode [93].

3.3.4.3 Mott-Schottky

Mott–Schottky (M-S) measurement is an important technique which has been widely applied to calculate the flat-band potential, charge carrier concentration at the interface (N_d for an n-type photoanode and N_a for a p-type photocathode) [91]. The junction capacitance at the interface of electrode and electrolyte has been measured over a range of applied potentials at different frequencies. The M-S study is closely related with the electrochemical impedance study. In impedance study, the space charge layer capacitance has been determined by the fitting with equivalent circuit model using constant phase elements [92]. In M-S, the real capacitances generated at the junction interface can be calculated [93]. The total capacitance of the double layer at the semiconductor-electrolyte interface is [94, 95];

$$\frac{1}{C} = \frac{1}{C_{sc}} + \frac{1}{C_H} \quad (3.45)$$

Where, $C \rightarrow$ total capacitance, $C_{sc} \rightarrow$ capacitance due to space charge layer and C_H for Helmholtz layer. According to previously reported literatures, the value of C_H is in the range of 0.1 – 0.2 F m^{-2} for semiconductor electrode [96, 97]. The capacitance for the space charge layer can be calculated from the Mott–Schottky equation. There are some assumptions, such as $C_H \gg C_{sc}$ and capacitance vary with the band bending. The $(E - E_{fb})$ represents the band bending [98]. The Mott–Schottky equation has been derived from the Poisson’s equation in one dimension which describes the relationship between potential difference (ϕ) and charge density (ρ);

$$\frac{\partial^2 \phi}{\partial x^2} = - \frac{\rho}{\epsilon \epsilon_0} \quad (3.46)$$

By applying the Boltzmann distribution which describes the distribution of electrons in space charge region and the Gauss’ law, related to the electric field, M-S equation can be derived [99].

$$\frac{1}{C^2} = \frac{2}{e N_d \epsilon \epsilon_0} \left(E - E_{fb} - \frac{KT}{e} \right) \quad (3.47)$$

where, $E_{fb} \rightarrow$ flat band potential (V), $N_d \rightarrow$ density of free charge carrier (cm^{-3}), $e \rightarrow$ electronic charge (C), $\epsilon_0 \rightarrow$ permittivity of free space, $\epsilon \rightarrow$ dielectric constant of the electrode, $K \rightarrow$ Boltzmann constant and $T \rightarrow$ temperature (K). From the slope of the linear portion of $1/C^2$ vs applied potential, N_d or N_a can be calculated which is inversely proportional to the slope. From the slope value the conductive nature of the semiconductor can be identified. For example, negative slope value indicates the p-type conductivity and positive slope reveals n-type conductivity of electrode material. Under the circumstances shown in Figure 3.23b, i.e. where $E_F > E_{F(\text{redox})}$, the

flat-band potential of the photoanode can be determined using Mott–Schottky equation (Eq. 3.47). Further, the space charge layer width can be calculated from the Eq. 3.48.

$$W = \sqrt{\left(\frac{2\epsilon\epsilon_0 V_s}{eN_d}\right)} \quad (3.48)$$

Where, $V_s \rightarrow$ applied potential. With the increase of space charge layer width the capacitance decreases which is analogous with a parallel-plate capacitor, i.e. capacitor in series with electrolyte resistance (ohmic contact) [100-102]. The impedance of the electrode-electrolyte interface can be represent as;

$$Z'' = -\frac{j}{\omega C_{\text{interface}}} \quad (3.49)$$

Figure 3.29 shows the basic equivalent circuit of a semiconductor electrode-electrolyte interface, where the impedance of the electronic circuit is;

$$Z_R = R_{\text{Faradaic}} + \frac{R_{\text{interface}}}{(1 + \omega^2 R_{\text{interface}}^2 C_{\text{interface}}^2)} \quad (3.50)$$

$$= -j \frac{\omega R_{\text{interface}}^2 C_{\text{interface}}}{(1 + \omega^2 R_{\text{interface}}^2 C_{\text{interface}}^2)} \quad (3.51)$$

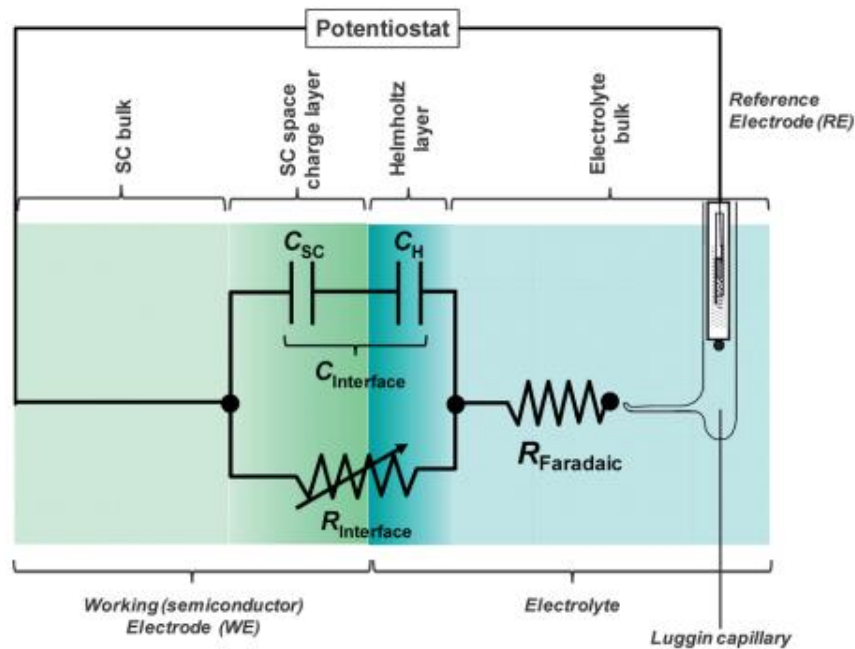


Figure 3.29 The schematic representation of electrode-electrolyte interface [85].

3.3.5 Vibrating Sample Magnetometer (VSM)

VSM is a useful and well-known technique for the measurement of magnetic moment of a sample at vibrating condition between a uniform magnetic field based on Faraday's law of magnetic induction [103]. In VSM, a magnetic sample is placed between two electromagnet poles horizontally after mounting on a sample holder (in-plane or out-of-plane sample holders), called “saddle point” (Figure 3.30). The sample is subjected to a constant vibration vertically at a fixed frequency and the change of magnetic flux (proportional to the magnetic moment in the sample) induces an AC voltage which is detected by a set of pickup coils, placed near the electromagnetic poles. With the change of coil position, applied magnetic field and sample position the flux will be changed and induced a voltage which further fed into a lock-in amplifier to obtain the magnetic moment resulted in the sample. The magnetic moment can be determined as a function of applied magnetic field which gives rise the information about coercivity, switching fields and their distribution. The Lake Shore Cryotronics VSM instrument has been employed at room temperature to measure the magnetic moment of the as prepared magnetic samples at a maximum field of 16 kOe.

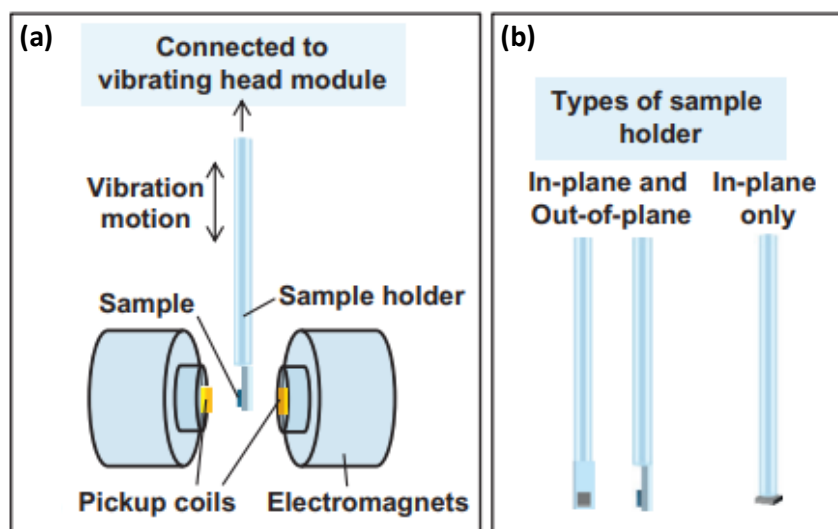


Figure 3.30 Schematic diagram of (a) part of the VSM setup and (b) types of sample holder used in VSM [97].

3.3.6 Gas Chromatography (GC)

To identify and quantify the produced gas in the photocatalytic H₂ generation, GC is employed. The sample is first vaporized by the heated injector and then injected onto the chromatographic column. An inert gas Argon (Ar) has been used as carrier gas to transport the sample through the

column. The separation of gas molecules happen during the transportation due to interaction between gaseous mobile phase of sample and stationary phase of column. Depending on the separation time, gas molecules are detected when it come out from the column and generate a signal. The mobile phase of the sample and the carrier gas must be chemically inert. The partition of solutes between stationary phases and mobile phase accounts for the separation of molecules, where the partition ratio depends on chemical characters of each component, affinity for the stationary phase and vapor pressure of solutes. Therefore, the stationary phase and the temperature program of column are greatly important. In this thesis work, YL6000 GC, with thermal conductivity detector (TCD) has been used to quantitatively measure the amount of H₂ produced by water reduction. Ar is employed as the carrier gas as it has lower thermal conductivity compared to H₂ and O₂. Basically, TCD detects change of the thermal conductivity between sample and carrier gas by a whetstone bridge coupled with resistors, which represent the heat loss depending on analyte. A graph of retention time vs detector response is obtained from GC, where the detector response depends on thermal conductivity and amount of element present. On the other hand, the retention time is specific to each element detected by the TCD detector. Therefore, the graph contains Gaussian peaks which are separated by time. By calculating the area under each peak, the amount of elemental presence can be determined.

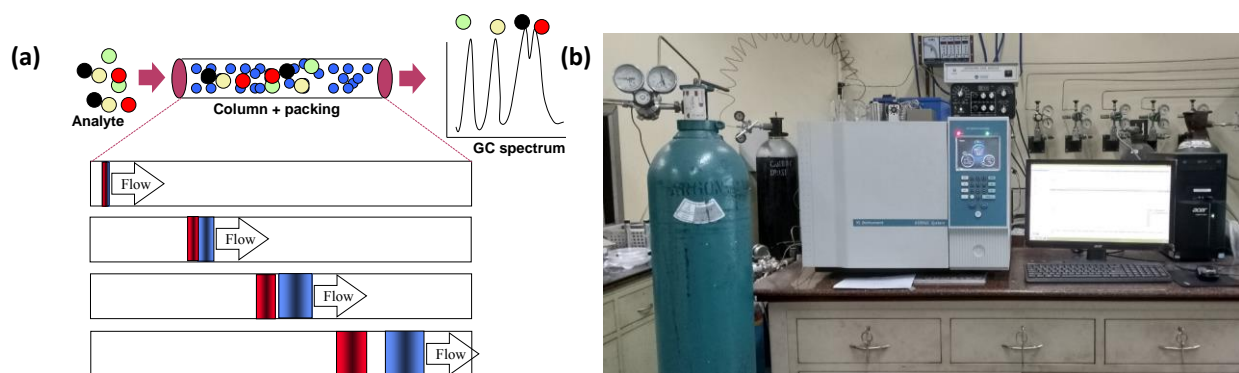


Figure 3.31 (a) Schematic presentation of the working principle of Gas Chromatography (GC) and (b) On-line GC setup.

3.4 Organic pollutant degradation

The photocatalytic activity of as developed semiconductor nanostructures has been studied for organic pollutant methyl orange (MO) degradation using under visible light. The initial concentration was $C_0 = 0.3 \times 10^{-4}$ M and the photodegradation carried out within a quartz cell reactor containing 50 mg catalyst powder in 50 mL of MO solution with stirring condition in

presence of O₂ flow. To attain adsorption-desorption equilibrium, each of the solution (containing organic dye and catalyst) first stirred in dark for 1h. The 250 W Xenon lamp is used as the visible light source which is placed at 15 cm above the solution. The schematic diagram of the photocatalytic experiment is shown in figure below (Figure 3.32). To investigate the photocatalytic activity of sample, 2 mL aliquots was collected from the reactor at a time interval of 15 mins. The degradation percentage (% DE) of the organic pollutant MO was founded using the following Eq.;

$$\% DE = \frac{C_0 - C}{C_0} \times 100 \quad (3.52)$$

Where, C₀ → initial intensity and C → intensity after light illumination. The optical density (OD) value are taken at maximum wavelength of λ_{max} = 463 nm.

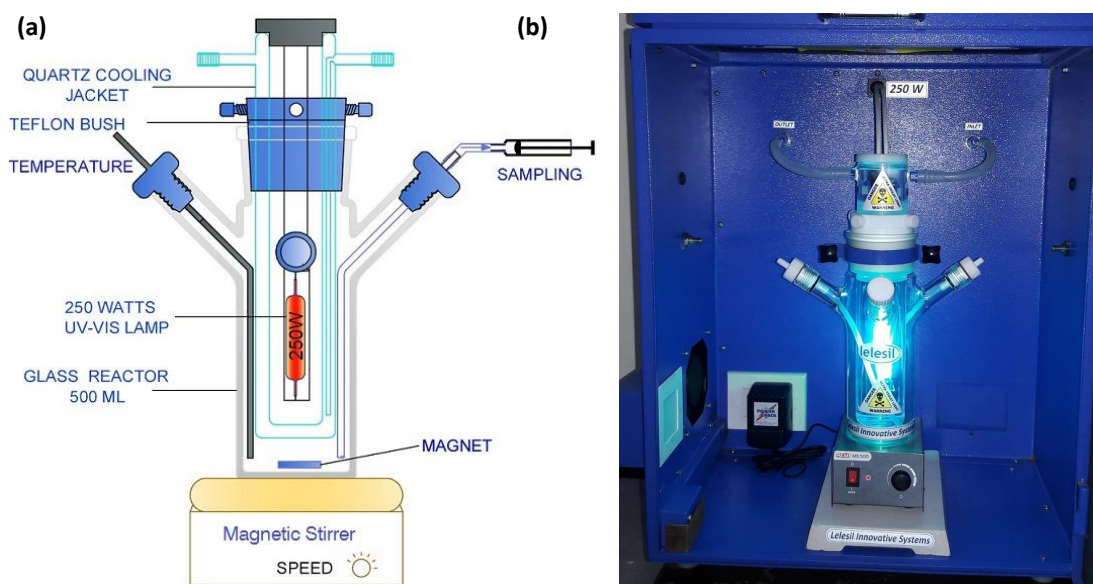


Figure 3.32 (a) Schematic presentation of quartz cell reactor for organic pollutant degradation. (b) Image of quartz cell reactor with light illumination.

3.5 Photocatalytic H₂ Generation Method

The photocatalytic H₂ generation experiment was conducted in a closed reactor containing water-methanol solution with vigorous stirring and saturated argon media. The 25 volume % of methanol (as hole scavenger) and 1 mg/mL catalyst concentration were used at room temperature. The online gas chromatography was employed to identify the product gases and quantitatively measure the generated H₂ through Gaussian fitting. The 250 W MPMVL lamp is used as the visible light source placed at 15 cm above the solution. The light source was covered with a double wall quartz jacket through which cold water circulation has been passed to maintain the reaction condition.

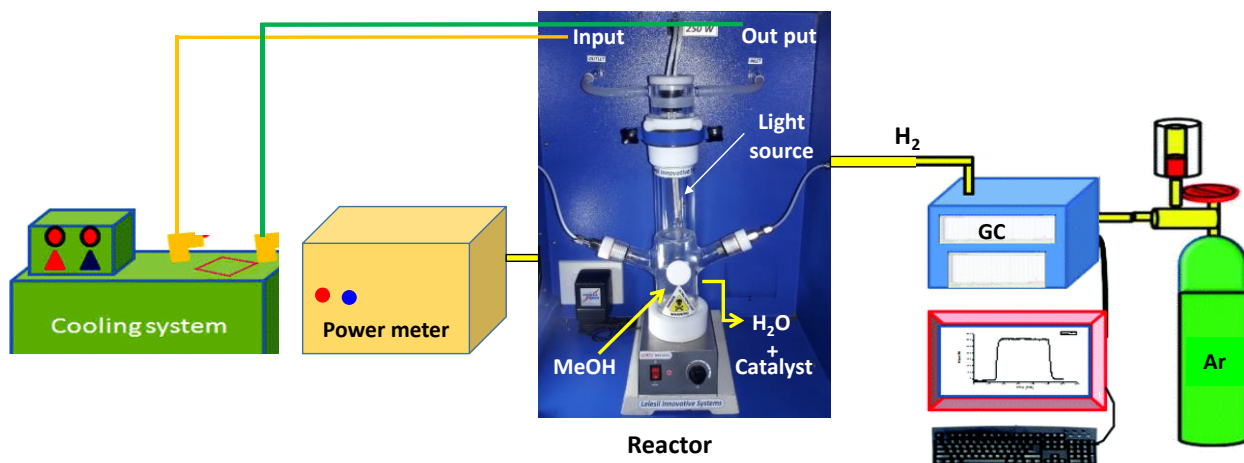


Figure 3.33 Online photocatalytic H₂ generation setup.

3.6 Photoelectrochemical Measurements

A galvanostat-potentiostat (Autolab, PGSTAT302N, The Netherlands) was used to measure the photoelectrochemical properties of the materials. For that, a standard three-electrode quartz cell containing 50 mL 0.1M N₂SO₄ electrolyte was taken where Pt wire and KCl saturated Ag/AgCl are used as counter and reference electrode, respectively.

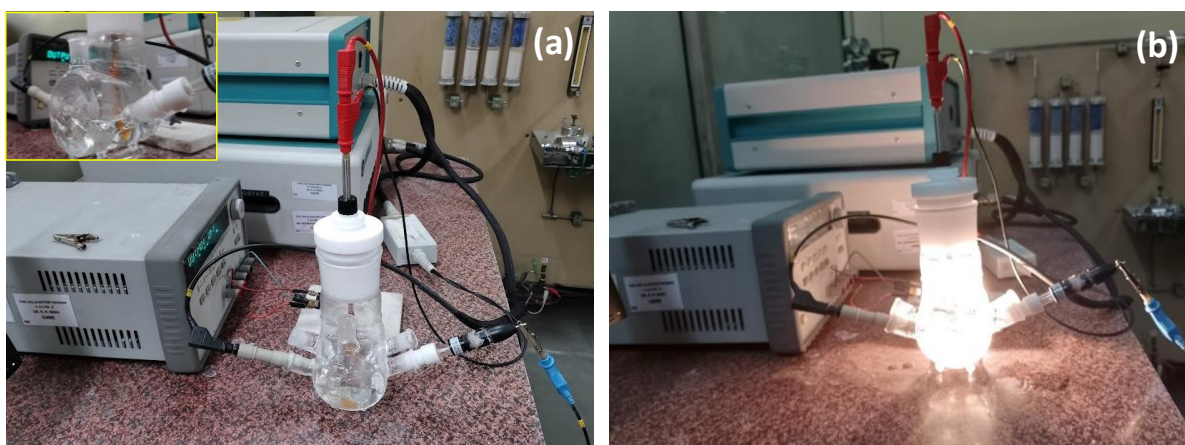


Figure 3.34 Three electrode photoelectrochemical cell (a) without light and (b) under light irradiation.

In order to prepare the working electrode of the as synthesized materials, doctor-blade method and spin coating method were employed. For the doctor-blade method, a paste was prepared as following: catalyst powder (1 mg) was mixed with ethylene glycol (2.5 mL) in a centrifuge tube at 20 min sonication. After that, the resulting paste was coated on Fluorine-doped Tin Oxide (FTO) glass (conducting side) to make a thin film using a doctor-blade method. Finally, the coated slides were then carefully placed inside a muffle furnace maintained at 400°C for 4 h. For spin coating,

a solutions was prepared at a catalyst concentration of 2 mg/mL in ethanol. During spin coating the rpm was fixed at 4000 for time 1 min, and 100 μ L used to prepare each of the thin film layer. Total three layers were coated on the FTO slides and dried at 200°C for 2 h.

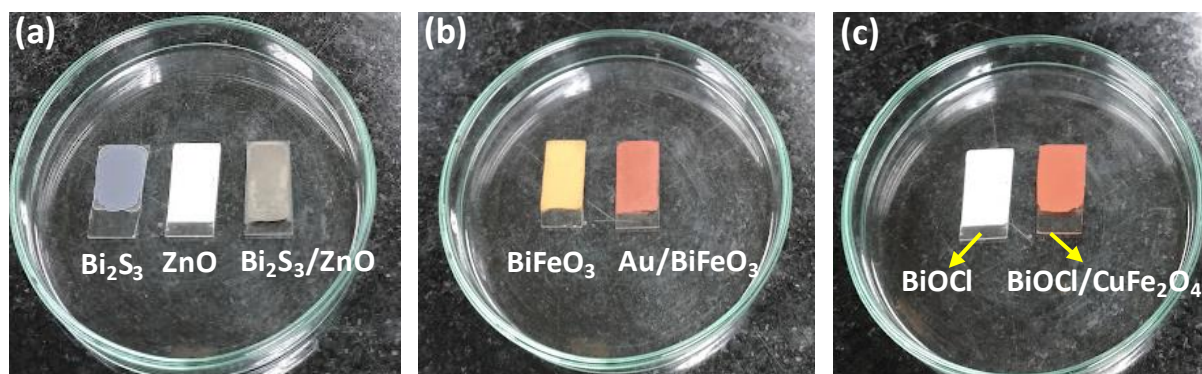


Figure 3.35 Prepared working electrode by doctor-blade method on FTO glass (a) Bi_2S_3 , ZnO , $\text{Bi}_2\text{S}_3/\text{ZnO}$, (b) BiFeO_3 , Au/BiFeO_3 , (c) BiOCl , $\text{BiOCl}/\text{CuFe}_2\text{O}_4$.

References

- [1] A. V. Nikam, B. L. V. Prasad, A. A. Kulkarni, Wet chemical synthesis of metal oxide nanoparticles: a review. *Cryst. Eng. Comm.* **20** (2018) 5091–5107.
- [2] N. Baig, I. Kammakakam, W. Falath, Nanomaterials: a review of synthesis methods, properties, recent progress, and challenges. *Mater. Adv.* **2** (2021) 1821–1871.
- [3] S. Ghosh, R. N. Basu, Electrochemistry of Nanostructured Materials: Implementation in Electrocatalysis for Energy Conversion Applications. *J. Indian Institute Sci.* **96** (2016) 293–314.
- [4] Z. Zhang, C. Dong, C. Yang, D. Hu, J. Long, L. Wang, H. Li, Y. Chen, D. Kong, Stabilized Copper(I) Oxide Nanoparticles Catalyze Azide-Alkyne Click Reactions in Water. *Adv. Synth. Catal.* **352** (2010) 1600–1604.
- [5] P. Garrigue, M. –H. Delville, C. Labrugère, E. Cloutet, P. J. Kulesza, J. P. Morand, A. Kuhn. Top–Down Approach for the Preparation of Colloidal Carbon Nanoparticles. *Chem. Mater.* **16** (2004) 2984–2986.
- [6] T. P. Yadav, R. M. Yadav, D. P. Singh, Mechanical Milling: a Top Down Approach for the Synthesis of Nanomaterials and Nanocomposites. *Nanosci. Nanotech.* **2** (2012) 22–48.
- [7] J. W. Lee, J.–S. Yoon, Y.–M. Kim, Y.–M. Sung, Wet chemical growth of semiconductor 1-D nanostructure arrays on conductive substrates. *J. Mater. Chem. C* **7** (2019) 12019–12047.
- [8] J. Yin, J. Wang, Y. Ma, J. Yu, J. Zhou, Z. Fan, Recent Advances in the Controlled Synthesis and Catalytic Applications of Two-Dimensional Rhodium Nanomaterials. *ACS Mater. Lett.* **3** (2021) 121–133.
- [9] S. K. Gupta, Y. Mao, Recent Developments on Molten Salt Synthesis of Inorganic Nanomaterials: A Review. *J. Phys. Chem. C* **125** (2021) 6508–6533.
- [10] A. C. Jones, M. L. Hitchman, Chemical Vapour Deposition, *Royal Society of Chemistry*, Cambridge. (2008) 1–36, Print ISBN 978-0-85404-465-8, PDF eISBN 978-1-84755-879-4.
- [11] X. Wu, G. Q. (Max) Lu, L. Wang, Shell-in-shell TiO₂ hollow spheres synthesized by one-pot hydrothermal method for dye-sensitized solar cell application. *Energy Environ. Sci.* **4** (2011) 3565.
- [12] A. E. Danks, S. R. Hall, Z. Schnepf, The evolution of ‘sol–gel’ chemistry as a technique for materials synthesis. *Mater. Horiz.* **3** (2016) 91–112.

- [13] Y. Liu, J. Goebel, Y. Yin, Templated synthesis of nanostructured materials. *Chem. Soc. Rev.* **42** (2013) 2610–2653.
- [14] M. A. Malik, M. Y. Wani, M. A. Hashim, Microemulsion method: A novel route to synthesize organic and inorganic nanomaterials: 1st Nano Update. *Arabian J. Chem.* **5** (2012) 397–417.
- [15] J. A. Darr, J. Zhang, N. M. Makwana, X. Weng, Continuous Hydrothermal Synthesis of Inorganic Nanoparticles: Applications and Future Directions. *Chem. Rev.* **117** (2017) 11125–11238.
- [16] J. Li, Q. Wu, J. Wu, Handbook of Nanoparticles, Springer International Publishing, Cham. (2015) 1–28.
- [17] G. J. A. A. Soler-Illia, M. Jobbágy, A. E. Regazzoni, M. A. Blesa, Synthesis of Nickel Hydroxide by Homogeneous Alkalinization. Precipitation Mechanism. *Chem. Mater.* **11** (1999) 3140–3146.
- [18] M.–H. Lee, T.–H. Kim, Y. S. Kim, H.–K. Song, Precipitation Revisited: Shape Control of LiFePO₄ Nanoparticles by Combinatorial Precipitation. *J. Phys. Chem. C* **115** (2011) 12255–12259.
- [19] S. Ghosh, A. Datta, A. Saha, Single Step Synthesis of Highly Stable Good Quality Water-soluble Semiconductor/Dendrimer nanocomposites: Distribution and Phase control of CdS nanocrystal in dendrimer matrix. *Colloids and Surfaces A: Physicochem. Eng. Aspects* **355** (2009) 130–138.
- [20] S. Ghosh, A. Datta, N. Biswas, A. Datta, A. Saha, Radiation-induced synthesis of self-organized assemblies of functionalized inorganic–organic hybrid nanocomposites. *RSC Adv.* **3** (2013) 14406–14412.
- [21] S. Ghosh, S. Bera, S. Bysakh, R. N. Basu, Highly Active Multimetallic Palladium nanoalloys Embedded in Conducting Polymer as Anode Catalysts for Electrooxidation of Ethanol. *ACS Appl. Mater. Interfaces* **9** (2017) 33775–33790.
- [22] S. Ghosh, S. Bera, S. Bysakh, R. N. Basu, Conducting Polymer Nanofibers Supported Pt Alloys: Unprecedented Materials for Methanol Oxidation with Enhanced Electrocatalytic Performance and Stability. *Sustainable Energy & Fuels* **1** (2017) 1148–1161.
- [23] Y. Lattach, C. Coletta, S. Ghosh, S. Remita, Radiation Induced Synthesis of Nanostructured PEDOT Conjugated Polymers in Aqueous Solution. *Chem. Phys. Chem* **15** (2014) 208–218.

- [24] A. I. El-Batal, A. F. El-Baz, F. M. Abo Mosalam, A. A. Tayel, Gamma irradiation induces silver nanoparticles synthesis by *Monascus purpureus*. *J Chem. Pharm. Res.* **8** (2013) 1–15.
- [25] B. I. Kharisov, O. V. Kharissova, U. O. Méndez Radiation synthesis of materials and compounds. CRC Press, (2013) ISBN 9781466505223.
- [26] G. G. Flores-Rojas, F. López-Saucedo, E. Bucio, Gamma-irradiation applied in the synthesis of metallic and organic nanoparticles: A short review. *Radiat. Phys. Chem.* **169** (2020) 107962–107985.
- [27] A. Abedini, A. R. Daud, M. A. Abdul Hamid, N. K. Othman, E. Saion, A review on radiation-induced nucleation and growth of colloidal metallic nanoparticles. *Nanoscale Res. Lett.* **8** (2013) 1–10.
- [28] J. Rojas, C. H. Castano, Production of palladium nanoparticles supported on multiwalled carbon nanotubes by gamma irradiation. *Radiat. Phys. Chem.* **81** (2012) 16–21.
- [29] J. Belloni, Nucleation, Growth and Properties of Nanoclusters Studied by Radiation Chemistry: Application to Catalysis. *Catal. Today* **113** (2006) 141–156.
- [30] S. Schorr, C. Stephan, T. Törndahl, R. Mainz, X-ray and neutron diffraction on materials for thin film solar cells. In: Advanced characterization techniques for thin film solar cells. Weinheim: Wiley-VCH Verlag GmbH & Co. KGaA (2011) 347–63.
- [31] B. D. Cullity, Elements of X-ray diffraction. Reading: Addison-Wesley Publishing Company (1956).
- [32] W. L. Bragg, The Crystalline State: Volume I. New York: The Macmillan Company (1934).
- [33] M. Hart, X-ray diffraction by L. V. Azaroff, R. Kaplow, N. Kato, R. J. Weiss, A. J. C. Wilson, R. A. Young. *Acta Crystallogr. A* **31** (1975) 878.
- [34] J. M. Hollander, W. L. Jolly, X-ray photoelectron spectroscopy. *Acc. Chem. Res.* **3** (1970) 193–200.
- [35] C. S. Fadley, X-ray photoelectron spectroscopy: progress and perspectives. *J. Electron Spectros. Relat. Phenom.* **178–179** (2010) 2–32.
- [36] D. P. Woodruff, T. A. Delchar, Modern techniques of surface science. Cambridge: Cambridge University Press (1994) 105–265.
- [37] A. Kahn, Fermi level, work function and vacuum level. *Mater. Horiz.* **3** (2016) 7–10.
- [38] D. Cahen, A. Kahn, Electron energetics at surfaces and interfaces: concepts and experiments. *Adv. Mater.* **15** (2003) 271–277.

- [39] D. R. Vij (editor), Handbook of applied solid state spectroscopy. Boston: Springer US; (2006).
- [40] I. Lindgren, Chemical shifts in X-ray and photo-electron spectroscopy: a historical review. *J. Electron Spectros. Relat. Phenom.* **137–140** (SPEC. ISS.) (2004) 59–71.
- [41] H. Bubert, J. Henning, editors. Surface and thin film analysis. Weinheim, FRG: Wiley-VCH Verlag GmbH (4) (2002).
- [42] L. Ley, R. A. Pollak, F. R. McFeely, S. P. Kowalczyk, D. A. Shirley, Total valence-band densities of states of III-V and II-VI compounds from X-ray photoemission spectroscopy. *Phys. Rev. B.* **9** (1974) 600–621.
- [43] J. Álvarez-García, V. Izquierdo-Roca, A. Pérez-Rodríguez, Raman spectroscopy on thin films for solar cells. In: Advanced characterization techniques for thin film solar cells. Weinheim: Wiley-VCH Verlag GmbH & Co. KGaA (2011) 365–386.
- [44] J.-Y. Ascencio, Electron Microscopy of Nanostructured and Ancient Materials, in Handbook of Nanostructured Materials and Nanotechnology. Academic Press, Cambridge, MA (2) (1999) 393.
- [45] K. S. Walton, R. Q. Snurr, Applicability of the BET Method for Determining Surface Areas of Microporous Metal–Organic Frameworks. *J. Am. Chem. Soc.* **129** (2007) 8552–8556.
- [46] S. Brunauer, P. H. Emmett, E. Teller, Adsorption of Gases in Multimolecular Layers. *J. Am. Chem. Soc.* **60** (1938) 309–319.
- [47] D. A. H. Hanaor, M. Ghadiri, W. Chrzanowski, Y. Gan, Scalable Surface Area Characterization by Electrokinetic Analysis of Complex Anion Adsorption. *Langmuir* **50** (2014) 15143–15152.
- [48] A. Galarneau, D. Mehlhorn, F. Guenneau, B. Coasne, F. Villemot, D. Minoux, C. Aquino, J. –P. Dath, Specific Surface Area Determination for Microporous/Mesoporous Materials: The Case of Mesoporous FAU-Y Zeolites. *Langmuir* **47** (2018) 14134–14142.
- [49] K. S. W. Sing, Adsorption by Powders and Porous Materials, Principles, Methodology and Applications by F. Rouquerol, J. Rouquerol, K. S. W. Sing. P. Llewellyn and G Maurin, eds., 2nd Edition. Amsterdam.NL: Academic Press/ Elsevier Ltd. (2014) 263–267 ISBN 978-0-08-097035-6.

- [50] J. Condon, Surface Area and Porosity Determinations by Physisorption, Measurement, Classical Theory and Quantum Theory, 2nd edition. Amsterdam.NL: Elsevier. Chapters 3, 4 and 5. (2020) ISBN 978-0-12-818785-2.
- [51] K. C. Ng, M. Burhan, M. Wakil Shahzad, A. Bin Ismail, A Universal Isotherm Model to Capture Adsorption Uptake and Energy Distribution of Porous Heterogeneous Surface. *Nat. Sci. Rep.* **7** (2017) 10634–10645.
- [52] J. M. Gay, J. Suzanne, J. P. Coulomb, Wetting, surface melting, and freezing of thin films of methane adsorbed on MgO (100). *Phys. Rev. B* **16** (1990) 11346–11351.
- [53] P. R. Griffiths, J. A. Hsueh, Fourier transform infrared spectrometry. Hoboken: Wiley; (2007).
- [54] C. Ghezzi, R. Magnanini, A. Parisini, B. Rotelli, L. Tarricone, A. Bosacchi, S. Franchi, Optical absorption near the fundamental absorption edge in GaSb. *Phys. Rev. B* **3** (1995) 1463–1466.
- [55] A. W. Coats, J. P. Redfern, Thermogravimetric Analysis: A Review. *Analyst.* **1053** (1963) 906–924.
- [56] J. A. Reyes-Labarta, A. Marcilla, Kinetic Study of the Decompositions Involved in the Thermal Degradation of Commercial Azodicarbonamide. *J. Appl. Polym. Sci.* **1** (2008) 339–346.
- [57] V. S. Ramachandran, Applications of differential thermal analysis in cement chemistry. Chap. V, Chemical Publishing Co., Inc., New York (1969) 92.
- [58] K. Oura, V. G. Lifshits, A. A. Saranin, A. V. Zotov, M. Katayama, Surface Science – An Introduction, Springer-Verlag Berlin Heidelberg (2003).
- [59] D. J. Smith, Characterization of Nanomaterials Using Transmission Electron Microscopy. 2015, pp. 1-29 DOI: 10.1039/9781782621867-0000. eISBN: 978-1-78262-186-7 From Book Series: Nanoscience & Nanotechnology Series.
- [60] D. Abou-Ras, M. Nichterwitz, M. J. Romero, S. S. Schmidt, Electron microscopy on thin films for solar cells. In: Advanced characterization techniques for thin film solar cells. Weinheim: Wiley-VCH Verlag GmbH & Co. KGaA (2011) 299–345.
- [61] J. H. Lambert, D. L. DiLaura, Photometry, or, on the measure and gradations of light, colors, and shade: Illuminating Engineering Society of North America, (2001).

- [62] A Beer, P. Beer, Determination of the absorption of red light in colored liquids. *Annalen der Physik und Chemie (in German)* **162** (1852) 78–88.
- [63] J. Tauc, R. Grigorovici, A. Vancu, Optical properties and electronic structure of amorphous Germanium. *Phys. Status. Solidi.* **15** (1966) 627–637.
- [64] J. Tauc, Optical properties and electronic structure of Amorphous Ge and Si. *Mater. Res. Bull.* **3** (1968) 37–46.
- [65] B. D. Viezbicke, S. Patel, B. E. Davis, D. P. Birnie, Evaluation of the Tauc method for optical absorption edge determination: ZnO thin films as a model system. *Phys. Status. Solidi.* **8** (2015) 1700–1710.
- [66] M. Tebyetekerwa, J. Zhang, Z. Xu, T. N. Truong, Z. Yin, Y. Lu, S. Ramakrishna, D. Macdonald, H. T. Nguyen, Mechanisms and Applications of Steady-State Photoluminescence Spectroscopy in Two-Dimensional Transition-Metal Dichalcogenides. *ACS Nano.* **14** (2020) 14579–14604.
- [67] K. Kash, J. Shah, Carrier energy relaxation in $\text{In}_{0.53}\text{Ga}_{0.47}\text{As}$ determined from picosecond luminescence studies. *Appl. Phys. Lett.* **4** (1984) 401.
- [68] W. G. Lawrence, T. Tozian, C. Stapels, J. F. Christian, G. D. Derderian, J. P. Derderian, G. Varadi, CMOS Geiger-mode avalanche photodiode detectors for time and intensity resolved measurements. *Proc. Spie.* **7594** (2014) 75940I-1–13.
- [69] R. Memming, *Semiconductor Electrochemistry*; Wiley-VCH: New York, (2001).
- [70] R. Krishnan, *Fundamentals of Semiconductor Electrochemistry and Photoelectrochemistry*. In *Encyclopedia of Electrochemistry*; Wiley-VCH: Weinheim, Germany, (2007).
- [71] S. R. Morrison, *Electrochemistry at Semiconductor and Oxidized Metal Electrodes*; Plenum Press: New York, (1980).
- [72] X. Yang, C. Du, R. Liu, J. Xie, D. W. Wang, Balancing photovoltage generation and charge-transfer enhancement for catalyst-decorated photoelectrochemical water splitting: A case study of the hematite/ MnO_x combination. *J. Catal.* **304** (2013) 86–91.
- [73] M. G. Walter, E. L. Warren, J. R. McKone, S. W. Boettcher, Q. Mi, E. A. Santori, N. S. Lewis, Solar water splitting cells. *Chem. Rev.* **110** (2010) 6446–6473.
- [74] C. Ding, J. Shi, Z. Wang, C. Li, Photoelectrocatalytic Water Splitting: Significance of Cocatalysts, Electrolyte, and Interfaces. *ACS Catal.* **7** (2017) 675–688.
- [75] P. T. Kissinger, W. R. Heineman, Cyclic Voltammetry. *J. Chem. Educ.* **60** (1983) 702.

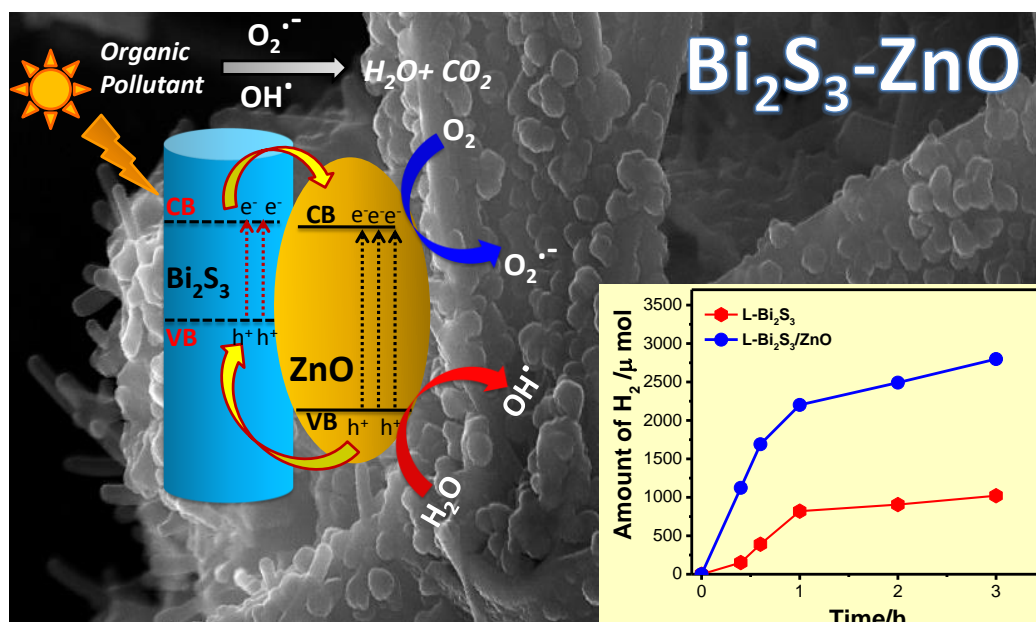
- [76] R. G. Compton, C. E. Banks, *Understanding Voltammetry*, 2nd (Ed.) Imperial College Press: London, (2011).
- [77] D. H. Evans, K. M. O'Connell, R. A. Petersen, M. J. Kelly, Cyclic voltammetry. *J. Chem. Educ.* **60** (1983) 290–293.
- [78] A. J. Bard, L. R. Faulkner, *Electrochemical Methods: Fundamentals and Applications*, 2nd ed.; John Wiley & Sons, Inc.: Hoboken, NJ, (2001).
- [79] L. Nadjo, J. M. Savéant, Linear sweep voltammetry: Kinetic control by charge transfer and/or secondary chemical reactions: I. Formal kinetics. *J. Electroanal. Chem. Interfacial Electrochem.* **48** (1973) 113–145.
- [80] T. J. Davies, R. G. Compton, The cyclic and linear sweep voltammetry of regular and random arrays of microdisc electrodes: Theory. *J. Electroanal. Chem.* **585** (2005) 63–82.
- [81] K. Aoki, K. Akimoto, K. Tokuda, H. Matsuda, J. Osteryoung, Linear sweep voltammetry at very small stationary disk electrodes. *J. Electroanal. Chem. Interfacial Electrochem.* **171** (1984) 219–230.
- [82] D. Garreau, J. M. Savéant, Linear sweep voltammetry—compensation of cell resistance and stability: Determination of the residual uncompensated resistance. *J. Electroanal. Chem. Interfacial Electrochem.* **35** (1972) 309–331.
- [83] G. Denuault, M. V. Mirkin, A. J. Bard, Direct determination of diffusion coefficients by chronoamperometry at microdisk electrodes. *J. Electroanal. Chem. Interfacial Electrochem.* **308** (1991) 27–38.
- [84] T. Gueshi, K. Tokuda, H. Matsuda, Voltammetry at partially covered electrodes: Part I. Chronopotentiometry and chronoamperometry at model electrodes. *J. Electroanal. Chem. Interfacial Electrochem.* **89** (1978) 247–260.
- [85] J. M. Saveant, E. Vianello, Potential-sweep chronoamperometry: Kinetic currents for first-order chemical reaction parallel to electron-transfer process (catalytic currents). *Electrochim. Acta* **9** (1965) 905–918.
- [86] M. Sluyters-Rehbach, J. H. O. J. Wijenberg, E. Bosco, J. H. Sluyters, The theory of chronoamperometry for the investigation of electrocrystallization: Mathematical description and analysis in the case of diffusion-controlled growth. *J. Electroanal. Chem. Interfacial Electrochem.* **236** (1987) 1–20.

- [87] R. L. Willis, C. Olson, B. O'Regan, T. Lutz, J. Nelson, J. R. Durrant, Electron Dynamics in Nanocrystalline ZnO and TiO₂ Films Probed by Potential Step Chronoamperometry and Transient Absorption Spectroscopy. *J. Phys. Chem. B* **106** (2002) 7605–7613.
- [88] G.-Y. Lee, J.-H. Park, Y. W. Chang, S. Cho, M. -J. Kang, J.-C. Pyun, Chronoamperometry-Based Redox Cycling for Application to Immunoassays. *ACS Sens.* **3** (2018) 106–112.
- [89] J. E. B. Randles, Kinetics of rapid electrode reactions. *Discuss. Faraday Soc.* **1** (1947) 11–19.
- [90] W. E. Armstrong et al. Catalyst comprising Ir or Ir and Ru for hydrazine decomposition. US Patent **4124** (1978) 538.
- [91] K. Sivula, Mott–Schottky Analysis of Photoelectrodes: Sanity Checks Are Needed. *ACS Energy Lett.* **6** (2021) 2549–2551.
- [92] J. Bisquert, S. Giménez, L. Bertoluzzi, I. Herraiz-Cardona, Analysis of Photoelectrochemical Systems by Impedance Spectroscopy. Springer International Publishing: Cham (2016) 281–321.
- [93] C. H. Hsu, F. Mansfeld, Technical Note: Concerning the Conversion of the Constant Phase Element Parameter Y_0 into a Capacitance. *Corrosion* **9** (2001) 747–748.
- [94] W. J. Albery, G. J. O'Shea, A. L. Smith, Interpretation and use of Mott-Schottky plots at the semiconductor/electrolyte interface. *J. Chem. Soc. Faraday Trans.* **20** (1996) 4083–4085.
- [95] R. D. Gryse, W. P. Gomes, F. Cardon, J. Vennik, On the Interpretation of Mott-Schottky Plots Determined at Semiconductor/Electrolyte Systems. *J. Electrochem. Soc.* **122** (1975) 711.
- [96] K. Uosaki, H. Kita, Effects of the Helmholtz Layer Capacitance on the Potential Distribution at Semiconductor/Electrolyte Interface and the Linearity of the Mott-Schottky Plot. *J. Electrochem. Soc.* **130** (1983) 895–897.
- [97] D. C. Grahame, The electrical double layer and the theory of electrocapillarity. *Chem. Rev.* **41** (1947) 441–501.
- [98] Y. V. Pleskov, Y. Y. Gurevich, Semiconductor Photoelectrochemistry, Consultants Bureau, New York, (1986).
- [99] K. Gelderman, L. Lee, S. W. Donne, Flat-Band Potential of a Semiconductor: Using the Mott–Schottky Equation. *J. Chem. Ed.* **84** (2007) 685–688.

- [100] A. Hankin, F. E. Bedoya-Lora, J. C. Alexander, A. Regoutz, G. H. Kelsall, Flat band potential determination: avoiding the pitfalls. *J. Mater. Chem. A* **7** (2019) 26162–26176.
- [101] G. A. Mabbott, An introduction to cyclic voltammetry. *J. Chem. Educ.* **60** (1983) 697–702.
- [102] H. Gerischer, Neglected problems in the pH dependence of the flatband potential of semiconducting oxides and semiconductors covered with oxide layers. *Electrochim. Acta* **34** (1989) 1005–1009.
- [103] A. O. Adeyeye, G. Shimon, Chapter 1 - Growth and Characterization of Magnetic Thin Film and Nanostructures. *Handbook of Surface Science* **5** (2015) 1–41.

CHAPTER 4

Fabrication of $\text{Bi}_2\text{S}_3/\text{ZnO}$ Heterostructures: an Excellent Photocatalyst for Visible-Light-Driven Hydrogen Generation and Photoelectrochemical Properties



4.1 Introduction

The challenges of environmental pollution and renewable energy production are both highly active areas of scientific research [1, 2]. Visible light induced photocatalysis is an effective clean approach for water splitting to generate clean solar fuels and converting solar energy to chemical energy [3, 4]. On the other hand, water purification and environmental protection pose an equally daunting challenge [5, 6]. Oxides based semiconductors have been utilized as active photocatalysts in various applications such as photochemical degradation of organic contaminants, photochemical water splitting to produce hydrogen, and photoelectrochemical cells [7-9]. Titanium dioxide (TiO_2) is one of the most popular photocatalyst possess high catalytic activity, low cost and non-toxicity [10, 11]. However, TiO_2 can absorb UV radiation (4% of total solar irradiation) due to wide bandgap and low charge separation efficiency which make them not suitable for visible light active photocatalysis [12, 13]. Moreover, TiO_2 doping with C, N, B, S or modified with metal nanoparticles (Au, Pt, Ag) exhibits Plasmon induced enhance visible light absorption, however, the high cost and low environmental stability of noble-metal-doped TiO_2 resists its economic potential [14-16]. Another semiconductor nanocrystal, zinc oxides (ZnO) having direct bandgap of 3.3 eV and a large excitation binding energy is widely tested for photocatalytic applications [17-19]. Moreover, ZnO has some advantageous properties over TiO_2 such as, high electron mobility for its electronic structure, room temperature luminescence etc. [18, 19]. In this regards, the loading of multiple catalysts or secondary semiconductors can improve catalytic efficiency of ZnO via formation of heterojunctions [20, 21]. This stimulated our interest to design a coupled heterojunction with ZnO to improve solar light absorption in visible region.

Significant efforts have been made on the fabrication of semiconductors based heterostructures such as ZnO/TiO_2 [22], $\text{Bi}_2\text{S}_3/\text{TiO}_2$ [23, 24] and CdS/TiO_2 [25] etc., which shows potential applications in water splitting and organic pollutant degradation. In fact, high charge separation has been achieved *via* coupling of a large bandgap semiconductor with a smaller one forming heterojunction, which in turn enhance the photocatalytic efficiency by decreasing the recombination rate of the photogenerated electron-hole pairs [26, 27]. In case of heterojunction, charge carriers are generated in one semiconductor and then vectorially transfer to the other material allowing for long lived electron hole pairs at the interface and able to produce potential gradient within the catalyst [5]. Due to presence of multiple active sites within the heterostructures, can provide high surface area for the decomposition of organic pollutant molecule at the surface

of the catalysts [28]. For example, TiO₂ based hybrid heterojunctions demonstrated high catalytic activity due to surface tunnelling of electrons between the surfaces of the semiconducting components of the heterostructure [29]. Till now, most of studies have been focused on hybridization of TiO₂ with semiconductor to improve photocatalytic efficiency under visible light [29-33]. In this regard, few reports have been developed on the modification of ZnO nanostructure with other semiconductors such as ZnO/TiO₂ [34], CdS/ZnO [35] etc. for improved visible light driven photocatalysis.

On the other hand, low bandgap semiconductors such as sulphides, nitrides, graphitic carbon nitrides, oxynitrides, chalcogenides etc., have been widely investigated to construct visible light active photocatalysts [36-39]. Among these, bismuth sulphide (Bi₂S₃), a low bandgap metal sulphides (1.3 eV) have shown absorption in visible region and considered as potential candidate for photocatalytic applications [40]. However, due to the rapid recombination of photo-induced electrons and holes, limits catalytic application of Bi₂S₃ under visible light. Recently, a series of Bi₂S₃ based heterostructures such as MoS₂/Bi₂S₃ [41], Bi₂S₃/CdS [42], Bi₂S₃/Bi₂WO₆ [43], Bi₂S₃/In₂S₃ [44], Bi₂S₃/BiVO₄ [45], Bi₂S₃/(BiO)₂CO₃ [46] etc., have been developed to improve the light absorption and charge separation efficiency. Recently, Bi₂S₃/g-C₃N₄ heterostructures exhibited high catalytic performance for organic dye (Rhodamine B) degradation, but its apparent kinetic rate was very low [47]. MoS₂/Bi₂S₃ and Bi₂S₃/In₂S₃ heterojunctions showed high catalytic activity for organic pollutant degradation but no report on hydrogen generation are available till now. Notably, semiconductor based heterostructures are effective catalyst for water oxidation as photogenerated electrons and holes on the surface of heterostructures have the potential to react the surface active site. Thus, the excited electrons reduce the water to form hydrogen and holes oxidize the water to generate oxygen [48]. The Bi₂S₃/CdS heterostructures displayed photocatalytic hydrogen generation under visible light irradiation but hydrogen evolution rate is low [42]. Recently, Wang et al. [49] have been used Z-scheme CdTe-Bi₂S₃ heterojunctions for photoelectrochemical performance. Hence, Bi₂S₃ based heterojunctions have been extensively utilized for organic dye degradation but photocatalytic hydrogen generation has not been tested yet. Herein, Bi₂S₃ with narrow bandgap has been integrated with ZnO nanoparticles to fabricate visible light active heterostructures. Various characterization techniques such as XRD, SEM, TEM and FTIR have been employed for characterizing the structure, morphology, and optical properties of heterostructures. To the best of our knowledge, for the first time, we studied the photocatalytic

performance and photoelectrochemical properties of Bi₂S₃/ZnO for hydrogen generation under visible light.

4.2 Experimental

Bismuth nitrate pentahydrate (Bi(NO₃)₃·5H₂O, 99.99%), L-cysteine hydro-chloride (99.99%), mercaptosuccinic acid (MSA, 99%), ethylenediaminetetraacetic acid disodium salt (EDTA-Na, 99%), methanol were procured from Sigma Aldrich, USA. For in-situ generation of ZnO, zinc acetate dehydrate (ZnCH₃COO)₂·2H₂O, 98%) and sodium hydroxide (NaOH, 98%) were procured from Merck, Germany.

In a typical synthesis, 0.5 mmol of ethylenediaminetetraacetic acid disodium salt (EDTA-Na) was dissolved in 100 mL of distilled water and stirred for 10 minutes. Then 0.4 mmol of Bi(NO₃)₃ was mixed and the solution mixture was ultrasonicated until the solution became transparent. After that, 0.6 mmol of L-cysteine hydrochloride was added to the solution. Finally, the solution was transferred into a 100 mL Teflon-lined autoclave with a stainless steel shell and heated at 180°C for 16 h. The Bi₂S₃ was collected and centrifuged, washed several times with distilled water and finally air-dried overnight at 50°C for further characterization. Similarly, Bi₂S₃ nanostructures were also prepared using mercaptosuccinic acid as a sulphur source [50]. The effect of sulphur source concentration (0.6, 1.2, 2.4 mmol) and different reaction times (10, 16, 24 h) to follow the growth mechanism of Bi₂S₃ nanostructure formation has been studied in detail.

In order to develop a coupled heterostructures of Bi₂S₃/ZnO, a facile in situ generation via co-precipitation technique has been employed using ethanol as a solvent [17]. Briefly, 20 mL of 4 mmol zinc acetate dehydrate solution was heated at 70°C for 30 min. Then a fixed amount of prepared Bi₂S₃ powder (1 mg mL⁻¹) was added and mixed thoroughly. In the next step, 20 mL of 4 mmol sodium hydroxide solution prepared at 70°C in ethanol was added slowly and the mixture was hydrolyzed for 2 h at 60°C to obtain ZnO NPs with average diameters of ~5 nm. The pure semiconductors and heterostructures are presented as L-Bi₂S₃, L-Bi₂S₃/ZnO (using L-cysteine hydro-chloride as a source of sulphur) and M-Bi₂S₃, M-Bi₂S₃/ZnO (using MSA as a source of sulphur). To understand the growth mechanism of Bi₂S₃, extensive experimental analyses were performed for varying reaction times, metal salt to surfactant ratios and sulphur sources.

The crystalline phase of Bi_2S_3 and the heterostructures was investigated by XRD (Philips X'Pert, The Netherlands) within the 2θ range of 10° to 80° at a slow scan rate of 1° min^{-1} with $\text{Cu K}\alpha$ radiation (at 40 kV and 40 mA). The structural morphology and EDS was recorded by Field Emission Scanning Electron Microscopy (LEO. 430i, Carl-Zeiss, Sigma). Transmission Electron Microscopy (TEM) images and the corresponding selected area electron diffraction (SAED) patterns were obtained on Tecnai G² 30ST (FEI) operating at 300 kV. The XPS study was performed using a PHI 5000 Versa Probe II spectrophotometer (Physical Electronics Inc., USA) with a monochromatized $\text{Al K}\alpha$ (B1486.6 eV) X-ray beam of size B100 mm. The samples were prepared in pallet form and the surfaces were sputtered with a 2 kV rastered Ar^+ ion beam for one minute to clean the surface. The thermal stability of the bare Bi_2S_3 and heterojunction was investigated using thermogravimetric analysis (TGA) apparatus (NETZSCH, STA 449 F3, Jupiter). The test was carried out in air with a heating rate of $10^\circ\text{C min}^{-1}$ from 30°C to 900°C . The porosity and specific surface area of the samples were determined through nitrogen adsorption at 200°C on the basis of the BET equation using a Quantachrome, FL-33426. The UV-Visible absorption spectra of the ethanolic solutions containing Bi_2S_3 , ZnO and $\text{Bi}_2\text{S}_3/\text{ZnO}$ were recorded using a Shimadzu, UV-3600 spectrophotometer. The hydrogen evolution was measured by online gas chromatography using an YL Instrument, 6500GC system with a thermos-conductive detector. The photoelectrochemical measurements have been tested using a galvanostat–potentiostat (PGSTAT302N, Autolab, The Netherlands) with a standard three-electrode cell and Pt wire as a counter electrode and saturated Ag/AgCl as a reference electrode. The working electrode was a thin film of as-prepared material on glassy carbon. The photocatalytic I–V characteristics have been measured using simulated illumination (60 mW cm^{-2}) by a white light source.

L- Bi_2S_3 , L- $\text{Bi}_2\text{S}_3/\text{ZnO}$, M- Bi_2S_3 and L- $\text{Bi}_2\text{S}_3/\text{ZnO}$ have been tested for dye degradation using methyl orange (MO) as model pollutant. It is a representative of hazardous azo dye. The photodegradation of MO (initial concentration $C_0 = 0.3 \times 10^{-4} \text{ M}$) was carried out within a quartz cell reactor containing 50 mL model solution with a concentration of 1 mg mL^{-1} under UV and visible lamp. A Xe-arc lamp (250W) with an incident beam intensity of 100 mW cm^{-2} (Oriol, Irvine, CA) was used as light source for visible irradiation and a 395 nm cutoff filter was used. For control experiment, bare L- Bi_2S_3 and M- Bi_2S_3 have been studied separately under similar reaction condition. The appropriate amount of aliquots was collected from the reactor at successive time

intervals. The percentage degradation (% DE) of MO was determined using the following equation.

$$\% DE = \frac{C_0 - C}{C_0} \times 100 \quad (4.1)$$

Where, C_0 is the initial absorption intensity of MO at $\lambda_{\max} = 463$ nm and C is the intensity after light illumination.

To study the hydrogen generation, online gas chromatography method was involved where the area under the Gaussian peak gives the amount of H_2 evolved. The H_2 production through water splitting was performed in a closed reactor in presence of methanol solution with saturated argon media and vigorous stirring. For this experiment, 25 volume % methanol solution was used at room temperature [51]. Here, methanol acts as sacrificial agent and use of methanol is very much advantageous than other alcohols because it reduce the formation of more carbon based sub products being the simplest organic molecule and also accelerate the main intermediate (free radical) formation process [51]. Here we report H_2 generation up to 3 h.

4.3 Results and Discussion

4.3.1 Structural Characterization

The XRD was carried out to study the crystalline phase of the as prepared materials. Figure 4.1a, b shows the X-Ray diffraction (XRD) patterns of L- Bi_2S_3 , L- Bi_2S_3/ZnO , M- Bi_2S_3 and M- Bi_2S_3/ZnO . X-ray patterns displayed narrow and sharp diffraction peaks, indicating the high crystallinity of the prepared samples. The strong peaks at 2θ value 15.54° , 17.41° , 22.21° , 23.57° , 24.92° , 28.43° , 31.71° correspond to characteristic diffraction from (020), (120), (220), (101), (130), (211) and (221) planes of pure Bi_2S_3 respectively (JCPDS card no. 17-0320) [47]. The diffraction peaks of ZnO at 2θ values 31.76° , 34.00° and 36.56° correspond to the (100), (002) and (101) plans indicating the wurtzite hexagonal phase of ZnO (JCPDS card no. 36-1451) [52]. The XRD pattern of the pure ZnO nanoparticles have been shown in inset Figure 4.1a which indicates high crystalline in nature. Therefore, the XRD patterns of heterostructures reveal the presence of wurtzite ZnO within orthorhombic Bi_2S_3 . Moreover, presence of all characteristic peaks of Bi_2S_3 and no additional peak in heterostructures confirms purity of Bi_2S_3/ZnO . Moreover, no remarkable changes was observed in the diffraction peak position and intensity of Bi_2S_3/ZnO at longer hydrothermal reaction time indicating formation of stable orthorhombic Bi_2S_3 (Figure 4.1c).

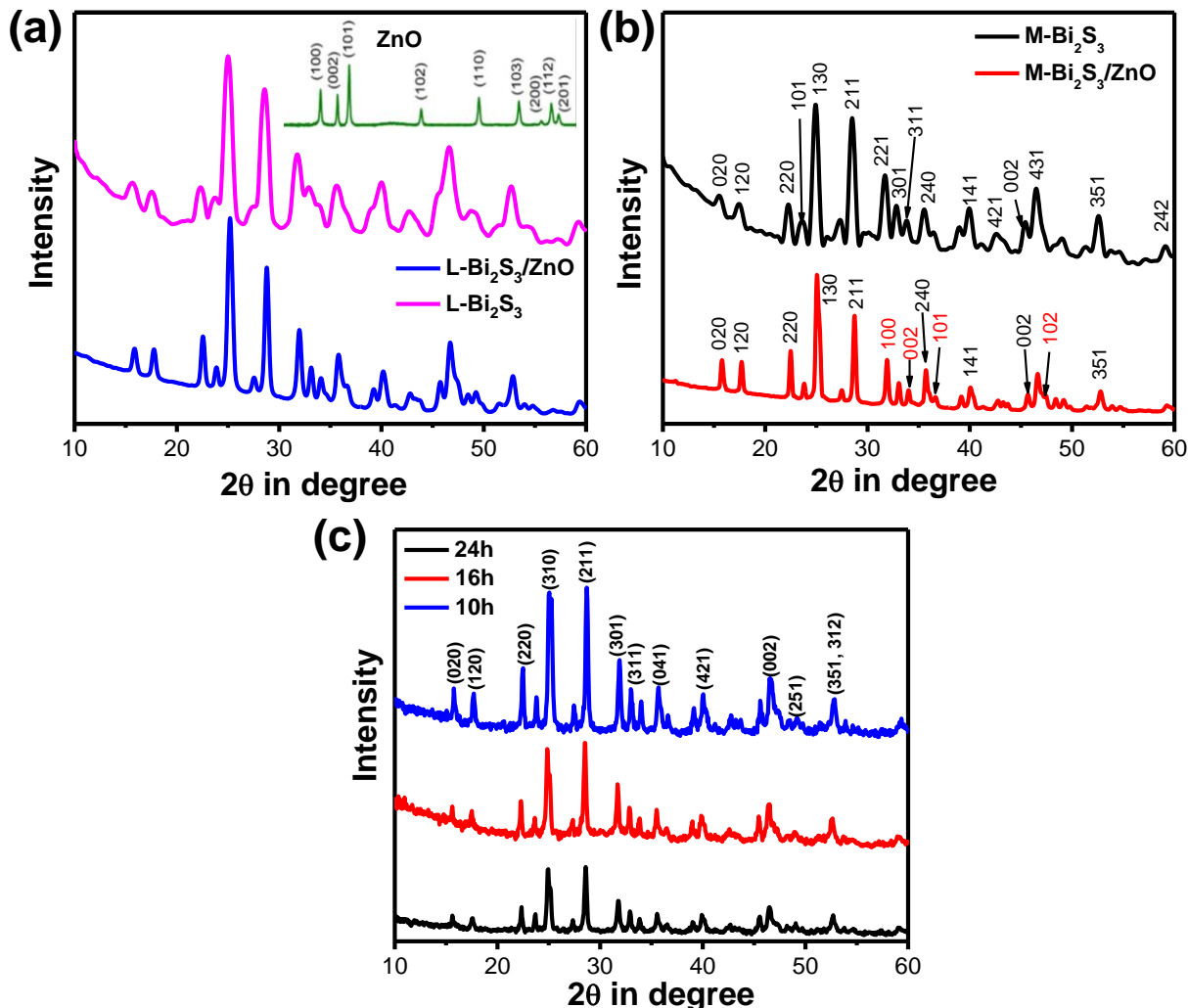


Figure 4.1 XRD patterns of as prepared (a) pure L-Bi₂S₃ and L-Bi₂S₃ decorated with ZnO NPs. Inset: XRD pattern of ZnO nanoparticles. (b) Pure M-Bi₂S₃ rod shaped structures and M-Bi₂S₃ decorated with ZnO NPs. The samples have been synthesized at 16 h and metal salt to surfactant ratio 1: 3. (c) XRD patterns of M-Bi₂S₃ at three different reaction times as 10 hours, 16 hours and 24 hours.

4.3.2 Morphology

The morphology and growth of Bi₂S₃ and Bi₂S₃/ZnO study were investigated by field emission scanning electron microscopy (FESEM). Figure 4.2a–c shows the assembled growth of Bi₂S₃ rods with increasing the reaction time. Figure 4.2a–c illustrates the growth of Bi₂S₃ rods with increasing the reaction time. It is clear from Figure 4.2a, when the hydrothermal reaction proceeds for 10 h, formation of rods like structures are obtained which are completely overlapped. At 16 h, the distinct rods with average length $\sim 3.81 \mu\text{m}$ (Figure 4.2b) are formed which are connected with each other and radiated from a centre.

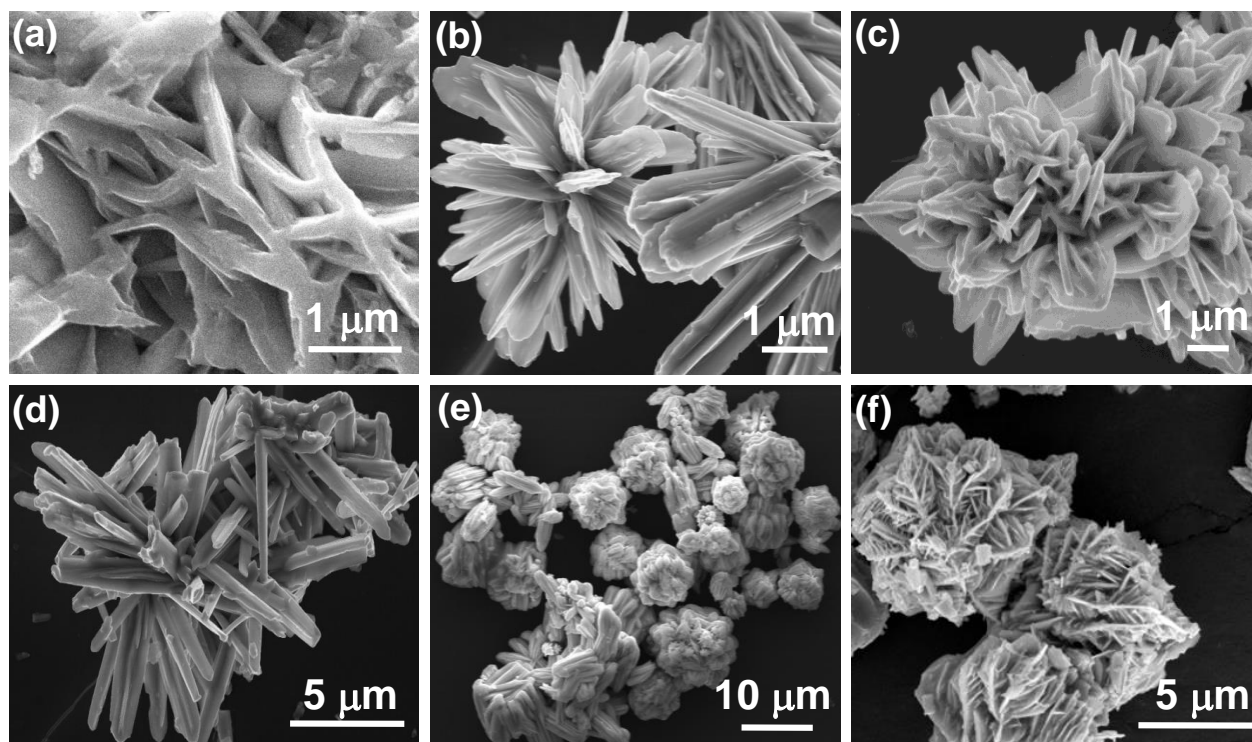


Figure 4.2 FESEM images of Bi_2S_3 using L-cysteine as structure controlling agent at three different reaction time (a) 10 h, (b) 16 h, (c) 24 h (metal: L-cysteine 1:1.5). Effect of surfactant concentrations during the formation of Bi_2S_3 at three different metal/surfactant ratio (d) 1:1.5, (e) 1:3 and (f) 1:6 at 16 h under similar condition.

Further increase in reaction time up to 24 h, the rods are more assembled and interestingly form lotus flower like morphology (Figure 4.2c). This may happened due to over growth of Bi_2S_3 nuclei in same direction [42]. In addition, the metal salt to surfactant ratio has been varied to investigate the role of surfactant as morphology controlling factor. Figure 4.2d–f display Bi_2S_3 synthesized at three different concentration of surfactant at 16 h keeping all other conditions similar. The metal salt : L-cysteine at 1 : 1.5, it can be observed that irregularly distributed rod shaped structures of average length $\sim 4.7 \mu\text{m}$ are formed (Figure 4.2d). In contrast, at 1:3, assembled morphology (length $\sim 5.5 \mu\text{m}$) consists of rods have been formed with bunched like structure.

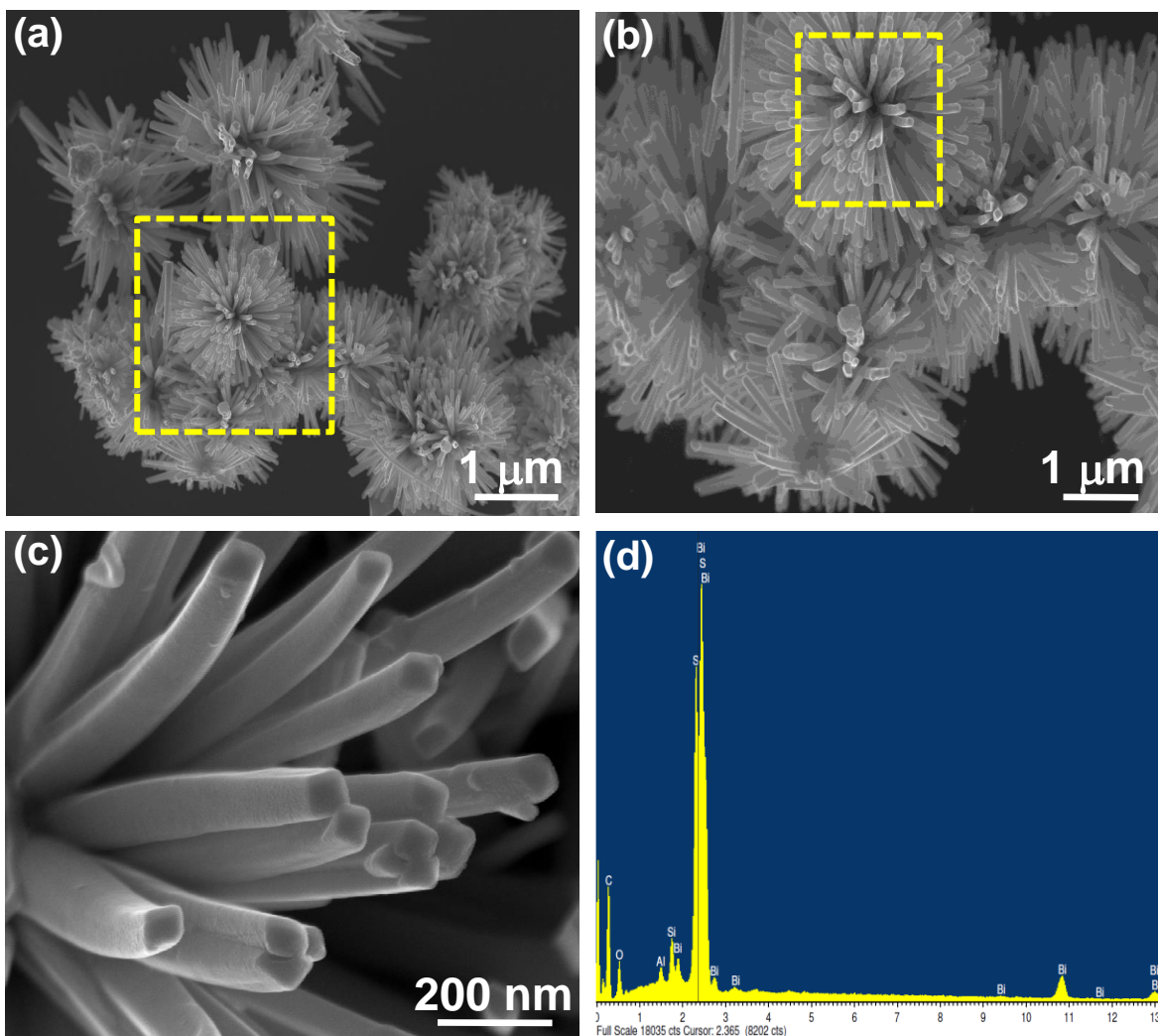


Figure 4.3 FESEM images of (a)–(c) flower like assembled structures of Bi_2S_3 using mercaptosuccinic acid as structure controlling agent at three different magnifications and (d) EDS spectrum of Bi_2S_3 synthesized at 16 h and metal salt to surfactant ratio 1 : 3.

Moreover, at higher concentration of L-cysteine (1:6 ratio), more assembled structures have been formed. Figure 4.2e displays Bi_2S_3 superstructure of diameter $\sim 8 \mu\text{m}$ which are built of two dimensional nanosheets. Hence, this highly assembled morphology is useful to provide more active site in photocatalytic applications. In general, assembled 1D morphology is more suitable for photocatalytic applications having large surface to volume ratio, synergistic interactions as the long length of nanorods will contact each other and multiple functionalities [53].

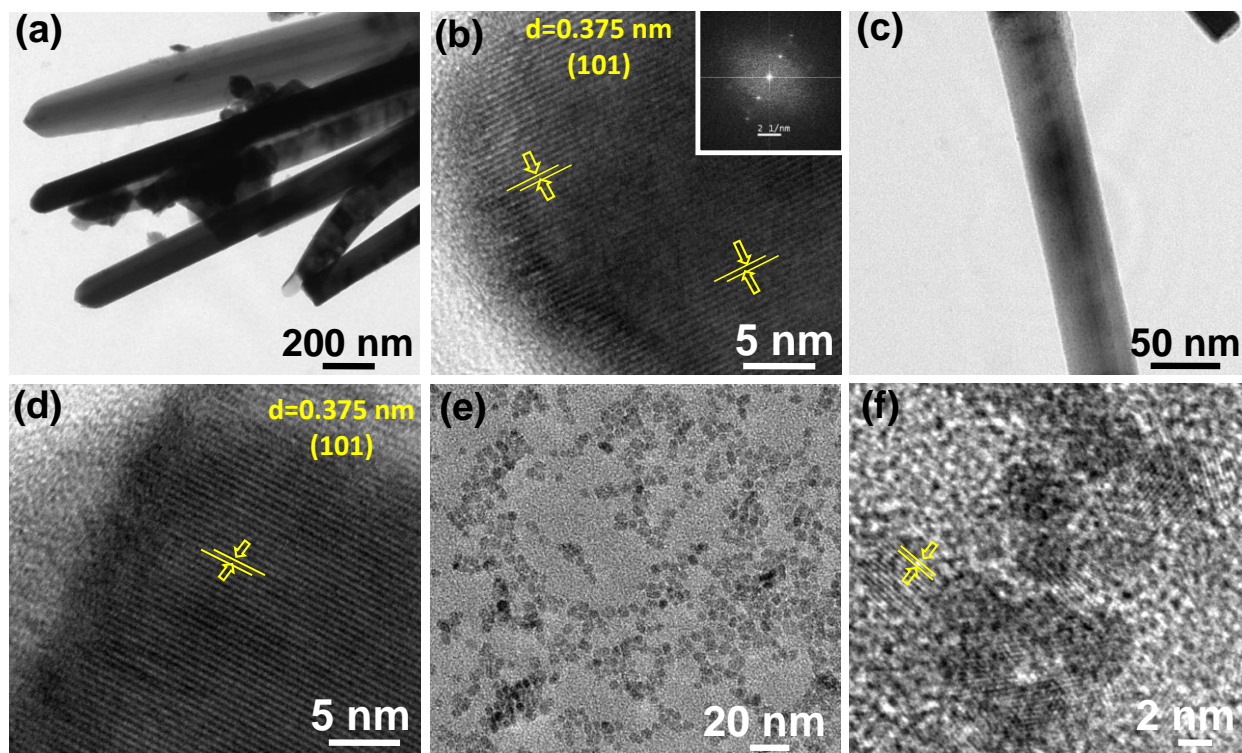


Figure 4.4 TEM images of (a) pure L-Bi₂S₃ nanostructures (b) HRTEM of L-Bi₂S₃ inset: SEAD pattern, (c) pure M-Bi₂S₃ nanostructures and (d) HRTEM image of M-Bi₂S₃ at metal: surfactant = 1:3 in reaction time 16 h.

Another kind of Bi₂S₃ nanostructures have been developed using mercaptosuccinic acid as structure controlling agent. Figure 4.3a–c illustrates FESEM images of pure Bi₂S₃ at different magnifications, clearly indicates solid rods radiated from a common centre and stack uniformly to form nanoflowers like morphology. At high magnification, it has been clearly observed that nanoflowers are consists of the solid rods of length ~ 500 nm with square edge of sides 60 to 70 nm (Figure 4.3c). To investigate the elemental composition, X-ray energy dispersive spectrometry (EDS) was carried out on Bi₂S₃ nanoflowers. Figure 4.3d suggests that the coexistence of Bi and S elements on the rod shaped structures. However, the presence of Al and Si signals has been originated from glass substrate. Additionally, detailed structural and crystalline nature of as prepared Bi₂S₃ and Bi₂S₃/ZnO have been investigated through TEM and HRTEM images (Figure 4.4). The TEM images (Figure 4.4a, c) clearly reveals the uniform 1D structure of L-Bi₂S₃ and M-Bi₂S₃ which are well consistent with FESEM images. The interplanar spacing of 0.375 nm reveals the characteristic (101) plane of Bi₂S₃ (Figure 4.4b, d) [54]. Therefore the preferential growth of Bi₂S₃ rods occurred along the (101) direction. The calculated size of bare ZnO NPs is in the range

5 nm as determined from TEM image which are also highly crystalline (Figure 4.4e and 4f). The microscopic images of L-Bi₂S₃/ZnO heterostructures are displayed in Figure 4.5. It can be clearly seen from SEM images (Figure 4.5a, b) that the spherical ZnO NPs have been formed uniformly on the L-Bi₂S₃ surface. Further detailed study on morphology of L-Bi₂S₃/ZnO heterostructures has been studied through the TEM images.

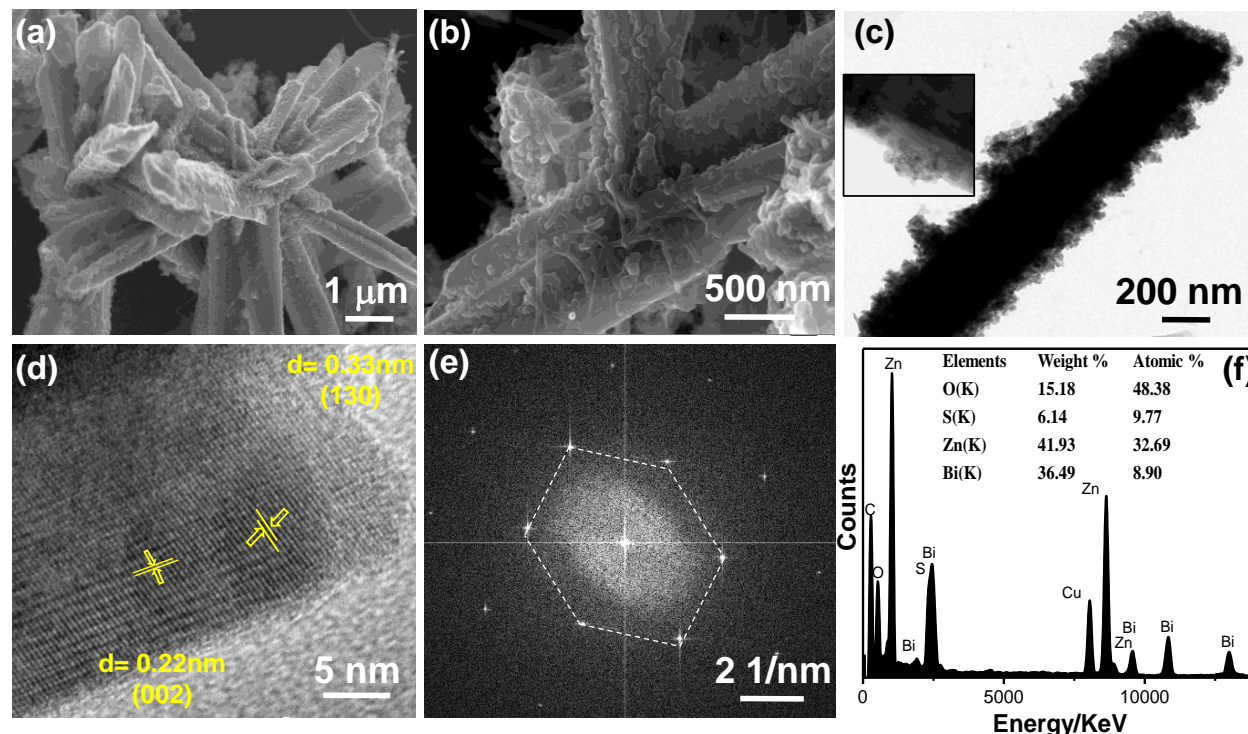


Figure 4.5 (a-b) FESEM images of L-Bi₂S₃/ZnO heterostructures at two different magnifications. TEM image of (c) ZnO nanoparticles decorated on rod shaped Bi₂S₃ structures, (d) HRTEM, (e) SAED and (f) EDX spectrum of L-Bi₂S₃/ZnO heterostructures.

Figure 4.5c clearly shows the rough surface of rod shaped L-Bi₂S₃ due to deposition of spherical hexagonal ZnO nanoparticles over the surface. The HRTEM image of L-Bi₂S₃/ZnO reveals high crystalline nature having the lattice spacing of about 0.33 nm related to (130) plane of Bi₂S₃ (Figure 4.5d) [55]. The SAED pattern depicts highly crystalline hexagonal structure of Bi₂S₃ (Figure 4.5e). For further analysis of chemical compositions and the elemental distribution, EDS was carried out (Figure 4.5f) where strong signals of Bi, S, O and Zn also confirm the formation of Bi₂S₃/ZnO heterostructures.

The morphology and crystalline nature of heterostructures using M-Bi₂S₃ was further investigated by FESEM and TEM images. Figure 4.6a shows *in situ* generation of ZnO NPs on the rod shaped M-Bi₂S₃ structures. It is evident that the assembled nanoflowers like structure are totally

transforms into nanofiber based network after formation of ZnO NPs. This is probably due to the strong interaction between ZnO and surface ligand (MSA) of Bi_2S_3 which is responsible for the formation of self-assemble nanoflowers like morphology. The FESEM image also illustrates that the single rod shaped structure of Bi_2S_3 is completely covered by small ZnO NPs (Figure 4.6b). Figure 4.6c shows that the M- $\text{Bi}_2\text{S}_3/\text{ZnO}$ rod like nanostructures are cover with smaller nanoparticles which consistent with the FESEM image (Figure 4.6a, b) and the cross fringes in HRTEM image indicates the crystallinity of heterostructures with lattice spacing value of 0.30 nm related to the (211) plane of Bi_2S_3 (Figure 4.6d) [56]. Due to high crystalline nature of Bi_2S_3 , it is difficult to observe crystal fringes of ZnO within the heterostructures.

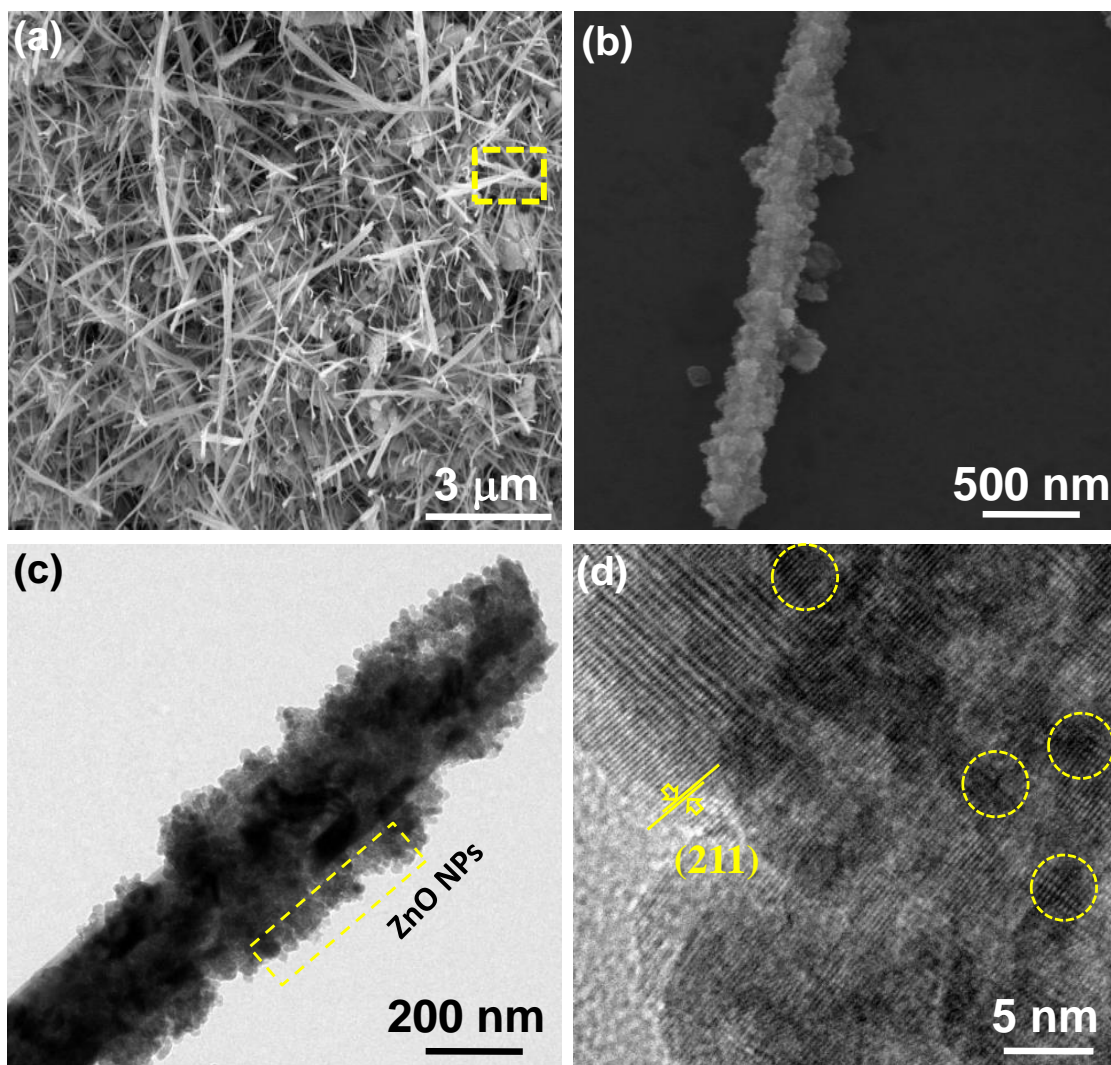
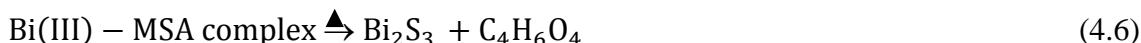
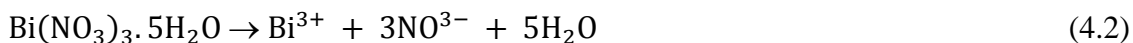


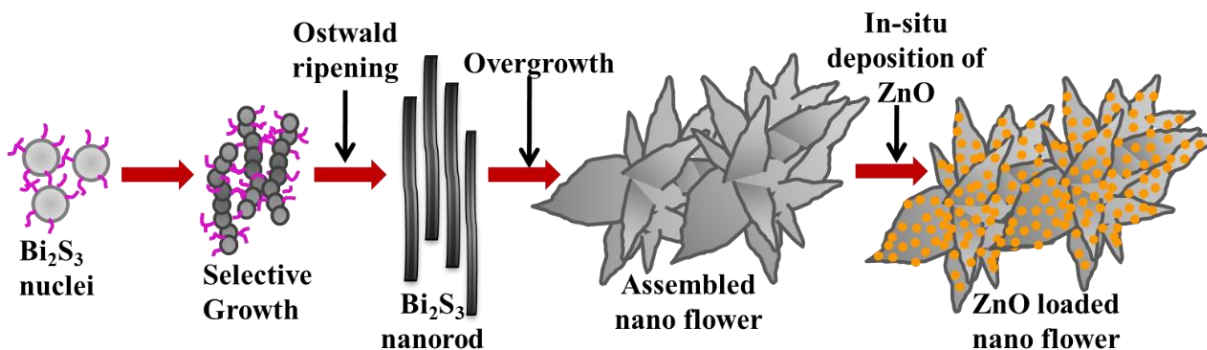
Figure 4.6 FESEM images of M- $\text{Bi}_2\text{S}_3/\text{ZnO}$ heterostructures at (a) low magnification, (b) high magnification. TEM image of (c) ZnO nanoparticle decorated on rod shaped Bi_2S_3 structures, (d) HRTEM of M- $\text{Bi}_2\text{S}_3/\text{ZnO}$ heterostructures.

4.3.3 Growth Mechanism

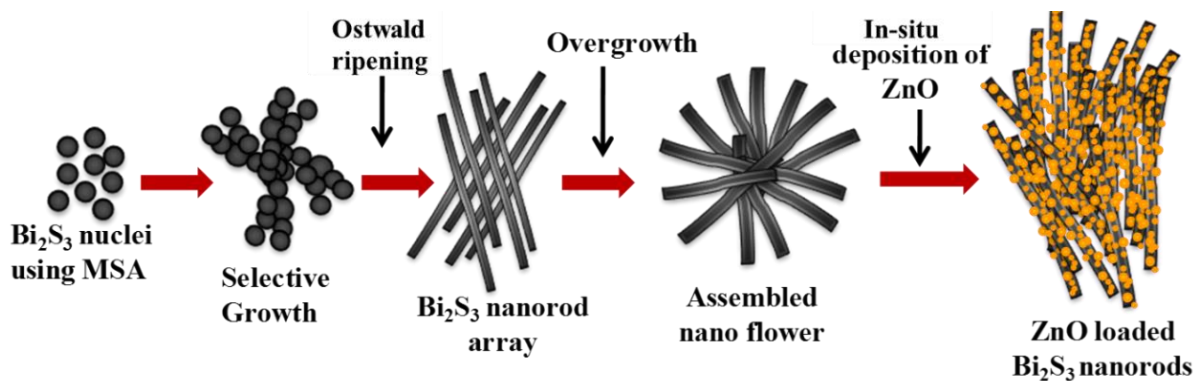
The growth of bare Bi_2S_3 and its heterostructures can be explained on the basis of coordination interaction between Bi^{3+} and surfactant. In the hydrothermal synthesis Bi_2S_3 nanostructure and *in-situ* generation method for heterojunction formation, the following reactions may involve:



Initially, as L-cysteine contain various functional groups such as $-\text{NH}_2$, $-\text{COOH}$, $-\text{SH}$ [57-59] and MSA contains $-\text{SH}$, $-\text{COOH}$ groups which have tendency to coordinate with inorganic cations and metals. Thereafter, the amino group reacts with the neighbouring carboxylic group of the surfactant to form dipeptide or polypeptide because of these complex forms are more stable relative to others [42, 54]. Moreover, this intermediated state serves as template in the successive nucleation of Bi_2S_3 nanocrystals. Finally, the rod shaped Bi_2S_3 are originated by continuous growth of Bi_2S_3 nuclei along one direction which may be caused by a typical Ostwald ripening process [42]. From the effect of different reaction time, it can be conclude that, the transformation of assembled flower from undefined structure may be caused due to recrystallization along the preferential growth axis to form the rod-composed flower as shown in FESEM images (Figure 4.2). To get the ZnO loaded Bi_2S_3 rods, direct adsorption as well as *in situ* generation of 5 nm ZnO NPs on the Bi_2S_3 have been followed. Possible mechanism of heterostructures formation are displayed in Scheme 1 and Scheme 2.



Scheme 4.1 Schematic illustration of ZnO nanoparticles decorated Bi_2S_3 assemblies structure synthesized by simple hydrothermal method using L-Cysteine hydrochloride as structure controlling agent.



Scheme 4.2 Schematic illustration of ZnO nanoparticles decorated Bi₂S₃ rods synthesized by simple hydrothermal method using mercaptosuccinic acid as structure controlling agent.

4.3.4 XPS Analysis

X-ray photon spectroscopy (XPS) was carried out further to elucidate the chemical compositions as well as the oxidation states of pure semiconductor and heterostructures. The overall XPS spectra (Figure 4.7a) indicate the presence of strong peaks of Bi, S, Zn, O and C. Here the 1S peak of C acts as reference point coming from the background. The strong peaks at binding energy ~157.84 eV and ~163.16 eV with typical spin orbit doublet splitting of 5.32 eV can be assigned to the binding energy of Bi 4f_{7/2} and Bi 4f_{5/2} respectively, closely matched with the Bi³⁺ in Bi₂S₃ (Figure 4.7b) [60]. The peaks found between the Bi 4f_{7/2} and Bi 4f_{5/2} at ~161.83 eV and ~160.56 eV are corresponding to the S 2p_{1/2} and S 2p_{3/2} (1.27 eV) refers the existence of S²⁻ within Bi₂S₃ [42]. Moreover, after heterojunction formation, blue shift of binding energy for Bi 4f_{7/2} (~ 0.3 eV), Bi 4f_{5/2} (~ 0.27 eV) and S (~ 0.19 eV) indicates the strong interaction between Bi₂S₃ and ZnO followed by formation of heterojunction. In addition, the strong oxidation peaks located at ~1021.9 eV and ~1045.1 eV of Zn 2p_{3/2} and 2p_{1/2} respectively (Figure 4.7c) suggests the Zn²⁺ state of ZnO [49]. It is also observed that binding energy of pure ZnO shift towards lower value of 0.23 eV after forming heterojunction. Figure 4.7d exhibits the asymmetric profile of O 1s which can be fitted to two symmetrical peaks at ~530.2 and ~531.72 eV, indicating two different kinds of O species presence in the sample. The peaks at ~531.72 eV and ~530.2 eV should be associated with the lattice oxygen (O_L) of ZnO and chemisorbed oxygen (OH) by the surface [61]. Thus, XPS spectra suggest the co-existence of Bi₂S₃ and ZnO within the heterostructures.

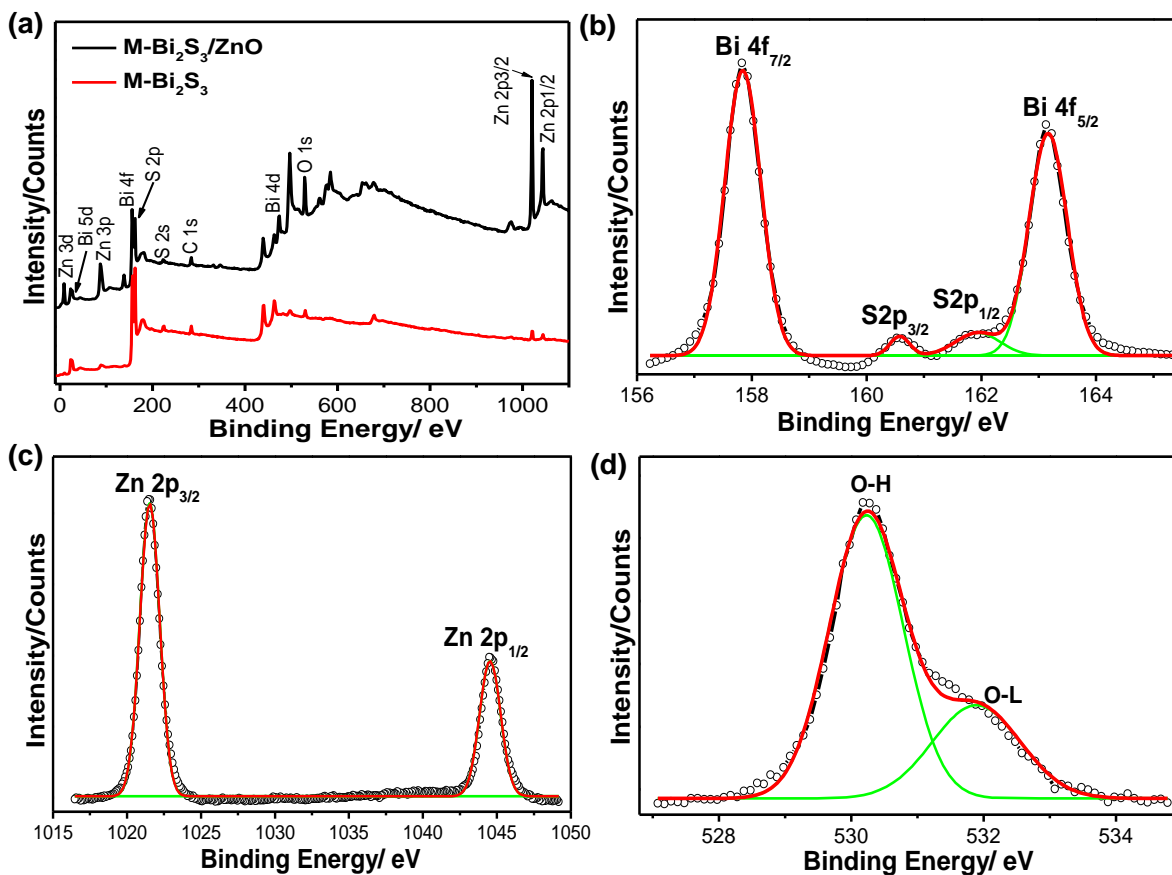


Figure 4.7 XPS spectra of as-prepared heterostructures. (a) The overall spectra of M-Bi₂S₃ and M-Bi₂S₃/ZnO. (b) The Bi 4f and S 2p spectra, (c) Zn 2p spectra and (d) O 1s spectra of M-Bi₂S₃/ZnO. Here the scatter and solid lines indicate the experimental and fitted data.

4.3.5 TG and BET Surface Area Analysis

Thermo-gravimetric analysis (TGA) was carried out to determine the loading of ZnO NPs after *in situ* deposition as well as the thermal stability of heterostructure. The loading of ZnO calculated from TGA curves, are found to be 10% and 15% for L-Bi₂S₃ and M-Bi₂S₃ respectively (Figure 4.8a and 8b). The initial mass losses in the range of 220°C to 230°C is originating from the removal of adsorbed O₂ and water molecules. The further mass loss above 380°C mainly attributed for decomposition of Bi₂S₃ into Bi metal. Notably, after 440°C, pure Bi₂S₃ curve is fairly stable whereas the Bi₂S₃/ZnO heterostructures is unstable and indicates a strong weight loss above 478°C which implies the formation of ZnO [42]. The porous structure of the pure semiconductor as well as heterostructures was studied by nitrogen adsorption desorption isotherm method. The specific surface areas calculated by BJH method are 3.13 m² g⁻¹ and 9.53 m² g⁻¹ for pure M-Bi₂S₃ and M-Bi₂S₃/ZnO heterostructures, respectively. This indicates that the specific BET surface area is

increased when heterojunction formed which may be useful for photocatalytic applications [56]. The hysteresis loop present in BET curve (Figure 4.8c) suggests about the type II pattern of the semiconductor heterostructures. Hence, incorporation of ZnO nanoparticles effectively generates porosity and active surface sites within the heterostructure.

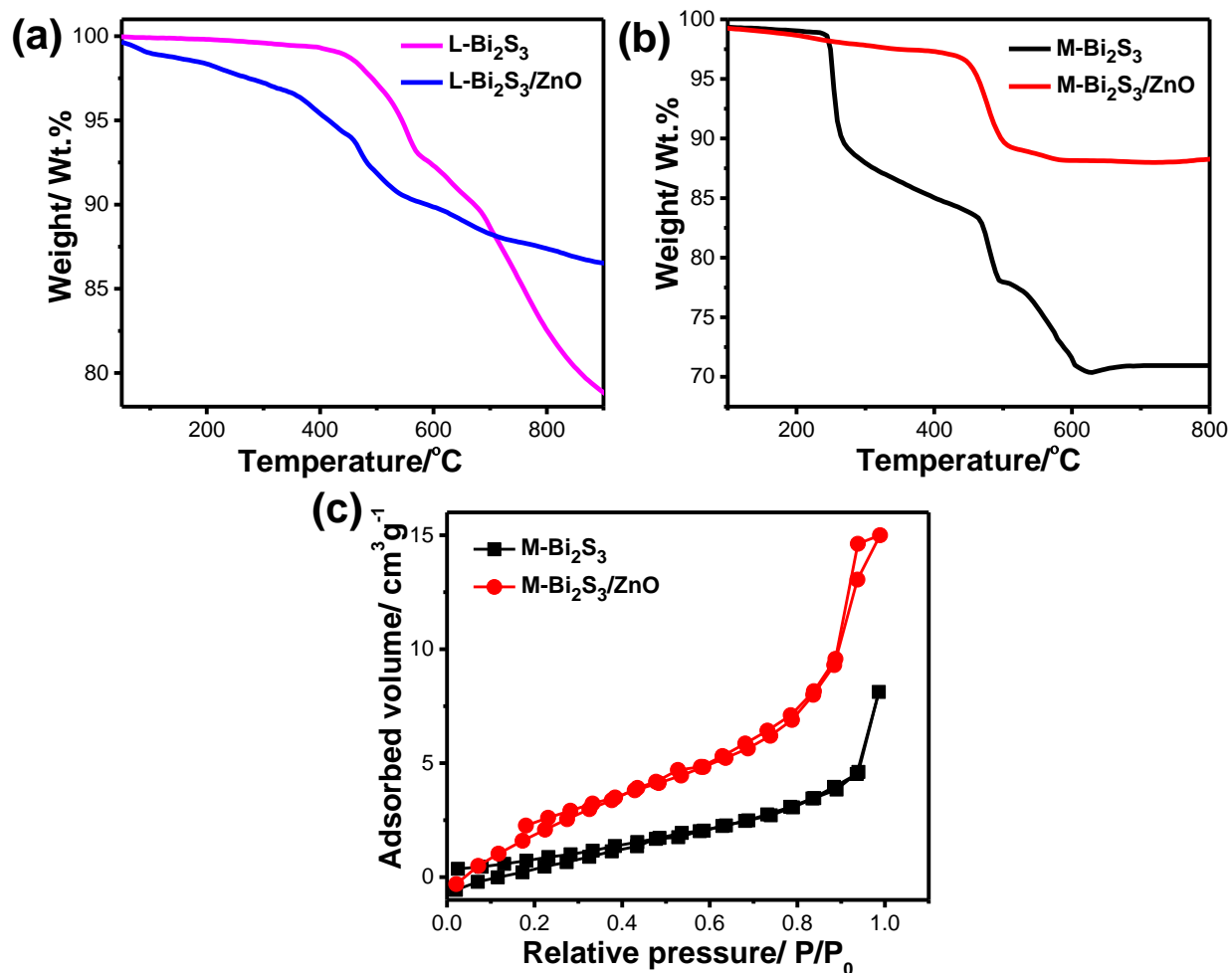


Figure 4.8 TG curves of (a) pure L-Bi₂S₃ and L-Bi₂S₃/ZnO, (b) pure M-Bi₂S₃ and M-Bi₂S₃/ZnO. (c) N₂ adsorption-desorption isotherm of bare M-Bi₂S₃ and M-Bi₂S₃/ZnO heterostructure.

4.3.6 Optical Characterization

The optical properties of pure semiconductor and semiconductor heterostructures have been evaluated by diffuse reflectance spectroscopy (DRS) and photoluminescence (PL) spectroscopy. Figure 4.9a shows the DRS of bare semiconductors and heterostructures where both L-Bi₂S₃/ZnO and M-Bi₂S₃/ZnO heterostructures demonstrated broad absorption in the visible range and it extends up to the near IR range. For the bare ZnO, the onset of light absorption is in the UV region with bandgap ~ 3.37 eV. The light absorption of Bi₂S₃/ZnO heterostructures increases in the visible

region compared to bare ZnO or Bi₂S₃ indicating that heterostructures are useful for efficient solar light harvesting applications. The photoluminescence spectra of ZnO display an emission peak at ~514 nm upon excitation to 320 nm as shown in Figure 4.9b. The intensity of the emission peak lowered significantly to 519 nm and 517 nm when L-Bi₂S₃ and M-Bi₂S₃ attached to the ZnO NPs. Thus, the quenching in emission intensity (65.5% for M-Bi₂S₃/ZnO and 83.25% for L-Bi₂S₃/ZnO) for heterostructure indicates the strong electronic interaction and improved charge carrier separation efficiency [17].

4.3.7 Photocatalytic MO Degradation

The photocatalytic activity has been studied under visible light using methyl orange (MO) as model pollutant. It is well known that MO is a very stable dye which is resistant to self-photo degradation. Figure 4.9c clearly shows the degradation of MO in presence of Bi₂S₃ and Bi₂S₃/ZnO under visible light irradiation. The M-Bi₂S₃/ZnO heterostructures exhibits significantly enhanced photocatalytic activity as compared with bare M-Bi₂S₃ and L-Bi₂S₃. Bare L-Bi₂S₃ has negligible photocatalytic activity (26%) but bare M-Bi₂S₃ shows high activity (63%). Whereas, photodegradation efficiency of MO reached 82% for M-Bi₂S₃/ZnO and 55% for L-Bi₂S₃/ZnO after 150 min of visible light irradiation, (Figure 4.9c) indicating that heterostructures possess superior photocatalytic activity. The photocatalytic activity of M-Bi₂S₃/ZnO heterostructures is ~8.6 times higher comparing to bare M-Bi₂S₃. The enhanced photocatalytic activity of heterostructures can be achieved due to strong absorption in visible range with high surface area of assembled structure [62]. As evident from TGA data, loading of ZnO NPs on M-Bi₂S₃ nanofibers may create more catalytic centres within the heterostructure and thereby show high catalytic activity. The enhanced catalytic activity of M-Bi₂S₃/ZnO may associated with the multiple reflection and scattering of light within the interconnected rods which results enhanced light absorption as reflected in absorption spectra [28]. Similarly, L-Bi₂S₃/ZnO demonstrated higher catalytic activity in comparison to bare L-Bi₂S₃.

Possible reactions involved in photocatalytic dye degradation are given below.



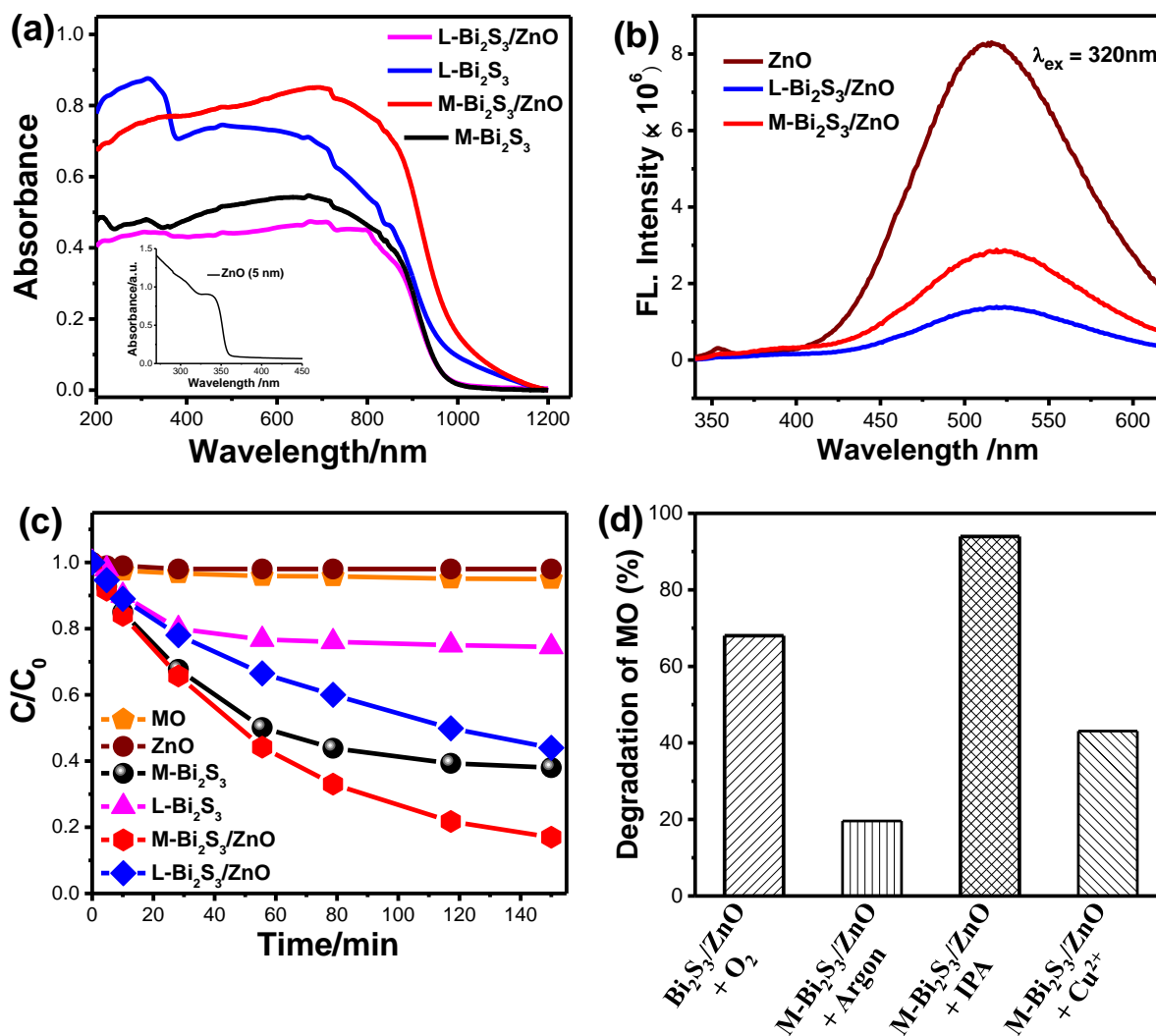


Figure 4.9 (a) Diffuse reflectance spectra of L-Bi₂S₃ (Pink line), L-Bi₂S₃/ZnO (Blue line), M-Bi₂S₃ (Black line) and M-Bi₂S₃/ZnO (red line) respectively. Inset: absorption spectra of ZnO nanoparticles (5 nm). (b) Photoluminescence spectra of ZnO (5 nm), L-Bi₂S₃/ZnO and M-Bi₂S₃/ZnO. (c) Photocatalytic degradation of methyl orange in presence of catalyst, bare semiconductors L-Bi₂S₃, M-Bi₂S₃ and heterostructures L-Bi₂S₃/ZnO, M-Bi₂S₃/ZnO under visible light irradiation. (d) Effect of argon, isopropanol, Cu²⁺ on the photocatalytic activity of M-Bi₂S₃/ZnO for methyl orange degradation.

In order to investigate the photocatalytic mechanism of heterostructures based catalyst, further study have been conducted in presence of sacrificial agents and contribution of excess electrons (Cu²⁺, isopropanol and saturated argon media) (Figure 4.9d) [62]. Semiconductor reacts with photoinduced electrons and holes from water to form various reactive species including O₂⁻ and OH[•] [63]. Herein, Cu²⁺ was used to understand the role of excess electrons as it reacts with electron very fast and convert into Cu⁺. The remarkable change of MO degradation in presence of 2×10^{-6} M Cu²⁺ (it changes 68 % to 43%) is presented in Figure 4.9d after 6 h visible light irradiation. This

suggests role of electron during photocatalytic reaction. In order to confirm the role of $O_2^{\bullet-}$, photodegradation experiment has been performed under argon saturated atmosphere. In general, argon saturated inert medium may suppress the $O_2^{\bullet-}$ radical production which may be the possible reason for inhibiting the degradation of MO by M-Bi₂S₃/ZnO [62]. It only degrades 20% of MO after 4h of visible light irradiation. Thus it can be concluded that oxygen has crucial role in photocatalytic reaction. Moreover, photocatalysis has been performed in presence of 0.1 M isopropanol (acts as hole scavenger) and oxygen to investigate the role of photoexcited holes in photocatalytic reactions. The decomposition kinetics of MO increased up to 94% in presence of isopropanol which clearly indicates the role of holes in photodegradation of MO.

4.3.8 Photocatalytic H₂ Generation

Figure 4.10a shows photocatalytic H₂ generation by Bi₂S₃ and Bi₂S₃/ZnO heterostructures via water splitting using 25 volume % of methanol solution as sacrificial agent. In general, the semiconductors with more negative CB can reduce water efficiently, thus increase the hydrogen production rate. Herein, relatively low bandgap semiconductor, Bi₂S₃ acts as recombination centre for ZnO and reduction process occur at the ZnO surface. The H₂ generation enhanced with the increase of irradiation time. The amount of H₂ production is higher for heterostructures, L-Bi₂S₃/ZnO (~2791 μmol). For comparison, the H₂ evolution activity has been investigated for bare semiconductors L-Bi₂S₃ and M-Bi₂S₃ under visible light irradiation. The heterojunction shows 2.74 fold enhancement in hydrogen generation compare to L-Bi₂S₃ (~1020 μmol). The H₂ generation for M-Bi₂S₃ and M-Bi₂S₃/ZnO are ~263 μmol and ~2450 μmol respectively. In contrast to dye degradation, L-Bi₂S₃/ZnO shows superior performance for photocatalytic hydrogen generation in comparison to M-Bi₂S₃/ZnO. The exact reason is not clear to us but the enhanced catalytic activity may associated with the assembled morphology of L-Bi₂S₃/ZnO which leads to intimate contact between metal sulphide and zinc oxide NPs. The three dimensional interconnected assembled structure may also facilitate the transport of photogenerated electrons and holes to the binding sites thereby water oxidation occurred in presence of sacrificial agent which is consistent with literature report [64]. Moreover, both of the heterostructures may provide facile electron transfer compare to bare semiconductors which can effectively enhance the hydrogen generation [65].

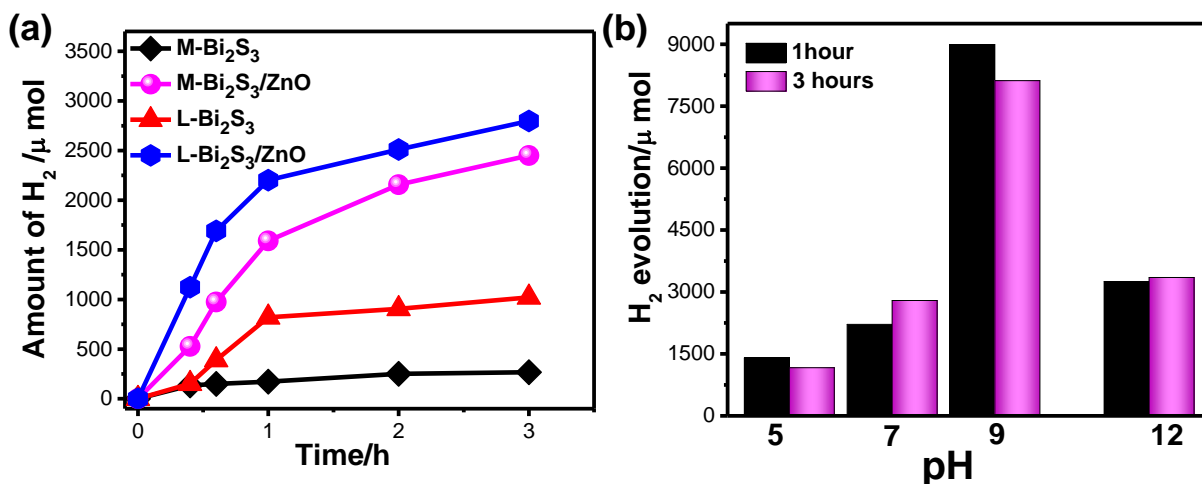


Figure 4.10 (a) Photocatalytic hydrogen generation in presence of catalyst L-Bi₂S₃, M-Bi₂S₃, L-Bi₂S₃/ZnO, M-Bi₂S₃/ZnO for 3h under visible light from an aqueous solution containing 25 volume % methanol at pH 7. (b) Effect of pH on hydrogen evolution from aqueous solution after 1h and 3h irradiation.

Further, the effect of pH on photocatalytic hydrogen evolution process has been studied to optimize the reaction condition. Figure 4.10b illustrates that higher activity for hydrogen evolution achieved at pH 9 ~8089 μmol whereas, at low pH condition i.e. acidic condition it generate only ~1159 μmol due to protonation of photocatalyst in acidic solution [65]. Generally in acidic condition the driving force for hydrogen generation decrease as the redox potential of H⁺/H₂ becomes more negative. On the other hand, high alkaline medium is also not preferable for hydrogen evolution because of insufficient protons [66]. In view of practical applications, reusability and stability of photocatalysts is an important parameter. Here, we checked recycling of M-Bi₂S₃/ZnO up to 5 successive cycles and result has been displayed in Figure 4.11a, which reveals nearly 10% loss in MO degradation. In hydrogen generation, recycling experiment of L-Bi₂S₃/ZnO has been performed up to 5th cycle displayed in Figure 4.11b. After 5th cycle, no remarkable decline was found in hydrogen evolution rate. Therefore, it can conclude that, M-Bi₂S₃/ZnO and L-Bi₂S₃/ZnO heterostructures are stable and reusable visible light active photocatalyst for organic pollutant degradation as well as hydrogen generation. To ensure about the structural stability and morphology of catalyst, XRD and FESEM were re-examined before and after catalytic reactions. As shown in Figure 4.11c, XRD pattern of ZnO decorated Bi₂S₃ heterostructures are almost remain same and all the characteristic peaks are present. The FESEM image of heterostructures reflects similar kind of morphology after photocatalytic reaction. Thus semiconductor based coupled

heterostructures is stable under long visible light irradiation and fruitful approach for solar light energy harvesting.

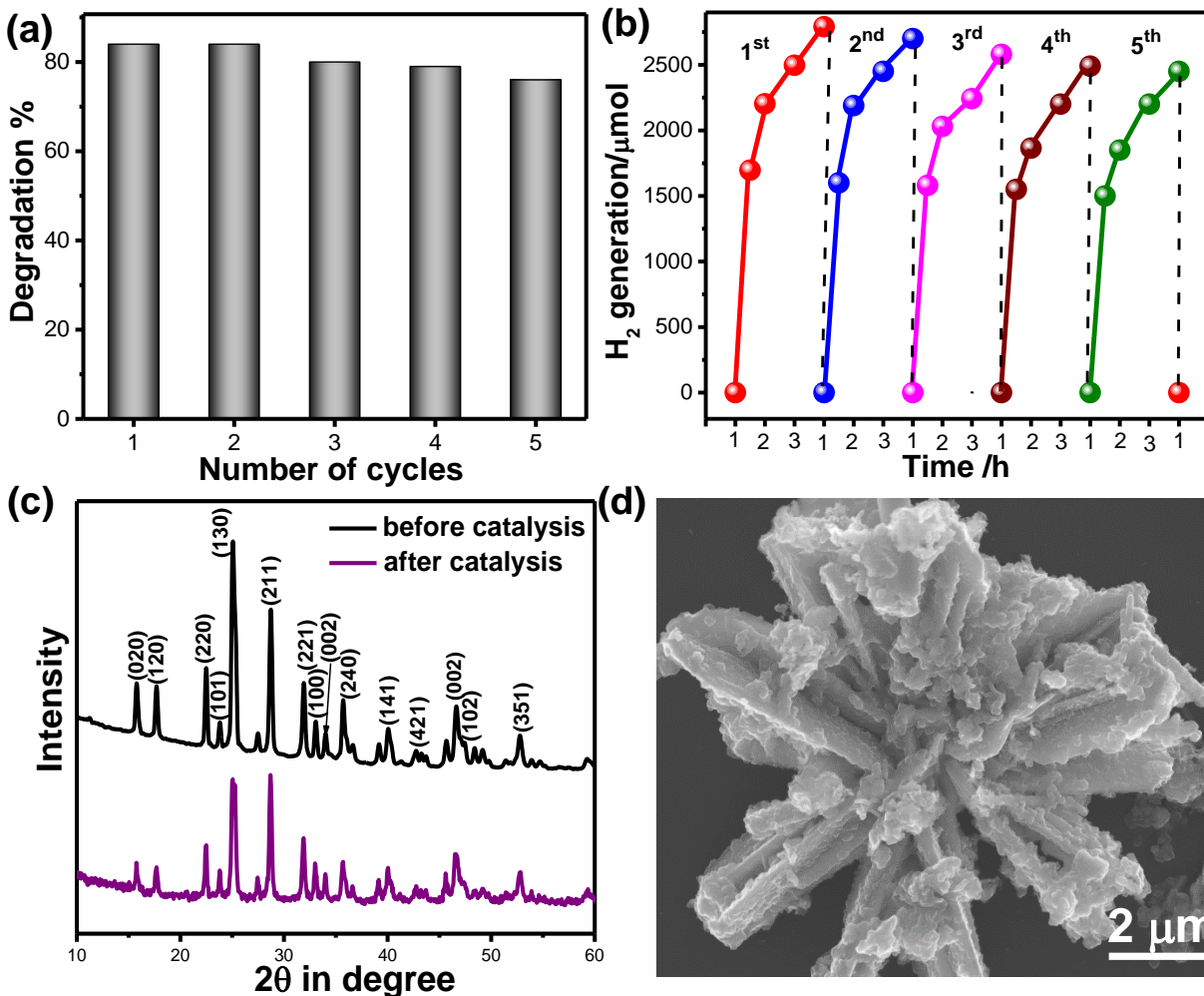


Figure 4.11 Recycling test of (a) M-Bi₂S₃/ZnO during MO degradation and (b) L-Bi₂S₃/ZnO during hydrogen generation. (c) The XRD pattern and (d) FESEM image of L-Bi₂S₃/ZnO after and before catalytic reaction of MO degradation and H₂ generation at pH 7.

4.3.9 Photoelectrochemical Performance

In order to investigate the photoelectrochemical activity of Bi₂S₃/ZnO heterostructures, it is important to find out the band edge potential of both Bi₂S₃ and ZnO as band edge potentials play a crucial role in determining the migration routes of photo generated electrons and holes. Additionally, photocatalytic activity directly depends on optical absorption, phase structure, morphology and separation efficiency of photo generated charge carriers. The valence band (VB) and conduction band (CB) of both the semiconductor had calculated following empirical equations [42].

$$E_{VB} = \chi - E_{fe} + \frac{1}{2}E_g \quad (4.11)$$

$$E_{CB} = \chi - E_{fe} - \frac{1}{2}E_g \quad (4.12)$$

Where, E_{VB} and E_{CB} are the valence and conduction band edge potential respectively, χ is the geometric mean of the electronegativity of constituent atoms. E_{fe} is the energy of electron in hydrogen scale (4.5 eV) and E_g is the bandgap of semiconductor. The VB and CB edge potentials of Bi_2S_3 calculated using above equations are 1.45 eV and 0.08 eV while for ZnO are 3 eV and -0.2 eV respectively [68]. This difference in band edge potential is useful for better charge separation and migration which is favourable for photoelectrochemical performance [68].

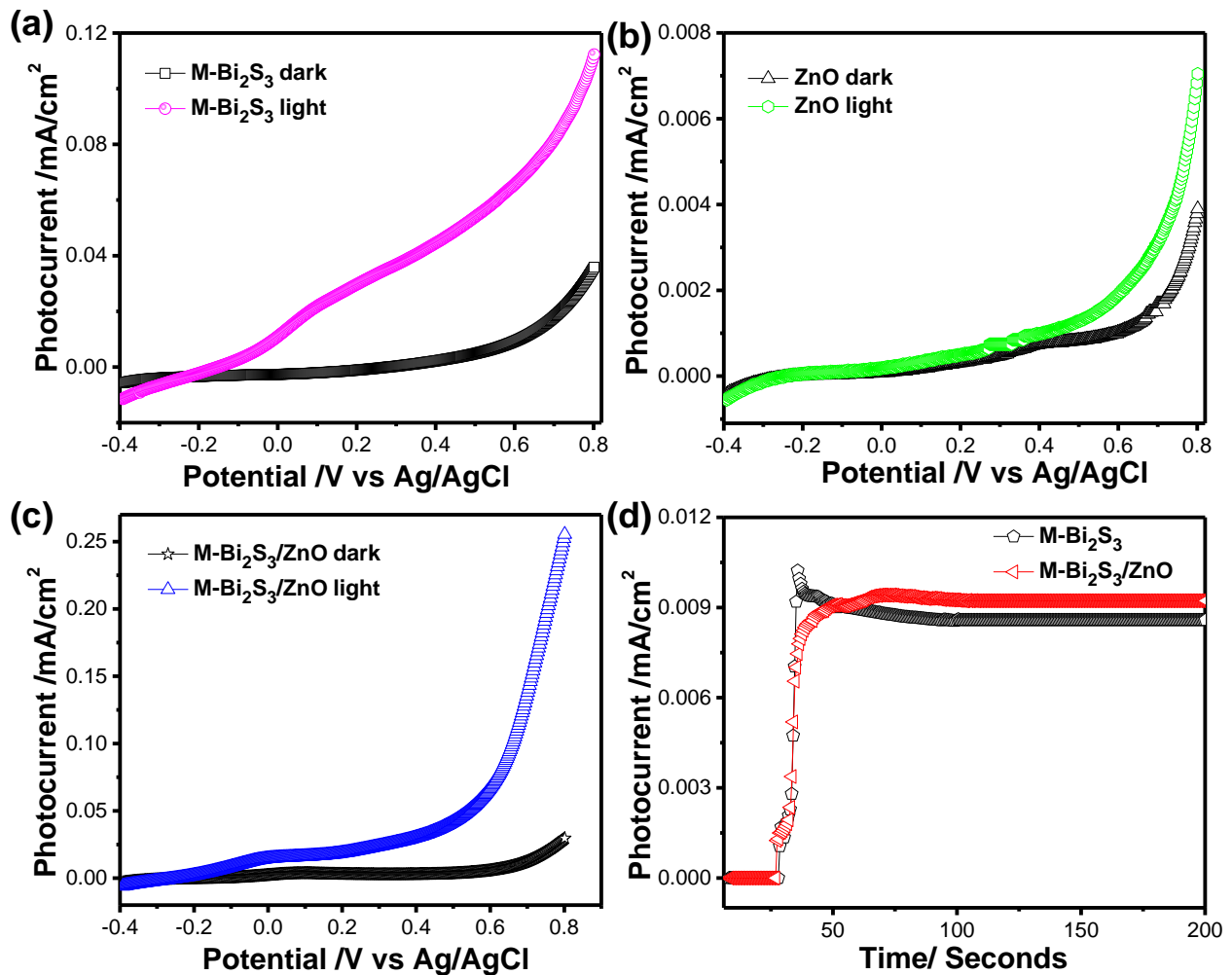


Figure 4.12 Photoelectrochemical current density vs potential plot of (a) M-Bi₂S₃, (b) ZnO (5 nm) and (c) M-Bi₂S₃/ZnO via LSV method without light (dark) and light illuminating condition at a scan rate 20 mV sec⁻¹ using 0.1 M KOH solution as electrolyte, Pt wire as counter electrode and Ag/AgCl as reference electrode and (d) time dependence of photocurrent density at external bias 0.26V vs Ag/AgCl with illumination, at scan rate 20 mV sec⁻¹ for bare M-Bi₂S₃ and heterojunction M-Bi₂S₃/ZnO.

The photoelectrochemical activity of catalyst has been examined by making a layer on the FTO coated glass substrate through linear sweep voltammetry (LSV) under dark and light condition with light irradiation. A 300 W Xenon lamp with a water filter of 1M NaNO₂ solution was used as the visible light (≥ 395 nm) source. Figure 4.12a–c shows the difference in photo current density measured *via* LSV of M-Bi₂S₃, ZnO and M-Bi₂S₃/ZnO catalyst in 0.1 M KOH solution using Pt wire as counter and Ag/AgCl as reference electrode at scan rate 20 mV sec⁻¹. The photoelectrochemical performance in terms of current density is presented in Table 1. Bi₂S₃ shows photocurrent response and photocurrent density reached up to 0.11 mA cm⁻² (Figure 4.12a). A weak photocurrent was obtained for bare ZnO upon illumination in the applied potential range as shown in Figure 4.12b. Whereas, Bi₂S₃/ZnO heterostructures demonstrated enhanced photocurrent density 0.25 mA cm⁻² which is 56% enhancement in comparison to bare ZnO NPs and Bi₂S₃. This result implies that heterostructures M-Bi₂S₃/ZnO shows higher photoelectrochemical activity and photo current gain which is ca. 3.05 times increased rather than single component M-Bi₂S₃. Notably, bare Bi₂S₃ also shows high photocurrent but due to fast recombination problem its photocurrent gain reduces. Thereby, introduction of ZnO with Bi₂S₃ enhances light absorption and charge separation efficiency.

Table 4.1 Comparative study of current density measured from photoelectrochemical studies performed in 0.1 M KOH solution as electrolyte, Pt wire as counter electrode and saturated Ag/AgCl as reference electrode within the voltage range -0.4V to 0.8V under dark and light condition.

| Catalyst | Dark Current (I_{dark}) mA/cm ² | Photo Current (I_{light}) mA/cm ² | Photo current gain $I_{\text{light}}/ I_{\text{dark}}$ |
|--|--|--|---|
| M-Bi₂S₃ | 0.039 | 0.112 | 2.88 |
| ZnO | 0.004 | 0.007 | 1.79 |
| M-Bi₂S₃/ZnO | 0.029 | 0.255 | 8.79 |

The stability of pure semiconductor as well as heterostructures was investigated by chronoamperometry method under light illumination for 200 seconds (Figure 4. 12d) [69]. In presence of light, a certain change in current density display for M-Bi₂S₃ whereas gradually increasing tendency exhibits for coupled system M-Bi₂S₃/ZnO because of charge transfer

mechanism [17]. As the photogenerated electrons migrate through the CB, more and more electrons are gathered at active surface site and gradually increases in current density. Remarkably, Figure 4.12d shows long time $i-t$ response (up to 600 sec) and current density remains almost stable which indicates catalyst are durable against photocorrosion. Hence, M-Bi₂S₃/ZnO shows enhance photoelectrochemical activity than bare Bi₂S₃ and ZnO. The photocurrent for Bi₂S₃ and heterostructures shows 7.39 and 8.06 fold enhancement in current density compare to dark condition at voltage 1.0 V respectively (Figure 4.13a and 13b). This enhancement in current density may happen for enhanced charge carrier separation in presence of light irradiation. The linear nature of $I-V$ plot indicates the good ohmic contact between the semiconductor and the ITO coated glass substrate which is a good sign for device application [69]. When light falls on the catalyst surface, excess photocarriers are generated which leads to charge separation and electrons are efficiently transfer to the electrode when voltage is applied [70]. The fluorescence decay curve at excitation wavelength 400 nm for ZnO and Bi₂S₃/ZnO have been examined to investigate the decay dynamics of heterostructures. It is observed that, the photocurrent is higher for heterostructures than single semiconductors. These charge carrier separation phenomena also enhance the mobility of electrons. The on/off photocurrent has been measured at 20 seconds interval at a bias voltage 500 mV (Figure 4. 13c), which exhibits two distinct state – one is high current state when light is on and another is low current state while light is off. This time dependent response of Bi₂S₃/ZnO coupled system is preferable for optoelectronic device applications. In the photocatalytic process, super oxide radicals and holes have crucial role in organic dye degradation which has been previously confirmed by lots of tested. Hence, the photo-excited electron and holes are responsible to generate these free radicals. Furthermore, the enhanced charge separation further studied *via* picosecond resolved time correlated single Figure 4. 13d shows decay curve of ZnO with average life time 4.34 ns. Interestingly, it decreases to 0.338 ns when Bi₂S₃ is attached with ZnO. From this sharp decrease in average life time, it can be concluded that fast electron transfer happen within the heterostructures through the CB of ZnO to Bi₂S₃ [17]. This charge transfer reduce the recombination rate which also understand by PL study, confirms more electrons may participate for photocatalytic water splitting and H₂ generation.

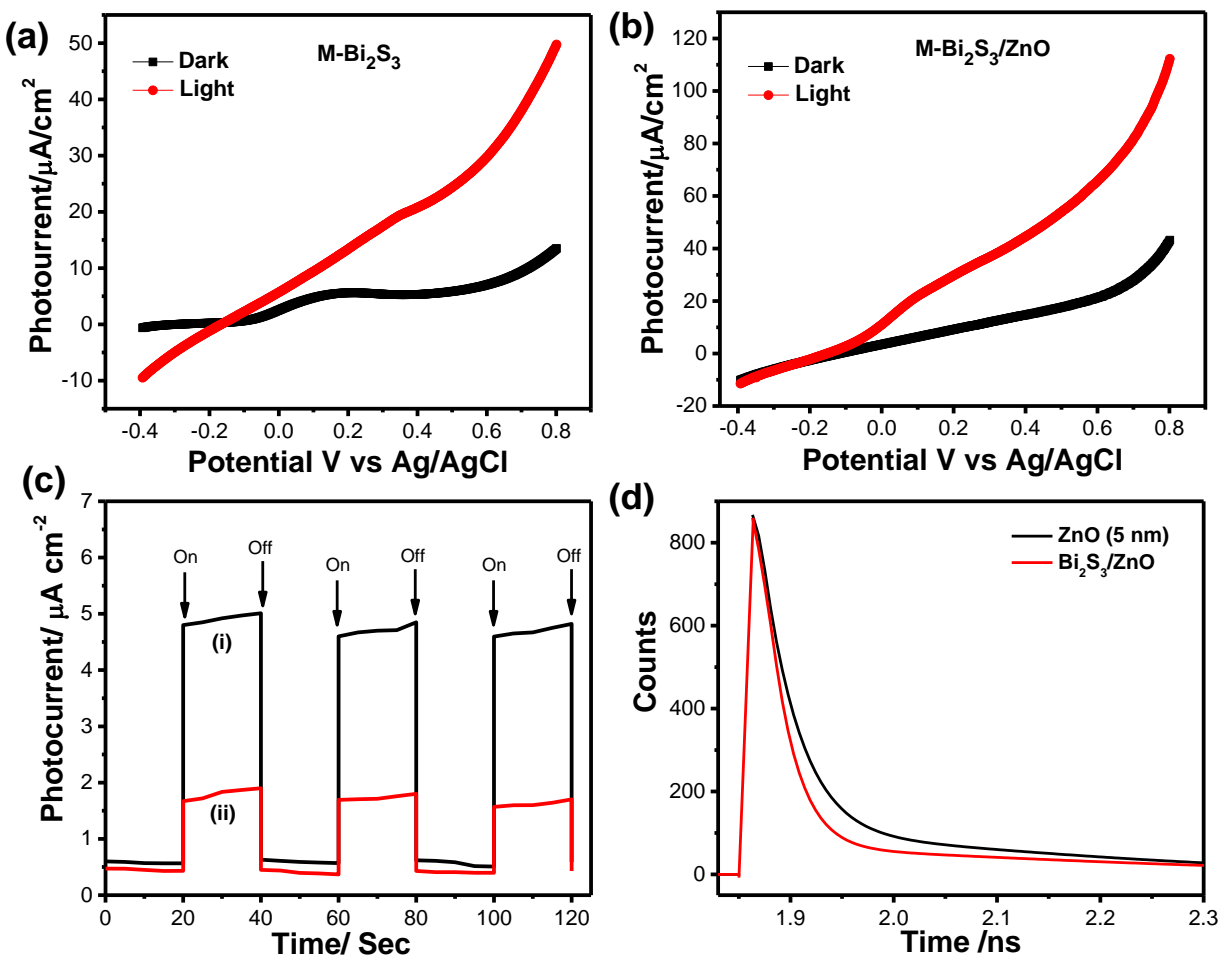


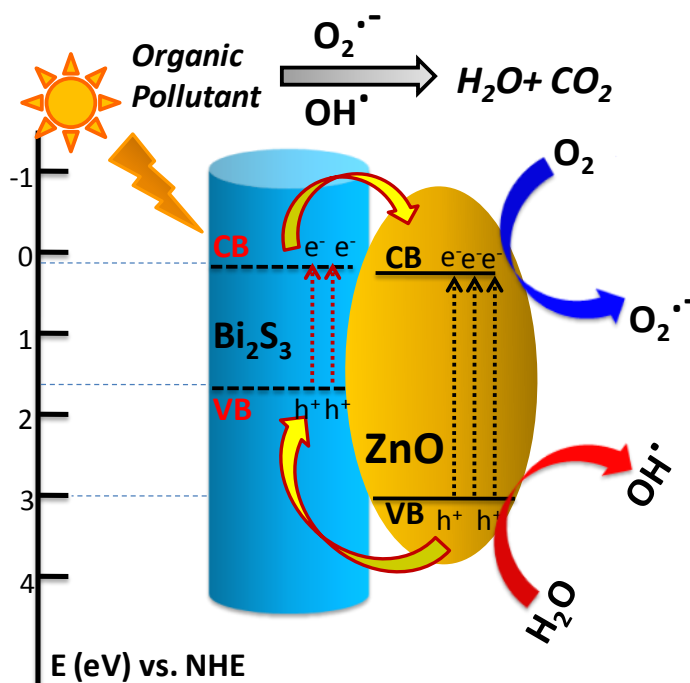
Figure 4.13. (a) Comparative time dependent photocurrent density response of the (i) heterostructures M-Bi₂S₃/ZnO and (ii) pure M-Bi₂S₃ with illumination (switched on) and off in air at a bias of 500 mV and (b) the picosecond-resolved PL spectra of ZnO (5 nm), M-Bi₂S₃ and M-Bi₂S₃/ZnO heterostructures.

Table 4.2 Dynamics of picosecond-resolved luminescence transients and decay parameters of ZnO (5 nm) and Bi₂S₃/ZnO.

| Sample | Excitation Wavelength (nm) | Detection Wavelength (nm) | τ_1 (ns) | τ_2 (ns) | τ_{avg} (ns) |
|-------------------------------------|----------------------------|---------------------------|---------------|---------------|-------------------|
| ZnO NPs | 400 | 500 | 0.82 (51.8%) | 29.30 (7.5%) | 4.42 |
| Bi ₂ S ₃ /ZnO | 400 | 500 | 0.25 (42.0%) | 5.02 (7.9%) | 0.338 |

4.3.10 Mechanism

Depending on the above results and discussion, a probable mechanism of photocatalytic activity can be described as follows. In presence of solar light, both of semiconductors absorb light and the electrons in VB gets excited up to higher potential of -1.53 eV for Bi_2S_3 and -0.2 eV for ZnO [55]. Therefore, effective charge transfer process proceeds within the semiconductor due to high photon energy [42]. Generally the excited electrons and holes always wish to transfer to the nearest recombination centre. The CB electrons of Bi_2S_3 rods can transfer to the CB of ZnO NPs and simultaneously the excited holes of ZnO can migrate to Bi_2S_3 rods and consequently reduce the first recombination process shown in schematic diagram 4.3.



Scheme 4.3 Proposed diagram for the possible band edge energy for charge separation and migration in the $\text{Bi}_2\text{S}_3/\text{ZnO}$ heterostructures.

These photo generated electrons and holes generate oxidative radicals (in presence of O_2) such as h^+ , OH^\bullet , $\text{O}_2^{\bullet-}$ by oxidation of O_2 and reduction of H_2O which are mainly responsible for dye degradation. In hydrogen evolution, sacrificial agent methanol acts as hole scavenger and generate more OH^\bullet free radicals and accelerate the H_2 production rate. As the band position of Bi_2S_3 is not suitable for H_2 production, so it can be concluded that, photochemical reactions occur at the ZnO surface and incorporation of narrow bandgap semiconductor helps in charge separation, leading more efficient activity in H_2 generation [69-71]. On the other hand, the visible light activity can

be explained on the basis of hole trapping mechanism which has explained in scheme diagram. Therefore, semiconductor heterojunction is suitable route in creating more recombination centre and thus increase the life time of electrons as well as reduce recombination rate.

4.4 Summary

In summary, assembled nanoflower morphology of Bi_2S_3 decorated with ZnO nanoparticles has been successfully synthesized by facile in situ deposition method. The strong absorption of $\text{Bi}_2\text{S}_3/\text{ZnO}$ heterostructures in visible region and enhanced charge separation in heterostructures makes them promising candidate for solar light harvesting applications. Experimental results indicate that M- $\text{Bi}_2\text{S}_3/\text{ZnO}$ demonstrate high catalytic activity for organic pollutant degradation whereas L- $\text{Bi}_2\text{S}_3/\text{ZnO}$ shows superior performance for photocatalytic H_2 generation through water splitting. The photocatalytic activity of heterostructures is ~ 8.6 times higher compared to bare Bi_2S_3 . The heterostructures L- $\text{Bi}_2\text{S}_3/\text{ZnO}$ ($\sim 2791 \mu\text{mol}$) illustrates 2.74 fold enhancements in photocatalytic hydrogen generation compare to L- Bi_2S_3 ($\sim 1020 \mu\text{mol}$) under visible light. Notably, $\text{Bi}_2\text{S}_3/\text{ZnO}$ demonstrate high photoelectrochemical activity with the photo current density is 0.25 mA cm^{-2} , which is 56% and 97 % higher than bare M- Bi_2S_3 and ZnO respectively under similar reaction condition. The band edge potential of heterostructures is suitable for sufficient charge separation which causes enhancement in photo current. Hence, the present synthetic methodology can be employed to prepare efficient, low cost heterostructure based photocatalysts to substitute the common use of noble metal based catalysts and $\text{Bi}_2\text{S}_3/\text{ZnO}$ has potential in environmental remedy and water splitting applications.

References

- [1] M. R. Hoffmann, S. T. Martin, W. Choi, D. W. Bahnemann, Environmental Applications of Semiconductor Photocatalysis. *Chem. Rev.* **95** (1995) 69–96.
- [2] T. Jafari, E. Moharreri, A. S. Amin, R. Miao, W. Song, S. L. Suib, Photocatalytic Water Splitting—The Untamed Dream: A Review of Recent Advances. *Molecules* **21** (2016) 900–929.
- [3] Z. G. Zou, J. H. Ye, K. Sayama, H. Arakawa, Direct splitting of water under visible light irradiation with an oxide semiconductor photocatalyst. *Nature* **414** (2001) 625–627.
- [4] D. J. Martin, K. Qiu, S. A. Shevlin, A. D. Handoko, X. Chen, Z. Guo, J. Tang, Highly Efficient Photocatalytic H₂ Evolution from Water using Visible Light and Structure-Controlled Graphitic Carbon Nitride. *Angew. Chem., Int. Ed.* **53** (2014) 9240–9245.
- [5] A. Kudo, Y. Miseki, Heterogeneous photocatalyst materials for water splitting. *Chem. Soc. Rev.* **38** (2009) 253–278.
- [6] S. Ghosh, N. A. Kouame, S. Remita, L. Ramos, F. Goubard, P.-H. Aubert, A. Dazzi, A. Deniset-Besseau, H. Remita, Visible-light active conducting polymer nanostructures with superior photocatalytic activity. *Sci. Rep.* **5** (2015) 18002–18011.
- [7] T. Hisatomi, J. Kubota, K. Domen, Recent advances in semiconductors for photocatalytic and photoelectrochemical water splitting. *Chem. Soc. Rev.* **43** (2014) 7520–7535.
- [8] Y. H. Ng, A. Iwase, A. Kudo, R. Amal, Reducing Graphene Oxide on a Visible-Light BiVO₄ Photocatalyst for an Enhanced Photoelectrochemical Water Splitting. *J. Phys. Chem. Lett.* **1** (2010) 2607–2612.
- [9] H. Wang, L. Zhang, Z. Chen, J. Hu, S. Li, Z. Wang, J. Liu, Semiconductor heterojunction photocatalysts: design, construction, and photocatalytic performances. *Chem. Soc. Rev.* **43** (2014) 5234–5244.
- [10] A. Fujishima, K. Honda, Electrochemical Photolysis of Water at a Semiconductor Electrode. *Nature* **238** (1972) 37–38.
- [11] J. Tian, Z. Zhao, A. Kumar, R. I. Boughton, H. Liu, Recent progress in design, synthesis, and applications of one-dimensional TiO₂ nanostructured surface heterostructures: a review. *Chem. Soc. Rev.* **43** (2014) 6920–6937.
- [12] L. Xu, G. A. Sewvandi, S. Uemura, T. Kusunose, S. Nakanishia, Q. Feng, Facile size-controllable synthesis process, bandgap blue shift, and enhanced photocatalytic

- performances of [111]-faceted anatase TiO₂ nanocrystals. *New J. Chem.* **41** (2017) 10998–11008.
- [13] G. Wang, H. Wang, Y. Ling, Y. Tang, X. Yang, R. C. Fitzmorris, C. Wang, J. Z. Zhang, Y. Li, Hydrogen-Treated TiO₂ Nanowire Arrays for Photoelectrochemical Water Splitting. *Nano Lett.* **11** (2011) 3026–3033.
- [14] J. Virkutyte, R. S. Varma, Fabrication and visible light photocatalytic activity of a novel Ag/TiO_{2-x}N_x nanocatalyst. *New J. Chem.* **34** (2010) 1094–1096.
- [15] M. D. Hernandez-Alonso, F. Fresno, S. Suarez, J. M. Coronado, Development of alternative photocatalysts to TiO₂: Challenges and opportunities. *Energy Environ. Sci.* **2** (2009) 1231–1257.
- [16] S. Piskunov, O. Lisovski, J. Begens, D. Bocharov, Y. F. Zhukovskii, M. Wessel and E. Spohr, C-, N-, S-, and Fe-Doped TiO₂ and SrTiO₃ Nanotubes for Visible-Light-Driven Photocatalytic Water Splitting: Prediction from First Principles. *J. Phys. Chem. C* **119** (2015) 18686–18696.
- [17] S. Sardar, P. Kar, H. Remita, B. Liu, P. Lemmens, S. K. Pal, S. Ghosh, Enhanced Charge Separation and FRET at Heterojunctions between Semiconductor Nanoparticles and Conducting Polymer Nanofibers for Efficient Solar Light Harvesting. *Sci. Rep.* **5** (2015) 17313–17327.
- [18] J. Dutta, M. A. Mahmood, S. Baruah, Mater. Enhanced visible light photocatalysis by manganese doping or rapid crystallization with ZnO nanoparticles. *Chem. and Phys.* **130** (2011) 531–535.
- [19] Q. Shen, X. Zhao, S. Zhou, W. Hou, J.-J. Zhu, ZnO/CdS Hierarchical Nanospheres for Photoelectrochemical Sensing of Cu²⁺. *J. Phys. Chem. C* **115** (2011) 17958–17964.
- [20] K. M. Lee, C. W. Lai, K. S. Ngai, J. C. Juan, Recent developments of zinc oxide based photocatalyst in water treatment technology: A review. *Water Res.* **88** (2016) 428–448.
- [21] L. Zhang, L. Du, X. Yu, S. Tan, X. Cai, P. Yang, Y. Gu, W. Mai, Significantly Enhanced Photocatalytic Activities and Charge Separation Mechanism of Pd-Decorated ZnO–Graphene Oxide Nanocomposites. *ACS Appl. Mater. Interfaces* **6** (2014) 3623–3629.
- [22] G. Marci, V. Augugliaro, M. J. López-Muñoz, C. Martin, L. Palmisano, V. Rives, M. Schiavello, R. J. D. Tilley, A. M. Venezia, Preparation Characterization and Photocatalytic Activity of Polycrystalline ZnO/TiO₂ Systems. 1. Surface and Bulk Characterization. *J.*

- Phys. Chem. B* **105** (2001) 1026–1032.
- [23] R. Brahim, Y. Bessekhoud, A. Bouguelia, M. Trari, Visible light induced hydrogen evolution over the heterosystem Bi₂S₃/TiO₂. *Catal. Today* **122** (2007) 62–65.
- [24] S. Boumaza, B. Bellal, A. Boudjemaa, M. Trari, Photodegradation of orange G by the hetero-junction x% Bi₂S₃/TiO₂ under solar light. *Solar Energy* **139** (2016) 444–451.
- [25] N. Qin, Y. Liu, W. Wu, L. Shen, X. Chen, Z. Li, L. Wu, One-Dimensional CdS/TiO₂ Nanofiber Composites as Efficient Visible-Light-Driven Photocatalysts for Selective Organic Transformation: Synthesis, Characterization, and Performance. *Langmuir* **31** (2015) 1203–1209.
- [26] S. J. Jum, G. K. Hyun, A. J. Upendra, W. J. Ji, S. L. Jae, Fabrication of CdS nanowires decorated with TiO₂ nanoparticles for photocatalytic hydrogen production under visible light irradiation. *Int. J. Hydrogen Energy* **33** (2008) 5975–5980.
- [27] S. K. Dutta, S. K. Mehetor, N. Pradhan, Metal Semiconductor Heterostructures for Photocatalytic Conversion of Light Energy. *J. Phys. Chem. Lett.* **6** (2015) 936–944.
- [28] X. Li, J. Yu, M. Jaroniec, Hierarchical photocatalysts. *Chem. Soc. Rev.* **45** (2016) 2603–2636.
- [29] J. Zhang, G. Xiao, F.-X. Xiao, B. Liu, Revisiting one-dimensional TiO₂ based hybrid heterostructures for heterogeneous photocatalysis: a critical review. *Mater. Chem. Front.* **1** (2017) 231–250.
- [30] L. Jing, J. Zhou, J. R. Durrant, J. Tang, D. Liu, Dynamics of photogenerated charges in the phosphate modified TiO₂ and the enhanced activity for photoelectrochemical water splitting. *Energy Environ. Sci.* **5** (2012) 6552–6558.
- [31] C. Sotelo-Vazquez, R. Quesada-Cabrera, M. Ling, D. O. Scanlon, A. Kafizas, P. K. Thakur, T.-L. Lee, A. Taylor, G. W. Watson, R. G. Palgrave, J. R. Durrant, C. S. Blackman, I. P. Parkin, Evidence and Effect of Photogenerated Charge Transfer for Enhanced Photocatalysis in WO₃/TiO₂ Heterojunction Films: A Computational and Experimental Study. *Adv. Funct. Mater.* **27** (2017) 1605413–1605423.
- [32] S. J. A. Moniz, S. A. Shevlin, X. An, Z.-X. Guo, J. Tang, Fe₂O₃-TiO₂ Nanocomposites for Enhanced Charge Separation and Photocatalytic Activity. *Chem. - A Eur. J.* **20** (2014) 15571–15579.
- [33] M. Xie, X. Fu, L. Jing, P. Luan, Y. Feng, H. Fu, Long-Lived, Visible-Light-Excited Charge

- Carriers of TiO₂/BiVO₄ Nanocomposites and their Unexpected Photoactivity for Water Splitting. *Adv. Energy Mater.* **4** (2013) 1300995–1301001.
- [34] F.-X. Xiao, onstruction of Highly Ordered ZnO–TiO₂ Nanotube Arrays (ZnO/TNTs) Heterostructure for Photocatalytic Application. *ACS Appl. Mater. Interfaces* **4** (2012) 7055–7063.
- [35] C. Eley, T. Li, F. Liao, S. M. Fairclough, J. M. Smith, G. Smith, S. C. E. Tsang, Nanojunction-Mediated Photocatalytic Enhancement in Heterostructured CdS/ZnO, CdSe/ZnO, and CdTe/ZnO Nanocrystals. *Angew. Chem. Int. Ed.* **53** (2014) 7838–7842.
- [36] A. Abdi, A. Denoyelle, N. Commenges-Bernole, M. Trari, Photocatalytic hydrogen evolution on new mesoporous material Bi₂S₃/Y-zeolite. *Int. J. Hydrogen Energy* **38** (2013) 2070–2078.
- [37] L. X. Hao, G. Chen, Y. G. Yu, Y. S. Zhou, Z. H. Han, Y. Liu, Sonochemistry synthesis of Bi₂S₃/CdS heterostructure with enhanced performance for photocatalytic hydrogen evolution. *Int. J. Hydrogen Energy* **39** (2014) 14479–14486.
- [38] F. Dong, Z. Ni, P. Li, Z. Wu, A general method for type I and type II g-C₃N₄/g-C₃N₄ metal-free isotype heterostructures with enhanced visible light photocatalysis. *New J. Chem.* **39** (2015) 4737–4744.
- [39] Q.-Z. Huang, Y. Xiong, Q. Zhang, H.-C. Yao, Z.-J. Li, Noble metal-free MoS₂ modified Mn_{0.25}Cd_{0.75}S for highly efficient visible-light driven photocatalytic H₂ evolution. *Appl. Catal. B: Environ.* **209** (2017) 514–522.
- [40] H. He, S. P. Berglund, P. Xiao, W. D. Chemelewski, Y. Zhang, C. B. Mullins, Nanostructured Bi₂S₃/WO₃ heterojunction films exhibiting enhanced photoelectrochemical performance. *J. Mater. Chem. A* **1** (2013) 12826–12834.
- [41] M. Li, J. Wang, P. Zhang, Q. Deng, J. Zhang, K. Jiang, Z. Hu, J. Chu, Superior adsorption and photoinduced carries transfer behaviors of dandelion-shaped Bi₂S₃@MoS₂: experiments and theory. *Sci. Rep.* **7** (2017) 42484–42492.
- [42] R. P. Panmand, Y. A. Sethi, R. S. Deokar, D. J. Late, H. M. Gholap, J.-O. Baeg, B. B. Kale, In situ fabrication of highly crystalline CdS decorated Bi₂S₃ nanowires (nano-heterostructure) for visible light photocatalyst application. *RSC Adv.* **6** (2016) 23508–23517.
- [43] C. Zhang, Y. Zhou, Y. Zhang, S. Zhao, J. Fang, X. Sheng, In situ doping of Pt active sites via Sn in double-shelled TiO₂ hollow nanospheres with enhanced photocatalytic H₂

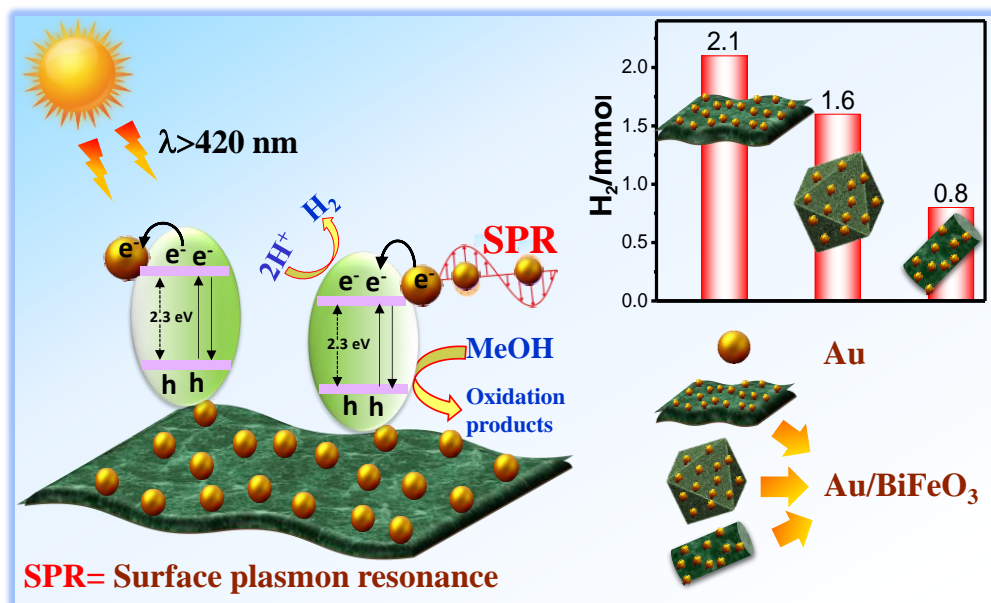
- production efficiency. *New J. Chem.* **41** (2017) 11089–11096.
- [44] J. Zhou, G. Tian, Y. Chen, Y. Shi, C. Tian, K. Pan, H. Fu, Growth rate controlled synthesis of hierarchical Bi₂S₃/In₂S₃ core/shell microspheres with enhanced photocatalytic activity. *Sci. Rep.* **4** (2014) 4027–4035.
- [45] X. Gao, H. B. Wu, L. Zheng, Y. Zhong, Y. Hu, X. W. Lou, Formation of mesoporous heterostructured BiVO₄/Bi₂S₃ hollow discoids with enhanced photoactivity. *Angew. Chem. Int. Ed.* **53** (2014) 5917–5921.
- [46] F. Dong, X. Feng, Y. Zhang, C. Gao, Z. Wu, An anion-exchange strategy for 3D hierarchical (BiO)₂CO₃/amorphous Bi₂S₃ heterostructures with increased solar absorption and enhanced visible light photocatalysis. *RSC Adv.* **5** (2015) 11714–11723.
- [47] D. Lu, H. Wang, X. Zhao, K. K. Kondamareddy, J. Ding, C. Li, P. Fang, Highly Efficient Visible-Light-Induced Photoactivity of Z-Scheme g-C₃N₄/Ag/MoS₂ Ternary Photocatalysts for Organic Pollutant Degradation and Production of Hydrogen. *ACS Sus. Chem. Eng.* **5** (2017) 1436–1445.
- [48] S. S. Thind, C. C. Mustapic, J. Wen, C. D. Goodwin, A. Chen, Facile synthesis of mesoporous carbon nitride and titanium dioxide nanocomposites with enhanced visible light photocatalytic activity. *New J. Chem.* **41** (2017) 10542–10549.
- [49] Q. Liu, J. Huan, N. Hao, J. Qian, H. Mao, K. Wang, Engineering of Heterojunction-Mediated Biointerface for Photoelectrochemical Aptasensing: Case of Direct Z-Scheme CdTe-Bi₂S₃ Heterojunction with Improved Visible-Light-Driven Photoelectrical Conversion Efficiency. *ACS Appl. Mater. Interfaces* **9** (2017) 18369–18376.
- [50] H. Bao, X. Cui, C. M. Li, Y. Gan, J. Zhang, J. Guo, Sonochemical Method for the Preparation of Bismuth Sulfide Nanorods. *J. Phys. Chem. C* **111** (2007) 12279–12283.
- [51] M. G. Mendez-Medrano, E. Kowalska, A. Lehoux, A. Herissan, B. Ohtani, S. Rau, C. Colbeau-Justin, J. L. Rodriguez-Lopez, H. Remita, Surface Modification of TiO₂ with Au Nanoclusters for Efficient Water Treatment and Hydrogen Generation under Visible Light. *J. Phys. Chem. C* **120** (2016) 25010–25022.
- [52] B. Li, Y. Zhang, R. Du, L. Gan, X. Yu, Synthesis of Bi₂S₃-Au Dumbbell Heteronanostructures with Enhanced Photocatalytic and Photoresponse Properties. *Langmuir* **32** (2016) 11639–11645.
- [53] S. Hernández, V. Cauda, A. Chiodoni, S. Dallorto, A. Sacco, D. Hidalgo, E. Celasco, C. F.

- Pirri, Optimization of 1D ZnO@TiO₂ Core–Shell Nanostructures for Enhanced Photoelectrochemical Water Splitting under Solar Light Illumination. *ACS Appl. Mater. Interfaces* **6** (2014) 12153–12167.
- [54] Y. Wang, J. Chen, P. Wang, L. Chen, Y.-B. Chen, L.-M. Wu, Syntheses, Growth Mechanism, and Optical Properties of [001] Growing Bi₂S₃ Nanorods. *J. Phys. Chem. C* **113** (2009) 16009–16014.
- [55] S. Khanchandani, S. Kundu, A. Patra, A. K. Ganguli, Bandgap Tuning of ZnO/In₂S₃ Core/Shell Nanorod Arrays for Enhanced Visible-Light-Driven Photocatalysis. *J. Phys. Chem. C* **117** (2013) 5558–5567.
- [56] J. Zhang, L. Zhang, N. Yu, K. Xu, S. Li, H. Wang, J. Liu, Flower-like Bi₂S₃/Bi₂MoO₆ heterojunction superstructures with enhanced visible-light-driven photocatalytic activity. *RSC Adv.* **5** (2015) 75081–75088.
- [57] A. Priyam, S. Ghosh, S. C. Bhattacharya, A. Saha, Supersaturation driven tailoring of photoluminescence efficiency and size distribution: A simplified aqueous approach for producing high-quality, biocompatible quantum dots. *J. Colloid Interface Sci.* **331** (2009) 195–201.
- [58] S. Ghosh, A. Priyam, S. C. Bhattacharya, A. Saha, Mechanistic Aspects of Quantum Dot Based Probing of Cu (II) Ions: Role of Dendrimer in Sensor Efficiency. *J. Fluoresc.* **19** (2009) 723–731.
- [59] S. Ghosh, M. Ray, M. Das, A. Chakrabarti, A. H. Khan, D. D. Sarma, S. Acharya, Modulation of glyceraldehyde-3-phosphate dehydrogenase activity by surface functionalized quantum dots. *Phys. Chem. Chem. Phys.* **16** (2014) 5276–5283.
- [60] M. Han, J. Jia, 3D Bi₂S₃/TiO₂ cross-linked heterostructure: An efficient strategy to improve charge transport and separation for high photoelectrochemical performance. *J. Power Sources* **329** (2016) 23–30.
- [61] X. Zhang, J. Qin, Y. Xue, P. Yu, B. Zhang, L. Wang, R. Liu, Effect of aspect ratio and surface defects on the photocatalytic activity of ZnO nanorods. *Sci. Rep.* **4** (2014) 4596–4604.
- [62] S. Ghosh, N. A. Kouame, L. Ramos, S. Remita, A. Dazzi, A. Deniset-Besseau, P. Beaunier, F. Goubard, P.-H. Aubert, H. Remita, Conducting polymer nanostructures for photocatalysis under visible light. *Nat. Mater.* **14** (2015) 505–511.

- [63] W. Cui, J. Li, F. Dong, Y. Sun, G. Jiang, W. Cen, S. C. Lee, Z. Wu, Highly Efficient Performance and Conversion Pathway of Photocatalytic NO Oxidation on SrO-Clusters@Amorphous Carbon Nitride. *Environ. Sci. Technol.* **51** (2017) 10682–10690.
- [64] J. Sun, J. Zhang, M. Zhang, M. Antonietti, X. Fu, X. Wang, Bioinspired hollow semiconductor nanospheres as photosynthetic nanoparticles. *Nat. Commun.* **3** (2012) 1139–1146.
- [65] S. Luo, F. Chai, L. Zhang, C. Wang, L. Li, X. Liu, Z. Su, Facile and fast synthesis of urchin-shaped $\text{Fe}_3\text{O}_4@ \text{Bi}_2\text{S}_3$ core-shell hierarchical structures and their magnetically recyclable photocatalytic activity. *J. Mater. Chem.* **22** (2012) 4832–4836.
- [66] F. Ozel, E. Aslan, B. Istanbulu, O. Akay, I. H. Patir, Photocatalytic hydrogen evolution based on $\text{Cu}_2\text{ZnSnS}_4$, $\text{Cu}_2\text{NiSnS}_4$ and $\text{Cu}_2\text{CoSnS}_4$ nanocrystals. *Applied Catal. B* **198** (2016) 67–73.
- [67] B. Tian, Y. Wu, Enhancing photoactivity for hydrogen generation by electron tunneling via flip-flop hopping over iodinated graphitic carbon nitride. *Applied Catal. B* **204** (2017) 33–42.
- [68] C. Liu, Y. Yang, W. Li, J. Li, Y. Li, Q. Chen, In situ synthesis of Bi_2S_3 sensitized WO_3 nanoplate arrays with less interfacial defects and enhanced photoelectrochemical performance. *Sci. Rep.* **6** (2016) 23451–23463.
- [69] J. Kundu, S. Khilari, D. Pradhan, Shape-Dependent Photocatalytic Activity of Hydrothermally Synthesized Cadmium Sulfide Nanostructures. *ACS Appl. Mater. Interfaces* **9** (2017) 9669–9680.
- [70] X. Zhang, Y. Liu, G. Zhang, Y. Wang, H. Zhang, F. Huang, Thermal Decomposition of Bismuth Oxysulfide from Photoelectric $\text{Bi}_2\text{O}_2\text{S}$ to Superconducting $\text{Bi}_4\text{O}_4\text{S}_3$. *ACS Appl. Mater. Interfaces* **7** (2015) 4442–4448.
- [71] Y.-Q. Zhang, S. Li, B.-P. Zhang, Controllable synthesis of $\text{Bi}_2\text{S}_3/\text{CuS}$ heterostructures by an in situ ion-exchange solvothermal process and their enhanced photocatalytic performance. *RSC Adv.* **6** (2016) 103215–103223.

CHAPTER 5

Photocatalytic Hydrogen Generation using Gold Decorated BiFeO₃ Heterostructures as an Efficient Catalyst under Visible Light Irradiation



5.1 Introduction

The concept of solar hydrogen generation by water splitting using photocatalysts has received significant attention as it is an eco-friendly and sustainable method [1-3]. In this regard, semiconductor based photocatalysis has been extensively investigated for potential applications in environmental remediation and water splitting [3, 4]. During the past few decades, tremendous efforts have been devoted to develop efficient, low-cost and stable photocatalysts under visible light for removal of environmental pollutants, photocatalytic and photoelectrochemical hydrogen generation through water splitting [4-7]. Among a large number of photocatalysts, perovskite oxides based semiconductors have drawn much interest because of their structural simplicity and flexibility, good stability and relatively narrow bandgaps of these materials allow them to harness the visible light of solar irradiation [8, 9]. Among these perovskite materials, bismuth ferrate (BiFeO_3 , BFO) is a potential multiferroic semiconductor in which ferroelectric and antiferromagnetic properties coexist at room temperature which generates internal electric field by switching the spontaneous polarization and applications focused on spintronics and memory devices [10, 11]. The low bandgap (~ 2.3 eV) with direct transition feature, suitable band alignment to oxidize or reduce water, good chemical stability, low cost and biocompatibility of BFO make it attractive for practical use in visible light induced photocatalysis. Moreover, Yang et al. [12] discovered a giant open-circuit photovoltage for ferroelectric semiconductors which enhances the charge separation efficiency of ferroelectric semiconductors compared to other conventional semiconductors. Inspired by this concept, it has been assumed that spontaneous polarization due to ferroelectricity of BFO could be an effective approach to harness solar energy in water splitting.

Recently, multidimensional BFO nanostructures have been fabricated to control the exposed facets, size and growth directions as these have significant effect in determining the electrical, magnetic, and optical properties [13]. For example, Fei et al. [14] prepared three different microstructures of BiFeO_3 where pills and rods showed an enhanced visible light response due to presence of {111} facets but catalytic application has not been performed yet. Further, Bui et al. [15] reported size dependent (30 nm to 190 nm) photocatalytic activity of BiFeO_3 NPs for organic dye (methyl orange, MO) degradation but efficiency was very low. Wang et al. [16] also prepared spindles, cubes and plates like morphology of BiFeO_3 where plates like morphology showed maximum efficiency (50%) in photocatalytic MO degradation. Therefore, to improve the photocatalytic activity of BFO, it has been coupled with other co-catalysts, such as SrTiO_3 ,

$\text{Bi}_2\text{Fe}_4\text{O}_9$, TiO_2 , CuS , $\text{g-C}_3\text{N}_4$ and reduced graphene oxide to develop heterostructured materials [17-20]. Generally, heterojunction is the interface between two different materials with unequal band structures resulting a band alignments which in turn creates a space-charge region at the interface and forms an electric field causes the diffusion of charge carriers [21]. As a result, spatial charge separation occurs at the interface which can promote the photocatalytic activity of the heterostructured materials [22-25]. More interestingly, charge carrier recombination may be suppressed in a heterostructures as the excited carriers can transfer to the nearest electronic state. For example, Zhang et al. [18] prepared $\text{BiFeO}_3/\text{Bi}_2\text{Fe}_4\text{O}_9$ heterojunction by an electrospinning technique where heterojunction showed enhanced photocatalytic activity compare to the single components due to fast charge transfer and lower recombination, although the kinetics of the catalytic reaction is very slow. Li et al. [20] reported that, heterojunction of BiFeO_3 with graphene effectively reduce the size of the BiFeO_3 particles which effectively enhance the photocatalytic activity due to increase specific surface area but the stability of the composite in air and multistep synthesis using strong oxidizing agent remains an issue. Upto now, these heterostructures based photocatalysts have been used mostly for organic pollutant degradation under visible light but clean solar fuel generation are still limited yet.

On the other hand, integration of noble metal NPs to semiconductor photocatalysts can offer an effective way to improve their photocatalytic activities under visible region. In fact, noble metal NPs (Au, Ag, Pt, Pd, Cu) modified semiconductor such TiO_2 , graphene and polymer also showed enhanced photocatalytic activity under visible light irradiation [26-31]. For instance, Niu et al. [32] reported Pt modified BFO exhibited 70% photocatalytic degradation activity for MO under visible light irradiation. Li et al. [33] also confirmed the enhanced photocatalytic activity of Au NPs deposited BiFeO_3 nanowires under visible-light for O_2 evolution due to surface-plasmon effect (SPR) of Au NPs. Recently, Li et al. [34] showed enhanced photovoltaic effect of noble metal Au modified La doped BiFeO_3 films. Moreover, Ag loaded BFO nanostructures showed enhanced photocatalytic degradation of methylene blue (MB) under visible light [35, 36]. It has been reported that, noble metal NPs can exhibit surface plasmon resonance effect, (a collective oscillation of conduction band electrons due to interaction with visible light photons) which induced a local electromagnetic field at the interface of the semiconductor photocatalyst, consequently promotes the charge-carrier separation efficiency [27, 28]. When plasmonic metal NPs brought into an approximate distance, coupling of their localized electromagnetic field may

happen and generate large number of hot electrons which may influence the photocatalytic reactions [37]. Moreover, noble metal NPs can also act as electron or hole acceptor and improves charge separation efficiency of the adjacent nanostructure as well as they provide active catalytic sites [38, 39]. However, to the best of our knowledge, the photocatalytic H₂ generation through water splitting using noble metal modified BFO as a catalyst is not reported yet.

In this work, BFO and BFO based metal-semiconductor heterostructures have been developed to study the photocatalytic H₂ generation and photoelectrochemical water splitting. Different morphologies of BFO have been successfully synthesized by hydrothermal method and, then plasmonic metal NPs have been deposited on BFO nanostructures by radiolysis technique. Experimental results reveal that, metal-semiconductor heterostructures are efficient photocatalyst for H₂ generation under visible light irradiation.

5.2 Experimental

Bismuth nitrate pentahydrate [Bi(NO₃)₃ · 5H₂O], gold(III) acetate, silver acetate, cadmium nitrate [Cd(NO₃)₂], zinc acetate [Zn(CH₃COO)₂ · 2H₂O], thiourea (99.0%), mercaptosuccinic acid (MSA, 99%), ethylenediaminetetraacetic acid disodium salt (EDTA-Na), methanol were obtained from Sigma Aldrich, USA. Anhydrous FeCl₃, sodium hydroxide (NaOH, 98%) were obtained from the Alfa Aesar chemicals and Merck, Germany respectively. All compounds were used as received and ultrapure water (Millipore System, 18.2 MU cm) was used as solvent.

In a typical synthesis of BFO nanostructures, Bi(NO₃)₃ · 5H₂O and FeCl₃ in a stoichiometric ratio (1 : 1 in molar ratio) were dissolved in acetone (50 ml) under stirring and ultrasonication until completely dissolved. Then, 50 ml distilled water was added with the solution and mixed properly. After that, NH₃ was added drop wise until the pH value of the mixed solution reached 10–11. The precipitation was then centrifuged and washed with distilled water several times until the pH value of the solution was neutral. Next, the brown co-precipitate was redispersed in 100 ml distilled water with vigorous stirring. Calculated amount of NaOH (2 M, 5M and 12 M) were added into the solution and stirred for 30 min. Finally, the solution was transferred into a stainless steel autoclave with a Teflon liner and heated at 180°C for 72 h. After cooling down to room temperature, the black powder was collected by filtration, washed with distilled water and ethanol for several times, and dried at 50°C for 12 h.

Au/BFO-Ns heterostructures were obtained using steady state gamma irradiation in presence of gold acetate salts [40-42]. In this experiment, to synthesize Au NPs on BFO-Ns, BFO solution (1 mg mL⁻¹) and gold (III) acetate (1 mM) solution were mixed in an ultrasonic bath for 30 min, followed by deoxygenated under Argon flow. Subsequently, the solution was irradiated for 1h (dose rate = 8 kGy h⁻¹) using a ⁶⁰Co gamma-facility. After that, black precipitation of Au/BFO-Ns was centrifuged and washed several times with ethanol and water and finally dried at 50°C for overnight. For comparison, control Au NPs were synthesized by colloidal method

The crystalline phase of BFO-Ns and Au/BFO-Ns heterostructures were investigated by XRD (Philips X'Pert, The Netherlands) within 2θ range 10° to 80° at slow scan rate of 1° min⁻¹ with Cu Kα radiation (at 40 kV and 40 mA). The structural morphology and EDX was recorded by Field Emission Scanning Electron Microscopy (LEO. 430i, Carl-Zeiss, Sigma). Transmission Electron Microscopy (TEM) images and the corresponding selected area electron diffraction (SAED) patterns were obtained on Tecnai G² 30ST (FEI) operating at 300 kV. The XPS-study was performed using PHI 5000 Versa Probe II spectrophotometer (Physical Electronics Inc., USA) using a monochromatized Al Kα (~1486.6 eV) X-ray beam of size ~ 100 μm. Samples were prepared in pallet form and surfaces were sputtered with a 2 kV rastered Ar⁺ ion beam for one minute to clean the surface. The porosity and specific surface area of the samples were determined through nitrogen adsorption at 200°C on the basis of BET equation using Quantachrome, FL-33426. The diffuse reflectance spectra of BFO-Ns and Au/BFO-Ns were recorded using a Shimadzu, UV-3600 spectrophotometer. The photoluminescence (PL) spectrum of as synthesized materials was taken by JASCO FP-8500. The hydrogen evolution was measured by online gas chromatography using YL Instrument, 6500GC system with thermoconductive detector. The magnetic properties of samples were measured using a VSM (Lake Shore Cryotronics) at a maximum field of 16 kOe at room temperature.

To study the hydrogen generation, online gas chromatography was used and the area under the Gaussian peak gives the amount of H₂ evolved. The experiment was performed in a closed reactor in presence of methanol solution with saturated argon media under vigorous stirring. For this experiment, 25 volume % methanol solution was used at room temperature. Here, methanol acts as sacrificial agent and a Xe-arc lamp (250W) with an incident beam intensity of 100 mW/cm² was used as light source for visible irradiation and a 420 nm cut-off filter was used.

Photoelectrochemical measurement was performed using a galvanostat-potentiostat (PGSTAT302N, Autolab, The Netherlands) with a standard three-electrode cell and Pt wire as counter electrode and saturated Ag/AgCl as reference electrode. The working electrode was thin film of as prepared material on FTO. The linear sweep voltammetry was carried out within the potential range -0.2V to 0.8V vs Ag/AgCl at a scan rate 10 mV/s using $0.1\text{ M Na}_2\text{SO}_4$ phosphate buffer (pH 7) as electrolyte. The PEC measurements of these electrodes were carried out with a 0.27 cm^2 geometric area exposure (using O-ring of the same inner area) to the electrolyte solution under light irradiation. The stability of BFO-Ns and Au/BFO-Ns were tested through chronoamperometry at 0.6V potential. The photoresponse of BFO-Ns and Au/BFO-Ns was measured under periodic chopped irradiation from Xe-arc lamp (300 W , Excelitas USA) as a white-light source with an incident beam intensity of 100 mW/cm^2 . The potential was then converted to the reversible hydrogen electrode (RHE) following the Eq. 5.1.

$$E_{\text{RHE}} = E_{\text{Ag/AgCl}} + 0.059\text{ pH} + 0.197(E_{\text{Ag/AgCl}}^0) \quad (5.1)$$

After that, photoelectrochemical action spectrum was studied through chronoamperometry under chopped monochromatic illumination (using an Oriel monochromator, USA) within the wavelength range of $300\text{--}700\text{ nm}$. Then incident photon to current conversion efficiency (IPCE) and absorbed photon to current conversion efficiency (APCE) was calculated according to the Eq. 5.2 and 5.3:

$$\text{IPCE (\%)} = \frac{I_{\text{ph}}}{P_{\text{in}}} \times \frac{1240}{\lambda} \times 100 \quad (5.2)$$

$$\text{APCE (\%)} = \frac{\text{IPCE}}{(1 - 10^{-A_\lambda})} \times 100 \quad (5.3)$$

Where, I_{ph} is the output photocurrent density (A/cm^2), P_{in} is the incident power density (W/cm^2), λ is wavelength (nm) and A_λ is the absorbance of the material at any particular wavelength (λ). Capacitance measurements were carried out using same instrument in a borosilicate glass cell with three-electrode configuration. To study the behaviour of the semiconductor-electrolyte interface, a phosphate buffer (pH 7) with $0.1\text{ M Na}_2\text{SO}_4$ was used as working solution. Experiments were done within the potential range of -0.6V to 0.2 V vs Ag/AgCl using ac RMS amplitude of 10 mV at 1000 Hz frequency.

5.3 Results and Discussion

5.3.1 Phase Purity and Crystal Structure

Figure 5.1a shows the XRD pattern of the pure BFO-Ns and Au/BFO-Ns heterostructures. All the diffraction peaks of pure BFO-Ns can be indexed as rhombohedral phase with R3c space group (JCPDS 86-1518). The corresponding lattice parameters are $a = 0.5577$ nm, $b = 0.5577$ nm and $c = 1.3862$ nm [32, 43]. No additional peaks are found, demonstrating that single-phase BFO-Ns powder has been successfully prepared. In Au/BFO-Ns heterostructures, the characteristic diffraction peaks of Au NPs at 2θ values 38.13° , 44.28° , 64.55° , 77.57° and 81.85° corresponds to (111), (200), (220), (311), and (222) planes respectively are present without changing the BFO-Ns peaks, which confirms the heterostructures formation [41, 42].

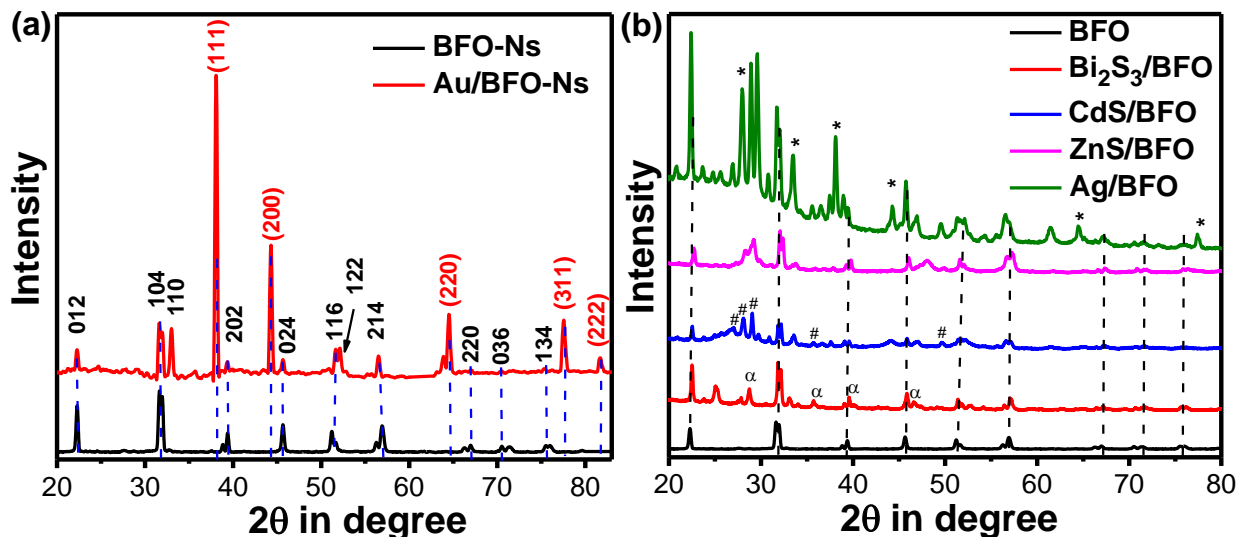


Figure 5.1 X-ray powder diffraction pattern of (a) pure BiFeO₃-Ns (BFO-Ns) and Au/BiFeO₃-Ns (Au/BFO-Ns) heterostructures, (b) BFO-Ns, Bi₂S₃/BFO-Ns, CdS/BFO-Ns, ZnS/BFO-Ns and Ag/BFO-Ns heterostructures.

Further, various sulfide based heterostructures with BFO-Ns have been developed (following previously reported hydrothermal methods) to compare the photocatalytic H₂ generation [25, 30, 44, 45]. The formation of other chalcogenide based heterostructures has been characterized by X-ray analysis (Figure 5.1b). The characteristic BFO-Ns peaks have been present for all the heterostructures. In addition, for Bi₂S₃/BFO heterostructures, the diffraction peaks of (130), (211), (240), (141), and (431) corresponds to 2θ value 25.06° , 28.65° , 35.59° , 39.97° , 46.60° are present for Bi₂S₃ [25]. The strong peaks at 2θ values of 26.89° , 27.93° , 28.96° , 35.59° , 49.46° correspond to the (100), (002), (101), (102) and (200) faces of CdS respectively in the heterostructures

CdS/BFO [44]. In ZnS/BFO heterostructures, the diffraction peaks of (111), (200), (220), and (311) corresponds to 2θ value of 28.71° , 33.09° , 47.82° , 56.70° are present for ZnS respectively [45]. The diffraction peaks at 2θ values of 38.08° , 44.17° , 64.37° , 77.40° corresponds to (111), (200), (220), (311) planes of Ag NPs in Ag/BFO heterostructures (Figure 5.1b) [30].

5.3.2 Microstructures

Figure 5.2 represents the FESEM and TEM images of pure BFO-Ns and Au/BFO-Ns heterostructures. The FESEM image illustrates that, microcubes (~ 922 nm sides) are formed at NaOH concentration of 5M along with small hexagonal nanosheets on the surface (Figure 5.2a). In addition, the TEM image clearly shows that cubes and hexagonal nanostructures of BFO in an irregular pattern are present (Figure 5.2b).

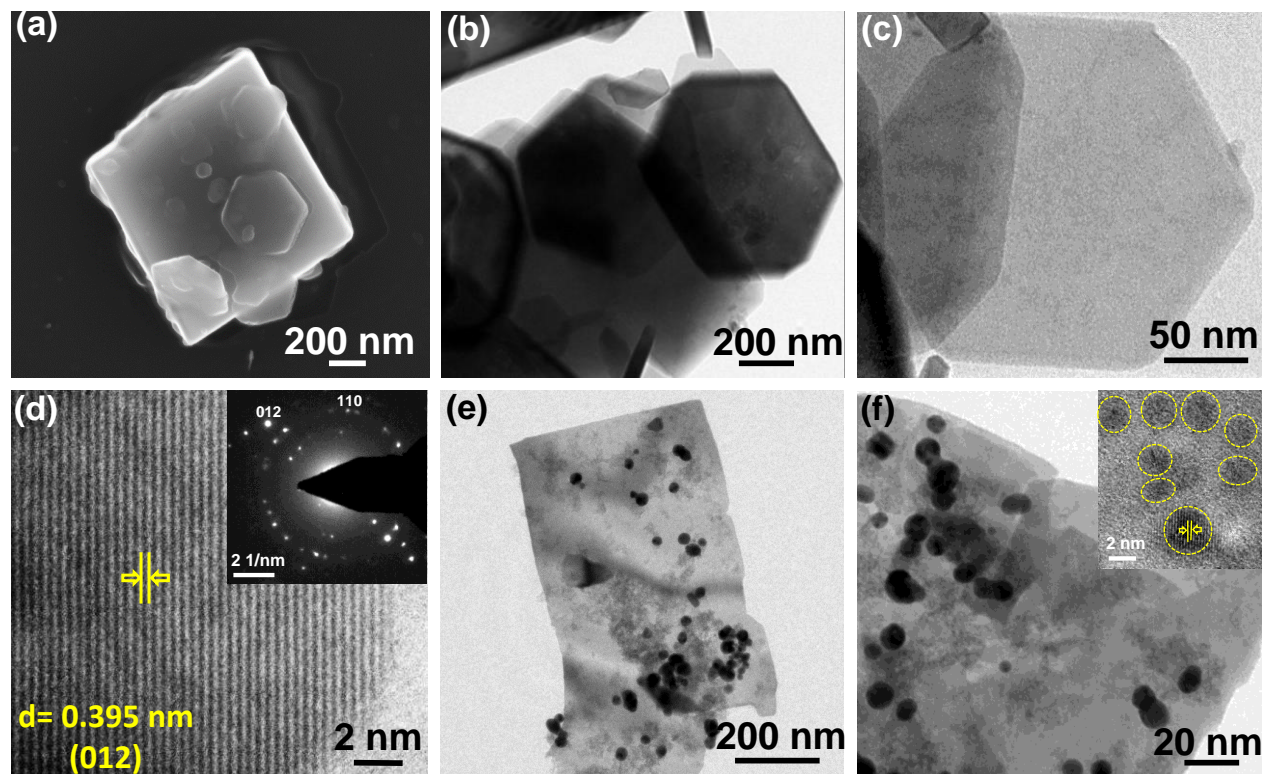


Figure 5.2 (a) FESEM image, (b, c) low and high magnification TEM images and (d) HRTEM of BiFeO₃ Nanosheets (BFO -Ns). Inset d: SAED pattern of BiFeO₃ nanosheets. (e, f) Low and high magnification TEM images of Au/BiFeO₃-Ns heterostructures. Inset f: HRTEM image of Au/BiFeO₃-Ns heterostructures. All the samples are prepared at NaOH concentration of 5M.

As BFO has magnetic property, the cubic structures may form due to the staking of hexagonal nanosheets. Interestingly, the high magnification TEM image (Figure 5.2c) shows that hexagonal

nanostructures with BFO of edges ~ 228 nm and width ~ 7.5 nm have been formed at NaOH concentration of 5M. The interplanar spacing of ~ 0.39 nm calculated from the HRTEM image (Figure 5.2d) is in good agreement with the spacing of (012) plane of BFO [14]. Moreover, a corresponding SAED pattern confirms the presence of (012) and (110) planes (Inset of Figure 5.2d) which has been taken from one single BFO-Ns. The SAED and HRTEM images reveal that the BFO-Ns are single-crystal. Figure 5.2e and 2f show the low and high magnification TEM images of Au/BFO-Ns heterostructures where Au NPs have been formed in a homogeneous distribution pattern on the BFO-Ns after γ radiation. The average particle size of the Au NPs is found to be ~ 17 nm. The energy-dispersive X-ray spectroscopy (EDX) spectrum of the Au/BFO-Ns heterostructures has been illustrated in Figure 5.3a. The strong peaks of Bi, Fe, O, and Au elements in EDX spectrum indicate that aforementioned elements are present within the heterostructures. Since, the atomic ratio of Bi, Fe and O is about 1:1:3, which is close to the stoichiometric ratio of BFO. Therefore, heterojunction formation of Au and BFO does not change the stoichiometric ratio of the BFO itself.

5.3.3 X-ray Photoelectron Spectroscopy and BET Surface Area

Furthermore, to study the chemical states of Au, Bi, Fe and O in the Au/BFO-Ns heterostructures and to investigate the detailed insight into the interaction between Au NPs and BFO nanostructures, X-ray photon spectroscopy (XPS) has been employed. Figure 5.3b shows the overall XPS spectra of pure BFO-Ns and Au/BFO-Ns heterostructures where oxidation states of Bi, Fe, O and Au are present. The XPS peaks observed for Au 4f at binding energy 53.5 eV and 87.17 eV corresponds to Au 4f_{7/2} and Au 4f_{5/2}, confirm the presence of Au(0) state within the heterostructures (Figure 5.3c) [33]. The presence of the doublet Bi 4f peaks at binding energy ~ 158.13 eV and ~ 163.41 eV corresponds to Bi 4f_{7/2} and Bi 4f_{5/2} indicate that bismuth existed in a single chemical state of Bi³⁺ (Figure 5. 3d) [32]. More interestingly, a red shifting has been observed for Bi 4f peaks after heterojunction formation which suggests the occurrence of strong interaction and charge transfer between Au NPs and BFO-Ns (Figure 5.4a).

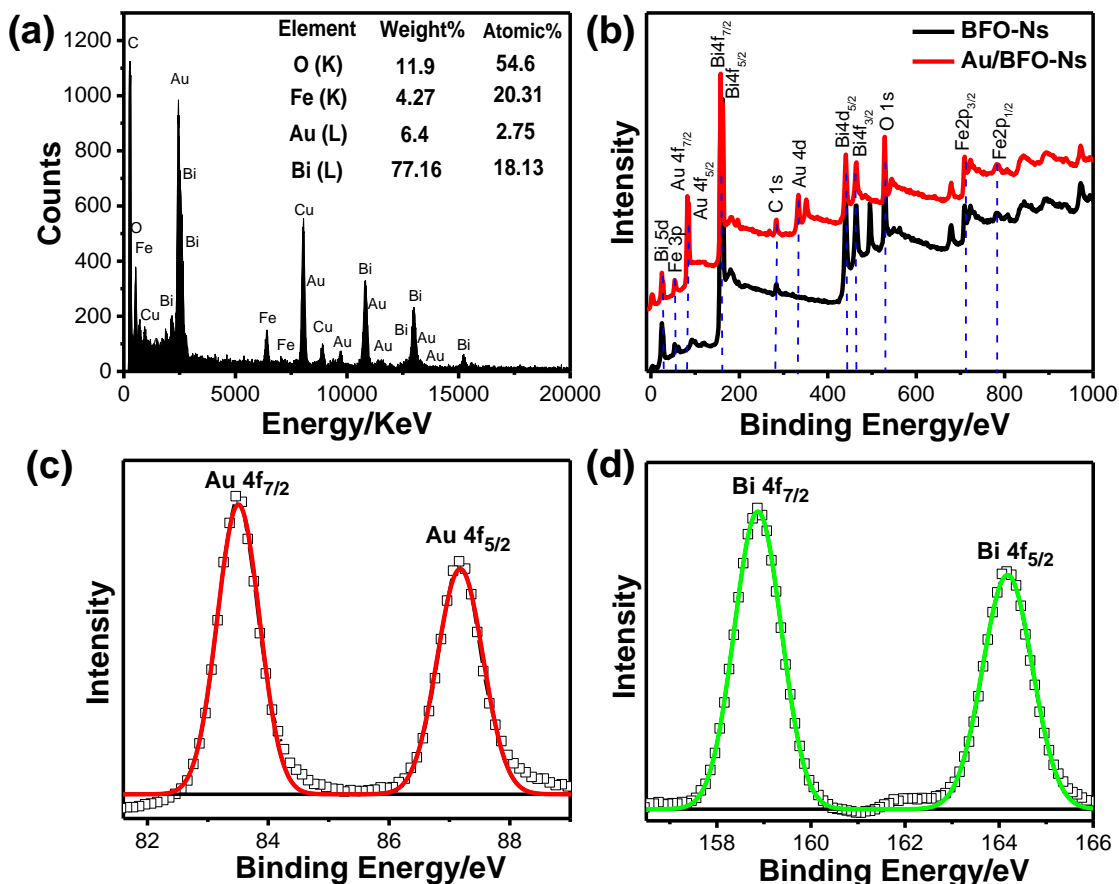


Figure 5.3 (a) Energy-dispersive X-ray spectra (EDX) of Au/BiFeO₃-Ns (Au/BFO-Ns) heterostructures. X-ray photon spectroscopy (XPS) of (b) pure BiFeO₃ Nanosheets (BFO-Ns) and Au/BFO-Ns heterostructures, (c) Au and (d) Bi of Au/BFO-Ns heterostructures.

The binding energy of peaks at ~ 710.15 eV and ~ 723.41 eV arise due to Fe 2p_{3/2} and Fe 2p_{1/2} states and the satellite peak at ~ 718.32 eV (8.17 eV above the Fe 2p_{3/2}) confirms that Fe is at Fe³⁺ state within BFO (Figure 5.4b) [32, 46]. Hence, the XPS spectrum of O1s for pure BFO-Ns shows (Figure 5.4c) two peaks at ~ 529.1 eV and ~ 530.77 eV correspond to oxygen-metal bonds and surface adsorbed oxygen respectively, whereas for Au/BFO-Ns heterostructures, single peak at 529.67 eV has been observed [47]. This observation indicates that, surface adsorbed oxygen are removed after heterostructures formation as the Au NPs occupy the surfaces of the BFO-Ns. Therefore, it can be conclude from XPS data, Bi and Fe exist in the states of Bi³⁺ and Fe³⁺ within BFO-Ns and Au in zero oxidation state within heterostructures. The porous structure of the pure semiconductor BFO-Ns and the heterostructures Au/BFO-Ns has been studied by the nitrogen adsorption desorption isotherm method. The hysteresis loop present in the BET curve (Figure 5.4d) suggests the type II pattern of BFO-Ns and Au/BFO-Ns heterostructures. The specific surface

areas calculated by the Barrett-Joyner-Halenda (BJH) method of pure BFO-Ns and Au/BFO-Ns heterostructures are $10 \text{ m}^2\text{g}^{-1}$ and $35 \text{ m}^2\text{g}^{-1}$, respectively. Therefore, it indicates that larger inter-aggregated pores were generated in heterostructures and became predominant with higher adsorption capacity. This could be confirmed by the TEM images that the total specific surface area of Au/BFO-Ns has been increased because of added surface area of the Au NPs with BFO nanosheet (Figure 5.2e and 2f). Hence, it is expected that photocatalytic activity of heterostructures might be enhanced due to increased surface area by the incorporation of Au NPs.

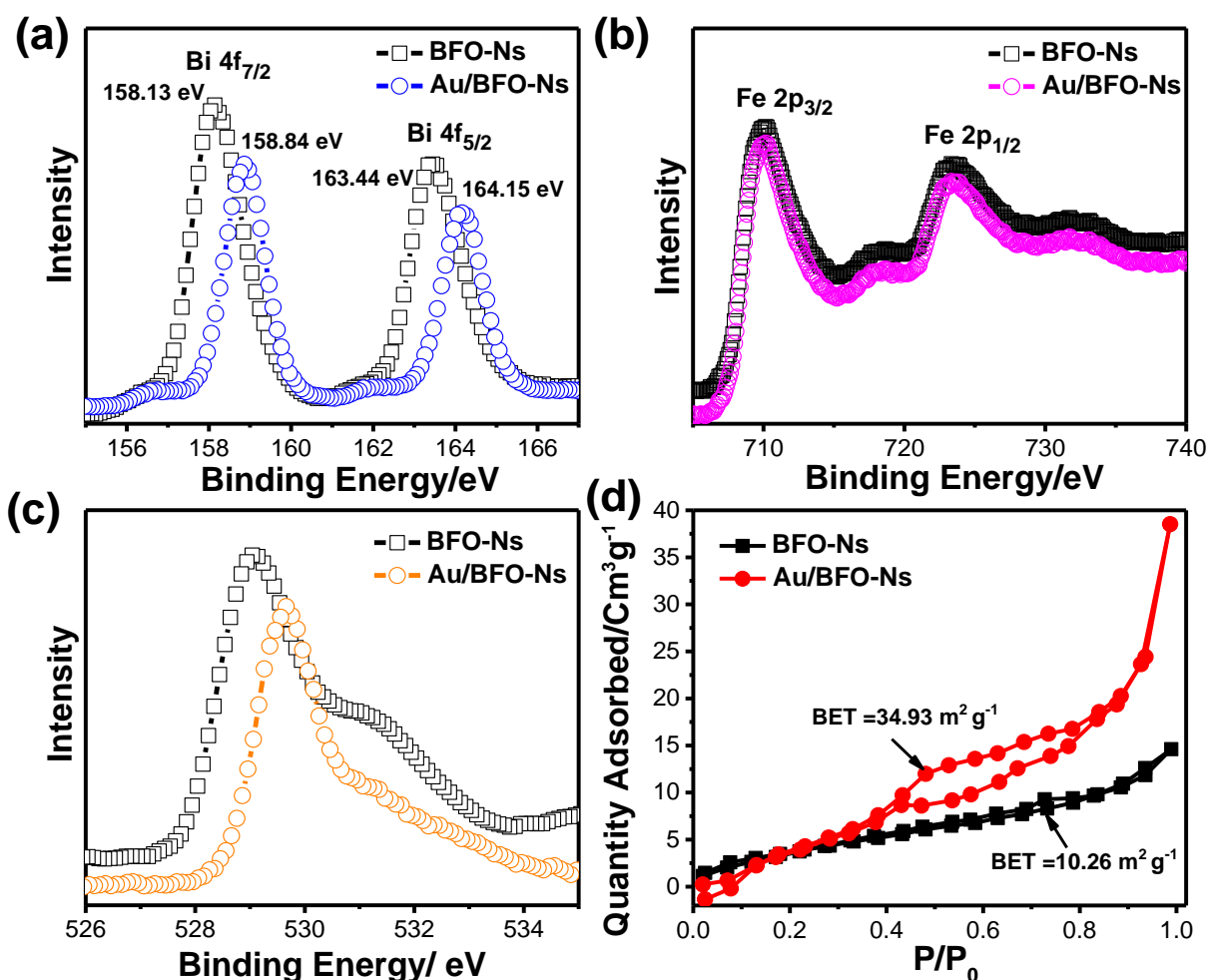


Figure 5.4 (a) X-ray photoelectron spectroscopy of (a) Bi, (b) Fe and (c) O for pure BiFeO₃ Nanosheets (BFO-Ns) and Au/BFO-Ns heterostructures. (d) Isothermal N₂ gas adsorption–desorption curves of the pure BFO-Ns and Au/BFO-Ns heterostructures.

5.3.4 UV-Vis Spectroscopy

To investigate the influence of heterostructures formation on the optical absorption and electronic band structure of the BFO-Ns, UV-Vis diffuse reflectance spectra (DRS) has been employed.

Figure 5.5 shows the UV–Vis absorption spectra of BFO-Ns and Au/BFO-Ns, which are converted from the measured diffuse reflectance spectra by means of the Kubelka–Munk Function [32]. Au/BFO-Ns show two striking features of the absorption spectra. First, a characteristic absorption peak at ~600 nm has been observed which is mainly attributed due to plasmonic absorption of Au NPs [27]. Secondly, the existing peaks of BFO-Ns at 350 nm and 450 nm have been increased which may arise due to strong electronic interaction of Au NPs with BFO-Ns. Further, the direct bandgaps of BFO-Ns (2.3 eV) and Au/BFO-Ns (2.1 eV) have been calculated from the Kubelka–Munk [$(\alpha h\nu)^2$ vs photon energy ($h\nu$)] plot (Figure 5.5b). This lowering of bandgap from 2.3 eV to 2.1 eV for Au/BFO-Ns heterostructures is useful for enhanced absorption in visible region and consequently may enhance the photocatalytic activity.

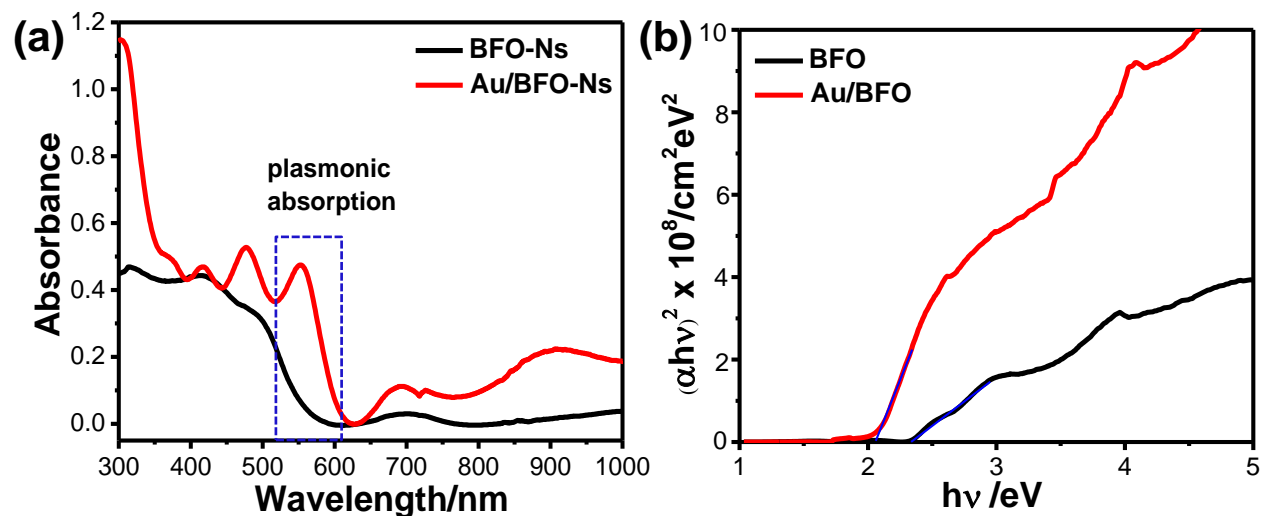


Figure 5.5 (a) Diffuse reflectance spectra of pure BiFeO₃ nanosheets (BFO-Ns) and Au/BFO-Ns heterostructures. (b) Kubelka–Munk [$(\alpha h\nu)^2$ vs photonenergy ($h\nu$)] plot of pure semiconductor BFO-Ns and Au/BFO-Ns heterostructures.

5.3.5 Photocatalytic Hydrogen Production

Photocatalytic activity of as synthesized materials has been evaluated by photocatalytic H₂ generation through water reduction. Figure 5.6a shows the photocatalytic H₂ generation of pure semiconductor BFO-Ns and Au/BFO-Ns heterostructures through water reduction under visible light irradiation ($\lambda > 420$ nm) in presence of methanol (25 volume %) as sacrificial agent at pH 7. Here methanol acts as hole scavenger, i.e. reacted with the photogenerated holes usually faster than water, lead to excess electron in the medium for H₂ generation by water reduction. Au/BFO-Ns heterostructures exhibit enhanced photocatalytic H₂ generation (~2.1 mmol) compared to pure BFO-Ns (~1.1 mmol) after 2h irradiation. Interestingly, the hydrogen evolution rate increased

linearly with time after a certain time (Figure 5.6b), demonstrating that the catalysts maintain a strong driving force for water reduction over the examined period [46]. To study the effect of BFO morphology on photocatalytic H₂ generation, two different morphologies (cylindrical and octahedron) of BFO have been synthesized by varying the NaOH concentration. At lower concentration of NaOH (2M), cylindrical shaped BFO (BFO-Cyl) of average length 500 nm and width 120 nm have been obtained, however, at higher concentration of NaOH (12 M), octahedral shaped BFO (BFO-Oct) nanostructures have been formed (Figure 5.6c and 6d). Hence, NaOH played a crucial role in controlling the morphology where sodium ions determine the available concentration of Fe³⁺ ions for further growth, which in turn affect the overall morphology of BFO nanostructures [47]. Photocatalytic activity of pure BFO with three different morphology and corresponding Au decorated BFO has been compared under visible light as shown in Figure 5.7a. The highest photocatalytic H₂ generation has been observed for BFO-Oct (BFO-Oct (~1.4 mmol) > BFO-Ns (~1.1 mmol) > BFO-Cyl (~0.5 mmol). Notably, BFO-Oct nanostructure shows strong absorption in the visible region in comparison to two other nanostructures (Figure 5.7b). Hence, more exposed surfaces of the BFO-Oct may led to better absorption and enhance the photocatalytic H₂ generation which is consistent with the literature report [48]. However, after formation of heterostructures, Au/BFO-Ns produces significant amount of H₂ generation, which is 2 times higher than pure BFO-Ns as shown in Figure 5.7a. The enhanced catalytic activity of Au/BFO-Ns may be due to the large surface area of two dimensional BFO-Ns which provide a strong coupling with the Au NPs. Thus, Au NPs can be exposed to the BFO-Ns surfaces and induce strong interaction [49]. Hence, BFO-Ns and Au/BFO-Ns have been taken for further studies. Next, the effect of pH on photocatalytic H₂ evolution has been studied to optimize the reaction condition. Figure 5.7c illustrates that higher catalytic activity for H₂ evolution achieved at pH 3 (~ 2.4 mmol) due to high availability of H⁺ in acidic solution and H₂ evolution activity decrease as the medium becomes more alkaline due to insufficient protons [50]. At more acidic medium protonation is happening due to presence of excess proton (H⁺) which may produce a filter effect by producing free molecules. It causes intermolecular energy transfer, resulting in a decrease in the photocatalytic efficiency [51].

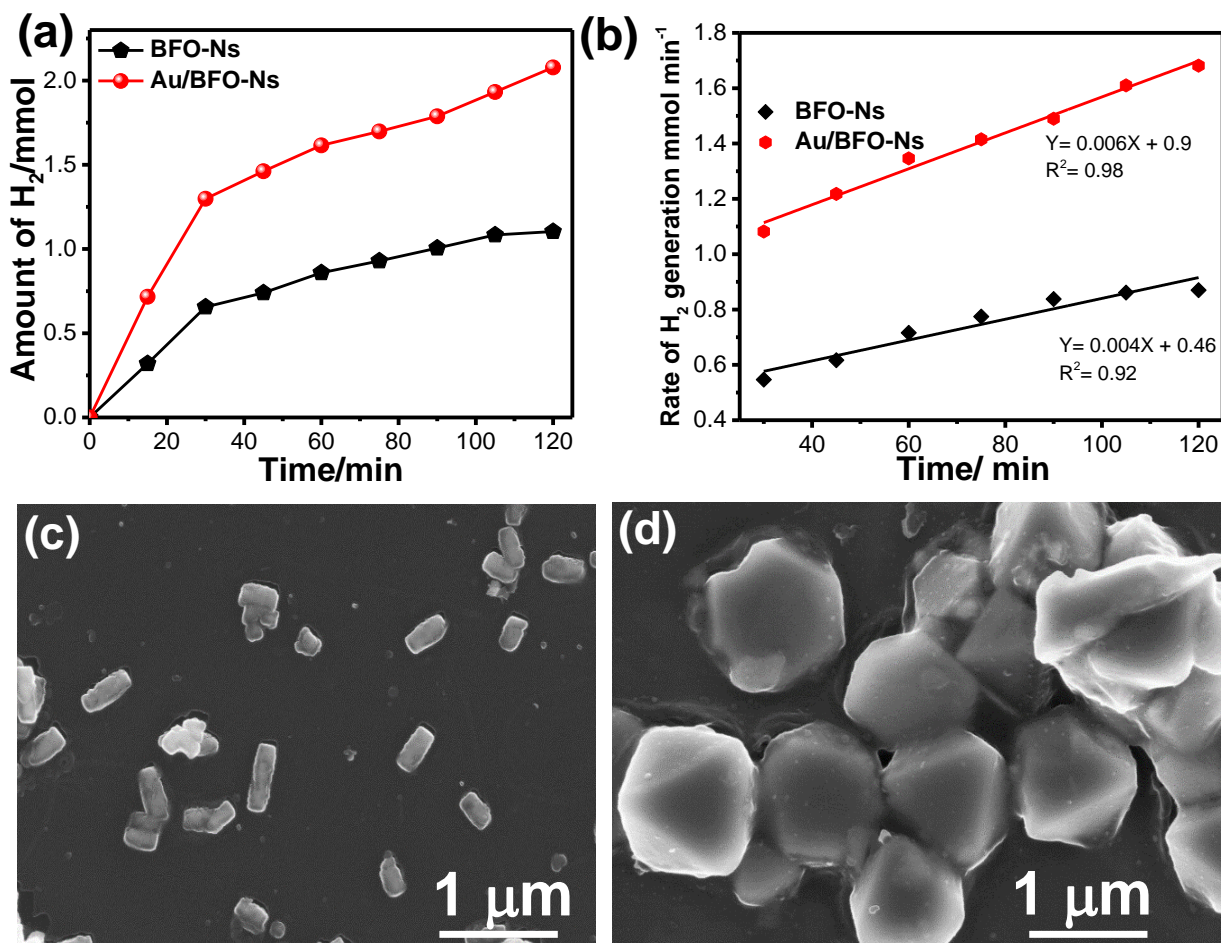


Figure 5.6 (a) Photocatalytic hydrogen generation and (b) H₂ evolution rate in presence of BiFeO₃ nanosheet (BFO-Ns, black line) and Au/BFO-Ns heterostructures (red line). (c) FESEM images of cylindrical shaped BiFeO₃ (BFO-Cyl) nanostructures using 2M NaOH, (d) octahedral shaped BiFeO₃ (BFO-Oct) nanostructures using 12M NaOH.

The same trend has been observed for pure BFO-Ns in H₂ generation. In order to further optimize the role of sacrificial agents in photocatalytic H₂ generation, commonly used alcohol and aldehydes have been tested under similar reaction condition (Figure 5.7d). In general, the redox potential of a sacrificial agent should be more negative than valence band of semiconductor, so that they can consume the holes and suppress the recombination of photogenerated electrons [52]. The highest photocatalytic H₂ generation has been observed for Au/BFO-Ns as photocatalyst using methanol (~ 2.1 mmol) as sacrificial agent compared to ethanol (~ 1.7 mmol), 2-propanol (~ 1.0 mmol), ethylene glycol (~ 0.6 mmol) and formaldehyde (~1.5 mmol). This result suggests that, the length of carbon chain is inversely proportional to photocatalytic H₂ generation. However, the oxidation potential and permittivity of sacrificial agents have also potential role in H₂ generation

as the sacrificial agents act as electron donors to consume the holes. According to Gouy-Chapman theory (Eq. 5.4), surface charge density is proportional to dielectric constant of the solvent [52].

$$\sigma_s = \frac{2RT\epsilon\epsilon_0}{F} \sinh \frac{F\psi_0}{2RT} \quad (5.4)$$

Where, σ_s is the surface charge density, ϵ is the dielectric constant of the solvent and ϵ_0 is the permittivity of free space, R is gas constant, T is the temperature, F is Faraday constant and ψ_0 is potential of the surface.

As shown in Table 5.1, the oxidation potential of methanol is lower than ethanol, 2-propanol and ethylene glycol but the permittivity is higher than ethanol and 2-propanol. Although, the permittivity of ethylene glycol is much higher compared to others, the higher oxidation potential (1.54 eV higher than water oxidation potential 1.23 eV) lowers its activity as it poorly oxidized. Therefore, methanol is considered as preferable sacrificial agent in photocatalytic hydrogen generation having lower oxidation potential and considerable permittivity. In case of pure BFO-Ns, the similar trend has been observed in H_2 generation (Figure 5.7d).

Table 5.1 Permittivity and oxidation potential of the sacrificial agents.

| Sacrificial agent | Permittivity (ϵ) | Oxidation Potential/ eV |
|--------------------------|---|--------------------------------|
| Methanol | 31.2 | 1.05 |
| Ethanol | 25.7 | 1.10 |
| 2-propanol | 18.23 | 1.15 |
| Ethylyne Glycol | 38.9 | 1.54 |

Furthermore, sulfide based other semiconductor-semiconductor heterostructures have been also prepared to compare the photocatalytic activity for H_2 generation with Au/BFO-Ns heterostructures. Figure 5.8a represents the hydrogen generation from a series of sulfide based semiconductor/BFO-Ns heterostructures along with other metal-semiconductor heterostructures (Ag/BFO-Ns) under similar conditions. The amount of H_2 evolution follow the order of Au/BFO-Ns (~2.1 mmol) > Ag/BFO-Ns (~1.8 mmol) > Bi_2S_3 /BFO-Ns (~1.4 mmol) > CdS/BFO-Ns (~1.2 mmol) > ZnS/BFO-Ns (~1.15 mmol) > BFO-Ns (~ 1.1 mmol) (Figure 5.8a).

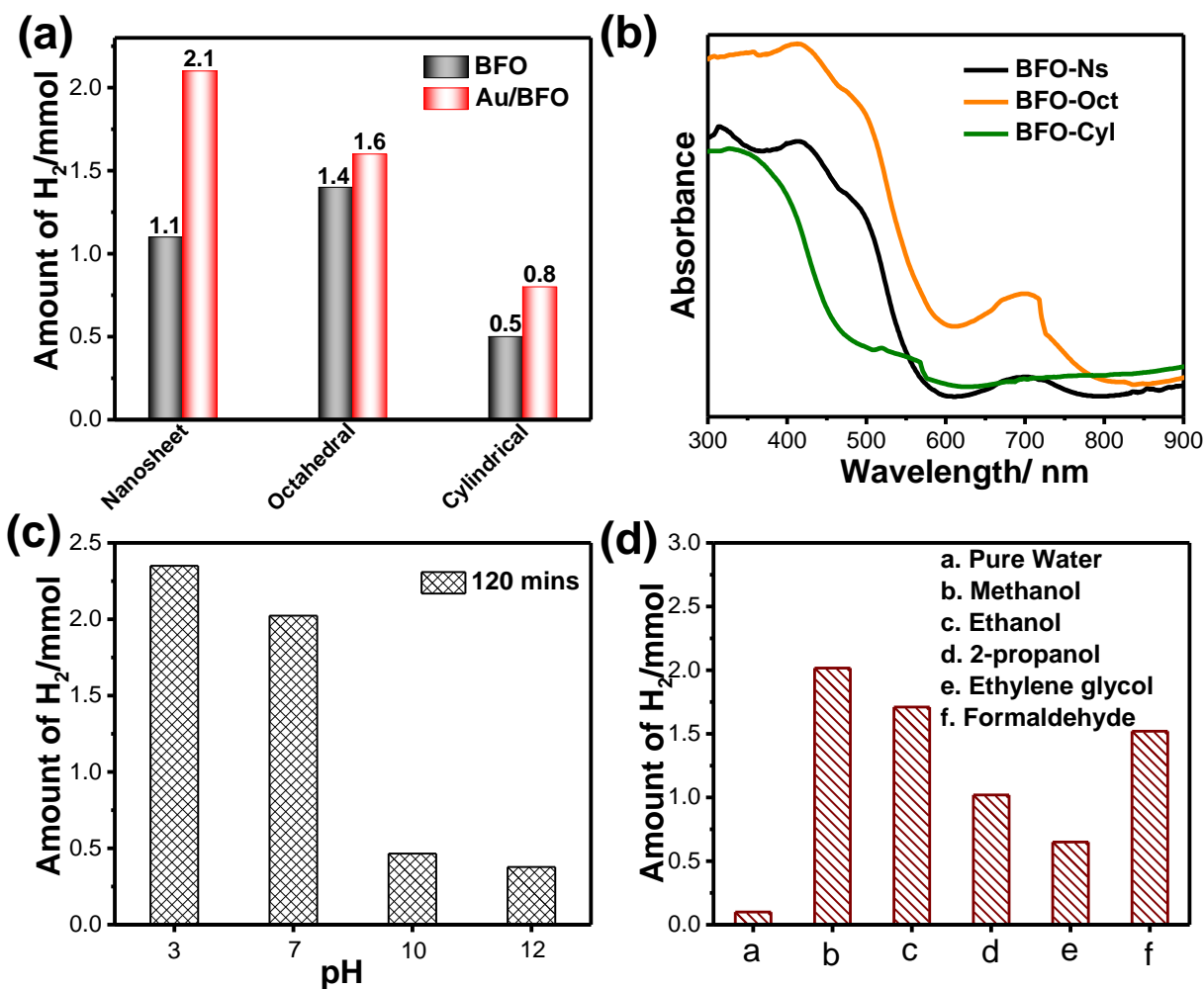


Figure 5. 7 (a) Comparative H₂ generation data after 2 h visible light irradiation using the catalysts of BiFeO₃ nanosheet (BFO-Ns), BiFeO₃ octahedral (BFO-Oct), cylindrical shaped BiFeO₃ (BFO-Cyl) and their heterostructures as Au/BFO-Ns, Au/BFO-Oct, Au/BFO -Cyl from an aqueous solution containing 25 volume % methanol at pH 7. (b) Diffuse reflectance spectra of BiFeO₃ nanostructures with different morphologies. Effect of (c) pH and (d) sacrificial agents on hydrogen generation using Au/BFO-Ns as photocatalyst under visible light illumination.

This suggests metal-semiconductor heterostructures are more effective for H₂ generation having an additional SPR effect of metal nanoparticles with Schottky barrier at the interfaces which greatly influence the dynamic behaviours of the photo excited charge carriers [33, 55]. Reusability and stability are important parameters of a photocatalyst for large scale application. Here, H₂ generation of Au/BFO-Ns heterostructures has been checked up to 5 successive cycles, which reveals nearly 13% loss in H₂ generation as shown in Figure 5.8b (13% loss also include catalysts mass loss). Figure 5.8c shows the TEM image of the heterostructures which reflects stability of nanosheet morphology after photocatalytic reaction. Interestingly, the gold NPs remain intact on

the BFO-Ns after cycling. Therefore, Au/BFO-Ns heterostructures are reusable catalyst for hydrogen generation and stable under long visible light irradiation.

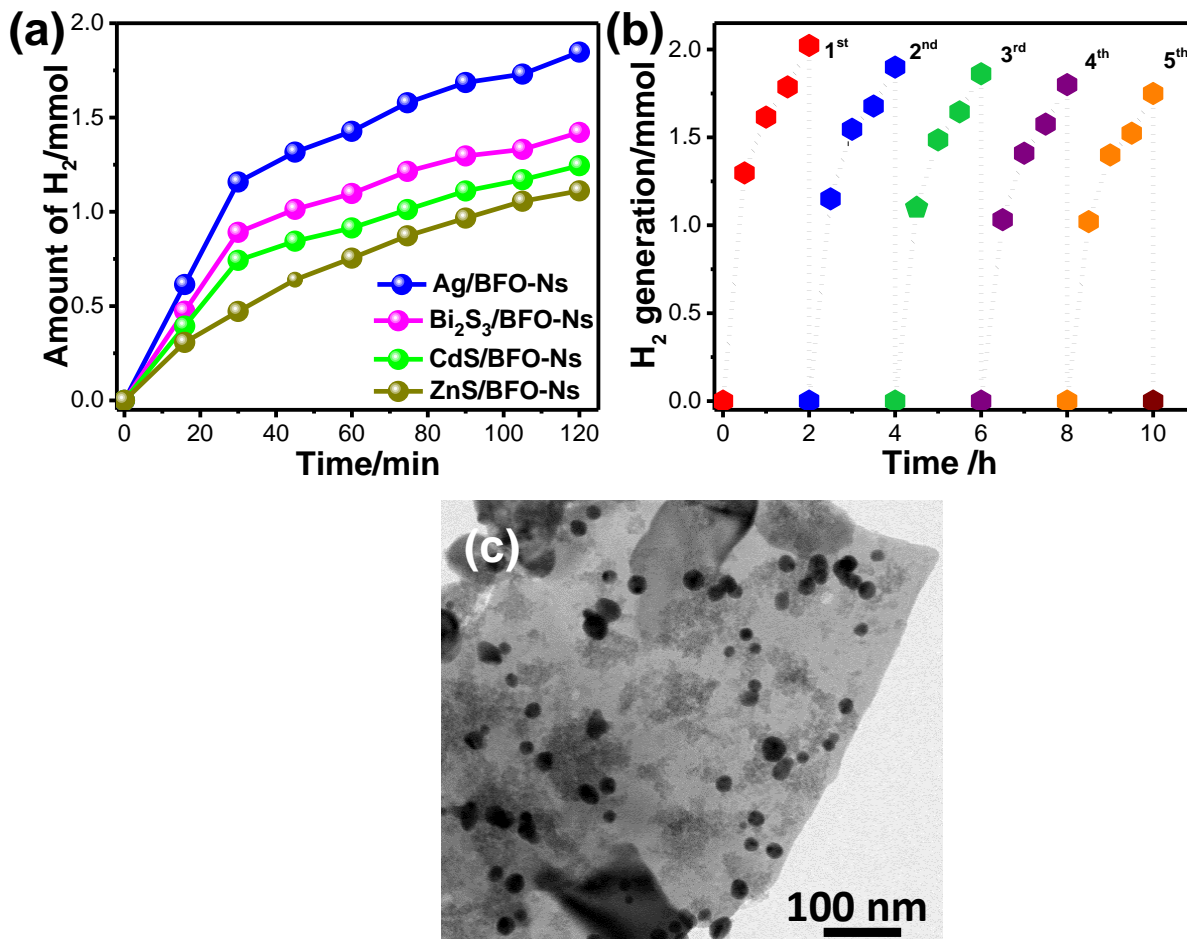


Figure 5.8 (a) Photocatalytic H₂ generation using as developed heterostructures. (b) Recycling test of Au/BFO-Ns heterostructures during photocatalytic hydrogen generation and (c) TEM image of Au/BFO-Ns heterostructures after catalytic reaction of H₂ generation at pH 7.

5.3.6 Photoelectrochemical (PEC) Activity

Photoelectrochemical measurement was performed using a galvanostat-potentiostat with a standard three-electrode cell and Pt wire as counter electrode and saturated Ag/AgCl as reference electrode. Here sacrificial agent has not been used but a potential is required to move the photogenerated electrons towards counter electrode from photoanode. To investigate the light sensitivity and stability of as synthesized material of BFO-Ns and Au/BFO-Ns heterostructures, photocurrent measurement *via* linear sweep voltammetry (LSV) and chronoamperometry (CA) have been studied. Figure 5.9a shows the LSV plot of pure BFO-Ns and Au/BFO-Ns heterostructures in dark and presence of continuous light illumination. In absence of light the

current density is negligible ($\sim 0.07 \mu\text{A cm}^{-2}$) for BFO-Ns, whereas, under continuous light illumination, the obtained current density is $\sim 0.56 \mu\text{A cm}^{-2}$ and $\sim 2.14 \mu\text{A cm}^{-2}$ for BFO-Ns and Au/BFO-Ns respectively at a potential of 0.6V vs Ag/AgCl , therefore 3.8 fold enhancement achieved for Au/BFO-Ns heterostructures. Additionally, we have measured H_2 generation under negative potentials in presence of light as reported earlier in literatures.

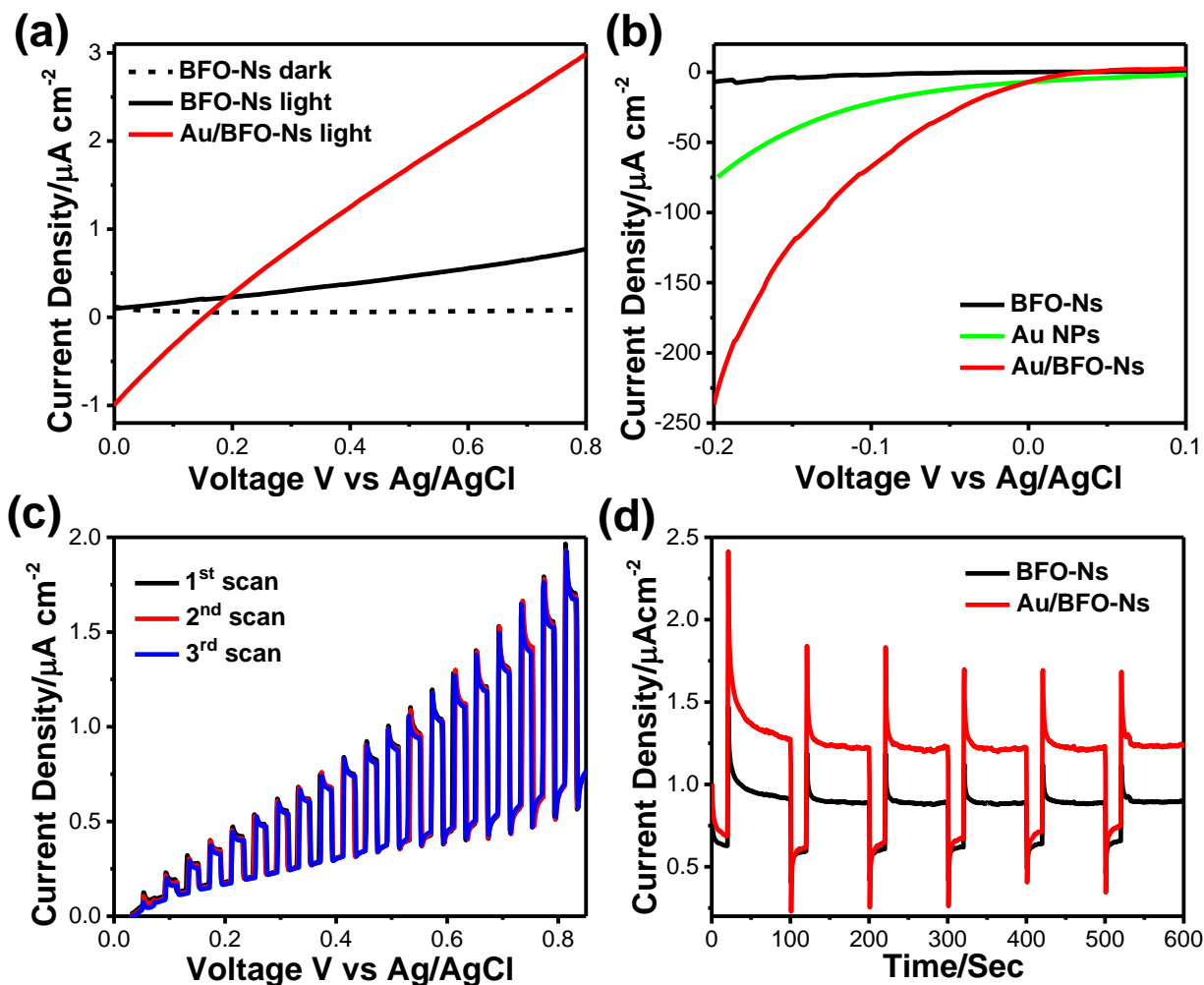


Figure 5.9 Linear sweep voltammograms (LSV) curves of BiFeO_3 nanosheet (BFO-Ns), Au NPs and Au/BFO-Ns at (a) positive potential (b) negative potential range in the presence of $0.1 \text{ M Na}_2\text{SO}_4$ -phosphate buffer solution (pH 7), under continuous light illumination of 100 mW/cm^2 . (b) Chopped LSV of BFO-Ns after three successive runs. (d) Chronoamperometry profile of the BFO-Ns and Au/BFO-Ns thin film semiconductor electrodes measured at 0.6 V vs Ag/AgCl , under chopped illumination.

A large current density ($\sim 235 \mu\text{A cm}^{-2}$) has been obtained for Au/BFO-Ns heterostructures, suggesting the H_2 generation by water reduction (Figure 5.9b) [53]. Kong et al. [54] also reported that CoSe_2 nanoparticles on carbon fiber paper generated a large photocurrent in negative potential

due to effective reduction of the water. In case of bare Au NPs, relatively lower current density ($75 \mu\text{A cm}^{-2}$) has been obtained at negative potential. Thus presence of Au NPs and its strong interaction with BFO-Ns may generate the large current density for Au/BFO-Ns heterostructures. Reusability of the semiconductor BFO-Ns has been tested through periodic voltammetry under continuous light illumination (Figure 5.9c), and almost constant photocurrent observed after three successive LSV scans under similar condition. Figure 5.9d represents the chopped chronoamperometric plot of pure BFO-Ns and Au/BFO-Ns heterostructures, indicating that materials are fairly stable against photocorrosion. The results of both LSV and CA indicate that the heterostructure exhibits increasing photoinduced electrons and holes separation, which could be on account of the enhanced photocurrent generation.

In order to get more details about quantum efficiency of as synthesized photoanodes, the incident photo-to-current efficiency (IPCE) of pure BFO-Ns and Au/BFO-Ns has been calculated using the action spectrums through chronoamperometry measurement. Figure 5.10a represents the plot of IPCE (%) and corresponding integrated current density *vs* wavelength where efficiency has been enhanced at lower wavelength for Au/BFO-Ns heterostructures compared to pure BFO-Ns. In action spectra (IPCE curve), BFO-Ns is practically inactive above 450 nm, whereas two distinct enhancement regions are prominent in Au/BFO-Ns photoanode. In the region of < 450 nm, the enhancement in efficiency is achieved mainly due to improve light harvesting by the heterojunction formation between Au and BiFeO₃. While in the wavelength of > 450 nm, the enhancement in efficiency may be attributed to the presence of Au nanoparticles which can induce localized surface plasmon resonance (SPR) with incident photons of visible light. The SPR effect of Au nanoparticles would generate hot electrons and inject to BiFeO₃ directly, as a result IPCE efficiency has been enhanced in the visible light region. The integrated current density of the photoanodes (product of the IPCE spectrum with the AM1.5G photon flux, blue stars) has been calculated further from the IPCE [55]. The integrated photocurrent density reaches to ~ 0.42 and $\sim 2 \mu\text{A/cm}^2$ for BFO-Ns and Au/BFO-Ns respectively, which is nearly identical to the photocurrent density from LSV measurement in Figure 5.9a, and the tiny deviation may be caused by the different design of the device. For instance, Zhao et al. [56] calculated integrated current density (0.08 mA/Cm^2) from the IPCE plot for Au/Pt/WO₃/TiO₂ composite which matches well with the photocurrent (0.45 mA/Cm^2). The similar trend has been followed in APCE (%) where Au/BFO-Ns heterostructures shows higher efficiency at lower wavelength (Figure 5.10b). The APCE

increases at significantly above 580 nm due to surface plasmonic effect of Au NPs. Therefore, it is obvious that, the surface modification of semiconductor BFO-Ns by metallic Au NPs improves the light absorption in visible region which may consequently increase photon to current conversion efficiency values.

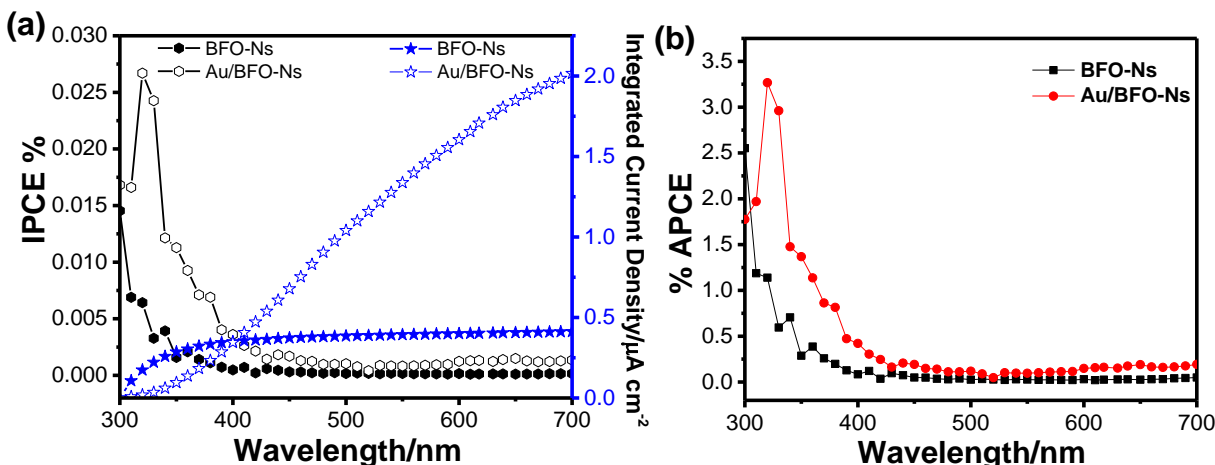


Figure 5.10 Calculated (a) IPCE (%) and corresponding integrated current density (product of the IPCE spectrum with the AM1.5G photon flux, blue stars) and (b) APCE (%) of BiFeO₃ nanosheet (BFO-Ns) and Au/BFO-Ns photoanodes using same electrolyte within the wavelength range 300 to 700 nm.

5.3.7 Mechanism

To elucidate the mechanism involved for enhanced photocatalytic activity of Au/BFO heterostructures, charge separation was investigated by various photoelectrochemical techniques including photoluminescence (PL), capacitance measurement and electrochemical impedance spectroscopy (EIS) measurements. Figure 5.11a shows the PL spectra of pure BFO-Ns and Au/BFO-Ns heterostructures at an excitation wavelength of 380 nm. It is observed that emission band for both BFO-Ns and Au/BFO-Ns is centered at 437 nm but PL intensity decreased for Au/BFO-Ns heterostructures [57]. This quenching of emission peak intensity for Au/BFO-Ns suggests the strong electronic interaction and improved charge carrier separation at the interface between Au and BFO-Ns [32]. Consequently, the improved charge separation lowers the number of surface trapped electrons by the oxygen vacancies and defects which is consistent with XPS result. Thus, the O 1s peaks at 530.77 eV which comes for surface adsorbed oxygen has been removed after heterojunction formation (Figure 5.4d). To further study the PEC properties of BFO-Ns and Au/BFO-Ns, Mott–Schottky (MS) analysis has been studied in details. Figure 5.11b shows the MS plot of pure BFO-Ns and Au/BFO-Ns heterostructures in which the positive characteristic slope in the MS plot following the Eq. 5.5, confirms the n-type behaviour of the samples.

$$\frac{1}{C^2} = \frac{2}{eN_A\epsilon\epsilon_0} \left(E - E_{fb} - \frac{KT}{e} \right) \quad (5.5)$$

where, C is the space charge capacitance (in F cm⁻²), e is electronic charge in C, ε is the dielectric constant of the semiconductors (30 for BFO, at room temperature) [10], ε₀ is the permittivity of free space, N_A is the charge carrier density in cm⁻³, E_{fb} is the flat band potential in V, K is the Boltzmann constant and T is the temperature in K. The flat band potentials of the synthesized materials have been calculated from the MS plot by extrapolating the slope of the plots at 1/C² = 0, shows that E_{fb} shift towards more negative potential for Au/BFO-Ns heterostructures, indicating the better catalytic activity of the materials towards water reduction reaction (Table 5.2). The VB and CB potentials of BFO-Ns and Au/BFO-Ns have been calculated (Table 5.2) and the bandgap of BFO-Ns significantly narrowed to 2.05 eV from 2.3 eV. Next, the charge carrier concentration (N_d) at the junction has been calculated following the Eq. 5.5 [58].

Table 5.2 Electrochemical parameters calculated from Mott–Schottky plot for BFO-Ns and Au/BFO-Ns catalysts.

| Catalyst | E_{fb} in V vs Ag/AgCl | E_{CB} in V vs RHE | E_{VB} in V vs RHE | E_g in eV | N_d in cm⁻³ | W_{sc} in nm | L_D in nm |
|-----------------|---|---|---|--------------------------------|---|---------------------------------|--------------------------------|
| BFO-Ns | -0.473 | 0.14 | 2.46 | 2.32 | 0.47×10 ¹⁷ | 225 | 30.2 |
| Au/BFO-Ns | -0.541 | 0.07 | 2.12 | 2.05 | 0.92×10 ¹⁷ | 163 | 21.6 |

Therefore, it is clear that N_d has been increased after Au/BFO-Ns heterojunction formation in comparison to pure semiconductor BFO-Ns. The increased charge N_d at the semiconductor-electrolyte interface helps in better reduction of water molecules [59]. The space charge layer width (W_{sc}) and Debye length (L_D) of the semiconductors have been calculated further following the Eq. 5.6 and 5.7 as given below [60].

$$W_{sc} = \sqrt{\left(\frac{2\epsilon\epsilon_0 V_s}{eN_d} \right)} \quad (5.6)$$

$$L_D = \sqrt{\left(\frac{\epsilon\epsilon_0 KT}{e^2 N_d} \right)} \quad (5.7)$$

According to Eq. 5.6, W_{sc} is inversely proportional to the N_d, therefore, the thickness of the space charge layer of BFO-Ns reduces after heterostructures formation with Au NPs. The calculated

space charge layer width reduces from 225 nm to 163 nm for Au/BFO-Ns heterostructures at an applied potential of 0.1V vs Ag/AgCl (Table 5.2). This reduction of W_{sc} strongly indicates the formation of band bending at the electrode – electrolyte surface due to electron transfer from semiconductor to electrolyte as the electron density of semiconductor is much higher compared to junction point [61]. This band bending greatly affect the space charge layer which contribute in formation of electric field near the interfaces. For BFO-Ns (n-type materials) photoexcited holes are accumulated on the semiconductor surface which are consumed by the oxidation reactions while the electrons are transferred to the counter electrode and used in proton reduction to H_2 [57]. On the other hand, Debye length (L_D) is an important parameter for photochemistry and it is inversely proportional to the N_d (Eq 5.7). Basically, L_D is a length in which the mobile charge carriers screen out the maximum electric field and it is closely related to the space charge region. So, the lowering value of L_D for Au/BFO-Ns indicates the better charge transfer through the junction. The morphological effect on junction capacitance has also been analyzed and the result reveals that, Au/BFO-Ns heterostructures possesses the higher amount of charge carrier which may results better H_2 generation in photochemical process (Table 5.3). The flat-band potential of BFO-Ns is almost frequency dependent (Figure 5.11c). In addition, flat-band potential of Au/BFO-Ns is negatively shifted compared to other heterostructures, indicating the reduced charge carrier recombination by enhancing band bending at the interface (Figure 5.11d). Moreover, the above results suggest that, heterojunction formation increase the carrier concentration at the electrode – electrolyte interfaces by enhancing the specific surface area, reduce the bad gap of the semiconductor and space charge layer width which have crucial role in enhancing the photocatalytic efficiency.

Table 5.3 Electrochemical parameters calculated from Mott-Schottky plot of the Au/BFO heterostructures for three different morphologies of BFO.

| Catalyst | N_A in cm^{-3} | W_{sc} in nm | L_D in nm |
|------------|-----------------------|----------------|-------------|
| BFO/Au-Ns | 1.48×10^{17} | 56.02 | 17.03 |
| BFO/Au-Oct | 0.92×10^{17} | 71.06 | 21.6 |
| BFO/Au-Cyl | 0.82×10^{17} | 85.07 | 32.88 |

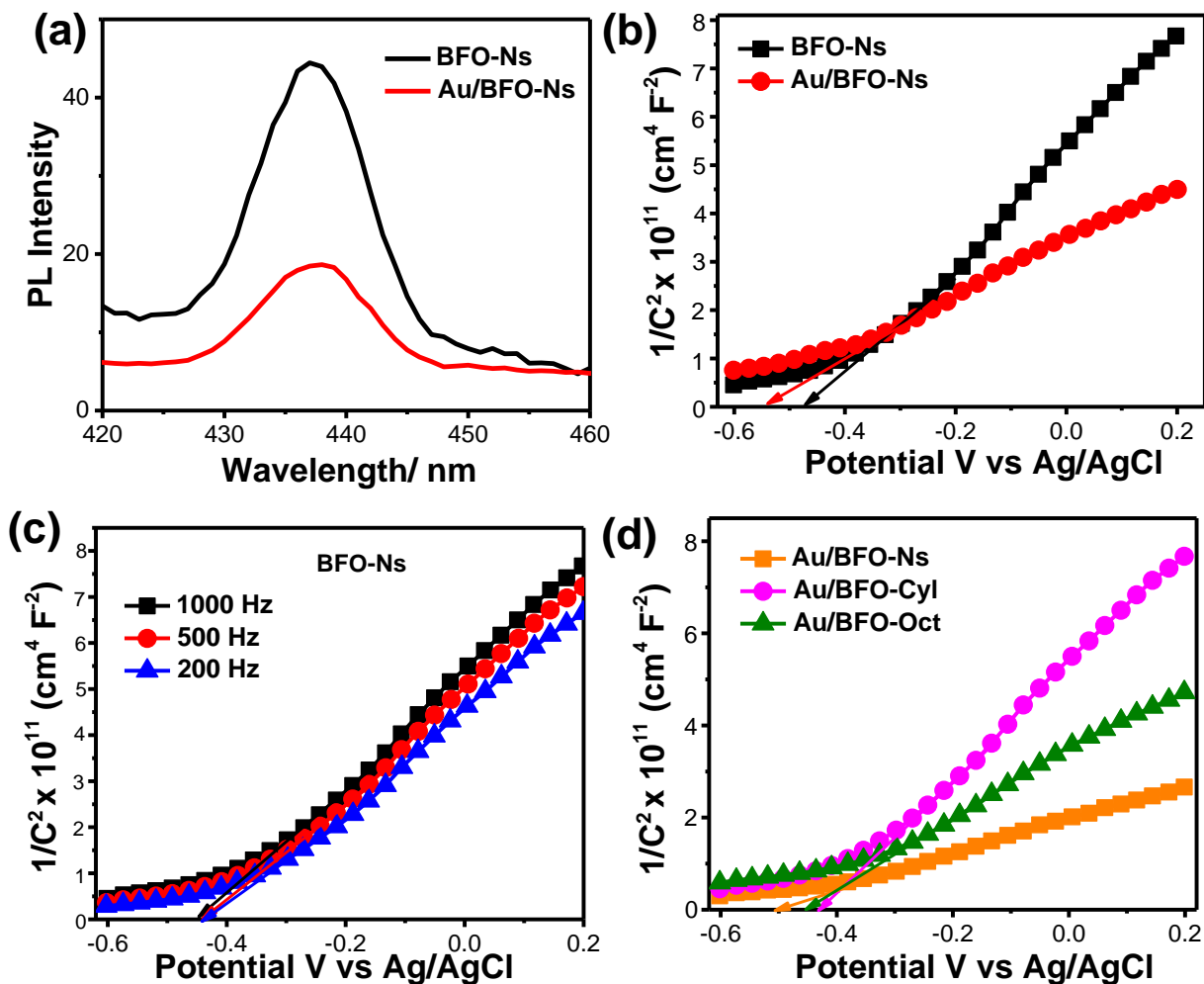


Figure 5.11 (a) Photoluminescence spectra of pure BiFeO_3 nanosheet (BFO-Ns) and Au/BFO-Ns heterostructures at an excitation of 380 nm. Mott–Schottky plots of (b) pure BFO-Ns and Au/BFO-Ns heterostructures and in the presence of 0.1 M Na_2SO_4 electrolytes (pH 7) using an AC frequency of 1000 Hz. The intercept of the plot (at $1/C^2 = 0$) has been used to determine the E_{fb} of the BFO-Ns and Au/BFO-Ns photoelectrodes. Effect of (c) frequency and (d) various morphology of BiFeO_3 (BFO nanosheet, octahedral shaped and cylindrical shaped nanostructures) on heterostructures in Mott–Schottky plot keeping other conditions same.

Further, the charge-transfer properties of the photocatalysts have been investigated by the electrochemical impedance spectra (EIS) measurement. Figure 5.12a represents the Nyquist plot of BFO-Ns and Au/BFO-Ns electrodes under light and dark, where a single semicircle has been obtained, confirms a single charge transfer mechanism of semiconductor–electrolyte interface under continuous light illumination [61]. The diameter of the semicircle represents the charge transfer resistance of the semiconductor–electrolyte interface. Thus, the low diameter for Au/BFO-Ns heterostructures implies the smaller resistance and better PEC performance compared to pure BFO-Ns semiconductor. The obtained curves are fitted with the Randles equivalent circuit model

and the fitting parameters are given in the Table 5.4. From the table, it is evident that, the ohmic resistance (R_s) decrease after heterostructures formation i.e. formation of better ohmic conductivity, which is helpful to improve the charge separation efficiency. Furthermore, the impedance study of Au/BFO-Ns electrode has been conducted in light and dark condition to understand the effect of light in charge transferring (Figure 5.12a). In presence of light, both BFO-Ns and Au/BFO-Ns show low charge-transfer resistance because of the enhanced diffusion of electrons with high mobility [62].

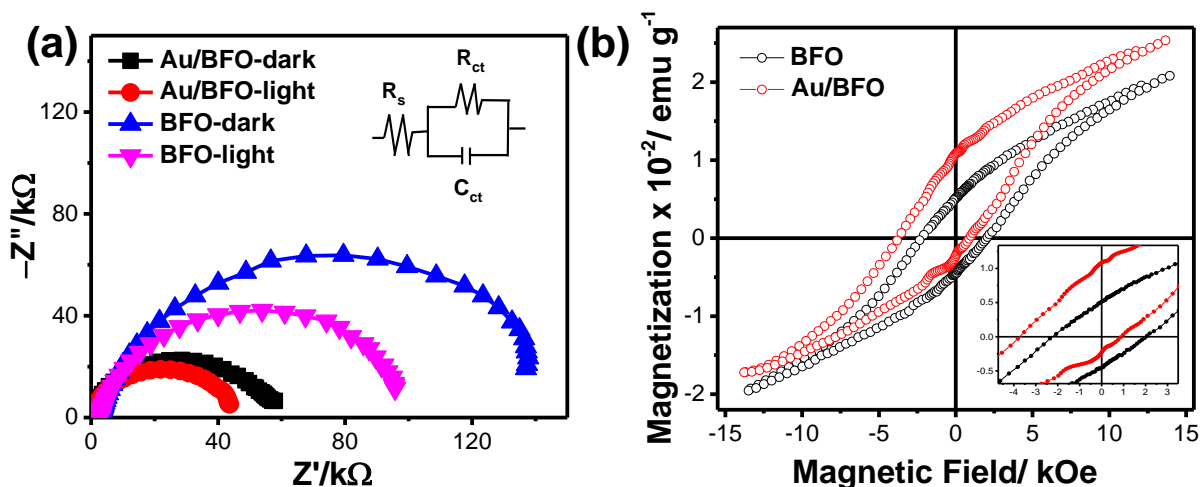


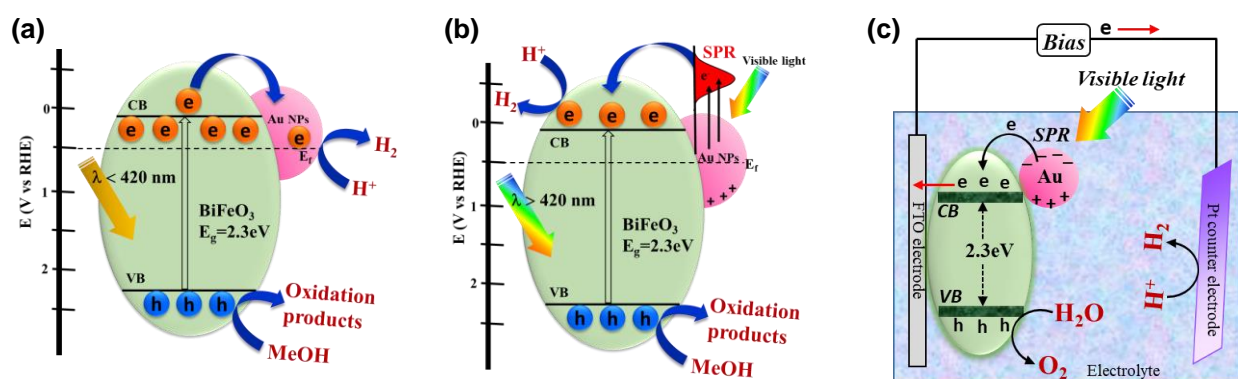
Figure 5.12 (a) Nyquist plot of BiFeO₃ nanosheet (BFO-Ns) and Au/BFO-Ns using same electrolyte under dark and light illumination of 100 mW/cm² at an applied potential 0.6V vs Ag/AgCl. Inset. Equivalent circuit model to analyze the Nyquist plot. (Nyquist plot under dark and light illumination. (b) Magnetic hysteresis loop for pure BiFeO₃ (BFO-Ns) and Au/BiFeO₃ heterostructures at room temperature. Inset: magnified views of the low field region.

Table 5.4 The Randles equivalent circuit fitting parameters of Nyquist plots for BFO and Au/BFO heterostructures.

| Catalyst | $R_s/k\Omega$ | $R_{ct}/k\Omega$ | $C_{ct}/\mu Mho$ | N |
|----------|---------------|------------------|------------------|-------|
| BFO | 161 | 137 | 4.39 | 0.911 |
| Au/BFO | 5.13 | 44.7 | 3.9 | 0.878 |

The magnetic hysteresis loop (M–H) for pure BFO-Ns and Au/BFO-Ns heterostructures have been measured at room temperature to understand the possible effect of magnetism on photocatalysis. As shown in Figure 5.12b, a typical ferromagnetic M–H curve with well-developed hysteresis loop has been observed for both BFO-Ns and Au/BFO-Ns heterostructures, however having low magnetization. The magnetization value is slightly increased for Au/BFO-Ns (0.025 emu/g)

compared to BFO-Ns (0.02 emu/g) at 1.5 kOe. Additionally, an exchange bias effect has been obtained for Au/BFO-Ns (inset Figure 5.12b) which may arise due to the suppression of spiral magnetic structure of BFO-Ns due to formation of heterostructure with Au NPs. However, there is an interface between Au and BFO within the Au/BFO heterostructures, which may induce a magnetic moment in metallic Au due to the magnetic proximity effect [63]. Such magnetic proximity effect arises in heterostructures due to the strong interfacial hybridization between BFO nanosheets and Au NPs which is described in the literatures [64]. As a result, the charge transfer property would be improved as both the elements of heterostructures possess magnetic moment and also a spin arrangement at the interface. Therefore, in presence of applied field, the injection rate of polarized carriers has been increased which leads to enhance current density as well as photocatalytic activity. From the above experimental results, it is clear that heterostructure formation facilitate the photocatalytic activity of BFO due to the combine effects of the strong absorption in visible region and compression of bandgap energy, efficient charge separation and the promotion of surface redox reactions. The photo generated charge separation within the Au/BFO heterostructures have been proposed in the schematic diagram (Scheme 5.1).



Scheme 5.1 Schematic representations of the band edges of Au/BiFeO₃ heterostructures and proposed mechanism of photocatalytic H₂ generation (a) when the incident light wavelength <math>< 420\text{ nm}</math>, (b) when the incident light wavelength $> 420\text{ nm}$, hot electron injection from the surface plasmon state of Au NPs to CB of BiFeO₃ in Au/BiFeO₃ heterostructures and (c) photoelectrochemical water splitting under visible light irradiation.

In general, the metal NPs possess the property of storing electrons and the electronic state within the metal NPs is continuous which follows the Fermi-Dirac distribution [37]. When the semiconductor and metal nanoparticles are in contact, a Schottky barrier would be formed *via* Fermi level equilibration between metals and semiconductor. First, the photogenerated electrons are distributed between the surface of BFO and Au NPs and then transfer of electrons from the

excited BFO into Au (Fermi level of Au +0.45 V vs RHE) occurs, which continues until the two systems attain equilibrium. The equilibrium alignment of the Fermi level for metal and semiconductor oxide built an electric field near the interface, which promotes the separation of photogenerated charge carriers and more reductive power for the heterostructured system (Scheme 5.1a) [65-67]. On the other hand, when visible light ($\lambda > 420$ nm) is illuminated on the Au/BFO heterostructures, resonance may happen with the incident photons and electrons, resulting the electronic oscillation with upshifted energy states which is greater than the conduction band (E_{CB}) of the neighbouring semiconductor. Under this circumstance, excited electrons of Au (generally called hot electrons) may transfer to the E_{CB} of the BFO (Scheme 5.1b) [68]. Next, reduction of water has been occurred by these excited electrons and generated H_2 from H^+ [26, 69, 70]. Simultaneously, holes are created in the valence band of BFO which can be quenched by the sacrificial agent (methanol) by reacting faster with it rather than water so that recombination of photogenerated electrons and holes would be hindered. Therefore, formation of metal-semiconductor heterojunction considered as a suitable route for enhancing the photocatalytic activity through water splitting under UV and visible light. Further, the possible mechanism of photoelectrochemical water splitting in presence of Au/BFO electrode, under visible light irradiation has been shown in Scheme 5.1c. Here, commercial Pt wire has been used as counter electrode. Under visible light illumination, hot electrons which are generated in the Au NPs due to SPR effect, are transferred into the CB of the BFO. These photogenerated electrons further transfer to the FTO and directly transported to the counter electrode as the external potential has been applied. Next, reduction of water has been occurred by these accumulated electrons at the counter electrode and generated H_2 . However, the photogenerated holes remaining in the photoanode can efficiently reduce the water molecules into H^+ and O_2 as they are located in the region of the water oxidation potential (1.23 eV).

Table 5.5 Comparative study of photocatalytic performance of $BiFeO_3$ based heterostructures for photocatalytic H_2 generation.

| S. No | Material | Amount of H_2 generation (μmol) | Reference |
|-------|--|--|-----------|
| 1. | $BiFeO_3/SrTiO_3$ composite | 4.2 | 17 |
| 2. | $BiFeO_3/Bi_2Fe_4O_9$ heterostructures | 800 | 18 |

| S. No | Material | Amount of H ₂ generation (μmol) | Reference |
|-------|--|--|---------------------|
| 3. | BiFeO ₃ –graphene nanohybrids | Not determined | 20 |
| 4. | Pt/ BiFeO ₃ | Not determined | 32 |
| 5. | Au/BiFeO ₃ | Water splitting, not determine the H ₂ generation | 33 |
| 6. | Au modified La doped BiFeO ₃ films | PEC water splitting, not determine the H ₂ generation | 34 |
| 7. | Ag/ BiFeO ₃ | Not determined | 36 |
| 8. | BiFeO ₃ /TiO ₂ Nanotube Arrays | Not determined | 62 |
| 9. | ITO/ BiFeO ₃ /Pt composite | 4000 | 70 |
| 10. | Au/BFO-Ns heterostructures | 20,200 | Present Work |
| 11. | Au/BFO-Oct heterostructures | 16800 | Present Work |
| 12. | Au/BFO- Cyl heterostructures | 8300 | Present Work |

5.4 Summary

In summary, we report a facile hydrothermal method followed by radiolysis for the fabrication of Au/BFO heterostructures without using any template and strong reducing agent and investigated photocatalytic H₂ generation as well as photoelectrochemical water splitting under visible light. The presence of Au NPs within BFO nanosheets enhances the visible light absorption by virtue of SPR effect. Consequently, two fold enhancements in photocatalytic H₂ generation have been achieved for Au/BFO heterostructures compared to pure BFO nanosheets. The heterostructure formation significantly improves the catalytic activity towards water oxidation by enhancing the photoelectrochemical current density (~3.8 times) and long-term stability under longer visible light illumination. In PEC measurements, 3.3% absorb photon to current conversion efficiency has been achieved for Au/BFO whereas 1.1% for pure BFO nanosheets at wavelength 320 nm. Further, Mott–Schottky and EIS measurements confirm effective charge separation at the interfaces of heterojunction which lead to enhance the photocurrent generation and H₂ evolution efficiencies compared to the bare BFO nanosheets. The present contribution represents a general route to synthesize other metal-perovskites based heterostructures as a visible light active photocatalysts for clean, sustainable, and renewable energy generation.

References

- [1] K. Sivula, R. V. Krol, Semiconducting materials for photoelectrochemical energy conversion. *Nat. Review Mater.* **1** (2016) 15010–15026.
- [2] S. J. A. Moniz, S. A. Shevlin, D. J. Martin, Z.-X. Guo, J. Tang, Visible-light driven heterojunction photocatalysts for water splitting – a critical review. *Energy Environ. Sci.* **8** (2015) 731–759.
- [3] T. Hisatomi, J. Kubota, K. Domen, Recent advances in semiconductors for photocatalytic and photoelectrochemical water splitting. *Chem. Soc. Rev.* **43** (2014) 7520–7535.
- [4] J. Xuan, W. J. Xiao, Visible-Light Photoredox Catalysis. *Angew. Chem., Int. Ed.* **51** (2012) 2–13.
- [5] S. Chen, T. Takata, K. Domen, Particulate photocatalysts for overall water splitting. *Nat. Rev. Mater.* **2** (2017) 17050–17067.
- [6] S. Ghosh, N. A. Kouame, L. Ramos, S. Remita, A. Dazzi, A. Deniset-Besseau, P. Beaunier, F. Goubard, P.-H. Aubert, H. Remita, Conducting polymer nanostructures for photocatalysis under visible light. *Nat. Mater.* **14** (2015) 505–511.
- [7] Y.-Y. Liu, H.-P. Zhang, B. Zhu, H.-W. Zhang, L.-D. Fan, X.-Y. Chai, Q.-L. Zhang, J.-H. Liu, C.-X. He, C/N-co-doped Pd coated Ag nanowires as a high-performance electrocatalyst for hydrogen evolution reaction. *Electrochim. Acta* **283** (2018) 221–227.
- [8] W. Wang, M. O. Tade, Z. Shao, Research progress of perovskite materials in photocatalysis- and photovoltaics-related energy conversion and environmental treatment. *Chem. Soc. Rev.* **44** (2015) 5371–5408.
- [9] G. Zhang, G. Liu, L. Wang, J. T. S. Irvine, Inorganic perovskite photocatalysts for solar energy utilization. *Chem. Soc. Rev.* **45** (2016) 5951–5984.
- [10] G. Catalan, J. F. Scott, Physics and Applications of Bismuth Ferrite. *Adv. Mater.* **21** (2009) 2463–2485.
- [11] T. Zhao, A. Scholl, F. Zavaliche, K. Lee, M. Barry, A. Doran, M. P. Cruz, Y. H. Chu, C. Ederer, N. A. Spaldin, R. R. Das, D. M. Kim, S. H. Baek, C. B. Eom, R. Ramesh, Electrical control of antiferromagnetic domains in multiferroic BiFeO₃ films at room temperature. *Nat. Mater.* **5** (2006) 823–829.

- [12] S. Y. Yang, J. Seidel, S. J. Byrnes, P. Shafer, C.-H. Yang, M. D. Rossell, P. Yu, Y.-H. Chu, J. F. Scott, J. W. Ager, L. W. Martin, R. Ramesh, Above-bandgap voltages from ferroelectric photovoltaic devices. *Nat. Nanotechnol.* **5** (2010) 143–147.
- [13] X. Wang, J. Zhang, Q. Peng, Y. D. Li, A general strategy for nanocrystal synthesis. *Nature* **437** (2005) 121–124.
- [14] L. Fei, J. Yuan, Y. Hu, C. Wu, J. Wang, Y. Wang, Visible Light Responsive Perovskite BiFeO₃ Pills and Rods with Dominant {111}c Facets. *Cryst. Growth Des.* **11** (2011) 1049–1053.
- [15] X. Bai, J. Wei, B. Tian, Y. Liu, T. Reiss, N. Guiblin, P. Gemeiner, . Dkhil, I. C. Infante, Size Effect on Optical and Photocatalytic Properties in BiFeO₃ Nanoparticles. *J. Phys. Chem. C* **120** (2016) 3595–3601.
- [16] X. Wang, W. Mao, Q. Zhang, Q. Wang, Y. Zhu, J. Zhang, T. Yang, J. Yang, X. Li, W. Huang, Magnetic phase transitions and giant magnetocaloric effect of Eu/TiO₃ nanowires. *J Alloys Compd.* **689** (2016) 63–68.
- [17] L. Lu, M. Lv, G. Liu, X. Xu, Photocatalytic hydrogen production over solid solutions between BiFeO₃ and SrTiO₃. *Appl. Surf. Sci.* **391** (2017) 535–541.
- [18] T. Zhang, Y. Shen, Y. Qiu, Y. Liu, R. Xiong, J. Shi, J. Wei, Facial Synthesis and Photoreaction Mechanism of BiFeO₃/Bi₂Fe₄O₉ Heterojunction Nanofibers. *ACS Sus. Chem. Eng.* **5** (2017) 4630–4636.
- [19] Y. P. Bhoi, B. G. Mishra, Photocatalytic degradation of alachlor using Type-II CuS/BiFeO₃ heterojunctions as novel photocatalyst under visible light irradiation. *Chem. Eng. J.* **344** (2018) 391–401.
- [20] Z. Li, Y. Shen, C. Yang, Y. Lei, Y. Guan, Y. Lin, D. Liu, C.-W. Nana, Significant enhancement in the visible light photocatalytic properties of BiFeO₃–graphene nanohybrids. *J. Mater. Chem. A* **1** (2013) 823–829.
- [21] J. Low, J. Yu, M. Jaroniec, S. Wageh, A. A. Al-Ghamdi, Heterojunction Photocatalysts. *Adv. Mater.* **29** (2017) 1601694–1601714.
- [22] S. J. A. Moniz, S. Ghosh (Ed), Visible-Light-Active Photocatalysis: Nanostructured Catalyst Design, Mechanisms and Applications, Wiley-VCH Verlag GmbH & Co. KGaA, Germany, Chapter 8, 2018, ISBN: 978-3-527-34293-8.

- [23] A. M. Díez, F. C. Moreira, B. A. Marinho, J. C. A. Espíndola, L. O. Paulista, M. A. Sanromán, M. Pazos, R. A. R. Boaventura, V. J. P. Vilar, A step forward in heterogeneous photocatalysis: Process intensification by using a static mixer as catalyst support. *Chem. Eng. J.* **343** (2018) 597–606.
- [24] S. Sardar, P. Kar, H. Remita, B. Liu, P. Lemmens, S. K. Pal, S. Ghosh, Enhanced Charge Separation and FRET at Heterojunctions between Semiconductor Nanoparticles and Conducting Polymer Nanofibers for Efficient Solar Light Harvesting. *Sci. Rep.* **5** (2015) 17313–17327.
- [25] S. Bera, S. Ghosh, R. N. Basu, Fabrication of Bi₂S₃/ZnO heterostructures: an excellent photocatalyst for visible-light-driven hydrogen generation and photoelectrochemical properties. *New J. Chem.* **42** (2018) 541–554.
- [26] S. Linic, P. Christopher, D. B. Ingram, Plasmonic-metal nanostructures for efficient conversion of solar to chemical energy. *Nat. Mater.* **10** (2011) 911–921.
- [27] S. Ghosh, A. K. Mallik, R. N. Basu, Enhanced photocatalytic activity and photoresponse of poly(3,4-ethylenedioxythiophene) nanofibers decorated with gold nanoparticle under visible light. *Solar Energy* **159** (2018) 548–560.
- [28] E. Grabowska, A. Zaleska, S. Sorgues, M. Kunst, A. Etcheberry, C. Colbeau-Justin, H. Remita, Modification of Titanium(IV) Dioxide with Small Silver Nanoparticles: Application in Photocatalysis. *J. Phys. Chem. C* **117** (2013) 1955–1962.
- [29] E. Kowalska, M. Janczarek, L. Rosa, S. Juodkazis, B. Ohtani, Mono- and bi-metallic plasmonic photocatalysts for degradation of organic compounds under UV and visible light irradiation. *Catal. Today* **230** (2014) 131–137.
- [30] A. L. Luna, D. Drago, K. Wang, P. Beaunier, E. Kowalska, B. Ohtani, D. B. Uribe, M. A. Valenzuela, H. Remita, C. Co.-Justin, Photocatalytic Hydrogen Evolution Using Ni–Pd/TiO₂: Correlation of Light Absorption, Charge-Carrier Dynamics, and Quantum Efficiency. *J. Phys. Chem. C* **121** (2017) 14302–14311.
- [31] S. Anwer, G. Bharath, S. Hongmei, Q. Tariq, M. Kin, L. Wesley, Synthesis of edge-site selectively deposited Au nanocrystals on TiO₂ nanosheets: An efficient heterogeneous catalyst with enhanced visible-light photoactivity. *Electrochim. Acta* **283** (2018) 1095–1104.

- [32] F. Niu, D. Chen, L. Qin, T. Gao, N. Zhang, S. Wang, Z. Chen, J. Wang, X. Sun, Y. Huang, Synthesis of Pt/BiFeO₃ heterostructured photocatalysts for highly efficient visible-light photocatalytic performances. *Sol. Energy Mater. Sol. Cells* **143** (2015) 386–396.
- [33] S. Li, J. Zhang, M. G. Kibria, Z. Mi, M. Chaker, D. Ma, R. Nechache, F. Rosei, Remarkably enhanced photocatalytic activity of laser ablated Au nanoparticle decorated BiFeO₃ nanowires under visible-light. *Chem. Commun.* **49** (2013) 5856–5858.
- [34] F. Z. Li, H. W. Zheng, M. S. Zhu, X. A. Zhang, G. L. Yuan, Z. S. Xie, X. H. Li, G. T. Yue, W. F. Zhang, Photovoltaic enhancement by Au surface-plasmon effect for La doped BiFeO₃ films. *J. Mater. Chem. C* **5** (2017) 10615–10623.
- [35] S. Mohan, B. Subramanian, G. Sarveswaran, A prototypical development of plasmonic multiferroic bismuth ferrite particulate and fiber nanostructures and their remarkable photocatalytic activity under sunlight. *J. Mater. Chem. C* **2** (2014) 6835–6842.
- [36] A. M. Schultz, Y. Zhang, P. A. Salvador, G. S. Rohrer, Effect of Crystal and Domain Orientation on the Visible-Light Photochemical Reduction of Ag on BiFeO₃. *ACS Appl. Mater. Interfaces* **3** (2011) 1562–1567.
- [37] P. Zhang, T. Wang, J. Gong, Mechanistic Understanding of the Plasmonic Enhancement for Solar Water Splitting. *Adv. Mater.* **27** (2015) 5328–5342.
- [38] J. Liu, Y. Liu, N. Liu, Y. Han, X. Zhang, H. Huang, Y. Lifshitz, S.-T. Lee, J. Zhong, Z. Kang, Metal-free efficient photocatalyst for stable visible water splitting via a two-electron pathway. *Science* **347** (2015) 970–974.
- [39] H. Suzuki, O. Tomita, M. Higashi, R. Abe, Two-step photocatalytic water splitting into H₂ and O₂ using layered metal oxide KCa₂Nb₃O₁₀ and its derivatives as O₂-evolving photocatalysts with IO³⁻/I⁻ or Fe³⁺/Fe²⁺ redox mediator. *Catal. Sci. Technol.* **5** (2015) 2640–2648.
- [40] J. Belloni, M. Mostafavi, H. Remita, J.-L. Marignier, M.-O. Delcourt, Radiation-induced synthesis of mono- and multi-metallic clusters and nanocolloids. *New J. Chem.* **22** (1998) 1239–1255.
- [41] S. Ghosh, S. Bera, S. Bysakh, R. N. Basu, Conducting polymer nanofiber-supported Pt alloys: unprecedented materials for methanol oxidation with enhanced electrocatalytic performance and stability. *Sustainable Energy Fuels* **1** (2017) 1148–1161.

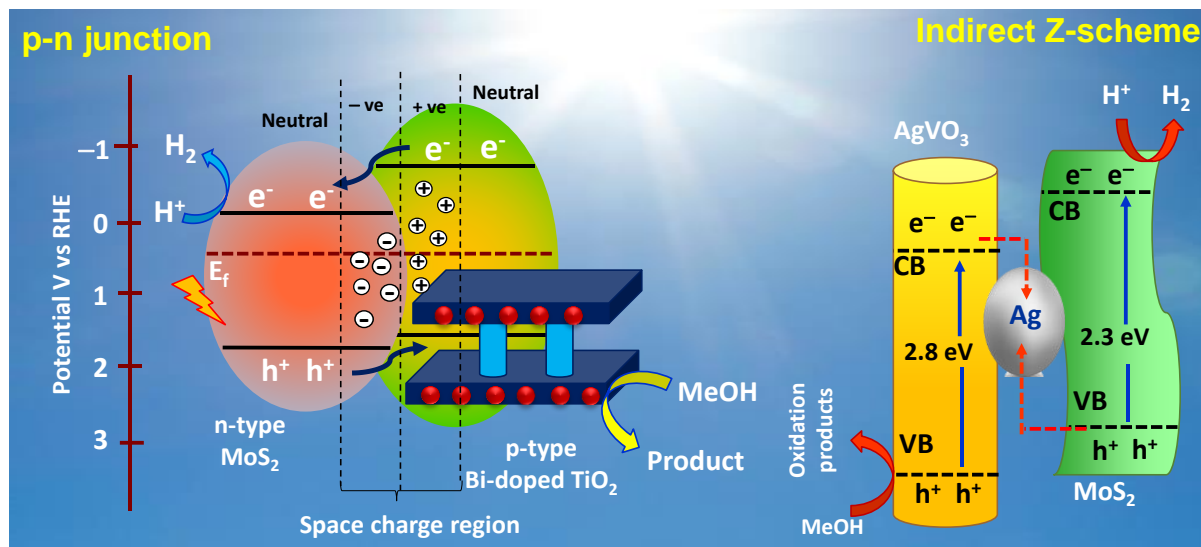
- [42] S. Ghosh, S. Bera, S. Bysakh, R. N. Basu, Highly Active Multimetallic Palladium Nanoalloys Embedded in Conducting Polymer as Anode Catalyst for Electrooxidation of Ethanol. *ACS Appl. Mater Interfaces* **9** (2017) 33775–33790.
- [43] S. J. A. Moniz, R. Q.-Cabrera, C. S. Blackman, J. Tang, P. Southern, P. M. Weaver, C. J. Carmalt, A simple, low-cost CVD route to thin films of BiFeO₃ for efficient water photo-oxidation. *J. Mater. Chem. A* **2** (2014) 2922–2927.
- [44] G. S. Pozan, M. Isleyen, S. Gokcen, Transition metal coated TiO₂ nanoparticles: Synthesis, characterization and their photocatalytic activity. *Appl. Catal. B: Environ.* **140** (2013) 537–545.
- [45] J. Jiang, J. Zou, M. N. Anjum, J. C. Yan, L. Huang, Y. X. Zhang, J. F. Chen, Synthesis and characterization of wafer-like BiFeO₃ with efficient catalytic activity. *Solid State Sci.* **13** (2011) 1779–1785.
- [46] I. Papadas, J. A. Christodoulides, G. Kioseoglou, G. S. Armatas, A high surface area ordered mesoporous BiFeO₃ semiconductor with efficient water oxidation activity. *J. Mater. Chem. A* **3** (2015) 1587–1593.
- [47] C.-J. Tsai, C.-Y. Yang, Y.-C. Liao, Y.-L. Chueh, Hydrothermally grown bismuth ferrites: controllable phases and morphologies in a mixed KOH/NaOH mineralizer. *J. Mater. Chem. C* **22** (2012) 17432–17436.
- [48] L. Gai, Q. Mei, X. Qin, W. Li, H. Jiang, X. Duan, Controlled synthesis of anatase TiO₂ octahedra with enhanced photocatalytic activity. *Mater. Res. Bull.* **48** (2013) 4469–4475.
- [49] A. H. Khan, S. Ghosh, B. Pradhan, A. Dalui, L. K. Shrestha, S. Acharya, K. Ariga, Two-Dimensional (2D) Nanomaterials towards Electrochemical Nanoarchitectonics in Energy-Related Applications. *Bull. Chem. Soc. Jpn.* **90** (2017) 1–21.
- [50] Y. Chao, J. Zheng, H. Zhang, F. Li, F. Yan, Y. Tan, Z. Zhu, Oxygen-incorporation in Co₂P as a non-noble metal cocatalyst to enhance photocatalysis for reducing water to H₂ under visible light. *Chem. Eng. J.* **346** (2018) 281–288.
- [51] M. Zhu, Y. Du, P. Yang, X. Wang, Donor–acceptor porphyrin functionalized Pt nano-assemblies for artificial photosynthesis: a simple and efficient homogeneous photocatalytic hydrogen production system. *Catal. Sci. Technol.* **3** (2013) 2295–2302.
- [52] M. Wang, S. Shen, L. Li, Z. Tang, J. Yang, Effects of sacrificial reagents on photocatalytic hydrogen evolution over different photocatalysts. *J. Mater. Sci.* **52** (2017) 5155–5164.

- [53] G. Liu, N. Li, Y. Zhao, R. Yao, M. Wang, D. He, J. Li, Fabrication of Fe-doped Co₂P nanoparticles as efficient electrocatalyst for electrochemical and photoelectrochemical water oxidation. *Electrochim. Acta* **283** (2018) 1490–1497.
- [54] D. Kong, H. Wang, Z. Lu, Yi Cui, CoSe₂ Nanoparticles Grown on Carbon Fiber Paper: An Efficient and Stable Electrocatalyst for Hydrogen Evolution Reaction. *J. Am. Chem. Soc.* **136** (2014) 4897–4900.
- [55] L.-C. Chen, J.-C. Chen, C.-C. Chen, C.-G. Wu, Fabrication and Properties of High-Efficiency Perovskite/PCBM Organic Solar Cells. *Nanoscale Res. Letters* **10** (2015) 312–317.
- [56] J. Zhao, P. Zhang, Z. Wang, S. Zhang, H. Gao, J. Hu, G. Shao, Direct evidence of multichannel improved charge-carrier mechanism for enhanced photocatalytic H₂ evolution. *Sci. Rep.* **7** (2017) 16116–16127.
- [57] A. Zhu, Q. Zhao, X. Li, Y. Shi, BiFeO₃/TiO₂ Nanotube Arrays Composite Electrode: Construction, Characterization, and Enhanced Photoelectrochemical Properties. *ACS Appl. Mater. Interfaces* **6** (2014) 671–679.
- [58] K. Gelderman, L. Lee, S. W. Donne, Flat-Band Potential of a Semiconductor: Using the Mott–Schottky Equation. *J. Chem. Educ.* **84** (2007) 685–689.
- [59] N. Zhang, D. Chen, F. Niu, S. Wang, L. Qin, Y. Huang, Enhanced visible light photocatalytic activity of Gd-doped BiFeO₃ nanoparticles and mechanism insight. *Sci. Rep.* **6** (2016) 26467–26478.
- [60] L. Palmisano, V. Augugliaro, A. Sclafani, M. Schiavello, Activity of chromium-ion-doped titania for the dinitrogen photoreduction to ammonia and for the phenol photodegradation. *J. Phys. Chem.* **92** (1988) 6710–6713.
- [61] S. Shyamal, P. Hajra, H. Mandal, A. Bera, D. Sariket, A. K. Satpati, S. Kundu, C. Bhattacharya, Benign role of Bi on an electrodeposited Cu₂O semiconductor towards photo-assisted H₂ generation from water. *J. Mater. Chem. A* **4** (2016) 9244–9252.
- [62] G. Zhang, L. Zhang, Y. Liu, L. Liu, C.-P. Huang, H. Liu, J. Li, Substitution Boosts Charge Separation for High Solar-Driven Photocatalytic Performance. *ACS Appl. Mater. Interfaces* **8** (2016) 26783–26793.

- [63] Z. Wang, C. Tang, R. Sachs, Y. Barlas, J. Shi, Proximity-Induced Ferromagnetism in Graphene Revealed by the Anomalous Hall Effect. *Phys. Rev. Lett.* **114** (2015) 016603–016606.
- [64] J. Li, Q. Pei, R. Wang, Y. Zhou, Z. Zhang, Q. Cao, D. Wang, W. Mi, Y. Du, Enhanced Photocatalytic Performance through Magnetic Field Boosting Carrier Transport. *ACS Nano* **12** (2018) 3351–3359.
- [65] C. Gu, B. C. Norris, F.-R. F. Fan, C. W. Bielawski, A. J. Bard, Is Base-Inhibited Vapor Phase Polymerized PEDOT an Electrocatalyst for the Hydrogen Evolution Reaction? Exploring Substrate Effects, Including Pt Contaminated Au. *ACS Catal.* **2** (2012) 746–750.
- [66] J. L. Fernández, V. Raghuvver, A. Manthiram, A. J. Bard, Pd-Ti and Pd-Co-Au Electrocatalysts as a Replacement for Platinum for Oxygen Reduction in Proton Exchange Membrane Fuel Cells. *J. Am. Chem. Soc.* **127** (2005) 13100–13101.
- [67] V. Subramanian, E. E. Wolf, P. V. Kamat, Catalysis with TiO₂/Gold Nanocomposites. Effect of Metal Particle Size on the Fermi Level Equilibration. *J. Am. Chem. Soc.* **126** (2004) 4943–4950.
- [68] X. Zhang, Y. L. Chen, R.-S. Liu, D. P. Tsai, Plasmonic photocatalysis. *Rep. Prog. Phys.* **76** (2013) 046401–046442.
- [69] D. Mateo, I. E.-Adell, J. Albero, J. F. S. Royo, A. Primo, H. Garcia, 111 oriented gold nanoplatelets on multilayer graphene as visible light photocatalyst for overall water splitting. *Nat. Commun.* **7** (2016) 11819–11827.
- [70] S. Gu, X. Zhou, F. Zheng, L. Fang, W. Dong, M. Shen, Improved photocathodic performance in Pt catalyzed ferroelectric BiFeO₃ films sandwiched by a porous carbon layer. *Chem. Commun.* **53** (2017) 7052–7055.

CHAPTER 6

Assemble of Bi-Doped TiO_2 and Ag-AgVO $_3$ onto 2D MoS $_2$: Efficient p-n Heterojunction and All Solid State Z-Scheme for Photocatalytic H $_2$ generation under Visible Light



6.1 Introduction

The ongoing concerns regarding environmental pollution and energy crisis have stimulated current research to explore sustainable and clean energy sources [1-3]. In this respect, sunlight-driven water splitting using particular photocatalyst has attracted significant attention as a green approach for large-scale production of renewable solar hydrogen, which in turn a promising alternative as renewable energy because of zero carbon emission and high energy density [4-10]. The steps in photocatalytic water splitting are absorption of photon by the catalyst, leading to formation of photogenerated electrons and photoinduced holes, then migration of excited charge carriers towards the surface where oxidation and reduction reactions take place [4, 6]. Thus, several parameters such as ability to absorb a wide range of the solar spectrum, efficient charge transfer and oxidation reduction are very crucial to improve the overall efficiency. Therefore, the focus of the current research is the development of novel photocatalysts which can possess a high light harvesting efficiency along with the improved charge migration.

Semiconductors are widely used as photocatalyst to harvest solar energy directly and convert into chemical energy which could be useful for organic pollutant removal, water reduction to generate H₂, CO₂ reduction etc. [10-13]. TiO₂ has been considered as most efficient photocatalyst because of its high oxidizing ability, however, the limited absorption in the UV region and slow charge transfer rate result in low hydrogen conversion efficiency and quantum efficiency. Moreover, the fast recombination rate of electrons and holes due to the high density of the trap state reduce the oxidation ability of TiO₂ [14]. To overcome this drawback and to extend its spectral response to visible light, different methods have been followed, including metal and non-metal doping [12, 15, 16], coupling of TiO₂ with other semiconductor materials [17, 18], polymers [19, 20], graphene [21], dye sensitization [22], Mott-Schottky junctions with metals such as Au, Ag, Pt, Bi, Cu, [23, 24] crystal facet engineering etc. Doping is considered as an effective route to extend the light absorption towards longer wavelengths by introducing additional energy states within the valence band (VB) and conduction band (CB) of the TiO₂. These additional states can inhibit the electrons-holes recombination by trapping the excited carriers [25]. In this way, more charge carriers could be successfully diffused to the surface of the photocatalyst and facilitates the charge separation. In particular, doping of Bi³⁺ into semiconductor photocatalysts may influence the luminescence efficiency by reducing the photo-induced electron-hole recombination, which further improves the catalytic performance [26-30]. Additionally, oxygen vacancy can be generated at the intermediate

level that may trap electrons to form the active radicals. Very recently, Li et al. [31] showed that doping of Bi^{3+} into ZnWO_4 semiconductor enhanced the photocatalytic activity for NO removal due to formation of oxygen vacancy. These oxygen vacancy increase the oxygen molecule adsorption at the semiconductor surface to generate superoxide radicals ($\text{O}_2^{\bullet-}$). Wu et al. [28] also reported that the optimal doping of Bi (1.0 mol%, both Bi^{3+} and Bi^0 state exists in ratio of 3: 1) into TiO_2 lattice enhanced the photocatalytic H_2 generation and Rhodamine B decolorization. On the other hand, semimetal Bi^0 can also exhibits a direct surface plasmonic resonance effect like novel metals (Au, Pd, Ag, Pt), that enhances the light absorption up to visible region [28]. Thus, Bi^0 has been considered as one of the promising candidate to increase the visible light harvesting and photocatalytic activity. For example, Lv et al. [32] fabricated Bi– $\text{Bi}_2\text{MoO}_6/\text{CdS}$ -DETA all-solid-state Z-scheme heterostructures which exhibited high H_2 generation through water splitting due to surface plasmonic resonance effect of Bi nanoparticles. Bi promoted a novel Z- Scheme Bi– BiOCl/AgCl heterojunction has been developed by Du et al. [33], which showed five times enhanced H_2 generation rate compared to bare BiOCl under visible light due to improved electron–hole transfer and separation through Bi. Moreover, Bi-nanoparticles can form Schottky barrier when it attached with other semiconductors and provide internal electric field to accelerate the charge separation efficiency. Recently, Hao et al. [34] demonstrated that presence of Bi^0 on the surface of Bi-doped (in Bi^{3+} state) TiO_2 formed Mott-Schottky junction, which promoted the light harvesting and the charge transfer ability. Magnussion et al. [35] also developed a Schottky barrier between Bi nanoparticles and ZnO through photoelectron spectroscopy under ultrahigh-vacuum conditions. It is clear that Bi doping either in Bi^0 state or Bi^{3+} state into the semiconductor band structure could lead a positive impact to improve the solar light absorption ability for longer wavelengths. However, the efficiency of the photocatalytic reaction may control by the oxidation state of the Bi which play a key role in bandgap engineering. Thus, mechanistic understanding of the valence state of metal dopant in the photocatalytic reactions is of significant important.

Beyond conventional semiconductors, transition-metal dichalcogenide materials, consisting of single or few-atom thick covalently bonded lattices have attracted immense interest in photocatalysis due to some unique properties, such as optical, electrical, photonic, mechanical, catalytic etc. which are originated from two-dimensional (2D) layered structure [36, 37]. Among transition-metal dichalcogenides, single or few layers molybdenum disulfide (MoS_2) found to be very attractive in terms of physical, electrochemical properties and mainly applied in diverse areas;

for examples photovoltaics [38], energy storage [39,40], supercapacitors [41], biosensors [42] and photocatalytic H₂ generation [43-47]. Bulk MoS₂ is an indirect bandgap semiconductor (bandgap~1.2 eV) and showed indirect to direct bandgap transition for monolayer MoS₂ (~1.9 eV) due to the quantum confinement effects [48, 49]. Interestingly, the coordination of the Mo atom and its d-electrons have a crucial role in determining the electronic structure of MoS₂, makes it an important candidate for photocatalysis. Moreover, the dangling bonds and unsaturated coordination of MoS₂ edges offers opportunities for surface-active applications [50-53]. MoS₂ can fabricate a van der Waals heterostructure by vertically stacked with other semiconductor, which overcome the weakness of single 2D layered material and extend its electronic and optoelectronic properties by introducing new physics at the interface. For example, n-type monolayer MoS₂ developed a p-n junction with type-II band alignment after stacking on p-type WSe₂ [54]. Ceballos et al. [55] showed ultrafast charge separation and long-lived interlayer excitons in out-of-plane MoS₂-MoSe₂ heterostructure. Recently, Li et al. [44] fabricated (MoS₂-TiO₂)/Au ternary component hybrid materials which enhance the photoelectrochemical current density under visible light. Moreover, MoS₂ has been reported as an efficient electrocatalyst for H₂ evolution reaction through water splitting, owing to the nanosized edge defects which are preferential for H₂ adsorption [45-47]. Thus, few-layered MoS₂ nanosheets may serve as co-catalyst for improving the efficiency of H₂ evolution.

On the other hand, silver vanadium oxide (AgVO₃) have attracted enormous attention in photocatalysis due to its high crystallinity and low bandgap (2.6 eV) with visible light absorption [48]. Unique hybridization of V 3d, O 2p and Ag 4d orbitals in AgVO₃ gives rise to a highly dispersed valence band (VB), resulting in a narrow bandgap, however, poor charge separation capability remains an unresolved issue [49]. In another example, Liu et al. [50] developed Z-scheme composite of g-C₃N₄@Ag/AgVO₃ which exhibited higher photocatalytic activity for dye degradation and antibacterial disinfection under visible light irradiation. Wang et al. [51] fabricated Z-scheme Ag/AgI/AgVO₃ nanocomposites by a facile *in-situ* ion-exchange method and showed selective oxidation of benzylic amine to imine and reduction of toxic Cr(VI) ions under visible light due to formation of charge migration bridge by Ag⁰ species which effectively enhance the charge separation between AgI and AgVO₃. Although, reported silver based Z-scheme system have shown excellent catalytic activity for organic pollutant degradation [52-54], water splitting

[55-58], CO₂ reduction [59, 60], degradation of antibiotics [51, 61] etc. but AgVO₃ based Z-scheme system for photocatalytic H₂ generation has not been tested yet.

Herein, a heterostructures has been developed by assemble of Bi modified TiO₂ nanoparticles on the surface MoS₂ nanosheets by chemical method. Introduction of Bi into the TiO₂ crystal reduce the bandgap of TiO₂ and make it suitable for visible light absorption whereas, presence of MoS₂ in the heterostructures enhances the H₂ generation activity by water reduction. At the same time, MoS₂/Ag-AgVO₃ heterostructures has been fabricated for photocatalytic H₂ generation under visible light. The fast interfacial charge transfer efficiency of MoS₂/Bi-TiO₂ and MoS₂/Ag-AgVO₃ heterostructures have been explained by photoelectrochemical analysis. Possible p-n junction and all solid state Z-scheme charge transfer mechanism have been proposed for MoS₂/Bi-TiO₂ and MoS₂/Ag-AgVO₃ heterostructures by analysing the energy-band structure of the component elements.

6.2 Experimental

Bulk molybdenum sulphide (MoS₂) powder, Bi(NO₃)₃. 5H₂O, polyvinylpyrrolidone (PVP), TiO₂ powder, Silver nitrate (AgNO₃, 99%), ammonium monovanadate (NH₄VO₃, 99%) and ethanol (C₂H₅OH), methanol (CH₃OH) were procured from the Sigma Aldrich, USA. All the chemicals had been used as received. Ultrapure water was used as solvent (18.2 MΩ cm).

Few layers of MoS₂ nanosheets were synthesized by surfactant assisted exfoliation method followed by the similar method developed by Wang et al. [56] with some modification. MoS₂ powder (0.4 g) and 0.5 g of PVP as stabilizer were dispersed in 200 ml of deionized water and stirred vigorously for 30 mins at 70°C. Then, the solution was bath sonicated for 1h and then probe sonicated for 4h at 50 kHz frequency. Finally, washing and centrifugation were done at 10,000 rpm for five times using water, ethanol and then dried in an oven at 60°C [45].

A series of Bi doped TiO₂ (Bi-TiO₂) having different molar concentration of Bi(NO₃)₃. 5H₂O, (1 – 5 mM) were prepared by a facile chemical reduction method. At first, 50 mg TiO₂ was dispersed in 50 ml deionized water by stirring for 30 mins. After that, the certain amount of Bi(NO₃)₃. 5H₂O was added and stirred for another 15 mins. At the same time, 10 ml NaBH₄ (3 –15 mM) solution was prepared which was added dropwise into the above solution and stirred for 10 mins. The amount of Bi(NO₃)₃. 5H₂O and the NaBH₄ was taken in a 1: 3 molar ratio. Next, the sample was collected by centrifugation with water, ethanol and dried overnight in an oven (60°C).

At first, 50 mg ultrasonicated MoS₂ was dispersed in 50 ml of deionized water and stirred for 30 min. Then 10 weight % of Bi-doped TiO₂ (using 2 mM of Bi) was added into the mixture with continuous vigorous stirring at room temperature for 24h in dark condition. The concentration of Bi-doped TiO₂ is varied from 1, 5, 10 to 20 weight % and levelled as MBT-1, MBT-5, MBT-10 and MBT-20. The final solution was centrifuged at 12000 rpm for several times. After drying the precipitate at 60°C for overnight, MoS₂/Bi-TiO₂ composites were ready for photocatalytic application.

The MoS₂/Ag-AgVO₃ heterostructures were synthesized by co-precipitation (CP) method. At first, the prepared MoS₂ nanosheet (35 mg) was dispersed in 35 ml of deionized water with vigorous stirring for 30 mins. Next, 10 mmol of AgNO₃ was added into the above solution and stirred for 30 mins at room temperature. At the same time 10 mmol of NH₄VO₃ solution were prepared in another 35 ml of water. After that, the NH₄VO₃ solutions were mixed with the above solution quickly. A precipitation had been occurred and the solution colour changed into yellow. The co-precipitation was collected, washed with distilled water and ethanol several times, and finally dried in an oven at 50°C for overnight. The Ag-AgVO₃ was prepared to compare the data by following the same method without using MoS₂.

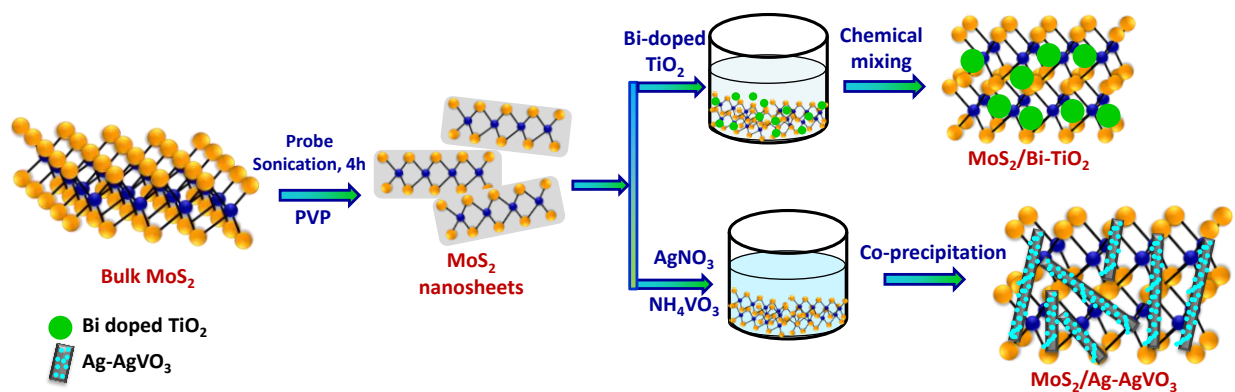
The morphology, size and analysis of elements were studied by FESEM (Carl-Zeiss, LEO. 430i, Sigma) and TEM (Tecnai G², 30ST). Phase purity of the synthesized materials was confirmed by XRD within 20° to 80° (2θ range) at 40 kV and 40 mA. A Cu Kα radiation was used in Philips X'Pert, The Netherlands to obtain the X-ray beam. Raman spectra of the synthesized material were studied by Jobin Yvon HR800 instrument to get the idea of number of layers, phase and defects in the MoS₂, as well as the crystallinity, phase composition of the TiO₂ and AgVO₃. A 540 nm laser beam had been employed on the sample surface. Further, valence of the elements was confirmed by XPS spectroscopy using PHI 5000 spectrophotometer, Versa Probe II. The optical properties of the materials were studied by Shimadzu, UV-3600 spectrophotometer and photocatalytic H₂ evolution rate were determined by online gas chromatography through the YL Instrument, 6500GC system. The thermal stability of the materials was investigated using thermogravimetric analysis (TGA, NETZSCH, STA 449 F3, Jupiter). The test was carried out in air with a heating rate of 10°C min⁻¹ from room temperature to 800°C. The Bi content in the TiO₂ was determined by a Spectro Ciros Vision inductively coupled plasma atomic-emission spectroscopy (ICPAES) instrument, Spectro GmbH, Germany.

Online gas chromatography was employed to measure the H₂ generation rate quantitatively. Water-methanol Ar saturated solution of 50 mL (25 volume % methanol) having 25 mg catalyst had been taken in a closed reactor. H₂ generation was measured under continuous light illumination of 100 mW cm⁻² from a Xe-arc lamp (250W). Photoelectrochemical properties of the materials were measured by galvanostat-potentiostat (Autolab, PGSTAT302N, The Netherlands). A Pt wire, saturated Ag/AgCl electrode and a thin film of as prepared material on FTO were used as counter electrode, reference electrode and working electrode respectively. The linear sweep voltammograms (LSV) of the prepared photoanodes were taken in presence of 0.1 M Na₂SO₄ phosphate buffer (pH 7) within the potential of -0.4V to 1V vs Ag/AgCl at a scan rate 10 mV s⁻¹ under light illumination. Chronoamperometry (CA) was employed to check the stability and light sensitivity of the prepared photoanodes at 0.26V vs Ag/AgCl under chopping condition. The obtained potentials were converted into reversible hydrogen electrode (RHE) by following the equation 5.1. Next, junction capacitance and the charge transfer resistance of the photoelectrodes were measured through Mott-Schottky (M-S, potential range -1.0V to 1.5V vs Ag/AgCl, frequency → 1000 Hz, voltage → 10 mV) and Nyquist experiments

6.3 Results and Discussion

6.3.1 Morphology

The synthesis strategy for MoS₂/Bi-TiO₂ and MoS₂/Ag-AgVO₃ heterostructures has been shown in Scheme 6.1.



Scheme 6.1 Schematic depiction of synthesis of MoS₂/Bi-TiO₂ and MoS₂/Ag-AgVO₃ heterostructures by chemical mixing and co-precipitation method, respectively.

The morphology and microstructural properties of the MoS₂ and the composites have been studied by FESEM, TEM and high resolution TEM (HRTEM). Figure 6.1a and 1b shows the FESEM images of MoS₂ powders before and after probe sonication.

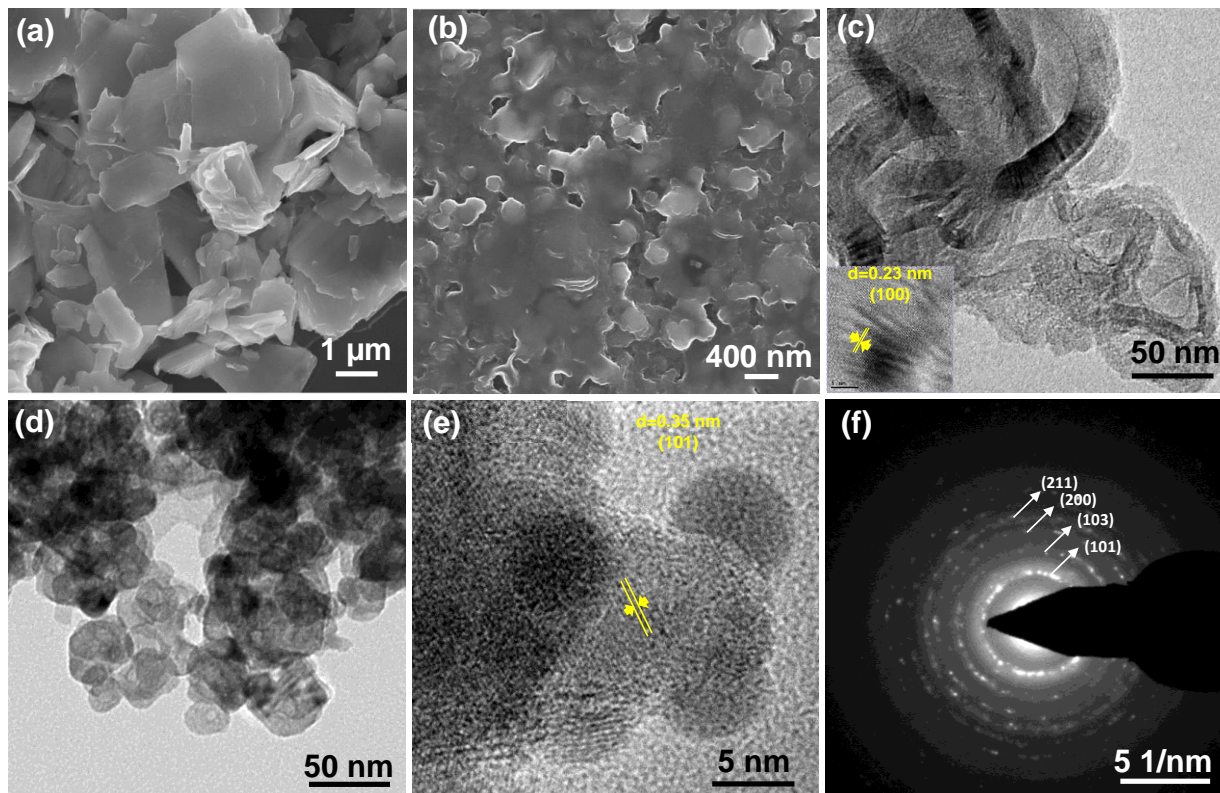


Figure 6.1 FESEM images of (a) bulk MoS₂ powder, (b) MoS₂ nanosheets. TEM images of (c) MoS₂ nanosheets, (d) Bi modified TiO₂ (using 2 mM Bi), (e) high resolution (HRTEM) and (f) selected area electron diffraction pattern of Bi modified TiO₂ (using 2 mM Bi).

It can be clearly observed that thin layers of MoS₂ nanosheets are formed after 4h probe sonication from MoS₂ powder (Figure 6.1b). Figure 6.1c shows the TEM image of MoS₂ nanosheets, consists of multiple layers which are highly crystalline. The HRTEM identifies lattice fringe of 0.23 nm (inset of Figure 6.1c) corresponding to the (100) hexagonal facets of MoS₂ [44]. Figure 6.1d and 1e present TEM and HRTEM images of TiO₂ nanoparticles after Bi modification, where the crystal fringe of 0.35 nm identifies the (101) planes of TiO₂ in anatase phase [47]. Moreover, polycrystalline nature of TiO₂ nanoparticles has been confirmed by the selected area electron diffraction pattern (SAED) (Figure 6.1f).

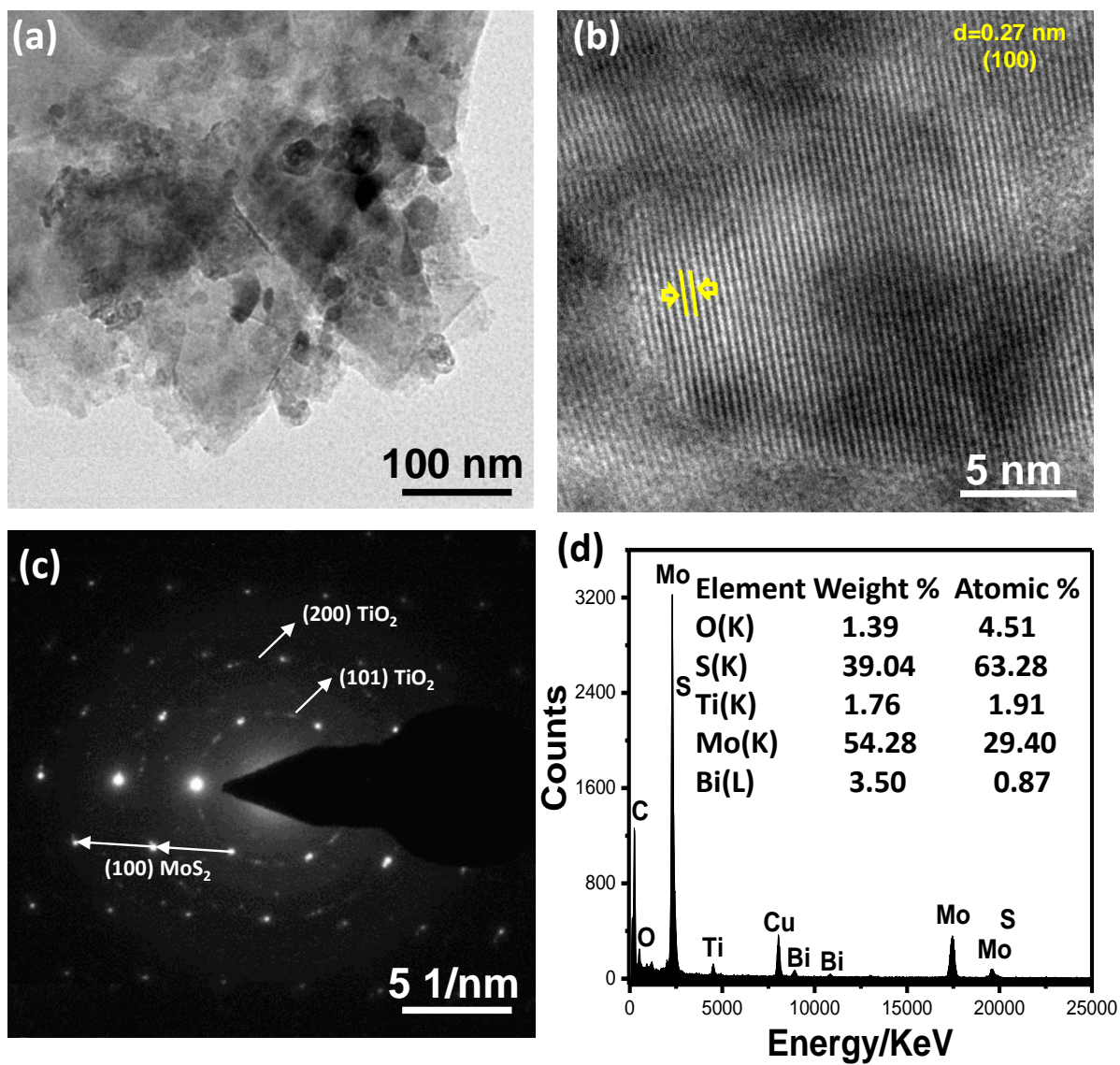


Figure 6.2 (a) TEM image, (b) HRTEM image, (c) SAED pattern and (d) EDX spectrum of MoS₂/Bi-TiO₂ (MBT-10) heterostructures.

Figure 6.2a shows the TEM image of MoS₂/Bi-TiO₂ composite (10 weight% Bi-TiO₂ (2 mM Bi) loaded MoS₂), where average ~40 nm spherical Bi modified TiO₂ nanoparticles are formed on the surface of MoS₂ nanosheets after 24h slow stirring. The HRTEM image shows the clear lattice fringes which are perfectly aligning across the entire surface (Figure 6.2b), reveals the single-crystallinity of MoS₂ nanosheet. The lattices fringes of ~0.27 nm can be indexed to (100) planes of hexagonal MoS₂ [45]. The corresponding SAED pattern shows an ordered array of bright spots, represents the single crystallinity of MoS₂ along with the rings correspond polycrystalline TiO₂ (Figure 6.2c). The energy-dispersive X-ray (EDX) spectrum illustrates the chemical composition

of MoS₂/Bi-TiO₂ heterostructures which composed of Mo, O, Bi, Ti and S (Figure 6.2d). Ag NPs decorated 1D AgVO₃ nanorods with a size of 200 nm in width and more than 6 μm in length have been obtained through co-precipitation method at room temperature (Figure 6.3a and 3b). The lattice spacing of ~0.236 nm correspond to the (111) plane of metal Ag (Figure 6.3c). The SEAD pattern identifies the (110) plane of AgVO₃ (Figure 6.3d).

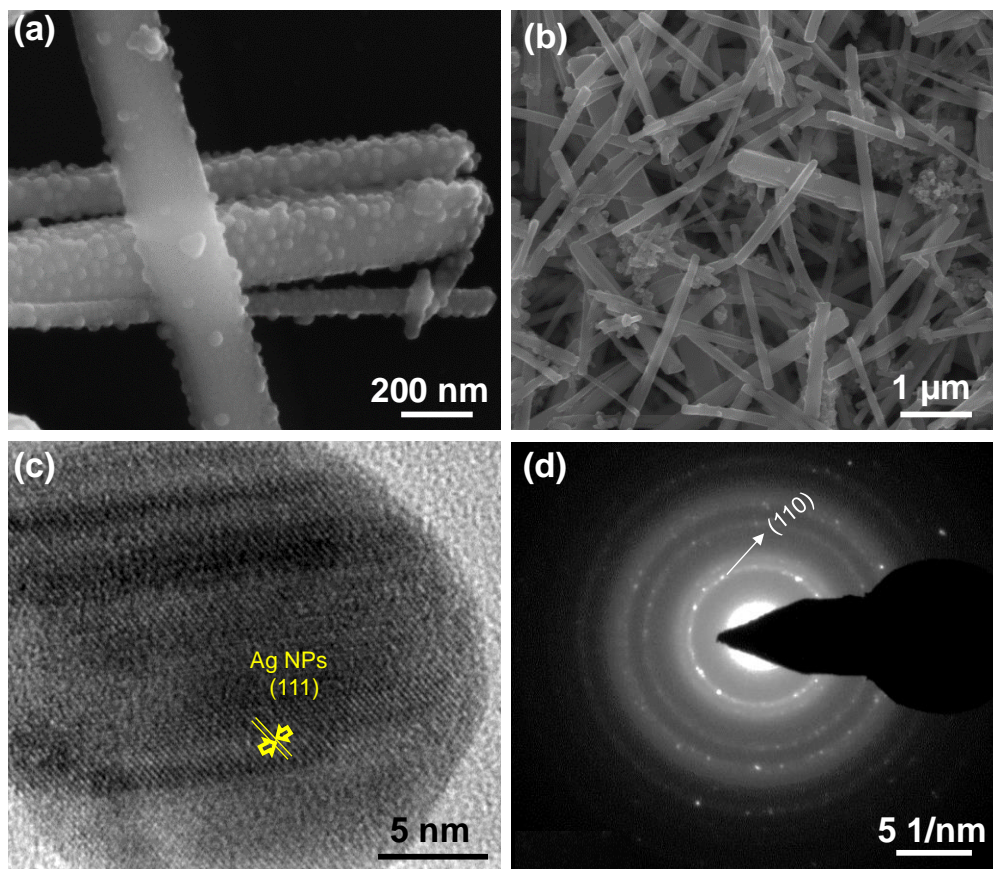


Figure 6.3 FESEM images of (a) Ag-AgVO₃ and (b) MoS₂/Ag-AgVO₃ heterostructures. (c) HRTEM image and (d) SEAD pattern of Ag nanoparticle.

TEM image of Ag-AgVO₃ further reveals that very small Ag NPs are formed on the surface of AgVO₃ nanorods (Figure 6.4a). Additionally, the high resolution TEM (HRTEM) identifies two set of different lattice fringes. The lattice fringe ~0.26 nm matches well with the (-131) plane of α-AgVO₃ NPs (Figure 6.4b) [51]. Moreover, the corresponding selected area electron diffraction (SAED) pattern supports the single crystallinity of each individual AgVO₃ nanorod in which the diffraction spots with d-values of ~0.35 nm and ~0.73 nm assigned to the (220) and (110) planes of the α-AgVO₃ (Figure 6.4c) [62]. The TEM images (Figure 6.4d and 6.4e) of heterostructures exhibit an interconnected architecture, consisting of thin layers of stacked 2D MoS₂ nanosheets

and AgVO_3 nanorods. Further, the magnified TEM image of the heterostructures shows that Ag NPs decorated AgVO_3 nanorods are dispersed on the surface of MoS_2 nanosheets, implies an assembly between nanorods and nanosheets through an electron mediator.

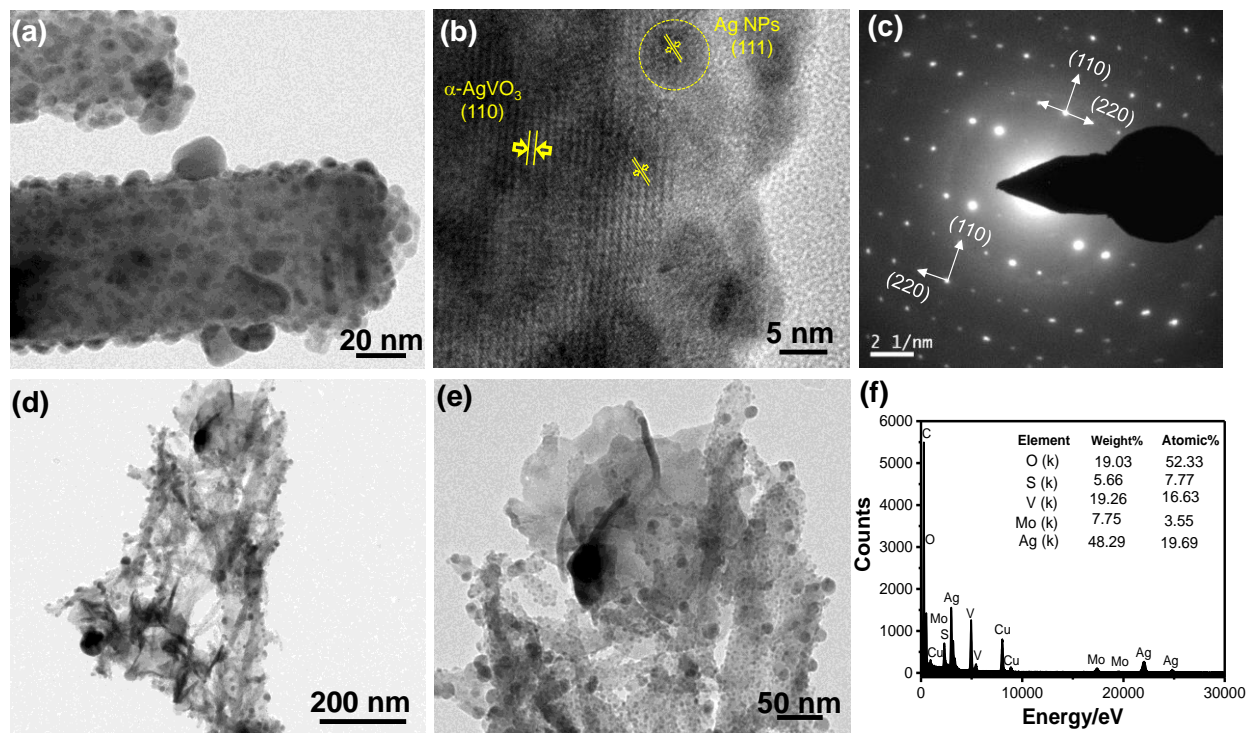


Figure 6.4 (a) TEM image, (b) HRTEM image and (c) SAED pattern of Ag-AgVO_3 synthesized at room temperature. (d) Low and (e) High magnification TEM images and (f) EDX spectrum of $\text{MoS}_2/\text{Ag-AgVO}_3$ heterostructures.

However, the energy-dispersive X-ray (EDX) spectrum illustrates the chemical composition of $\text{MoS}_2/\text{Ag-AgVO}_3$ heterostructures which composed of Ag, V, O, Mo and S (Figure 6.4f). The atomic ratio of Mo and S is 1:2 calculated from EDX. However, the atomic ratio of Ag, V and O is about 1.2:1:3, which is close to the stoichiometric ratio of AgVO_3 (1:1:3). As Ag NPs are also formed, total atomic weight is slightly greater for Ag. Thus, heterostructures formation between MoS_2 and AgVO_3 does not change the stoichiometric ratio of individual MoS_2 and AgVO_3 .

6.3.2 Structural Analysis

The XRD pattern of TiO_2 nanoparticles match very well with the JCPDS No. 21-1272, can be indexed to anatase phase (Figure 6.5a) [44]. After Bi modification (using 1 mM and 2 mM Bi), no shifting or extra significant diffraction peak of Bi species have been observed, indicating the doping of Bi does not affect the crystal structure of TiO_2 at low concentration.

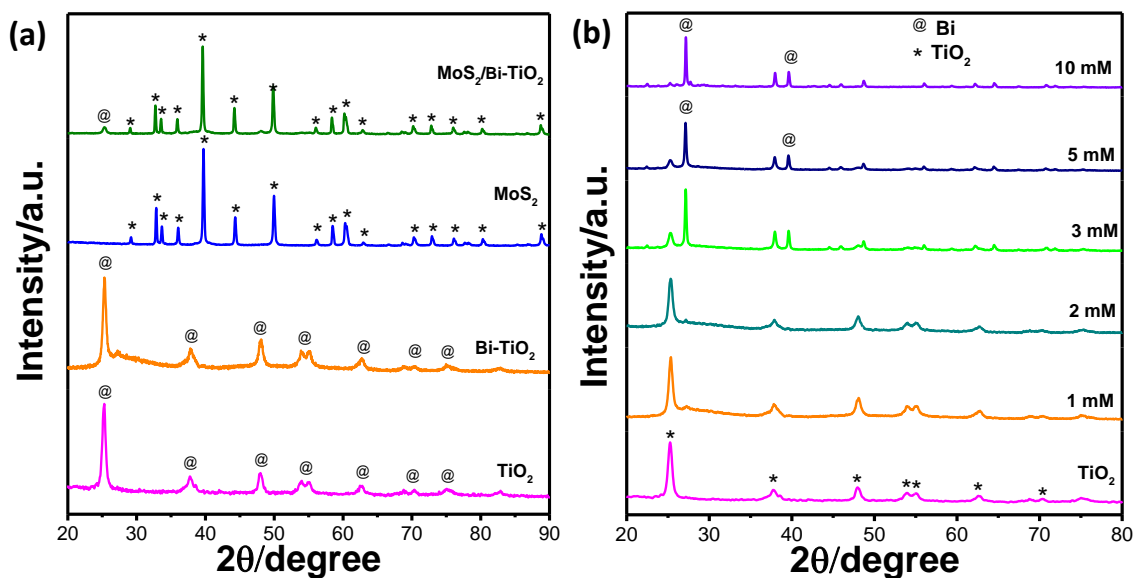


Figure 6.5 (a) XRD pattern of TiO₂, Bi-doped TiO₂ (using 2mM Bi), MoS₂ and MoS₂/Bi-TiO₂ (MBT-10) heterostructures. (b) XRD of Bi-modified TiO₂ materials which are synthesized using 1 mM, 2 mM, 3 mM, 5 mM and 10 mM Bi-salt.

However, at higher loading concentration (using 3 mM, 5 mM Bi and 10 mM Bi), prominent diffraction peaks of metallic Bi arises (Figure 6.5b). Therefore, 2 mM Bi concentration has been fixed for doping. On the other hand, the XRD pattern of the MoS₂ indicates the hexagonal phase of MoS₂ (JCPDS no. 37-1492) [63]. However, the XRD pattern of MoS₂/Bi-TiO₂ shows mainly MoS₂ peaks along with (101) diffraction peaks of anatase TiO₂ (Figure 6.5a). This result demonstrates the heterostructures formation and co-existence of MoS₂ and TiO₂ in the composite sample.

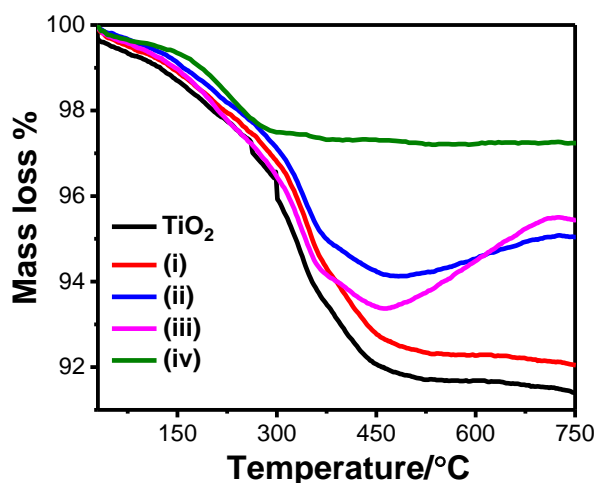


Figure 6.6 TG analysis of Bi-doped TiO₂ as photocatalyst with various loading concentration. The Bi doping samples are marked as (i), (ii), (iii), (iv) according to the amount of Bi-salt used during the synthesis (1 mM, 2 mM, 3 mM and 5 mM) respectively.

Further, the quantity of Bi concentration in Bi-TiO₂ samples has been calculated from the thermogravimetric analysis and the inductively coupled plasma atomic-emission spectroscopy. With increase the loading concentration, the stability of the TiO₂ has been improved (Figure 6.6). The wt% of Bi calculated from TG and ICP-AES are summarized in Table 6.1.

Table 6.1 Bi loading (wt %) calculated from the TGA and ICP-AES.

| Bi-doped TiO ₂ material | Loading % Bi | |
|--|--------------|--------------|
| | From TGA | From ICP-AES |
| TiO ₂ doped with 1mM Bi-salt | 0.63 | 1.14 |
| TiO ₂ doped with 2 mM Bi-salt | 3.64 | 3.39 |
| TiO ₂ doped with 3 mM Bi-salt | 4.04 | 4.12 |
| TiO ₂ doped with 5 mM Bi-salt | 5.85 | 7.04 |

Figure 6.7a illustrates the XRD patterns of Ag-AgVO₃, MoS₂ and MoS₂/Ag-AgVO₃. The strong peaks at 2θ values of 25°, 27.5°, 28.32°, 29.8°, 31.58°, 32.14°, 32.95°, 34.97°, 39.5° and 40.5° can be assigned to the diffraction plans of (220), (310), (20-1), (-311), (221), (-131), (002), (311), (400) and (420) for AgVO₃ which confirms the monoclinic α-phase of AgVO₃ with space group C2/c (JCPDS No. 15-50645) [64]. The diffraction peaks at 2θ values of 38.1° and 44.3° are represent the presence of Ag nanoparticles [JCPDF card 04-0783] [64]. The characteristic (100), (103), (105) and (110) peaks of MoS₂ indicate the hexagonal phase of MoS₂ (JCPDS no. 37-1492) [65]. After heterostructures formation, (220), (310), (20-1), (-131), (311), (400) and (420) remains unchanged, whereas a new diffraction peak comes at 31.75° which may be the combined peak of (221) and (-131) located at 31.58° and 32.14° for pure Ag-AgVO₃.

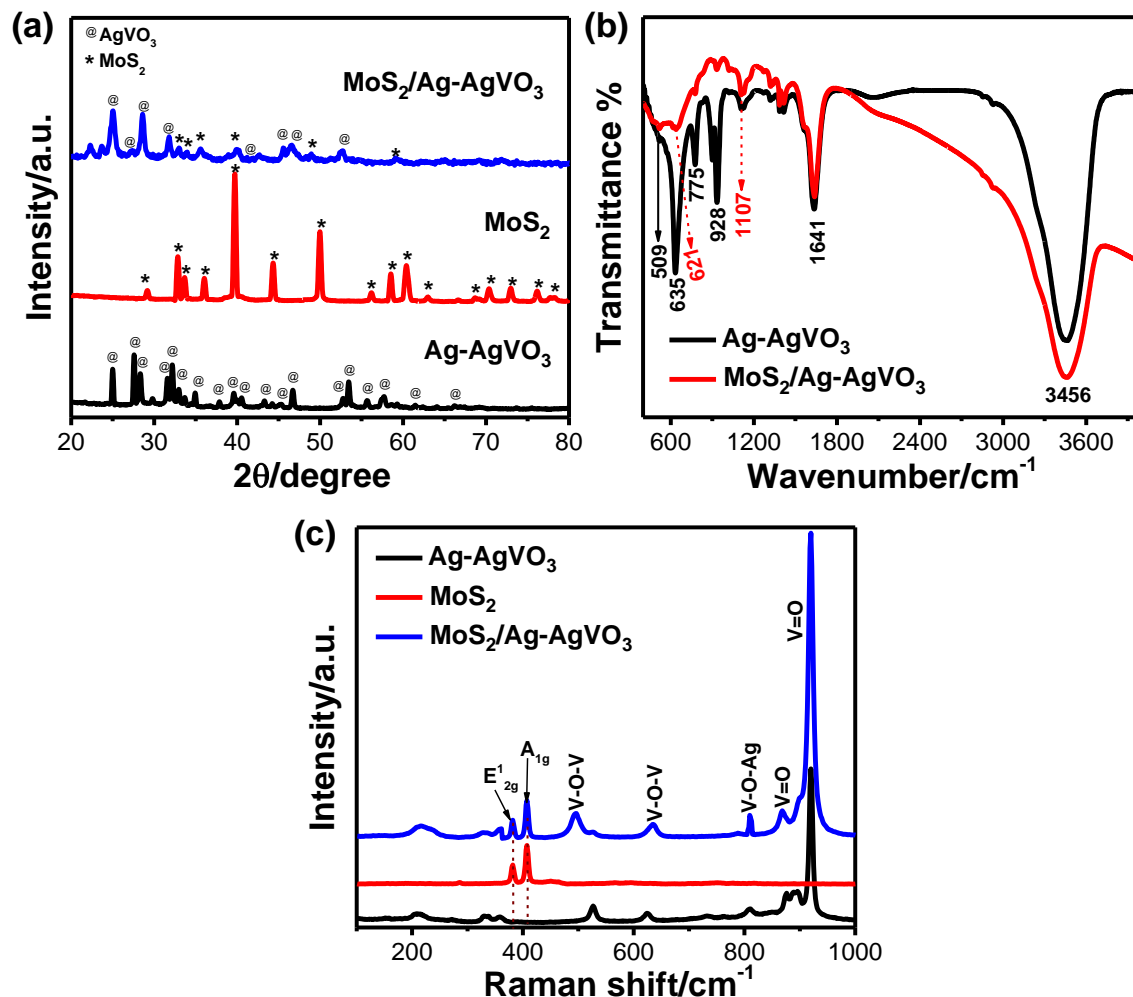


Figure 6.7 (a) XRD patterns, (b) FTIR spectra and (c) Raman spectra of the synthesized Ag-AgVO₃, bare MoS₂ and MoS₂/Ag-AgVO₃ heterostructures.

The chemical structures of the heterostructures and the interactions between MoS₂ and AgVO₃ have been further studied by FT-IR and Raman analysis. The Ag-AgVO₃ shows characteristic peaks at ~3456, ~1641, ~1383, ~1113, ~928, ~775, ~635 and ~509 cm⁻¹ (Figure 6.7b). The peaks at ~3456 cm⁻¹ correspond to O–H stretching vibration and bending vibration of physisorbed water molecules and ~1641 cm⁻¹ correspond to surface hydroxyl groups [50]. A peak at ~928 cm⁻¹ arises due to the symmetric stretching vibrations of VO₃ whereas, additional peaks at ~775 and ~635 cm⁻¹ are assigned to the antisymmetric stretching vibrations of VO₃ [55]. The symmetric stretching mode of V–O–V units are confirmed by the presence of FTIR peak at ~509 cm⁻¹ as reported earlier [59]. New vibration peaks appear at ~1107 cm⁻¹ and ~621 cm⁻¹ in heterostructures, which are attributed to the characteristic peaks of MoS₂ [56]. Furthermore, the as-prepared materials have

been characterized by the Raman spectroscopy. Figure 6.7c shows the Raman peaks of Ag-AgVO₃, bare MoS₂ and MoS₂/Ag-AgVO₃ heterostructures. The characteristic peaks of Ag-AgVO₃ at ~919 cm⁻¹, ~867 cm⁻¹, ~809 cm⁻¹, ~624 cm⁻¹, ~526 cm⁻¹, ~332 cm⁻¹ and ~213 cm⁻¹ are well matched with the previously reported literatures (Figure 6.7c) [51]. The Raman peaks at ~919 and ~867 cm⁻¹ correspond to V=O stretching vibration and peaks at ~624 and ~526 cm⁻¹ are attributed to the V–O–V stretching vibration. Further, peak at ~809 cm⁻¹ is originated from the V–O–Ag stretching vibration [51]. However, the MoS₂ exhibits characteristics Raman peaks at ~380 and ~407 cm⁻¹ corresponds to in-plane E_{2g}¹ mode and the out-of-plane A_{1g} mode respectively which are consistent with Raman results of monolayer MoS₂ in the reported literature. The inplane E_{2g}¹ mode originates due to opposite vibration of two S atoms with respect to the Mo atom and the A_{1g} mode arises due to the out-of-plane vibration of S atoms [57]. In heterostructures, both Raman peaks of MoS₂ and AgVO₃ are present whereas, a blue shift has been observed for V–O–V bands which suggests the bond length becomes weaker due to presence of a covalent bond between MoS₂ and AgVO₃ [57]. Moreover, this result again confirms the heterostructures formation between AgVO₃ and MoS₂.

6.3.3 XPS Analysis

XPS analysis has been studied further to analyze the surface chemical composition and valance state of the components. The XPS survey spectra confirms that the sample is composed of Mo, S, Ti, Bi and O (Figure 6.8a). The peaks at ~229.4 eV and ~232.7 eV having spin–orbit separation of ~3.2 eV are ascribed to Mo 3d_{5/2} and Mo 3d_{3/2} state respectively, indicating Mo⁴⁺ state of Mo [45]. The characteristic peaks corresponding to S 2p_{1/2} and S 2p_{3/2} in MoS₂/Bi-TiO₂ composite are located at ~163.1 eV and ~161.9 eV respectively. The peaks are separated by ~1.22 eV which confirms the S²⁻ of S (Figure 6.8b) [45]. The XPS peaks at ~164.5 eV (Bi 4f_{5/2}) and ~159.2 eV (Bi 4f_{7/2}) indicate the Bi³⁺ state of Bi (Figure 6.8c) [66]. Moreover, the binding energies of ~464.3 eV and ~458.8 eV correspond to the Ti 2p_{1/2} and Ti 2p_{3/2} confirms that Ti present in Ti⁴⁺ state within the heterostructures (Figure 6.8d) [44]. The fitted O 1s spectra shows two peaks (Figure 6.8e), one for the lattice oxygen (at 530.2 eV) and another for surface hydroxyl oxygen (at ~531.7 eV) [46]. Figure 6.9a represents the XPS survey spectra of Ag-AgVO₃, MoS₂ and MoS₂/Ag-AgVO₃ heterostructures where peaks at binding energy ~159.5, ~229.7, ~364.2, ~515.6, ~528.6 and ~571.3 eV correspond to S, Mo, Ag, V and O respectively, supporting the formation of heterostructures. Figure 6.9b–d illustrates the magnified XPS spectra of Ag 3d, V 2p, O 1s,

regions. The core level Ag 3d spectra display a doublet signal with binding energies of 367.9 eV and 373.9 eV corresponds to $\text{Ag}^+ 3d_{5/2}$ and $\text{Ag}^+ 3d_{3/2}$ respectively. Notably, a strong peaks at 368.4 eV has been observed after fitting which is ascribed to the presence of Ag^0 state [67].

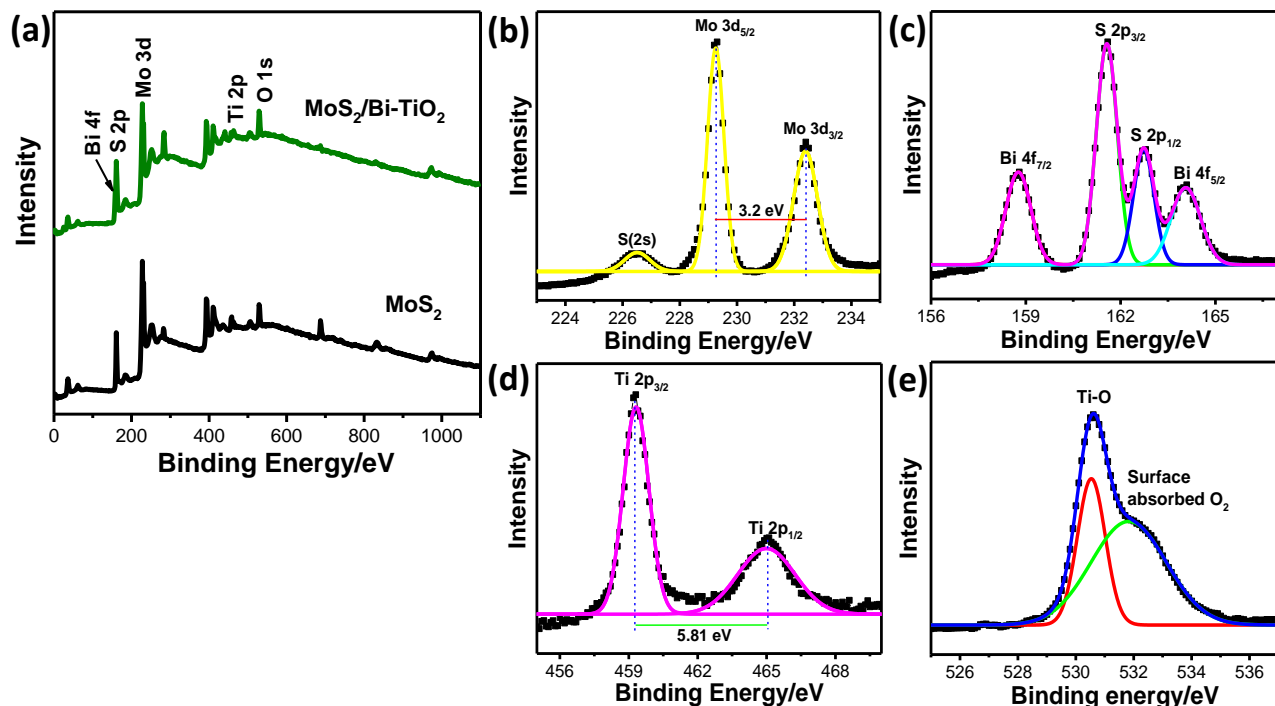


Figure 6.8 (a) The surface survey XPS spectra of the $\text{MoS}_2/\text{Bi-TiO}_2$ (MBT-10) heterostructures and the bare MoS_2 . Magnified XPS spectra for (b) Mo 3d, (c) Bi 4f, S 2p, (d) Ti 2p and (e) O 1s of $\text{MoS}_2/\text{Bi-TiO}_2$ (MBT-10) heterostructures. The scattered lines represent the experimental data and solid lines for fitted data.

In addition, the heterostructures formation with MoS_2 leads to a shift of the Ag 3d peaks toward the higher binding energy side with a value of ~ 0.38 eV (Figure 6.9e). Peak shifting indicates a possibility of sharing electrons with neighbouring atoms in terms of asymmetry in the bond arrangements, which creates an extra pressure on the electrons. So, slightly high binding energy is required for ejection of electrons compared to base material during the excitation process. Moreover, the shifting towards high binding energy implies a band bending which results a charge redistribution at the interface as well as indicates the decrease of electron density in the Ag^+ cation, which implies an electron transfer from the AgVO_3 to MoS_2 [67]. As shown in Figure 6.9c, V 2p signal represents two peaks at ~ 516.4 eV and ~ 523.9 eV are attributed to the binding energies of $\text{V}^{5+} 2p_{5/2}$ and $\text{V}^{5+} 2p_{3/2}$ [68].

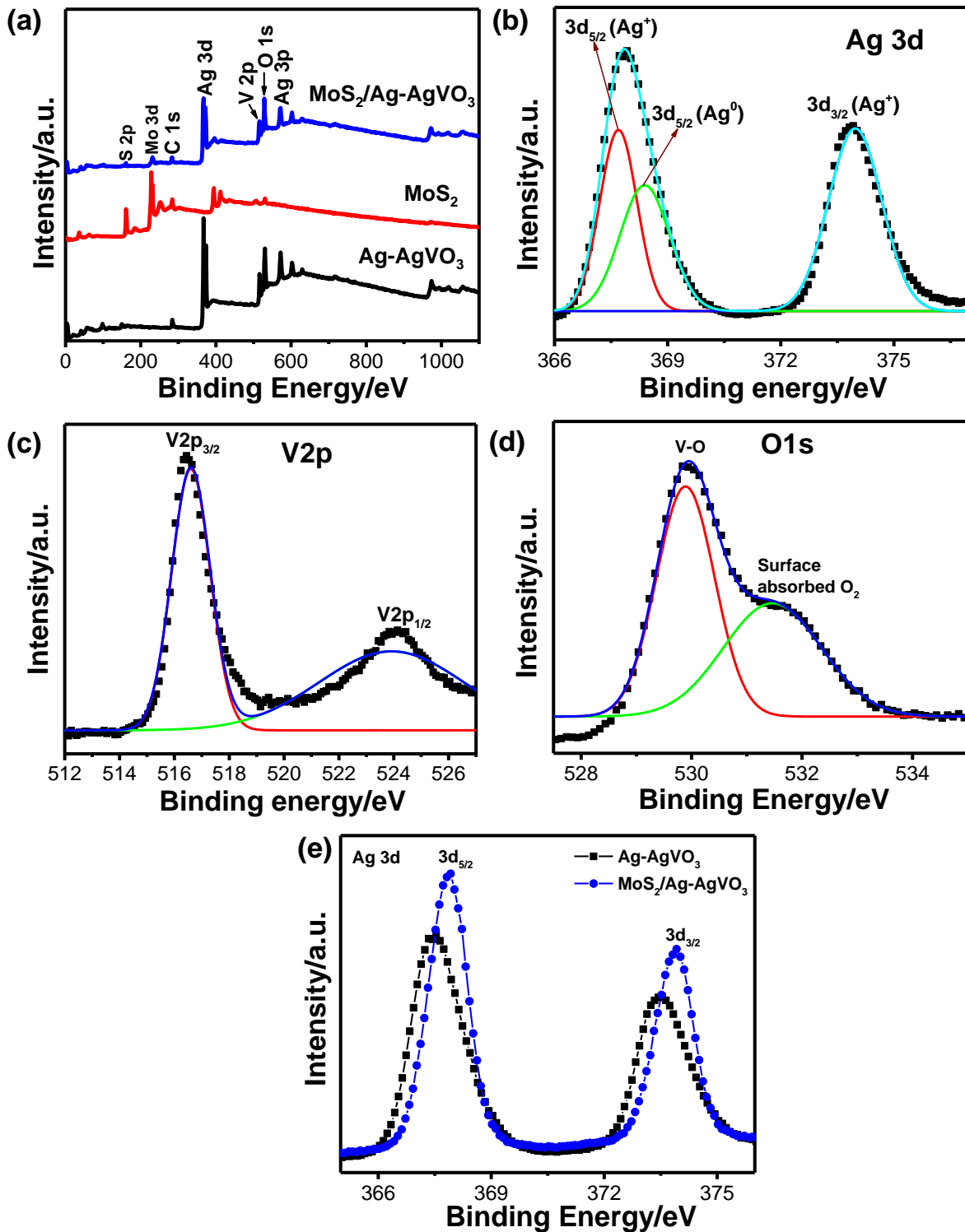


Figure 6.9 (a) The XPS spectra of the Ag-AgVO₃, bare MoS₂ and MoS₂/Ag-AgVO₃ heterostructures. Magnified XPS spectra of (b) Ag 3d, (c) V 2p, (d) O 1s of MoS₂/Ag-AgVO₃ heterostructures. The magnified XPS spectra of (e) Ag 3d of the bare Ag-AgVO₃ and MoS₂/Ag-AgVO₃ heterostructures.

Hence, the XPS spectrum of O1s shows two peaks at ~ 529.9 eV and ~ 531.6 eV, which could be assigned to the binding energies of V–O bond and surface adsorbed oxygen respectively (Figure 6.9d) [69]. Figure 6.10a and 10b shows the magnified XPS spectra of Mo 3d and S 2p. The strong peaks located at binding energies of ~ 232.7 eV and ~ 229.4 eV are ascribed to Mo $3d_{3/2}$ and Mo $3d_{5/2}$ respectively, in which the spin–orbit separation of 3.2 eV suggests Mo⁴⁺ state of Mo (Figure 6.10a) [70].

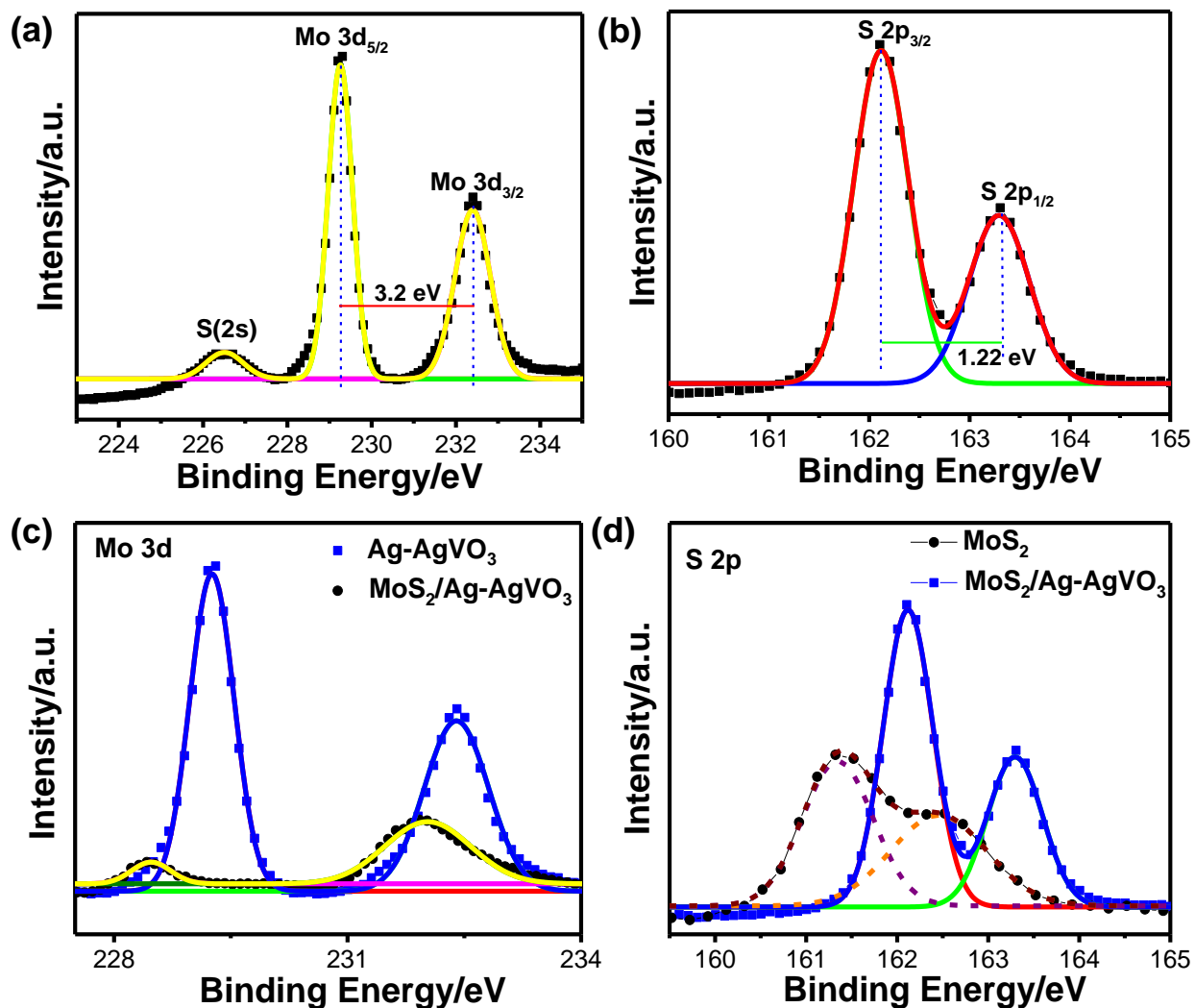


Figure 6.10 Magnified XPS spectra of (a) Mo 3d, (b) S 2p of MoS₂/Ag-AgVO₃ heterostructures. The magnified XPS spectra of (c) Mo 3d and (d) S 2p of the bare MoS₂ and MoS₂/Ag-AgVO₃ heterostructures.

In addition, the characteristic peaks obtained at ~ 161.9 eV and ~ 163.1 eV (separated by 1.22 eV) correspond to S $2p_{3/2}$ and S $2p_{1/2}$ respectively, confirming S²⁻ state of S within the MoS₂/Ag-AgVO₃ heterostructures (Figure 6.10b) [71]. Moreover, the peak intensity of Mo 3d and S 2p peaks have

been increased after heterostructures formation, indicating electrons are diffused towards the surface (Figure 6.10c and 6.10d) as the intensity of peak is directly depends on the number of electron in the respective chemical state [71]. Thus, XPS spectra suggest the co-existence of MoS₂, AgVO₃ and heterostructures formation.

6.3.4 Optical properties

The optical absorbance of MoS₂, TiO₂, MoS₂/TiO₂ and MoS₂/Bi-TiO₂ heterostructures has been measured by UV-Vis spectroscopy from 300 nm to 900 nm wavelength at room temperature which shows three distinct absorption peaks (Figure 6.11a). The doublet peak at ~629 nm and ~685 nm with splitting energy ~0.16 eV is well consistent with the ideal value for MoS₂ (0.15 eV, theoretically calculated) [72]. The peaks arise due to the direct electronic transition at the K point of first Brillouin zone. However, the energy difference between two peaks arises from the spin-orbit coupling of the VB [73]. A broad peak at 400 to 600 nm has been observed which originates from the interband transition between occupied and unoccupied Mo 3d orbitals in the K-point of first Brillouin zone [60]. In comparison to the pure MoS₂, the peak positions of MoS₂/Bi-TiO₂ are slightly red shifted because of the interaction between two components, indicating a decrease in the bandgap.

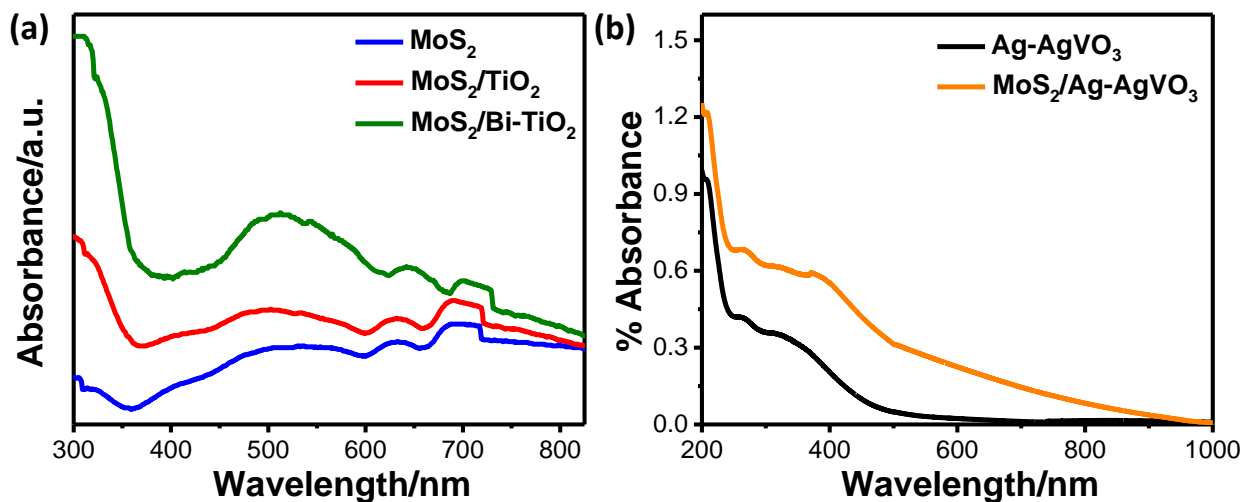


Figure 6.11 UV-Vis absorption spectra of (a) bare MoS₂, MoS₂/TiO₂ and MoS₂/Bi-TiO₂ (MBT-10) heterostructures and (b) Ag-AgVO₃, MoS₂/Ag-AgVO₃ heterostructures.

Figure 6.11b illustrates the UV-Vis absorption spectra of Ag-AgVO₃, and MoS₂/Ag-AgVO₃ heterostructures. The bare Ag-AgVO₃ exhibits absorption both in the UV and visible regions. Interestingly, after heterostructure formation absorption intensities of MoS₂/Ag-AgVO₃ increase

at each wavelength and the absorption edge shifts to near IR region. Thus, presence of Ag NPs remarkably enhance the absorption of light by virtue of SPR effect which induce a local electromagnetic field at the interfaces of the semiconductors. As a result, electron-hole pair formation and separation ability at the interfaces increases, which would be helpful to achieve efficient photocatalytic activity under visible light.

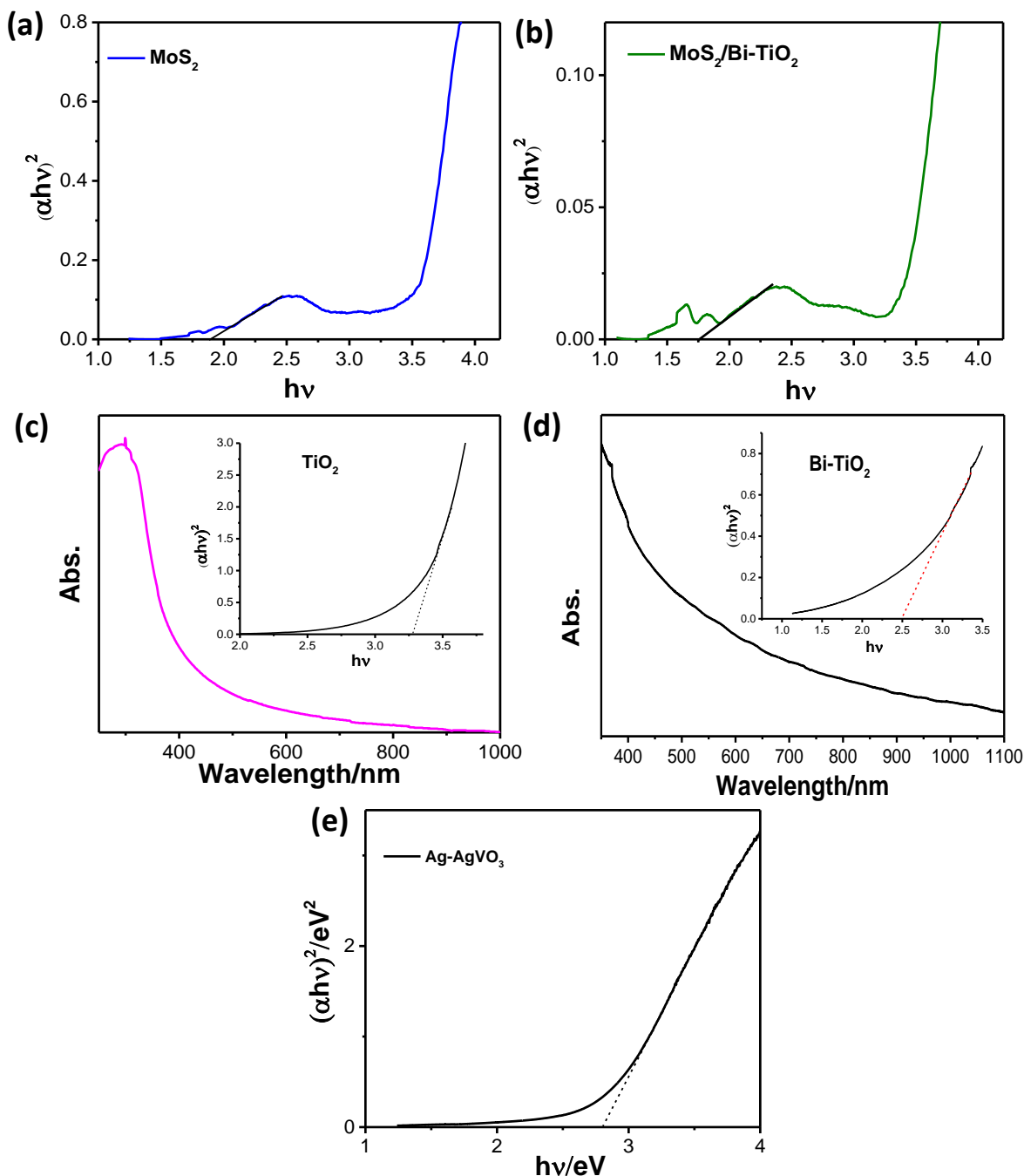


Figure 6.12 Kubelka–Munk [$(\alpha h\nu)^2$ vs photonenergy ($h\nu$)] plot of (a) bare MoS_2 and (b) $\text{MoS}_2/\text{Bi-TiO}_2$. (c) UV-Vis spectra of TiO_2 (Inset: Kubelka–Munk of TiO_2) and (d) Bi-doped TiO_2 , (Inset: Kubelka–Munk of Bi-doped TiO_2). (e) Kubelka–Munk plot of Ag-AgVO_3 .

Further, the bandgap of the materials was calculated by extrapolating the tangent of Kubelka–Munk $(\alpha hv)^2$ vs hv plot. Here “ α ” is absorption coefficient and “ hv ” is photon energy [62]. Initially, the calculated bandgap for Bi-TiO₂ was ~2.5 eV which is lowered from the pure TiO₂ (3.21 eV) and further significantly lowered after formation of heterostructures with MoS₂ (~1.74 eV) (Figure 6.12b–d). The doping of Bi ions is mainly responsible for the bandgap reduction of TiO₂, because of the formation of intermediate energy levels between the top of the Bi³⁺ 6s band and the bottom of the Ti⁴⁺ 3d band [28, 29]. However, Bi³⁺ 6s level is located above the VB of TiO₂ [30]. Thus, it can be concluded that, incorporation of Bi-content effectively narrowing the bandgap of TiO₂ and make active for visible light absorption. The calculated E_g of the MoS₂ and Ag-AgVO₃ are 1.63 eV and 2.8 eV respectively (Figure 6.12a and 12e).

6.3.5 Photocatalytic H₂ Generation

The photocatalytic activity of the as synthesized materials has been studied by measuring the amount of H₂ generation through water reduction under visible light illumination. For this experiment, 25 volume % of methanol has been taken as hole scavenger as it can react with the photo-induced holes usually faster compare to water, leaving excess photogenerated electrons in the electrolyte for reduction reactions. The effect of Bi-doping on TiO₂ for the photocatalytic H₂ generation has been studied (Figure 6.13a). With the increase of Bi-content, the H₂ generation rate has been improved due to presence of additional electronic states between the VB and CB of TiO₂. Consequently, probability of electron hole recombination may be reduced which enhance the catalytic activity. Moreover, the effect of Bi-TiO₂ loading on MoS₂ has been studied. It has been clearly shown from the Figure 6.13b that with increase the Bi-TiO₂ loading (1 to 20 wt %), H₂ generation rate has been increased up to a certain concentration because of the increment of active sites on the MoS₂ surface for water reduction. Further increase in loading concentration falling down the photocatalytic activity, which may happen because of excessive loading of Bi-doped TiO₂ on the MoS₂, leads aggregation of Bi-TiO₂ nanoparticles. Clearly, after heterostructures formation with MoS₂, the photocatalytic activity of TiO₂ has been enhanced. The MoS₂/TiO₂ (10% loading of TiO₂, MT-10) heterostructures shows six and three fold enhanced H₂ generation (~367 $\mu\text{mol g}^{-1}$) compared to pristine TiO₂ (57 $\mu\text{mol g}^{-1}$) and bare MoS₂ (~130 $\mu\text{mol g}^{-1}$) respectively. However, the heterostructures composed of MoS₂ and Bi-doped TiO₂ shows highest H₂ generation of ~512 $\mu\text{mol g}^{-1}$ in 4h of visible light illumination, which may be attributed to the enhance light

absorption by Bi-doped TiO₂ and availability of active sites for hydrogen evolution (Figure 6.13c) [75]. Moreover, MoS₂/Bi-TiO₂ heterostructures displayed a linear evolution of H₂ for the entire period (Figure 6.13d).

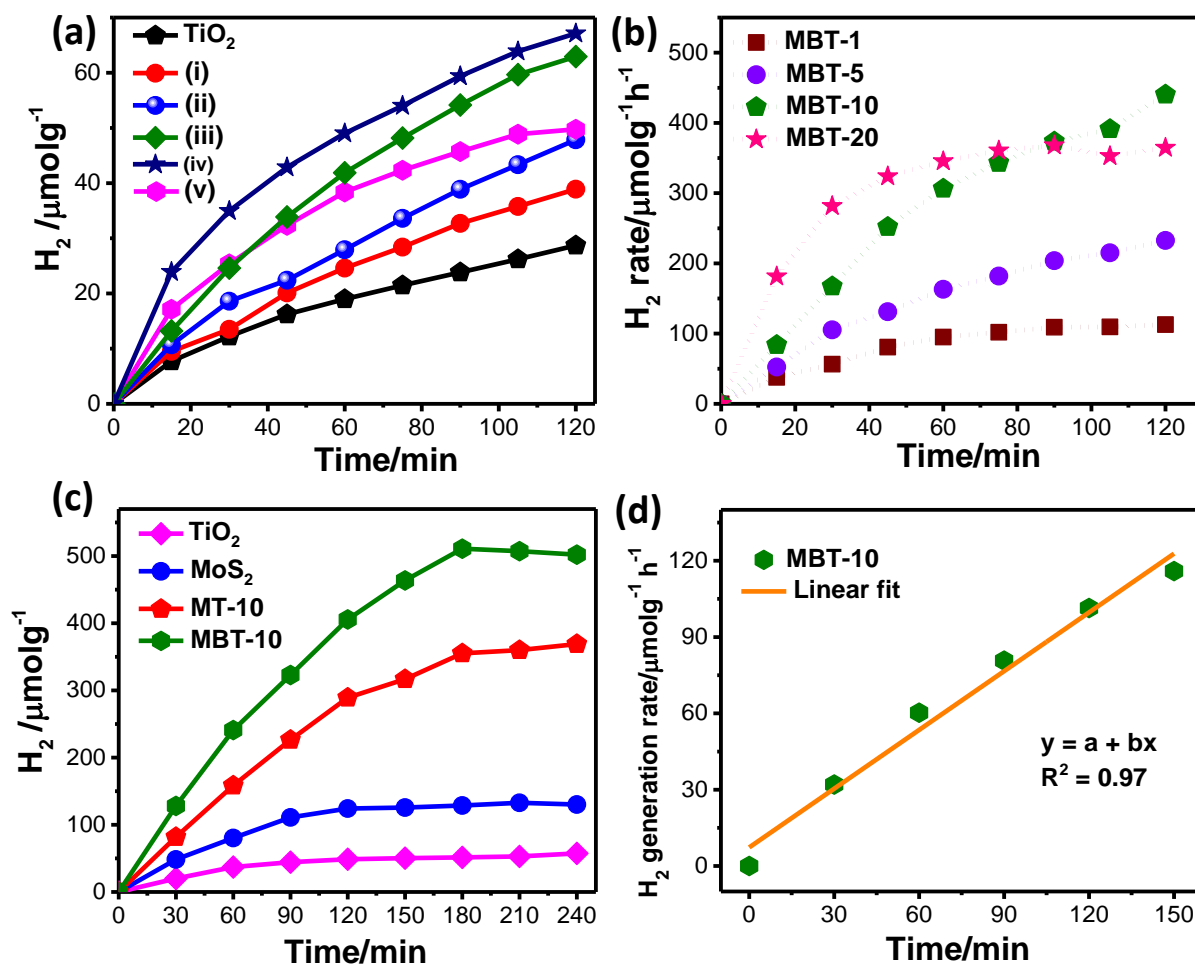


Figure 6.13 (a) Photocatalytic H₂ generation using Bi-doped TiO₂ as photocatalyst with various loading concentration which are synthesized using (i) 1 mM, (ii) 2 mM, (iii) 3 mM and (iv) 5 mM Bi-salt. The H₂ data of bare TiO₂ has been incorporated to compare the doping effect. (b) Effect of Bi-TiO₂ loading on MoS₂. (c) Photocatalytic H₂ generation in presence of MoS₂, MoS₂/TiO₂-10 (MT-10) and MoS₂/Bi-TiO₂ heterostructures (MBT-10) after 240 mins of visible light irradiation. (d) Photocatalytic H₂ generation rate of MBT-10 with linear fitting.

On the other hand, solution pH has a crucial role in controlling the photocatalytic activity of the catalyst. At neutral pH (pH 7) MBT-10 showed highest activity (Figure 6.14a). Figure 6.14b implies that the MoS₂/Bi-TiO₂ heterostructure can be reused at least three times for H₂ generation. To check the structural stability, XRD and FESEM of MoS₂/Bi-TiO₂ heterostructure have been studied before and after catalysis. All the characteristic peaks are present after catalytic reaction and no other extra peak has been observed (Figure 6.14c). As shown in Figure 6.14d and 14e, a

similar kind of morphology has been observed after 2h of photocatalytic H₂ generation. Therefore, it can be concluded that, the heterostructures is stable under light illumination and photocatalytic reactions, represent a green way for solar light harvesting applications.

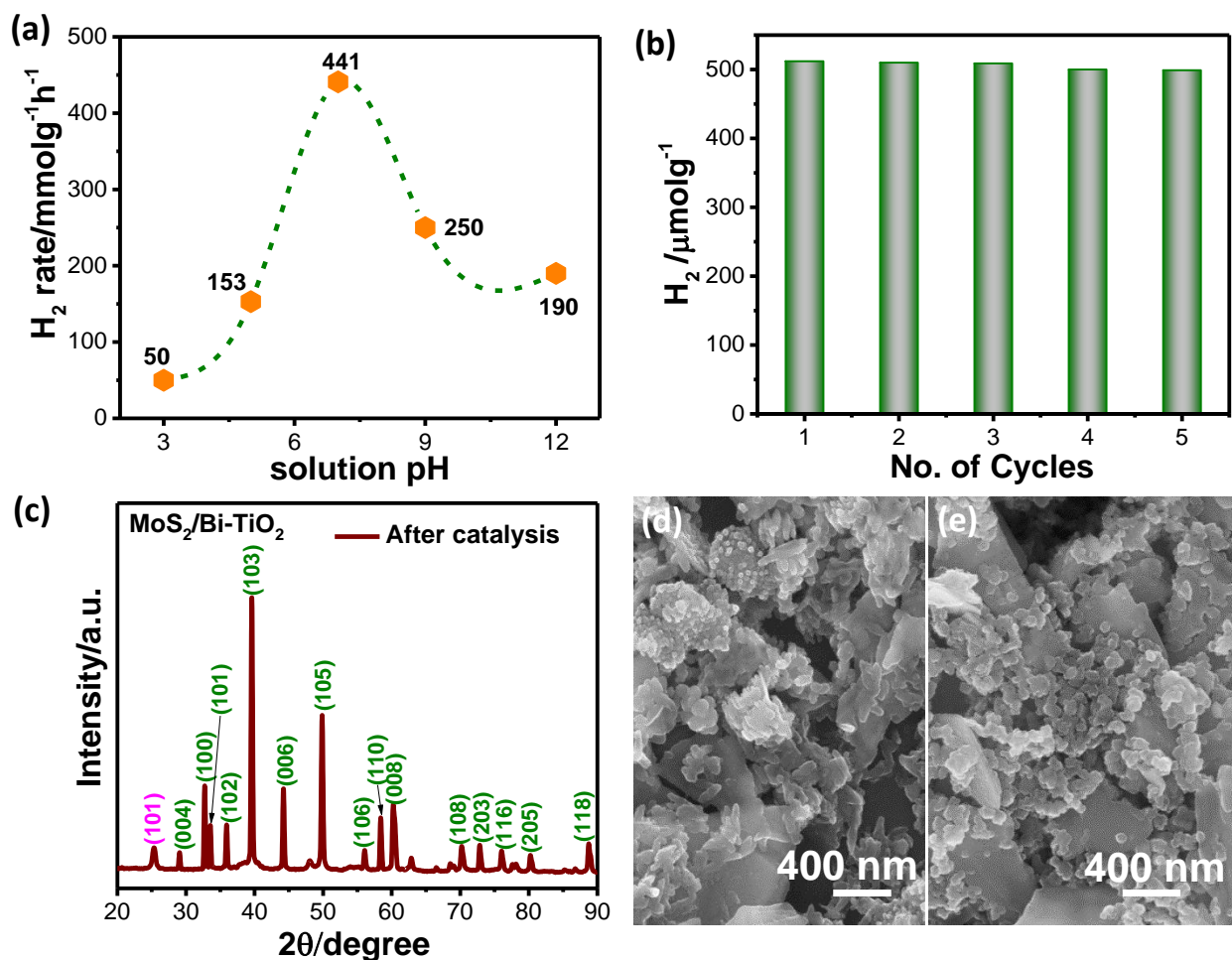


Figure 6.14 (a) Effect of pH for photocatalytic H₂ generation under visible light. (b) Recycling test of MoS₂/Bi-TiO₂ during H₂ generation. (c) The XRD pattern and (d-e) FESEM image of MoS₂/Bi-TiO₂ after and before catalytic reaction for H₂ generation.

Figure 6.15a shows the photocatalytic H₂ generation of Ag-AgVO₃, bare MoS₂ and MoS₂/Ag-AgVO₃ heterostructures through water reduction. In the absence of light as well as catalyst, there is no generation of H₂ gas. The considerable increase in H₂ generation rate (~8.9 mmol g⁻¹ h⁻¹) have been observed for Ag-AgVO₃, which may be attributed due to the presence of Ag NPs on the surface of 1D AgVO₃. The SPR generated by Ag NPs and high carrier density at the catalyst surface may result in the enhancement of the photocatalytic activity. However, MoS₂/Ag-AgVO₃ heterostructures exhibits highest H₂ generation rate of around 38.6 mmol g⁻¹ h⁻¹ because of fast

electron transfer between the MoS₂ and AgVO₃ through bridged Ag NPs. Interestingly, the H₂ generation rate increases linearly with time for heterostructures, indicating that a strong driving force has been maintained by the catalyst for water reduction over the examined period.

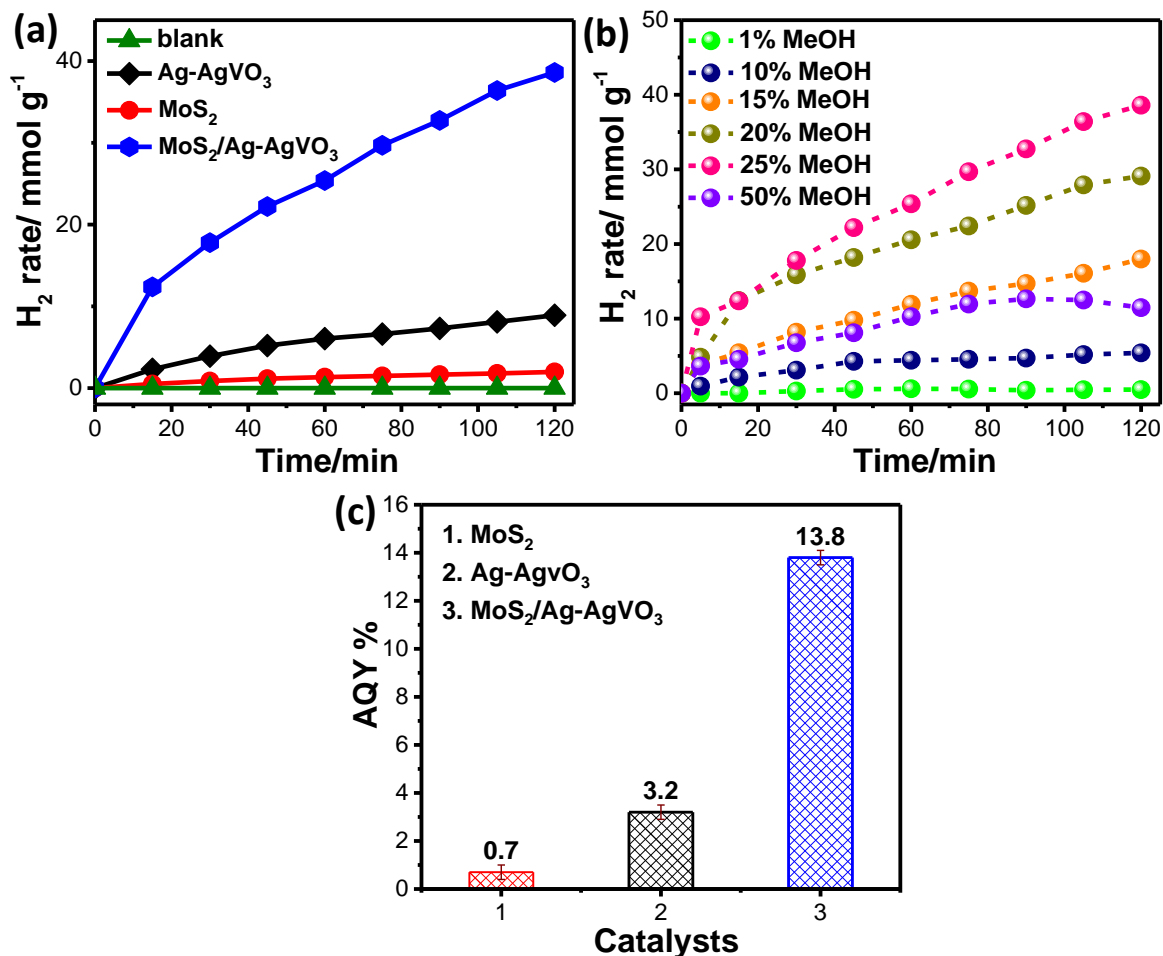


Figure 6.15 (a) Photocatalytic hydrogen generation in presence of Ag-AgVO₃ (black line), bare MoS₂ (red line) and MoS₂/Ag-AgVO₃ heterostructures (blue line) after 120 mins of visible light irradiation. (b) Photocatalytic H₂ generation of MoS₂/Ag-AgVO₃ heterostructures at different volume % of methanol and (c) apparent quantum yield (AQY %) of Ag-AgVO₃, bare MoS₂ and MoS₂/Ag-AgVO₃ heterostructures.

Further, to understand the role of sacrificial agent in H₂ generation, a set of experiments have been carried out by varying the volume % of methanol. Figure 6.15b reflects the effect of methanol (volume %) on the H₂ generation as sacrificial agent. Photocatalytic H₂ generation increase with the increase of methanol upto 25 volume % because of fast capturing the photogenerated holes which hinder the rapid recombination rate of charge carriers, and then goes to decrease due to back reaction and photocorrosion. Figure 6.15c presents the calculated AQY% for the catalysts, where MoS₂/Ag-AgVO₃ heterostructures exhibits highest photocatalytic H₂ generation efficiency of

13.8% followed by Ag-AgVO₃ (3.2%) and bare MoS₂ (0.7%). Thus, heterostructures formation improve the H₂ generation rate as well as AQY% which indicate that efficient electron-hole generation and separation processes may be happened at the interfaces of the heterostructures.

6.3.6 Photoelectrochemical Properties

To gain deeper insights into the photogenerated charge separation and transport process in the photocatalytic reactions, electrochemical measurements have been conducted further by preparing electrodes of as synthesized materials on FTO glass by doctor-blade method in presence of light. The transient photocurrent responses of MoS₂, MoS₂/TiO₂ and MoS₂/Bi-TiO₂ heterostructures have been recorded for several on off cycles under illumination. The MBT-10 heterostructures (10 wt % loading of Bi-TiO₂ on MoS₂) exhibits highest photocurrent density of $\sim 3.6 \mu\text{A cm}^{-2}$, which is 3.2 fold of bare MoS₂ ($\sim 1.2 \mu\text{A cm}^{-2}$) (Figure 6.16a). Thus, transient photocurrent results are well consistent with the H₂ generation and further supports that the existence of MoS₂ and Bi-doped TiO₂ in the heterostructures could result in high active sites for oxidation – reduction reactions. Furthermore, the charge carrier separation efficiency of MoS₂/Bi-TiO₂ has been studied by impedance spectroscopy. As shown in Figure 6.16b, a smaller semi-circular arc has been obtained for MBT-10 compared to MT-10 and bare MoS₂ electrodes, indicating that the heterostructures formation with Bi-doped TiO₂ reduces the charge-transfer resistance at the electrode electrolyte interface [76]. Further detailed electrochemical study has been carried out for MBT heterostructures with different loading of Bi-TiO₂. It can be clearly observed that 10 wt % loading exhibits smallest charge transfer resistance among the all materials. However, at higher loading (20 wt %), charge transfer resistance at the electrode-electrolyte interface has been increased (Figure 6.16c). Similar trend has been observed in LSV measurements of MoS₂/Bi-TiO₂ heterostructures at various loading of Bi-doped TiO₂ (Figure 6.16d). Therefore, it can be concluded that 10 wt % loading of Bi-TiO₂ on the MoS₂ surface is the optimal condition which offers minimum resistance with significant amount of available catalytic active sites. At higher loading concentration, photo-current density has been decreased due to the surface agglomeration.

For better understanding the enhanced catalytic activity of MoS₂/Bi-TiO₂ heterostructures, the Mott–Schottky study has been further carried out. Figure 6.17a – 17d shows the Mott–Schottky plots of bare MoS₂, MoS₂/TiO₂ (MT-10), Bi-doped TiO₂ (using 2 mM Bi) and MoS₂/Bi-TiO₂

(MBT-10) heterostructures. The positive slopes in the linear regions confirm n-type conductivity of MoS₂ and MoS₂/TiO₂ (Figure 6.17a and 17b).

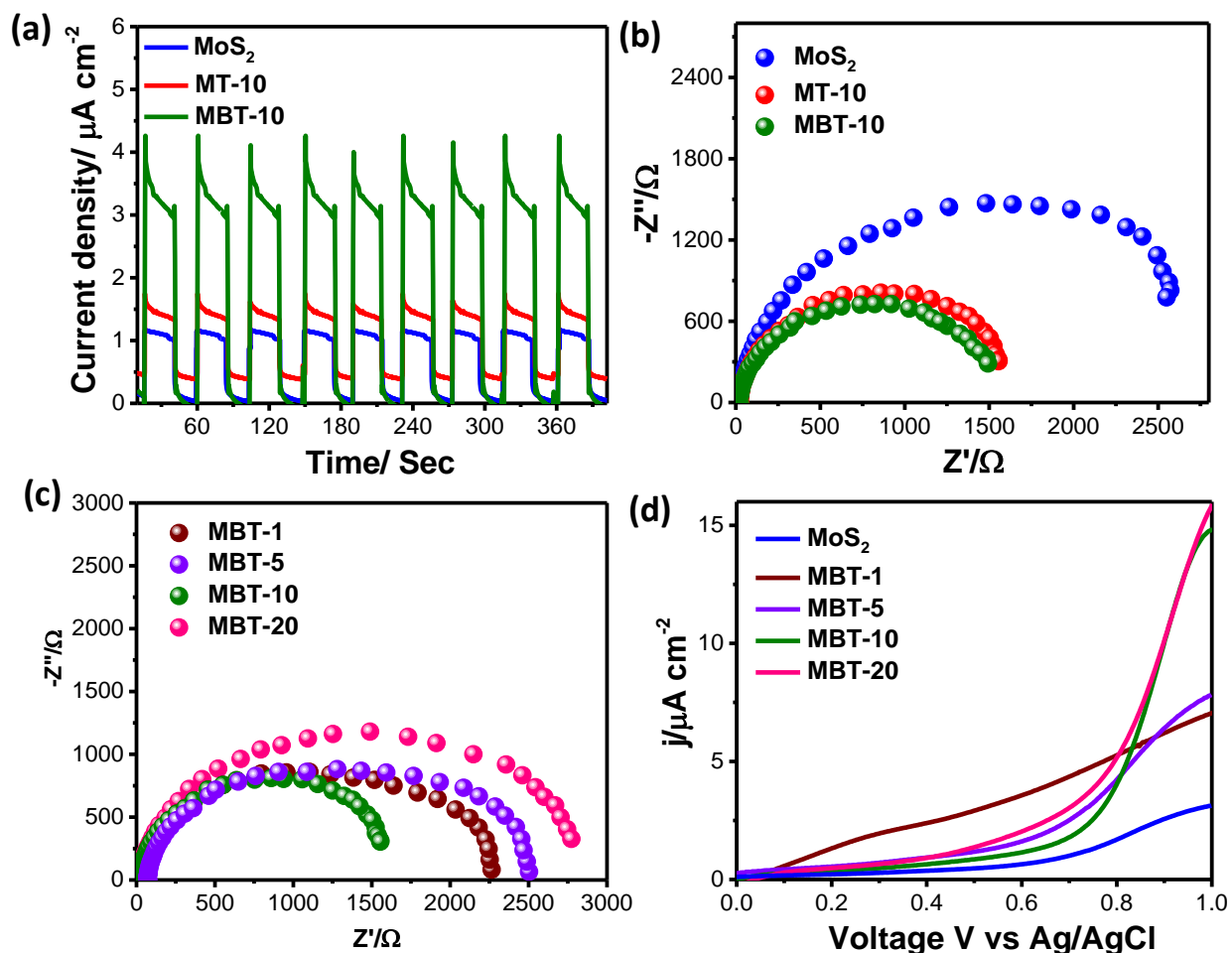


Figure 6.16 (a) Transient photocurrent spectra of MoS₂, MoS₂/TiO₂ and MoS₂/Bi-TiO₂ heterostructure-modified ITO electrodes at a bias of 0.26 V versus Ag/AgCl reference electrode in presence of 0.1M Na₂SO₄ buffer solution (suppress photogenerated holes and drive photogenerated electrons to reduce protons to H₂). Nyquist plots of the electrodes (b) MoS₂, MoS₂/TiO₂ and MoS₂/Bi-TiO₂ heterostructure, (c) MoS₂/Bi-TiO₂ heterostructures with various Bi-TiO₂ loading concentration at potential 0.1 V vs Ag/AgCl under continuous light illumination. (d) Linear sweep voltammetry curves of MoS₂/Bi-TiO₂ samples at various loading of Bi-doped TiO₂.

Flatband (E_{fb}) potentials have been obtained by calculating of the intersection of the linear fit to the $1/C^2$ measurements with the x-axis, which is $-0.69V$ (vs Ag/AgCl) for bare MoS₂ and -1.06 V (vs Ag/AgCl) for MoS₂/TiO₂. The negative shift of E_{fb} reveals that heterostructure formation with TiO₂ accelerate the charge transferring and catalyze the reduction reactions for H₂ generation [45]. The E_{fb} potentials could be near to the CB edges ($CB = E_{fb} - 0.2$ V) for the n-type conductors [77]. Thus, the CB potentials of MoS₂ is $-0.28V$ after converting the potential vs RHE scale by

following the equation 5.1. As a consequence, the VB potentials have been calculated using the optical bandgap, which is 1.63V (vs RHE) for MoS₂. However, the Bi doping in the TiO₂ lattice change the conductivity of TiO₂ and shows p-type conductivity with E_{fb} potential of 1.16 V (vs Ag/AgCl). As Bi³⁺ replace the Ti⁴⁺ so an extra hole remains in the crystal which play the crucial role as free carrier in conductivity (Figure 6.17c). The VB and CB potentials of Bi-doped TiO₂ are 1.57 V and -1.28 V vs RHE respectively. As expected, MoS₂/Bi-TiO₂ heterostructures shows both p-type and n-type conductivity for the presence of n-type MoS₂ and p-type Bi-doped TiO₂, i.e. a p-n junction may be formed at the interface between two semiconductors (Figure 6.17d). As a result, enhanced electron–hole transfer efficiency has been achieved through the junction due to presence of internal electric field.

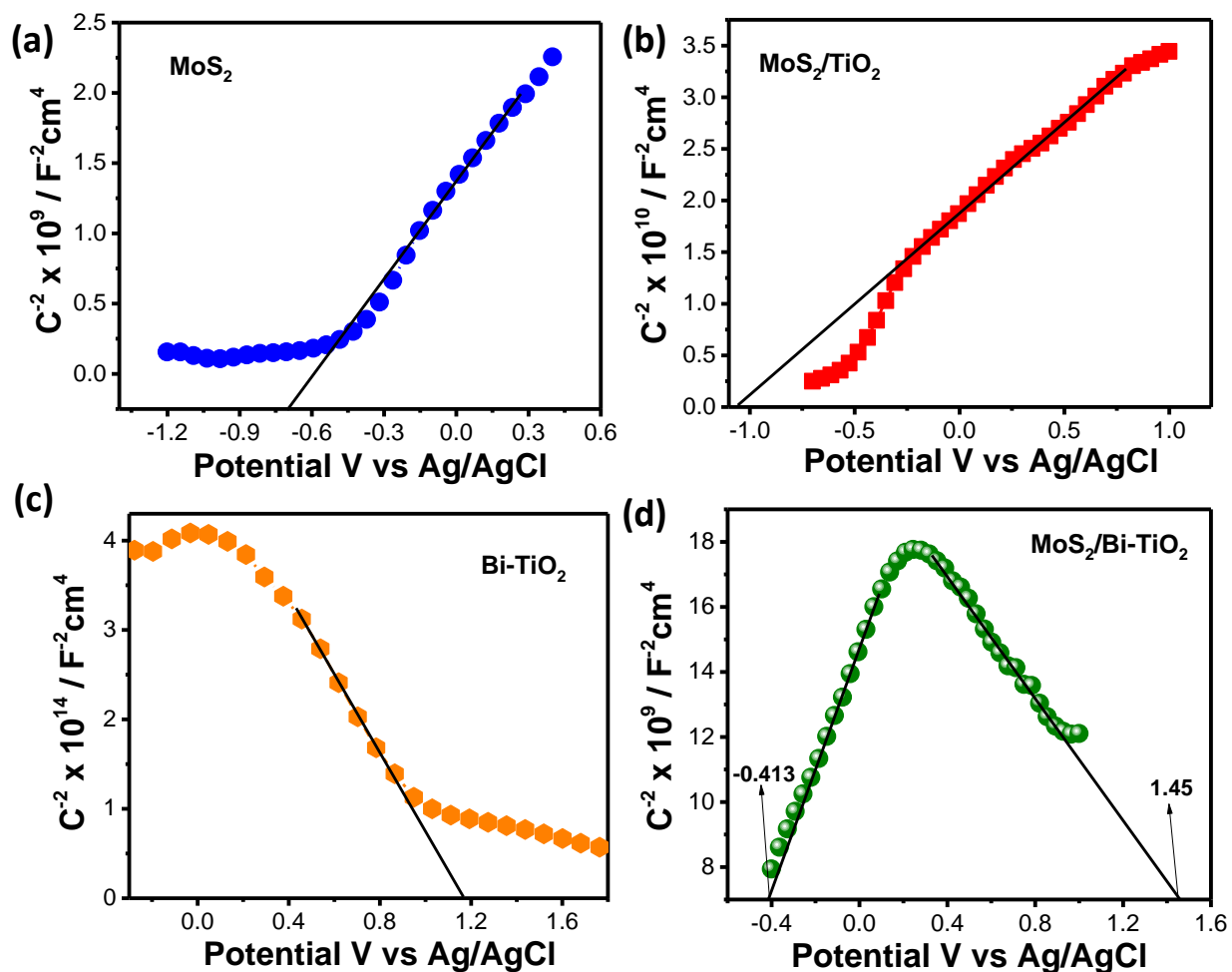


Figure 6.17 Mott–Schottky plots of (a) bare MoS₂, (b) MoS₂/TiO₂ (MT-10), (c) Bi-doped TiO₂ and (d) MoS₂/Bi-TiO₂ (MBT-10) heterostructures. The experiment was carried out in Na₂SO₄ solution (0.1 M) under 1000 Hz AC frequency. E_{fb} of photoelectrodes have been calculated from the intercept of the plots at 1/C² = 0.

Cyclic voltammetry (CV) has been carried out to study the electrochemical properties of the as prepared electrodes of MoS₂, Ag-AgVO₃ and MoS₂/Ag-AgVO₃ using 0.5M Na₂SO₄-phosphate buffer solution (pH 7) as electrolyte and Ag/AgCl electrode as reference electrode at a scan rate of 10 mV s⁻¹ (Figure 6.18a). In the cathodic polarization process, two peaks have been observed for Ag-AgVO₃ at ~0.31 V and ~0.59 V vs Ag/AgCl with current density of ~69 μA cm⁻² and ~336 μA cm⁻², which corresponds to the initial reduction of Ag⁺ to Ag⁰ and V⁵⁺ to V⁴⁺ respectively. Similarly, two characteristic peaks have been appeared in the anodic scan at ~0.27 V and ~0.12 V vs Ag/AgCl, which are in well agreement with the previously reported literatures [78, 79]. On the other hand, no prominent cathodic peak is present in MoS₂ electrode, but a broad peak is observed around ~0.8 V vs Ag/AgCl. However, the CV of the MoS₂/Ag-AgVO₃ electrode shows a single peak at ~0.45 V vs Ag/AgCl in cathodic scan with current density of ~519 μA cm⁻². This large current density of heterostructures demonstrate an enhanced electron transfer rate through the interfaces [80]. Further, linear sweep voltammetry (LSV) have been studied under chopped light illumination of 100 mW cm⁻² (Figure 6.18b). The bare MoS₂ photoanode shows low current density in the full potential range, because of its poor ability of charge separation, which leads to the fast recombination of photoinduced electron–hole pairs. However, an enhanced current density has been obtained for Ag-AgVO₃ and MoS₂/Ag-AgVO₃ electrodes and it reaches maximum value of ~80 μA cm⁻² at 0.8 V vs Ag/AgCl for MoS₂/Ag-AgVO₃ heterostructures. This result demonstrates that presence of Ag NPs significantly improves visible-light absorption by plasmonic effect and efficiently separates the photoinduced electrons and holes by making electron migration bridge between two semiconductors, leading to a remarkable enhancement in PEC water splitting. Transient photocurrent measurements through chronoamperometry (CA) and electrochemical impedance spectroscopy (EIS) have been performed further to gain insight into the carrier separation and transport efficiency of the photoanodes. It can be clearly observed that the current density increases for MoS₂/Ag-AgVO₃ heterostructures (~64 μA cm⁻²) compared to bare MoS₂ (~25 μA cm⁻²) and Ag-AgVO₃ (~35 μA cm⁻²) after 500 sec and remains almost constant with time (Figure 6.18c). Therefore, it can be concluded that heterojunction formation can promote the charge separation and suppress the recombination of photogenerated electron–holes. Figure 6.18d represents the Nyquist diagram of as prepared electrodes, where the radius of each arc is associated with the charge transfer resistance (R_{ct}) at the electrode electrolyte interface.

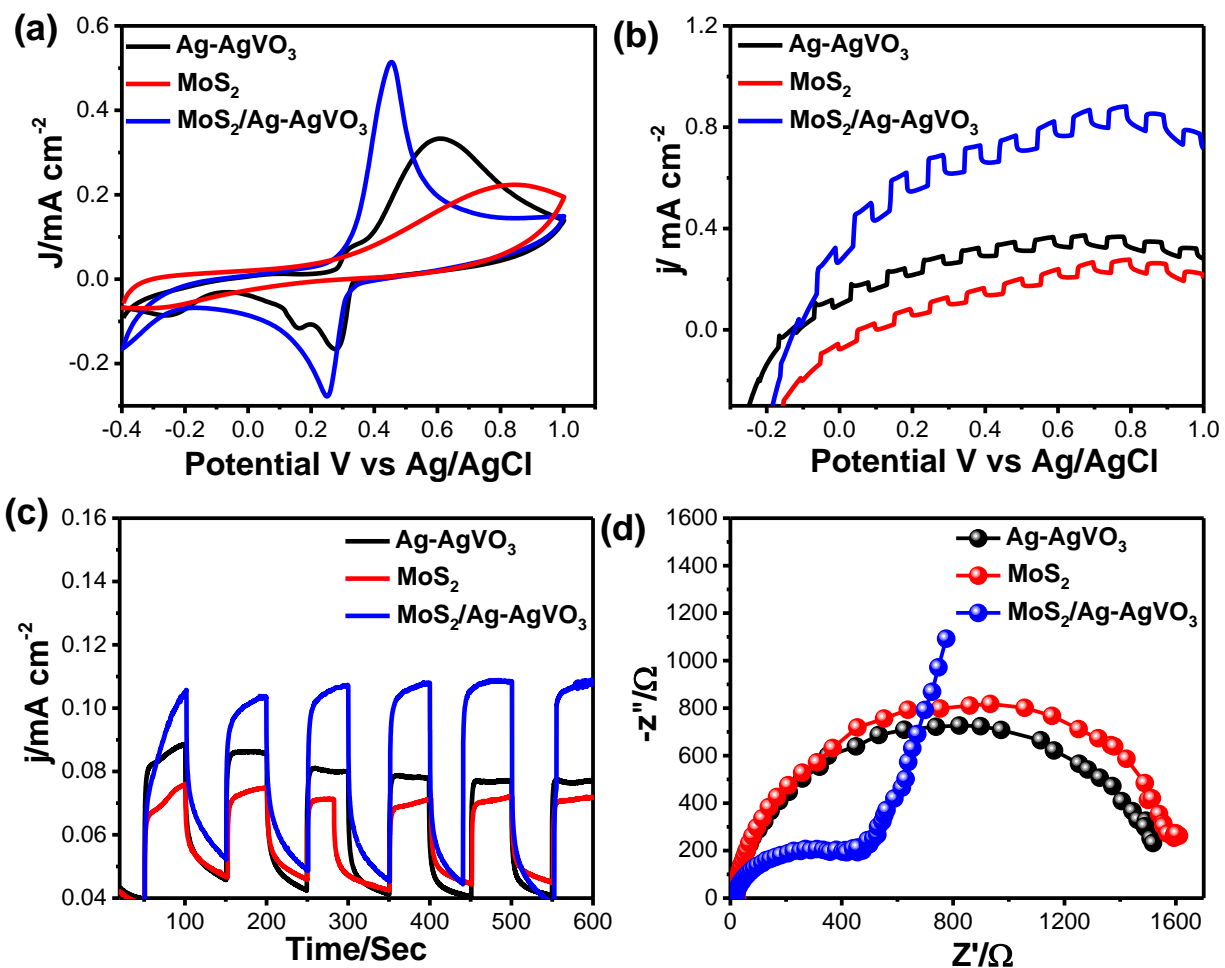


Figure 6.18 (a) Cyclic voltammogram (CV) of prepared electrodes in presence of 0.1M Na₂SO₄-phosphate buffer solution (pH 7) as electrolyte at a scan rate of 10 mV s⁻¹. (b) Linear sweep voltammetry (LSV) and (c) chronoamperometry (CA) profile under chopped light illumination of 100 mW cm⁻² of as prepared electrodes in presence of 0.1M Na₂SO₄-phosphate buffer solution at a scan rate of 10 mV s⁻¹. (d) Nyquist plots of Ag-AgVO₃, bare MoS₂ and MoS₂/Ag-AgVO₃ heterostructures recorded at 0.1 V vs Ag/AgCl under light illumination.

A single semicircle has been obtained for both MoS₂ and Ag-AgVO₃ electrodes, whereas a distorted semicircle has been observed for MoS₂/Ag-AgVO₃ heterostructures. This may results due to the increase of electron diffusion to the catalyst surface [77]. The straight line in the lower frequency region arises due to more diffusion process of the electrolyte. The diameter presents the R_{ct} over the electrode-electrolyte interface. As shown in Figure 6.18d the diameter of heterostructures (0.46 KΩ) is considerably smaller than that of bare MoS₂ (1.6 kΩ) and Ag-AgVO₃ (1.5 kΩ), suggests that heterostructures provide facile access for charge carrier interpolation during the water splitting process. Thus, all electrochemical investigations demonstrate that,

heterostructures formation between MoS₂ and Ag-AgVO₃ accelerates the interfacial transfer and separation of photogenerated charges which results high activity in photocatalytic H₂ generation.

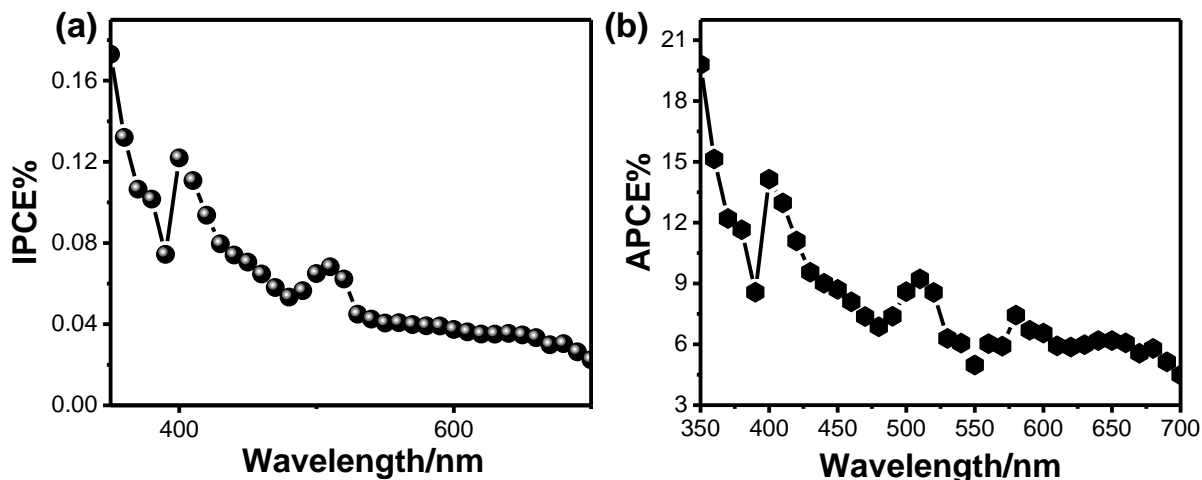


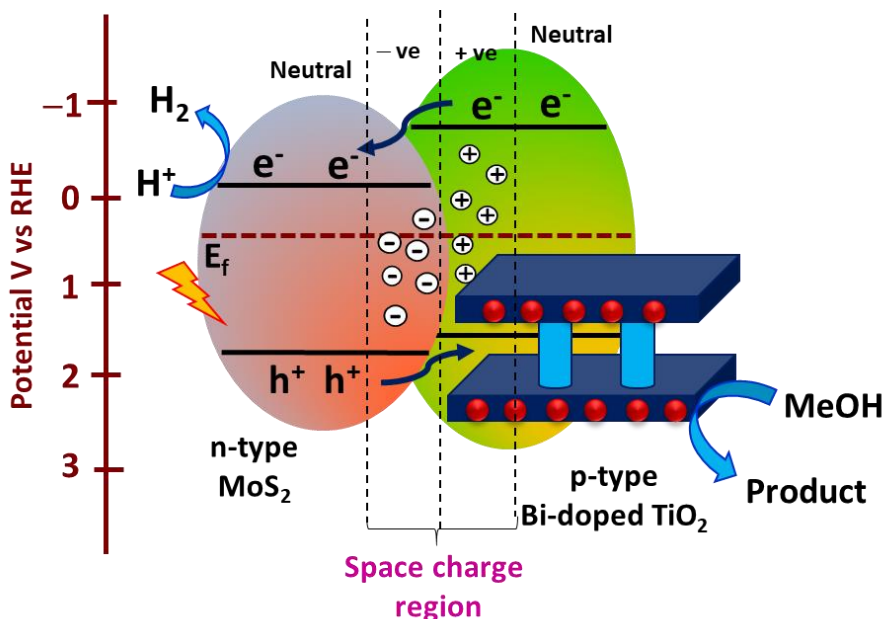
Figure 6.19 (a) Calculated incident photon to current conversion efficiency (IPCE %) and (b) Absorbed photon to current conversion efficiency (APCE %) of MoS₂/Ag-AgVO₃ photoanode within the wavelength range 350–700 nm.

Moreover, the quantum efficiency of the MoS₂/Ag-AgVO₃ heterostructures has been studied in details by calculating incident photon to current conversion efficiency (IPCE) and absorbed photon to current conversion efficiency (APCE) from the action spectra through CA measurements within the wavelength range of 350 to 700 nm [77]. Figure 6.19a represents the IPCE vs wavelength plot where two distinct enhanced regions are observed at 400 nm and 510 nm with efficiency of 0.12% and 0.06% respectively. The integrated current density of the MoS₂/Ag-AgVO₃ photoanode reaches to 21 μA cm⁻² which well consistent with the photo current density calculated from LSV curve. The APCE plot represents the similar trend like IPCE with two enhanced region at visible region (Figure 6.19b). Thus, heterostructures formation is beneficial to enhance the light absorption, charge separation and surface catalytic reactions which consequently enhance the incident photon to current conversion efficiency.

6.3.7 Photocatalytic Mechanism

Before light illumination on the MoS₂/Bi-TiO₂ heterostructures, the electrons of MoS₂ near the junction try to diffuse into the p-type Bi-doped TiO₂, leaving the holes. Similarly, the holes on the p-type Bi-doped TiO₂ near the junction tend to diffuse into the n-type MoS₂, leaving negatively charged electrons. This diffusion of electrons and holes will be continued until the Fermi level

equilibrium of the system is achieved, which results a space charge region both sides of the junction interface and creates an internal electric field. Now, when this equilibrium system is irradiated by light energy (greater than the work function energy of the constituent semiconductors) then both the semiconductors will excited and produce excitons (excited electrons and holes). The photo-generated electrons of p-type Bi-doped TiO_2 will transfer to the CB of the n-type MoS_2 and the holes of MoS_2 will transfer to the VB of the Bi-doped TiO_2 by the influence of internal electric field (Scheme 6. 1). In this way, special separation of electrons and holes will occur which can reduce the formation of electron-hole pairs [81]. Consequently, the excited electrons accumulated on the CB of MoS_2 which have higher negative potential compared to the water reduction potential (0 V vs RHE). These electrons can easily reduce the water and generate H_2 from H^+ . Simultaneously, oxidation of the water molecules takes place by the accumulated holes on the VB of Bi-doped TiO_2 which are highly positive and can oxidize the water.



Scheme 6.1 Schematic illustration of the charge transfer in $\text{MoS}_2/\text{Bi-TiO}_2$ p-n heterojunction.

In order to investigate the enhanced photocatalytic activity of $\text{MoS}_2/\text{Ag-AgVO}_3$ heterostructures, the separation and recombination processes of photoinduced charge carriers of the as-prepared samples have been further examined by the Photoluminescence (PL) spectra. Generally, the PL emission are originated from the recombination of electron hole pairs in a semiconductor. The low

PL intensity presents low recombination of photoinduced electron hole pairs, thereby high photocatalytic performance. Figure 6.20a shows the PL spectra of Ag-AgVO₃ and MoS₂/Ag-AgVO₃ heterostructures upon excitation at 340 nm. The band to band recombination and distortion in the [O–Ag–O] and [O–V–O] bonds in AgVO₃ lattice are mainly responsible for PL emissions. In the PL spectra a pronounced maximum at 467 nm has been observed which corresponds to band to band recombination of photoinduced charge carriers. Additionally, a peak at 450 nm comes due to distortions in the tetrahedral [VO₄] clusters [82]. In addition, a weak emission peak has also been presented at 560 nm, indicates an ordered structure of AgVO₃. However, the PL emission peak intensity has been decreased after heterostructure formation with MoS₂ without effecting the spectral position of the peaks, suggesting improve charge separation and transfer ability of heterostructures. Furthermore, to understand the ultrafast charge transfer processes associated at the interface between MoS₂ and AgVO₃, picosecond resolved time correlated single photon counting (TCSPC) of the materials have been recorded. Figure 6.20b shows the decay curve of Ag-AgVO₃ which is properly fitted with a double exponential with average lifetime of ~1.30 ns. However, the average decay time for MoS₂ (~0.71 ns) is lower than Ag-AgVO₃, which has an ultrafast component of ~ 25 ps (21.3%). The average decay time decreases significantly from 0.71 ns to 0.36 ns after heterostructure formation between MoS₂ and Ag-AgVO₃ (Table 6.2). Interestingly, the contribution of the fast component of MoS₂/Ag-AgVO₃ heterostructure has been increased to nearly 40% from 21.3% compared to bare MoS₂. This result clearly indicated that, electron transfer occurs from AgVO₃ to MoS₂ after heterostructure formation and reduce the recombination rate which is well consistent with the PL data (Figure 6.20a).

Table 6.2 Decay parameters of Ag-AgVO₃, MoS₂ and MoS₂/Ag-AgVO₃ heterostructures.

| sample | Excitation wavelength (nm) | Detection wavelength (nm) | τ_1 (a1 %) ns | τ_2 (a2 %) ns | τ_3 (a3 %) ns | τ_{avg} (ns) |
|--|----------------------------|---------------------------|--------------------|--------------------|--------------------|-------------------|
| Ag-AgVO ₃ | 375 | 450 | 1.31 (55.6) | 1.30 (44.4) | – | 1.30 |
| MoS ₂ | 375 | 450 | 0.26 (10.5) | 0.99 (68.2) | 0.025 (21.3) | 0.71 |
| MoS ₂ /Ag-AgVO ₃ | 375 | 450 | 0.13 (26.4) | 0.91 (34.2) | 0.051 (39.4) | 0.36 |

Finally, Mott-Schottky (M-S) experiment of as prepared electrodes has been carried out to find out the band edge potentials of constituent semiconductors as they play crucial role in determining the transfer route of the charge carriers. Figure 6.20c shows the M-S plot of Ag-AgVO₃ and bare MoS₂ electrodes in the presence of 0.5 M Na₂SO₄ electrolytes (pH 7) using an AC frequency of 1000 Hz, where the positive slopes confirm the n-type behaviour of the materials.

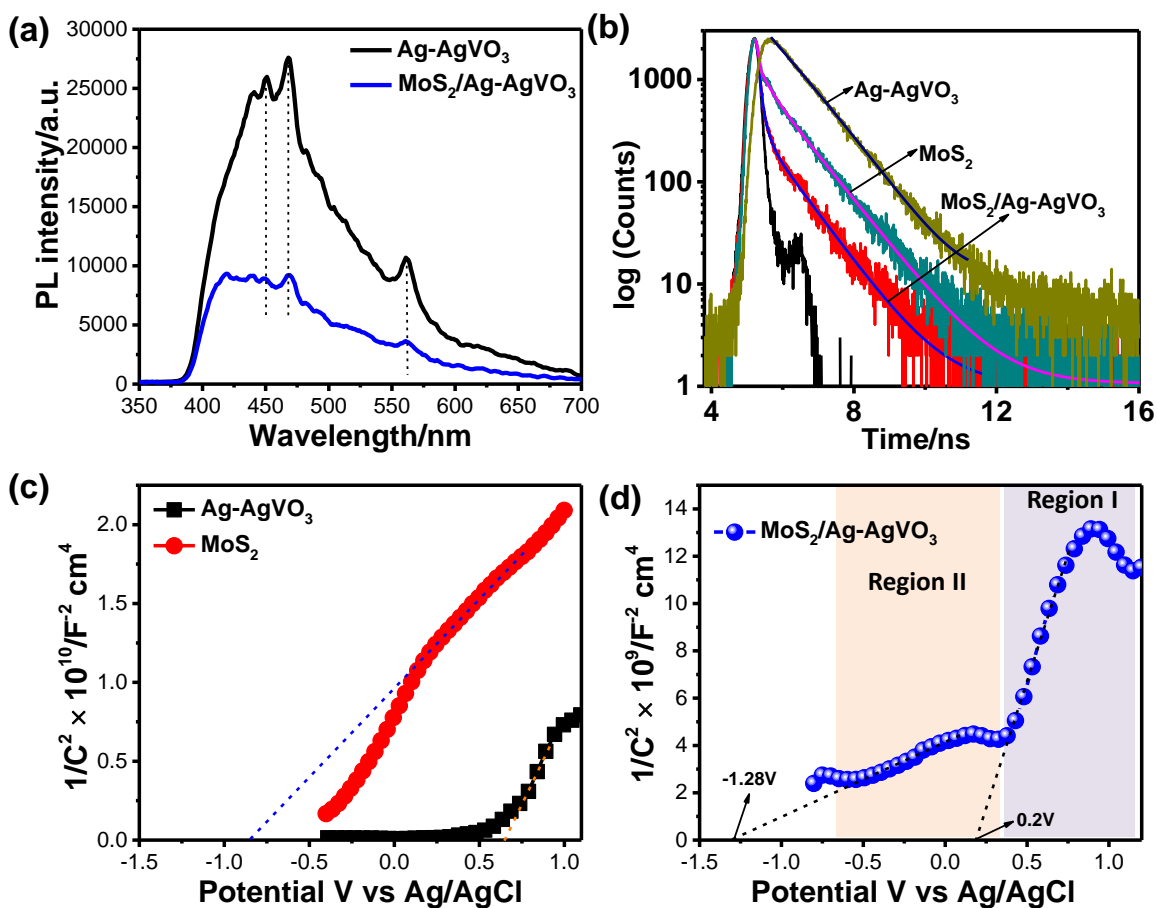


Figure 6.20 (a) Photoluminescence (PL) spectra of Ag-AgVO₃ and MoS₂/Ag-AgVO₃ heterostructures upon excitation at 340 nm. (b) The picosecond-resolved TCSPC spectra of as prepared materials upon excitation at 375 nm. Mott-Schottky plots of (c) Ag-AgVO₃, bare MoS₂ and the MoS₂/Ag-AgVO₃ heterostructures in the presence of 0.1 M Na₂SO₄ electrolytes (pH 7) using an AC frequency of 1000 Hz. The intercept of the plot (at $1/C^2 = 0$) has been used to determine the flat band potential (E_{fb}) of the photoelectrodes.

The flat band potentials (E_{fb}) of the electrodes have been determined by taking an intercept of the plot (at $1/C^2 = 0$). Notably, a negative shift in the flat band potential (E_{fb}) has been observed for MoS₂ ($-0.83 \text{ V vs Ag/AgCl}$) compare to Ag-AgVO₃ ($0.65 \text{ V vs Ag/AgCl}$). As the E_{fb} is near to the CB for n-type semiconductor, thus the positions of CB are 0.45 V and -1.03 V (*vs Ag/AgCl*,

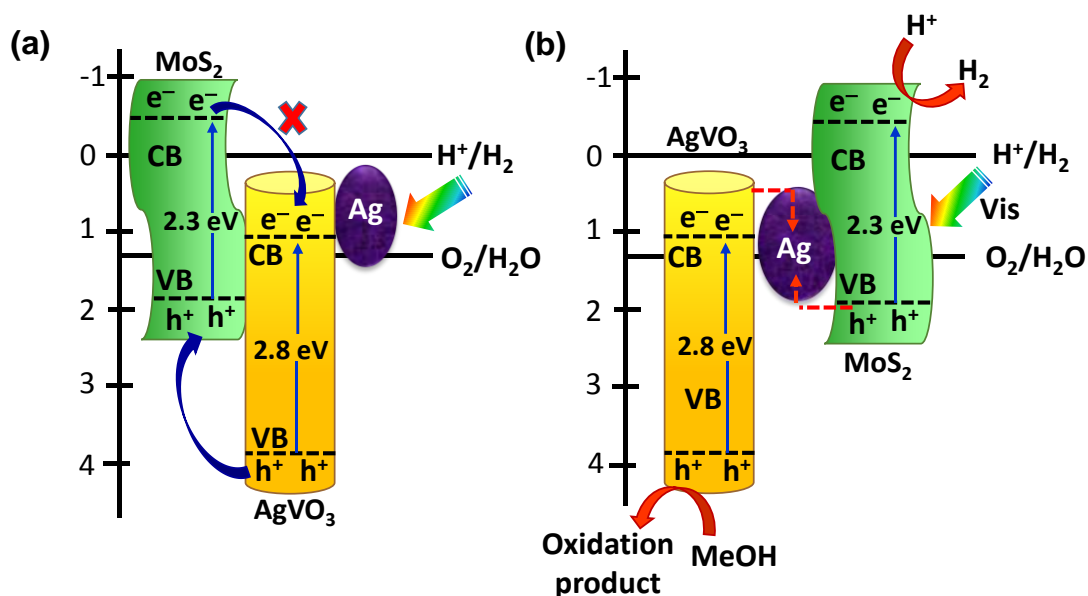
CB = $E_{fb} - 0.2$ V), therefore they are 1.06 V and -0.42 V vs NHE (Normal Hydrogen Electrode) for Ag-AgVO₃ and bare MoS₂ electrodes respectively. So, the VB positions of Ag-AgVO₃ and bare MoS₂ electrodes would be 3.86 V and 1.88 V vs NHE respectively (Table 6.2) which corresponds to the results of UV-Vis DRS analysis. The M-S plot of heterostructures also exhibits n-type nature with flat band potential of 0.2 V vs Ag/AgCl which is shifted towards negative potential than Ag-AgVO₃ (0.65 V vs Ag/AgCl), clearly reveals a strong interaction after heterostructures formation (Figure 6.20d).

Table 6.3 Electrochemical parameters calculated from Mott-Schottky plots for prepared electrodes.

| Catalyst | E_{fb} in V vs Ag/AgCl | CB in V vs NHE | VB in V vs NHE | E_g in eV |
|----------------------|--------------------------|----------------|----------------|-------------|
| Ag-AgVO ₃ | 0.65 | 1.06 | 3.86 | 2.8 |
| MoS ₂ | -0.83 | -0.42 | 1.88 | 2.3 |

Based on the experimental results, it can be proposed that the improved photocatalytic activity achieves due to the enhancement of light absorption capacity as well as efficient charge separation of photogenerated electron hole pairs. Generally, the charge transfer mechanism of heterostructures follow type-II heterojunction pathway, where the CB electrons (more negative potential) of one semiconductor transfer to the CB of another semiconductor and the VB holes (more positive potential) transfer to the relatively low positive potential VB of another semiconductor. Consequently, electrons and holes may accumulated in CB and VB of two different semiconductors respectively. Hence, in the present system, the photogenerated CB electron of MoS₂ may preferably transfer to the CB of AgVO₃ due to more negative CB potential of MoS₂ and the holes in the VB of AgVO₃ would simultaneously transfer to the VB of MoS₂. However, the CB potential of AgVO₃ (+1.06 V vs NHE) is more positive than the potential required for the water reduction (0 V vs NHE, H⁺/H₂), therefore the electrons in the CB of AgVO₃ cannot reduce the water into H₂ [83]. So, this type-II heterojunction charge-transfer mechanism may not be possible for MoS₂/Ag-AgVO₃ hetrostructures (Scheme 6.2a). Consequently, a plausible Z-scheme charge-transfer mechanism for the MoS₂/Ag-AgVO₃ hetrostructures can be proposed in Scheme 6.2b. Under visible light illumination, the photoexcited electrons on the CB of AgVO₃ easily transfer into the Ag NPs because the CB edge is more negative than the Fermi level of the metallic Ag NPs. At the same time, the holes on the VB of MoS₂ may migrate into the metal Ag NPs, as

the valence band of MoS₂ is more positive than the Fermi level of metallic Ag. Meanwhile, Ag NPs also absorb visible light and generate photoexcited electron and a hole due to the SPR effect and dipolar character of metallic Ag. The plasmon-induced electrons of Ag nanoparticles can be transported to the CB of MoS₂ because of electronic oscillation with upshifted energy states which is greater than the CB of the neighboring semiconductor [84]. Therefore, enrichment of photoexcited electrons occurs on the CB of MoS₂ with a more negative potential than of water reduction (0 V vs NHE) and accumulation of holes take place on the valence band of AgVO₃ with a more positive potential, greater than water oxidation potential (1.23 V vs NHE). This synergistic charge transfer process through Z-scheme bridge made by Ag NPs remarkably enhance the separation of photogenerated charge carriers and reduce the rapid recombination on the surface of individual AgVO₃ and MoS₂. Additionally, metallic Ag NPs enhance the catalytic performance towards H₂ generation through SPR effect of a resonant collective oscillation of photoinduced electrons over Ag NPs which extend the absorption up to visible region. However, the existence of Ag-AgVO₃ nanocrystals on the surfaces of the MoS₂ nanosheets form an uniquely hierarchical nanostructure, which provides a high surface area and a large number of interfaces between the Ag-AgVO₃ and MoS₂. The high surface areas and interfaces provide numerous active sites for the photocatalytic reactions. Consequently, it can be conclude that the enhanced photocatalytic performance of MoS₂/Ag-AgVO₃ hetrostructures mainly ascribed to the efficient separation of charge carriers according to the Ag-promoted Z-scheme mechanism.



Scheme 6.2 Proposed (a) Type II heterostructures and (b) Z-scheme mechanism of MoS₂/Ag-AgVO₃ heterostructures for photocatalytic H₂ generation under visible light irradiation.

6.4 Summary

A p-n junction of MoS₂/Bi-TiO₂ heterostructures was developed for visible light sensitive water splitting. The introduction of Bi into the TiO₂ crystal leads to more efficient light absorption by hybridized VB. The photoexcited electrons in the CB of Bi-modified TiO₂ transferred to MoS₂ and holes of MoS₂ transfer to the VB of Bi-TiO₂ through the junction between them. The p-n junction provide an internal driving force to accelerate the charge separation. As a result, four fold enhanced H₂ generation rate achieved for MoS₂/Bi-TiO₂ p-n junction compared to bare MoS₂. Moreover, the MoS₂/Bi-TiO₂ heterostructures shows superior catalytic activity in photoelectrochemical measurements because of low charge transfer resistance at the electrode-electrolyte interfaces. On the other hand, Z-scheme heterostructures has been developed with Ag NPs decorated 1D AgVO₃ nanorods by facile coprecipitation method on MoS₂ nanosheet at room temperature. The introduction of metallic Ag NPs between AgVO₃ and MoS₂ enhance the light absorption capacity in visible region by virtue of surface plasmonic resonance effect. Moreover, it develops the Z-scheme bridge mechanism between AgVO₃ and MoS₂ to drive the efficient separation of photoinduced charge carriers. In addition, the well-matched band positions of AgVO₃ and MoS₂ composite conforms the Z-scheme charge transfer mechanism with a higher reducing capability, leading to the enhancement of photocatalytic H₂ generation under visible light illumination. MoS₂/Ag-AgVO₃ Z-scheme heterostructures show four fold and twenty fold enhanced H₂ generation rate compared to Ag-AgVO₃ and bare MoS₂ respectively. Moreover, MoS₂/Ag-AgVO₃ Z-scheme heterostructures significantly improve the catalytic activity towards water oxidation by enhancing the photoelectrochemical current density and long-term stability under visible light irradiation. Thus, this work represents a paradigm of the p-n junction and all-solid-state Z-scheme photocatalyst having the advantages of enhanced visible light harvesting, efficient charge separation and transfer, low photocorrosion and provides a possible way to develop more MoS₂ based heterostructures with useful properties for environmental and energy applications.

References

- [1] A. J. Bard, M. A. Fox, Artificial Photosynthesis: Solar Splitting of Water to Hydrogen and Oxygen. *Acc. Chem. Res.* **28** (1995) 141–145.
- [2] J. H. Kim, D. Hansora, P. Sharma, J.-W. Jang, J. S. Lee, Toward practical solar hydrogen production – an artificial photosynthetic leaf-to-farm challenge. *Chem. Soc. Rev.* **48** (2019) 1908–1971.
- [3] T. Hisatomi, J. Kubota, K. Domen, Recent advances in semiconductors for photocatalytic and photoelectrochemical water splitting. *Chem. Soc. Rev.* **43** (2014) 7520–7535.
- [4] Q. Wang, K. Domen, Particulate Photocatalysts for Light-Driven Water Splitting: Mechanisms, Challenges, and Design Strategies. *Chem. Rev.* **120** (2020) 919–985.
- [5] B. A. Pinaud, J. D. Benck, L. C. Seitz, A. J. Forman, Z. Chen, T. G. Deutsch, B. D. James, K. N. Baum, G. N. Baum, S. Ardo, H. Wang, E. Millere, T. F. Jaramillo, Technical and economic feasibility of centralized facilities for solar hydrogen production via photocatalysis and photoelectrochemistry. *Energy Environ. Sci.* **6** (2013) 1983–2002.
- [6] S. Ghosh (Ed), Visible-Light-Active Photocatalysis: Nanostructured Catalyst Design, Mechanisms and Applications, Wiley-VCH Verlag GmbH & Co. KGaA, Germany, 2018, ISBN: 978-3-527-34293-8.
- [7] Z. Wang, C. Li, K. Domen, Recent developments in heterogeneous photocatalysts for solar-driven overall water splitting. *Chem. Soc. Rev.* **48** (2019) 2109–2125.
- [8] J. Jian, G. Jiang, R. Krol, B. Wei, H. Wang, Recent Advances in Rational Engineering of Multinary Semiconductors for Photoelectrochemical Hydrogen Generation. *Nano Energy* **51** (2018) 457–480.
- [9] S. Ghosh, M. Thandavarayan, R. N. Basu, Nanostructured conducting polymers for energy applications: towards a sustainable platform. *Nanoscale* **8** (2016) 6921–6947.
- [10] K. Sivula, R. Krol, Semiconducting Materials for Photoelectrochemical Energy Conversion. *Nat. Rev. Mater.* **1** (2016) 1–15.
- [11] X. Yuan, D. Floresyona, P. H. Aubert, T. T. Bui, S. Remita, S. Ghosh, F. Brisset, F. Goubard, H. Remita, Photocatalytic degradation of organic pollutant with polypyrrole nanostructures under UV and visible light. *Appl. Catal. B* **242** (2019) 284–292.
- [12] I. Gu, M. Sayed, N. S. Shah, J. A. Khan, K. Polychronopoulou, J. Iqbal, F. Rehman, Solar light responsive bismuth doped titania with Ti^{3+} for efficient photocatalytic degradation of

- flumequine: Synergistic role of peroxymonosulfate. *Chem. Eng. J.* **384** (2020) 123255–123272.
- [13] S. Ghosh, H. Remita, R. N. Basu, Visible-light-induced reduction of Cr (VI) by PDPB-ZnO nanohybrids and its photo-electrochemical response. *Appl. Catal. B* **239** (2018) 362–72.
- [14] M. D. Hernandez-Alonso, F. Fresno, S. Suarez, J. M. Coronado, Development of alternative photocatalysts to TiO₂: Challenges and opportunities. *Energy Environ. Sci.* **2** (2009) 1231–1257.
- [15] F. Wang, R. J. Wong, J. H. Ho, Y. Jiang, R. Amal, Sensitization of Pt/TiO₂ Using Plasmonic Au Nanoparticles for Hydrogen Evolution under Visible-Light Irradiation. *ACS Appl. Mater. Interfaces* **9** (2017) 30575–30581.
- [16] N. A. Kouamé, O. T. Alaoui, A. Herissan, E. Larios, M. José-Yacaman, A. Etcheberry, C. Colbeau-Justina, H. Remita, Visible light-induced photocatalytic activity of modified titanium (IV) oxide with zero-valent bismuth clusters. *New J. Chem.* **39** (2015) 2316–2322.
- [17] Y. Chen, C.-H. Chuang, Z. Qin, S. Shen, T. Doane, C. Burd, Electron-transfer dependent photocatalytic hydrogen generation over cross-linked CdSe/TiO₂ type-II heterostructure. *Nanotechnol.* **28** (2017) 084002–084006.
- [18] S. B. Kubakaddi, S. Chirakkara, G. Hosamani, S. M. Shivaprasad, Nanostructured p-TiO₂/n-GaN heterostructure as a potential photoelectrode for efficient charge separation. *Nanotechnol.* **29** (2018) 50LT02–50LT07.
- [19] Y. Zhao, Q. Zeng, T. Feng, C. Xia, C. Liu, F. Yang, K. Zhang, B. Yang, Carbonized polymer dots/TiO₂ photonic crystal heterostructures with enhanced light harvesting and charge separation for efficient and stable photocatalysis. *Mater. Chem. Front.* **3** (2019) 2659–2667.
- [20] X. Wang, S. Jiang, X. Huo, R. Xia, E. Muhire, M. Gao, Facile preparation of a TiO₂ quantum dot/graphitic carbon nitride heterojunction with highly efficient photocatalytic activity. *Nanotechnol.* **29** (2018) 205702–205705.
- [21] K. Wang, M. Endo-Kimura, R. Belchi, D. Zhang, A. Habert, J. Bouclé, B. Ohtani, E. Kowalska, N. Herlin-Boime, Carbon/Graphene-Modified Titania with Enhanced Photocatalytic Activity under UV and Vis Irradiation. *Materials* **12** (2019) 4158–4164.

- [22] U. Bach, D. Lupo, P. Comte, J. E. Moser, F. Weissörtel, J. Salbeck, H. Spreitzer, M. Grätzel, Solid-state dye-sensitized mesoporous TiO₂ solar cells with high photon-to-electron conversion efficiencies. *Nature* **395** (1998) 583–585.
- [23] M. G. Mendez-Medrano, E. Kowalska, A. Lehoux, A. Herissan, B. Ohtani, S. Rau, C. Colbeau-Justin, J. L. Rodríguez-Lopez, H. Remita, Surface modification of TiO₂ with Au nanoclusters for efficient water treatment and hydrogen generation under visible light. *J. Phys. Chem. C* **120** (2016) 25010–25022.
- [24] M. Nischk, P. Mazierski, Z. Wei, K. Siuzdak, N. A. Kouame, E. Kowalska, H. Remita, A. Zaleska-Medynska, Enhanced photocatalytic, electrochemical and photoelectrochemical properties of TiO₂ nanotubes arrays modified with Cu, AgCu and Bi nanoparticles obtained via radiolytic reduction. *Appl. Surface Sci.* **387** (2016) 89–102.
- [25] T. H. Ji, F. Yang, Y. Y. Lv, J. Y. Zhou, J. Y. Sun, Synthesis and visible-light photocatalytic activity of Bi-doped TiO₂ nanobelts. *Mater. Lett.* **63** (2009) 2044–2048.
- [26] S. Murcia-López, M. C. Hidalgo, J. A. Navío, Synthesis, characterization and photocatalytic activity of Bi-doped TiO₂ photocatalysts under simulated solar irradiation. *Appl. Catal., A* **404** (2011) 59–67.
- [27] P. A. K. Reddy, B. Srinivas, P. Kala, V. D. Kumari, M. Subrahmanyam, Preparation and characterization of Bi-doped TiO₂ and its solar photocatalytic activity for the degradation of isoproturon herbicide. *Mater. Res. Bull.* **46** (2011) 1766–1771.
- [28] Y. Q. Wu, G. X. Lu, S. B. Li, The doping effect of Bi on TiO₂ for photocatalytic hydrogen generation and photodecolorization of rhodamine B. *J. Phys. Chem. C* **113** (2009) 9950–9955.
- [29] J. J. Xu, M. D. Chen, D. G. Fu, Study on highly visible light active Bi-doped TiO₂ composite hollow sphere. *Appl. Surf. Sci.* **257** (2011) 7381–7384.
- [30] Y. Hu, Y. T. Cao, P. X. Wang, D. Z. Li, W. Chen, Y. H. He, X. Z. Fu, Y. Shao, Y. Zheng, A new perspective for effect of Bi on the photocatalytic activity of Bi-doped TiO₂. *Appl. Catal. B* **125** (2012) 294–301.
- [31] S. Li, L. Chang, J. Peng, J. Gao, J. Lu, F. Zhang, G. Zhu, M. Hojamberdiev, Bi⁰ nanoparticle loaded on Bi³⁺-doped ZnWO₄ nanorods with oxygen vacancies for enhanced photocatalytic NO removal. *J. Alloys Compd.* **818** (2020) 152837–152846.

- [32] J. Lv, J. Zhang, J. Liu, Z. Li, K. Dai, C. Liang, Bi SPR-Promoted Z- Scheme $\text{Bi}_2\text{MoO}_6/\text{CdS}$ -Diethylenetriamine Composite with Effectively Enhanced Visible Light Photocatalytic Hydrogen Evolution Activity and Stability. *ACS Sus. Chem. Eng.* **6** (2018) 696–706.
- [33] M. Du, S. Zhang, Z. Xing, Z. Li, J. Yin, J. Zou, Q. Zhu, W. Zhou, All-Solid Z Scheme Bi– BiOCl/AgCl Heterojunction Microspheres for Improved Electron–Hole Separation and Enhanced Visible Light Driven Photocatalytic Performance. *Langmuir* **35** (2019) 7887–7895.
- [34] W. Hao, F. Teng, Z. Liu, Z. Yang, Z. Liu, W. Gu, Synergistic effect of Mott-Schottky junction with oxygen defect and dramatically improved charge transfer and separation of Bi@Bi-doped TiO_2 , *Sol. Energy Mater. Sol. Cells* **203** (2019) 110198–110206.
- [35] K. O. Magnusson, S. Wiklund, Interface formation of Bi on ceramic ZnO: A simple model varistor grain boundary. *J. Appl. Phys.* **76** (1994) 7405–7409.
- [36] Y. Liu, X. Duan, Y. Huang, X. Duan, Two-dimensional transistors beyond graphene and TMDCs. *Chem. Soc. Rev.* **47** (2018) 6388–6409.
- [37] Q. Lu, Y. Yu, Q. Ma, B. Chen, H. Zgang, 2D Transition-Metal-Dichalcogenide-Nanosheet-based composites for photocatalytic and electrocatalytic hydrogen evolution reactions. *Adv. Mater.* **28** (2016) 1917–1933.
- [38] S. Wi, H. Kim, M. Chen, H. Nam, L. J. Guo, E. Meyhofer, X. Liang, Enhancement of photovoltaic response in multilayer MoS_2 induced by plasma doping. *ACS Nano* **8** (2014) 5270–5281.
- [39] Q. Pang, Y. Zhao, X. Bian, Y. Ju, X. Wang, Y. Wei, B. Liu, F. Du, C. Wang, G. Chen, Hybrid graphene@ MoS_2 @ TiO_2 microspheres for use as a high performance negative electrode material for lithium ion batteries. *J. Mater. Chem. A* **5** (2017) 3667–3674.
- [40] T. Stephenson, Z. Li, B. Olsen, D. Mitlin, Lithium ion battery applications of molybdenum disulfide (MoS_2) nanocomposites. *Energy Environ. Sci.* **7** (2014) 209–231.
- [41] T. Wang, S. Chen, H. Pang, H. Xue, Y. Yu, MoS_2 - Based nanocomposites for electrochemical energy storage. *Adv. Sci.* **4** (2016) 1600289–1600315.
- [42] D. Sarkar, W. Liu, X. Xie, A. C. Anselmo, S. Mitragotri, K. Banerjee, MoS_2 field-effect transistor for next-generation label-free biosensors. *ACS Nano* **8** (2014) 3992–4003.

- [43] L. Guo, Z. Yang, K. Marcus, Z. Li, B. Luo, L. Zhou, X. Wang, Y. Du, Y. Yang, MoS₂/TiO₂ heterostructures as nonmetal plasmonic photocatalysts for highly efficient hydrogen evolution. *Energy Environ. Sci.* **11** (2018) 106–114.
- [44] Y.-Y. Li, J.-H. Wang, Z.-J. Luo, K. Chen, Z.-Q. Cheng, L. Ma, S.-J. Ding, L. Zhou, Q.-Q. Wang, Plasmon-enhanced photoelectrochemical current and hydrogen production of (MoS₂-TiO₂)/Au hybrids. *Sci. Rep.* **7** (2017) 7178–7216.
- [45] S. Bera, S. Ghos, R. N. Basu, Silver as solid-state electron mediator in MoS₂/Ag–AgVO₃ Z-Scheme heterostructures for photocatalytic H₂ generation. *J. Alloys Compd.* **830** (2020) 154527–154539.
- [46] X. Zong, H. Yan, G. Wu, G. Ma, F. Wen, L. Wang, C. Li, Enhancement of Photocatalytic H₂ Evolution on CdS by Loading MoS₂ as Cocatalyst under Visible Light Irradiation. *J. Am. Chem. Soc.* **130** (2008) 7176–7177.
- [47] Q. Xiang, J. Yu, M. Jaroniec, Synergetic effect of MoS₂ and graphene as co-catalysts for enhanced photocatalytic H₂ production activity of TiO₂ nanoparticles. *J. Am. Chem. Soc.* **134** (2012) 6575–6578.
- [48] R. Wang, L. Cao, Facile synthesis of a novel visible-light-driven AgVO₃/BiVO₄ heterojunction photocatalyst and mechanism insight. *J. Alloys Compd.* **722** (2017) 445–451.
- [49] A. Beltrán, L. Gracia, J. Andrés, E. Longo, First-Principles study on polymorphs of AgVO₃: assessing to structural stabilities and pressure-induced transitions. *J. Phys. Chem. C* **121** (2017) 27624–27642.
- [50] B. Liu, L. Mu, X. Han, J. Zhang, H. Shi, Highly efficient visible-light-driven photocatalytic activity of g-C₃N₄@Ag/AgVO₃ composites for dye degradation and bacterial inactivation. *J. Photochem. Photobio. A: Chem.* **380** (2019) 111866–111871.
- [51] X. Wang, J. Yang, S. Ma, D. Zhao, J. Dai, D. Zhang, In situ fabrication of AgI/AgVO₃ nanoribbon composites with enhanced visible photocatalytic activity for redox reactions. *Catal. Sci. Technol.* **6** (2016) 243–253.
- [52] F. Wu, X. Li, W. Liu, S. Zhang, Highly enhanced photocatalytic degradation of methylene blue over the indirect all-solid-state Z-scheme g-C₃N₄-RGO-TiO₂-Nanoheterojunctions, *Appl. Surf. Sci.* **405** (2017) 60–70.

- [53] X. Wang, S. Li, Y. Ma, H. Yu, J. Yu, H₂WO₄.H₂O/Ag/AgCl composite nanoplates: a plasmonic Z-scheme visible-light photocatalyst. *J. Phys. Chem. C* **115** (2011) 14648–14655.
- [54] F. Chen, Q. Yang, X. Li, G. Zeng, D. Wang, C. Niu, J. Zhao, H. An, T. Xie, Y. Deng, Hierarchical assembly of graphene-bridged Ag₃PO₄/Ag/BiVO₄ (040) Z-scheme photocatalyst: an efficient, sustainable and heterogeneous catalyst with enhanced visible-light photoactivity towards tetracycline degradation under visible light irradiation. *Appl. Catal. B* **200** (2017) 330–342.
- [55] Y. Liu, H. Zhang, J. Ke, J. Zhang, W. Tian, X. Xu, X. Duan, H. Sun, M. O. Tade, S. Wang, 0D (MoS₂)/2D (g-C₃N₄) heterojunctions in Z-scheme for enhanced photocatalytic and electrochemical hydrogen evolution. *Appl. Catal. B* **228** (2018) 64–74.
- [56] H. J. Yun, H. Lee, N. D. Kim, D. M. Lee, S. Yu, J. Yi, A combination of two visible light responsive photocatalysts for achieving the Z-scheme in the solid state. *ACS Nano* **5** (2011) 4084–4090.
- [57] R. Kobayashi, S. Tanigawa, T. Takashima, B. Ohtani, H. Irie, Silver-inserted heterojunction photocatalysts for Z-scheme overall pure-water splitting under visible-light irradiation. *J. Phys. Chem. C* **118** (2014) 22450–22456.
- [58] R. Q. Ye, H. B. Fang, Y.-Z. Zheng, N. Li, Y. Wang, X. Tao, Fabrication of CoTiO₃/g-C₃N₄ hybrid photocatalysts with enhanced H₂ evolution: Z-scheme photocatalytic mechanism insight. *ACS Appl. Mater. Interfaces* **8** (2016) 13879–13889.
- [59] K. Qi, B. Cheng, J. Yu, W. Ho, A review on TiO₂-based Z-scheme Photocatalysts. *Chinese J. Catal.* **38** (2017) 1936–1955.
- [60] A. Bafaqeer, M. Tahir, A. A. Khan, N. A. S. Amin, Indirect Z-scheme Assembly of 2D ZnV₂O₆/RGO/g-C₃N₄ Nanosheets with RGO/pCN as solid-state electron mediators toward Visible Light-enhanced CO₂ reduction. *Ind. Eng. Chem. Res.* **58** (2019) 208612–208624.
- [61] S.-Y. Yu, L.-P. Mei, Y.-T. Xu, T.-Y. Xue, G.-C. Fan, D.-M. Han, G. Chen, W.-W. Zhao, Liposome-mediated in situ formation of AgI/Ag/BiOI Z-scheme heterojunction on foamed nickel electrode: a proof-of-concept study for cathodic liposomal photoelectrochemical bioanalysis. *Bioanalysis. Anal. Chem.* **91** (2019) 3800–3804.

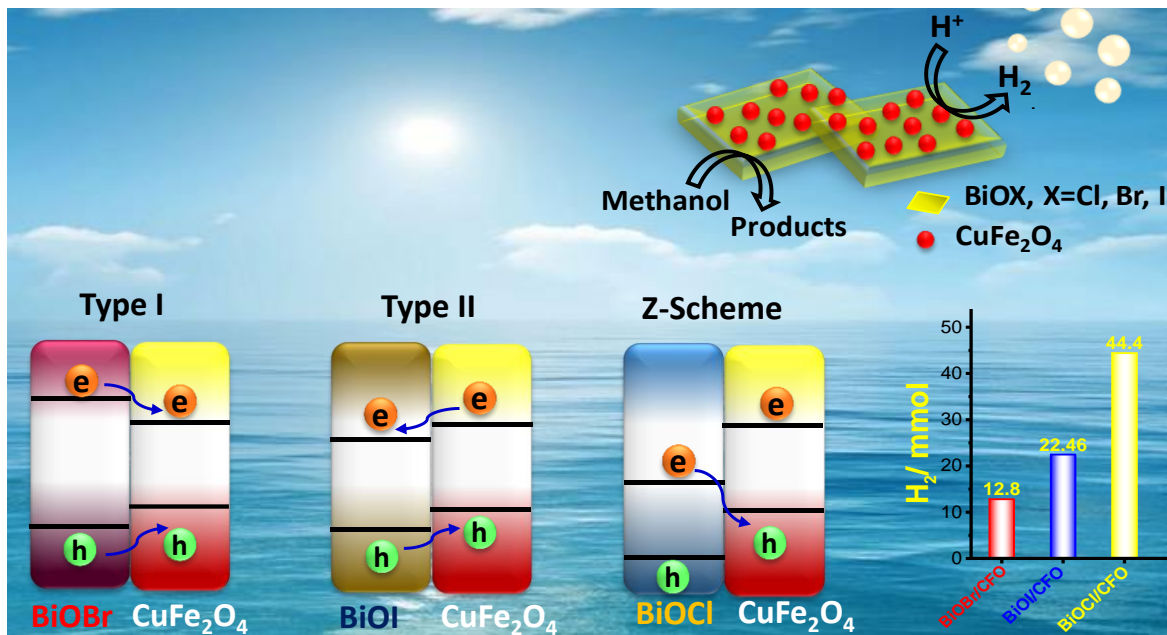
- [62] Y. Sang, L. Kuai, C. Chen, Z. Fang, B. Geng, Fabrication of a visible-light-driven Plasmonic Photocatalyst of $\text{AgVO}_3@\text{AgBr}@\text{Ag}$ Nano belt Heterostructures. *ACS Appl. Mater. Interfaces* **6** (2014) 5061–5068.
- [63] K. F. Mak, C. Lee, J. Hone, J. Shan, T. F. Heinz, Atomically thin MoS_2 : A new direct-gap semiconductor. *Phys. Rev. Lett.* **105** (2010) 136805–136808.
- [64] A. Radisavljevic, J. Radenovic, V. Brivio, A. K. Giacometti, Single-layer MoS_2 transistors. *Nat. Nanotechnol.* **6** (2011) 147–150.
- [65] D. Lu, Q. Wang, K.K. Kondamareddy, A. Wang, H. Hao, Q. Wu, Efficiently visible-light-induced photoactivity of MoS_2 nanoflowers/chromic oxide/protonated titanatenanoflakes edge-on ternary heterostructures for production of hydrogen. *J. Alloys Compd.* **761** (2018) 31–40.
- [66] K. F. Mak, C. Lee, J. Hone, J. Shan, T. F. Heinz, Atomically thin MoS_2 : a new direct-gap semiconductor. *Phys. Rev. Lett.* **105** (2010) 136805–136809.
- [67] D. Lu, H. Wang, X. Zhao, K.K. Kondamareddy, J. Ding, C. Li, P. Fang, Highly efficient visible-light-induced photoactivity of Z-scheme $\text{g-C}_3\text{N}_4/\text{Ag}/\text{MoS}_2$ ternary photocatalysts for organic pollutant degradation and production of hydrogen. *ACS Sustain. Chem. Eng.* **5** (2017) 1436–1445.
- [68] M. J. Islam, D. A. Reddy, N. S. Han, J. Choi, J. K. Song, T. K. Kim, An oxygen-vacancy rich 3D novel hierarchical $\text{MoS}_2/\text{BiOI}/\text{AgI}$ ternary nanocomposite: enhanced photocatalytic activity through photogenerated electron shuttling in a Zscheme manner. *Phys. Chem. Chem. Phys.* **18** (2016) 24984–24993.
- [69] W. K. Jo, T. Adinaveen, J. J. Vijaya, N. C. S. Selvam, Synthesis of MoS_2 nanosheet supported Z-scheme $\text{TiO}_2/\text{g-C}_3\text{N}_4$ photocatalysts for the enhanced photocatalytic degradation of organic water pollutants. *RSC Adv.* **6** (2016) 10487–10497.
- [70] R. C. Oliveira, C. C. Foggi, M. M. Teixeira, M. D. P. Silva, M. Assis, E. M. Francisco, N. A. S. Pimentel, P. F. S. Pereira, C. E. Vergani, A. L. Machado, J. Andres, L. Gracia, E. Longo, Mechanism of antibacterial activity via morphology change of $\alpha\text{-AgVO}_3$: theoretical and experimental insights. *ACS Appl. Mater. Interfaces* **9** (2017) 11472–11481.
- [71] Q. Pang, Y. Zhao, X. Bian, Y. Ju, X. Wang, Y. Wei, B. Liu, F. Du, C. Wang, G. Chen, Hybrid $\text{graphene}@\text{MoS}_2@\text{TiO}_2$ microspheres for use as a high performance negative electrode material for lithium ion batteries. *J. Mater. Chem.* **5** (2017) 3667–3674.

- [72] Z. Y. Zhu, Y. C. Cheng, U. Schwingenschlögl, Giant spin-orbit-induced spin splitting in two-dimensional transition-metal dichalcogenide semiconductors. *Phys. Rev. B* **84** (2011) 153402–153407.
- [73] S. Umrao, J. Jeon, S. M. Jeon, Y. J. Choi, S. Lee, A homogeneous atomic layer $\text{MoS}_{2(1-x)}\text{Se}_{2x}$ alloy prepared by low-pressure chemical vapor deposition, and its properties. *Nanoscale* **9** (2017) 594–603.
- [74] R. Ahmad, R. Srivastava, S. Yadav, D. Singh, G. Gupta, S. Chand, S. Sapra, Functionalized molybdenum disulphide nanosheets for 0D-2D hybrid nanostructure photoinduced charge transfer and enhanced photoresponse. *J. Phys. Chem. Lett.* **8** (2017) 1729–38.
- [75] Y.-F. Zhao, Z.-Y. Yang, Y.-X. Zhang, L. Jing, X. Guo, Z. Ke, P. Hu, G. Wang, Y.-M. Yan, K.-N. Sun, Cu_2O decorated with cocatalyst MoS_2 for solar hydrogen production with enhanced efficiency under visible light. *J. Phys. Chem. C* **118** (2014) 14238–45.
- [76] H. Wang, C. Li, P. Fang, Z. Zhang, J. Z. Zhang, Synthesis, properties, and optoelectronic applications of two-dimensional MoS_2 and MoS_2 -based heterostructures. *Chem. Soc. Rev.* **47** (2018) 6101–27.
- [77] S. Ghosh, S. R. Keshri, S. Bera, R. N. Basu, Enhanced solar hydrogen generation using $\text{Cu-Cu}_2\text{O}$ integrated polypyrrole nanofibers as heterostructured catalysts. *Int. J. Hydrogen Energy* **45** (2019) 6159–73.
- [78] D. McNulty, Q. Ramasse, C. O' Dwyer, The structural conversion from $\alpha\text{-AgVO}_3$ to $\beta\text{-AgVO}_3$: Ag nanoparticle decorated nanowires with application as cathode materials for Li-ion batteries. *Nanoscale* **8** (2016) 16266–16275.
- [79] S. Zhang, W. Li, C. Li, J. Chen, Characterization, and electrochemical properties of $\text{Ag}_2\text{V}_4\text{O}_{11}$ and AgVO_3 1-D nano/microstructures. *J. Phys. Chem. B* **110** (2006) 24855–24863.
- [80] S. Zhang, J. Li, X. Wang, Y. Huang, M. Zeng, J. Xu, Rationally designed 1D Ag@AgVO_3 nanowire/graphene/protonated $g\text{-C}_3\text{N}_4$ nanosheet heterojunctions for enhanced photocatalysis via electrostatic self-assembly and photochemical reduction methods. *J. Mater. Chem.* **3** (2015) 10119–10126.
- [81] P. P. Patel, P. J. Hanumantha, O. I. Velikokhatnyi, M. K. Datta, D. Hong, B. Gattu, J. A. Poston, A. Manivannan, P. N. Kumta, Nitrogen and cobalt co-doped zinc oxide nanowires

- Viable photoanodes for hydrogen generation via photoelectrochemical water splitting. *J. Power Sources* **299** (2015) 11–24.
- [82] P. Chen, P. Xing, Z. Chen, X. Hu, H. Lin, L. Zhao, Y. He, In-situ synthesis of AgNbO₃/g-C₃N₄ photocatalyst via microwave heating method for efficiently photocatalytic H₂ generation. *J. Colloid Interface Sci.* **534** (2019) 163–171.
- [83] S. Bera, S. Ghosh, S. Shyamal, C. Bhattacharya, R. N. Basu, Photocatalytic hydrogen generation using gold decorated BiFeO₃ heterostructures as an efficient catalyst under visible light irradiation. *Sol. Energy Mater. Sol. Cells* **194** (2019) 195–206.
- [84] L. Jiang, K. Wang, X. Wu, G. Zhang, S. Yin, Amorphous bimetallic cobalt nickel sulfide cocatalysts for significantly boosting photocatalytic hydrogen evolution performance of graphitic carbon nitride: efficient interfacial charge transfer. *ACS Appl. Mater. Interfaces* **11** (2019) 26898–26908.

CHAPTER 7

Band Edge Engineering of BiOX/CuFe₂O₄ Heterostructures for Efficient Water Splitting



7.1 Introduction

Solar energy conversion to generate renewable fuel H_2 through water splitting by developing sustainable, low cost and efficient photocatalysts, provides a potential approach to meet the global energy demand [1–4]. On account of the photocatalyst development, various metal oxides (such as TiO_2 , ZnO , Fe_2O_3 , Cu_2O , WO_3 , $BiVO_4$), hydroxides, chalcogenides (like MoS_2 , $MoSe_2$, WS_2 , WSe_2), MXenes, black phosphorus, and organic semiconductors such as conjugated polymers, graphitic carbon nitrides, graphene, metal organic frameworks, covalent organic frameworks, etc. are fabricated and studied for water splitting over the past decades [5–10]. However, the efficiency is still not significant for the large scale application as most of these photocatalysts suffer from fast charge carrier recombination and low absorption in the visible region, which accounts for 53% of the total solar spectrum. Therefore, it is required to exploit efficient catalysts with high photocatalytic activity and stability under visible light.

In this regard, bismuth oxyhalides ($BiOX$, $X = Cl, Br, I$) a new family of photocatalyst, have attracted intense interest in various photocatalytic applications due to its layered structure which is composed of $[Bi_2O_2]^+$ slabs interleaved by double halogen atoms $[X]^-$ with open crystalline nature. The Van der Waals force within the halide layers and the covalent bond between $[Bi_2O_2]^+$ and $[X]^-$ make the intrinsic structure of $BiOX$ very stable [11,12]. Besides, the open crystalline structure benefits a large space for the polarization of atoms and induces a static electric field perpendicular to the $[Bi_2O_2]^+$ slabs, which further accelerates the charge separation along the (001) direction [13]. In addition, $BiOX$ generate facile O-vacancy during photocatalysis under UV light due to low energy Bi–O bond at the surface [14–16]. As example, Guan et al. [17] experimentally demonstrated the enhanced photocatalytic activity of $BiOCl$ nanosheets towards organic pollutant Rhodamine B degradation because of O-defects generated at the exposed (001) surface under UV light. Further, L. Zhang [18] showed selective transfer of photogenerated electrons to the (001) surface of $BiOCl$ as the vacancy state lying below the CB which act as trapping state. On the other hand, $BiOX$ shows indirect transition bandgap, i.e electrons have to travel a certain k-spacing to be emitted to the VB, thus electron-hole recombination is low compared to direct bandgap semiconductors [14]. However, the wide bandgap of $BiOCl$ (2.4–3.4 eV) limits its photocatalytic activity under visible light and owing to positive conduction band minima (CBM), $BiOCl$ is improper for water splitting, CO_2 reduction and N_2 fixation. Thus, photocatalytic activity is confined only for organic pollutant degradation under UV light [14, 19]. Although, $BiOBr$ (2.3–2.9

eV) could absorb visible light, the large bandgap still restricts its effective performance, while relatively smaller bandgap of BiOI (1.8–2.1 eV) suffers from the fast recombination of electrons and holes [17, 18]. Thus, coupling of secondary semiconductors with BiOBr and BiOI may improve the photocatalytic performance under visible light. As example, binary and ternary heterojunctions have been fabricated with BiOBr, such as SnWO₄/BiOBr [20], N-CQDs/OV-BiOBr [21], Ag/AgBr/BiOBr [22], BiOBr/ZnO/BiOI [23] to increase visible light driven photocatalytic activity towards organic pollutant degradation. Significant efforts have been made on BiOI *via* heterostructures formation with other semiconductors, like CdS [24], CuI [25], g-C₃N₄ [26] to prolong the lifetime of the excited charge carriers by lowering the fast recombination rate. However, these BiOI-based heterostructures are tested mainly for organic dye degradation and very limited reports on photocatalytic H₂ generation, up to date. Meanwhile, some literatures demonstrated BiOI as O₂ evolving catalyst through photocatalytic and photoelectrochemical (PEC) water oxidation, although the efficiency is still too low for large scale applications [27, 28]. This simulate our interest to design BiOX-based efficient catalysts which can have strong redox potentials to drive the water splitting reactions along with minimal recombination, high charge separation and visible light absorption capabilities. In this regard, the direct Z-scheme heterostructures which consists of a reduction semiconductor with a highly negative CB and another oxidative semiconductor having highly positive VB, is gaining intense research interest as it offers strong redox capability to drive catalytic reactions [4, 29]. Apart from that, this Z-scheme system benefits an internal potential gradient and spatial charge separation *via* recombination of low energy electrons and holes within the body [4].

Recently, considerable attention has been paid on the narrow bandgap spinel ferrites (MFe₂O₄, M = Co, Ni, Mn, Cu, and Zn) in photocatalysis due to the varied chemical composition, multiple oxidation states, environmental compatibility, stability, easy synthesis and low cost. In addition, the available large number of active sites is a potential factor of spinel ferrites for the catalytic reactions [30]. Y. Matsumoto [31] reported that, the electrical conductivity and surface electrochemical reactivity of spinel ferrites are much higher compared to corresponding single component iron oxides, due to the improved electron transport process *via* different metal cations. The magnetic properties of spinel ferrites would be helpful for the removal of catalyst from the reaction medium by a magnet. As an outstanding member of the spinel ferrite family, CuFe₂O₄, with bandgap of 1.65 eV and strong visible light response has paid more attention in PEC water

splitting both as photoanode [32] and photocathode [33, 34]. The chemical stability at high temperature and the phase transition of CFO give rise to interesting electrical and magnetic properties. However, it suffers from low surface area, irregular morphology and limited catalytic activity due to fast charge carrier recombination. Besides, single semiconductor CFO is unable to evolve O_2 through water oxidation because of low VB potential. At the same time, the large difference between CB potential and water reduction potential leads to poor activity in photocatalytic H_2 generation. There have been reports on modification of CFO to overcome the aforesaid issues [35-38]. For example, Hussain et al. [35] fabricated Fe_2O_3/CFO composite to modulate the charge separation by developing a Z-shaped path for enhanced water oxidation and reduction. A Type-II heterostructures was developed by Cheng et al [36]. between CFO and $g-C_3N_4$, which exhibited photocatalytic H_2 generation in presence of Pt (3 wt%) co-catalyst and triethanolamine (10 vol%) sacrificial electron donor under visible light. Very recently, S. Das and co-workers [37] fabricated p-n junction of CFO/NiAl LDH and demonstrated enhanced photocatalytic H_2 generation rate compared to bare LDH and CFO, which is associated with the increased trapping sites by multiple oxidation states of charge carries that effectively prolong the lifetimes. However, the H_2 generation rates of these heterostructures are very low. In particular, the highly negative CB potential, the p-type conductivity and narrow bandgap of CFO fascinate our interest to couple with BiOX for develop Z-scheme heterostructures. To the best of our knowledge BiOX/CFO heterostructures are not prepared and tested for photocatalytic H_2 generation.

In this work, heterostructures are fabricated between n-type BiOX and p-type CFO by facile hydrothermal method followed by co-precipitation method. Depending on the position of VB and CB of BiOX, three types of heterostructures (Type-I, Type-II and Z-scheme) are formed. The new band edges position with respect to the redox potentials for both H_2 and O_2 evolution is suitable for efficient water splitting. The Z-scheme heterostructures showed significantly high catalytic efficiency in photocatalytic H_2 generation through water reduction and PEC water oxidation under visible light. Moreover, possible charge transfer mechanisms of the as prepared heterostructures have been proposed to explain the catalytic reactions.

7.2 Experimental

Bismuth nitrate penta-hydrate $\text{Bi}(\text{NO}_3)_3 \cdot 5\text{H}_2\text{O}$, potassium iodide (KI), sodium chloride (NaCl), potassium bromide (KBr), mannitol, methanol, and ethanol were obtained from Merck chemicals. DI water, 18.2 M Ω .cm (Millipore System) was used as solvent.

The BiOCl , BiOBr , BiOI are synthesized by one step hydrothermal method [35]. To prepare BiOCl , 0.5M $\text{Bi}(\text{NO}_3)_3 \cdot 5\text{H}_2\text{O}$ dissolved in 20 mL of 0.1 M mannitol solution under magnetic stirring for 20 min. Then 10 mL of 0.5M KCl solution was added dropwise into the Bi-solution under vigorous stirring. The solution colour changed into white which was then transferred into a 50 mL capacity stainless still autoclave, heated to 150°C for 3h. After cooling down the sample was collected and washed with DI water and ethanol several times. The final white precipitation was dried into an oven at 60°C for overnight. The BiOBr and BiOI were also prepared by similar method using KBr and KI as Br and I-source respectively.

BiOX/CFO heterostructures were synthesized by facile co-precipitation method. At first 30 mg BiOX were mixed in 30 mL of DI water by 10 min ultrasonication. At the same time, 0.57 g $\text{Cu}(\text{NO}_3)_2 \cdot 6\text{H}_2\text{O}$ and 1.92 g $\text{Fe}(\text{NO}_3)_3 \cdot 9\text{H}_2\text{O}$ were dissolved in 30 mL of DI water. After that, the mixed solution was added dropwise into the BiOX solution and mixed for 15 min to yield a homogeneous mixture. The whole mixture was then refluxed at 75°C under stirring condition for another 30 mins. After cooling down, the solid precipitation was collected by centrifugation with DI water and ethanol for several times and then dried in an oven at 75°C for overnight.

Powder X-ray diffraction (XRD) of as synthesized materials were collected using a Philips X'Pert. To analysis size and morphology of the bare semiconductors and heterostructures, field emission scanning electron microscopy (FESEM) were employed using Carl-Zeiss, Sigma (LEO. 430i). The transmission electron microscopy (TEM) was used to further study the crystallinity properties by employing Tecnai G² 30ST, FEI. Formation of heterostructures and the oxidation states were investigated by X-ray photoelectron spectroscopy (XPS). The PHI 5000 Versa Probe II spectrophotometer was used to conduct this experiment. Here, the charge correction was performed by considering C 1s (284.5 eV) spectra as standard. Furthermore, the thermal stability of the as prepared heterostructures was studied by NETZSCH, STA 449 F3 Jupiter instrument through thermogravimetric analysis (TGA). The Fourier transform infrared (FTIR) spectra and Raman spectra were collected using JASCO FTIR-6300 spectrometer and Jobin Yvon HR800 confocal Raman system (540 nm laser beam). Room temperature UV-Visible absorption spectra

of the bare semiconductors and the heterostructures were taken using Cary 5000 UV-VIS-NIR spectrophotometer.

The photoelectrochemical properties of pure BiOX, CFO and the heterostructures were studied by preparing thin films on FTO coated glass slides (2 cm × 2cm) by spin coating method at 4000 rpm for 1 min. Catalysts solutions were prepared at a concentration of 2 mg/mL in ethanol and 100 μL was used for preparing each thin film layer. Total three layers were coated on the FTO slides and dried at 200°C for 2h. A three electrode quartz cell containing 0.1 M Na₂SO₄ (~pH 7) electrolyte, a Pt wire and KCl saturated Ag/AgCl as counter and reference electrode, respectively was used as photoelectrochemical cell and the measurements performed by a galvanostat-potentiostat (PGSTAT302 N, Autolab, The Netherlands) under 35W Xenon lamp. The current density was recorded between the applied potential ranges of -0.4 V to 1V vs Ag/AgCl at 50 mV s⁻¹ scan rate through linear sweep voltammetry (LSV). Further, photocurrent density and the stability was checked *via* chopped chronoamperometry (CA) at applied potential of 0.6V vs Ag/AgCl. The electrochemical impedance spectra (EIS) were measured at an AC frequency range of 100 KHz to 0.1 Hz with 0.1 V amplitude to calculate the charge transfer resistance at electrode-electrolyte interfaces. Junction capacitance of the electrodes was recorded at 1000 Hz frequency *via* Mott-Schottky (M-S) study for determining the flat band potentials as well as free charge carrier density. The Nernst equation was employed to convert the potentials ($E_{\text{Ag/AgCl}}$) to normal hydrogen electrode scale (E_{NHE}), equation 5.1.

Photocatalytic H₂ generation of the as synthesized materials was tested through water reduction in a closed quartz cell containing 30 mL solution with catalyst concentration of 1 mg/mL under visible light irradiation (250 W Xenon lamp) through online gas chromatography (GC) using 25 vol % methanol as sacrificial agent. The solution was argon purged for 15 min before the experiment. The area under Gaussian peak in GC gives the amount of H₂ evolved. The apparent quantum yield (AQY) of H₂ generation has been calculated further using the following Equation of:

$$\text{AQY}\% = \frac{2 \times \text{moles of H}_2 \text{ produced}}{\text{no. of incident photons}} \times 100 \quad (7.1)$$

7.3 Results and Discussion

7.3.1. Structural analysis

The phase composition and crystalline structure of bare semiconductors and prepared heterostructures have been investigated by powder X-ray diffractometer. Figures 7.1a and 7.1b show the XRD pattern of bare semiconductors BiOI, BiOCl, BiOBr and CuFe₂O₄ (CFO) nanoparticles, BiOI/CFO, BiOCl/CFO, BiOBr/CFO heterostructures. In case of BiOI, the diffraction peaks at 2θ of 29.53°, 31.53°, 36.96°, 39.31°, 45.29°, 51.27°, 55.08° related to (012), (110), (013), (004), (200), (114), (212) planes clearly indicates the tetragonal phase of BiOI (JCPDS No. 73–2062) [38].

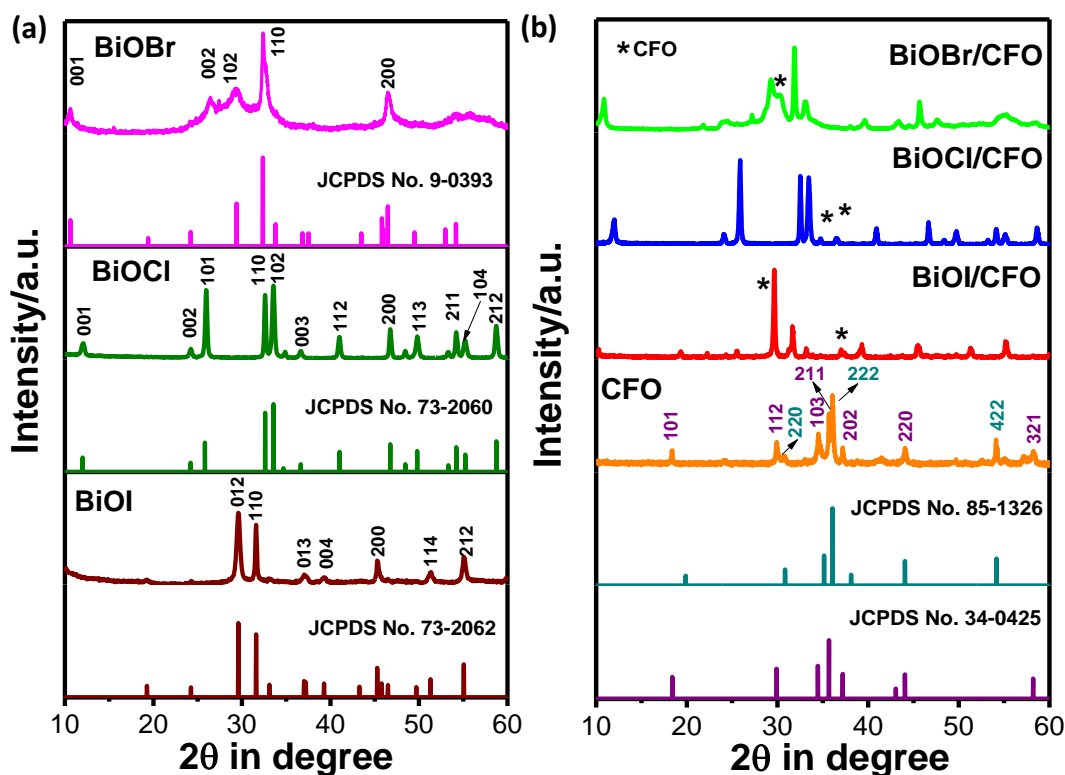


Figure 7.1 XRD pattern of (a) bare semiconductors BiOI, BiOCl, BiOBr with the standard XRD patterns, (b) CuFe₂O₄ (CFO) nanoparticles with standard XRD patterns, BiOI/CFO, BiOCl/CFO and BiOBr/CFO heterostructures.

The diffraction peaks at 2θ of 12.12°, 24.25°, 26.04°, 32.67°, 33.56°, 36.61°, 41.08°, 46.81°, 49.86°, 54.34°, 55.23°, 58.81° indexed to (001), (002), (101), (110), (102), (003), (112), (200), (113), (211), (104), (212) planes of the tetragonal BiOCl (JCPDS No. 73–2060) [39]. The XRD pattern of BiOBr exhibits five characteristic peaks of (001), (002), (102), (110), (200) at 2θ of 10.51°, 26.27°, 29.35°, 32.43°, 46.56° which are well matched with tetragonal phase of BiOBr

(JCPDS No. 9–0393) [40]. Interestingly, the presence of (001) peak for BiOCl and BiOBr strongly reveals the [X–Bi–O–Bi–O–X] stacking structure along c-axis [39]. The characteristic peaks at 2θ of 18.36° , 29.89° , 34.42° , 35.69° , 37.14° , 44.03° , 58.16° correspond to (101), (112), (103), (211), (202), (220) and (321) planes confirm the tetragonal spinel structure of CuFe_2O_4 (JCPDS No. 34–0425) [36]. However, three characteristic peaks of (220), (222) and (422) which are marked by green at 2θ value 30.8° , 36.05° , 54.17° represents the cubic phase of CuFe_2O_4 (JCPDS No. 85–1326) [41]. After heterostructures formation, no shifting of the BiOX peaks have been observed and the characteristic peaks of CFO are present (marked by ‘*’), implies the successful heterostructures formation between BiOX and CFO (Figure 1b).

X-ray photoelectron spectroscopy (XPS) analysis is performed to study the surface and sub-surface chemical states of heterostructures samples. The surface survey scan spectra of BiOCl/CFO confirm the presence of Bi, Cl, O, Fe and Cu in heterostructures (Figure 7.2a).

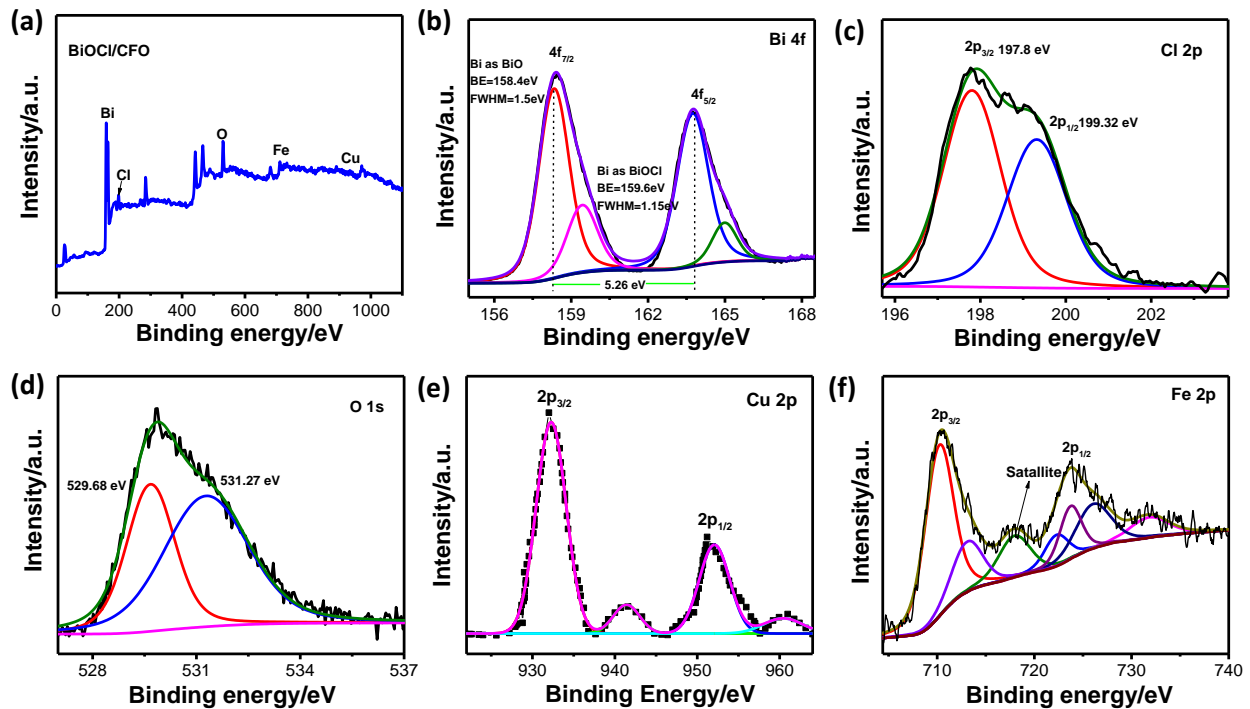


Figure 7.2 (a) Surface survey XPS spectra of BiOCl/CFO heterostructures. High resolution XPS spectra of (b) Bi 4f, (c) Cl 2p, (d) O 1s, (e) Cu 2p and (f) Fe 2p of BiOCl/CFO heterostructures.

In Bi 4f spectra, two peaks at binding energy of ~ 163.75 eV and ~ 158.41 eV might be assigned to be Bi $4f_{5/2}$ and Bi $4f_{7/2}$, respectively which are further fitted properly (Figure 7.2b) [42]. The characteristic Bi $4f_{7/2}$ peak can be fitted with two peaks located at binding energies of ~ 158.4 eV

and ~ 159.62 eV, correspond to Bi=O and O=Bi-Cl bonds. Similar results have been obtained for BiOBr/CFO heterostructures (Figure 7.3). However, the Bi $4f_{7/2}$ of BiOI/CFO has been fitted with single peaks located at binding energy of 158.54 eV (Figure 7.4). Now, it is well known that the Bi $4f_{7/2}$ located at binding energy between 157.2 eV to 158.1 eV corresponds to metallic Bi⁰ state (Bi-Bi), whereas peak position at 158.4 ± 0.4 eV and 158.8 ± 0.3 eV indicate presence of Bi(OH)₃, (Bi-OH) and BiOOH (O=Bi-OH) states, respectively [43-45]. Therefore, it can be concluded that surface is mainly composed of Bi(OH)₃, i.e. Bi³⁺ state for all the heterostructures, which further verified by the obtained O/Bi atomic ratio. In addition the binding energy difference of ~ 5.3 eV between Bi $4f_{7/2}$ and Bi $4f_{5/2}$ strongly supports the presence of Bi³⁺ state [46].

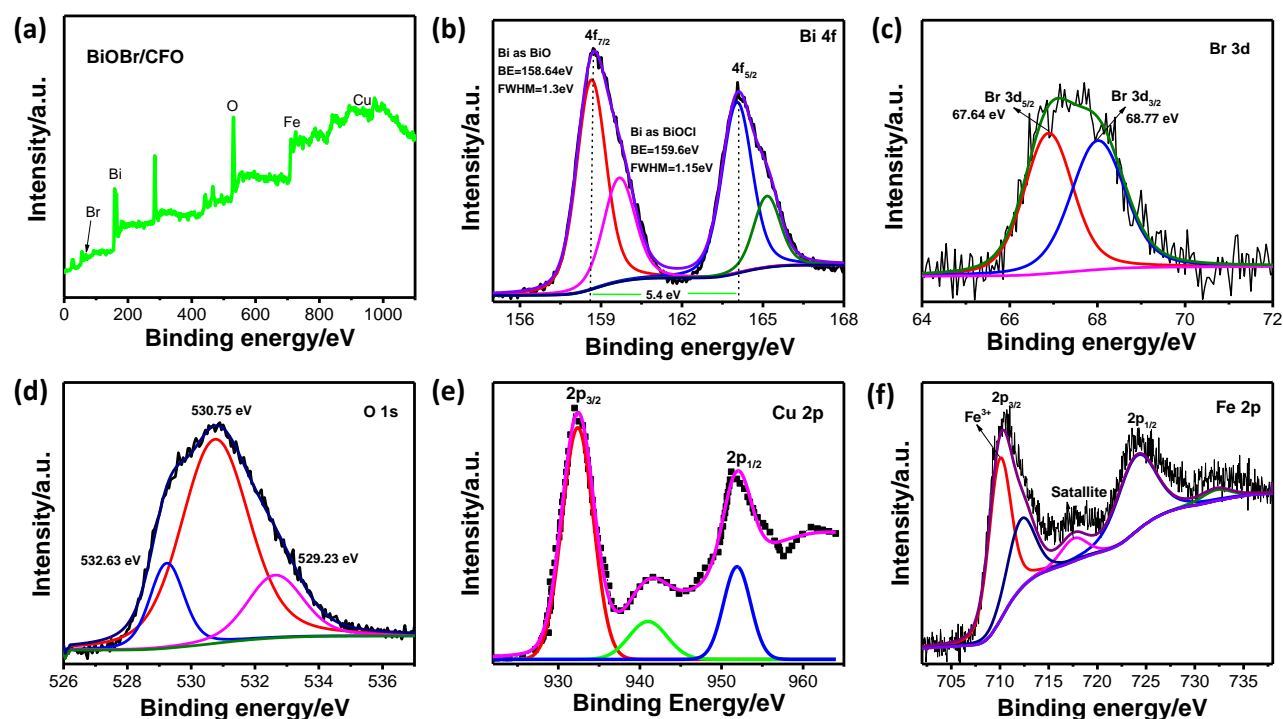


Figure 7.3 (a) Surface survey XPS spectra of BiOBr/CFO heterostructures. High resolution XPS spectra of (b) Bi 4f, (c) Br 3d, (d) O 1s, (e) Cu 2p and (f) Fe 2p.

The Cl 2p spectrum has been fitted into two peaks, at ~ 197.8 eV and ~ 199.32 eV binding energies belongs to Cl $2p_{3/2}$ and Cl $2p_{1/2}$, confirms the Cl⁻ state in heterostructures (Figure 7.2c) which is well consistency with the reported literatures [47-49]. The O 1s spectrum of BiOCl/CFO heterostructures are fitted into two peaks, one located at ~ 529.83 eV corresponds to lattice oxygen which are chemically bonded and another at ~ 531.59 eV related to adsorbed oxygen (Figure 7.2d) [42]. The Cu 2p spectrum showed two main peaks at ~ 932.36 eV (Cu $2p_{3/2}$) and ~ 951.97 eV (Cu $2p_{1/2}$) with two satellite peaks at ~ 941.3 eV and ~ 961.06 eV which are well consistency with the

Cu^{2+} state (Figure 7.2e) [50]. The Fe 2p peaks located at binding energies of ~ 710.28 eV and ~ 723.83 eV correspond to Fe $2p_{3/2}$ and Fe $2p_{1/2}$, arising from the spin orbital interaction (Figure 7.2f) [57].

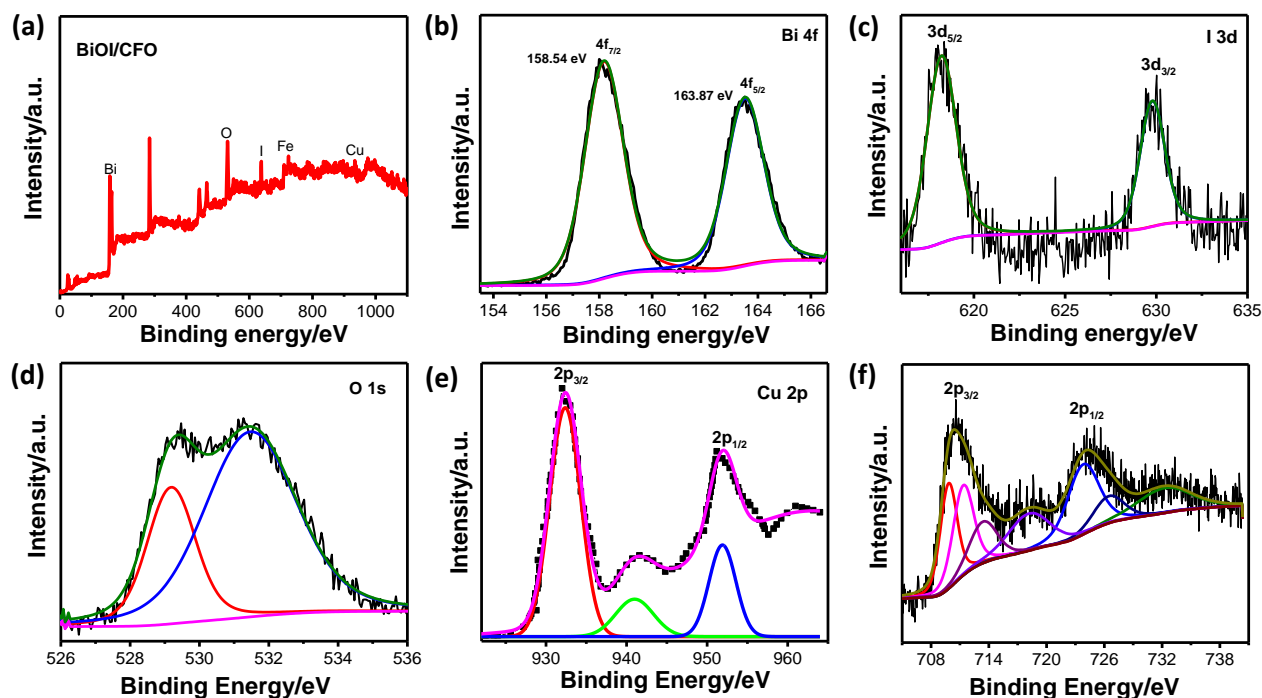


Figure 7.4 (a) Surface survey XPS spectra of BiOI/CFO heterostructures. High resolution XPS spectra of (b) Bi 4f, (c) I 3d, (d) Fe 2p, (e) Cu 2p and (f) O 1s.

Due to different d orbital electron configurations, Fe2p and Fe3p generally exhibit a satellite peak at 6 or 8 eV above their $2p_{3/2}$ principal peaks, respectively. Here, satellite peak at ~ 718.09 eV has been found about 7.8 eV above the Fe $2p_{3/2}$ peak, could be considered as the characteristic of Fe^{3+} state. The XPS spectra of BiOBr/CFO and BiOI/CFO are presented in Figure 7.3 and Figure 7.4, which reveals that Bi, I, Br, Cu, Fe and O are present. Furthermore, the Bi 4f core level XPS spectra of bare BiOX (X=Cl, Br, I) and BiOX/CFO heterostructures have been investigated, where a shifting of the peaks towards lower binding energy observed after heterostructures formation (Figure 7.5). Peak shifting indicates a possibility of sharing electrons with neighboring atoms in terms of asymmetry in the bond arrangements. Moreover, the shifting towards lower binding energy implies a band bending which results a charge redistribution at the interface as well as indicates the increase of electron density on BiOX [60].

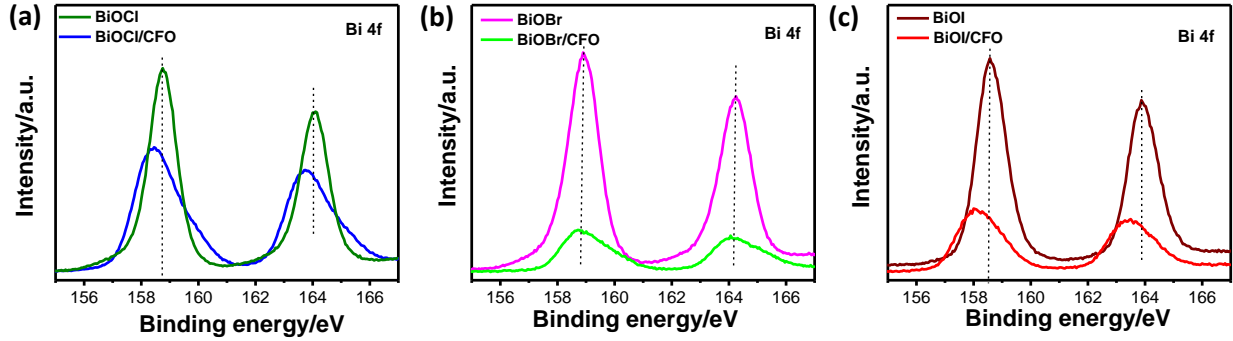


Figure 7.5 Core level Bi 4f XPS spectra of (a) BiOCl and BiOCl/CFO heterostructures (b) BiOBr and BiOBr/CFO heterostructures and (c) BiOI and BiOI/CFO heterostructures.

Furthermore, TG analysis of bare semiconductors and heterostructures are studied to check the thermal stability of as prepared materials. As shown in Figure 7.6, formation of heterostructures between BiOX and CFO enhance the thermal stability of the materials.

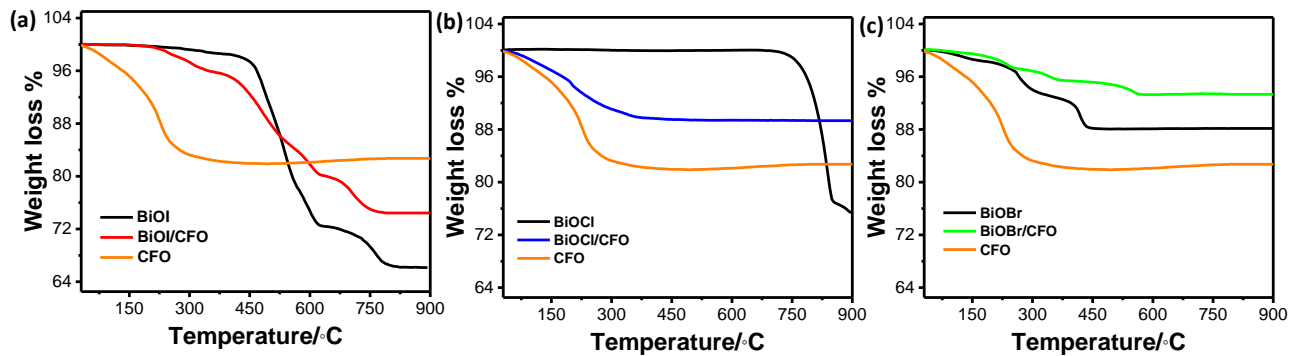


Figure 7.6 TG curves of (a) BiOI, CFO, BiOI/CFO, (b) BiOCl, CFO, BiOCl/CFO and (c) BiOBr, CFO, BiOBr/CFO under Ar atmosphere.

The Raman and FTIR analysis of the prepared materials have been carried out further to analysis the chemical structures. Figure 7.7a represents the Raman spectra of bare CFO, BiOCl and BiOCl/CFO heterostructures. The two prominent Raman peaks have been observed for BiOCl, centered at $\sim 142.74 \text{ cm}^{-1}$ and $\sim 198.52 \text{ cm}^{-1}$, well agreed with A_{1g} and E_g internal Bi–Cl stretching modes, respectively [51]. In case of CFO, three characteristic peaks at 213 cm^{-1} , 274 cm^{-1} and 472 cm^{-1} are assigned to the spinel copper ferrite [52]. After heterostructures formation, the prominent Bi–Cl A_{1g} and E_g stretching modes with the CFO vibration peaks have been observed, which strongly reveals the heterostructures formation. Figure 7.7b shows the FTIR spectra of BiOCl, CFO and BiOCl/CFO heterostructures, where the characteristic band around $\sim 1623 \text{ cm}^{-1}$ confirms the O–H bending vibrations. The absorption band at $\sim 528 \text{ cm}^{-1}$ corresponds to the symmetrical

vibrations of Bi–O stretching mode. Moreover, the absorption peaks at $\sim 1400\text{ cm}^{-1}$ might be assigned as the asymmetric stretching vibration of Bi–Cl band [52]. For CFO, absorption band at the range of $330\text{ to }350\text{ cm}^{-1}$ arises due to stretching vibrations of octahedral metal–oxygen bonding and at $\sim 580\text{ cm}^{-1}$ for tetrahedral metal–oxygen bonding [53]. However, the strong CFO absorption band is absent in BiOCl/CFO which might be resulted for strong interaction between BiOCl and CFO.

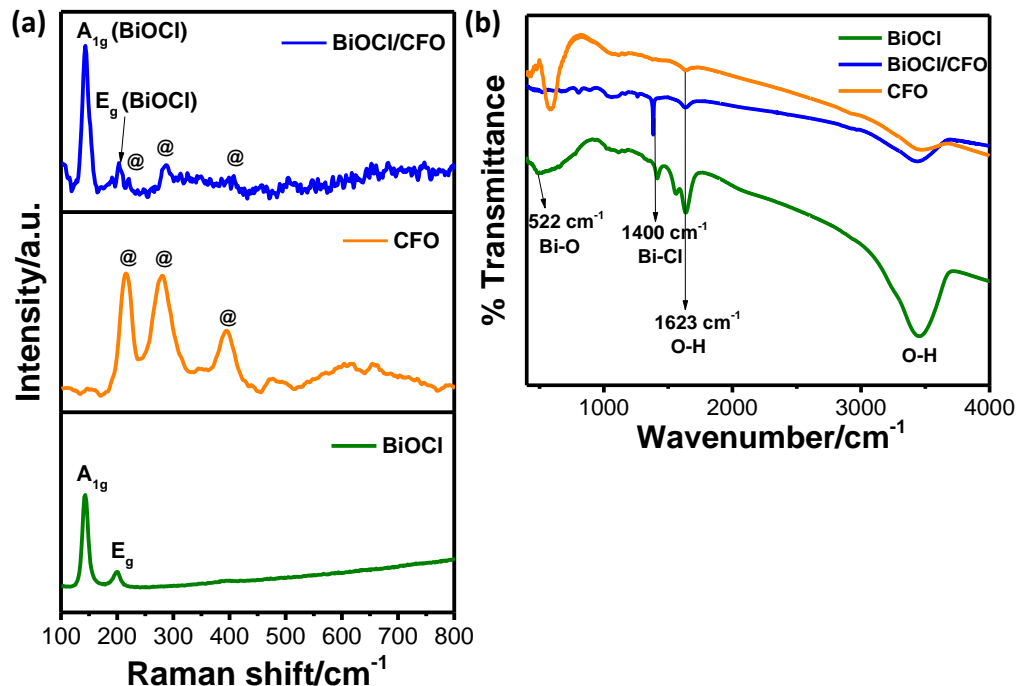


Figure 7.7 (a) Raman spectra and (b) FTIR spectra of bare semiconductors BiOCl, CFO and BiOCl/CFO heterostructures.

7.3.2. Morphology

The morphology and structure of heterostructures are analyzed by FESEM and TEM. Figure 7.8 (a–c) illustrate TEM image of BiOI/CuFe₂O₄, BiOCl/CuFe₂O₄ and BiOBr/CuFe₂O₄ heterostructures respectively. It has been clearly observed that all the pure bismuth oxyhalides possess nanosheet like morphology. The average size of BiOX nanosheets are $\sim 450\text{ nm}$, $\sim 110\text{ nm}$ and $\sim 300\text{ nm}$ for BiOI, BiOCl and BiOBr, respectively. Moreover, all the BiOX nanosheets are fully covered with the small CFO nanoparticles. High resolution TEM (HRTEM) images of the BiOX/CFO heterostructures clearly exhibit good crystallinity with clear lattice fringes. Figure 7.8d represents the cross fringes of (102) and (112) planes of BiOI and CFO having the d-space spacing of 0.3 nm and 0.29 nm , respectively [54]. Two set of lattice fringes having the interplanar spacing

of ~ 0.275 nm and ~ 0.29 nm related to (110) and (112) planes of BiOCl and CFO, respectively (Figure 7.8e) [17]. At the same time, two set of bright spots are presented in the selected area electron diffraction pattern (SAED), which also confirm the heterostructures formation between BiOCl and CFO (Inset of Figure 7.8e).

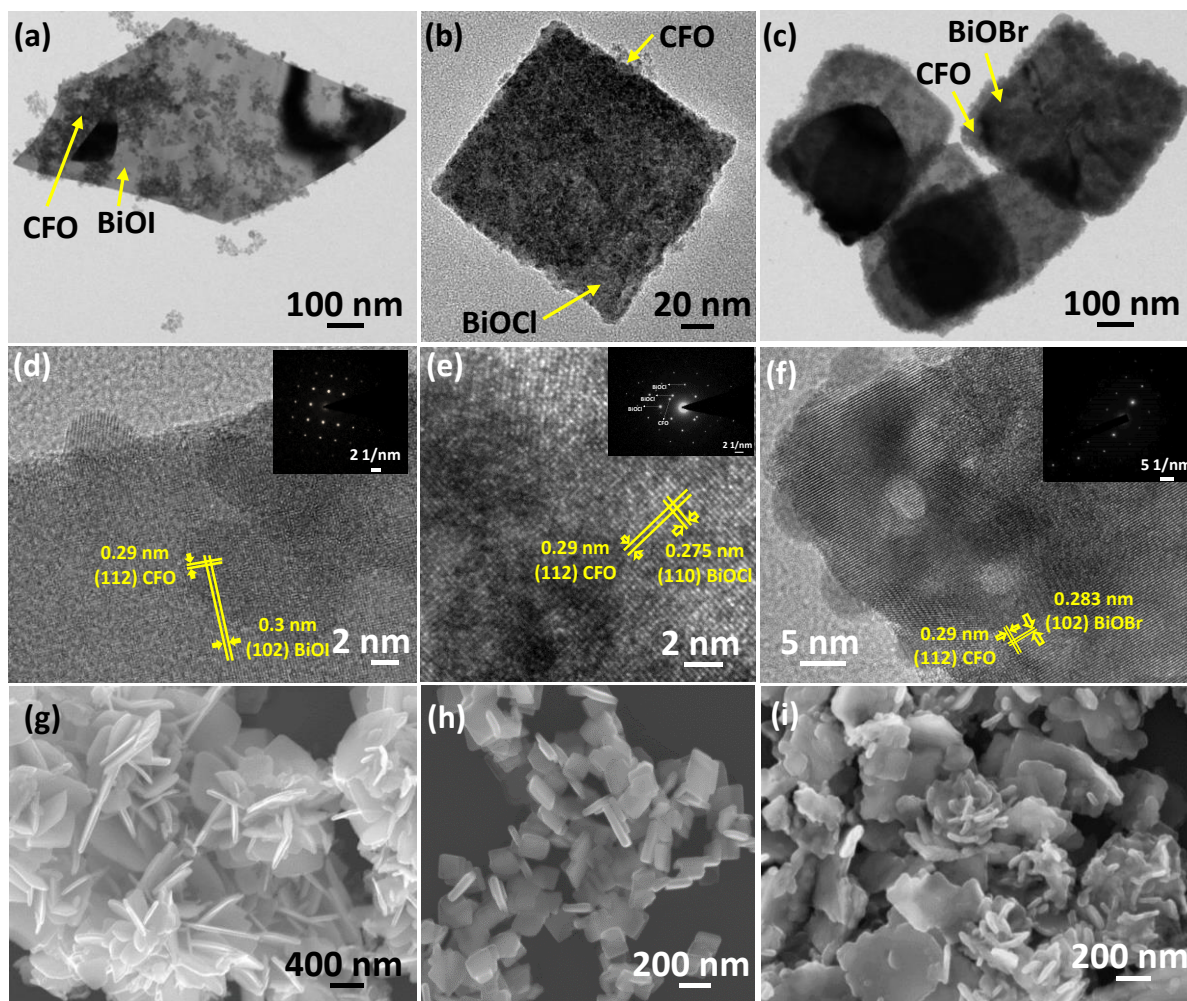


Figure 7.8 TEM image of (a) BiOI/CFO, (b) BiOCl/CFO and (c) BiOBr/CFO. HRTEM images of (d) BiOI/CFO, (e) BiOCl/CFO and (f) BiOBr/CFO heterostructures. Insets: corresponding SAED pattern. FESEM images of bare semiconductors (g) BiOI, (h) BiOCl and (i) BiOBr.

The HRTEM images of BiOBr/CFO displays presence of both crystal planes (102) and (112) having d-spacing of 0.283 nm and 0.29 nm correspond to BiOBr and CFO, respectively (Figure 7.8f) [37]. The spot pattern in the SEAD pattern clearly indicates the single crystalline nature of BiOBr nanosheets. Furthermore, FESEM images of the bare BiOX semiconductors have been presented in Figure 7.8 (g-i), where nanosheets like morphology are also observed for BiOI, BiOCl and BiOBr which is consistent with TEM images. However, BiOI and BiOBr have a trend to form

assembled structure, whereas BiOCl showed uniform square like nanosheets. The TEM image of the bare CFO has been shown in Figure 7.9, average ~13 nm CFO spherical nanoparticles are formed.

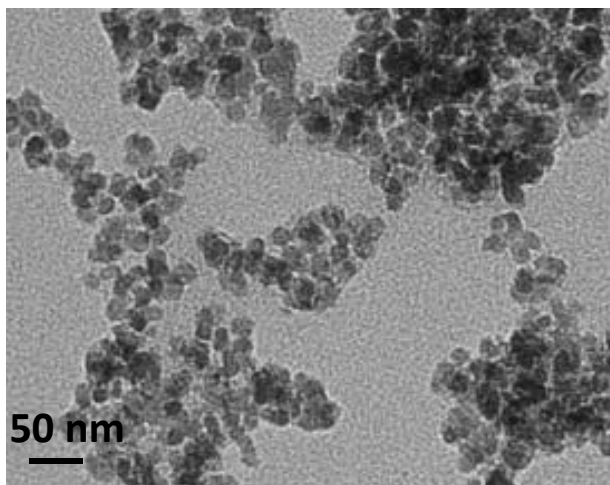


Figure 7.9 TEM image of CuFe_2O_4 nanoparticles.

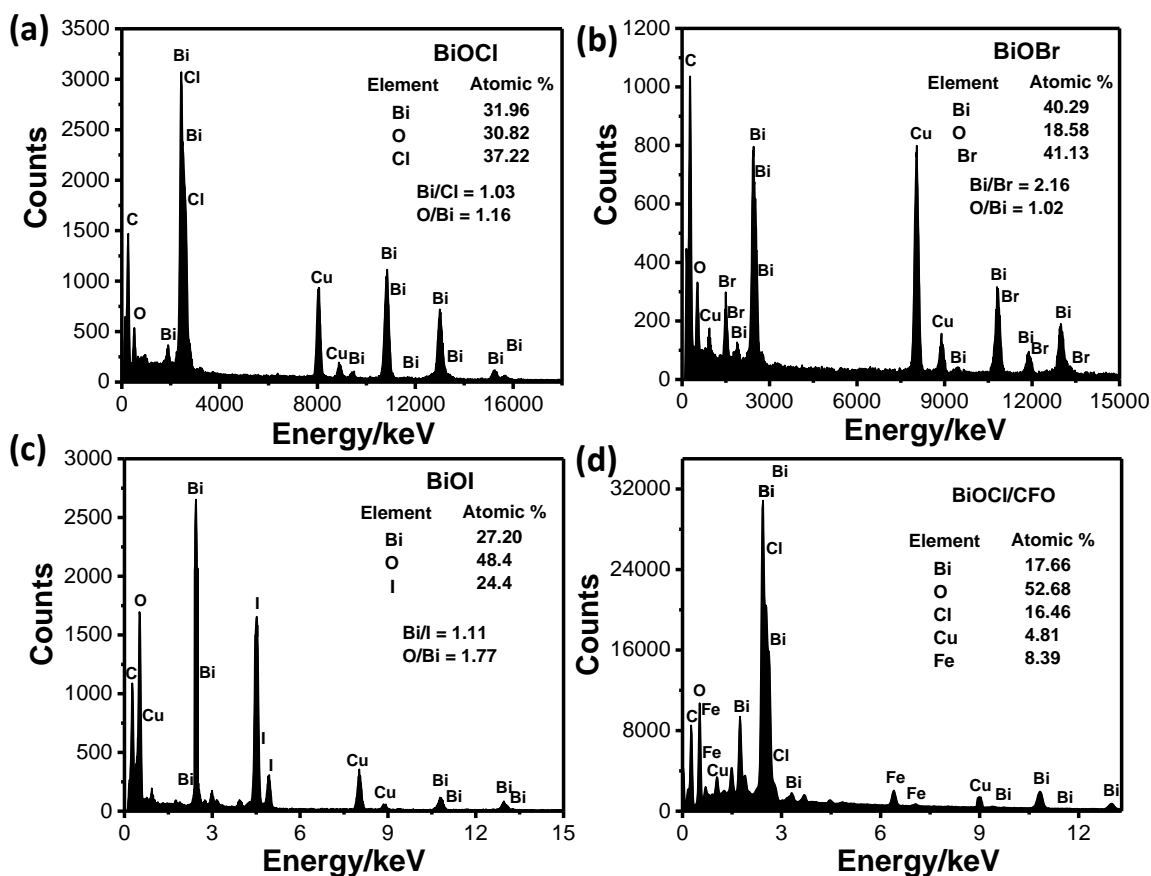


Figure 7.10 TEM-EDX (a) BiOCl, (b) BiOBr (c) BiOI and (d) BiOCl/CFO heterostructures.

The O/Bi and Bi/X atomic ratios have been calculated further from the TEM-EDX for the bare BiOX (X=Cl, Br, I) to have the insightful information about types of material formed [Figure 7.10 (a-c)]. The values of O/Bi atomic ratio are 1.16, 1.02 and 1.77 for BiOCl, BiOBr and BiOI, respectively. The atomic ratios of Bi/X (X=Cl, Br, I) are 1.03, 2.16 and 1.11 in case of BiOCl, BiOBr and BiOI, respectively are well consistent with the reported literature and confirm the formation of BiOX [55]. Further, the FESEM-EDX of BiOCl/CFO heterostructures has been investigated, where the Bi/Cl atomic ratio is 1.07 nearly equal to the bare BiOCl (Figure 7.10d). Therefore, it can be confirmed that heterostructures formation does not change the atomic ratio of the elements.

7.3.3. Electrochemical properties

Besides the structural characterization, intrinsic electronic properties like bandgap, band edge position, free carrier density, space charge layer width have significant role to optimize the photocatalytic activity. To further address the relative band structure of BiOX and CFO samples under study, the flat-band potential (E_{fb}) is measured using the electrochemical method in 0.1 M Na_2SO_4 solution (pH 7) and the Mott–Schottky plots are shown in Figure 7.11. The Mott–Schottky plots of all the BiOX samples show a positive slope, which is typical for n-type semiconductors and associated with the O-vacancy in crystal lattice originated from the high oxygen density in (001) facet. The E_{fb} is located at -0.86 V, -0.017 V and -0.92 V *vs* Ag/AgCl for BiOI, BiOCl and BiOBr, respectively. The E_{fb} values are obtained as -0.24 V, 0.59 V and -0.31 V *vs* RHE by using the Nernst equation (Eq. 7.1). It is generally accepted that the E_{fb} of n-type semiconductor is located just below the CBM and for BiOX the difference between CBM and E_{fb} is around 0.3V [42]. Therefore, the CB are -0.54 V, 0.29 V and -0.61 V *vs* RHE for BiOI, BiOCl and BiOBr, respectively ($\text{CB} = E_{fb} - 0.3$ V). The VB was estimated to be 1.22 V, 2.52 V and 2.32 V for BiOI, BiOCl and BiOBr, respectively using their bandgaps, calculated from the UV-Vis spectra ($\text{VB} - \text{CB} = E_g$). However, bare CFO shows negative slope, i.e. p-type conductivity and the E_{fb} at 0.18 V *vs* Ag/AgCl, thereby 0.79 V *vs* RHE. As the E_{fb} of p-type semiconductor lies just above the valence band maxima (VBM), thus VB and CB would be at 1.09 V and -0.56 V *vs* RHE, respectively. The calculated E_{fb} , CB, VB potentials are presented in the Table 7.1.

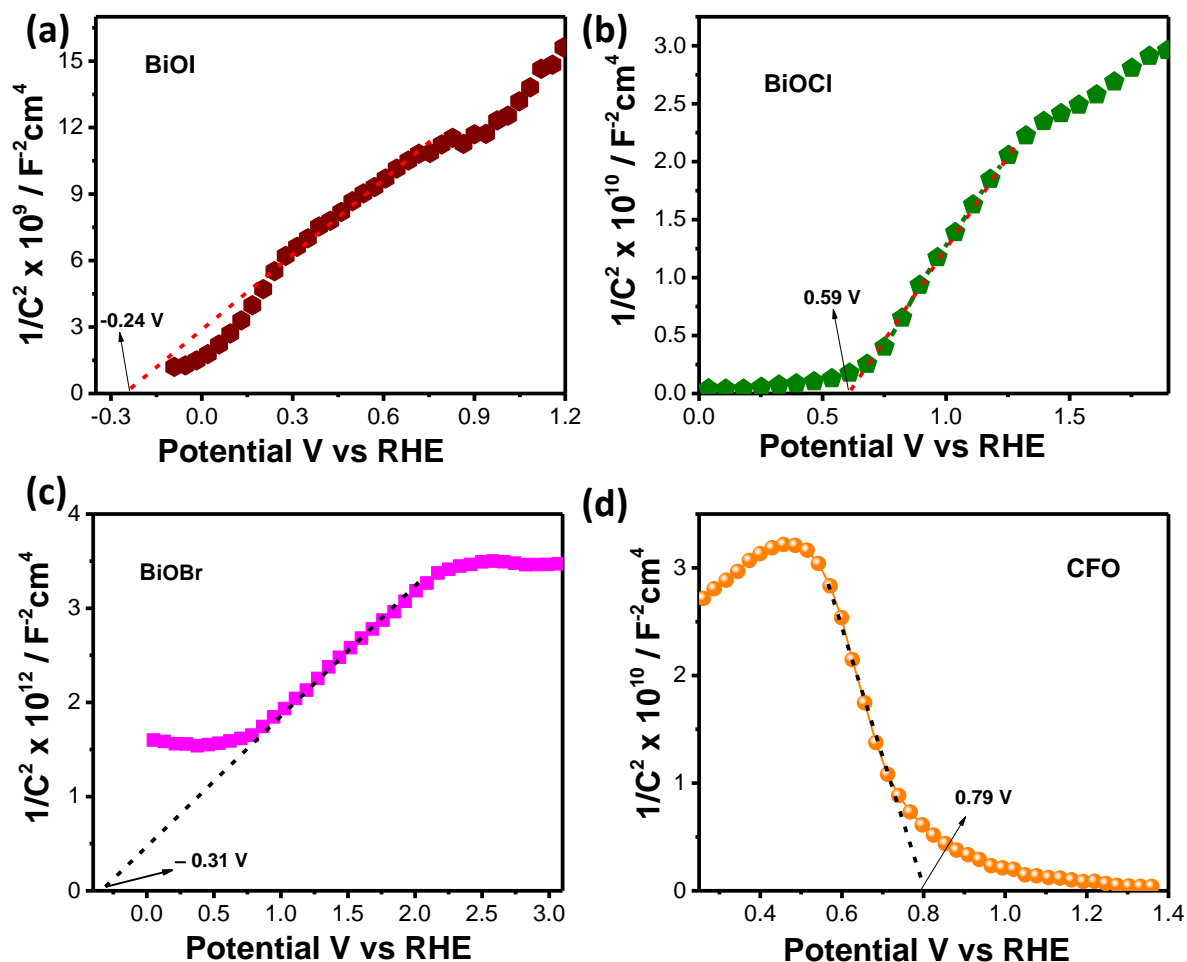


Figure 7.11 Mott-Schottky plots of pure semiconductors (a) BiOI, (b) BiOCl, (c) BiOBr and (d) CFO.

The Mott-Schottky plot of the bare BiOX (X = Cl, Br, I) at three different frequencies are shown in Figure 7.12, where frequency independent nature has been observed, indicating the flat band potential of the materials are frequency independent.

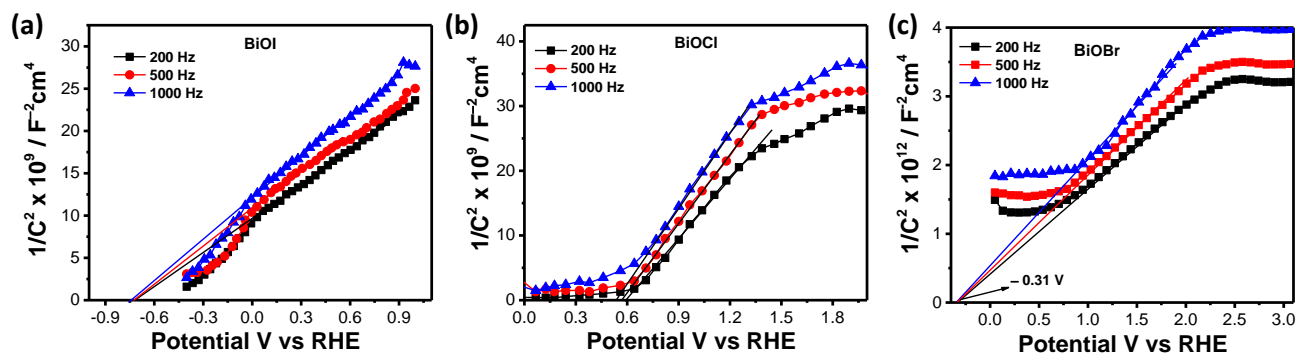


Figure 7.12 Mott-Schottky plots of (a) BiOI, (b) BiOCl and (c) BiOBr at three different frequencies.

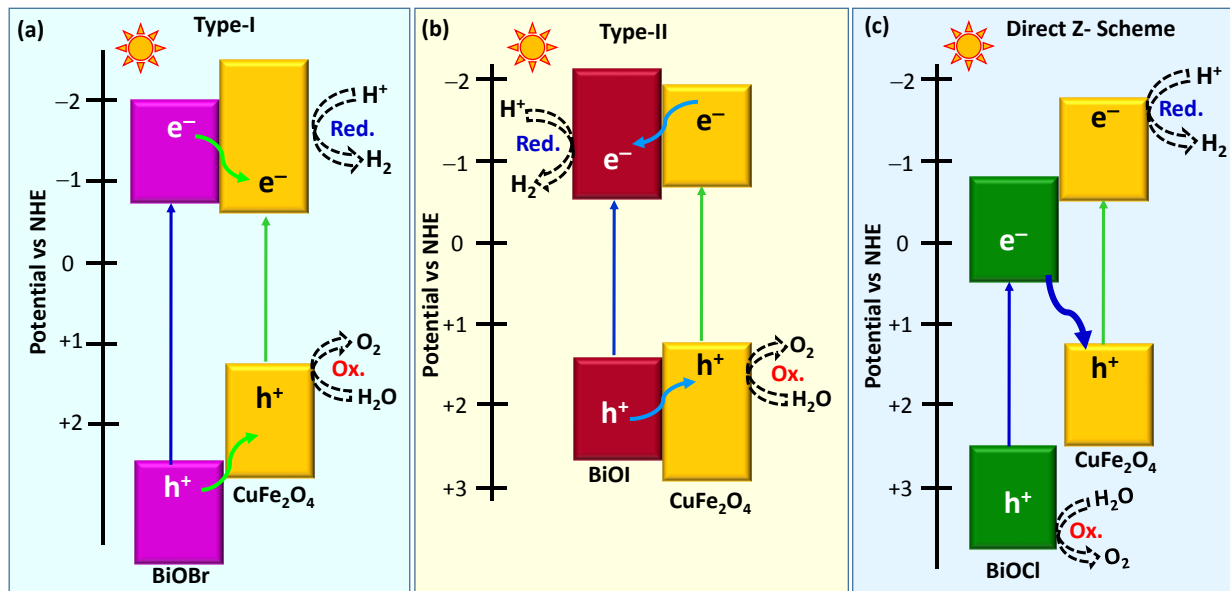
Depending on the position of VB and CB of BiOX and CFO, plausible charge transfer band diagram have been schematically presented in Scheme 7.1. It has been clearly observed that, the band alignments of BiOBr with CFO are well matched with the conventional Type-I heterostructures. The CBM and VBM of BiOBr both have higher potential than CFO (Scheme 7.1a). Thus, in presence of light energy, photo-generated electrons and holes of BiOBr will migrate to the CB and VB of CFO, respectively, due to lower potential of CFO. Thus, special charge separation of electrons and holes may not possible in this system, rather the recombination rate will be increased which reduces the number of excited carriers for water splitting.

Table 7.1 Calculated flat band potentials (E_{fb}), position of the VB and CB potentials and bandgaps the as synthesized materials.

| Material | Type of material | E_{fb} (V) vs RHE | CB (V) vs RHE | VB (V) vs RHE | E_g eV |
|--------------------------------------|-------------------------|---------------------------------------|----------------------|----------------------|----------------------------|
| BiOI | n-type | -0.24 | -0.54 | 1.22 | 1.76 |
| BiOCl | n-type | 0.59 | 0.29 | 2.52 | 2.23 |
| BiOBr | n-type | -0.31 | -0.61 | 2.32 | 2.63 |
| CuFe₂O₄ | P-type | 0.79 | -0.56 | 1.09 | 1.65 |

On the other hand, the CBM of both BiOI and CFO are negative and CFO has higher potential than BiOI, whereas the VBM of BiOI located at higher potential compared to CFO (Scheme 7.1b). Thus, in presence of light energy, photo-generated electrons of CFO will migrate to the CB of BiOI and the photo-induced holes will follow the opposite direction (BiOI to VB of CFO), due to lower potential of CFO. In this way, the charge separation will happen at two different semiconductors and the water oxidation and reduction occur by the CB electrons of BiOI and VB holes of CFO, respectively. Meanwhile, in BiOCl/CFO heterostructures the difference between CBM of BiOCl and CFO is large enough and the electrons of BiOCl lies at positive potential, which is insufficient for water reduction reaction (Scheme 7.1c). At the same time, holes of CFO will not oxidize the water molecules due to low positive potential of 0.99 V vs RHE. Thus, these electrons will try to recombine with the VB holes of CFO to form electron-hole pairs. Thereby, spatial charge separation occurs between BiOCl and CFO by accumulating highly negative excited electrons at CB of CFO and photo-induced holes at VB of BiOCl with enough potentials for water

splitting. Thus, BiOCl/CFO offers optimized redox ability with low charge carrier recombination rate and minimal energy loss due to backward reactions [56].



Scheme 7.1 Band alignments of (a) BiOI/CFO, (b) BiOBr/CFO and (c) BiOCl/CFO heterostructures.

Furthermore, the junction capacitance of the as prepared heterostructures have been studied through M-S measurement, where a ‘V’ shaped nature observed for all the heterostructures, confirming the presence of n-type BiOX and p-type CFO (Figure 7.13).

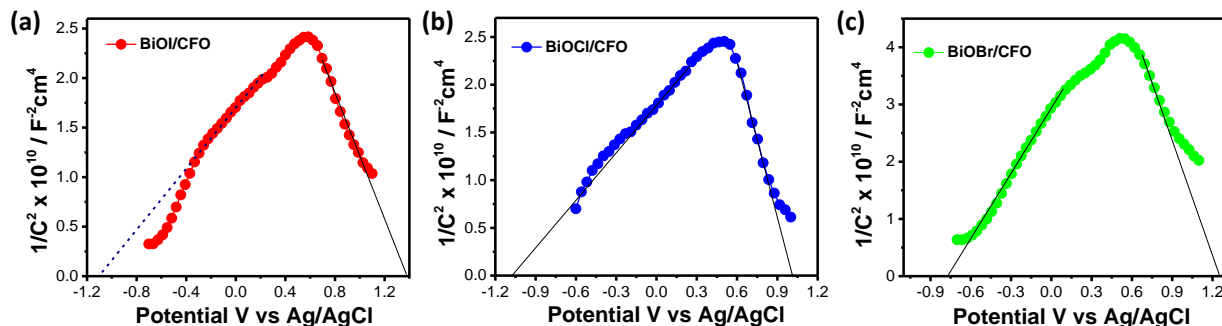


Figure 7.13 Mott-Schottky plots of (a) BiOI/CFO, (b) BiOCl/CFO and (c) BiOBr/CFO heterostructures.

The carrier concentrations of the bare semiconductors and the heterostructures have been calculated using following equation:

$$\frac{1}{C^2} = \frac{2}{eN_d\epsilon\epsilon_0} \left(E - E_{fb} - \frac{KT}{e} \right) \quad (7.2)$$

where, C is space charge capacitance at the junction interface ($F\text{ cm}^{-2}$), E_{fb} is flat band potential (V), N_d is free charge carrier density (cm^{-3}), e is the charge of electron (C), ϵ is dielectric constant

of the semiconductors, ϵ_0 is permittivity of free space, K is Boltzmann constant and T is temperature (K). The calculated N_d values are tabulated in Table 7.2, where BiOCl/CFO shows 2.5 times and 7 times higher carrier concentration compared to BiOI/CFO and BiOBr/CFO, respectively. Thus, the Z-scheme heterostructures is more effective to promote the catalytic redox reactions.

Table 7.2 Calculated charge carrier concentrations from the Mott-Schottky measurements.

| Material | Intercept | Slope | R ² | ϵ | N_d/cm^{-3} |
|--------------------------------------|-----------------------|------------------------|----------------|------------|-------------------------|
| BiOI | 1.00×10^{10} | 1.16×10^{10} | 0.990 | 40 | 302.31×10^{16} |
| BiOCl | 4.19×10^{10} | 3.08×10^{10} | 0.993 | 14.5 | 316.26×10^{16} |
| BiOBr | 2.34×10^{10} | 1.12×10^{12} | 0.996 | 45 | 2.8×10^{16} |
| CuFe₂O₄ | 2.33×10^{10} | -1.21×10^{11} | 0.990 | 19.6 | 59.65×10^{16} |
| BiOI/CFO | 1.69×10^{10} | 1.44×10^{10} | 0.990 | - | 245.21×10^{16} |
| BiOCl/CFO | 1.80×10^{10} | 1.61×10^{10} | 0.997 | - | 606.53×10^{16} |
| BiOBr/CFO | 5.30×10^{10} | 3.64×10^{10} | 0.994 | - | 186.32×10^{16} |

Space charge layer width is also an important parameter to optimize the charge transfer efficiency of a photocatalyst. The space charge layer width (W_{sc}) has been calculated further following the equation of

$$W_{sc} = \sqrt{\left(\frac{2\epsilon\epsilon_0V_s}{eN_d}\right)} \quad (7.3)$$

where V_s is the applied potential. The variation of space charge layer width with the applied potential for bare BiOX and the heterostructures have been shown in the Figure 7.14, where a drift assisted transport in the space charge region has been evident at lower potentials. After heterostructures formation, the W_{sc} decreases for each BiOX, indicating efficient charge transfer through the electrode-electrolyte interface *via* band bending due to presence of internal potential gradient at the junction interface [57]. More interestingly, the Z-scheme heterostructures exhibited lowest W_{sc} which is indicative of high catalytic efficiency.

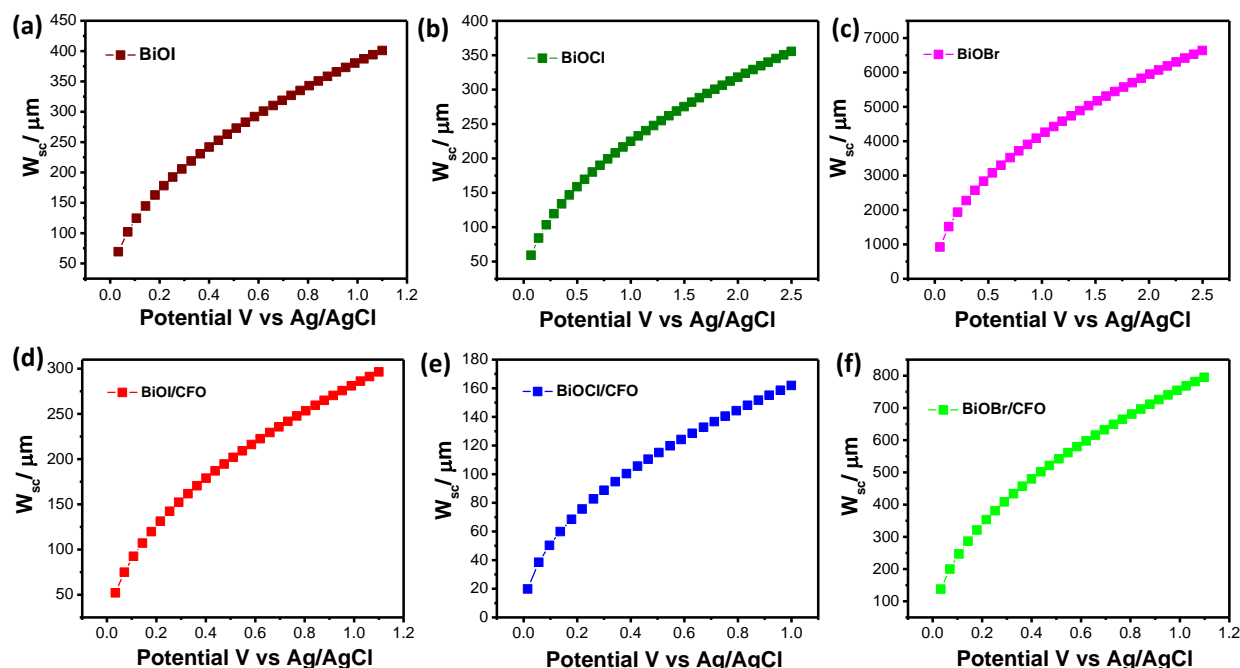


Figure 7.14 Space charge layer width vs applied potential plots of bare semiconductors (a) BiOI, (b) BiOCl, (c) BiOBr, and the heterostructures of (d) BiOI/CFO, (e) BiOCl/CFO and (f) BiOBr/CFO.

To investigate the better charge transfer efficiency of prepared heterostructures at electrode-electrolyte interface, electrochemical impedance measurement has been performed in presence of light. Figure 7.15a represents the Nyquist plots of the bare BiOX and the CFO, where, much higher resistance has been obtained for bare CFO ($\sim 639 \text{ k}\Omega$, Inset of Figure 7.15a). Among the BiOX, BiOBr shows single semicircular arc with charge transfer resistance of $\sim 1749 \Omega$, whereas BiOCl and BiOI exhibit a semicircle in high frequency, small Warburg line in intermediate frequency and almost a vertical line in low frequency region. Semicircular part corresponds to the electron transfer between redox species and the electrode *via* surface states or reaction intermediates and the steep region arises due to the diffusion of redox species, indicates the capacitive nature of the electrode. Interestingly, the smaller semicircle radius of the Nyquist plots has been noticed after heterostructures formation between BiOX and CFO, signifies the improved electron-hole transfer than that of component semiconductors. However, direct Z-scheme BiOCl/CFO exhibits smallest charge transfer resistance ($\sim 41.08\Omega$) compared to BiOI/CFO ($\sim 766.4 \Omega$) and BiOBr/CFO ($\sim 819.7 \Omega$), which means faster interfacial charge transfer occur in Z-scheme system to result the effective separation of electron-hole pairs (Figure 7.15b). In other words, Z-scheme heterostructures significantly improves the electrical conductivity at the interface in presence of light, which may

useful for water splitting reactions. All the Nyquist spectra further fitted with Randles equivalent circuit model via Z-View software and the fitted parameters are tabulated in the Table 7.3 and the plots are represented in Figure 7.16.

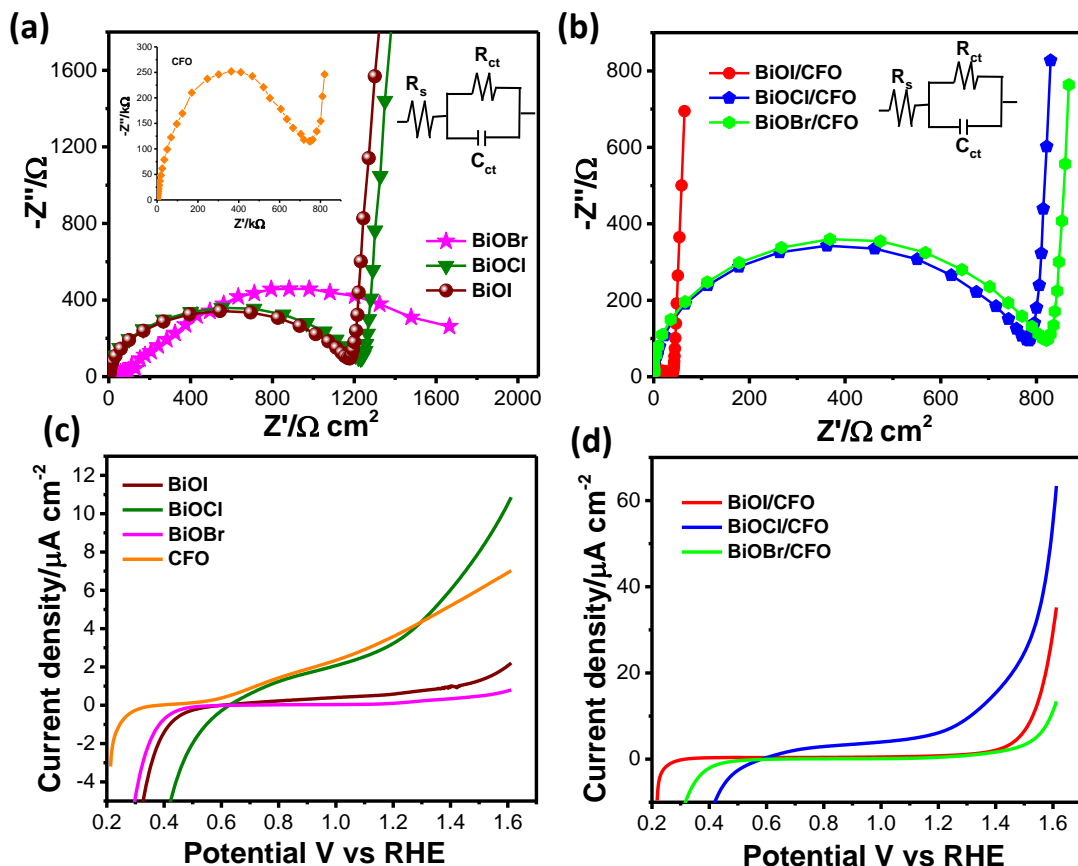


Figure 7.15 Impedance spectra of (a) bare BiOI, BiOCl, BiOBr, Inset: bare CFO, (b) BiOI/CFO, BiOCl/CFO, BiOBr/CFO heterostructures. The equivalent circuit parameters are shown in the inset of (a) and (b). Linear sweep voltammetry (LSV) curves of (c) bare semiconductors BiOI, BiOCl, BiOBr, CFO and (d) BiOI/CFO, BiOCl/CFO, BiOBr/CFO heterostructures under continuous light illumination (35W Xenon lamp) in 0.1 M Na₂SO₄ electrolyte.

Table 7.3 Fitting parameters of linearly fitted photocatalytic H₂ generation.

| Material | R _s /Ω | R _{ct} /Ω | C _{ct} /μMho |
|-----------|-------------------|--------------------|-----------------------|
| BiOI | 0.23 | 1180 | 0.16 |
| BiOCl | 0.16 | 1190 | 0.19 |
| BiOBr | 65.0 | 1749 | 0.84 |
| BiOI/CFO | 0.47 | 766 | 0.25 |
| BiOCl/CFO | 0.72 | 41.1 | 0.27 |
| BiOBr/CFO | 0.20 | 819 | 0.34 |
| CFO | 2.48 | 639000 | 0.02 |

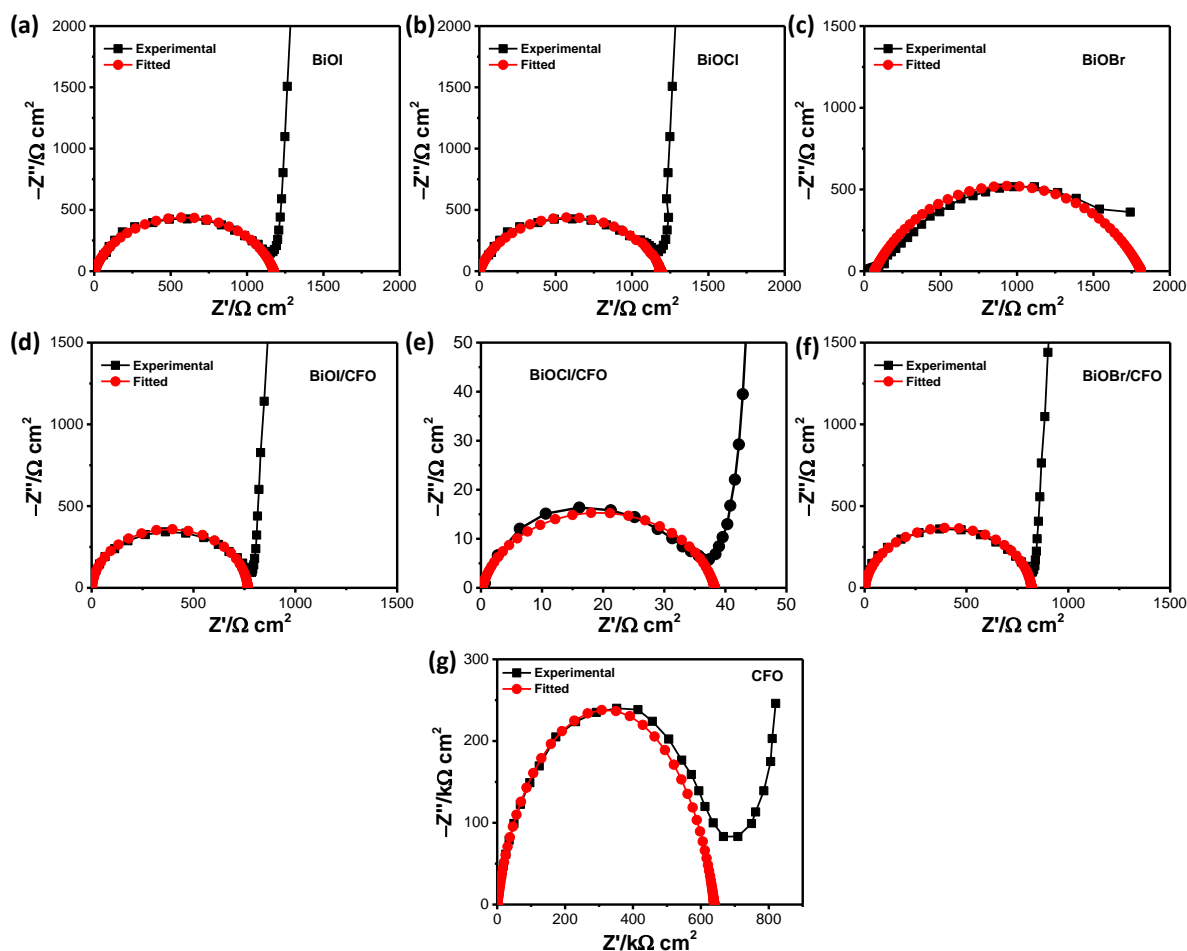


Figure 7.16 Fitted Nyquist plots of (a) BiOI, (b) BiOCl, (c) BiOBr, (d) BiOI/CFO, (e) BiOCl/CFO, (f) BiOBr/CFO and (g) bare CFO under light illumination.

To further explore the catalytic properties of the as synthesized materials, a series of electrochemical and optical measurements have been conducted. Figure 7.15(c-d) and Figure 7.17 exhibit the linear sweep voltammetry curves of bare semiconductors and the heterostructures in 0.1M Na₂SO₄ aqueous solution under continuous visible light illumination using 35W Xenon lamp as light source. Clearly, heterostructures formation effectively enhances the current density compared to their component semiconductors, which might be attributed due to the synergetic effects of low charge transfer resistance, high charge carrier concentration and efficient charge separation through the interfaces. In addition, the CFO nanoparticles may serve as effective active sites to promote the redox reactions for H₂ generation by accumulating the photogenerated electrons, which is further verified by the transient photocurrent measurement.

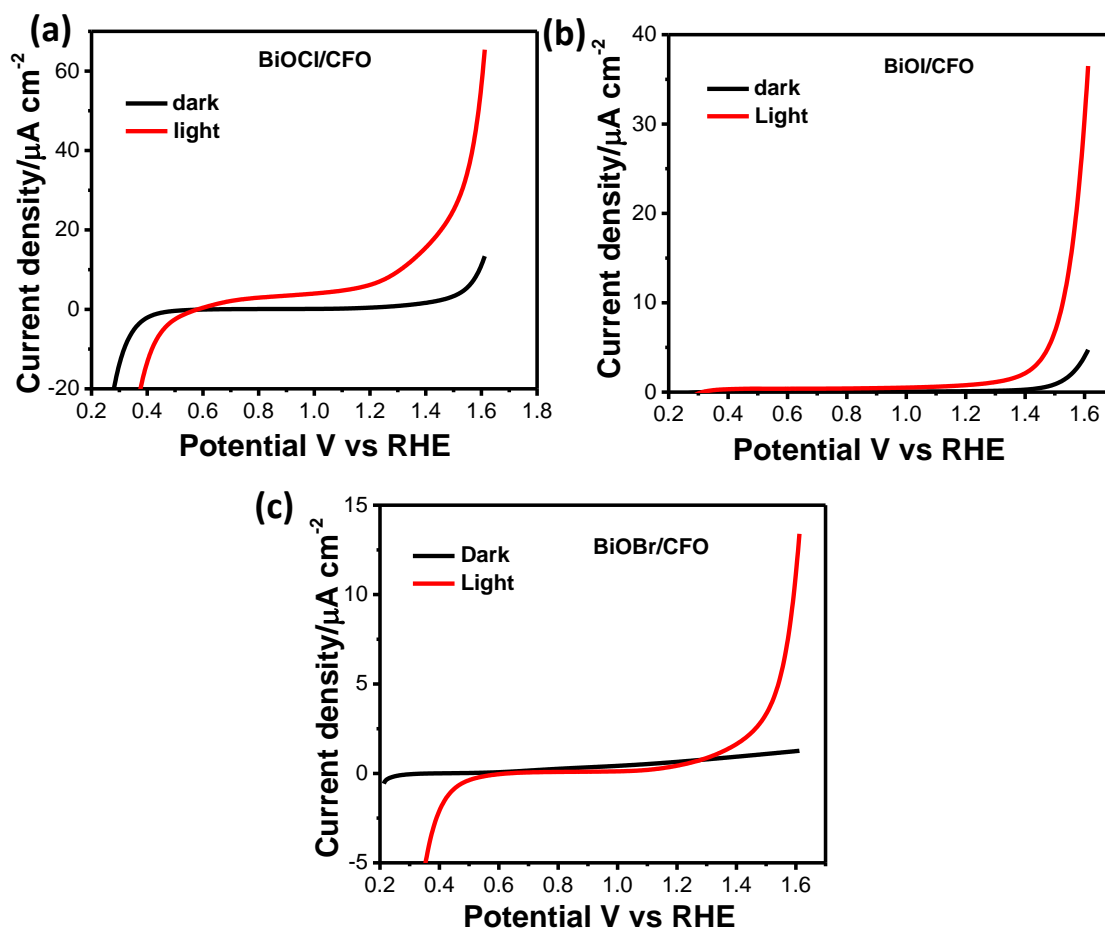


Figure 7.17 Linear sweep voltammetry (LSV) curves of (a) BiOCl/CFO, (b) BiOI/CFO and (c) BiOBr/CFO heterostructures under dark and continuous light illumination (35W Xenon lamp) in 0.1 M Na₂SO₄ electrolyte.

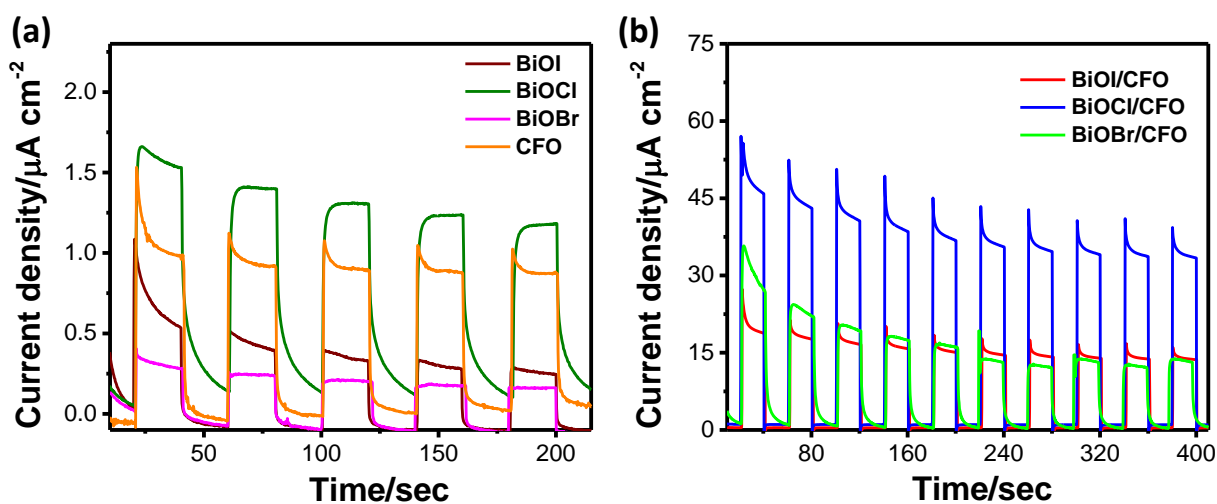


Figure 7.18 Transient photocurrent spectra of (a) bare semiconductors CFO, BiOI, BiOCl, BiOBr and (b) the BiOI/CFO, BiOCl/CFO, BiOBr/CFO heterostructures under chopped light condition, measured by chronoamperometry at a fixed potential of 0.6V vs Ag/AgCl.

The photo-stability of the anodes have been determined by measuring transient photocurrent density through chopped chronoamperometry. The BiOCl exhibited highest photocurrent density compared to other BiOX semiconductors which is consistency with the LSV result (Figure 7.18a). As expected, the Z-scheme BiOCl/CFO heterostructures shows remarkably increased photocurrent density compared to Type-II heterostructures, implying that direct Z-scheme system is more efficient in water oxidation reaction (Figure 7.18b). The theoretical PEC H₂ generation for the Z-scheme BiOCl/CFO heterostructures further calculated from the chronoamperometry spectra by determining the charge (Q) passed through the photoanode. The charge has been determined by integrating the current over the time and the moles of H₂ is equal to $\frac{Q}{2F}$, where F is the faraday constant (F = 96500) [61]. The estimated PEC H₂ generation for BiOCl/CFO heterostructures reaches to 0.05 μmol at 450 sec (Figure 7.19).

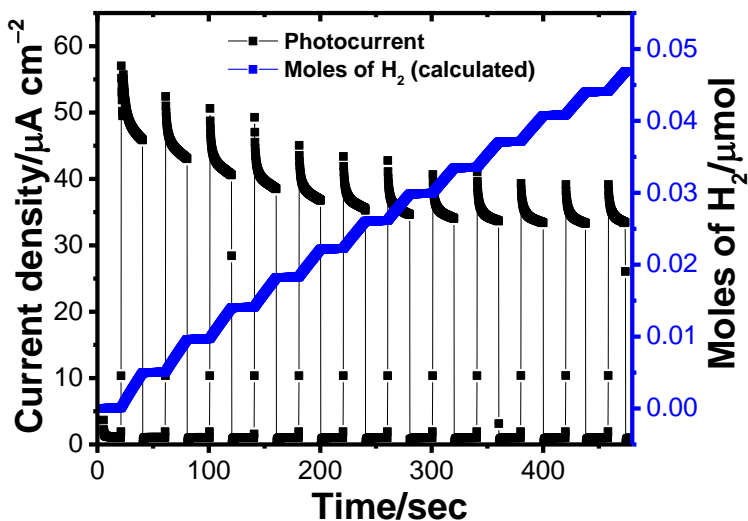


Figure 7.19 Chopped chronoamperometry profile and calculated PEC H₂ spectra of BiOCl/CFO Z-scheme heterostructure.

In order to get more details about quantum efficiency of the Z-scheme heterostructures, incident photon-to-current conversion efficiency (IPCE) has been calculated from the action spectrums through chopped chronoamperometry measurement within the visible region (400 – 750 nm). Z-scheme BiOCl/CFO heterostructures has very low efficiency at wavelength region of > 600 nm, whereas it shows prominent enhanced efficiency at the range of < 600 nm and maximum at 450 nm (~25%) (Figure 7.20). The enhanced activity within the range of 450 nm – 750 nm could possibly achieve by effective visible light absorption and electron-hole separation which is in accordance with the consequence of electrochemical impedance measurements.

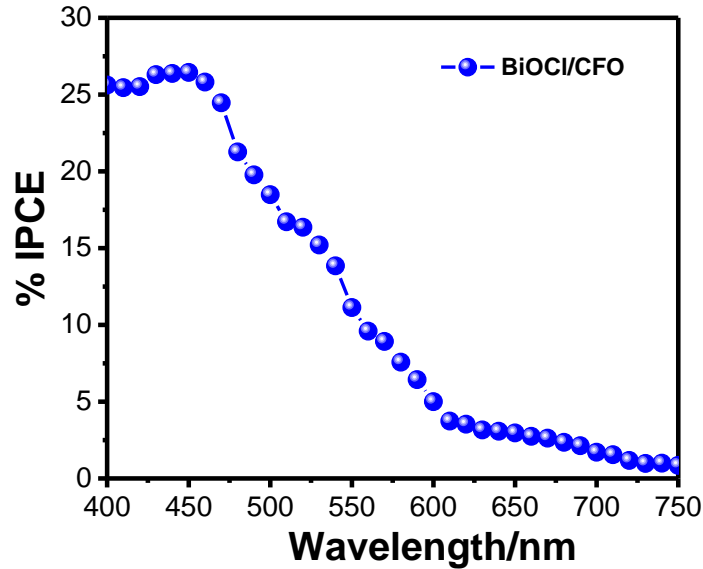


Figure 7.20 Incident Photon to Current Conversion Efficiency (IPCE %) spectra of BiOCl/CFO heterostructures using 0.1 M Na₂SO₄ electrolyte within the wavelength range 400–750 nm.

7.3.4 UV-Vis Absorption and Bandgap Calculation

Furthermore, the optical absorption of bare semiconductors and the heterostructures are studied by diffuse reflectance spectra (DRS) to investigate the influence of heterostructures on light absorption. Figure 7.21 represents the DRS of bare CFO, BiOCl and BiOCl/CFO heterostructures. BiOCl has strong absorption in UV and visible region which significantly boosted up after heterostructures formation with CFO at each wavelength. Interestingly, a prominent absorption hump has been observed within the wavelength range of 380 nm to 550 nm, which may be arise due to strong interaction between BiOCl and CFO, is well consistent with the IPCE result. Therefore, it can be concluded that, improved light absorption at this region enhances the photon to current conversion efficiency of the Z-scheme heterostructures. Furthermore, the absorption spectra of the BiOI, BiOBr, BiOI/CFO and BiOBr/CFO are studied and shown in Figure 7.22, where prominent enhancement observed in intensity as well as in absorption edge for heterostructures compared to bare BiOX. A classical Kubelka–Munk $[(\alpha hv)^2 \text{ vs photon energy } (hv)]$ equation has been used to calculate the bandgap of the materials (Inset of Figure 7.21 and Figure 7.23).

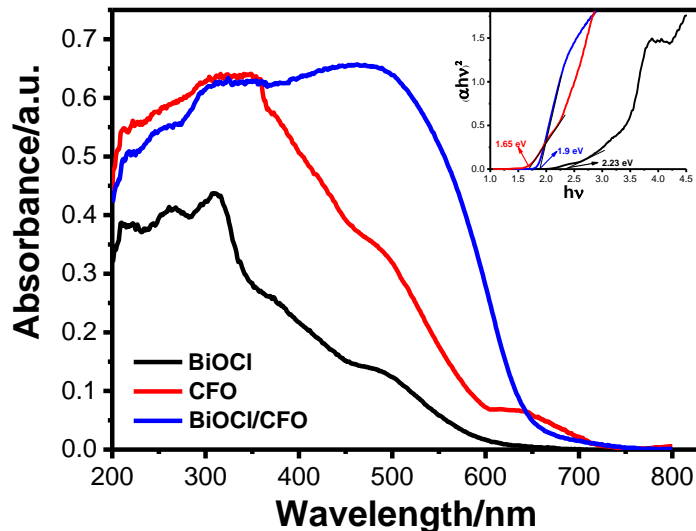


Figure 7.21 Diffuse reflectance spectra of BiOCl, BiOCl/CFO, and bare CFO. Inset: Kubelka–Munk $[(\alpha hv)^2 \text{ vs photon energy (} hv)]$ plots of CFO, BiOCl and BiOCl/CFO.

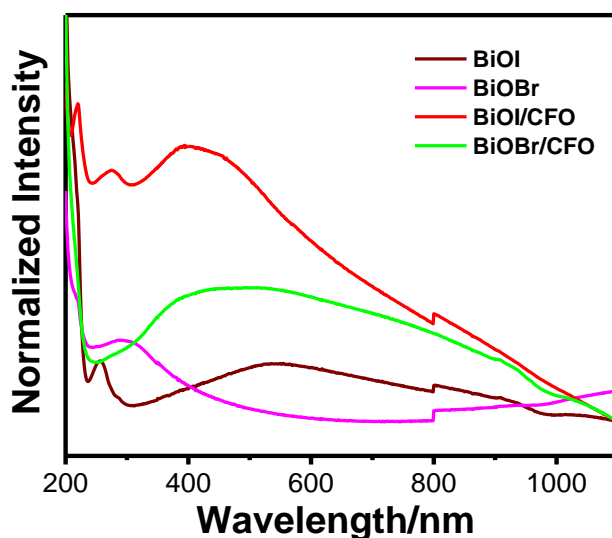


Figure 7.22 UV-Vis absorption spectra of BiOI, BiOBr, BiOI/CFO and BiOBr/CFO heterostructures.

It is widely accepted that the BiOX and CFO follow indirect and direct transition, respectively. Thus, the calculated indirect bandgaps are 1.76 eV, 2.23 eV and 2.63 eV for BiOI, BiOCl and BiOBr respectively and direct bandgap of 1.65 eV for CFO, well matched with the previously reported literatures [12]. The calculated bandgap of BiOCl nanosheet is 2.2 eV which reduces to 1.9 eV after CFO nanoparticle deposition on the surface. The bandgap reduction may attributed due to formation of heterostructures between BiOCl and CFO, which further facilities the photon absorption, photogenerated charge carrier generation and separation.

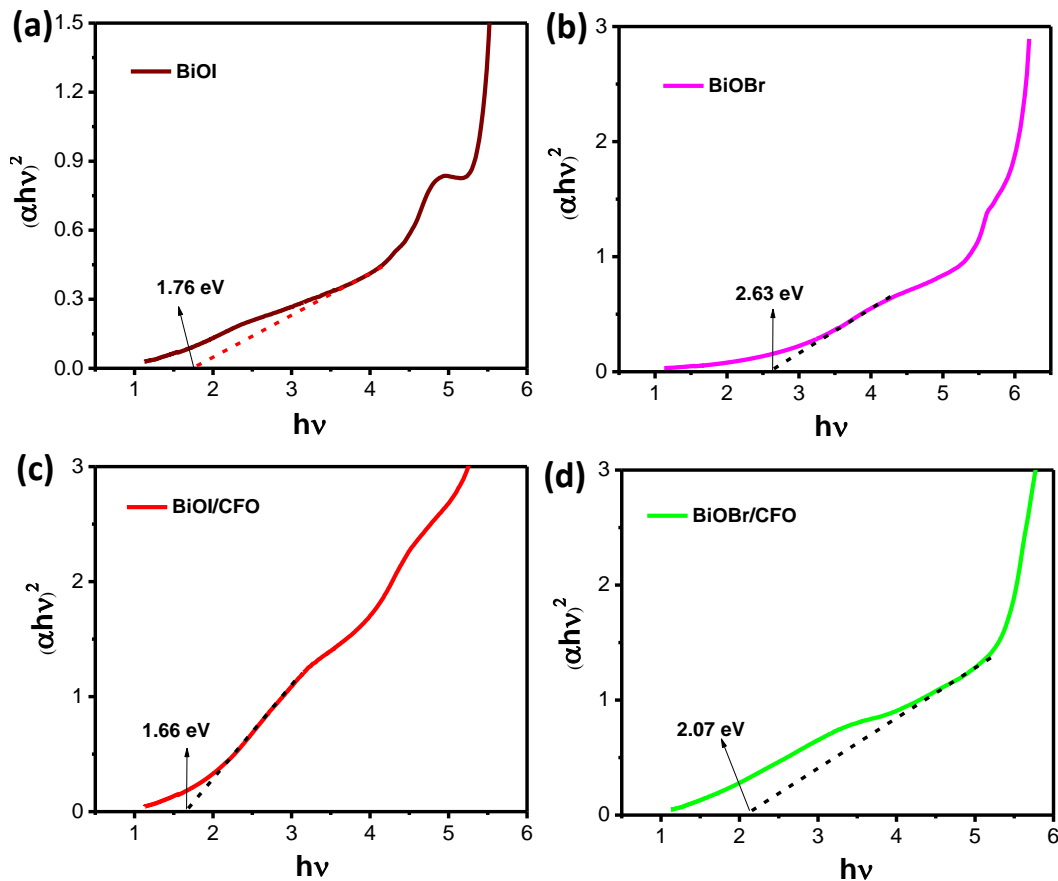


Figure 7.23 Kubelka–Munk $[(\alpha h\nu)^2$ vs photon energy ($h\nu$)] plots of (a) BiOI, (b) BiOBr, (c) BiOI/CFO, (d) BiOBr/CFO.

7.3.5 Photocatalytic H₂ Generation

The photocatalytic activity of BiOX and the heterostructures was measured through H₂ generation from water under visible light illumination. The time course of hydrogen generation has been measured under continuous visible light illumination (250W Xe lamp) and in presence of 25 vol % methanol as sacrificial agent (Figure 7.24). Here catalysts (1mg/ml concentration) are dispersed in the water medium under light illumination without any external potential. BiOI exhibits highest H₂ generation (~18.45 mmol) among the BiOX due to more negative CB which provides high reduction potential. However, the H₂ generation of CFO is very low (~4.2 mmol) because of fast recombination of the excited charge carriers owing to narrow bandgap. Interestingly, the H₂ generation has been significantly increased after heterostructures formation in a steady manner which validates the aforesaid estimated reasons of high conductivity, large number of active sites and efficient charge separation. Under visible light, BiOCl/CFO exhibits the highest mass specific activity (~22.2 mmol h⁻¹), followed by BiOI/CFO (~ 12.5 mmol h⁻¹) and then BiOBr/CFO (~6.5

mmol h⁻¹), consistent with their ability to absorb the visible light (Figure 7.24b). For comparison, a mixing sample of BiOCl and CFO (at equal mass ratio) have been prepared and tested the photocatalytic H₂ generation, where eight times lower activity obtained than that of BiOCl/CFO heterostructures at similar reaction condition. This result clearly confirms the intimate contact between BiOCl and CFO after heterostructures formation which facilitate the charge separation and transfer through the junction.

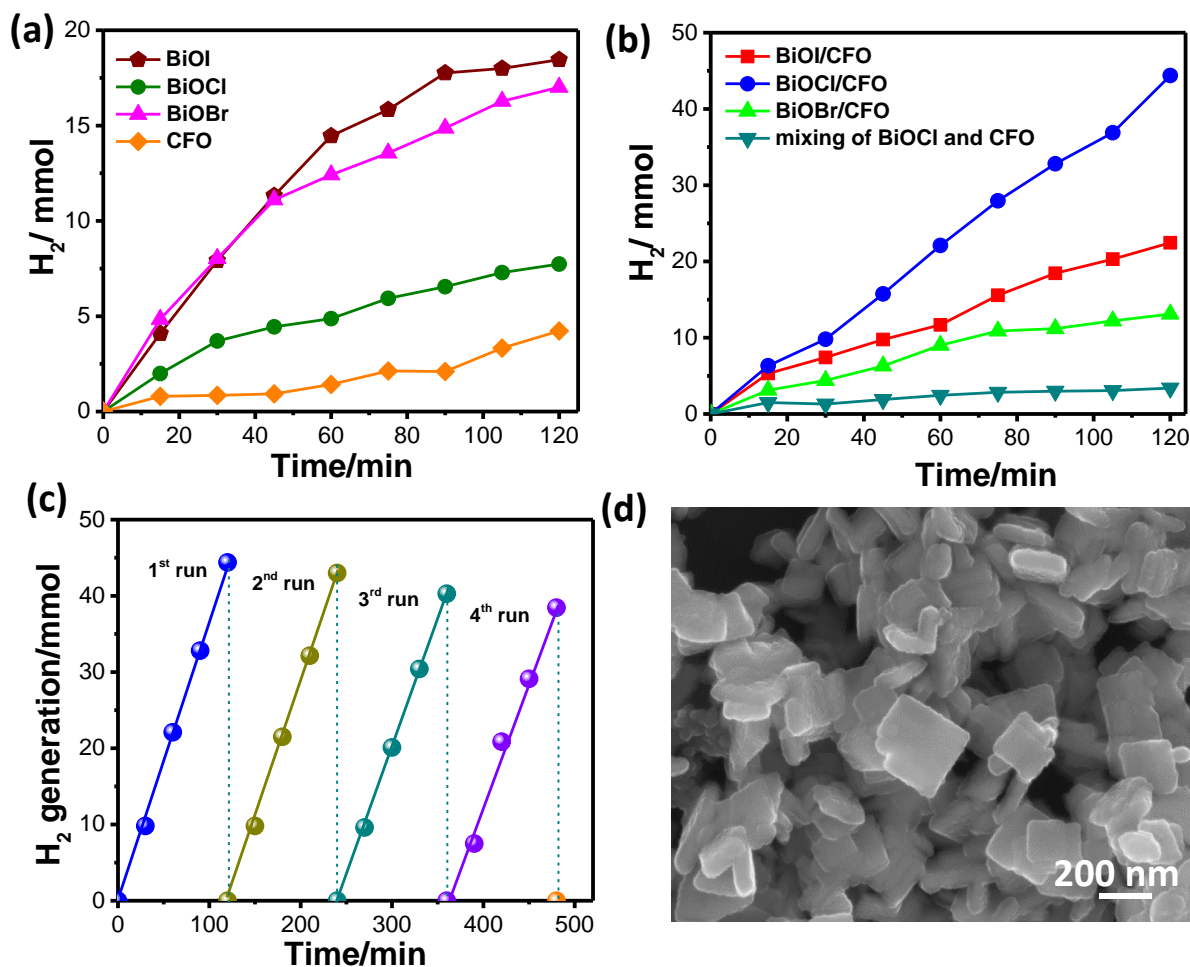


Figure 7.24 Photocatalytic hydrogen generation in the presence of (a) bare BiOX (X= Cl, Br, I) and CFO, (b) BiOX/CFO (X= Cl, Br, I) heterostructures for 2 h under visible light from an aqueous solution containing 25 volume% methanol as sacrificial agent at pH 7, (c) Recycling test of BiOCl/CFO heterostructures for H₂ generation, (d) FESEM image of BiOCl/CFO after the catalytic reaction of H₂ generation under visible light.

Further, the H₂ generation data of all the bare BiOX (X=Cl, Br, I) and CuFe₂O₄ as well as heterostructures are linearly fitted (Figure 7.25a and 25b) and the fitted parameters are represented in Table 7.4. The H₂ generation of bare BiOX and CFO are roughly linear may be associated with

fast recombination. Additionally, the H₂ generation increases up to a certain time then get saturated due to presence of limited sacrificial agent in the reaction system. However, Z-scheme BiOCl/CFO and Type-II BiOI/CFO exhibit linear H₂ generation for the entire time period because of efficient charge separation and transfer to the surface of the catalyst. On the other hand, roughly linear trend has been observed for Type-I BiOBr heterostructures as the photogenerated charge carrier accumulation on the CFO, which may increase the electron-hole recombination rate, thereby reduce the number of free electrons for water reduction.

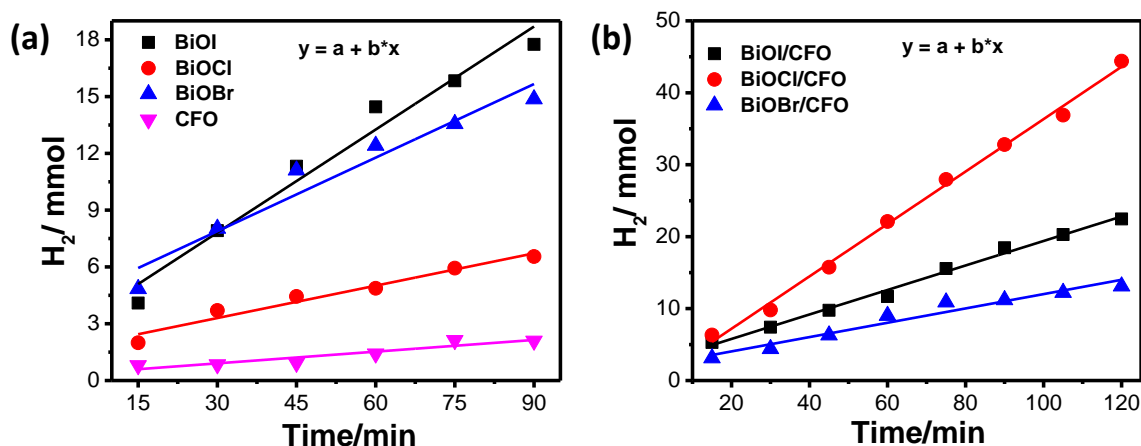


Figure 7.25 Linearly fitted H₂ generation of (a) bare BiOX and CFO, (b) BiOX/CFO heterostructures.

Table 7.4 Fitting parameters of Nyquist plots.

| Material | Linear equation | Adj. R ² | Intercept | Slope |
|--|-----------------|---------------------|-----------|-------|
| BiOI | $y = a + b*x$ | 0.96 | 2.37 | 0.18 |
| BiOCl | $y = a + b*x$ | 0.95 | 1.59 | 0.05 |
| BiOBr | $y = a + b*x$ | 0.92 | 3.99 | 0.12 |
| CuFe ₂ O ₄ (CFO) | $y = a + b*x$ | 0.85 | 0.28 | 0.02 |
| BiOI/CFO | $y = a + b*x$ | 0.99 | 2.37 | 0.17 |
| BiOCl/CFO | $y = a + b*x$ | 0.99 | - 0.08 | 0.38 |
| BiOBr/CFO | $y = a + b*x$ | 0.94 | 2.05 | 0.09 |

Figure 7.26 presents the calculated AQY% for the catalysts (calculated using Eq. 7.1), where BiOCl/CFO heterostructures exhibits highest photocatalytic H₂ generation efficiency of 9.9 % followed by BiOI/CFO (5 %) and BiOBr/CFO (4 %). Thus, direct Z-scheme heterostructures

formation improve the H₂ generation rate as well as AQY% which can be described on the basis of charge transfer process.

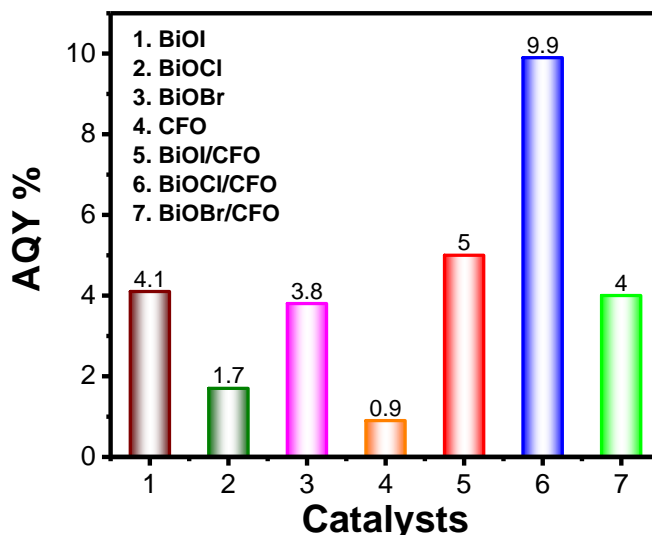


Figure 7.26 Apparent quantum yield (AQY %) of the as developed bare semiconductors and heterostructures.

The effect of sacrificial agents (commonly used alcohol and aldehydes) in H₂ generation has been investigated (Figure 7.27a). The redox potential of a sacrificial hole scavenger for H₂ generation should be more negative than valence band of semiconductor, so that it can consume the holes and suppress the recombination of photogenerated electrons [58]. Notably, methanol shows the highest H₂ generation (~44.4 mmol) compared to ethanol (~38.5 mmol), formaldehyde (34.1 mmol), 2-propanol (~24.8 mmol), and ethylene glycol (~18.7 mmol) suggesting the length of carbon chain is inversely proportional to water reduction ability. However, the oxidation potential and permittivity of sacrificial agents have play potential role in H₂ generation as it act as electron donors to consume the holes. According to Gouy-Chapman theory, surface charge density is proportional to dielectric constant of the solvent [57]. As shown in Table 7.5, the oxidation potential of methanol is lower than ethanol, 2-propanol and ethylene glycol but the permittivity is higher than ethanol and 2-propanol. Although, the permittivity of ethylene glycol is much higher compared to other solvent, the higher oxidation potential (1.54 eV, which is higher than water oxidation potential 1.23 eV) lowers its activity as it poorly oxidized. Therefore, methanol is considered as preferable sacrificial agent in photocatalytic hydrogen generation having lower oxidation potential and considerable permittivity. The effect of sacrificial donor/solvent ratio in photocatalytic H₂ generation has been investigated for BiOCl/CFO heterostructures (Figure 7.27b).

The volume % of methanol has been varied from 5 to 50%, where the amount of H₂ generation increases with the increase of methanol concentration up to a certain percentage, then decreases. The 25 volume % and 30 volume % shows almost similar result, however decreases when 50 volume % was used. Methanol generally acts as hole scavenger, i.e. it reacts with photoinduced holes very fast than water and reduces the probability of electron-hole recombination. Therefore, an optimized percentage may boost the catalytic reactions in a forward direction. The higher concentration of methanol may generate higher amount of reactant products which further sluggish the reaction rate kinetics due to unwanted backward reaction.

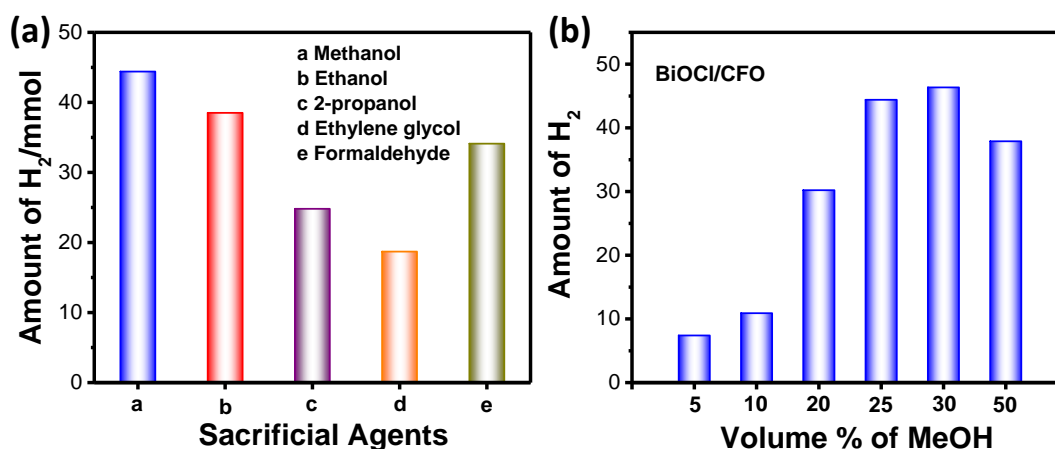


Figure 7.27 Effect of (a) different sacrificial hole scavengers and (b) sacrificial donor/solvent ratio in photocatalytic H₂ generation for BiOCl/CFO heterostructures.

Table 7.5 Permittivity and oxidation potential of the sacrificial agents.

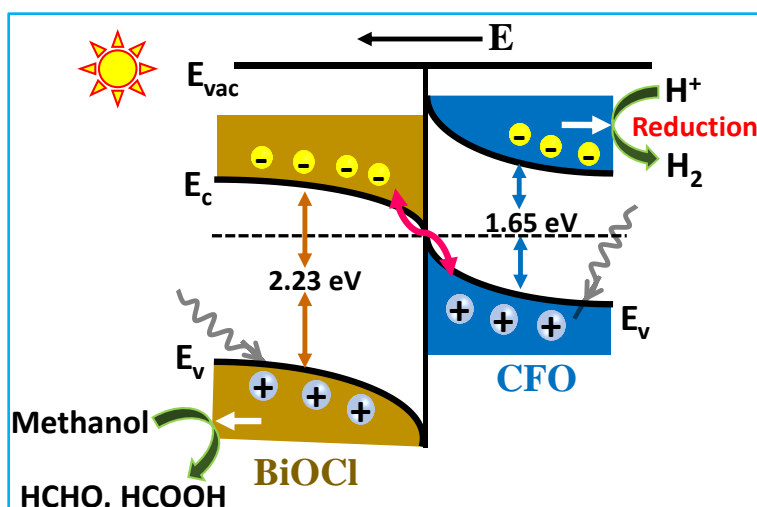
| Sacrificial agent | Permittivity (ϵ) | Oxidation Potential/ eV |
|-------------------|-----------------------------|-------------------------|
| Methanol | 31.2 | 1.05 |
| Ethanol | 25.7 | 1.10 |
| 2-propanol | 18.23 | 1.15 |
| Ethylene Glycol | 38.9 | 1.54 |

In addition to its remarkable photocatalytic activity, BiOCl/CFO heterostructures exhibits very good stability as a photocatalyst. As shown in Figure 7.24c, no noticeable decrease in the activity for photo catalytic hydrogen production can be observed in the cycling tests (a minimal 14% loss

after 4th run), indicating that the as-prepared heterostructures may effectively restrain photocorrosion under visible light and possess stable photocatalytic H₂ generation activity. Moreover, no obvious structural modification can be observed for BiOCl/CFO heterostructures even after photocatalytic reactions (Figure 7.24d). Therefore, the remarkable catalytic activity and stability make heterostructures as a promising photocatalyst for hydrogen production from water splitting under visible light.

7.3.6 Proposed Mechanism for H₂ Generation

Conceptually, when two semiconductor comes in contact with each other, a junction will create which in turn facilitate electron transfer from higher energy level to the lower energy level to achieve equilibrium. At equilibrium, bands of the material bended according to their fermi level position and tried to line up the fermi level (Scheme 7.2). Under light irradiation, photoinduced electrons and holes are generated both at BiOCl and CFO. As the CB of BiOCl is nearly located to the VB of CFO, thus low energy electrons of BiOCl may directly recombine with the holes of CFO by leaving excited electrons on the CB of CFO as shown in Scheme 2. Due to upward band bending, CB electrons of CFO may not transfer from CFO to BiOCl, may flow away from the junction. These electrons can easily reduce the water molecules into H₂ (H⁺/H₂, 0V vs RHE) due to strong redox capability (-0.65 V). At the same time, photo-induced holes are consumed by the scavenger methanol and reduce the recombination rate as holes react faster with methanol than water. Thus, the direct Z-scheme photocatalytic system may effectively lower the backward reactions and enhances the amount of H₂ generation under visible light. On the other hand, the high energy photo generated electron and holes are migrated in the BiOI/CFO and BiOBr/CFO Type-II and Type-I heterostructures and lost their redox ability for water splitting, resulting lower H₂ generation compared to Z-scheme photocatalytic system (Scheme 1). The H₂ production rate of some reported CFO and BiOX-based materials and patent photocatalysts [59] are listed in Table 7.6 to compare the photocatalytic activity, where very high photocatalytic activity has been achieved for developed Z-scheme BiOCl/CFO heterostructures. Therefore, it can be concluded that, the position of the energy bands has strong role in controlling the electron hole transfer as well as formation of different type heterostructures.



Scheme 7.2 Schematic illustration of the charge transfer process and the photocatalytic H₂ generation of the novel Z-scheme BiOCl/CFO heterostructures under visible light irradiation.

Table 7.6 Comparison table of photocatalytic applications of CFO and BiOX based materials.

| Material | Light Source | Sacrificial agent | Photocatalytic H ₂ /O ₂ generation μmolh^{-1} | PEC activity $\mu\text{A cm}^{-2}$ at 1V vs Ag/AgCl | Referece |
|---|---|--|--|---|----------|
| CuFe ₂ O ₄ photoanodes | Xenon, 450 W | – | – | 500 | 62 |
| CuFe ₂ O ₄ /BiVO ₄ | 400 W metal halogen lamp with 420 nm cutoff filters | 0.5 M NaClO ₄ electrolyte | – | 450 | 63 |
| CuFe ₂ O ₄ / α -Fe ₂ O ₃ Composite | AM 1.5, 100 mW/cm ² | – | – | 2400 | 64 |
| CdS/CuFe ₂ O ₄ | Xenon lamp | – | – | 10 | 65 |
| CuFe ₂ O ₄ /g-C ₃ N ₄ | 300 W Xe lamp, 420 nm band-pass filter | 3 wt% Pt, triethanolamine (TEA, 10 vol%) | 76 | – | 66 |
| CuFe ₂ O ₄ /WO ₃ nanocomposite | AM 1.5G illumination | – | – | 800 | 67 |
| CuFe ₂ O ₄ /ZnO | 500 W Xe lamp | – | – | – | 68 |
| Flame-Annealed CuFe ₂ O ₄ | AM 1.5 G, 100mW/cm ² | – | – | 2000 | 69 |
| graphene oxide–CuFe ₂ O ₄ –ZnO | Xenon lamp | 0.5 M Na ₂ SO ₄ aqueous solution | – | – | 70 |

| Material | Light Source | Sacrificial agent | Photocatalytic H ₂ /O ₂ generation $\mu\text{mol h}^{-1}$ | PEC activity $\mu\text{A cm}^{-2}$ at 1V vs Ag/AgCl | Reference |
|--|--|---|---|---|-----------|
| p-CuFe ₂ O ₄ /n-NiAl LDH | – | 20 mL aqueous methanol | 345.76 (H ₂) | 1.5 | 71 |
| TiO ₂ -x/BiOCl heterojunctions | 300W Xe lamp, cutoff filter was used as a light source ($\lambda > 400$ nm) | - | – | 700 | 72 |
| Bi ₄ NbO ₈ Cl | – | Methanol | 25 (H ₂) 12 (O ₂) | – | 73 |
| Fe(III) modified BiOCl | 300 W Xe lamp, 1.5 solar light irradiation | – | 30 (H ₂) | 350 | 74 |
| BiOCl/ β -FeOOH heterojunction | xenon lamp (500 W) | triethanolamine (TEA; 15 vol%) | 13650(H ₂) | – | 75 |
| BiOCl/copper(II) | 500 W Xe lamp | 20vol% of methanol | 16 (H ₂) | 40 | 76 |
| {0 0 1} Facets BiOCl | – | – | 58.6 (O ₂) | – | 77 |
| Oxygen Vacancy-Mediated BiOCl | 300 W Xe lamp | methanol triethanolamine (10 vol%) | 4 (H ₂) 90(O ₂) | – | 78 |
| BiOI | 250 W metal halide lamp and a 300 W xenon lamp without any filter | – | 2730 (H ₂) | – | 79 |
| g-C ₃ N ₄ /BiOI | 300 W Xe lamp | – | – | 800 | 80 |
| BiOI Nanoplatelet | 300 W Xe lamp | – | – | 1200 | 81 |
| g-C ₃ N ₄ /Bi ₄ NbO ₈ Cl | 300 W Xe lamp, with optical filter ($\lambda > 420$ nm) | 10 mL of lactic acid, 1 wt % Pt co-catalyst | 287.71(H ₂) | 0.8 | 82 |
| CeO ₂ /BiOI | 125 W medium pressure Hg lamp ($\lambda \geq 420$ nm) | 0.05 M aqueous AgNO ₃ | 323 (O ₂) | – | 83 |
| Bi-BiOCl/AgCl | 300 W Xe lamp | – | 198.2 (H ₂) | 45 | 84 |
| 2.2% W/C on TiO ₂ | 500 W Hg lamp | MeOH (50 vol%aq) | 5350 (H ₂) | – | 85 |
| Pt/TiO ₂ | 740 mW cm ⁻² , Hg | MeOH (50 vol%aq) | 1950 (H ₂) | – | 86 |
| 19% Printex-G + 65% TiO ₂ + 16% (5 wt% RuO ₂ /TiO ₂) | 50 mW cm ⁻² Hg | EtOH-H ₂ O | 45 (H ₂) | – | 87 |

| Material | Light Source | Sacrificial agent | Photocatalytic H ₂ /O ₂ generation μmolh^{-1} | PEC activity $\mu\text{A cm}^{-2}$ at 1V vs Ag/AgCl | Reference |
|---|--|---|---|---|------------|
| (5 wt%)Ag/TiO ₂ NT | Hg or Xe | MeOH (5 vol% aq) | 3200 (H ₂) | – | 88 |
| Pt/TiO ₂ | 300 W, Xe | Glycerol (20 vol% aq) | 7280 (H ₂) | – | 89 |
| C,N-co-doped TiO ₂ | 8 W, Hg (365 nm) | Na ₂ S–Na ₂ SO ₃ | 0380 (H ₂) | – | 90 |
| TiO ₂ /BiVO ₄ | 300 W, Xe | MeOH–H ₂ O | 1240 (H ₂) | – | 91 |
| TiO ₂ /Cu ₂ O | 300 W, Xe 420 nm | MeOH–H ₂ O | 1520 (H ₂) | – | 92 |
| Ag/AgBr/TiO ₂ | 300 W, Xe | HCOONa HCOONa–MeOH | 1430 (H ₂) 3930 (H ₂) | – | 93 |
| ZnO | 500 W, Xe | H ₂ S | 2900 (H ₂) | – | 94 |
| (0.8 wt%)Pt/CdS | 125 W, Hg (4260 nm) | Na ₂ SO ₃ | 9360 (H ₂) | – | 95 |
| CdS/TiO ₂ /conductive polymer fiber membrane | 500 W, Xe | MeOH (25 vol %)–H ₂ O | 1800 (H ₂) | – | 96 |
| NiS–PdS/CdS | 300 W, Xe (420 nm) | 30% lactic acid | 31000 (H ₂) | – | 97 |
| BiOI BiOCl BiOBr CuFe ₂ O ₄ | 35 W Xe lamp for PEC, 250 W Xe lamp for H ₂ generation | 25 vol% of methanol | 9200 (H ₂) 3860(H ₂) 8500 (H ₂) 2110 (H ₂) | 2.4 11 0.76 7.13 | Our result |
| BiOI/CuFe ₂ O ₄ BiOCl/CuFe ₂ O ₄ BiOBr/CuFe ₂ O ₄ | 35 W Xe lamp for PEC, 250 W Xe lamp for H ₂ generation | 25 vol% of methanol | 11230 (H ₂) 22200 (H ₂) 12500 (H ₂) | 36.67 13.63 64.47 | Our result |

7.4 Summary

In summary, we developed three types of heterostructures (direct Z-scheme, Type-I and Type-II) between n-type layered oxyhalides (BiOX) and p-type CuFe₂O₄ as photocatalyst for water splitting. The highest activity was achieved over the BiOCl/CFO photocatalyst, with an H₂ production rate of 22.2 mmolh⁻¹ compared to BiOI/CFO and BiOBr/CFO heterostructures, highlighting the intense promoting effect of direct Z-scheme charge transfer mechanism. The self-induced internal field gradient of BiOCl along with the intimate contact between BiOCl and CFO accelerates the charge separation efficiency as well as extends the visible light absorption at longer wavelengths. Additionally, the highly dispersed O-2p band of BiOX helps in narrowing the

bandgaps and enhances stability against water oxidation. The electrochemical measurements confirmed that the synergetic effects of high carrier concentration, low charge transfer resistance and sufficient redox potentials resulted highest photocatalytic activity of BiOCl/CFO towards H₂ generation. Hence, present study strongly suggests that fine and extensive regulation of band edge energies have key role to control the charge separation efficiency, which in turn influence the photocatalytic activity. These band edge engineered nanostructures are promising for efficient and stable H₂ generation through water reduction under visible light.

References:

- [1] S. Protti, M. Fagnoni, The sunny side of chemistry: green synthesis by solar light. *J. Photochem. Photobio. Sci.* **8** (2009) 1499–1516.
- [2] Q. Wang, T. Hisatomi, Q. Jia, H. Tokudome, M. Zhong, C. Wang, Z. Pan, T. Takata, M. Nakabayashi, N. Shibata, Y. Li, I. D. Sharp, A. Kudo, T. Yamada, K. Domen, Scalable water splitting on particulate photocatalyst sheets with a solar-to-hydrogen energy conversion efficiency exceeding 1%. *Nat. mater.* **15** (2016) 611–615.
- [3] D. Ravelli, S. Protti, M. Fagnoni, A. Albini, Visible Light Photocatalysis. A Green Choice?. *Curr. Org. Chem.* **17** (2013) 2366–2373.
- [4] S. Ghosh (ed), Heterostructured photocatalysts for solar energy conversion, Elsevier Inc., 2020, ISBN: 9780128200735.
- [5] L. Jing, W. Zhou, G. Tian, H. Fu, Surface tuning for oxide-based nanomaterials as efficient photocatalysts. *Chem. Soc. Rev.* **42** (2013) 9509–9549.
- [6] C. Prasad, X. Yang, Q. Liu, H. Tang, A. Rammohan, S. Zulfiqar, G. V. Zyryanov, S. Shah, Recent advances in MXenes supported semiconductors based photocatalysts: Properties, synthesis and photocatalytic applications. *J. Ind. Eng. Chem.* **85** (2020) 1–33.
- [7] D. Floresyona, F. Goubard, P.-H. Aubert, I. Lampre, J. Mathurin, A. Dazzi, S. Ghosh, P. Beaunier, F. Brisset, S. Remita, L. Ramos, H. Remita, Highly active poly(3-hexylthiophene) nanostructures for photocatalysis under solar light. *Appl. Catal. B* **209** (2017) 23–32.
- [8] R. Djara, M. A. Lacour, A. Merzouki, J. Cambedouzou, D. Cornu, S. Tingry, Y. Holade, Iridium and Ruthenium Modified Polyaniline Polymer Leads to Nanostructured Electrocatalysts with High Performance Regarding Water Splitting. *Polymers* **13** (2021) 190.
- [9] Q. Xiang, B. Cheng, J. Yu, Graphene-Based Photocatalysts for Solar-Fuel Generation. *Angew. Chem., Int. Ed.* **54** (2015) 11350–11366.
- [10] J. W. Colson, A. R. Woll, A. Mukherjee, M. P. Levendorf, E. L. Spitler, V. B. Shields, M. G. Spencer, J. Park, W. R. Dichtel, Oriented 2D covalent organic framework thin films on single-layer graphene. *Science* **332** (2011) 228–231.
- [11] J. Li, Y. Yu, L. Zhang, Bismuth oxyhalide nanomaterials: layered structures meet photocatalysis. *Nanoscale* **6** (2014) 8473–8488.

- [12] A. Shoja, A. H.-Yangjeh, M. Mousavi, S. Ghosh, T. Maiyalagan, Carbon dots and Bi₄O₅Br₂ adhered on TiO₂ nanoparticles: Impressively boosted photocatalytic efficiency for removal of pollutants under visible light. *Sep. Purif. Technol.* **250** (2020) 117179–117190.
- [13] M. Shi, G. Li, J. Li, X. Jin, X. Tao, B. Zeng, E. A. Pidko, R. Li, C. Li, Intrinsic Facet-dependent Reactivity of Well-defined BiOBr Nanosheets on Photocatalytic Water Splitting. *Angew. Chem. Int. Ed.* **59** (2020) 6590–6595.
- [14] H. Li, J. Li, Z. Ai, F. Jia, L. Zhang, Oxygen Vacancy-Mediated Photocatalysis of BiOCl: Reactivity, Selectivity, and Perspectives. *Angew. Chem. Int. Ed.* **57** (2018) 122–138.
- [15] X. Zhang, Y. Zhang, Z. Feng, J. Zhao, Z. Yang, X. Wang, W. Wang, Self-accelerating photocharge separation in BiOBr ultrathin nanosheets for boosting photoreversible color switching. *Chem. Eng. J.* **428** (2022) 131235.
- [16] Q. Zhou, W. Huang, C. Xu, X. Liu, K. Yang, D. Li, Y. Hou, D. D. Dionysiou, Novel hierarchical carbon quantum dots-decorated BiOCl nanosheet/carbonized eggshell membrane composites for improved removal of organic contaminants from water via synergistic adsorption and photocatalysis. *Chem. Eng. J.* **420** (2021) 129582.
- [17] J. Sun, X. Li, Q. Zhao, B. Liu, Ultrathin nanoflake-assembled hierarchical BiOBr microflower with highly exposed {001} facets for efficient photocatalytic degradation of gaseous ortho-dichlorobenzene. *Appl. Catal. B* **281** (2021) 119478–119489.
- [18] L. Zhang, W. Wang, S. Sun, D. Jiang, E. Gao, Selective transport of electron and hole among {0 0 1} and {1 1 0} facets of BiOCl for pure water splitting. *Appl. Catal. B* **162** (2015) 470–474.
- [19] J. Cao, J. Li, W. Chu, W. Cen, Facile synthesis of Mn-doped BiOCl for metronidazole photodegradation: Optimization, degradation pathway, and mechanism. *Chem. Eng. J.* **400** (2020) 125813.
- [20] A. P. Chowdhury, B. H. Shambharkar, Fabrication and characterization of BiOBr-SnWO₄ heterojunction nanocomposites with boosted photodegradation capability. *Chem. Eng. J. Adv.* **4** (2020) 100040.
- [21] H. Yu, J. Huang, L. Jiang, Y. Shi, K. Yi, W. Zhang, J. Zhang, H. Chen, X. Yuan, Enhanced photocatalytic tetracycline degradation using N-CQDs/OV-BiOBr composites: Unraveling the complementary effects between N-CQDs and oxygen vacancy. *Chem. Eng. J.* **402** (2020) 126187.

- [22] L. Ye, J. Liu, C. Gong, L. Tian, T. Peng, L. Zan, Insights into the interfacial carrier behaviour of copper ferrite (CuFe_2O_4) photoanodes for solar water oxidation. *ACS Catal.* **2** (2012) 1677–1683.
- [23] S. Zarezadeh, A. Habibi-Yangjeh, M. Mousavi, S. Ghosh, Synthesis of novel p-n-p BiOBr/ZnO/BiOI heterostructures and their efficient photocatalytic performances in removals of dye pollutants under visible light. *J. Photochem. Photobio. A* **389** (2020) 112247.
- [24] C. Song, Y. Feng, W. Shi, C. Liu, Fabrication and mechanism of a novel direct solid-state Z-scheme photocatalyst CdS/BiOI under visible light. *Cryst. Eng. Commun.* **18** (2016) 7796–7804.
- [25] M. Sun, J. Hu, C. Zhai, M. Zhu, J. Pan, CuI as Hole-Transport Channel for Enhancing Photoelectrocatalytic Activity by Constructing CuI/BiOI Heterojunction. *ACS Appl. Mater. Interfaces* **9** (2017) 13223–13230.
- [26] L. Hu, H. He, D. Xia, Y. Huang, J. Xu, H. Li, C. He, W. Yang, D. Shu, P. K. Wong, Highly Efficient Performance and Conversion Pathway of Photocatalytic CH_3SH Oxidation on Self-Stabilized Indirect Z-Scheme $\text{g-C}_3\text{N}_4/\text{I}^{3-}$ -BiOI. *ACS Appl. Mater. Interfaces* **10** (2018) 18693–18708.
- [27] T.-H. Chen, M. Yoshida, S. Tsunekawa, J.-H. Wu, K.-Y. A. Lind, C. Hu, Development of BiOI as an effective photocatalyst for oxygen evolution reaction under simulated solar irradiation. *Catal. Sci. Technol.* **10** (2020) 3223–3231.
- [28] K. M. Alam, P. Kumar, P. Kar, U. K. Thakur, S. Zeng, K. Cui, K. Shankar, Enhanced charge separation in $\text{g-C}_3\text{N}_4$ -BiOI heterostructures for visible light driven photoelectrochemical water splitting. *Nanoscale Adv.* **1** (2019) 1460–1471.
- [29] Q. Wang, T. Hisatomi, Y. Suzuki, Z. Pan, J. Seo, M. Katayama, T. Minegishi, H. Nishiyama, T. Takata, K. Seki, A. Kudo, T. Yamada, K. Domen, Particulate photocatalyst sheets based on carbon conductor layer for efficient Z-scheme pure-water splitting at ambient pressure. *J. Am. Chem. Soc.* **139** (2017) 1675–1683.
- [30] V A. N. V, P. K. Rastogi, T. S., V. S., S. Shaji, R. R. V., M. A. Garza-Navarro, S. Thomas, T. N. Narayanan, M. R. Anantharaman, Engineering nanostructured spinel ferrites by co-substitution for total water electrolysis by preferential exposure of metal cations on the surface. *Sustain. Energy Fuels* **4** (2020) 3915–3925.

- [31] Y. Matsumoto, Energy Positions of Oxide Semiconductors and Photocatalysis with Iron Complex Oxides. *J. Solid State Chem.* **126** (1996) 227–234.
- [32] Y. Liu, F. L. Formal, F. Boudoire, L. Yao, K. Sivula, N. Guijarro, Insights into the interfacial carrier behaviour of copper ferrite (CuFe_2O_4) photoanodes for solar water oxidation. *J. Mater. Chem. A* **7** (2019) 1669–1677.
- [33] Y. Matsumoto, M. Omae, K. Sugiyama, E. -I. Sato, New photocathode materials for hydrogen evolution: calcium iron oxide (CaFe_2O_4) and strontium iron oxide ($\text{Sr}_7\text{Fe}_{10}\text{O}_{22}$). *J. Phys. Chem.* **91** (1987) 577–581.
- [34] S. Park, J. H. Baek, L. Zhang, J. M. Lee, K. H. Stone, I. S. Cho, J. Guo, H. S. Jung, X. Zheng, Rapid Flame-Annealed CuFe_2O_4 as Efficient Photocathode for Photoelectrochemical Hydrogen Production. *ACS Sus. Chem. Eng.* **7** (2019) 5867–5874.
- [35] S. Hussain, S. Hussain, A. Waleed, M. M. Tavakoli, Z. Wang, S. Yang, Z. Fan, M. A. Nadeem, Fabrication of $\text{CuFe}_2\text{O}_4/\alpha\text{-Fe}_2\text{O}_3$ Composite Thin Films on FTO Coated Glass and 3-D Nanospire Structures for Efficient Photoelectrochemical Water Splitting. *ACS Appl. Mater. Interfaces* **8** (2016) 35315–35322.
- [36] R. Cheng, X. Fan, M. Wang, M. Li, J. Tian, L. Zhang, Facile construction of $\text{CuFe}_2\text{O}_4/\text{g-C}_3\text{N}_4$ photocatalyst for enhanced visible-light hydrogen evolution. *RSC Adv.* **6** (2016) 18990–18995.
- [37] S. Das, S. Patnaik, K. Parida, Dynamic charge transfer through Fermi level equilibration in the p- CuFe_2O_4 /n-NiAl LDH interface towards photocatalytic application. *Catal. Sci. Technol.* **10** (2020) 6285–6298.
- [38] G. Li, F. Qin, R. Wang, S. Xiao, H. Sun, R. Chen, BiOX (X = Cl, Br, I) nanostructures: Mannitol-mediated microwave synthesis, visible light photocatalytic performance, and Cr(VI) removal capacity. *J. Colloid. Interface Sci.* **409** (2013) 43–51.
- [39] W. Tang, Y. Zhang, H. Guo, Y. Liu, Heterogeneous activation of peroxydisulfate for bisphenol AF degradation with $\text{BiOI}_{0.5}\text{Cl}_{0.5}$. *RSC Adv.* **9** (2019) 14060–14071.
- [40] J. Lv, Q. Hu, C. Cao, Y. Zhao, Modulation of valence band maximum edge and photocatalytic activity of BiOX by incorporation of halides. *Chemosphere* **191** (2018) 427–437.
- [41] S. -M. Chen, R. Umamaheswari, G. Mani, T. -W. Chen, M. A. Ali, A. H. F. M. A., M. S. Elshikh, M. A. Farah, Hierarchically structured CuFe_2O_4 ND@RGO composite for the

- detection of oxidative stress biomarker in biological fluids. *Ing. Chem. Front.* **5** (2018) 944–950.
- [42] D. S. Bhachu, S. J. A. Moniz, S. Sathasivam, D. O. Scanlon, A. Walsh, S. M. Bawaked, M. Mokhtar, A. Y. Obaid, I. P. Parkin, J. Tang, C. J. Carmalt, Bismuth oxyhalides: synthesis, structure and photoelectrochemical activity. *Chem. Sci.* **7** (2016) 4832–4841.
- [43] P. Morandi, V. Flaud, S. Tingry, D. Cornu, Y. Holade, Tartaric acid regulated the advanced synthesis of bismuth-based materials with tunable performance towards the electrocatalytic production of hydrogen peroxide. *J. Mater. Chem. A* **8** (2020) 18840–18855.
- [44] A. Zalineeva, A. Serov, M. Padilla, U. Martinez, K. Artyushkova, S. Baranton, C. Coutanceau, P. B. Atanassov, Self-Supported Pd_xBi Catalysts for the Electrooxidation of Glycerol in Alkaline Media. *J. Am. Chem. Soc.* **136** (2014) 3937–3945.
- [45] I. G. Casella, M. Contursi, Characterization of bismuth adatom-modified palladium electrodes: The electrocatalytic oxidation of aliphatic aldehydes in alkaline solutions. *Electrochim. Acta* **52** (2006) 649–657.
- [46] S. Bera, S. Ghosh, R. N. Basu, Fabrication of Bi₂S₃/ZnO heterostructures: an excellent photocatalyst for visible-light-driven hydrogen generation and photoelectrochemical properties. *New J. Chem.* **42** (2018) 541–554.
- [47] M. Guo, Z. Zhou, S. Yan, P. Zhou, F. Miao, S. Liang, J. Wang, X. Cui, Bi₂WO₆-BiOCl heterostructure with enhanced photocatalytic activity for efficient degradation of oxytetracycline. *Sci. Rep.* **10** (2020) 18401–18415.
- [48] J. Hu, W. Fan, W. Ye, C. Huang, X. Qiu, Insights into the photosensitivity activity of BiOCl undervisible light irradiation. *Appl. Catal. B* **158–159** (2014) 182–189.
- [49] J. Di, J. Xia, S. Yin, H. Xu, L. Xu, Y. Xu, M. He, H. Li, One-pot solvothermal synthesis of Cu-modified BiOCl via a Cu-containing ionic liquid and its visible-light photocatalytic properties. *RSC Adv.* **4** (2014) 14281–14290.
- [50] S. Ghosh, S. R. Keshri, S. Bera, R. N. Basu, Enhanced solar hydrogen generation using Cu-Cu₂O integrated polypyrrole nanofibers as heterostructured catalysts. *International Journal of Hydrogen Energy. Int. J. Hydrogen Energy* **45** (2020) 6159–6173.
- [51] B. K. Chatterjee, K. Bhattacharjee, A. Dey, C. K. Ghosh, K. K. Chattopadhyay, Influence of spherical assembly of copper ferrite nanoparticles on magnetic properties: orientation of magnetic easy axis. *Dalton Trans.* **43** (2014) 7930–7944.

- [52] L. Li, M. Zhang, Z. Zhao, B. Sun, X. Zhang, Visible/near-IR-light-driven TNFePc/BiOCl organic–inorganic heterostructures with enhanced photocatalytic activity. *Dalton Trans.* **45** (2016) 9497–9505.
- [53] R. D. Waldron, Infrared spectra of ferrites. *Phys. Rev.* **99** (1955) 1727.
- [54] T. B. Li, G. Chen, C. Zhou, Z. Y. Shen, R. C. Jin, J. X. Sun, New photocatalyst BiOCl/BiOI composites with highly enhanced visible light photocatalytic performances, *Dalton Trans.* **40** (2011) 6751–6758.
- [55] X. Chang, S. Wang, Q. Qi, M. A. Gondal, S. G. Rashid, S. Gao, D. Yang, K. Shen, Q. Xu, P. Wang, Insights into the growth of bismuth nanoparticles on 2D structured BiOCl photocatalysts: an in situ TEM investigation. *Dalton Trans.* **44** (2015) 15888–15896.
- [56] S. Kumar, N. Yadav, P. Kumar, A. K. Ganguli, Design and Comparative Studies of Z-Scheme and Type II Based Heterostructures of NaNbO₃/CuInS₂/In₂S₃ for Efficient Photoelectrochemical Applications. *Inorg. Chem.* **57** (2018) 15112–15122.
- [57] S. Bera, S. Ghosh, S. Shyamal, C. Bhattacharya, R. N. Basu, Photocatalytic hydrogen generation using gold decorated BiFeO₃ heterostructures as an efficient catalyst under visible light irradiation. *Sol. Energy Mater. Sol. Cell.* **194** (2019) 195–206.
- [58] M. Wang, S. Shen, L. Li, Z. Tang, J. Yang, Effects of sacrificial reagents on photocatalytic hydrogen evolution over different photocatalysts, *J. Mater. Sci.* **52** (2017) 5155–5164.
- [59] S. Protti, A. Albini, N. Serpone, Photocatalytic generation of solar fuels from the reduction of H₂O and CO₂: a look at the patent literature. *Phys. Chem. Chem. Phys.* **16** (2014) 19790–19827.
- [60] S. Zhang, J. Li, X. Wang, Y. Huang, M. Zeng, J. Xu, Rationally designed 1D Ag@AgVO₃ nanowire/graphene/protonated g-C₃N₄ nanosheet heterojunctions for enhanced photocatalysis via electrostatic self-assembly and photochemical reduction methods. *J. Mater. Chem.* **3** (2015) 10119–10126.
- [61] C. G. Morales-Guio, S. D. Tilley, H. Vrubel, M. Graetzel, X. Hu, Hydrogen evolution from a copper(I) oxide photocathode coated with an amorphous molybdenum sulphide catalyst. *Nat. Commun.* **5** (2014) 3059–3066.
- [62] M. Wang, S. Shen, L. Li, Z. Tang, J. Yang, Effects of sacrificial reagents on photocatalytic hydrogen evolution over different photocatalysts. *J. Mater. Sci.* **52** (2017) 5155–5164.

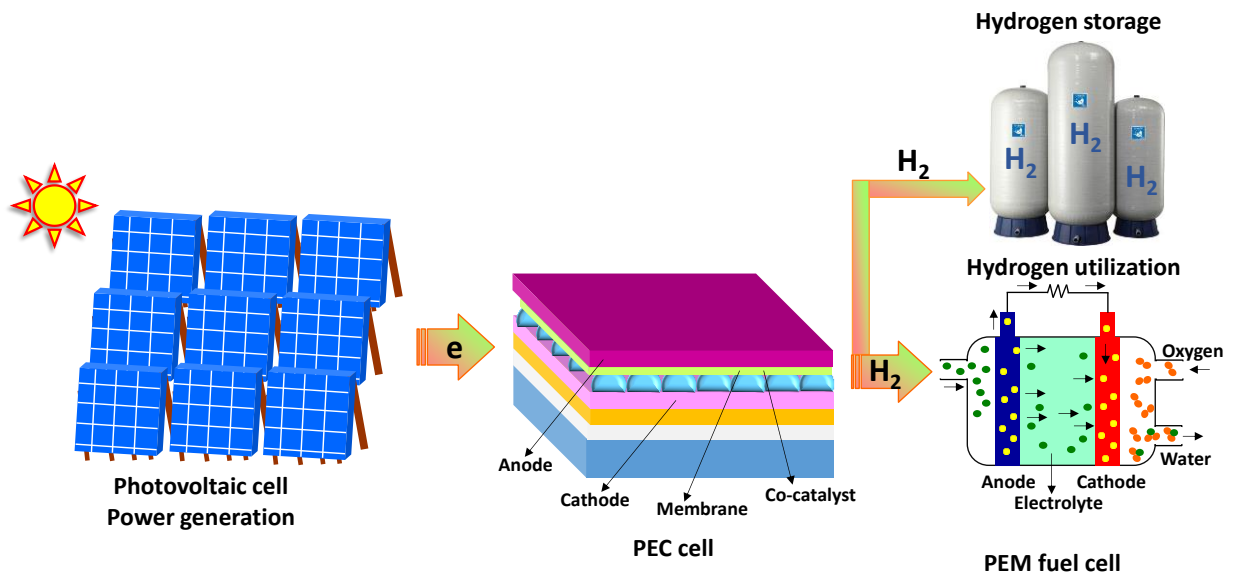
- [63] G. Liu, N. Li, Y. Zhao, R. Yao, M. Wang, D. He, J. Li, Fabrication of Fe-doped Co₂P nanoparticles as efficient electrocatalyst for electrochemical and photoelectrochemical water oxidation. *Electrochim. Acta* **283** (2018) 1490–1497.
- [64] D. Kong, H. Wang, Z. Lu, Yi Cui, CoSe₂ Nanoparticles Grown on Carbon Fiber Paper: An Efficient and Stable Electrocatalyst for Hydrogen Evolution Reaction. *J. Am. Chem. Soc.* **136** (2014) 4897–4900.
- [65] L.-C. Chen, J.-C. Chen, C.-C. Chen, C.-G. Wu, Fabrication and Properties of High-Efficiency Perovskite/PCBM Organic Solar Cells. *Nanoscale Res. Letters* **10** (2015) 312–317.
- [66] J. Zhao, P. Zhang, Z. Wang, S. Zhang, H. Gao, J. Hu, G. Shao, Direct evidence of multichannel improved charge-carrier mechanism for enhanced photocatalytic H₂ evolution. *Sci. Rep.* **7** (2017) 16116–16127.
- [67] A. Zhu, Q. Zhao, X. Li, Y. Shi, BiFeO₃/TiO₂ Nanotube Arrays Composite Electrode: Construction, Characterization, and Enhanced Photoelectrochemical Properties. *ACS Appl. Mater. Interfaces* **6** (2014) 671–679.
- [68] K. Gelderman, L. Lee, S. W. Donne, Flat-Band Potential of a Semiconductor: Using the Mott–Schottky Equation. *J. Chem. Educ.* **84** (2007) 685–689.
- [69] N. Zhang, D. Chen, F. Niu, S. Wang, L. Qin, Y. Huang, Enhanced visible light photocatalytic activity of Gd-doped BiFeO₃ nanoparticles and mechanism insight. *Sci. Rep.* **6** (2016) 26467–26478.
- [70] L. Palmisano, V. Augugliaro, A. Sclafani, M. Schiavello, Activity of chromium-ion-doped titania for the dinitrogen photoreduction to ammonia and for the phenol photodegradation. *J. Phys. Chem.* **92** (1988) 6710–6713.
- [71] S. Shyamal, P. Hajra, H. Mandal, A. Bera, D. Sariket, A. K. Satpati, S. Kundu, C. Bhattacharya, Benign role of Bi on an electrodeposited Cu₂O semiconductor towards photo-assisted H₂ generation from water. *J. Mater. Chem. A* **4** (2016) 9244–9252.
- [72] G. Zhang, L. Zhang, Y. Liu, L. Liu, C.-P. Huang, H. Liu, J. Li, Substitution Boosts Charge Separation for High Solar-Driven Photocatalytic Performance. *ACS Appl. Mater. Interfaces* **8** (2016) 26783–26793.

- [73] Z. Wang, C. Tang, R. Sachs, Y. Barlas, J. Shi, Proximity-Induced Ferromagnetism in Graphene Revealed by the Anomalous Hall Effect. *Phys. Rev. Lett.* **114** (2015) 016603–016606.
- [74] J. Li, Q. Pei, R. Wang, Y. Zhou, Z. Zhang, Q. Cao, D. Wang, W. Mi, Y. Du, Enhanced Photocatalytic Performance through Magnetic Field Boosting Carrier Transport. *ACS Nano* **12** (2018) 3351–3359.
- [75] C. Gu, B. C. Norris, F.-R. F. Fan, C. W. Bielawski, A. J. Bard, Is Base-Inhibited Vapor Phase Polymerized PEDOT an Electrocatalyst for the Hydrogen Evolution Reaction? Exploring Substrate Effects, Including Pt Contaminated Au. *ACS Catal.* **2** (2012) 746–750.
- [76] J. L. Fernández, V. Raghuvver, A. Manthiram, A. J. Bard, Pd-Ti and Pd-Co-Au Electrocatalysts as a Replacement for Platinum for Oxygen Reduction in Proton Exchange Membrane Fuel Cells. *J. Am. Chem. Soc.* **127** (2005) 13100–13101.
- [77] V. Subramanian, E. E. Wolf, P. V. Kamat, Catalysis with TiO₂/Gold Nanocomposites. Effect of Metal Particle Size on the Fermi Level Equilibration. *J. Am. Chem. Soc.* **126** (2004) 4943–4950.
- [78] X. Zhang, Y. L. Chen, R.-S. Liu, D. P. Tsai, Plasmonic photocatalysis. *Rep. Prog. Phys.* **76** (2013) 046401–046442.
- [79] D. Mateo, I. E.-Adell, J. Albero, J. F. S. Royo, A. Primo, H. Garcia, 111 oriented gold nanoplatelets on multilayer graphene as visible light photocatalyst for overall water splitting. *Nat. Commun.* **7** (2016) 11819–11827.
- [80] S. Gu, X. Zhou, F. Zheng, L. Fang, W. Dong, M. Shen, Improved photocathodic performance in Pt catalyzed ferroelectric BiFeO₃ films sandwiched by a porous carbon layer. *Chem. Commun.* **53** (2017) 7052–7055.
- [81] N. T. Hahn, S. Hoang, J. L. Self, C. B. Mullins, N.T. Hahn, S. Hoang, J. L. Self, C. B. Mullins, Spray pyrolysis deposition and photoelectrochemical properties of n-type BiOI nanoplatelet thin films. *ACS nano* **60** (2012) 7712–7722.
- [82] Y. You, S. Wang, K. Xiao, T. Ma, Y. Zhang, H. Huang, Z-Scheme g-C₃N₄/Bi₄NbO₈Cl Heterojunction for Enhanced Photocatalytic Hydrogen Production. *ACS Sustainable Chem. Eng.* **6** (2018) 16219–16227.
- [83] S. Sultana, S. Mansingh, K. M. Parida, Facile Synthesis of CeO₂ Nanosheets Decorated upon BiOI Microplate: A Surface Oxygen Vacancy Promoted Z-Scheme-Based 2D-2D

- Nanocomposite Photocatalyst with Enhanced Photocatalytic Activity. *J. Phys. Chem. C* **122** (2018) 808–819.
- [84] M. Du, S. Zhang, Z. Xing, Z. Li, J. Yin, J. Zou, Q. Zhu, W. Zhou, All-Solid Z-Scheme Bi-BiOCl/AgCl Heterojunction Microspheres for Improved Electron-Hole Separation and Enhanced Visible Light-Driven Photocatalytic Performance. *Langmuir* **35** (2019) 7887–7895.
- [85] H. Nakanishi, T. Nakayama, Toshiba corporation, Jpn Pat. (1985) 60044053A.
- [86] H. Yamakita, T. H. Masato, T. Kiyoshi, Jpn. Pat. (1988) 63035402A.
- [87] T. Ravindranathan, The Hydrogen Solar Production Company Limited, World Pat. (2002) 2002022497A1.
- [88] D. Liao, Y. Ou, J. Lin, S. Fang, Chin. Pat. (2008) 100396373C.
- [89] G. Chen, Z. Shang, Z. Li, Chin. Pat. (2010) 101229514B.
- [90] Z. Feng, J. Zhang, Q. Xu, C. Li, X. L. Wang, Y. Ma, Chin. Pat. (2010) 101884914A.
- [91] X. Cui, X. Zhang, Chin. Pat. (2009) 101513610A.
- [92] L. Jing, M. Xie, H. Fu, X. Fu, Chin. Pat. (2013) 103157498A.
- [93] W. Huang, Y. Liu, W. Wang, Chin. Pat. (2013) 103263920A.
- [94] B. Tian, F. Yang, Y. Li, J. Zhang, T. Wang, T. Xiong, X. Chen, R. Dong, T. Li, Chin. Pat. (2013) 102874751A.
- [95] D.-C. Park, J.-O. Baeg, US Pat. (2001) 6300274B1.
- [96] N. Buehler, J. F. Reber, K. Meier, M. Rusek, Eur. Pat. (1982) 58136A1.
- [97] H. Cheng, X. Wang, L. Wang, G. Liu, F. Li, G. Lu, Chin. Pat. (2014)102641741B.
- [98] P. Lin, Q. Li, Y. Yang, J. Su, W. Shangguan, Y. Sun, Chin. Pat. (2013)102861597A.

CHAPTER 8

Conclusions & Future Scope



8.1 Conclusions

In this thesis, visible light driven photocatalysis is revisited from an experimental and engineering point of view, using semiconductor based nanostructures. As low cost, non-toxic and chemically stable material, bismuth (Bi)-based semiconductors are focussed as photocatalyst for water splitting with tunable morphology, bandgap and band edge potentials. Therefore, fabrication of a series of Bi-based semiconductors by green and cost-effective method is the important attempt of this thesis work. On the other hand, Bi-based semiconductors suffer some limitations, for example, rapid recombination of photogenerated charge carriers, wide bandgap for some materials, low redox potential to drive the water oxidation and reduction reactions. Therefore, heterostructures have been developed with other semiconductors to overcome the aforesaid issues and boost the photocatalytic efficiency. Moreover, the free charge carrier concentration and number of active sites have been improved by heterostructure formation. In this study, various types Bi-based semiconductor heterostructures (Type-II, p-n heterojunction, Schottky junction, direct and indirect Z-scheme heterojunctions) have been fabricated by in-situ methods and presented as a promising photocatalysts for organic pollutant degradation, renewable fuel H₂ generation through water reduction and photoelectrochemical (PEC) water splitting under visible light. As Bi-based semiconductor, Bi₂S₃, BiFeO₃ and BiOX (X = Cl, Br, I) are synthesized by facile hydrothermal method and further coupled with other semiconductors or metals to develop heterostructures.

A novel Type-II heterostructures has been developed between low bandgap bismuth sulphide (Bi₂S₃) and wide bandgap zinc oxide (ZnO) to reduce the fast electron-hole recombination rate of Bi₂S₃ and enhance the absorption of ZnO in visible region. Flower like Bi₂S₃ has been synthesized by facile hydrothermal method and further ZnO nanoparticles deposited on the surface of Bi₂S₃ flowers *via* in-situ precipitation method. Successful formation of heterostructures enhances the light absorption in visible region and improves the charge separation ability. Moreover, the growth of Bi₂S₃ during hydrothermal reaction time has been studied in details and based on which a growth mechanism proposed. The effect of sulphur precursors (L-cysteine and mercaptosuccinic acid) in morphology has been studied, where more fine structure of Bi₂S₃ (assembly of rods forms flower like structure) obtained by using mercaptosuccinic acid. The photocatalytic activity of bare Bi₂S₃ and the heterostructures has been tested for organic pollutant methyl orange (MO) degradation, where M-Bi₂S₃/ZnO demonstrate highest catalytic activity. Further, as synthesized materials have been used as heterogeneous catalyst for photocatalytic H₂ generation through water reduction, in

which L-Bi₂S₃/ZnO showed ~ 8.6 time higher H₂ generation compared to bare Bi₂S₃ under visible light illumination. Moreover, PEC activity has been studied, where Bi₂S₃/ZnO demonstrated high photocurrent density of 0.25 mA cm⁻², which is 56% and 97 % higher than bare M-Bi₂S₃ and ZnO respectively. From the band edge potential calculation, a Type-II charge transfer pathway between Bi₂S₃ and ZnO has been proposed and on the basis of the experimental findings the higher activity of Bi₂S₃/ZnO heterostructures described.

Furthermore, a new strategy has been developed through two steps comprising of hydrothermal method followed by radiolysis for an efficient Schottky junction between noble metal gold nanoparticles (Au NPs) and bismuth ferrite (BiFeO₃) has been developed. The hydrothermal method has been followed to synthesis hexagonal BiFeO₃ and then average ~ 17 nm Au nanoparticles are developed by radiolysis on the surface of the BiFeO₃ without using any template or strong reducing agent. In addition, cylindrical and octahedral morphology of BiFeO₃ is synthesized by changing the solution pH during the hydrothermal reaction. The catalytic activity of as developed metal-semiconductor Schottky junction was investigated by photocatalytic H₂ generation and PEC water splitting under visible light. The presence of Au NPs on the surface of BiFeO₃ effectively enhances the light absorption in visible region due to the surface plasmonic resonance effect and the strong interaction between Au and BiFeO₃. Consequently, two-fold enhanced H₂ generation have been achieved for Au/BiFeO₃ Schottky junction than that of bare BiFeO₃. The effect of pH, various sacrificial agent, catalyst loading have been tested in details to optimize the reaction parameters of photocatalytic H₂ generation. The hot electron generation by the virtue of plasmonic absorption of Au significantly improves the PEC current density due to the large number of free charge carriers, which are gathered at electrode-electrolyte interface. The effective transfer of excited electrons from Au to conduction band of BiFeO₃ results lower charge transfer resistance for Au/BiFeO₃ Schottky junction. Moreover, the intimate contact hinders the photobleaching effect and improves the long-term stability under visible light irradiation. The absorb photon to current conversion efficiency for the bare BiFeO₃ and Au/BiFeO₃ are 1.1% and 3.3%, respectively at 320 nm wavelength. Furthermore, the shifting of onset potential towards negative w.r.t. water reduction observed for Au/BiFeO₃ at Mott-Schottky measurement, implies the low overpotential of Schottky junction towards H₂ generation. The electrochemical impedance measurement confirms effective charge transfer at the interfaces of heterojunction which lead to

enhance photocurrent generation and H₂ evolution than bare BFO nanosheets. The charge transfer mechanism of Schottky junction has been described.

The performance of TiO₂ has been further enhanced through the formation of p-n heterojunction between Bi-doped TiO₂/MoS₂ for visible light active water splitting. The Bi doping into TiO₂ crystal has been carried out to reduce the bandgap and enhance the solar light absorption range. Further, to hinder the fast electron-hole recombination and efficient charge separation, a p-n heterojunction has been fabricated between Bi-doped TiO₂ and MoS₂. The excited electrons of Bi-doped TiO₂ transferred to MoS₂ and holes of MoS₂ transfer to the Bi-doped TiO₂ through the junction between them by the influence of internal electric field. As a result, four times higher H₂ generation rate obtained for Bi-doped TiO₂/MoS₂ p-n heterojunction compared to bare MoS₂. Moreover, the as developed p-n heterojunction showed superior catalytic activity in PEC measurements due to the synergistic effects of low charge transfer resistance and improved light absorption. In addition, an indirect Z-scheme heterostructures has been developed between MoS₂ nanosheet and Ag NPs decorated AgVO₃ nanorods by facile co-precipitation method. The introduction of metallic Ag NPs between AgVO₃ and MoS₂ enhance the light absorption capacity in visible region by virtue of surface plasmonic resonance effect. It develops the Z-scheme bridge mechanism between AgVO₃ and MoS₂ to drive the efficient separation of photoinduced charge carriers. In addition, the well-matched band positions of AgVO₃ and MoS₂ composite confirms the Z-scheme charge transfer mechanism with a higher reducing capability, leading to the enhancement of photocatalytic H₂ generation under visible light. The charge transfer mechanisms at p-n heterojunction and indirect Z-scheme have been investigated along with their effects in photocatalytic H₂ generation.

Bandgap engineering is an effective approach to tune the catalytic activity of semiconductor-based nanostructures has also been studied in this thesis. We have enhanced the photocatalytic performance of bismuth oxyhalides (BiOX, X=Cl, Br, I) through the coupling of low bandgap spinel structure copper ferrite (CuFe₂O₄) via *in-situ* co-precipitation method. Three types of heterostructures (Type-I, Type-II and direct Z-scheme) have been formed between BiOX and CuFe₂O₄ depending on the position of their valence band, conduction band location and Fermi level. The highest efficiency towards H₂ generation was achieved for BiOCl/CuFe₂O₄ direct Z-scheme heterostructures (~22.2 mmol h⁻¹), which is two times higher than BiOI/CFO and BiOBr/CFO heterostructures, highlighting the intense promoting effect of direct Z-scheme charge

transfer mechanism. The self-induced internal field gradient of BiOCl along with the intimate contact between BiOCl and CuFe₂O₄ boosts the electron-hole separation efficiency and extends the absorption at visible region. The electrochemical measurements confirmed that the synergetic effects of high carrier concentration, low charge transfer resistance and sufficient redox potentials resulted highest photocatalytic activity of BiOCl/CFO towards H₂ generation. Hence, present study strongly suggests that fine and extensive regulation of band edge energies have key role to control the charge separation efficiency, which in turn influence the photocatalytic activity.

Therefore, in this thesis attempts have been taken to solve the problem of fast charge carrier recombination and limited light absorption using Bi-based heterostructures as photocatalyst. In the first attempt, a novel Type-II heterostructure has been developed between Bi₂S₃ and ZnO to overcome the fast recombination of Bi₂S₃ and reduce the bandgap of ZnO. The coupling of low bandgap Bi₂S₃ and wide bandgap of ZnO effectively improve the light absorption range towards visible region. Additionally, the heterostructures formation enhances the number of active surface sites for redox reactions. In another approach, a novel Schottky junction has been developed between Au and BiFeO₃ which produced hot electrons by the surface plasmonic resonance effect under visible light. Moreover, the band bending due to development of schottky junction boosts the hot electron transfer from metal to semiconductor for water reduction to generate H₂. In another attempt, the bandgap of benchmark photocatalyst TiO₂ has been successfully reduced (2.5 eV from 3.2 eV) by Bi-doping. Interestingly, after doping, the conductivity of TiO₂ changes from n-type to p-type due to the formation of acceptor level near the VB of TiO₂. Further, to lower the fast electron-hole recombination problem, a novel p-n heterojunction has been developed between p-type Bi-doped TiO₂ and n-type MoS₂ nanosheets. The p-n heterojunction formation effectively improves the charge separation by the influence of internal electric field (generated at the interface between two semiconductors), which resulted increased catalytic activity towards H₂ generation. However, the electron transfer from one semiconductor/metal to adjacent semiconductor in case of as developed Type-II, p-n heterojunction and Schottky junction reduces the redox capability for H₂ generation. Thus, an efficient direct Z-scheme heterostructures between BiOCl and CuFe₂O₄ have been finally developed through bandgap engineering which resulted highest H₂ generation rate than that of Type-II, p-n heterojunction and Schottky junction because of low recombination rate and high redox potential than water reduction. Notably, all the attempts of heterostructures formation improve the photo-stability of Bi-based semiconductors. The as developed

heterostructures not only suitable for H₂ generation, but also capable for CO₂ reduction, N₂ fixation and green NH₃ production from under visible light.

8.2 Future Scope

The low cost, facile synthesis, chemical stability, layered structure and excellent visible-light response endow Bi-based semiconductors as promising photocatalysts for energy and environmental applications. Therefore, the detailed structural, optical, electrochemical properties as well as photocatalytic performance of Bi-based semiconductor nanostructures and the heterostructures would be beneficial for the future development of photocatalysts. This can also lead to large volume production as several up-scalable approaches have been introduced in this study. In addition, there are many areas of opportunity and possible valuable approaches for future work which are summarized below:

- The band structures of the as prepared heterostructures are proposed on the basis of Mott-Schottky experiment and bandgap values. Most of the Bi-based semiconductors are n-type, thus location of the conduction band can be estimated from the flat band potential. Therefore, the valence band XPS is a good technique to explore the experimentally determine the position of the valence band.
- The theoretical calculation of valence and conduction band, Fermi level, bandgap, density of state by density functional theory might be effective for the investigation of electronic structure of as prepared semiconductor nanostructures and the heterostructures can also be explored.
- The industrial waste which consists of toxic chemicals, is one of the major challenge for the environment. The photodegradation of toxic chemicals may possible by using these Bi-based heterostructures and decrease the impact of industries on the environment. The developed Bi-based heterostructures may degrade the organic pollutant under gaseous conditions instead of aqueous solutions due to the efficient utilization of visible light in gas phase. Therefore, these photocatalyst could be used as indoor air purifier by the removal of formaldehyde and benzene.
- The heterostructures formation shifted the reduction potential of Bi-based semiconductors to the more negative w.r.t. reversible hydrogen scale, thus, can be used as catalysts for CO₂

reduction to CO or CH₄ under visible light illumination. This could also be extended under visible light and explored in detail.

- Recently, the scaling up of PEC water splitting has shown high demand to generate green H₂ for the implementation of H₂ economy. In this regard, the conversion of H₂, generated from PEC water splitting, into electricity through fuel cell stacks, is becoming an attractive pathway for clean energy storage. The developed Bi-based heterostructures could be used as electrodes or integrated with the commercial metal foam electrodes to drive the H₂ generation efficiently.
- The integration of PEC-PV tandem cell is also a potential option for the green H₂ generation, where the PV cell generates electricity under light illumination which provides further potential during water splitting to generate H₂. The Bi-based heterostructures may be a suitable component for PEC or PV system due to the enhanced light absorption in visible region. This exciting area needs further in-depth study.
- The reactor design for large scale H₂ generation is a challenge for future H₂ economy. As H₂ and O₂ both are generated during water splitting, thus collection of these gaseous products in large scale is another challenge. Moreover, H₂ generation without using any co-catalyst or sacrificial agent is also an issue for green H₂ economy and needs to be looked into.

List of Publications

Journal Paper:

1. S. Bera, S. Ghosh, R. N. Basu, "Fabrication of Bi₂S₃/ZnO heterostructures: An excellent photocatalyst for visible-light- driven hydrogen generation and photoelectrochemical properties" *New J. Chem.* **42** (2018) 541–554.
2. S. Bera, S. Ghosh, S. Shyamal, C. Bhattacharya, R. N. Basu, "Gold Decorated BiFeO₃ Heterostructure as Efficient Photocatalyst for Hydrogen Generation" *Sol. Energy Mater. Sol. Cells* **194** (2019) 195–206.
3. S. Bera, S. Ghosh, R. N. Basu, "Silver as Solid-State Electron Mediator in MoS₂/Ag-AgVO₃ Z-Scheme Heterostructures for Photocatalytic H₂ Generation" *J. Alloy Compd.* **830** (2020) 154527–154539.
4. S. Bera, A. Kumari, S. Ghosh, R. N. Basu, "Assemble of Bi-doped TiO₂ onto 2D MoS₂: an efficient p–n heterojunction for photocatalytic H₂ generation under visible light" *Nanotechnology* **32** (2021) 195402–195414.
5. S. Bera, S. Ghosh, T. Maiyalagan, R. N. Basu, "Band Edge Engineering of BiOX/CuFe₂O₄ Heterostructures for Efficient Water Splitting" *ACS Appl. Energy Mater.* **5** (2022) 3821–3833.
6. S. Ghosh, S. Bera, S. Bysakh, R. N. Basu, "Highly active multimetallic palladium nanoalloys embedded in conducting polymer as anode catalyst for electrooxidation of ethanol" *ACS Appl. Mater. Interfaces* **9** (2017) 33775–33790.
7. S. Ghosh, S. Bera, S. Bysakh, R. N. Basu, "Conducting polymer nanofiber-supported Pt alloys: unprecedented materials for methanol oxidation with enhanced electrocatalytic performance and stability" *Sustainable Energy Fuels* **1** (2017) 1148–1161.
8. S. Ghosh, S. Bera, N. Karmakar, R. N. Basu, "Enhanced electrocatalytic activity of branched Pd nanostructures decorated conducting polymer nanofibers for alkaline fuel cells" *Materials Today Proceedings* **5** (2018) 9733–9742.
9. S. Ghosh, D. Rashmi, S. Bera, R. N. Basu, "Functionalized conjugated polymer with plasmonic Au nanoalloy for photocatalytic hydrogen generation under visible-NIR" *Int. J. Hydrogen Energy* **44** (2019) 13262–13272.
10. S. Ghosh, S. R. Keshri, S. Bera, R. N. Basu, "Enhanced solar hydrogen generation using Cu-Cu₂O integrated polypyrrole nanofibers as heterostructured catalysts" *Int. J. Hydrogen Energy* **45** (2020) 6159 – 6173.
11. S. Bhattacharjee, S. Bera, R. Das, D. Chakraborty, A. Basu, P. Banerjee, S. Ghosh, A. Bhaumik, "A Ni(II) Metal–Organic Framework with Mixed Carboxylate and Bipyridine Ligands for Ultrafast and Selective Sensing of Explosives and Photoelectrochemical Hydrogen Evolution" *ACS Appl. Mater. Interfaces* (2022) DOI: 10.1021/acsami.2c01647.

Book Chapters:

1. S. Bera, S. Ghosh, R. N. Basu, Chapter 8, “Bismuth-based heterostructured photocatalysts” in “Heterostructured photocatalysts for solar energy conversion” Elsevier Inc., 2020, ISBN: 9780128200735.
2. S. Bera, S. Ghosh, Chapter 23, “Bandgap Engineering of Heterostructures for Visible Light-Driven Water Splitting” in “Green Photocatalytic Semiconductors”, Springer, Cham, 2022, ISBN: 978-3-030-77371-7.
3. S. Ghosh, S. Bera, Chapter 8, “Advances in 2D nanomaterials and their heterostructures for photocatalytic energy conversion” in “2D Materials for Energy Storage and Conversion” IOP Publisher, 2021, ISBN: 978-0-7503-3319-1.

Conferences Attended

2022

- Oral presentation on “Fabrication of a hierarchical Mo-Bi₂WO₆/Fe₂O₃ heterojunction via simultaneously metal doping and coupling with metal oxides for photoelectrochemical water splitting” by S. Bera, V. R. Dhanak, S. Ghosh, at on day workshop on ADVANCED ENERGY MATERIALS & DEVICES (AEMD), held on 3rd March 2022. (*Selected for Oral Presentation Award*)

2021

- Oral presentation on “Enhanced Photocatalytic Activity of Metal Doped Bi₂WO₆ for Water Splitting under Visible Light’ by S. Bera, S. Samajdar, P. S. Das, S. Ghosh, at 85th Annual Session of Indian Ceramic Society on “Advances in Ceramics & Cement Technologies: Materials & Manufacturing” held on 13-14th December, 2021 virtually. (*Best Oral Presentation Award*)
- Oral presentation on “Engineering of BiOX/CuFe₂O₄ heterostructures for sustainable fuel H₂ generation through water splitting’ by S. Bera, S. Ghosh, at 5th National Symposium on “Shaping the Energy Future : Challenges and Opportunities” (SEFCO-2021) held on 27th August, 2021 virtually.
- Attended 6 day Short Term Training Programme (STTP) on “Chemistry of Advanced Materials & Their Applications” at MAKAUT, WB, held on 6th December – 11th December, 2021, virtually.
- Attended Webinar Internship Course on “Emerging Trends in Nanomaterials for Different Device Architectures” (ETNDDA-2021), held on 15th September to 28th November, 2021 Organized by Indian Chemical Society, Kolkata, virtually.
- Attended the Indo-French International virtual workshop on “Recent Advances and Applications of Conducting Polymer Nanostructures and Nanocomposites” (RA2CPNC), held on 23rd–24th June 2021, virtually.

2020

- Poster presentation on “Temperature Dependent Phase Transition of AgVO_3 and its effect on Photocatalytic Activity” by S. Bera, S. Ghosh, R. N. Basu at the 22nd DAE – BRNS Workshop & Symposium on Thermal Analysis (THERMANS- 2020), held on January 28- February 1, 2020 at Multipurpose Hall, BARC Training School Hostel Anushaktinagar, Mumbai, India.

2019

- Oral presentation on “Solar Light Driven Photocatalytic H_2 Generation by $\text{MoS}_2/\text{Bi-TiO}_2$ Nanocomposites” by S. Bera, S. Ghosh, R. N. Basu at the 83rd Annual Session of Indian Ceramic Society (InCerS) which would be held on 11th-12th December, 2019 at CSIR-National Institute for Interdisciplinary Science and Technology (NIIST), Thiruvananthapuram, Kerala, India.
- Poster presentation on “Use of Heterogeneous Photocatalysts to Produce Hydrogen” by S. Bera, S. Ghosh, R. N. Basu at the Young Scientist Colloquium -2019, MRSI, Kolkata Chapter held on 17th September, 2019 at Saha Institute of Nuclear Physics, Kolkata.

2018

- Poster Presentation on “A Ternary Plasmonic Cu-Ag/AgVO_3 Heterostructured Photocatalyst for Solar Photocatalytic H_2 Generation” by S. Bera, S. Ghosh and R. N. Basu in “International Conference on Complex and Functional Materials (ICCFM)” organized by S. N. Bose National Centre for Basic Sciences, Kolkata, India, held during 13th -16th December, 2018.
- Poster Presentation on “Plasmonic Metal Nanostructure Modified BiFeO_3 Heterostructured Photocatalysts for Visible Light Driven Photocatalytic H_2 Generation” by S. Bera, S. Ghosh and R. N. Basu in National Symposium on “Advances in Functional and Exotic Materials” organized by MRSI–Trichy Chapter, Bharathidasan University, Tiruchirappalli held at SRM Hotel during 14 -16th February 2018.

2017

- Poster Presentation on “Heterojunction Construction between Bi_2S_3 Nanowires and Crystalline ZnO Nanoparticles for Enhanced Photocatalysis under Visible Light” by S. Bera, S. Ghosh, R. N. Basu in “International Conference on Energy Options for Tomorrow: Technology to Sustainability (ICEOT 2017)” organized by The Neotia University at Eco Vista, Kolkata, India during 17 – 19th April 2017. (*Best Poster Award*)
- Poster Presentation on “Visible-light-driven enhanced photoresponse of $\text{Bi}_2\text{S}_3/\text{ZnO}$ heterostructures: Photocatalytic hydrogen evolution and photoelectrochemical performance” by S. Bera, S. Ghosh, R. N. Basu in “National Symposium on Recent Advance in Chemistry & Industry (2017)” organized by Department of Chemistry, Indian Institute of Engineering Science and Technology, Shibpur and Indian Chemical Society, Kolkata during 2nd & 3rd August 2017. (*Young Chemist Award*)

- Poster Presentation on “Synthesis of Au-BiFeO₃ heterostructured photocatalysts for visible light driven photocatalytic hydrogen generation” by S. Bera, S. Ghosh, R. N. Basu in National Conference on “Recent Trends in Condensed Matter Physics (RTCMP)” organized by Bose Institute, Kolkata, India during 31st October to 3rd November, 2017.
- Participated 2nd International Conference on “Alumina and Other Functional Ceramics (AOFc 2017)” jointly organized by CSIR-Central Glass & Ceramic Research Institute and Indian ceramic Society, Kolkata, India, during 15th to 17th February, 2017.
- Participated National Seminar on “Carbon Capture and Utilization Technology” organized by Calcutta Regional Centre, IChE, Kolkata held on 24-25th February 2017.
- Participated Young Scientist Colloquium, 2017 (MRSI) on 11th October 2017, held at IEST Shibpur, Kolkata, India.

2016

- Participated “International Conference on Functional Nanomaterials (IC-FNM 2016)” organized by Center of Excellence on Micro-structurally Designed Advanced Materials under TEQIP and M.N. Dastur School of Materials Science and Engineering of IEST, Shibpur, India held during 28th – 29th September, 2016.
- Poster Presentation on “Enhanced Electrocatalytic Activity of Conducting Polymer Supported Pt Nanoparticles for Anodic Oxidation of Methanol in Alkali” by S. Bera, S. Ghosh, R. N. Basu in “International Conference on Ceramics, Glass and Refractories-Emerging Innovations” organized by Indian Ceramic Society 80th annual session, held during 13-15th December, 2016 at IICT, Hyderabad, India.

Reprint of Publications



Cite this: DOI: 10.1039/c7nj03424e

Fabrication of Bi₂S₃/ZnO heterostructures: an excellent photocatalyst for visible-light-driven hydrogen generation and photoelectrochemical properties†

Susmita Bera, Srabanti Ghosh * and Rajendra N. Basu*

Fabrication of heterostructures is considered as one of the effective strategies to improve photocatalytic performance for organic pollutant degradation and hydrogen production under solar light irradiation. Here, Bi₂S₃/ZnO heterostructures with a flower-like architecture have been successfully synthesized by a facile *in situ* generation method. The as-synthesized Bi₂S₃/ZnO heterostructures showed enhanced visible-light absorption and charge separation efficiency of photoinduced electron–hole pairs. This heterojunction exhibits 3 fold enhancement in organic pollutant degradation and 2.7 fold enhancement in photocatalytic hydrogen generation under visible irradiation compared to rod-shaped Bi₂S₃. The high current gain (*ca.* 8.79) and low photocorrosion in photoelectrochemical water splitting reveal the superior photocatalytic activity of the heterojunction under visible light. The superior photocatalytic activities are attributed to the synergetic effects of ZnO nanoparticles and rod-shaped Bi₂S₃ in the Bi₂S₃/ZnO heterostructures, which result in fast separation and slow recombination of photoinduced electron–hole pairs. The reusability and stability of the photocatalysts has been checked by recycling experiments. X-ray diffraction and scanning electron microscopy reveal that the structure and morphology of the heterostructures remain unchanged after photocatalytic cycling tests. The visible light active catalysts have potential for efficient solar light harvesting and overall water splitting. This work demonstrates the potential use of heterostructures as a highly efficient photocatalyst for dye degradation and hydrogen production under visible light irradiation.

Received 9th September 2017,
Accepted 25th November 2017

DOI: 10.1039/c7nj03424e

rsc.li/njc

Introduction

The challenges of environmental pollution and renewable energy production are both highly active areas of scientific research.^{1,2} Visible light-induced photocatalysis is an effective clean approach for water splitting to generate clean solar fuels and converting solar energy to chemical energy.^{3,4} On the other hand, water purification and environmental protection pose an equally daunting challenge.^{5,6} Oxide-based semiconductors have been utilized as active photocatalysts in various applications such as photochemical degradation of organic contaminants, photochemical water splitting to produce hydrogen and photoelectrochemical cells.^{7–9} Titanium dioxide (TiO₂) is one of the most popular photocatalysts and possesses high catalytic activity, low cost and non-toxicity.^{10,11} However, TiO₂ can only absorb UV radiation (4% of the total solar irradiation) due to its wide band gap and low charge separation efficiency, which makes it unsuitable for visible

light active photocatalysis.^{12,13} Moreover, TiO₂ doping with C, N, B, or S or modification with metal nanoparticles (Au, Pt, Ag) results in plasmon-induced enhanced visible light absorption; however, the high cost and low environmental stability of noble-metal-doped TiO₂ restricts its economic potential.^{14–16} Another semiconductor nanocrystal, zinc oxide (ZnO), having a direct band gap of 3.3 eV and a large excitation binding energy has been widely tested for photocatalytic applications.^{17–19} Moreover, ZnO has some advantageous properties over TiO₂ such as high electron mobility due to its electronic structure, room temperature luminescence *etc.*^{18,19} In this regard, the loading of multiple catalysts or secondary semiconductors can improve the catalytic efficiency of ZnO *via* the formation of heterojunctions.^{20,21} This stimulated our interest in designing a coupled heterojunction with ZnO to improve solar light absorption in the visible region.

Significant efforts have been made on the fabrication of semiconductor-based heterostructures such as ZnO/TiO₂,²² Bi₂S₃/TiO₂,^{23,24} and CdS/TiO₂,²⁵ *etc.*, which show potential applications in water splitting and organic pollutant degradation. In fact, high charge separation has been achieved *via* coupling of a large band gap semiconductor with a smaller one forming

CSIR-Central Glass and Ceramic Research Institute, 196, Raja S.C. Mullick Road, Kolkata – 700032, India. E-mail: ghosh.srabanti@gmail.com, rnbasu@cgcri.res.in

† Electronic supplementary information (ESI) available. See DOI: 10.1039/c7nj03424e

a heterojunction, which in turn enhances the photocatalytic efficiency by decreasing the recombination rate of the photo-generated electron-hole pairs.^{26,27} In the case of a heterojunction, charge carriers are generated in one semiconductor and then vectorially transfer to the other material allowing for long lived electron hole pairs at the interface and are able to produce a potential gradient within the catalyst.⁵ The presence of multiple active sites within the heterostructures can provide a high surface area for the decomposition of organic pollutant molecules at the surface of the catalysts.²⁸ For example, TiO₂-based hybrid heterojunctions demonstrated high catalytic activity due to surface tunnelling of electrons between the surfaces of the semiconducting components of the heterostructure.²⁹ Until now, most of the studies have been focused on the hybridization of TiO₂ with semiconductors to improve the photocatalytic efficiency under visible light.^{29–33} In this regard, few reports have been published on the modification of ZnO nanostructures with other semiconductors such as ZnO/TiO₂,³⁴ CdS/ZnO³⁵ *etc.* for improved visible light-driven photocatalysis.

On the other hand, low band gap semiconductors such as sulphides, nitrides, graphitic carbon nitrides, oxynitrides, chalcogenides *etc.*, have been widely investigated to construct visible light active photocatalysts.^{36–39} Among these, bismuth sulphide (Bi₂S₃), a low band gap metal sulphide (1.3 eV), has shown absorption in the visible region and has been considered a potential candidate for photocatalytic applications.⁴⁰ However, the rapid recombination of photo-induced electrons and holes limits the catalytic application of Bi₂S₃ under visible light. Recently, a series of Bi₂S₃-based heterostructures such as MoS₂/Bi₂S₃,⁴¹ Bi₂S₃/CdS,⁴² Bi₂S₃/Bi₂WO₆,⁴³ Bi₂S₃/In₂S₃,⁴⁴ Bi₂S₃/BiVO₄,⁴⁵ Bi₂S₃/(BiO)₂CO₃⁴⁶ *etc.*, have been developed to improve the light absorption and charge separation efficiency. Recently, Bi₂S₃/g-C₃N₄ heterostructures exhibited high catalytic performance for organic dye (Rhodamine B) degradation, but the apparent kinetic rate was very low.⁴⁷ MoS₂/Bi₂S₃ and Bi₂S₃/In₂S₃ heterojunctions showed high catalytic activity for organic pollutant degradation but no report on hydrogen generation is available to date. Notably, semiconductor-based heterostructures are effective catalysts for water oxidation as the photogenerated electrons and holes on the surface of heterostructures have the potential to react at the surface active site. Thus, the excited electrons reduce the water to form hydrogen and the holes oxidize the water to generate oxygen.⁴⁸ The Bi₂S₃/CdS heterostructures displayed photocatalytic hydrogen generation under visible light irradiation but the hydrogen evolution rate is low.⁴² Recently, Wang *et al.*⁴⁹ have used Z-scheme CdTe–Bi₂S₃ heterojunctions for photoelectrochemical performance. Hence, Bi₂S₃-based heterojunctions have been extensively utilized for organic dye degradation but photocatalytic hydrogen generation has not been tested yet. Herein, Bi₂S₃ with a narrow band gap has been integrated with ZnO nanoparticles to fabricate visible light active heterostructures. Various characterization techniques such as XRD, SEM, TEM and FTIR have been employed for characterizing the structure, morphology and optical properties of the heterostructures. To the best of our knowledge, for the first time, we studied the photocatalytic

performance and photoelectrochemical properties of Bi₂S₃/ZnO for hydrogen generation under visible light.

Experimental section

Materials

Bismuth nitrate pentahydrate (Bi(NO₃)₃·5H₂O, 99.99%), L-cysteine hydrochloride (99.99%), mercaptosuccinic acid (MSA, 99%), ethylenediaminetetraacetic acid disodium salt (EDTA-Na, 99%), methanol were procured from Sigma Aldrich, USA. For the *in situ* generation of ZnO, zinc acetate dehydrate (Zn(CH₃COO)₂·2H₂O, 98%) and sodium hydroxide (NaOH, 98%) were procured from Merck, Germany.

Synthesis of Bi₂S₃ nanostructures

In a typical synthesis, 0.5 mmol of ethylenediaminetetraacetic acid disodium salt (EDTA-Na) was dissolved in 100 mL of distilled water and stirred for 10 minutes. Then 0.4 mmol of Bi(NO₃)₃ was mixed and the solution mixture was ultrasonicated until the solution became transparent. After that, 0.6 mmol of L-cysteine hydrochloride was added to the solution. Finally, the solution was transferred into a 100 mL Teflon-lined autoclave with a stainless steel shell and heated at 180 °C for 16 h. The Bi₂S₃ was collected and centrifuged, washed several times with distilled water and finally air-dried overnight at 50 °C for further characterization. Similarly, Bi₂S₃ nanostructures were also prepared using mercaptosuccinic acid as a sulphur source.⁵⁰ The effect of sulphur source concentration (0.6, 1.2, 2.4 mmol) and different reaction times (10, 16, 24 h) to follow the growth mechanism of Bi₂S₃ nanostructure formation has been studied in detail.

Synthesis of Bi₂S₃/ZnO heterostructures

In order to develop a coupled heterostructure of Bi₂S₃/ZnO, a facile *in situ* generation *via* co-precipitation technique has been employed using ethanol as a solvent.¹⁷ Briefly, 20 mL of 4 mmol zinc acetate dehydrate solution was heated at 70 °C for 30 min. Then a fixed amount of prepared Bi₂S₃ powder (1 mg mL⁻¹) was added and mixed thoroughly. In the next step, 20 mL of 4 mmol sodium hydroxide solution prepared at 70 °C in ethanol was added slowly and the mixture was hydrolyzed for 2 h at 60 °C to obtain ZnO NPs with average diameters of ~5 nm. The pure semiconductors and heterostructures are presented as L-Bi₂S₃, L-Bi₂S₃/ZnO (using L-cysteine hydrochloride as a source of sulphur) and M-Bi₂S₃, M-Bi₂S₃/ZnO (using MSA as a source of sulphur). To understand the growth mechanism of Bi₂S₃, extensive experimental analyses were performed for varying reaction times, metal salt to surfactant ratios and sulphur sources.

Instrumentation

The crystalline phase of Bi₂S₃ and the heterostructures was investigated by XRD (Philips X'Pert, The Netherlands) within the 2θ range of 10° to 80° at a slow scan rate of 1° min⁻¹ with Cu Kα radiation (at 40 kV and 40 mA). The structural morphology

and EDS was recorded by Field Emission Scanning Electron Microscopy (LEO. 430i, Carl-Zeiss, Sigma). Transmission Electron Microscopy (TEM) images and the corresponding selected area electron diffraction (SAED) patterns were obtained on Tecnai G² 30ST (FEI) operating at 300 kV. The XPS study was performed using a PHI 5000 Versa Probe II spectrophotometer (Physical Electronics Inc., USA) with a monochromatized Al K α (~ 1486.6 eV) X-ray beam of size ~ 100 μm . The samples were prepared in pallet form and the surfaces were sputtered with a 2 kV rastered Ar⁺ ion beam for one minute to clean the surface. The thermal stability of the bare Bi₂S₃ and heterojunction was investigated using thermogravimetric analysis (TGA) apparatus (NETZSCH, STA 449 F3, Jupiter). The test was carried out in air with a heating rate of 10 °C min⁻¹ from 100 °C to 900 °C. The porosity and specific surface area of the samples were determined through nitrogen adsorption at 200 °C on the basis of the BET equation using a Quantachrome, FL-33426. The UV-visible absorption spectra of the ethanolic solutions containing Bi₂S₃, ZnO and Bi₂S₃/ZnO were recorded using a Shimadzu, UV-3600 spectrophotometer. The hydrogen evolution was measured by online gas chromatography using a YL Instrument, 6500GC system with a thermoconductive detector. The photoelectrochemical measurements have been tested using a galvanostat-potentiostat (PGSTAT302N, Autolab, The Netherlands) with a standard three-electrode cell and Pt wire as a counter electrode and saturated Ag/AgCl as a reference electrode. The working electrode was a thin film of as-prepared material on glassy carbon. The photocatalytic *I*-*V* characteristics have been measured using simulated illumination (60 mW cm⁻²) by a white light source.

Photocatalytic test

L-Bi₂S₃, L-Bi₂S₃/ZnO, M-Bi₂S₃ and M-Bi₂S₃/ZnO have been tested for dye degradation using methyl orange (MO) as a model pollutant. It is a representative of hazardous azo dyes. The photodegradation of MO (initial concentration $C_0 = 0.3 \times 10^{-4}$ M) was carried out within a quartz cell reactor containing 50 mL model solution with a concentration of 1 mg mL⁻¹ under UV and visible lamps. A Xe-arc lamp (250 W) with an incident beam intensity of 100 mW cm⁻² (Oriel, Irvine, CA) was used as a light source for visible irradiation and a 395 nm cutoff filter was used. For a control experiment, bare L-Bi₂S₃ and M-Bi₂S₃ have been studied separately under similar reaction conditions. The appropriate amount of aliquots was collected from the reactor at successive time intervals. The percentage degradation (% DE) of MO was determined using the following equation:

$$\% \text{ DE} = \frac{C_0 - C}{C_0} \times 100 \quad (1)$$

where C_0 is the initial absorption intensity of MO at $\lambda_{\text{max}} = 463$ nm and C is the intensity after light illumination.

Photocatalytic hydrogen generation

To study the hydrogen generation, the online gas chromatography method was used where the area under the Gaussian peak gives the amount of H₂ evolved. The H₂ production

through water splitting was performed in a closed reactor in the presence of methanol solution with saturated argon media and vigorous stirring. For this experiment, a 25 volume% methanol solution was used at room temperature.⁵¹ Here, methanol acts as a sacrificial agent and use of methanol is very much advantageous compared to other alcohols because it reduces the formation of more carbon-based sub-products being the simplest organic molecule and also accelerates the main intermediate (free radical) formation process.⁵¹ Here we report H₂ generation up to 3 h.

Results and discussion

Structural characterization

XRD was carried out to study the crystalline phase of the as-prepared materials. Fig. 1a and b show the X-ray diffraction (XRD) patterns of L-Bi₂S₃, L-Bi₂S₃/ZnO, M-Bi₂S₃ and M-Bi₂S₃/ZnO. The X-ray patterns displayed narrow and sharp diffraction peaks, indicating the high crystallinity of the prepared samples. The strong peaks at 2θ values of 15.54, 17.41, 22.21, 23.57, 24.92, 28.43, and 31.71 correspond to characteristic diffraction from the (020), (120), (220), (101), (130), (211) and (221) planes of pure Bi₂S₃ respectively (JCPDS card no. 17-0320).⁴⁷ The diffraction peaks of ZnO at 2θ values of 31.76, 34.00 and 36.56 correspond to the (100), (002) and (101) planes indicating the wurtzite hexagonal phase of ZnO (JCPDS card no. 36-1451).⁵² The XRD pattern of the pure ZnO nanoparticles is shown in the inset of Fig. 1a which indicates that the nanoparticles are highly crystalline in nature. Therefore, the XRD patterns of the heterostructures reveal the presence of wurtzite ZnO

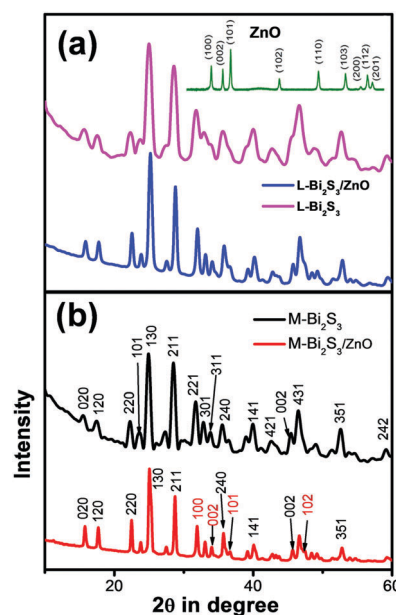


Fig. 1 XRD patterns of as-prepared (a) pure L-Bi₂S₃ and L-Bi₂S₃ decorated with ZnO NPs. Inset: XRD pattern of ZnO nanoparticles. (b) Pure M-Bi₂S₃ rod-shaped structures and M-Bi₂S₃ decorated with ZnO NPs. The samples have been synthesized at 16 h and metal salt to surfactant ratio 1: 3.

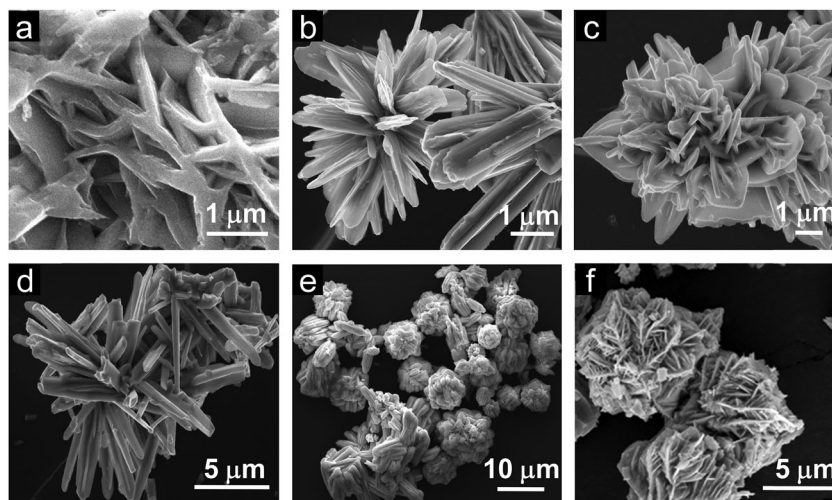


Fig. 2 FESEM images of Bi_2S_3 using L-cysteine as a structure controlling agent at three different reaction times: (a) 10 h, (b) 16 h, and (c) 24 h (metal : L-cysteine 1 : 1.5). Effect of surfactant concentration during the formation of Bi_2S_3 at three different metal/surfactant ratios: (d) 1 : 1.5, (e) 1 : 3 and (f) 1 : 6 at 16 h under similar conditions.

within orthorhombic Bi_2S_3 . Moreover, the presence of all the characteristic peaks of Bi_2S_3 and no additional peak in the heterostructures confirms the purity of $\text{Bi}_2\text{S}_3/\text{ZnO}$. Moreover, no remarkable changes were observed in the diffraction peak position and intensity of $\text{Bi}_2\text{S}_3/\text{ZnO}$ at longer hydrothermal reaction times indicating the formation of stable orthorhombic Bi_2S_3 (Fig. S1, ESI†).

The morphology and growth of Bi_2S_3 and $\text{Bi}_2\text{S}_3/\text{ZnO}$ were investigated by field emission scanning electron microscopy (FESEM). Fig. 2a–c illustrates the assembled growth of Bi_2S_3 rods with increasing reaction time. It is clear from Fig. 2a that when the hydrothermal reaction proceeds for 10 h, the formation of rod-like structures is obtained which are completely overlapped. At 16 h, distinct rods with an average length of $\sim 3.81 \mu\text{m}$ (Fig. 2b) are formed which are connected with each other and radiated from a centre.

With further increase in the reaction time up to 24 h, the rods are more assembled and interestingly form a lotus flower-like morphology (Fig. 2c). This may happen due to over growth of Bi_2S_3 nuclei in the same direction.⁴² In addition, the metal salt to surfactant ratio has been varied to investigate the role of the surfactant as a morphology controlling factor. Fig. 2d–f display Bi_2S_3 synthesized at three different concentrations of surfactant at 16 h keeping all other conditions similar.

When the metal salt:L-cysteine ratio is 1:1.5, it can be observed that irregularly distributed rod-shaped structures of average length $\sim 4.7 \mu\text{m}$ are formed (Fig. 2d). In contrast, at 1:3, the assembled morphology (length $\sim 5.5 \mu\text{m}$) consists of rods that have been formed with a bunched-like structure.

Moreover, at a higher concentration of L-cysteine (1:6 ratio), more assembled structures have been formed. Fig. 2e displays Bi_2S_3 superstructures of diameter $\sim 8 \mu\text{m}$ which are built of two-dimensional nanosheets. Hence, this highly assembled morphology is useful to provide more active sites in photocatalytic applications. In general, an assembled 1D morphology is more suitable for photocatalytic applications having a large

surface to volume ratio, synergistic interactions as the long lengths of the nanorods will contact each other, and multiple functionalities.⁵³

Another kind of Bi_2S_3 nanostructure has been developed using mercaptosuccinic acid as a structure controlling agent. Fig. 3a–c illustrates the FESEM images of pure Bi_2S_3 at different magnifications, and clearly indicates solid rods radiated from a common centre and stacked uniformly to form a nanoflower-like morphology.

At high magnification, it has been clearly observed that the nanoflowers consist of solid rods of length $\sim 500 \text{ nm}$ with the square edge of the sides at 60 to 70 nm (Fig. 3c). To investigate the elemental composition, X-ray energy-dispersive spectrometry (EDS)

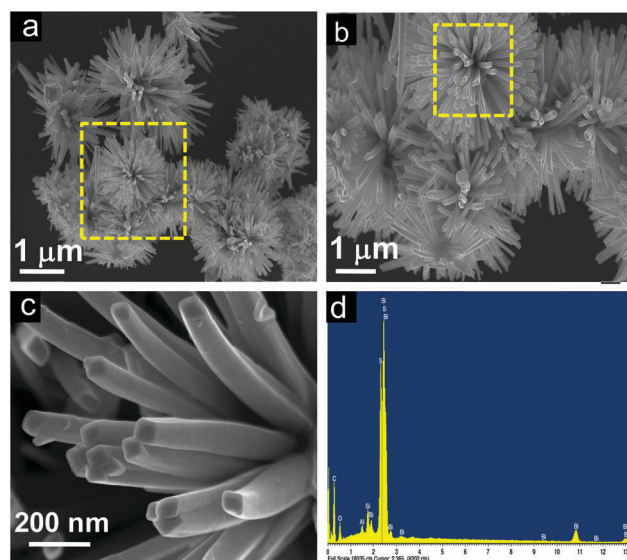


Fig. 3 FESEM images of (a)–(c) flower-like assembled structures of Bi_2S_3 using mercaptosuccinic acid as a structure controlling agent at three different magnifications and (d) EDS spectrum of Bi_2S_3 synthesized at 16 h and a metal salt to surfactant ratio of 1 : 3.

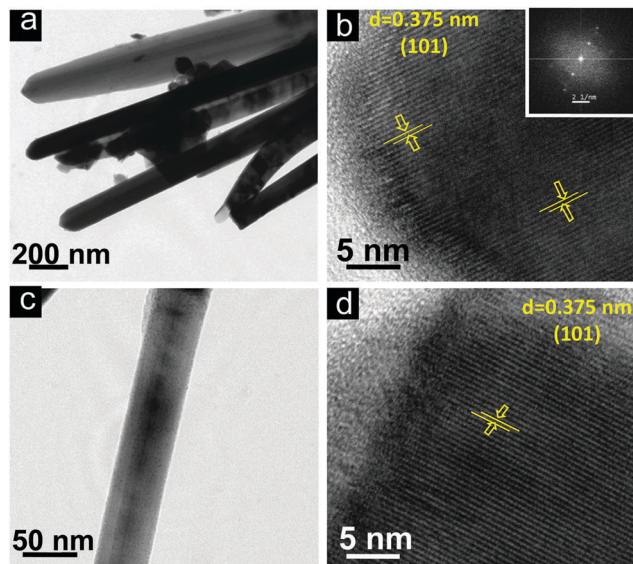


Fig. 4 TEM images of (a) pure L-Bi₂S₃ nanostructures, (b) HRTEM of L-Bi₂S₃, inset: SEAD pattern, (c) pure M-Bi₂S₃ nanostructures and (d) HRTEM image of M-Bi₂S₃ at metal : surfactant = 1 : 3 in reaction time 16 h.

was carried out on the Bi₂S₃ nanoflowers. Fig. 3d indicates the coexistence of Bi and S elements on the rod-shaped structures. However, the presence of Al and Si signals originated from the glass substrate.

Additionally, the detailed structural and crystalline nature of the as-prepared Bi₂S₃ and Bi₂S₃/ZnO has been investigated through TEM and HRTEM images (Fig. 4). The TEM images (Fig. 4a and c) clearly reveal the uniform 1D structures of L-Bi₂S₃ and M-Bi₂S₃ and are well consistent with the FESEM images. The interplanar spacing of 0.375 nm reveals the characteristic (101) plane of Bi₂S₃ (Fig. 4b and d).⁵⁴ Therefore, the preferential growth of Bi₂S₃ rods occurred along the (101) direction. The calculated size of the bare ZnO NPs is in the range of 5 nm as determined from the TEM image (Fig. S2, ESI[†]).

The microscopic images of the L-Bi₂S₃/ZnO heterostructures are displayed in Fig. 5. It can clearly be seen from the SEM images (Fig. 5a and b) that the spherical ZnO NPs have been formed uniformly deposited on the L-Bi₂S₃ surface. A further detailed study on the morphology of the L-Bi₂S₃/ZnO heterostructures has been performed through the TEM images. Fig. 5c clearly shows the rough surface of the rod-shaped L-Bi₂S₃ due to deposition of spherical hexagonal ZnO nanoparticles over the surface. The HRTEM image of L-Bi₂S₃/ZnO reveals its highly crystalline nature having a lattice spacing of about 0.33 nm related to the (130) plane of Bi₂S₃ (Fig. 5d).⁵⁵ The SAED pattern depicts the highly crystalline hexagonal structure of Bi₂S₃ (Fig. 5e). For further analysis of chemical compositions and the elemental distribution, EDS was carried out (Fig. 5f) where strong signals of Bi, S, O and Zn also confirm the formation of Bi₂S₃/ZnO heterostructures.

The morphology and crystalline nature of the heterostructures using M-Bi₂S₃ was further investigated using FESEM and TEM images. Fig. 6a shows the *in situ* generation of ZnO NPs on the rod-shaped M-Bi₂S₃ structures. It is evident that the assembled nanoflower-like structures are totally transformed into a nanofibre-based network after the formation of ZnO NPs. This is probably due to the strong interaction between ZnO and the surface ligand (MSA) of Bi₂S₃ which is responsible for the formation of the self-assembled nanoflower-like morphology. The FESEM image also illustrates that the single rod-shaped structure of Bi₂S₃ is completely covered by small ZnO NPs (Fig. 6b). Fig. 6c shows that the M-Bi₂S₃/ZnO rod-like nanostructures are covered with smaller nanoparticles which is consistent with the FESEM image (Fig. 6a and b) and the cross fringes in the HRTEM image indicate the crystallinity of the heterostructures with a lattice spacing value of 0.30 nm related to the (211) plane of Bi₂S₃ (Fig. 6d).⁵⁶ Owing to the highly crystalline nature of Bi₂S₃, it is difficult to observe crystal fringes of ZnO within the heterostructures.

The growth of bare Bi₂S₃ and its heterostructures can be explained on the basis of coordination interaction between Bi³⁺

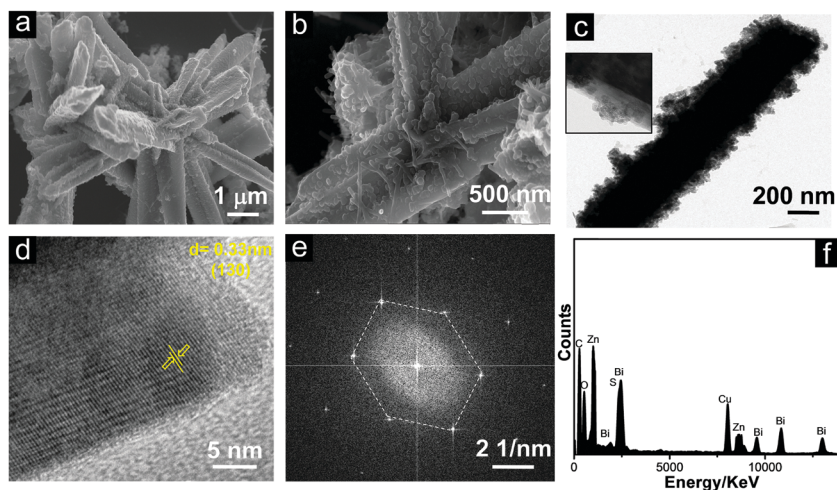


Fig. 5 (a and b) FESEM images of L-Bi₂S₃/ZnO heterostructures at two different magnifications. TEM image of (c) ZnO nanoparticles decorated on rod-shaped Bi₂S₃ structures, and (d) HRTEM, (e) SAED and (f) EDX spectrum of L-Bi₂S₃/ZnO heterostructures.

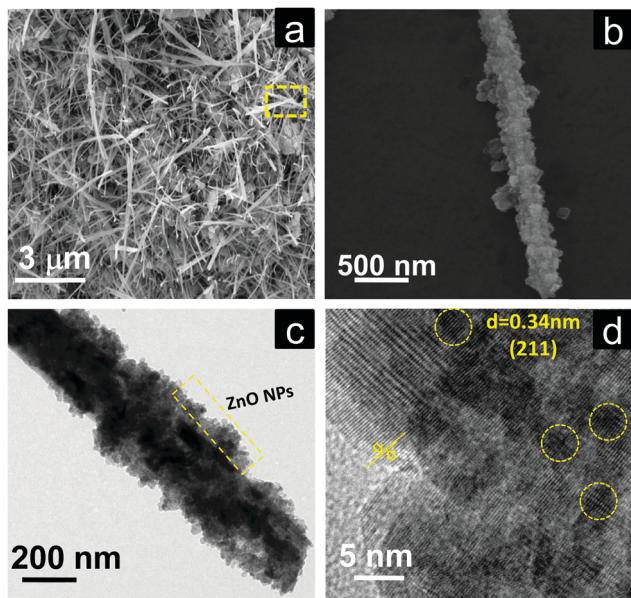
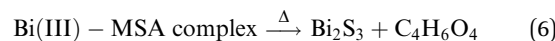
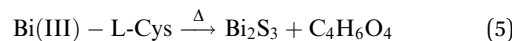
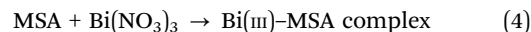
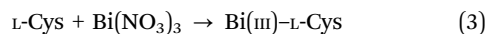
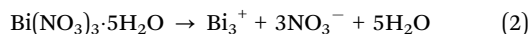


Fig. 6 FESEM images of M-Bi₂S₃/ZnO heterostructures at (a) low magnification, and (b) high magnification. TEM image of (c) ZnO nanoparticles decorated on rod-shaped Bi₂S₃ structures, and (d) HRTEM of M-Bi₂S₃/ZnO heterostructures.

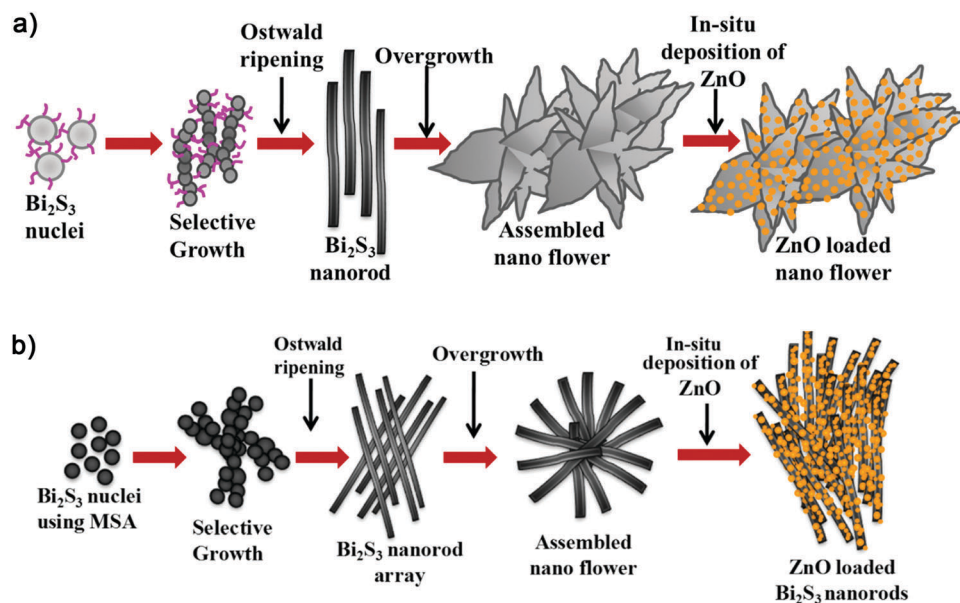
and the surfactant. In the hydrothermal synthesis of the Bi₂S₃ nanostructures and *in situ* generation method for heterojunction formation, the following reactions may be involved:



Initially, L-cysteine contains various functional groups such as -NH₂, -COOH, and -SH⁵⁷⁻⁵⁹ and MSA contains -SH, and -COOH groups which have a tendency to coordinate with inorganic cations and metals. Thereafter, the amino group reacts with the neighbouring carboxylic group of the surfactant to form a dipeptide or polypeptide because these complex forms are more stable relative to others.^{42,54} Moreover, this intermediated state serves as a template in the successive nucleation of Bi₂S₃ nanocrystals. Finally, the rod-shaped Bi₂S₃ originates from continuous growth of Bi₂S₃ nuclei along one direction which may be caused by a typical Ostwald ripening process.⁴² From the effect of different reaction times, it can be concluded that the transformation of the assembled flowers from an undefined structure may be caused due to recrystallization along the preferential growth axis to form the rod-composed flower as shown in the FESEM images (Fig. 2). To get the ZnO-loaded Bi₂S₃ rods, direct adsorption and *in situ* generation of 5 nm ZnO NPs on the Bi₂S₃ have been followed. Possible mechanisms of heterostructure formation are displayed in Scheme 1a and b.

X-ray photon spectroscopy (XPS) was carried out to further elucidate the chemical compositions as well as the oxidation states of the pure semiconductor and heterostructures. The overall XPS spectra (Fig. 7a) indicate the presence of strong peaks of Bi, S, Zn, O and C. Here, the 1S peak of C acts as a reference point coming from the background.

The strong peaks at binding energies of 157.84 eV and 163.16 eV with typical spin orbit doublet splitting of 5.32 eV



Scheme 1 (a) Schematic illustration of ZnO nanoparticle decorated Bi₂S₃ assembled structures synthesized by a simple hydrothermal process using L-cysteine hydrochloride as a structure controlling agent. (b) Schematic illustration of ZnO nanoparticle decorated Bi₂S₃ rods synthesized by a simple hydrothermal method using mercaptosuccinic acid as a structure controlling agent.

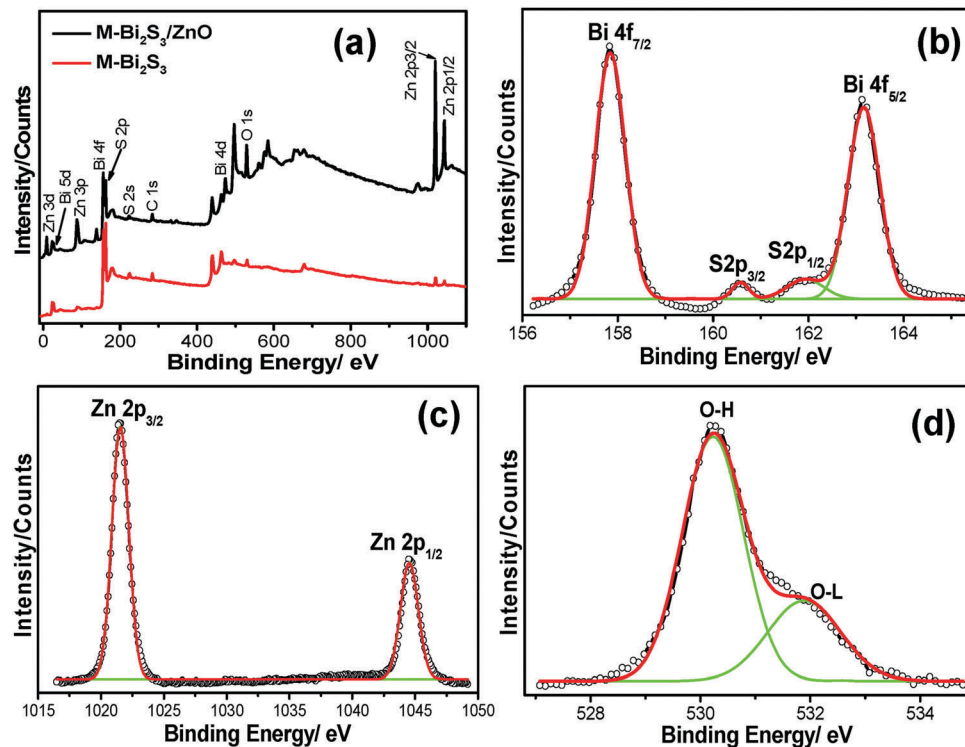


Fig. 7 XPS spectra of the as-prepared heterostructures. (a) The overall spectra of M-Bi₂S₃ and M-Bi₂S₃/ZnO. (b) The Bi 4f and S 2p spectra, (c) Zn 2p spectra and (d) O 1s spectra of M-Bi₂S₃/ZnO. Here, the scatter and solid lines indicate the experimental and fitted data.

can be assigned to the binding energy of Bi 4f_{7/2} and Bi 4f_{5/2} respectively, closely matched with the Bi³⁺ in Bi₂S₃ (Fig. 7b).⁶⁰ The peaks found between Bi 4f_{7/2} and Bi 4f_{5/2} at 161.83 eV and 160.56 eV correspond to S 2p_{1/2} and S 2p_{3/2} (1.27 eV), which indicates the existence of S²⁻ within Bi₂S₃.⁴² Moreover, after the heterojunction formation, the blue shift of the binding energy for Bi 4f_{7/2} (~0.3 eV), Bi 4f_{5/2} (~0.27 eV) and S (~0.19 eV) indicates the strong interaction between Bi₂S₃ and ZnO followed by the formation of a heterojunction. In addition, the strong oxidation peaks located at 1021.9 eV and 1045.1 eV of Zn 2p_{3/2} and 2p_{1/2} respectively (Fig. 7c) suggest the Zn²⁺ state of ZnO.⁴⁹ It is also observed that the binding energy of pure ZnO shifts towards a lower value of 0.23 eV after forming a heterojunction. Fig. 7d exhibits the asymmetric profile of O 1s which can be fitted to two symmetrical peaks at 530.2 and 531.72 eV, indicating the presence of two different kinds of O species in the sample. The peaks at 531.72 eV and 530.2 eV should be associated with the lattice oxygen (O_L) of ZnO and chemisorbed oxygen (OH) by the surface.⁶¹ Thus, the XPS spectra suggest the co-existence of Bi₂S₃ and ZnO within the heterostructures.

Thermo gravimetric analysis (TGA) was carried out to determine the loading of ZnO NPs after *in situ* deposition as well as the thermal stability of the heterostructure. The loading of ZnO calculated from the TGA curves is found to be 10% and 15% for l-Bi₂S₃ and M-Bi₂S₃ respectively (Fig. 8a and b). The initial mass losses in the range of 220 °C to 230 °C originate from the removal of adsorbed O₂ and water molecules. The further mass loss above 380 °C is mainly attributed to the decomposition of Bi₂S₃ into Bi metal.

Notably, after 440 °C, the pure Bi₂S₃ curve is fairly stable whereas the Bi₂S₃/ZnO heterostructures are unstable and indicate a strong weight loss above 478 °C which implies the formation of ZnO.⁴² The porous structure of the pure semiconductor as well as the heterostructures was studied by the nitrogen adsorption-desorption isotherm method. The specific surface areas calculated by the BJH method are 3.13 m² g⁻¹ and 9.53 m² g⁻¹ for the pure M-Bi₂S₃ and M-Bi₂S₃/ZnO heterostructures, respectively. This indicates that the specific BET surface area is increased when the heterojunction is formed which may be useful for photocatalytic applications.⁵⁶ The hysteresis loop present in the BET curve (Fig. S3, ESI[†]) suggests the type II pattern of the semiconductor heterostructures. Hence, incorporation of ZnO nanoparticles effectively generates porosity and active surface sites within the heterostructure.

The optical properties of the pure semiconductor and semiconductor heterostructures have been evaluated by diffuse reflectance and photoluminescence (PL) spectroscopy. Fig. 8c shows the diffuse reflectance spectroscopy of the bare semiconductors and heterostructures where both the l-Bi₂S₃/ZnO and M-Bi₂S₃/ZnO heterostructures demonstrated broad absorption in the visible range that extends up to the near IR range. For the bare ZnO, the onset of light absorption is in the UV region with a band gap of ~3.37 eV. The light absorption of the Bi₂S₃/ZnO heterostructures increases in the visible region compared to bare ZnO or Bi₂S₃ indicating that heterostructures are useful for efficient solar light harvesting applications. The photoluminescence spectra of ZnO display an emission peak at ~514 nm upon excitation to 320 nm, as shown in Fig. 8d.

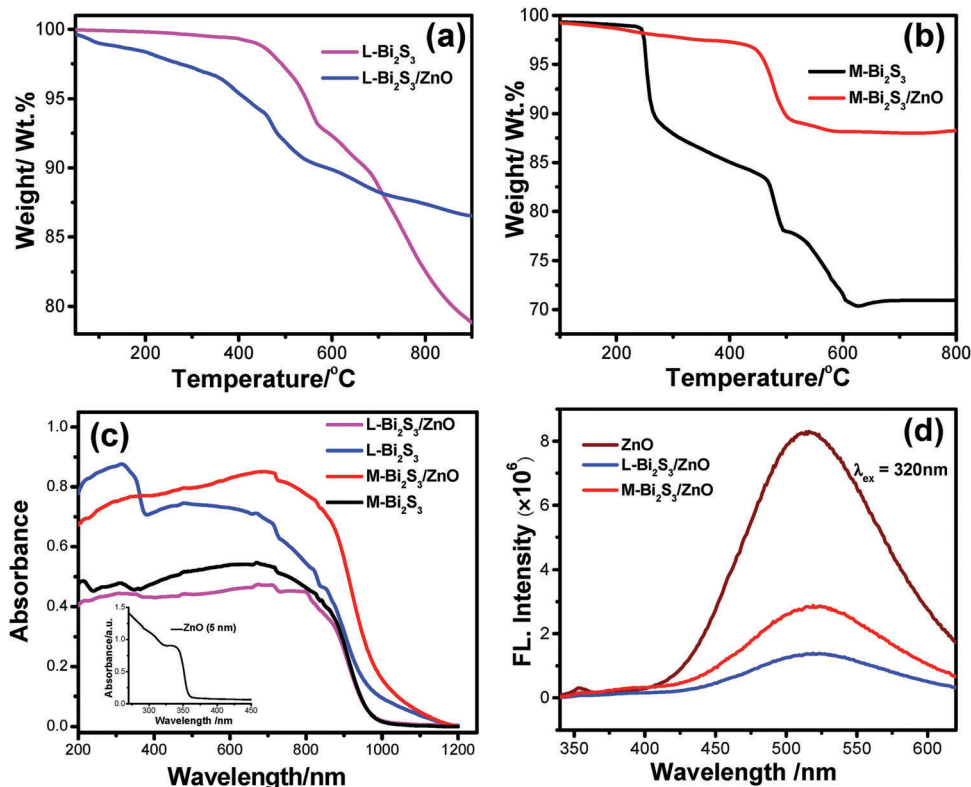


Fig. 8 TG curves of (a) pure L-Bi₂S₃ and L-Bi₂S₃/ZnO, and (b) pure M-Bi₂S₃ and M-Bi₂S₃/ZnO. (c) Diffuse reflectance spectra of L-Bi₂S₃ (pink line), L-Bi₂S₃/ZnO (blue line), M-Bi₂S₃ (black line) and M-Bi₂S₃/ZnO (red line) respectively. Inset: Absorption spectra of ZnO nanoparticles (5 nm). (d) Photoluminescence spectra of ZnO (5 nm), L-Bi₂S₃/ZnO and M-Bi₂S₃/ZnO.

The intensity of the emission peak lowered significantly to 519 nm and 517 nm when L-Bi₂S₃ and M-Bi₂S₃ attached to the ZnO NPs. Thus, the quenching in emission intensity (65.5% for M-Bi₂S₃/ZnO and 83.25% for L-Bi₂S₃/ZnO) for the heterostructures (Fig. 8d) indicates the strong electronic interaction and improved charge carrier separation efficiency.¹⁷

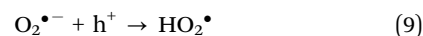
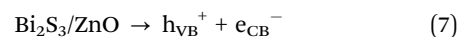
Photocatalytic MO degradation

The photocatalytic activity has been studied under visible light using methyl orange (MO) as a model pollutant. It is well known that MO is a very stable dye which is resistant to self-photo degradation. Fig. 9a clearly shows the degradation of MO in the presence of Bi₂S₃ and Bi₂S₃/ZnO under visible light irradiation. The M-Bi₂S₃/ZnO heterostructures exhibit significantly enhanced photocatalytic activity as compared with bare M-Bi₂S₃ and L-Bi₂S₃. Bare L-Bi₂S₃ has negligible photocatalytic activity (26%) but bare M-Bi₂S₃ shows high activity (63%). In contrast, the photodegradation efficiency of MO reached 82% for M-Bi₂S₃/ZnO and 55% for L-Bi₂S₃/ZnO after 150 min of visible light irradiation (Fig. 9a), indicating that heterostructures possess superior photocatalytic activity. The photocatalytic activity of the M-Bi₂S₃/ZnO heterostructures is ~8.6 times higher compared to bare M-Bi₂S₃.

The enhanced photocatalytic activity of heterostructures can be achieved due to strong absorption in the visible range with high surface area of the assembled structure.⁶² As evident from the TGA data, loading of ZnO NPs on the M-Bi₂S₃ nanofibres

may create more catalytic centres within the heterostructure and thereby show high catalytic activity. The enhanced catalytic activity of M-Bi₂S₃/ZnO may be associated with the multiple reflections and scattering of light within the interconnected rods which results in enhanced light absorption as reflected in the absorption spectra (Fig. 8c).²⁸ Similarly, L-Bi₂S₃/ZnO demonstrated higher catalytic activity in comparison with bare L-Bi₂S₃. The photocatalytic activity under UV light irradiation was also studied where M-Bi₂S₃/ZnO degrades only 48% of MO concentration (Fig. S4, ESI†).

Possible reactions involved in photocatalytic dye degradation are given below.



In order to investigate the photocatalytic mechanism of the heterostructure-based catalysts, a further study has been conducted in the presence of sacrificial agents and the contribution of excess electron–holes (Cu²⁺, isopropanol and saturated argon media) (Fig. 9b).⁶² Semiconductors react with photoinduced electrons and holes from water to form various reactive species including O₂^{•−} and OH[•].⁶³ Herein, Cu²⁺ was used to understand the role of excess electrons as it reacts with electrons very quickly and converts into Cu⁺. The remarkable

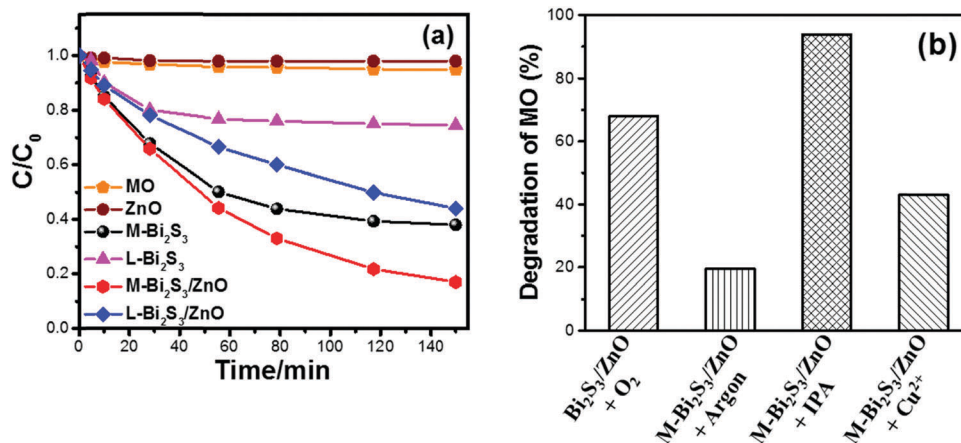


Fig. 9 (a) Photocatalytic degradation of methyl orange in the presence of catalyst, bare semiconductors L-Bi₂S₃ and M-Bi₂S₃, and heterostructures L-Bi₂S₃/ZnO and M-Bi₂S₃/ZnO under visible light irradiation. (b) Effect of argon, isopropanol, and Cu²⁺ on the photocatalytic activity of M-Bi₂S₃/ZnO for methyl orange degradation.

change of MO degradation in the presence of 2×10^{-6} M Cu²⁺ (it changes 68% to 43%) is presented in Fig. 9b after 6 h visible light irradiation. This suggests a role of electrons during the photocatalytic reaction. In order to confirm the role of O₂^{•-}, a photodegradation experiment has been performed under argon saturated atmosphere. In general, the argon-saturated inert medium may suppress the O₂^{•-} radical production which may be the possible reason for inhibiting the degradation of MO by M-Bi₂S₃/ZnO.⁶² It only degrades 20% of MO after 4 h of visible light irradiation. Thus, it can be concluded that oxygen has a crucial role in the photocatalytic reaction. Moreover, photocatalysis has been performed in the presence of 0.1 M isopropanol (acts as a hole scavenger) and oxygen to investigate the role of photoexcited holes in the photocatalytic reactions. The decomposition kinetics of MO increased up to 94% in the presence of isopropanol which clearly indicates the role of holes in the photodegradation of MO.

Photocatalytic H₂ generation

Fig. 10a shows photocatalytic H₂ generation by Bi₂S₃ and Bi₂S₃/ZnO heterostructures *via* water splitting using 25 volume%

of methanol solution as a sacrificial agent. In general, the semiconductors with more negative CB can reduce water efficiently, and thus increase the hydrogen production rate. Herein, a relatively low band gap semiconductor, Bi₂S₃, acts as a recombination centre for ZnO and the reduction process occurs at the ZnO surface. The H₂ generation enhanced with the increase in irradiation time. The amount of H₂ production is higher for heterostructures, L-Bi₂S₃/ZnO (2791 μmol). For comparison, the H₂ evolution activity has been investigated for bare semiconductors L-Bi₂S₃ and M-Bi₂S₃ under visible light irradiation. The heterojunction shows 2.74-fold enhancement in hydrogen generation compared to L-Bi₂S₃ (1020 μmol). The H₂ generation for M-Bi₂S₃ and M-Bi₂S₃/ZnO is 263 μmol and 2450 μmol respectively. In contrast to dye degradation, L-Bi₂S₃/ZnO shows superior performance for photocatalytic hydrogen generation in comparison to M-Bi₂S₃/ZnO.

The exact reason is not clear to us but the enhanced catalytic activity may be associated with the assembled morphology of L-Bi₂S₃/ZnO which leads to intimate contact between metal sulphide and the zinc oxide NPs. The three-dimensional interconnected assembled structure may also facilitate the transport of photogenerated electrons and holes to the binding sites;

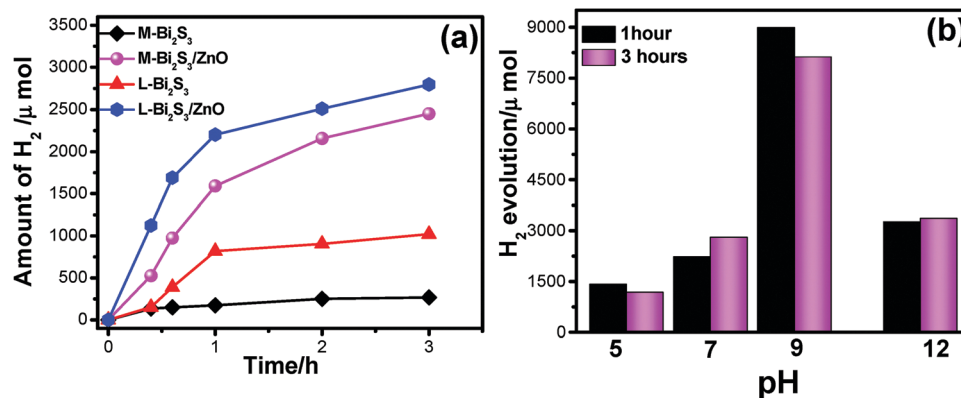


Fig. 10 (a) Photocatalytic hydrogen generation in the presence of catalyst L-Bi₂S₃, M-Bi₂S₃, L-Bi₂S₃/ZnO, and M-Bi₂S₃/ZnO for 3 h under visible light from an aqueous solution containing 25 volume% methanol at pH 7. (b) Effect of pH on hydrogen evolution from aqueous solution after 1 h and 3 h of irradiation.

thereby water oxidation occurred in the presence of a sacrificial agent which is consistent with the literature report.⁶⁴ Moreover, both the heterostructures may provide facile electron transfer compared with bare semiconductors which can effectively enhance the hydrogen generation.⁶⁵

Furthermore, the effect of pH on the photocatalytic hydrogen evolution process has been studied to optimize the reaction conditions. Fig. 10b illustrates that higher activity for hydrogen evolution is achieved at pH 9, $\sim 8089 \mu\text{mol}$, whereas under low pH conditions, *i.e.* acidic conditions, it generates only $1159 \mu\text{mol}$ due to protonation of the photocatalyst in acidic solution.⁶⁵ Generally under acidic conditions the driving force for hydrogen generation decreases as the redox potential of H^+/H_2 becomes more negative. On the other hand, a highly alkaline medium is also not preferable for hydrogen evolution because of insufficient protons.⁶⁶

In view of practical applications, reusability and stability of photocatalysts is an important parameter. Here, we checked the recycling of M-Bi₂S₃/ZnO up to 5 successive cycles and the result is displayed in Fig. 11a, which reveals nearly 10% loss in MO degradation. In hydrogen generation, a recycling experiment of L-Bi₂S₃/ZnO has been performed up to the 5th cycle displayed in Fig. 11b. After the 5th cycle, no remarkable decline was found in the hydrogen evolution rate. Therefore, it can be concluded that the M-Bi₂S₃/ZnO and L-Bi₂S₃/ZnO heterostructures are stable and reusable visible light active photocatalysts for organic pollutant degradation as well as for hydrogen generation.

of the catalyst, XRD and FESEM were re-examined before and after catalytic reactions. As shown in Fig. 11c, the XRD patterns of the ZnO decorated Bi₂S₃ heterostructures almost remain the same and all the characteristic peaks are present. The FESEM image of the heterostructures reflects a similar kind of morphology after the photocatalytic reaction. Thus the semiconductor-based coupled heterostructures are stable under long visible light irradiation and represent a fruitful approach for solar light energy harvesting.

Photoelectrochemical performance

In order to investigate the photoelectrochemical activity of the Bi₂S₃/ZnO heterostructures, it is important to find out the band edge potential of both Bi₂S₃ and ZnO as band edge potentials play a crucial role in determining the migration routes of photo-generated electrons and holes. Additionally, photocatalytic activity directly depends on optical absorption, phase structure, morphology and separation efficiency of photo-generated charge carriers. The valence band (VB) and conduction band (CB) of both the semiconductors were calculated using the following empirical equations,⁴²

$$E_{\text{VB}} = x - E_{\text{fe}} + 1/2E_{\text{g}} \quad (11)$$

$$E_{\text{CB}} = x - E_{\text{fe}} - 1/2E_{\text{g}} \quad (12)$$

where E_{VB} and E_{CB} are the valence and conduction band edge potential respectively, and x is the geometric mean of the

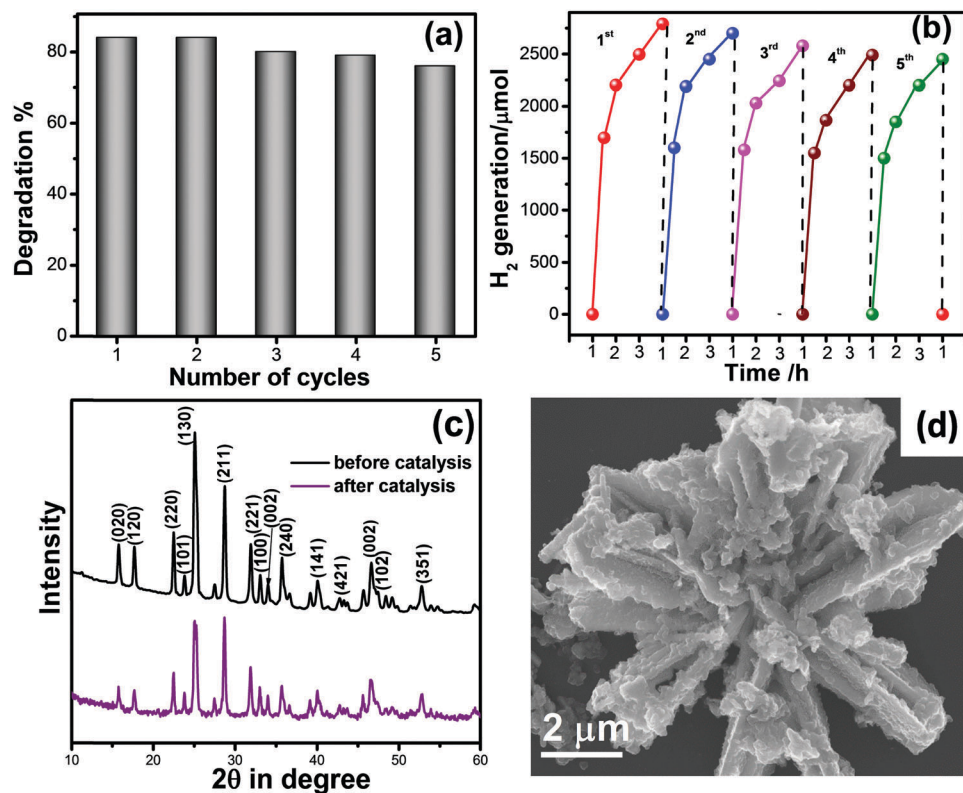


Fig. 11 Recycling test of (a) M-Bi₂S₃/ZnO during MO degradation and (b) L-Bi₂S₃/ZnO during hydrogen generation. (c) The XRD pattern and (d) FESEM image of L-Bi₂S₃/ZnO after and before the catalytic reaction of MO degradation and H₂ generation at pH 7.

electronegativity of the constituent atoms. E_{fe} is the energy of an electron on the hydrogen scale (4.5 eV) and E_g is the band gap of the semiconductor. The VB and CB edge potentials of Bi_2S_3 calculated using the above equations are 1.45 eV and 0.08 eV while for ZnO they are 3 eV and -0.2 eV respectively.^{67,68}

This difference in band edge potential is useful for better charge separation and migration which is favourable for photoelectrochemical performance.^{68,69} The photoelectrochemical activity of the catalyst has been examined by making a layer on an FTO-coated glass substrate through linear sweep voltammetry (LSV) under dark and light conditions with light irradiation. A 300 W xenon lamp with a water filter of 1 M NaNO_2 solution was used as the visible light (≥ 395 nm) source. Fig. 12a–c shows the difference in photo current density measured *via* LSV of the M- Bi_2S_3 , ZnO and M- $\text{Bi}_2\text{S}_3/\text{ZnO}$ catalysts in 0.1 M KOH solution using Pt wire as a counter and Ag/AgCl as a reference electrode at a scan rate of 20 mV s^{-1} . The photoelectrochemical performance in terms of current density is presented in Table 1. Bi_2S_3 shows a photocurrent response and the photocurrent density reached up to 0.11 mA cm^{-2} (Fig. 12a). A weak photocurrent was obtained for bare ZnO upon illumination in the applied potential range as shown in Fig. 12b. In contrast, the $\text{Bi}_2\text{S}_3/\text{ZnO}$ heterostructures demonstrated an enhanced photocurrent density of 0.25 mA cm^{-2} which is a 56% enhancement in comparison with bare ZnO NPs and Bi_2S_3 .

This result implies that the M- $\text{Bi}_2\text{S}_3/\text{ZnO}$ heterostructures show higher photoelectrochemical activity and a photo current

Table 1 Comparative study of current density measured from the photoelectrochemical studies performed in 0.1 M KOH solution as an electrolyte, Pt wire as a counter electrode and saturated Ag/AgCl as a reference electrode within the voltage range -0.4 V to 0.8 V under dark and light conditions

| Catalyst | Dark current (I_{dark}) (mA cm^{-2}) | Photo current (I_{light}) (mA cm^{-2}) | Photo current gain $I_{\text{light}}/I_{\text{dark}}$ |
|---------------------------------------|--|--|---|
| M- Bi_2S_3 | 0.039 | 0.112 | 2.88 |
| ZnO | 0.004 | 0.007 | 1.79 |
| M- $\text{Bi}_2\text{S}_3/\text{ZnO}$ | 0.029 | 0.255 | 8.79 |

gain which is *ca.* 3.05 times increased compared to the single component M- Bi_2S_3 . Notably, bare Bi_2S_3 also shows high photocurrent but due to fast recombination problems its photocurrent gain reduces. Thereby, the introduction of ZnO with Bi_2S_3 enhances light absorption and charge separation efficiency. The stability of pure semiconductor as well as heterostructures was investigated by the chronoamperometry method under light illumination for 200 seconds (Fig. 12d).⁶⁹ In the presence of light, a certain change in current density is displayed for M- Bi_2S_3 whereas a gradually increasing tendency is exhibited for the coupled system M- $\text{Bi}_2\text{S}_3/\text{ZnO}$ because of a charge transfer mechanism.¹⁷ As the photogenerated electrons migrate through the CB, more and more electrons are gathered at the active surface site and gradually increase the current density. Remarkably, Fig. 12d shows the long time $i-t$ response (up to 600 s) and the

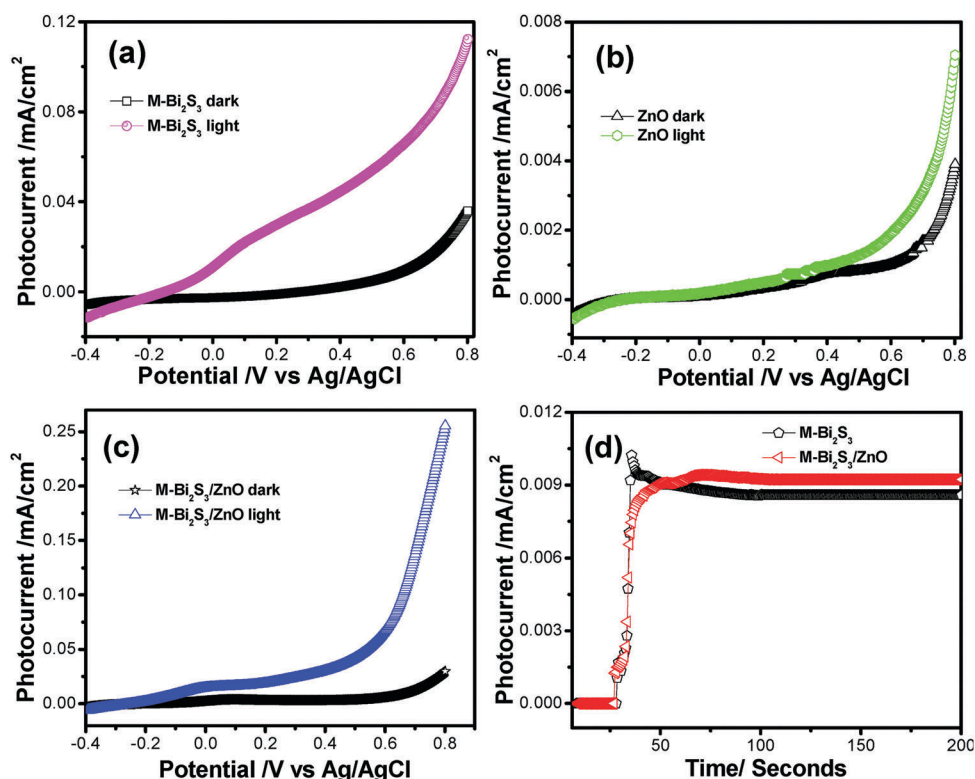


Fig. 12 Photoelectrochemical current density vs. potential plot of (a) M- Bi_2S_3 , (b) ZnO (5 nm) and (c) M- $\text{Bi}_2\text{S}_3/\text{ZnO}$ *via* the LSV method without light (dark) and under light illumination conditions at a scan rate 20 mV s^{-1} using 0.1 M KOH solution as an electrolyte, Pt wire as a counter electrode and Ag/AgCl as a reference electrode and (d) time dependence of photocurrent density at an external bias of 0.26 V vs. Ag/AgCl with illumination, at a scan rate of 20 mV s^{-1} for bare M- Bi_2S_3 and heterojunction M- $\text{Bi}_2\text{S}_3/\text{ZnO}$.

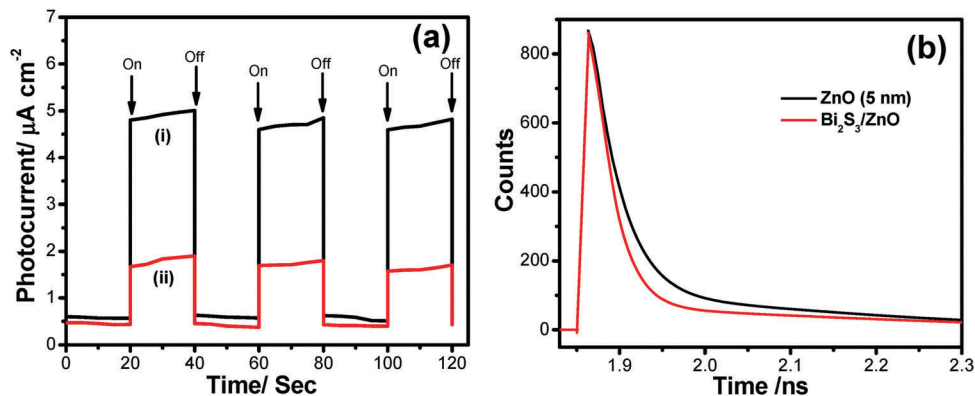


Fig. 13 (a) Comparative time-dependent photocurrent density response of the (i) M-Bi₂S₃/ZnO heterostructures and (ii) pure M-Bi₂S₃ with illumination switched on and off in air at a bias of 500 mV and (b) the picosecond-resolved PL spectra of ZnO (5 nm), M-Bi₂S₃ and M-Bi₂S₃/ZnO heterostructures.

current density remains almost stable which indicates that the catalysts are durable against photocorrosion. Hence, M-Bi₂S₃/ZnO shows enhanced photoelectrochemical activity compared to bare Bi₂S₃ and ZnO.

The photocurrent for Bi₂S₃ and the heterostructures shows 7.39 and 8.06 fold enhancement in current density compared with dark conditions at a voltage of 1.0 V respectively (Fig. S5, ESI[†]). This enhancement in current density may happen due to enhanced charge carrier separation in the presence of light irradiation. The linear nature of the *I*-*V* plot indicates the good ohmic contact between the semiconductor and the ITO-coated glass substrate which is a good sign for device applications.⁷⁰ When light falls on the catalyst surface, excess photocarriers are generated which leads to charge separation and electrons are efficiently transferred to the electrode when voltage is applied.⁷¹ The fluorescence decay curves at an excitation wavelength of 400 nm for ZnO and Bi₂S₃/ZnO have been examined to investigate the decay dynamics of the heterostructures.

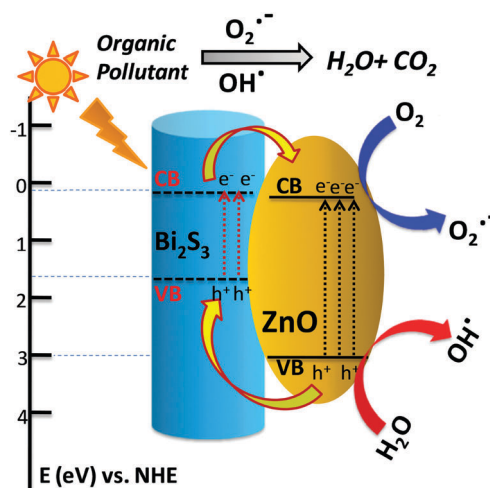
It is observed that the photocurrent is higher for heterostructures than single semiconductors. These charge carrier separation phenomena also enhance the mobility of electrons. The on/off photocurrent has been measured at 20 second intervals at a bias voltage 500 mV (Fig. 13a), which exhibits two distinct states – one is a high current state when the light is on and the other is a low current state while the light is off. This time-dependent response of the Bi₂S₃/ZnO-coupled system is preferable for optoelectronic device applications. In the photocatalytic process, super oxide radicals and holes have a crucial role in organic dye degradation which has been previously confirmed by lots of tests. Hence, the photo-excited electron and holes are responsible for generating these free radicals. Moreover, the enhanced charge separation have been studied *via* picosecond resolved time correlated single photon counting (TCSPC). Fig. 13b shows a decay curve of ZnO with an average life time of 4.34 ns. Interestingly, it decreases to 0.338 ns when Bi₂S₃ is attached with ZnO. From this sharp decrease in average life time, it can be concluded that fast electron transfer happens within the heterostructures through the CB of ZnO to Bi₂S₃.¹⁷ This charge transfer reduces the recombination rate, which can also be understood from the PL study, confirming

Table 2 Dynamics of picosecond-resolved luminescence transients and decay parameters of ZnO (5 nm) and Bi₂S₃/ZnO

| Sample | Excitation wavelength (nm) | Detection wavelength (nm) | τ_1 (ns) | τ_2 (ns) | τ_{avg} (ns) |
|-------------------------------------|----------------------------|---------------------------|---------------|---------------|--------------------------|
| ZnO NPs | 400 | 500 | 0.82 (51.8%) | 29.30 (7.5%) | 4.42 |
| Bi ₂ S ₃ /ZnO | 400 | 500 | 0.25 (42.0%) | 5.02 (7.9%) | 0.338 |

that more electrons may participate for photocatalytic water splitting and H₂ generation (Table 2).

Depending on the above results and discussion, a probable mechanism of photocatalytic activity can be described as follows. In the presence of solar light, both the semiconductors absorb light and the electrons in the VB get excited up to a higher potential of -1.53 eV for Bi₂S₃ and -0.2 eV for ZnO.⁵⁵ Therefore, the effective charge transfer process proceeds within the semiconductor due to high photon energy.⁴² Generally, the excited electrons and holes always wish to transfer to the nearest recombination centre. The CB electrons of the Bi₂S₃ rods can transfer to the CB of the ZnO NPs and simultaneously



Scheme 2 Proposed diagram for the possible band edge energy for charge separation and migration in the Bi₂S₃/ZnO heterostructures.

the excited holes of ZnO can migrate to the Bi₂S₃ rods and consequently reduce the first recombination process shown in Scheme 2. These photo-generated electrons and holes generate oxidative radicals (in the presence of O₂) such as h⁺, OH[•], and O₂^{•-} by the oxidation of O₂ and the reduction of H₂O which are mainly responsible for dye degradation. In hydrogen evolution, the sacrificial agent methanol acts as a hole scavenger and generates more OH[•] free radicals and accelerates the H₂ production rate. As the band position of Bi₂S₃ is not suitable for H₂ production, it can be concluded that photochemical reactions occur at the ZnO surface and incorporation of a narrow band gap semiconductor helps in charge separation, leading to more efficient activity in H₂ generation.^{69–72} On the other hand, the visible light activity can be explained on the basis of a hole-trapping mechanism which has been explained in the scheme diagram. Therefore, semiconductor heterojunctions are a suitable route for creating more recombination centres and thus increase the life time of electrons as well as reduce the recombination rate.

Conclusions

In summary, an assembled nanoflower morphology of Bi₂S₃ decorated with ZnO nanoparticles has been successfully synthesized by a facile *in situ* deposition method. The strong absorption of Bi₂S₃/ZnO heterostructures in the visible region and enhanced charge separation in the heterostructures makes them promising candidates for solar light harvesting applications. The experimental results indicate that M-Bi₂S₃/ZnO demonstrates high catalytic activity for organic pollutant degradation, whereas L-Bi₂S₃/ZnO shows superior performance for photocatalytic H₂ generation through water splitting. The photocatalytic activity of the heterostructures is ~8.6 times higher compared to bare Bi₂S₃. The L-Bi₂S₃/ZnO heterostructures (2791 μmol) exhibit 2.74 fold enhancements in photocatalytic hydrogen generation compared to L-Bi₂S₃ (1020 μmol) under visible light. Notably, Bi₂S₃/ZnO demonstrates high photoelectrochemical activity with a photo current density of 0.25 mA cm⁻², which is 56% and 97% higher than that of bare M-Bi₂S₃ and ZnO respectively under similar reaction conditions. The band edge potential of the heterostructures is suitable for sufficient charge separation which causes enhancement in photo current. Hence, the present synthetic methodology can be employed to prepare efficient, low cost heterostructure-based photocatalysts to substitute the common use of noble metal-based catalysts, and Bi₂S₃/ZnO has potential in environmental remediation and water-splitting applications.

Conflicts of interest

There are no conflicts to declare.

Acknowledgements

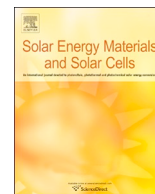
One of the authors (SB) is thankful to Department of Science & Technology (DST), India, for providing an INSPIRE fellowship.

Another author (SG) is thankful to the Council of Scientific & Industrial Research (CSIR), India, for providing a CSIR-Senior Research Associateship (Scientists' Pool Scheme). The authors also wish to thank Dr Sunirmal Jana and Dr Rajat Banerjee of this institute for their help by providing some of the instrumental facilities. The authors acknowledge Director, CSIR-CGCRI for his kind permission to publish the work.

References

- 1 M. R. Hoffmann, S. T. Martin, W. Choi and D. W. Bahnemann, *Chem. Rev.*, 1995, **95**, 69–96.
- 2 T. Jafari, E. Moharreri, A. S. Amin, R. Miao, W. Song and S. L. Suib, *Molecules*, 2016, **21**, 900–929.
- 3 Z. G. Zou, J. H. Ye, K. Sayama and H. Arakawa, *Nature*, 2001, **414**, 625–627.
- 4 D. J. Martin, K. Qiu, S. A. Shevlin, A. D. Handoko, X. Chen, Z. Guo and J. Tang, *Angew. Chem., Int. Ed.*, 2014, **53**, 9240–9245.
- 5 A. Kudo and Y. Miseki, *Chem. Soc. Rev.*, 2009, **38**, 253–278.
- 6 S. Ghosh, N. A. Kouame, S. Remita, L. Ramos, F. Goubard, P.-H. Aubert, A. Dazzi, A. Deniset-Besseau and H. Remita, *Sci. Rep.*, 2015, **5**, 18002–18011.
- 7 T. Hisatomi, J. Kubota and K. Domen, *Chem. Soc. Rev.*, 2014, **43**, 7520–7535.
- 8 Y. H. Ng, A. Iwase, A. Kudo and R. Amal, *J. Phys. Chem. Lett.*, 2010, **1**, 2607–2612.
- 9 H. Wang, L. Zhang, Z. Chen, J. Hu, S. Li, Z. Wang and J. Liu, *Chem. Soc. Rev.*, 2014, **43**, 5234–5244.
- 10 A. Fujishima and K. Honda, *Nature*, 1972, **238**, 37–38.
- 11 J. Tian, Z. Zhao, A. Kumar, R. I. Boughton and H. Liu, *Chem. Soc. Rev.*, 2014, **43**, 6920–6937.
- 12 L. Xu, G. A. Sewwandi, S. Uemura, T. Kusunose, S. Nakanishia and Q. Feng, *New J. Chem.*, 2017, **41**, 10998–11008.
- 13 G. Wang, H. Wang, Y. Ling, Y. Tang, X. Yang, R. C. Fitzmorris, C. Wang, J. Z. Zhang and Y. Li, *Nano Lett.*, 2011, **11**, 3026–3033.
- 14 J. Virkutyte and R. S. Varma, *New J. Chem.*, 2010, **34**, 1094–1096.
- 15 M. D. Hernandez-Alonso, F. Fresno, S. Suarez and J. M. Coronado, *Energy Environ. Sci.*, 2009, **2**, 1231–1257.
- 16 S. Piskunov, O. Lisovski, J. Begens, D. Bocharov, Y. F. Zhukovskii, M. Wessel and E. Spohr, *J. Phys. Chem. C*, 2015, **119**, 8686–18696.
- 17 S. Sardar, P. Kar, H. Remita, B. Liu, P. Lemmens, S. K. Pal and S. Ghosh, *Sci. Rep.*, 2015, **5**, 17313–17327.
- 18 J. Dutta, M. A. Mahmood and S. Baruah, *Mater. Chem. Phys.*, 2011, **130**, 531–535.
- 19 Q. Shen, X. Zhao, S. Zhou, W. Hou and J.-J. Zhu, *J. Phys. Chem. C*, 2011, **115**, 17958–17964.
- 20 K. M. Lee, C. W. Lai, K. S. Ngai and J. C. Juan, *Water Res.*, 2016, **88**, 428–448.
- 21 L. Zhang, L. Du, X. Yu, S. Tan, X. Cai, P. Yang, Y. Gu and W. Mai, *ACS Appl. Mater. Interfaces*, 2014, **6**, 3623–3629.

- 22 G. Marci, V. Augugliaro, M. J. López-Muñoz, C. Martin, L. Palmisano, V. Rives, M. Schiavello, R. J. D. Tilley and A. M. Venezia, *J. Phys. Chem. B*, 2001, **105**, 1026–1032.
- 23 R. Brahim, Y. Bessekhouad, A. Bouguelia and M. Trari, *Catal. Today*, 2007, **122**, 62–65.
- 24 S. Boumaza, B. Bellal, A. Boudjemaa and M. Trari, *Sol. Energy*, 2016, **139**, 444–451.
- 25 N. Qin, Y. Liu, W. Wu, L. Shen, X. Chen, Z. Li and L. Wu, *Langmuir*, 2015, **31**, 1203–1209.
- 26 S. J. Jum, G. K. Hyun, A. J. Upendra, W. J. Ji and S. L. Jae, *Int. J. Hydrogen Energy*, 2008, **33**, 5975–5980.
- 27 S. K. Dutta, S. K. Mehetor and N. Pradhan, *J. Phys. Chem. Lett.*, 2015, **6**, 936–944.
- 28 X. Li, J. Yu and M. Jaroniec, *Chem. Soc. Rev.*, 2016, **45**, 2603–2636.
- 29 J. Zhang, G. Xiao, F.-X. Xiao and B. Liu, *Mater. Chem. Front.*, 2017, **1**, 231–250.
- 30 L. Jing, J. Zhou, J. R. Durrant, J. Tang and D. Liu, *Energy Environ. Sci.*, 2012, **5**, 6552–6558.
- 31 C. Sotelo-Vazquez, R. Quesada-Cabrera, M. Ling, D. O. Scanlon, A. Kafizas, P. K. Thakur, T.-L. Lee, A. Taylor, G. W. Watson, R. G. Palgrave, J. R. Durrant, C. S. Blackman and I. P. Parkin, *Adv. Funct. Mater.*, 2017, **27**, 1605413.
- 32 S. J. A. Moniz, S. A. Shevlin, X. An, Z.-X. Guo and J. Tang, *Chem. – Eur. J.*, 2014, **20**, 15571–15579.
- 33 M. Xie, X. Fu, L. Jing, P. Luan, Y. Feng and H. Fu, *Adv. Energy Mater.*, 2013, **4**, 1300995.
- 34 F.-X. Xiao, *ACS Appl. Mater. Interfaces*, 2012, **4**, 7055–7063.
- 35 C. Eley, T. Li, F. Liao, S. M. Fairclough, J. M. Smith, G. Smith and S. C. E. Tsang, *Angew. Chem., Int. Ed.*, 2014, **53**, 7838–7842.
- 36 A. Abdi, A. Denoyelle, N. Commenges-Bernole and M. Trari, *Int. J. Hydrogen Energy*, 2013, **38**, 2070–2078.
- 37 L. X. Hao, G. Chen, Y. G. Yu, Y. S. Zhou, Z. H. Han and Y. Liu, *Int. J. Hydrogen Energy*, 2014, **39**, 14479–14486.
- 38 F. Dong, Z. Ni, P. Li and Z. Wu, *New J. Chem.*, 2015, **39**, 4737–4744.
- 39 Q.-Z. Huang, Y. Xiong, Q. Zhang, H.-C. Yao and Z.-J. Li, *Appl. Catal., B*, 2017, **209**, 514–522.
- 40 H. He, S. P. Berglund, P. Xiao, W. D. Chemelewski, Y. Zhang and C. B. Mullins, *J. Mater. Chem. A*, 2013, **1**, 12826–12834.
- 41 M. Li, J. Wang, P. Zhang, Q. Deng, J. Zhang, K. Jiang, Z. Hu and J. Chu, *Sci. Rep.*, 2017, **7**, 42484–42492.
- 42 R. P. Panmand, Y. A. Sethi, R. S. Deokar, D. J. Late, H. M. Gholap, J.-O. Baeg and B. B. Kale, *RSC Adv.*, 2016, **6**, 23508–23517.
- 43 C. Zhang, Y. Zhou, Y. Zhang, S. Zhao, J. Fang and X. Sheng, *New J. Chem.*, 2017, **41**, 11089–11096.
- 44 J. Zhou, G. Tian, Y. Chen, Y. Shi, C. Tian, K. Pan and H. Fu, *Sci. Rep.*, 2014, **4**, 4027–4035.
- 45 X. Gao, H. B. Wu, L. Zheng, Y. Zhong, Y. Hu and X. W. Lou, *Angew. Chem., Int. Ed.*, 2014, **53**, 5917–5921.
- 46 F. Dong, X. Feng, Y. Zhang, C. Gao and Z. Wu, *RSC Adv.*, 2015, **5**, 11714–11723.
- 47 D. Lu, H. Wang, X. Zhao, K. K. Kondamareddy, J. Ding, C. Li and P. Fang, *ACS Sustainable Chem. Eng.*, 2017, **5**, 1436–1445.
- 48 S. S. Thind, C. C. Mustapic, J. Wen, C. D. Goodwin and A. Chen, *New J. Chem.*, 2017, **41**, 10542–10549.
- 49 Q. Liu, J. Huan, N. Hao, J. Qian, H. Mao and K. Wang, *ACS Appl. Mater. Interfaces*, 2017, **9**, 18369–18376.
- 50 H. Bao, X. Cui, C. M. Li, Y. Gan, J. Zhang and J. Guo, *J. Phys. Chem. C*, 2007, **111**, 12279–12283.
- 51 M. G. Mendez-Medrano, E. Kowalska, A. Lehoux, A. Herissan, B. Ohtani, S. Rau, C. Colbeau-Justin, J. L. Rodriguez-Lopez and H. Remita, *J. Phys. Chem. C*, 2016, **120**, 25010–25022.
- 52 B. Li, Y. Zhang, R. Du, L. Gan and X. Yu, *Langmuir*, 2016, **32**, 11639–11645.
- 53 S. Hernández, V. Cauda, A. Chiodoni, S. Dallorto, A. Sacco, D. Hidalgo, E. Celasco and C. F. Pirri, *ACS Appl. Mater. Interfaces*, 2014, **6**, 12153–12167.
- 54 Y. Wang, J. Chen, P. Wang, L. Chen, Y.-B. Chen and L.-M. Wu, *J. Phys. Chem. C*, 2009, **113**, 16009–16014.
- 55 S. Khanchandani, S. Kundu, A. Patra and A. K. Ganguli, *J. Phys. Chem. C*, 2013, **117**, 5558–5567.
- 56 J. Zhang, L. Zhang, N. Yu, K. Xu, S. Li, H. Wang and J. Liu, *RSC Adv.*, 2015, **5**, 75081–75088.
- 57 A. Priyam, S. Ghosh, S. C. Bhattacharya and A. Saha, *J. Colloid Interface Sci.*, 2009, **331**, 195–201.
- 58 S. Ghosh, A. Priyam, S. C. Bhattacharya and A. Saha, *J. Fluoresc.*, 2009, **19**, 723–731.
- 59 S. Ghosh, M. Ray, M. Das, A. Chakrabarti, A. H. Khan, D. D. Sarma and S. Acharya, *Phys. Chem. Chem. Phys.*, 2014, **16**, 5276–5283.
- 60 M. Han and J. Jia, *J. Power Sources*, 2016, **329**, 23–30.
- 61 X. Zhang, J. Qin, Y. Xue, P. Yu, B. Zhang, L. Wang and R. Liu, *Sci. Rep.*, 2014, **4**, 4596–4604.
- 62 S. Ghosh, N. A. Kouame, L. Ramos, S. Remita, A. Dazzi, A. Deniset-Besseau, P. Beaunier, F. Goubard, P.-H. Aubert and H. Remita, *Nat. Mater.*, 2015, **14**, 505–511.
- 63 W. Cui, J. Li, F. Dong, Y. Sun, G. Jiang, W. Cen, S. C. Lee and Z. Wu, *Environ. Sci. Technol.*, 2017, **51**, 10682–10690.
- 64 J. Sun, J. Zhang, M. Zhang, M. Antonietti, X. Fu and X. Wang, *Nat. Commun.*, 2012, **3**, 1139.
- 65 S. Luo, F. Chai, L. Zhang, C. Wang, L. Li, X. Liu and Z. Su, *J. Mater. Chem.*, 2012, **22**, 4832–4836.
- 66 F. Ozel, E. Aslan, B. Istanbulu, O. Akay and I. H. Patir, *Appl. Catal., B*, 2016, **198**, 67–73.
- 67 B. Tian and Y. Wu, *Appl. Catal., B*, 2017, **204**, 33–42.
- 68 C. Liu, Y. Yang, W. Li, J. Li, Y. Li and Q. Chen, *Sci. Rep.*, 2016, **6**, 23451–23463.
- 69 C. Liu, Y. Yang, W. Li, J. Li, Y. Li and Q. Chen, *Int. J. Hydrogen Energy*, 2016, **41**, 1–9.
- 70 J. Kundu, S. Khilari and D. Pradhan, *ACS Appl. Mater. Interfaces*, 2017, **9**, 9669–9680.
- 71 X. Zhang, Y. Liu, G. Zhang, Y. Wang, H. Zhang and F. Huang, *ACS Appl. Mater. Interfaces*, 2015, **7**, 4442–4448.
- 72 Y.-Q. Zhang, S. Li and B.-P. Zhang, *RSC Adv.*, 2016, **6**, 103215–103223.



Photocatalytic hydrogen generation using gold decorated BiFeO₃ heterostructures as an efficient catalyst under visible light irradiation

Susmita Bera^a, Srabanti Ghosh^{a,*}, Sanjib Shyamal^b, Chinmoy Bhattacharya^b, Rajendra N. Basu^{a,*}

^a Fuel Cell & Battery Division, CSIR - Central Glass and Ceramic Research Institute, 196, Raja S. C. Mullick Road, Kolkata 700032, India

^b Department of Chemistry, Indian Institute of Engineering Science & Technology (IIEST), Shibpur, Howrah 711103, West Bengal, India



ARTICLE INFO

Keywords:

Visible light photocatalyst
BiFeO₃
Heterostructures
Plasmonic Au nanoparticles
Photoelectrochemical properties
H₂ generation

ABSTRACT

Perovskites based oxides materials with a suitable energy level have been considered as efficient photocatalysts for solar hydrogen generation. Gold nanoparticles (Au NPs)-sensitized BiFeO₃ (BFO) perovskite heterostructures were synthesized, characterized and tested for hydrogen generation under visible light ($\lambda > 420$ nm) irradiation. Au/BFO heterostructures were synthesized using a facile hydrothermal method followed by radiolysis without using any surfactant or strong reducing agent. The shape-dependent photocatalysis revealed that the BFO octahedron (BFO-Oct) exhibited higher hydrogen generation ($1.4 \text{ mmol h}^{-1} \text{ g}^{-1}$) than the BFO nanosheets (BFO-Ns) ($1.1 \text{ mmol h}^{-1} \text{ g}^{-1}$) and BFO cylindrical shaped (BFO-Cyl) ($0.5 \text{ mmol h}^{-1} \text{ g}^{-1}$). After radiolytic construction of the Au/BFO heterostructure, more efficient hydrogen generation was obtained due to the photoinduced electron transfer. The photoresponse of the Au/BFO heterostructures was also assessed in terms of the photocurrent via photoelectrochemical (PEC) measurement which showed Au/BFO-Ns generated higher photocurrents than BFO-Ns by a factor of ~ 3.8 . The Nyquist plot demonstrated facile charge transfer of BFO-Ns after formation of heterojunction with Au NPs. The Mott-Schottky plot revealed that catalysts are n-type and photo-generated charge carrier concentration has been increased for Au/BFO heterostructures ($0.92 \times 10^{17} \text{ cm}^{-3}$) compared to pure BFO ($0.47 \times 10^{17} \text{ cm}^{-3}$). On the basis of experimental results, the enhanced photocatalytic activities of Au/BFO heterostructures could be ascribed to the significant visible light absorption and the efficient charge carrier separation. This study offers a new route to design noble metal modified perovskites based heterostructure as photocatalysts for water splitting.

1. Introduction

The concept of solar hydrogen generation by water splitting using photocatalysts has received significant attention as it is an ecofriendly and sustainable method [1–3]. In this regard, semiconductor based photocatalysis has been extensively investigated for potential applications in environmental remediation and water splitting [3,4]. During the past few decades, tremendous efforts have been devoted to develop efficient, low-cost and stable photocatalysts under visible light for removal of environmental pollutants, photocatalytic and photoelectrochemical hydrogen generation through water splitting [4–7]. Among a large number of photocatalysts, perovskite oxides based semiconductors have drawn much interest because of their structural simplicity and flexibility, good stability and relatively narrow band gaps of these materials allow them to harness the visible light of solar irradiation [8,9]. Among these perovskite materials, bismuth ferrite (BiFeO₃, BFO) is a potential multiferroic semiconductor in which

ferroelectric and antiferromagnetic properties coexist at room temperature which generates internal electric field by switching the spontaneous polarization [10,11]. The moderate band gap (~ 2.3 eV) with direct transition feature, suitable band alignment to oxidize or reduce water, good chemical stability, low cost and biocompatibility of BFO make it attractive for practical use in visible light induced photocatalysis. Moreover, Yang et al. [12] discovered a giant open-circuit photovoltage for ferroelectric semiconductors which enhances the charge separation efficiency of ferroelectric semiconductors compared to other conventional semiconductors. Inspired by this concept, it has been assumed that spontaneous polarization due to ferroelectricity of BFO could be an effective approach to harness solar energy in water splitting.

Recently, multidimensional BFO nanostructures have been fabricated to control the exposed facets, size and growth directions as these have significant effect in determining the electrical, magnetic, and optical properties [13]. For example, Fei et al. [14] prepared three

* Corresponding authors.

E-mail addresses: ghosh.srabanti@gmail.com (S. Ghosh), rmbasu@cgcrci.res.in (R.N. Basu).

different microstructures of BiFeO₃ where pills and rods showed an enhanced visible light response due to presence of {111} facets but catalytic application has not been performed yet. Further, Bai et al. [15] reported size dependent (30–190 nm) photocatalytic activity of BiFeO₃ NPs for organic dye (methyl orange, MO) degradation but efficiency was very low. Wang et al. [16] also prepared spindles, cubes and plates like morphology of BiFeO₃ where plates like morphology showed maximum efficiency (50%) in photocatalytic MO degradation. Therefore, to improve the photocatalytic activity of BFO, it has been coupled with other co-catalysts, such as SrTiO₃, Bi₂Fe₄O₉, TiO₂, CuS, g-C₃N₄ and reduced graphene oxide to develop heterostructured materials [17–20]. Generally, heterojunction is the interface between two different materials with unequal band structures resulting a band alignments which in turn creates a space-charge region at the interface and forms an electric field causes the diffusion of charge carriers [21]. As a result, spatial charge separation occurs at the interface which can promote the photocatalytic activity of the heterostructured materials [22–25]. More interestingly, charge carrier recombination may be suppressed in a heterostructure as the excited carriers can transfer to the nearest electronic state. For example, Zhang et al. [18] prepared BiFeO₃/Bi₂Fe₄O₉ heterojunction by an electrospinning technique where heterojunction showed enhanced photocatalytic activity compared to the single components due to fast charge transfer and lower recombination, although the kinetics of the catalytic reaction is very slow. Li et al. [20] reported that, heterojunction of BiFeO₃ with graphene effectively reduce the size of the BiFeO₃ particles which effectively enhance the photocatalytic activity due to increase specific surface area but the stability of the composite in air and multistep synthesis using strong oxidizing agent remains an issue. Upto now, these heterostructure based photocatalysts have been used mostly for organic pollutant degradation under visible light but clean solar fuel generation are still limited yet.

On the other hand, integration of noble metal NPs to semiconductor photocatalysts can offer an effective way to improve their photocatalytic activities under visible region. In fact, noble metal NPs (Au, Ag, Pt, Pd, Cu) modified TiO₂, graphene and polymer also showed enhanced photocatalytic activity under visible light irradiation [26–31]. For instance, Niu et al. [32] reported Pt modified BFO exhibited 70% photocatalytic degradation activity for MO under visible light irradiation. Li et al. [33] also confirmed the enhanced photocatalytic activity of Au NPs deposited BiFeO₃ nanowires under visible-light for O₂ evolution due to Surface-Plasmon effect (SPR) of Au NPs. Recently, Li et al. [34] showed enhanced photovoltaic effect of noble metal Au modified La doped BiFeO₃ films. Moreover, Ag loaded BFO nanostructures showed enhanced photocatalytic degradation of methylene blue (MB) under visible light [35,36]. It has been reported that, noble metal NPs can exhibit SPR effect, (a collective oscillation of conduction band electrons due to interaction with visible light photons) which induced a local electromagnetic field at the interface of the semiconductor photocatalyst, consequently promotes the charge-carrier separation efficiency [27,28]. When plasmonic metal NPs brought into an approximate distance, coupling of their localized electromagnetic field may happen and generate large number of hot electrons which may influence the photocatalytic reactions [37]. Moreover, noble metal NPs can also act as electron or hole acceptor and improves charge separation efficiency of the adjacent nanostructure as well as they provide active catalytic sites [38,39]. However, to the best of our knowledge, the photocatalytic H₂ generation through water splitting using noble metal modified BFO as a catalyst is not reported yet.

In this work, BFO and BFO based metal-semiconductor heterostructures have been developed to study the photocatalytic H₂ generation and photoelectrochemical water splitting. Different morphologies of BFO have been successfully synthesized by hydrothermal method and, then plasmonic metal NPs have been deposited on BFO nanostructures by radiolysis technique. Experimental results reveal that, metal-semiconductor heterostructures are efficient photocatalyst for H₂ generation under visible light irradiation.

2. Experimental section

2.1. Reagents

Bismuth nitrate pentahydrate [Bi(NO₃)₃·5H₂O, 99.99%], gold(III) acetate, methanol were obtained from Sigma Aldrich, USA. Anhydrous FeCl₃ and sodium hydroxide (NaOH, 98%) were obtained from the Alfa Aesar chemicals and Merck, Germany respectively. All compounds were used as received and ultrapure water (Millipore System, 18.2 MU cm) was used as solvent.

2.2. Synthesis of BiFeO₃ nanosheets (BFO-Ns)

In a typical synthesis of BFO nanostructures, Bi(NO₃)₃·5H₂O and FeCl₃ in a stoichiometric ratio (1:1 in molar ratio) were dissolved in acetone (50 ml) under stirring and ultrasonication until completely dissolved. Then, 50 ml distilled water was added with the solution and mixed properly. After that, NH₃ was added drop wise until the pH value of the mixed solution reached 10–11. The precipitation was then centrifuged and washed with distilled water several times until the pH value of the solution was neutral. Next, the brown co-precipitate was redispersed in 100 ml distilled water with vigorous stirring. Calculated amount of NaOH (2 M, 5 M and 12 M) were added into the solution and stirred for 30 min. Finally, the solution was transferred into a stainless steel autoclave with a Teflon liner and heated at 180 °C for 72 h. After cooling down to room temperature, the black powder was collected by filtration, washed with distilled water and ethanol for several times, and dried at 50 °C for 12 h.

2.3. Synthesis of Au/BFO-Ns heterostructures

Au/BFO-Ns heterostructures were obtained using steady state gamma irradiation in presence of gold acetate salts [40–42]. In this experiment, to synthesize Au NPs on BFO-Ns, BFO solution (1 mg ml⁻¹), gold (III) acetate (1 mM), solution were mixed in an ultrasonic bath for 30 min, followed by deoxygenated under Argon flow. Subsequently, the solution was irradiated for 1 h (dose rate = 8 kGy h⁻¹) using a ⁶⁰Co gamma-facility. After that, black precipitation of Au/BFO-Ns was centrifuged and washed several times with ethanol and water and finally dried at 50 °C for overnight. For comparison, control Au NPs were synthesized by colloidal method

2.4. Characterizations

The crystalline phase of BFO-Ns and Au/BFO-Ns heterostructures were investigated by XRD (Philips X'Pert, The Netherlands) within 2θ range 10–80° at slow scan rate of 1° min⁻¹ with Cu Kα radiation (at 40 kV and 40 mA). The structural morphology and EDS was recorded by Field Emission Scanning Electron Microscopy (LEO. 430i, Carl-Zeiss, Sigma). Transmission Electron Microscopy (TEM) images and the corresponding selected area electron diffraction (SAED) patterns were obtained on Tecnai G² 30ST (FEI) operating at 300 kV. The XPS-study was performed using PHI 5000 Versa Probe II spectrophotometer (Physical Electronics Inc., USA) using a monochromatized Al Kα (~1486.6 eV) X-ray beam of size ~100 μm. Samples were prepared in pallet form and surfaces were sputtered with a 2 kV rastered Ar⁺ ion beam for one minute to clean the surface. The porosity and specific surface area of the samples were determined through nitrogen adsorption at 200 °C on the basis of BET equation using Quantachrome, FL-33426. The diffuse reflectance spectra of BFO-Ns and Au/BFO-Ns were recorded using a Shimadzu, UV-3600 spectrophotometer. The photoluminescence (PL) spectrum of as synthesized materials was taken by JASCO FP-8500. The hydrogen evolution was measured by online gas chromatography using YL Instrument, 6500GC system with thermo conductive detector. The magnetic properties of the samples were measured using a VSM (Lake Shore Cryotronics) at a maximum field of 16 kOe at room temperature.

2.5. Photocatalytic H₂ generation

To study the hydrogen generation, online gas chromatography was used and the area under the Gaussian peak gives the amount of H₂ evolved. The experiment was performed in a closed reactor containing 50 ml solution with a catalyst concentration of 1 mg ml⁻¹ with saturated argon media under vigorous stirring. For this experiment, 25 vol% methanol solution was used at room temperature. Here, methanol acts as sacrificial agent and a Xe-arc lamp (250 W) with an incident beam intensity of 100 mW/cm² was used as light source for visible irradiation and a 420 nm cutoff filter was used.

2.6. Photoelectrochemical measurements

Photoelectrochemical measurement was performed using a galvanostat-potentiostat (PGSTAT302N, Autolab, The Netherlands) with a standard three-electrode cell and Pt wire as counter electrode and saturated Ag/AgCl as reference electrode. The working electrode was thin film of as prepared material on FTO by doctor-blade method. For the doctor-blade method, a BFO and Au/BFO paste was prepared as following: BFO or Au/BFO powder (1 mg) was mixed with ethylene glycol (EG, 2.5 ml) in a centrifuge tube under sonication for 20 min. After that, the resulting paste was coated on FTO glass (conducting side) to make a thin film using a doctor-blade method. Finally, the coated slides were then carefully placed inside a muffle furnace maintained at 400 °C for 4 h. Yellowish BiFeO₃ and Au/BiFeO₃ coated FTO glasses were obtained successfully. The linear sweep voltammetry was carried out within the potential range -0.2 V to 0.8 V vs Ag/AgCl at a scan rate 10 mV/s using 0.1 M Na₂SO₄ phosphate buffer (pH 7) as electrolyte. The PEC measurements of these electrodes were carried out with a 0.27 cm² geometric area exposure (using O-ring of the same inner area) to the electrolyte solution under light irradiation. The stability of BFO-Ns and Au/BFO-Ns were tested through chronoamperometry at 0.6 V vs Ag/AgCl potential (~1.2 V vs RHE), which is the theoretical onset voltage for water splitting in absence of light where normally no current would flow. The photo response of BFO-Ns and Au/BFO-Ns was measured under periodic chopped irradiation from Xe-arc lamp (100 W, Hamaan, India) as a white-light source with an incident beam intensity of 100 mW/cm². The potential was then converted to the reference hydrogen electrode (RHE) following the Eq. (1).

$$E_{\text{RHE}} = E_{\text{Ag/AgCl}} + 0.059 \text{ pH} + 0.197 (E_{\text{Ag/AgCl}}^0) \quad (1)$$

After that, photoelectrochemical action spectrum was studied through chronoamperometry under chopped monochromatic illumination (using an Oriol monochromator, USA) within the wavelength range of 300–700 nm. Then incident photon to current conversion efficiency (IPCE) and absorbed photon to current conversion efficiency (APCE) was calculated according to the Eqs. (2) and (3):

$$\text{IPCE}(\%) = \frac{I_{\text{ph}}}{P_{\text{in}}} \times \frac{1240}{\lambda} \times 100 \quad (2)$$

$$\text{APCE}(\%) = \frac{\text{IPCE}}{(1-10^{-A_{\lambda}})} \times 100 \quad (3)$$

where, I_{ph} is the output photocurrent density (A/cm²), P_{in} is the incident power density (W/cm²), λ is wavelength (nm) and A_{λ} is the absorbance of the material at any particular wavelength (λ).

Capacitance measurements were carried out using same instrument in a borosilicate glass cell with three-electrode configuration. The capacitance measurements of the electrodes were carried out with a 0.27 cm² geometric area exposure (using O-ring of the same inner area) to the electrolyte solution under light irradiation. To study the behavior of the semiconductor-electrolyte interface, a phosphate buffer (pH 7) with 0.1 M Na₂SO₄ was used as working solution. Experiments were done within the potential range of -0.6 V to 0.2 V vs Ag/AgCl using ac RMS amplitude of 10 mV at 1000 Hz frequency.

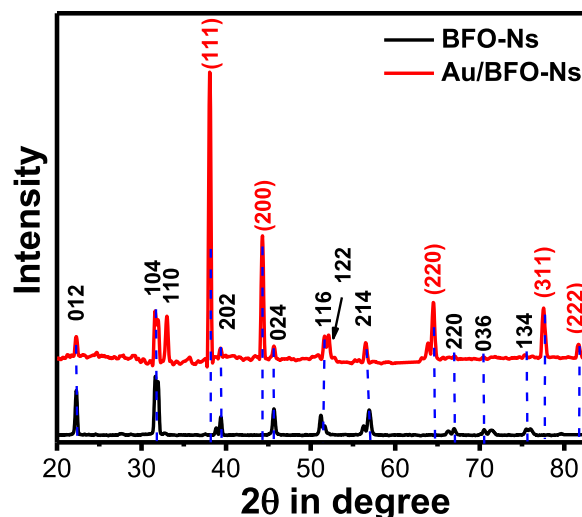


Fig. 1. X-ray powder diffraction pattern of pure BFO-Ns and Au/BFO-Ns heterostructures.

3. Results and discussion

3.1. Phase purity and crystal structure

Fig. 1 shows the XRD pattern of the pure BFO-Ns and Au/BFO-Ns heterostructures. All the diffraction peaks of pure BFO-Ns can be indexed as rhombohedral phase with R3c space group (JCPDS 86–1518). The corresponding lattice parameters are $a = 0.5577$ nm, $b = 0.5577$ nm and $c = 1.3862$ nm [32,43]. No additional peaks are found, demonstrating that single crystalline phase BFO-Ns powder has been successfully prepared. In Au/BFO-Ns heterostructures, the characteristic diffraction peaks of Au NPs at 2θ values 38.13°, 44.28°, 64.55°, 77.57° and 81.85° corresponds to (111), (200), (220), (311), and (222) planes respectively are present without changing the BFO-Ns peaks, which confirms the heterostructure formation [41,42].

3.2. Microstructures

Fig. 2 represents the FESEM and TEM images of pure BFO-Ns and Au/BFO-Ns heterostructures. The FESEM image illustrates that, microcubes (~922 nm sides) are formed at NaOH concentration of 5 M along with small hexagonal nanosheets on the surface (Fig. 2a). In addition, the TEM image clearly shows that cubes and hexagonal nanostructures of BFO in an irregular pattern are present (Fig. 2b). As BFO has magnetic property, the cubic structures may form due to the staking of hexagonal nanosheets. Interestingly, the high magnification TEM image (Fig. 2c) shows that hexagonal nanostructures of BFO with edges ~228 nm and width 7.5 nm have been formed at NaOH concentration of 5 M. The interplanar spacing of 0.39 nm calculated from the HRTEM image (Fig. 2d) is in good agreement with the spacing of (012) plane of BFO [14]. Moreover, a corresponding SAED pattern confirms the presence of (012) and (110) planes (Inset of Fig. 2d) which has been taken from one single BFO-Ns. The SAED and HRTEM images reveal that the BFO-Ns are single-crystal.

Fig. 2e and f show the low and high magnification TEM images of Au/BFO-Ns heterostructures where Au NPs have been formed in a homogeneous distribution pattern on the BFO-Ns after γ radiation. The average particle size of the Au NPs is found to be ~17 nm. The energy-dispersive X-ray spectroscopy (EDX) spectrum of the Au/BFO-Ns heterostructures has been illustrated in Fig. 3a. The strong peaks of Bi, Fe, O, and Au elements in EDX spectrum indicate that aforementioned elements are present within the heterostructures. Since, the atomic ratio of Bi, Fe and O is about 1:1:3, which is close to the stoichiometric

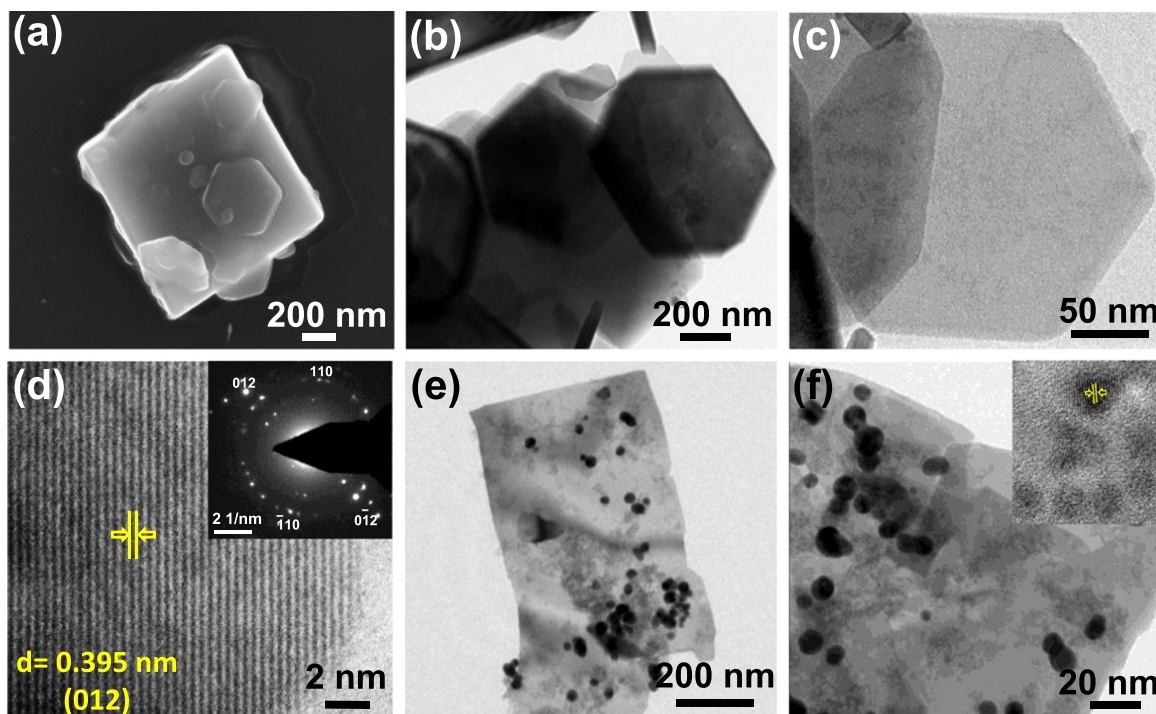


Fig. 2. (a) FESEM image, (b, c) low and high magnification TEM images and (d) HRTEM of BFO Nanosheets (BFO-Ns). Inset d: SAED pattern of BFO nanosheets. (e, f) Low and high magnification TEM images of Au/BFO-Ns heterostructures. Inset f: HRTEM image of Au/BFO-Ns heterostructure. All the samples are prepared at NaOH concentration of 5 M.

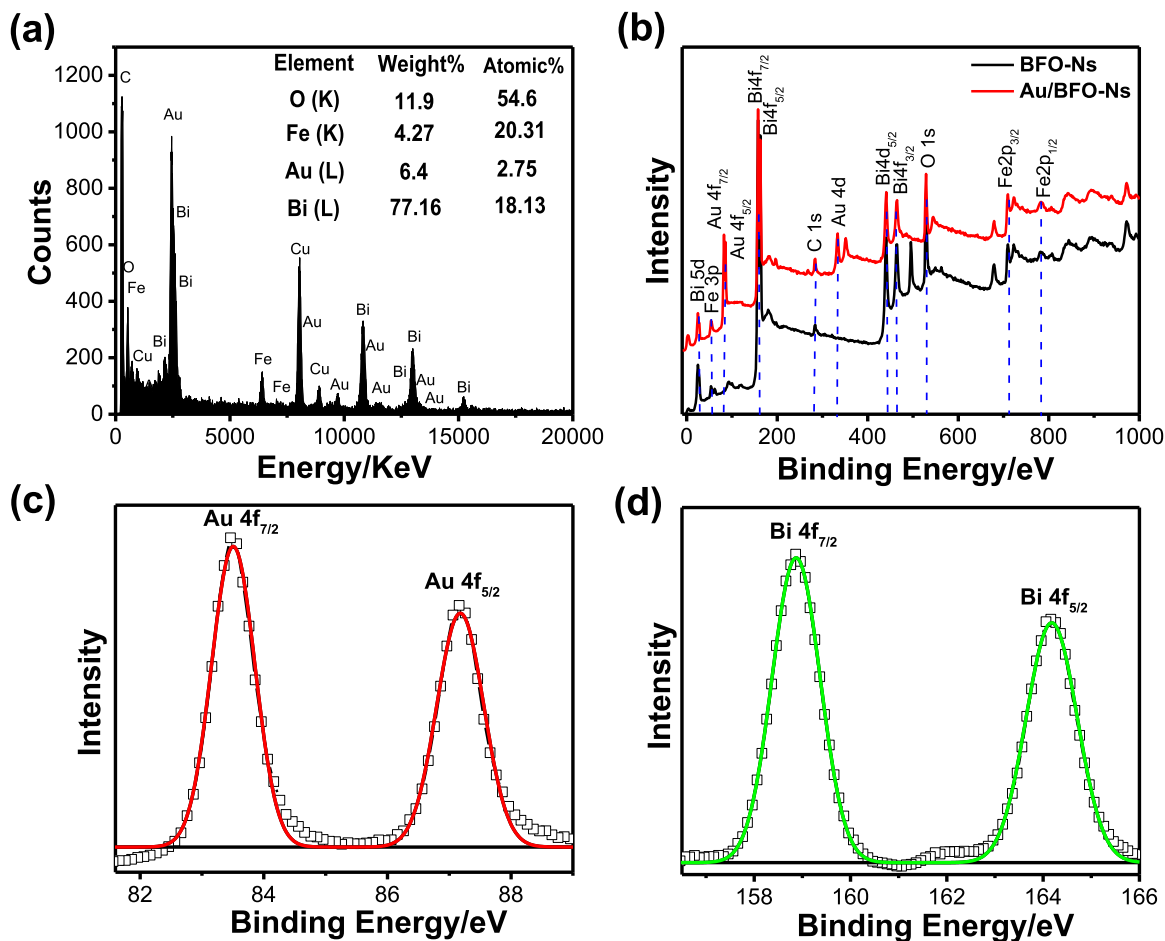


Fig. 3. (a) Energy-dispersive X-ray spectra (EDX) of Au/BFO-Ns heterostructures. X-ray photoelectron spectroscopy (XPS) of (b) pure BFO-Ns and Au/BFO-Ns heterostructures, (c) Au and (d) Bi of Au/BFO-Ns heterostructures.

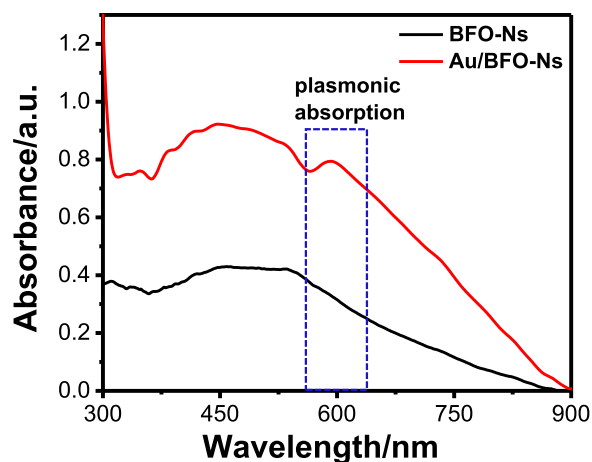


Fig. 4. Diffuse reflectance spectra of pure BFO nanosheets (BFO-Ns) and Au/BFO-Ns heterostructures.

ratio of BFO. Therefore, heterojunction formation of Au and BFO does not change the stoichiometric ratio of the BFO itself.

3.3. X-ray photoelectron spectroscopy and surface compositions

Furthermore, to study the chemical states of Au, Bi, Fe and O in the Au/BFO-Ns heterostructures and to investigate the detailed insight into the interaction between Au NPs and BFO nanostructures, X-ray photoelectron spectroscopy (XPS) has been employed. Fig. 3b shows the overall XPS spectra of pure BFO-Ns and Au/BFO-Ns heterostructures where oxidation states of Bi, Fe, O and Au are present. The XPS peaks observed for Au 4f at binding energy 53.5 eV and 87.17 eV corresponds to Au 4f_{7/2} and Au 4f_{5/2}, confirm the presence of Au(0) state within the heterostructures (Fig. 3c) [33]. The presence of the doublet Bi 4f peaks at binding energy 158.13 eV and 163.41 eV corresponds to Bi 4f_{7/2} and Bi 4f_{5/2} indicate that bismuth existed in a single chemical state of Bi³⁺ (Fig. 3d) [32]. More interestingly, a red shifting has been observed for Bi 4f peaks after heterojunction formation which suggests the occurrence of strong interaction and charge transfer between Au NPs and BFO-Ns (Fig. S1a). The binding energy of peaks at 710.15 eV and 723.41 eV arise due to Fe 2p_{3/2} and Fe 2p_{1/2} states and the satellite peak at 718.32 eV (8.17 eV above the Fe 2p_{3/2}) confirms that Fe is at Fe³⁺ state within BFO (Fig. S1b) [32,44]. Hence, the XPS spectrum of O1s for pure BFO-Ns shows (Fig. S1c) two peaks at 529.1 eV and 530.77 eV correspond to oxygen-metal bonds and surface adsorbed oxygen respectively, whereas for Au/BFO-Ns heterostructure, single peak at 529.67 eV has been observed [45]. This observation indicates that, surface adsorbed oxygen are removed after heterostructure formation as the Au NPs occupy the surfaces of the BFO-Ns. Therefore, it can be concluded from XPS data, Bi and Fe exist in the states of Bi³⁺ and Fe³⁺ within BFO-Ns and Au in zero oxidation state within heterostructures.

The porous structure of the pure semiconductor BFO-Ns and the heterostructures Au/BFO-Ns has been studied by the nitrogen adsorption desorption isotherm method. The hysteresis loop present in the BET curve (Fig. S2) suggests the type II pattern of BFO-Ns and Au/BFO-Ns heterostructures. The specific surface areas calculated by the Barrett-Joyner-Halenda (BJH) method of pure BFO-Ns and Au/BFO-Ns heterostructures are 10 m² g⁻¹ and 35 m² g⁻¹, respectively. Therefore, it indicates that larger inter-aggregated pores were generated in heterostructures and became predominant with higher adsorption capacity. This could be confirmed by the TEM images that the total specific surface area of Au/BFO-Ns has been increased because of added surface area of the Au NPs with BFO nanosheet (Fig. 2e and f). Hence, it is expected that photocatalytic activity of heterostructures might be enhanced due to increased surface area by the incorporation of Au NPs.

3.4. UV-Vis spectroscopy

To investigate the influence of heterostructure formation on the optical absorption and electronic band structure of the BFO-Ns, UV-Vis diffuse reflectance spectra (DRS) has been employed. Fig. 4 shows the UV-Vis absorption spectra of BFO-Ns and Au/BFO-Ns, which are converted from the measured diffuse reflectance spectra by means of the Kubelka-Munk Function [32]. Au/BFO-Ns show two striking features of the absorption spectra. First, a characteristic absorption peak at ~600 nm has been observed which is mainly attributed due to plasmonic absorption of Au NPs [27]. Secondly, the existing peaks of BFO-Ns at 350 nm and 450 nm have been increased which may arise due to strong electronic interaction of Au NPs with BFO-Ns.

Further, the direct band gaps of BFO-Ns (2.3 eV) and Au/BFO-Ns (2.1 eV) have been calculated from the Kubelka-Munk [(αhν)² vs photon energy (hν)] plot (Fig. S3). This lowering of band gap from 2.3 eV to 2.1 eV for Au/BFO-Ns heterostructures is useful for enhanced absorption in visible region and consequently may enhance the photocatalytic activity.

3.5. Photocatalytic hydrogen production

Photocatalytic activity of as synthesized materials has been evaluated by photocatalytic H₂ generation through water reduction. Fig. 5a shows the photocatalytic H₂ generation of pure semiconductor BFO-Ns and Au/BFO-Ns heterostructures through water reduction under visible light irradiation (λ > 420 nm) in presence of methanol (25 vol%) as sacrificial agent at pH 7. Here methanol acts as hole scavenger, i.e. reacted with the photogenerated holes usually faster than water, lead to excess electron in the medium for H₂ generation by water reduction. Au/BFO-Ns heterostructures exhibit enhanced photocatalytic H₂ generation (2.1 mmol) compared to pure BFO-Ns (1.1 mmol) after 2 h irradiation. Interestingly, the hydrogen evolution rate increased linearly with time after a certain time (Fig. S4a), demonstrating that the catalysts maintain a strong driving force for water reduction over the examined period [46]. To study the effect of BFO morphology on photocatalytic H₂ generation, two different morphologies (cylindrical and octahedron) of BFO have been synthesized by varying the NaOH concentration. At lower concentration of NaOH (2 M), cylindrical shaped BFO (BFO-Cyl) of average length 500 nm and width 120 nm have been obtained, however, at higher concentration of NaOH (12 M), octahedral shaped BFO (BFO-Oct) nanostructures have been formed (Fig. S4b and c). Hence, NaOH played a crucial role in controlling the morphology where sodium ions determine the available concentration of Fe³⁺ ions for further growth, which in turn affect the overall morphology of BFO nanostructures [47]. Photocatalytic activity of pure BFO with these three different morphology and corresponding Au decorated BFO has been compared under visible light as shown in Fig. 5b. The highest photocatalytic H₂ generation has been observed for BFO-Oct (BFO-Oct (1.4 mmol) > BFO-Ns (1.1 mmol) > BFO-Cyl (0.5 mmol)). Notably, BFO-Oct nanostructure shows strong absorption in the visible region in comparison to two other nanostructures (Fig. S4d). Hence, more exposed surfaces of the BFO-Oct may led to better absorption and enhance the photocatalytic H₂ generation which is consistent with the literature report [48]. However, after formation of heterostructures, Au/BFO-Ns produces significant amount of H₂ generation, which is 2 times higher than pure BFO-Ns as shown in Fig. 5b. The enhanced catalytic activity of Au/BFO-Ns may be due to the large surface area of two dimensional BFO-Ns which provide a strong coupling with the Au NPs. Thus, Au NPs can be exposed to the BFO-Ns surfaces and induce strong interaction [49]. Hence, BFO-Ns and Au/BFO-Ns have been taken for further studies.

Next, the effect of pH on photocatalytic H₂ evolution has been studied to optimize the reaction condition. Fig. 5c illustrates that higher catalytic activity for H₂ evolution achieved at pH 3 (~2.4 mmol) due to high availability of H⁺ in acidic solution and H₂ evolution activity

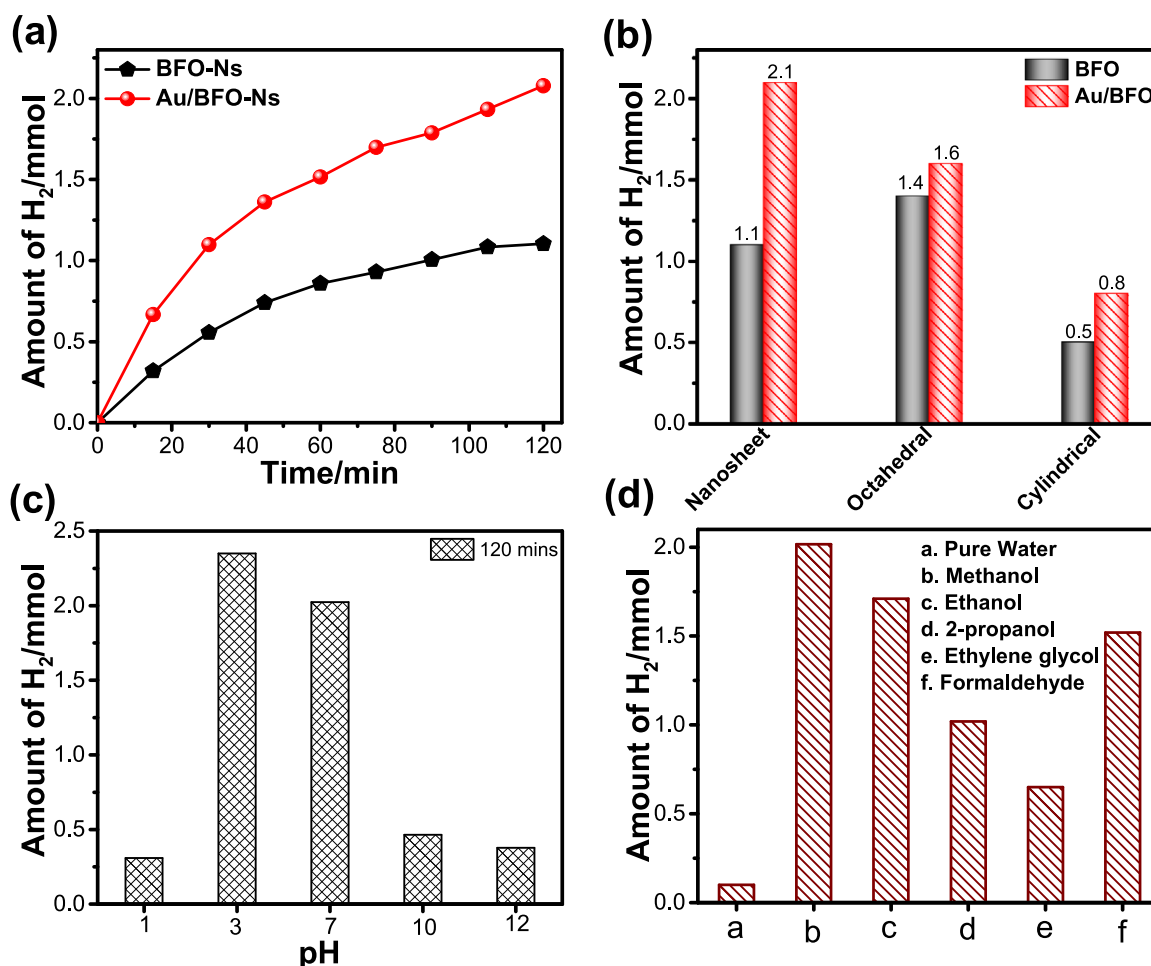


Fig. 5. (a) Photocatalytic hydrogen generation in presence of BFO nanosheet (BFO-Ns, black line) and Au/BFO-Ns heterostructures (red line) (b) Comparative H₂ generation data after 2 h visible light irradiation using the catalysts of BFO nanosheet (BFO-Ns), BFO octahedral (BFO-Oct), cylindrical shaped BFO (BFO-Cyl) and their heterostructures as Au/BFO-Ns, Au/BFO-Oct, Au/BFO-Cyl from an aqueous solution containing 25 vol% methanol at pH 7. Effect of (c) pH and (d) sacrificial agents on hydrogen generation using Au/BFO-Ns as photocatalyst under 2 h visible light illumination. (For interpretation of the references to color in this figure legend, the reader is referred to the web version of this article.)

decrease as the medium becomes more alkaline due to insufficient protons [50]. At more acidic medium protonation is happening due to presence of excess proton (H⁺) which may produce a filter effect by producing free molecules. It causes intermolecular energy transfer, resulting in a decrease in the photocatalytic efficiency [51]. The same trend has been observed for pure BFO-Ns in H₂ generation (Fig. S4e). In order to further optimize the role of sacrificial agents in photocatalytic H₂ generation, commonly used alcohol and aldehydes have been tested under similar reaction condition (Fig. 5d). In general, the redox potential of a sacrificial agent should be more negative than valence band of semiconductor, so that they can consume the holes and suppress the recombination of photogenerated electrons [52].

The highest photocatalytic H₂ generation has been observed for Au/BFO-Ns as photocatalyst using methanol (~2.1 mmol) as sacrificial agent compared to ethanol (~1.7 mmol), 2-propanol (~1.0 mmol), ethylene glycol (~0.6 mmol) and formaldehyde (1.5 mmol). This result suggests that, the length of carbon chain is inversely proportional to photocatalytic H₂ generation. However, the oxidation potential and permittivity of sacrificial agents have also potential role in H₂ generation as the sacrificial agents act as electron donors to consume the holes. According to Gouy-Chapman theory (Eq. (4)), surface charge density is proportional to dielectric constant of the solvent [52].

$$\sigma_s = \frac{2RT\epsilon\epsilon_0}{F} \sinh \frac{F\psi_0}{2RT} \quad (4)$$

where, σ_s is the surface charge density, ϵ is the dielectric constant of the solvent and ϵ_0 is the permittivity of free space, R is gas constant, T is the temperature, F is Faraday constant and ψ_0 is potential of the surface.

As shown in Table S1, the oxidation potential of methanol is lower than ethanol, 2-propanol and ethylene glycol but the permittivity is higher than ethanol and 2-propanol. Although, the permittivity of ethylene glycol is much higher compared to others, the higher oxidation potential (1.54 eV higher than water oxidation potential 1.23 eV) lowers its activity as it poorly oxidized. Therefore, methanol is considered as preferable sacrificial agent in photocatalytic hydrogen generation having lower oxidation potential and considerable permittivity. In case of pure BFO-Ns, the similar trend has been observed in H₂ generation (Fig. S4f).

Reusability and stability are important parameters of a photocatalyst for large scale application. Here, H₂ generation of Au/BFO-Ns heterostructures has been checked up to 5 successive cycles, which reveals nearly 13% loss in H₂ generation as shown in Fig. 6a (13% loss also include catalysts mass loss). Fig. 6b shows the TEM image of the heterostructures which reflects stability of nanosheet morphology after photocatalytic reaction. Interestingly, the gold NPs remain intact on the BFO-Ns after cycling. Therefore, Au/BFO-Ns heterostructures are reusable catalyst for hydrogen generation and stable under long visible light irradiation.

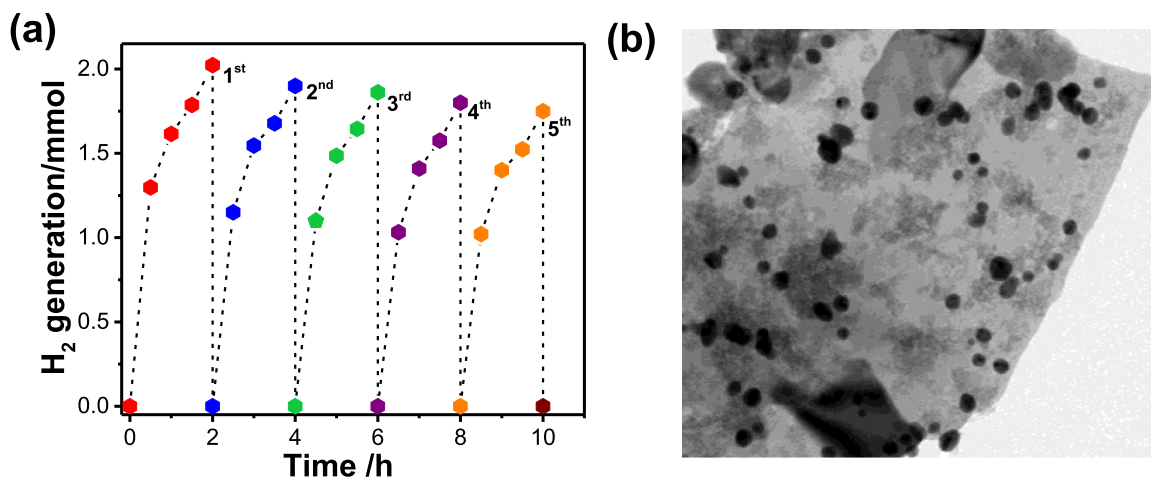


Fig. 6. (a) Recycling test of Au/BFO-Ns heterostructures during photocatalytic hydrogen generation and (b) TEM image of Au/BFO-Ns heterostructures after catalytic reaction of H_2 generation at pH 7.

3.6. Photoelectrochemical (PEC) activity

Photoelectrochemical measurement was performed using a galvanostat-potentiostat with a standard three-electrode cell and Pt wire as counter electrode and saturated Ag/AgCl as reference electrode. Here sacrificial agent has not been used but a potential is required to move

the photogenerated electrons towards counter electrode from photoanode. To investigate the light sensitivity and stability of as synthesized material of BFO-Ns and Au/BFO-Ns heterostructures, photocurrent measurement via linear sweep voltammetry (LSV) and chronoamperometry (CA) have been studied. Fig. 7a shows the LSV plot of pure BFO-Ns and Au/BFO-Ns heterostructures in dark and presence of

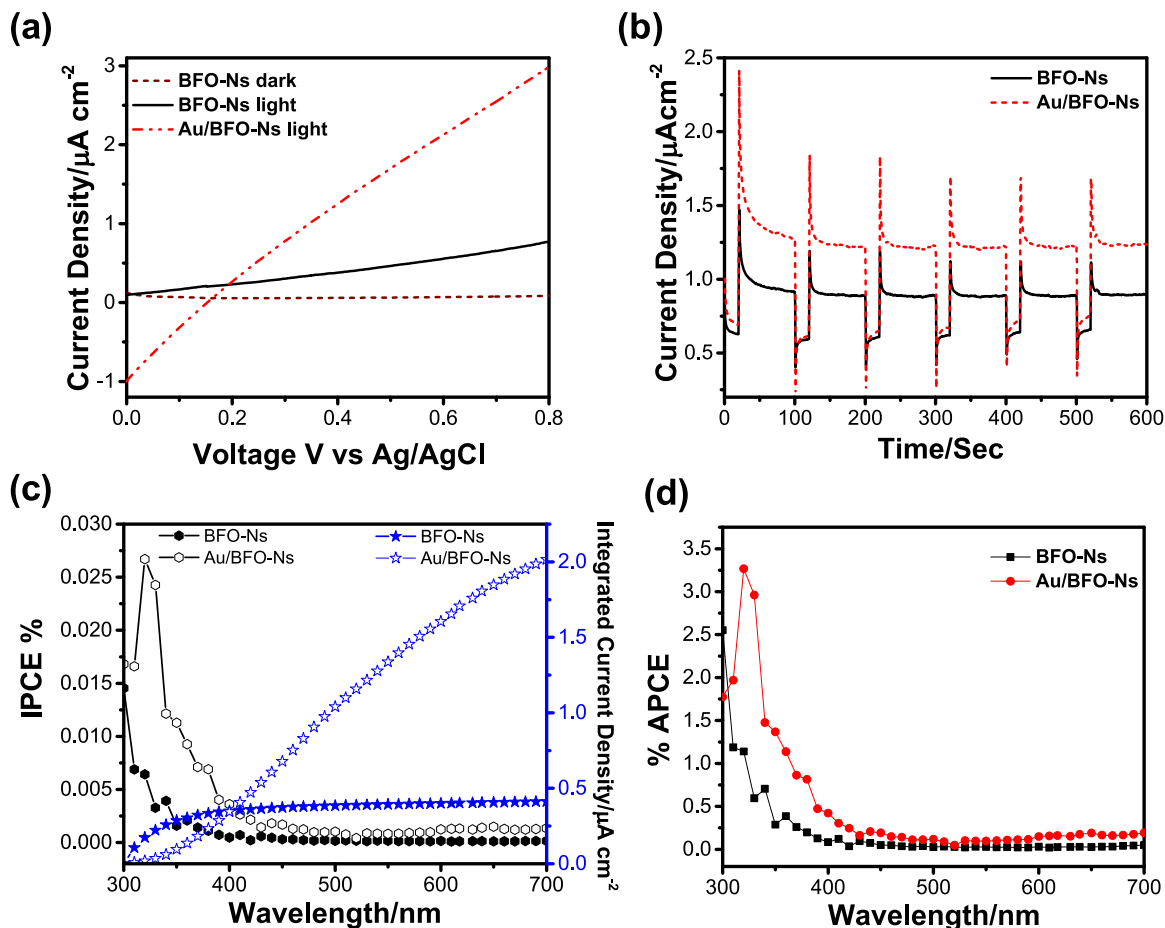


Fig. 7. (a) Linear sweep voltammograms (LSV) curves and (b) chronoamperometric plot of the BFO-Ns and Au/BFO-Ns thin film semiconductor electrodes on FTO substrates in the presence of 0.1 M Na_2SO_4 -phosphate buffer solution (pH 7) under continuous light illumination of 100 mW/cm^2 . The chronoamperometric plot measured at 0.6 V vs Ag/AgCl, under chopped illumination of 100 mW/cm^2 light. Calculated (c) IPCE (%) and corresponding integrated current density (product of the IPCE spectrum with the AM1.5G photon flux, blue spheres) and (d) APCE (%) of BFO-Ns and Au/BFO-Ns photoanodes using same electrolyte within the wavelength range 300–700 nm. (For interpretation of the references to color in this figure legend, the reader is referred to the web version of this article.)

continuous light illumination. In absence of light the current density is negligible ($0.07 \mu\text{A cm}^{-2}$) for BFO-Ns, whereas, under continuous light illumination, the obtained current density is $0.56 \mu\text{A cm}^{-2}$ and $2.14 \mu\text{A cm}^{-2}$ for BFO-Ns and Au/BFO-Ns respectively at a potential of 0.6 V vs Ag/AgCl , therefore 3.8 fold enhancement achieved for Au/BFO-Ns heterostructures. Additionally, we have measured H_2 generation under negative potentials in presence of light as reported earlier in literatures. A large current density ($\sim 235 \mu\text{A cm}^{-2}$) has been obtained for Au/BFO-Ns heterostructures, suggesting the H_2 generation by water reduction (Fig. S5a) [53]. Kong et al. [54] also reported that CoSe_2 nanoparticles on carbon fiber paper generated a large photocurrent in negative potential due to effective reduction of the water. In case of bare Au NPs, relatively lower current density ($75 \mu\text{A cm}^{-2}$) has been obtained at negative potential. Thus presence of Au NPs and its strong interaction with BFO-Ns may generate the large current density for Au/BFO-Ns heterostructures.

Fig. 7b represents the chopped chronoamperometric plot of pure BFO-Ns and Au/BFO-Ns heterostructures, indicating that materials are fairly stable against photocorrosion. Reusability of the semiconductor BFO-Ns has been tested through periodic voltammetry under continuous light illumination (Fig. S5b), and almost constant photocurrent observed after three successive LSV scans under similar condition. The results of both LSV and CA indicate that the heterostructure exhibits increasing photoinduced electrons and holes separation, which could be on account of the enhanced photocurrent generation.

In order to get more details about quantum efficiency of as synthesized photoanodes, the incident photon-to-current efficiency (IPCE) of pure BFO-Ns and Au/BFO-Ns has been calculated using the action spectrums through chronoamperometry measurement. Fig. 7c represents the plot of IPCE (%) and corresponding integrated current density vs wavelength where efficiency has been enhanced at lower wavelength for Au/BFO-Ns heterostructures compared to pure BFO-Ns. In action spectra (IPCE curve), BFO-Ns is practically inactive above 450 nm , whereas two distinct enhancement regions are prominent in Au/BFO-Ns photoanode. In the region of $< 450 \text{ nm}$, the enhancement in efficiency is achieved mainly due to improve light harvesting by the heterojunction formation between Au and BiFeO_3 . While in the wavelength of $> 450 \text{ nm}$, the enhancement in efficiency may be attributed to the presence of Au nanoparticles which can induce localized surface plasmon resonance (SPR) with incident photons of visible light. The SPR effect of Au nanoparticles would generate hot electrons and inject to BiFeO_3 directly, as a result IPCE efficiency has been enhanced in the visible light region. The integrated current density of the photoanodes (product of the IPCE spectrum with the AM1.5G photon flux, blue stars) has been calculated further from the IPCE [55]. The integrated photocurrent density reaches to ~ 0.42 and $\sim 2 \mu\text{A/cm}^2$ for BFO-Ns and Au/BFO-Ns respectively, which is nearly identical to the photocurrent density from LSV measurement in Fig. 7a, and the tiny deviation may be caused by the different design of the device. For instance, Zhao et al. [56] calculated integrated current density (0.08 mA/Cm^2) from the IPCE plot for Au/Pt/ WO_3/TiO_2 composite which matches well with the photocurrent (0.45 mA/Cm^2). The similar trend has been followed in APCE (%) where Au/BFO-Ns heterostructures shows higher efficiency at lower wavelength (Fig. 7d). The APCE increases at significantly above 580 nm due to surface plasmonic effect of Au NPs. Therefore, it is obvious that, the surface modification of semiconductor BFO-Ns by metallic Au NPs improves the light absorption in visible region which may consequently increase photon to current conversion efficiency values.

3.7. Mechanism

To elucidate the mechanism involved for enhanced photocatalytic activity of Au/BFO heterostructures, charge separation was investigated by various photoelectrochemical techniques including photoluminescence (PL), capacitance measurement and electrochemical

impedance spectroscopy (EIS) measurements. Fig. 8a shows the PL spectra of pure BFO-Ns and Au/BFO-Ns heterostructures at an excitation wavelength of 380 nm . It is observed that emission band for both BFO-Ns and Au/BFO-Ns is centered at 437 nm but PL intensity decreased for Au/BFO-Ns heterostructures [57]. This quenching of emission peak intensity for Au/BFO-Ns suggests the strong electronic interaction and improved charge carrier separation at the interface between Au and BFO-Ns [32]. Consequently, the improved charge separation lowers the number of surface trapped electrons by the oxygen vacancies and defects which is consistent with XPS result. Thus, the O 1s peaks at 530.77 eV which comes for surface adsorbed oxygen has been removed after heterojunction formation (Fig. S3).

To further study the PEC properties of BFO-Ns and Au/BFO-Ns, Mott–Schottky (MS) analysis has been studied in details. Fig. 8b shows the MS plot of pure BFO-Ns and Au/BFO-Ns heterostructures in which the positive characteristic slope in the MS plot following the Eq. (5), confirms the n-type behavior of the samples.

$$\frac{1}{C_{sc}^2} = \frac{2}{eN_d\epsilon\epsilon_0} \left(E - E_{fb} - \frac{KT}{E} \right) \quad (5)$$

where, C_{sc} is the space charge capacitance (in F cm^{-2}), e is electronic charge in C , ϵ is the dielectric constant of the semiconductors (30 for BFO, at room temperature) [10], ϵ_0 is the permittivity of free space, N_d is the charge carrier density in cm^{-3} , E_{fb} is the flat band potential in V , K is the Boltzmann constant and T is the temperature in K .

The flat band potentials of the synthesized materials have been calculated from the MS plot by extrapolating the slope of the plots at $1/C^2 = 0$, shows that E_{fb} shift towards more negative potential for Au/BFO-Ns heterostructures, indicating the better catalytic activity of the materials towards water reduction reaction (Table 1). The VB and CB potentials of BFO-Ns and Au/BFO-Ns have been calculated (Table 1) and the band gap of BFO-Ns significantly narrowed to 2.05 eV from 2.3 eV . Next, the charge carrier concentration (N_d) at the junction has been calculated following the Eq. (5) [58].

Therefore, it is clear that N_d has been increased after Au/BFO-Ns heterojunction formation in comparison to pure semiconductor BFO-Ns. The increased charge N_d at the semiconductor-electrolyte interface helps in better reduction of water molecules [59]. The space charge layer width (W_{sc}) and Debye length (L_D) of the semiconductors have been calculated further following the Eqs. (6) and (7) as given below [60].

$$W_{sc} = \sqrt{\left(\frac{2\epsilon\epsilon_0 V_s}{eN_d} \right)} \quad (6)$$

$$L_D = \sqrt{\left(\frac{\epsilon\epsilon_0 KT}{e^2 N_d} \right)} \quad (7)$$

According to Eq. (6), W_{sc} is inversely proportional to the N_d , therefore, the thickness of the space charge layer of BFO-Ns reduces after heterostructures formation with Au NPs. The calculated space charge layer width reduces from 225 nm to 163 nm for Au/BFO-Ns heterostructures at an applied potential of 0.1 V vs Ag/AgCl (Fig. S6a). This reduction of W_{sc} strongly indicates the formation of band bending at the electrode – electrolyte surface due to electron transfer from semiconductor to electrolyte as the electron density of semiconductor is much higher compared to junction point [61]. This band bending greatly affect the space charge layer which contribute in formation of electric field near the interfaces. For BFO-Ns (n-type materials) photo-excited holes are accumulated on the semiconductor surface which are consumed by the oxidation reactions while the electrons are transferred to the counter electrode and used in proton reduction to H_2 [57].

On the other hand, Debye length (L_D) is an important parameter for photochemistry and it is inversely proportional to the N_d (Eq. (4)). Basically, L_D is a length in which the mobile charge carriers screen out the maximum electric field and it is closely related to the space charge

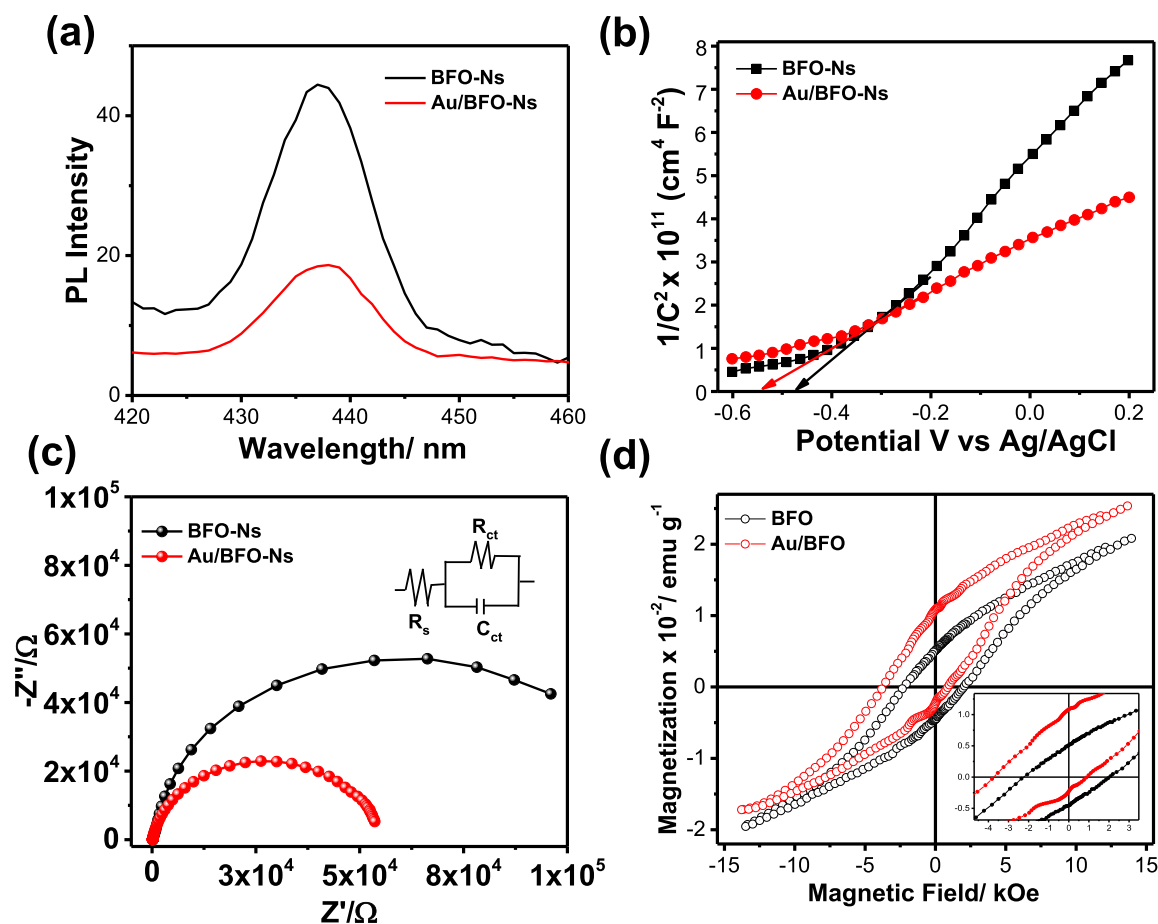


Fig. 8. (a) Photoluminescence spectra of pure BFO-Ns and Au/BFO-Ns heterostructures at an excitation of 380 nm. (b) Mott–Schottky plots pure BFO-Ns and Au/BFO-Ns heterostructures in the presence of 0.1 M Na₂SO₄ electrolytes (pH 7) using an AC frequency of 1000 Hz. The intercept of the plot (at $1/C^2 = 0$) has been used to determine the E_{fb} of the BFO-Ns and Au/BFO-Ns photoelectrodes. (c) Nyquist plot of BFO-Ns and Au/BFO-Ns using same electrolyte under continuous light illumination of 100 mW/cm² at an applied potential 0.6 V vs Ag/AgCl. Inset: (c) Equivalent circuit model to analyze the Nyquist plot. (d) Magnetic hysteresis loop for pure BFO and Au/BFO heterostructures at room temperature. Inset: magnified views of the low field region.

Table 1

Electrochemical parameters calculated from Mott–Schottky plot for BFO-Ns and Au/BFO-Ns catalysts.

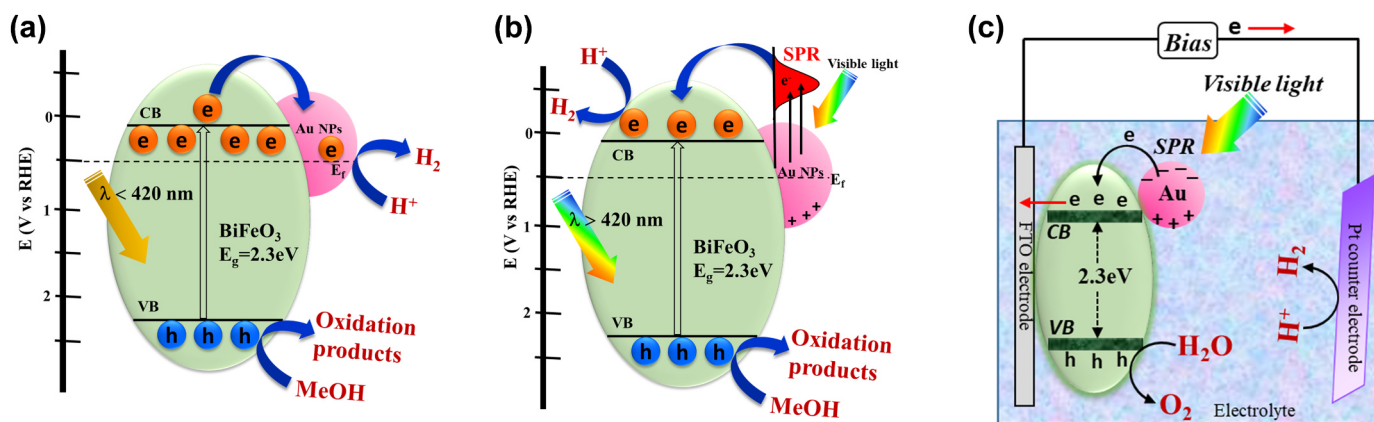
| Catalyst | E_{fb} in V vs Ag/AgCl | E_{CB} in V vs RHE | E_{VB} in V vs RHE | E_g in eV | N_d in cm ⁻³ | W_{sc} in nm | L_D in nm |
|-----------|--------------------------|----------------------|----------------------|-------------|---------------------------|----------------|-------------|
| BFO-Ns | -0.473 | 0.14 | 2.46 | 2.32 | 0.47×10^{17} | 225 | 30.2 |
| Au/BFO-Ns | -0.541 | 0.07 | 2.12 | 2.05 | 0.92×10^{17} | 163 | 21.6 |

region. So, the lowering value of L_D for Au/BFO-Ns indicates the better charge transfer through the junction. The morphological effect on junction capacitance has also been analyzed and the result reveals that, Au/BFO-Ns heterostructures possesses the higher amount of charge carrier which may results better H₂ generation in photochemical process (Table S3). In addition, flat-band potential of Au/BFO-Ns is negatively shifted compared to other heterostructures, indicating the reduced charge carrier recombination by enhancing band bending at the interface (Fig. S6b). Moreover, the above results suggest that, heterojunction formation increase the carrier concentration at the electrode–electrolyte interfaces by enhancing the specific surface area, reduce the bad gap of the semiconductor and space charge layer width which have crucial role in enhancing the photocatalytic efficiency.

Further, the charge-transfer properties of the photocatalysts have been investigated by the electrochemical impedance spectra (EIS) measurement. Fig. 8c represents the Nyquist plot of BFO-Ns and Au/BFO-Ns electrodes where a single semicircle has been obtained, confirms a single charge transfer mechanism of semiconductor–electrolyte interface under continuous light illumination [61]. The diameter of the

semicircle represents the charge transfer resistance of the semiconductor–electrolyte interface. Thus, the low diameter for Au/BFO-Ns heterostructures implies the smaller resistance and better PEC performance compared to pure BFO-Ns semiconductor. The obtained curves are fitted with the Randles equivalent circuit model and the fitting parameters are given in the Table S4. From the table, it is evident that, the ohmic resistance (R_s) decrease after heterostructure formation i.e. formation of better ohmic conductivity, which is helpful to improve the charge separation efficiency. Furthermore, the impedance study of Au/BFO-Ns electrode has been conducted in light and dark condition to understand the effect of light in charge transferring (Fig. S6c). In presence of light, both BFO-Ns and Au/BFO-Ns show low charge-transfer resistance because of the enhanced diffusion of electrons with high mobility [62].

The magnetic hysteresis loop (M–H) for pure BFO-Ns and Au/BFO-Ns heterostructures have been measured at room temperature to understand the possible effect of magnetism on photocatalysis. As shown in Fig. 8d, a typical ferromagnetic M–H curve with well-developed hysteresis loop has been observed for both BFO-Ns and Au/BFO-Ns



Scheme 1. Schematic representations of the band edges of Au/BiFeO₃ heterostructures and proposed mechanism of photocatalytic H₂ generation (a) when the incident light intensity < 420 nm, (b) when the incident light intensity > 420 nm, hot electron injection from the surface plasmon state of the Au NPs to the CB of BiFeO₃ in Au/BiFeO₃ heterostructures and (c) Photoelectrochemical water splitting under visible light irradiation.

heterostructures, however having low magnetization. The magnetization value is slightly increased for Au/BFO-Ns (0.025 emu/g) compared to BFO-Ns (0.02 emu/g) at 1.5 kOe. Additionally, an exchange bias effect has been obtained for Au/BFO-Ns (inset Fig. 8d) which may arise due to the suppression of spiral magnetic structure of BFO-Ns due to formation of heterostructure with Au NPs. However, there is an interface between Au and BFO within the Au/BFO heterostructures, which may induce a magnetic moment in metallic Au due to the magnetic proximity effect [63]. Such magnetic proximity effect arises in heterostructures due to the strong interfacial hybridization between BFO nanosheets and Au NPs which is described in the literatures [64]. As a result, the charge transfer property would be improved as both the elements of heterostructures possess magnetic moment and also a spin arrangement at the interface. Therefore, in presence of applied field, the injection rate of polarized carriers has been increased which leads to enhance current density as well as photocatalytic activity.

From the above experimental results, it is clear that heterostructure formation facilitate the photocatalytic activity of BFO due to the combine effects of the strong absorption in visible region and compression of band gap energy, efficient charge separation and the promotion of surface redox reactions. The photo generated charge separation within the Au/BFO heterostructures have been proposed in the schematic diagram (Scheme 1).

In general, the metal NPs possess the property of storing electrons and the electronic state within the metal NPs is continuous which follows the Fermi-Dirac distribution [37]. When the semiconductor and metal nanoparticles are in contact, a Schottky barrier would be formed via Fermi level equilibration between metals and semiconductor. First, the photogenerated electrons are distributed between the surface of BFO and Au NPs and then transfer of electrons from the excited BFO into Au (Fermi level of Au +0.45 V vs RHE) occurs, which continues until the two systems attain equilibrium. The equilibrium alignment of the Fermi level for metal and semiconductor oxide built an electric field near the interface, which promotes the separation of photogenerated charge carriers and more reductive power for the heterostructured system (Scheme 1a) [65–67].

On the other hand, when visible light ($\lambda > 420$ nm) is illuminated on the Au/BFO heterostructures, resonance may happen with the incident photons and electrons, resulting the electronic oscillation with upshifted energy states which is greater than the conduction band (E_{CB}) of the neighboring semiconductor. Under this circumstance, excited electrons of Au (generally called hot electrons) may transfer to the E_{CB} of the BFO (Scheme 1b) [68]. Next, reduction of water has been occurred by these excited electrons and generated H₂ from H⁺ [26,69,70]. Simultaneously, holes are created in the valence band of BFO which can be quenched by the sacrificial agent (methanol) by

reacting faster with it rather than water so that recombination of photogenerated electrons and holes would be hindered. Therefore, formation of metal-semiconductor heterojunction considered as a suitable route for enhancing the photocatalytic activity through water splitting under UV and visible light.

Further, the possible mechanism of photoelectrochemical water splitting in presence of Au/BFO electrode, under visible light irradiation has been shown in Scheme 1c. Here, commercial Pt wire has been used as counter electrode. Under visible light illumination, hot electrons which are generated in the Au NPs due to SPR effect, are transferred into the CB of the BFO. These photo-generated electrons further transfer to the FTO and directly transported to the counter electrode as the external potential has been applied. Next, reduction of water has been occurred by these accumulated electrons at the counter electrode and generated H₂. However, the photogenerated holes remaining in the photoanode can efficiently reduce the water molecules into H⁺ and O₂ as they are located in the region of the water oxidation potential (1.23 eV).

4. Conclusion

In summary, we report a facile hydrothermal method followed by radiolysis for the fabrication of Au/BFO heterostructures without using any template and strong reducing agent and investigated photocatalytic H₂ generation as well as photoelectrochemical water splitting under visible light. The presence of Au NPs within BFO nanosheets enhances the visible light absorption by virtue of SPR effect. Consequently, two fold enhancements in photocatalytic H₂ generation have been achieved for Au/BFO heterostructures compared to pure BFO nanosheets. The heterostructure formation significantly improves the catalytic activity towards water oxidation by enhancing the photoelectrochemical current density (~3.8 times) and long-term stability under longer visible light illumination. In PEC measurements, 3.3% absorb photon to current conversion efficiency has been achieved for Au/BFO whereas 1.1% for pure BFO nanosheets at wavelength 320 nm. Further, Mott-Schottky and EIS measurements confirm effective charge separation at the interfaces of heterojunction which lead to enhance the photocurrent generation and H₂ evolution efficiencies compared to the bare BFO nanosheets. The present contribution represents a general route to synthesize other metal-perovskites based heterostructures as a visible light active photocatalysts for clean, sustainable, and renewable energy generation.

Acknowledgement

The authors acknowledge Director, CSIR-CGCRI for his kind permission to publish the work. One of the authors (SB) is thankful to Department of Science & Technology (DST), India, for providing

INSPIRE fellowship award. Another author (SG) is thankful to the Council of Scientific & Industrial Research (CSIR), India, for providing a CSIR-Senior Research Associate (Scientists' Pool Scheme) award. One of the author (SS) is thankful to the Board of Research in Nuclear Science (BRNS), Department of Atomic Energy, Government of India, for providing financial support.

Appendix A. Supporting information

Supplementary data associated with this article can be found in the online version at doi:10.1016/j.solmat.2019.01.042.

References

- [1] K. Sivula, R.V. Krol, Semiconducting materials for photoelectrochemical energy conversion, *Nat. Rev. Mater.* 1 (2016) 15010–15026.
- [2] S.J.A. Moniz, S.A. Shevlin, D.J. Martin, Z.-X. Guo, J. Tang, Visible-light driven heterojunction photocatalysts for water splitting – a critical review, *Energy Environ. Sci.* 8 (2015) 731–759.
- [3] T. Hisatomi, J. Kubota, K. Domen, Recent advances in semiconductors for photocatalytic and photoelectrochemical water splitting, *Chem. Soc. Rev.* 43 (2014) 7520–7535.
- [4] J. Xuan, W.J. Xiao, Visible-light photoredox catalysis, *Angew. Chem. Int. Ed.* 51 (2012) 2–13.
- [5] S. Chen, T. Takata, K. Domen, Particulate photocatalysts for overall water splitting, *Nat. Rev. Mater.* 2 (2017) 17050–17067.
- [6] S. Ghosh, N.A. Kouame, L. Ramos, S. Remita, A. Dazzi, A. Deniset-Besseau, P. Beunier, F. Goubard, P.-H. Aubert, H. Remita, Conducting polymer nanostructures for photocatalysis under visible light, *Nat. Mater.* 14 (2015) 505–511.
- [7] Y.-Y. Liu, H.-P. Zhang, B. Zhu, H.-W. Zhang, L.-D. Fan, X.-Y. Chai, Q.-L. Zhang, J.-H. Liu, C.-X. He, C/N-co-doped Pd coated Ag nanowires as a high-performance electrocatalyst for hydrogen evolution reaction, *Electrochim. Acta* 283 (1) (2018) 221–227.
- [8] W. Wang, M.O. Tade, Z. Shao, Research progress of perovskite materials in photocatalysis- and photovoltaics-related energy conversion and environmental treatment, *Chem. Soc. Rev.* 44 (2015) 5371–5408.
- [9] G. Zhang, G. Liu, L. Wang, J.T.S. Irvine, Inorganic perovskite photocatalysts for solar energy utilization, *Chem. Soc. Rev.* 45 (2016) 5951–5984.
- [10] G. Catalan, J.F. Scott, Physics and applications of bismuth ferrite, *Adv. Mater.* 21 (2009) 2463–2485.
- [11] T. Zhao, A. Scholl, F. Zavaliche, K. Lee, M. Barry, A. Doran, M.P. Cruz, Y.H. Chu, C. Ederer, N.A. Spaldin, R.R. Das, D.M. Kim, S.H. Baek, C.B. Eom, R. Ramesh, Electrical control of antiferromagnetic domains in multiferroic BiFeO₃ films at room temperature, *Nat. Mater.* 5 (2006) 823–829.
- [12] S.Y. Yang, J. Seidel, S.J. Byrnes, P. Shafer, C.-H. Yang, M.D. Russell, P. Yu, Y.-H. Chu, J.F. Scott, J.W. Ager, L.W. Martin, R. Ramesh, Above-bandgap voltages from ferroelectric photovoltaic devices, *Nat. Nanotechnol.* 5 (2010) 143–147.
- [13] X. Wang, J. Zhang, Q. Peng, Y.D. Li, A general strategy for nanocrystal synthesis, *Nature* 437 (2005) 121–124.
- [14] L. Fei, J. Yuan, Y. Hu, C. Wu, J. Wang, Y. Wang, Visible light responsive perovskite BiFeO₃ pills and rods with dominant {111}c facets, *Cryst. Growth Des.* 11 (2011) 1049–1053.
- [15] X. Bai, J. Wei, B. Tian, Y. Liu, T. Reiss, N. Guiblin, P. Gemeiner, Dkhill, I.C. Infante, Size effect on optical and photocatalytic properties in BiFeO₃ nanoparticles, *J. Phys. Chem. C* 120 (2016) 3595–3601.
- [16] X. Wang, W. Mao, Q. Zhang, Q. Wang, Y. Zhu, J. Zhang, T. Yang, J. Yang, X. Li, W. Huang, Magnetic phase transitions and giant magnetocaloric effect of Eu/TiO₃ nanowires, *J. Alloy. Compd.* 689 (2016) 63–68.
- [17] L. Lu, M. Lv, G. Liu, X. Xu, Photocatalytic hydrogen production over solid solutions between BiFeO₃ and SrTiO₃, *Appl. Surf. Sci.* 391 (2017) 535–541.
- [18] T. Zhang, Y. Shen, Y. Qiu, Y. Liu, R. Xiong, J. Shi, J. Wei, Facial synthesis and photoreaction mechanism of BiFeO₃/Bi₂Fe₄O₉ heterojunction nanofibers, *ACS Sustain. Chem. Eng.* 5 (2017) 4630–4636.
- [19] Y.P. Bhoi, B.G. Mishra, Photocatalytic degradation ofalachlor using Type-II CuS/BiFeO₃ heterojunctions as novel photocatalyst under visible light irradiation, *Chem. Eng. J.* 344 (2018) 391–401.
- [20] Z. Li, Y. Shen, C. Yang, Y. Lei, Y. Guan, Y. Lin, D. Liu, C.-W. Nana, Significant enhancement in the visible light photocatalytic properties of BiFeO₃-graphene nanohybrids, *J. Mater. Chem. A* 1 (2013) 823–829.
- [21] J. Low, J. Yu, M. Jaroniec, S. Wageh, A.A. Al-Ghamdi, Heterojunction photocatalysts, *Adv. Mater.* 29 (2017) 1601694–1601714.
- [22] S.J.A. Moniz, S. Ghosh (Eds.), Visible-Light-Active Photocatalysis: Nanostructured Catalyst Design, Mechanisms and Applications, Wiley-VCH Verlag GmbH & Co. KGaA, Germany, 2018 (ISBN: 978-3-527-34293-8).
- [23] A.M. Díez, F.C. Moreira, B.A. Marinho, J.C.A. Espíndola, L.O. Paulista, M.A. Sanromán, M. Pazos, R.A.R. Boaventura, V.J.P. Vilar, A step forward in heterogeneous photocatalysis: process intensification by using a static mixer as catalyst support, *Chem. Eng. J.* 343 (2018) 597–606.
- [24] S. Sardar, P. Kar, H. Remita, B. Liu, P. Lemmens, S.K. Pal, S. Ghosh, Enhanced charge separation and FRET at heterojunctions between semiconductor nanoparticles and conducting polymer nanofibers for efficient solar light harvesting, *Sci. Rep.* 5 (2015) 17313–17327.
- [25] S. Bera, S. Ghosh, R.N. Basu, Fabrication of Bi₂S₃/ZnO heterostructures: an excellent photocatalyst for visible-light-driven hydrogen generation and photoelectrochemical properties, *New J. Chem.* 42 (2018) 541–554.
- [26] S. Linić, P. Christopher, D.B. Ingram, Plasmonic-metal nanostructures for efficient conversion of solar to chemical energy, *Nat. Mater.* 10 (2011) 911–921.
- [27] S. Ghosh, A.K. Mallik, R.N. Basu, Enhanced photocatalytic activity and photo-response of poly(3,4-ethylenedioxythiophene) nanofibers decorated with gold nanoparticle under visible light, *Sol. Energy* 159 (2018) 548–560.
- [28] E. Grabowska, A. Zaleska, S. Sorgues, M. Kunst, A. Etcheberry, C. Colbeau-Justin, H. Remita, Modification of titanium(IV) dioxide with small silver nanoparticles: application in photocatalysis, *J. Phys. Chem. C* 117 (2013) 1955–1962.
- [29] E. Kowalska, M. Janczarek, L. Rosa, S. Juodkazis, B. Ohtani, Mono- and bi-metallic plasmonic photocatalysts for degradation of organic compounds under UV and visible light irradiation, *Catal. Today* 230 (2014) 131–137.
- [30] A.L. Luna, D. Drago, K. Wang, P. Beunier, E. Kowalska, B. Ohtani, D.B. Uribe, M.A. Valenzuela, H. Remita, C. Co.-Justin, Photocatalytic hydrogen evolution using Ni-Pd/TiO₂: correlation of light absorption, charge-carrier dynamics, and quantum efficiency, *J. Phys. Chem. C* 121 (2017) 14302–14311.
- [31] S. Anwer, G. Bharath, S. Hongmei, Q. Tariq, M. Kin, L. Wesley, Synthesis of edge-site selectively deposited Au nanocrystals on TiO₂ nanosheets: an efficient heterogeneous catalyst with enhanced visible-light photoactivity, *Electrochim. Acta* 283 (2018) 1095–1104.
- [32] F. Niu, D. Chen, L. Qin, T. Gao, N. Zhang, S. Wang, Z. Chen, J. Wang, X. Sun, Y. Huang, Synthesis of Pt/BiFeO₃ heterostructured photocatalysts for highly efficient visible-light photocatalytic performances, *Sol. Energy Mater. Sol. Cells* 143 (2015) 386–396.
- [33] S. Li, J. Zhang, M.G. Kibria, Z. Mi, M. Chaker, D. Ma, R. Nechache, F. Rosei, Remarkably enhanced photocatalytic activity of laser ablated Au nanoparticle decorated BiFeO₃ nanowires under visible-light, *Chem. Commun.* 49 (2013) 5856–5858.
- [34] F.Z. Li, H.W. Zheng, M.S. Zhu, X.A. Zhang, G.L. Yuan, Z.S. Xie, X.H. Li, G.T. Yue, W.F. Zhang, Photovoltaic enhancement by Au surface-plasmon effect for La doped BiFeO₃ films, *J. Mater. Chem. C* 5 (2017) 10615–10623.
- [35] S. Mohan, B. Subramanian, G. Sarveswaran, A prototypical development of plasmonic multiferroic bismuth ferrite particulate and fiber nanostructures and their remarkable photocatalytic activity under sunlight, *J. Mater. Chem. C* 2 (2014) 6835–6842.
- [36] A.M. Schultz, Y. Zhang, P.A. Salvador, G.S. Rohrer, Effect of crystal and domain orientation on the visible-light photochemical reduction of Ag on BiFeO₃, *ACS Appl. Mater. Interfaces* 3 (2011) 1562–1567.
- [37] P. Zhang, T. Wang, J. Gong, Mechanistic understanding of the plasmonic enhancement for solar water splitting, *Adv. Mater.* 27 (2015) 5328–5342.
- [38] J. Liu, Y. Liu, N. Liu, Y. Han, X. Zhang, H. Huang, Y. Lifshitz, S.-T. Lee, J. Zhong, Z. Kang, Metal-free efficient photocatalyst for stable visible water splitting via a two-electron pathway, *Science* 347 (2015) 970–974.
- [39] H. Suzuki, O. Tomita, M. Higashi, R. Abe, Two-step photocatalytic water splitting into H₂ and O₂ using layered metal oxide KCa₂Nb₂O₁₀ and its derivatives as O₂-evolving photocatalysts with IO₃³⁻/I⁻ or Fe³⁺/Fe²⁺ redox mediator, *Catal. Sci. Technol.* 5 (2015) 2640–2648.
- [40] J. Belloni, M. Mostafavi, H. Remita, J.-L. Marignier, M.-O. Delcourt, Radiation-induced synthesis of mono- and multi-metallic clusters and nanocolloids, *New J. Chem.* 22 (1998) 1239–1255.
- [41] S. Ghosh, S. Bera, S. Bysakh, R.N. Basu, Conducting polymer nanofiber-supported Pt alloys: unprecedented materials for methanol oxidation with enhanced electrocatalytic performance and stability, *Sustain. Energy Fuels* 1 (2017) 1148–1161.
- [42] S. Ghosh, S. Bera, S. Bysakh, R.N. Basu, Highly active multimetallic palladium nanoalloys embedded in conducting polymer as anode catalyst for electrooxidation of ethanol, *ACS Appl. Mater. Interfaces* 9 (2017) 33775–33790.
- [43] S.J.A. Moniz, R. Q.-Cabrera, C.S. Blackman, J. Tang, P. Southern, P.M. Weaver, C.J. Carmalt, A simple, low-cost CVD route to thin films of BiFeO₃ for efficient water photo-oxidation, *J. Mater. Chem. A* 2 (2014) 2922–2927.
- [44] G.S. Pozan, M. Isleyen, S. Gokcen, Transition metal coated TiO₂ nanoparticles: synthesis, characterization and their photocatalytic activity, *Appl. Catal. B: Environ.* 140 (2013) 537–545.
- [45] J. Jiang, J. Zou, M.N. Anjum, J.C. Yan, L. Huang, Y.X. Zhang, J.F. Chen, Synthesis and characterization of wafer-like BiFeO₃ with efficient catalytic activity, *Solid State Sci.* 13 (2011) 1779–1785.
- [46] I. Papadas, J.A. Christodoulides, G. Kioseoglou, G.S. Armatas, A high surface area ordered mesoporous BiFeO₃ semiconductor with efficient water oxidation activity, *J. Mater. Chem. A* 3 (2015) 1587–1593.
- [47] C.-J. Tsai, C.-Y. Yang, Y.-C. Liao, Y.-L. Chueh, Hydrothermally grown bismuth ferrites: controllable phases and morphologies in a mixed KOH/NaOH mineralizer, *J. Mater. Chem. C* 22 (2012) 17432–17436.
- [48] L. Gai, Q. Mei, X. Qin, W. Li, H. Jiang, X. Duan, Controlled synthesis of anatase TiO₂ octahedra with enhanced photocatalytic activity, *Mater. Res. Bull.* 48 (2013) 4469–4475.
- [49] A.H. Khan, S. Ghosh, B. Pradhan, A. Dalui, L.K. Shrestha, S. Acharya, K. Ariga, Two-dimensional (2D) nanomaterials towards electrochemical nanoarchitectonics in energy-related applications, *Bull. Chem. Soc. Jpn.* 90 (2017) 1–21.
- [50] Y. Chao, J. Zheng, H. Zhang, F. Li, F. Yan, Y. Tan, Z. Zhu, Oxygen-incorporation in Co₂P as a non-noble metal cocatalyst to enhance photocatalysis for reducing water to H₂ under visible light, *Chem. Eng. J.* 346 (2018) 281–288.
- [51] M. Zhu, Y. Du, P. Yang, X. Wang, Donor-acceptor porphyrin functionalized Pt nanoassemblies for artificial photosynthesis: a simple and efficient homogeneous photocatalytic hydrogen production system, *Catal. Sci. Technol.* 3 (2013) 2295–2302.

- [52] M. Wang, S. Shen, L. Li, Z. Tang, J. Yang, Effects of sacrificial reagents on photocatalytic hydrogen evolution over different photocatalysts, *J. Mater. Sci.* 52 (2017) 5155–5164.
- [53] G. Liu, N. Li, Y. Zhao, R. Yao, M. Wang, D. He, J. Li, Fabrication of Fe-doped Co₂P nanoparticles as efficient electrocatalyst for electrochemical and photoelectrochemical water oxidation, *Electrochim. Acta* 283 (2018) 1490–1497.
- [54] D. Kong, H. Wang, Z. Lu, Yi Cui, CoSe₂ nanoparticles grown on carbon fiber paper: an efficient and stable electrocatalyst for hydrogen evolution reaction, *J. Am. Chem. Soc.* 136 (2014) 4897–4900.
- [55] L.-C. Chen, J.-C. Chen, C.-C. Chen, C.-G. Wu, Fabrication and properties of high-efficiency perovskite/PCBM organic solar cells, *Nanoscale Res. Lett.* 10 (2015) 312–317.
- [56] J. Zhao, P. Zhang, Z. Wang, S. Zhang, H. Gao, J. Hu, G. Shao, Direct evidence of multichannel improved charge-carrier mechanism for enhanced photocatalytic H₂ evolution, *Sci. Rep.* 7 (2017) 16116–16127.
- [57] A. Zhu, Q. Zhao, X. Li, Y. Shi, BiFeO₃/TiO₂ nanotube arrays composite electrode: construction, characterization, and enhanced photoelectrochemical properties, *ACS Appl. Mater. Interfaces* 6 (2014) 671–679.
- [58] K. Gelderman, L. Lee, S.W. Donne, Flat-band potential of a semiconductor: using the Mott–Schottky equation, *J. Chem. Educ.* 84 (2007) 685–689.
- [59] N. Zhang, D. Chen, F. Niu, S. Wang, L. Qin, Y. Huang, Enhanced visible light photocatalytic activity of Gd-doped BiFeO₃ nanoparticles and mechanism insight, *Sci. Rep.* 6 (2016) 26467–26478.
- [60] L. Palmisano, V. Augugliaro, A. Sclafani, M. Schiavello, Activity of chromium-ion-doped titania for the dinitrogen photoreduction to ammonia and for the phenol photodegradation, *J. Phys. Chem.* 92 (1988) 6710–6713.
- [61] S. Shyamal, P. Hajra, H. Mandal, A. Bera, D. Sariket, A.K. Satpati, S. Kundu, C. Bhattacharya, Benign role of Bi on an electrodeposited Cu₂O semiconductor towards photo-assisted H₂ generation from water, *J. Mater. Chem. A* 4 (2016) 9244–9252.
- [62] G. Zhang, L. Zhang, Y. Liu, L. Liu, C.-P. Huang, H. Liu, J. Li, Substitution boosts charge separation for high solar-driven photocatalytic performance, *ACS Appl. Mater. Interfaces* 8 (2016) 26783–26793.
- [63] Z. Wang, C. Tang, R. Sachs, Y. Barlas, J. Shi, Proximity-induced ferromagnetism in graphene revealed by the anomalous hall effect, *Phys. Rev. Lett.* 114 (2015) 016603–016606.
- [64] J. Li, Q. Pei, R. Wang, Y. Zhou, Z. Zhang, Q. Cao, D. Wang, W. Mi, Y. Du, Enhanced photocatalytic performance through magnetic field boosting carrier transport, *ACS Nano* 12 (2018) 3351–3359.
- [65] C. Gu, B.C. Norris, F.-R.F. Fan, C.W. Bielawski, A.J. Bard, Is base-inhibited vapor phase polymerized PEDOT an electrocatalyst for the hydrogen evolution reaction? Exploring substrate effects, including Pt contaminated Au, *ACS Catal.* 2 (2012) 746–750.
- [66] J.L. Fernaández, V. Raghuvver, A. Manthiram, A.J. Bard, Pd-Ti and Pd-Co-Au electrocatalysts as a replacement for platinum for oxygen reduction in proton exchange membrane fuel cells, *J. Am. Chem. Soc.* 127 (2005) 13100–13101.
- [67] V. Subramanian, E.E. Wolf, P.V. Kamat, Catalysis with TiO₂/gold nanocomposites. Effect of metal particle size on the fermi level equilibration, *J. Am. Chem. Soc.* 126 (2004) 4943–4950.
- [68] X. Zhang, Y.L. Chen, R.-S. Liu, D.P. Tsai, Plasmonic photocatalysis, *Rep. Prog. Phys.* 76 (2013) 046401–046442.
- [69] D. Mateo, I. E.-Adell, J. Albero, J.F.S. Royo, A. Primo, H. Garcia, 111 oriented gold nanoplatelets on multilayer graphene as visible light photocatalyst for overall water splitting, *Nat. Commun.* 7 (2016) 11819.
- [70] S. Gu, X. Zhou, F. Zheng, L. Fang, W. Dong, M. Shen, Improved photocathodic performance in Pt catalyzed ferroelectric BiFeO₃ films sandwiched by a porous carbon layer, *Chem. Commun.* 53 (2017) 7052–7055.



Silver as solid-state electron mediator in MoS₂/Ag–AgVO₃ Z-Scheme heterostructures for photocatalytic H₂ generation



Susmita Bera, Srabanti Ghosh^{**1}, Rajendra N. Basu^{*}

Fuel Cell & Battery Division, CSIR - Central Glass and Ceramic Research Institute, 196, Raja S. C. Mullick Road, Kolkata, 700032, India

ARTICLE INFO

Article history:

Received 23 December 2019

Received in revised form

20 January 2020

Accepted 25 February 2020

Available online 4 March 2020

Keywords:

Solid-state Z-scheme heterostructures

Electron mediator

Water splitting

H₂ generation

Electrochemical properties

ABSTRACT

Heterostructured photocatalysts have attracted enormous research interest in H₂ generation through water splitting because of highly efficient interfacial charge-transfer characteristics of nanoarchitectures. Herein, Ag nanoparticles decorated AgVO₃ nanorods and MoS₂ nanosheets are combined to fabricate MoS₂/Ag–AgVO₃ heterostructures, in which Ag NPs act as a solid-state electron mediator. Owing to unique nanoarchitecture, MoS₂/Ag–AgVO₃ exhibited the best H₂ generation (reaches 38.6 mmol g⁻¹ in 2 h) which is four times and twenty times higher than Ag–AgVO₃ and bare MoS₂ under visible light respectively. Transient photocurrent and Nyquist spectra reveal that the enhanced photocatalytic performance of MoS₂/Ag–AgVO₃ is mainly attributed to its effective carrier separation and transfer through the surfaces. Moreover, the band structures of the materials have been calculated from Mott-Schottky study, demonstrated a Z-scheme interfacial charge-transfer mechanism. This study describes a promising approach for harvesting solar energy to generate H₂ from water by designing an efficient Ag mediated Z-scheme heterostructures.

© 2020 Elsevier B.V. All rights reserved.

1. Introduction

Generation of H₂ from water using sunlight is one of the most promising pathway to fulfil the growing global demand for clean and renewable energy [1–3]. Semiconductor based photocatalysts have been extensively studied in the field of solar light driven catalysis since TiO₂ was discovered as photoanode for photoelectrochemical water splitting [4–6]. However, the photocatalytic activities of single catalysts are still not satisfactory due to inefficient light absorption in visible range, fast recombination of photogenerated charge carriers and the lack of active sites [7,8]. Thus, designing a visible light harvesting photocatalyst having sufficient charge carriers separation and transport efficiency for water splitting is highly desirable. Semiconductor based heterostructures, where charge-carriers are generated in one semiconductor and subsequently vectorially transferred to the neighboring semiconductor allowing for long-lived electron-hole pairs, are

extensively studied for photocatalysis, however, the redox ability of photogenerated electrons and holes weakened after charge transfer, leading to lower redox ability [9–12]. Thus, heterostructured system is unable to possess high charge separation efficiency and redox ability simultaneously. Therefore, development of a novel photocatalytic system to resolve the aforementioned problems and significantly improve the photocatalytic efficiency is required.

Z-scheme photocatalytic system, involves two step photoreaction for harvest solar energy and transfer electrons to higher electronic state similar to natural photosynthesis, has emerged as an efficient photocatalyst due to enhance charge separation efficiency and high redox capacity for water splitting [13–17]. Although, the concept of Z-scheme photocatalytic system for water splitting was first reported by Bard et al. [18], the idea of all-solid-state Z-scheme for TiO₂–Au–CdS system was proposed by Tada et al. [19] in 2006. All-solid-state Z-scheme photocatalytic system has been composed of two photocatalysts with well-matched band structures and an electron mediator (ionic redox shuttles or solid electron mediators) which forms Ohmic contact between semiconductors with low resistance to boost the charge migration through the interfaces and prolong the life time of photoinduced charges [17,20,21]. Such favorable aligned band position may helpful to maintain the sufficient energy for the water oxidation and reduction as well as inhibiting the undesirable charge carrier recombination [13–15].

* Corresponding author.

** Corresponding author.

E-mail addresses: ghosh.srabanti@gmail.com (S. Ghosh), rnbasu@cgcri.res.in, rajnbasu54@gmail.com (R.N. Basu).

¹ Present address: Department of Organic and Inorganic Chemistry, Universidad de Alcalá (UAH), Madrid, Spain.

Thus, fabrication of Z-scheme heterojunction is expected to enhance the charge carrier separation to boost the redox ability of electrons for water splitting. In Z-scheme photocatalytic system, silver based semiconductors like Ag_3PO_4 [22], AgX ($X = \text{Cl}, \text{Br}, \text{I}$) [23] exhibited enhanced catalytic activity due to tunable band gap and electronic structures in combination with other semiconductor photocatalysts. For example, Bu et al. [22] fabricated Z-scheme heterojunction of $\text{Ag}_3\text{PO}_4/\text{Ag}/\text{WO}_{3-x}$ which showed improved the photocatalytic RhB dye degradation due to prolonged lifetime of photogenerated electrons and photoinduced holes. Recently, a series of reports showed enhanced catalytic activity of Z-scheme system using plasmonic Ag nanoparticles (NPs) as solid state electron mediator under visible light because of their excellent electron conductivity [24–26,32,39]. Owing to the unique properties of surface plasmon resonance (SPR) effect, the Ag NPs can extend the absorption of light in the visible region and boost the photoinduced electron transfer due to generation of an induced local electric field. Similarly, silver vanadium oxide (AgVO_3) have attracted enormous attention in photocatalysis due to its high crystallinity and low band gap (2.6 eV) with visible light absorption [27]. On the other hand, unique hybridization of V 3d, O 2p and Ag 4d orbitals in AgVO_3 gives rise to a highly dispersed valence band (VB), resulting in a narrow band gap. However, the poor charge separation remains an unresolved issue [28]. In another example, Liu et al. [29] developed Z-scheme composite of $g\text{-C}_3\text{N}_4/\text{Ag}/\text{AgVO}_3$ which exhibited higher photocatalytic activity for dye degradation and antibacterial disinfection under visible light irradiation. Wang et al. [30] fabricated Z-scheme $\text{Ag}/\text{AgI}/\text{AgVO}_3$ nanocomposites by a facile *in-situ* ion-exchange method and showed selective oxidation of benzylic amine to imine and reduction of toxic Cr(VI) ions under visible light due to formation of charge migration bridge by Ag^0 species which effectively enhance the charge separation between AgI and AgVO_3 . Although, reported silver based Z-scheme system have shown excellent catalytic activity for organic pollutant degradation [31–33], water splitting [34–37], CO_2 reduction [14,38], degradation of antibiotics [30,39] etc. but AgVO_3 based Z-scheme system for photocatalytic H_2 generation has not been tested yet.

2D layer structured materials are widely utilized in photocatalysis due to high specific surface area, more available catalytic active sites, large number of exposed edges and shorter diffusion length of the charge carriers [40]. Molybdenum disulfide (MoS_2 , belongs to 2D layered transition metal dichalcogenides family) has attracted enormous research interest in photocatalysis because of excellent electrochemical, optoelectronic and energy harvesting properties [41,42]. In addition, the active S atoms on the exposed edges of MoS_2 is potential for H_2 adsorption [43]. Recently, a series of MoS_2 based Z-scheme photocatalytic system such as 0D (MoS_2)/2D ($g\text{-C}_3\text{N}_4$) [34], $g\text{-C}_3\text{N}_4/\text{Ag}/\text{MoS}_2$ [44], $\text{MoS}_2/\text{BiOI}/\text{AgI}$ [45], $\text{MoS}_2/\text{TiO}_2/g\text{-C}_3\text{N}_4$ [46] have been developed which showed high photocatalytic efficiency for H_2 generation. As the CB potential of MoS_2 is sufficiently high from water reduction potential, a novel all-solid-state Z-scheme photocatalytic system could be constructed in presence of a suitable electron mediator between AgVO_3 and MoS_2 .

Herein a novel all-solid-state Z-scheme $\text{MoS}_2/\text{Ag}\text{-}\text{AgVO}_3$ heterostructures using metallic Ag NPs as electron mediator has been fabricated for photocatalytic H_2 generation under visible light. Initially, MoS_2 nanosheets have been prepared by chemical exfoliation method from bulk MoS_2 powder and then Ag NPs decorated AgVO_3 nanorods have been deposited on the surface of the MoS_2 nanosheets by co-precipitation method to fabricate $\text{MoS}_2/\text{Ag}\text{-}\text{AgVO}_3$ heterostructures. The as-prepared heterostructures exhibits much higher photocatalytic activity compared to single MoS_2 and $\text{Ag}\text{-}\text{AgVO}_3$ for H_2 generation under visible light. The superfast interfacial charge-transfer efficiency and high redox

ability of $\text{MoS}_2/\text{Ag}\text{-}\text{AgVO}_3$ heterostructures have been explain by both the photoelectrochemical analysis and photoluminescence (PL) decay spectra. On the basis of band structure, a possible Z-scheme charge-transfer mechanism of $\text{MoS}_2/\text{Ag}\text{-}\text{AgVO}_3$ heterostructures for the enhanced H_2 generation has been proposed.

2. Experimental

2.1. Reagents

Silver nitrate (AgNO_3 , 99%), ammonium monovanadate (NH_4VO_3 , 99%), polyvinylpyrrolidone (PVP) and MoS_2 were obtained from Sigma Aldrich, USA. All compounds were used as received and ultrapure water (Millipore System, 18.2 $\text{M}\Omega$ cm) was used as solvent.

2.2. Synthesis of $\text{MoS}_2/\text{Ag}\text{-}\text{AgVO}_3$ heterostructures

The $\text{MoS}_2/\text{Ag}\text{-}\text{AgVO}_3$ heterostructures were synthesized by co-precipitation (CP) method following the previous method with some modifications [47]. At first, 0.4 g of MoS_2 powder was dispersed in 200 ml of deionized water. Then 0.5 g of PVP as stabilizer was added into the mixture with continuous vigorous stirring at 70 °C for 30 min. After that, bath sonication of MoS_2 solution was carried out for 1 h followed by ultrasound probe sonication for 4 h at frequency 40 kHz. The centrifugation was carried out further for several times using water and ethanol at 12000 rpm. The obtained black powder was then collected and dried at 50 °C overnight.

Finally, the prepared MoS_2 powder (35 mg) was dispersed in 35 ml of deionized water with vigorous stirring for 30 min. Next, 10 mmol of AgNO_3 was added into the above solution and stirred for 30 min at room temperature. At the same time 10 mmol of NH_4VO_3 solution were prepared in another 35 ml of water. After that, the NH_4VO_3 solutions were mixed with the above solution quickly. A precipitation had been occurred and the solution colour changed into yellow. The co-precipitation was collected, washed with distilled water and ethanol several times, and finally dried in an oven at 50 °C for overnight. The synthesis strategy for $\text{MoS}_2/\text{Ag}\text{-}\text{AgVO}_3$ heterostructures has been shown in Fig. 1a. The $\text{Ag}\text{-}\text{AgVO}_3$ was prepared to compare the data by following the same method without using MoS_2 .

3. Characterizations

The crystalline phase of as synthesized materials were studied by XRD (Philips X'Pert, The Netherlands) within 20°–80° (2 θ range) with Cu K α radiation at 40 kV and 40 mA. The morphology and elemental analysis was investigated by Field Emission Scanning Electron Microscopy (LEO. 430i, Carl-Zeiss, Sigma) and Transmission Electron Microscopy (Tecnai G² 30ST). The XPS was performed using PHI 5000 Versa Probe II spectrophotometer with a monochromatized Al K α (~1486.6 eV) X-ray beam of size ~ 100 μm . To clean the surface of the pallet samples 2 kV rastered Ar⁺ ion beam was used for 1 min. JASCO FTIR-6300 spectrometer was used to record the Fourier transform infrared (FTIR) spectra of the as prepared materials and the Raman spectra were collected using a JobinYvon HR800 confocal Raman system by employing 540 nm laser beam on the sample surface. To study the optical properties of as prepared materials, Shimadzu, UV-3600 spectrophotometer (for diffuse reflectance spectra, DRS) and JASCO FP-8500 (for photoluminescence spectra, PL) was used. Finally, photocatalytic H_2 evolution through water reduction was measured by online gas chromatography using YL Instrument, 6500 GC system with thermoconductive detector.

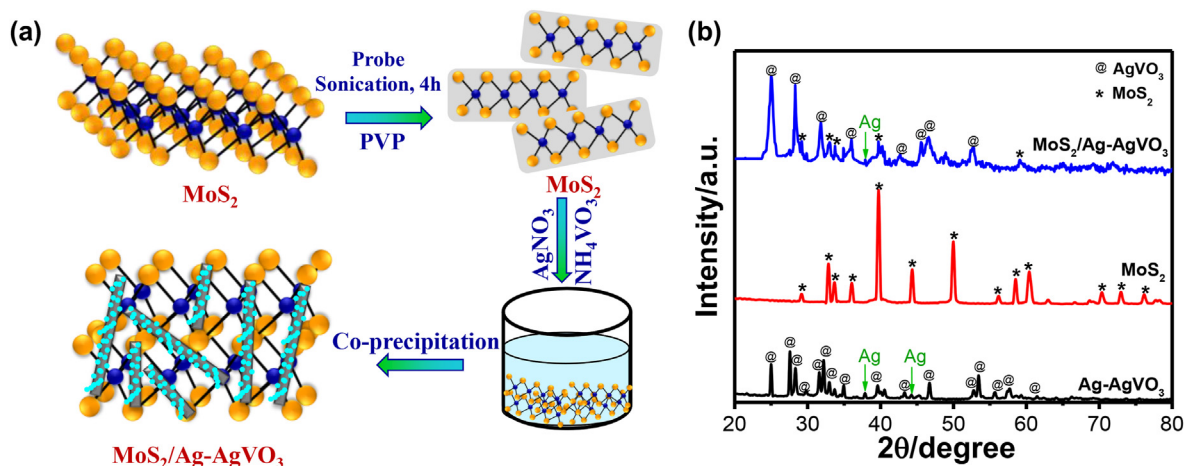


Fig. 1. (a) Schematic depiction of synthesis of MoS₂/Ag-AgVO₃ heterostructures by co-precipitation method. (b) XRD patterns of the synthesized Ag-AgVO₃, bare MoS₂ and MoS₂/Ag-AgVO₃ heterostructures.

3.1. Photocatalytic H₂ generation

To quantitatively measure the amount of H₂ generation and H₂ generation rate, online gas chromatography was used. A closed reactor containing 50 mL Ar saturated water-methanol (25 vol % methanol) solution with catalyst concentration of 1 mg mL⁻¹ was used as reactor. In presence of Xe-arc lamp (250W) with an incident beam intensity of 100 mWcm⁻², H₂ generation had been measured. A 420 nm cutoff filter was used to get the visible light. The apparent quantum yield (AQY) of H₂ generation has been calculated further using the following Eq. of [58]:

$$AQY = \frac{2 \times \text{moles of } H_2 \text{ produced}}{\text{no. of incident photons}} \times 100 \quad (1)$$

3.2. Photoelectrochemical measurements

To measure the photoelectrochemical properties of the as synthesized materials, a galvanostat-potentiostat (PGSTAT302 N, Autolab, The Netherlands) with standard three-electrode cell where saturated Ag/AgCl electrode as reference electrode and Pt wire as counter electrode. The working electrode was thin film of as prepared material on FTO. The cyclic voltammetry (CV) and linear sweep voltammetry (LSV) was carried out within the potential range -0.4V to 1V vs Ag/AgCl at a scan rate 10 mV s⁻¹ in presence of 0.5 M Na₂SO₄ phosphate buffer (pH 7) as electrolyte under light illumination. The light sensitivity and stability of the photo anodes were checked through chronoamperometry (CA) at 0.26V vs Ag/AgCl under periodic chopped irradiation. To convert the obtained potential into reference hydrogen electrode (RHE) Eq. (2) has been followed.

$$E_{RHE} = E_{Ag/AgCl} + 0.059 \text{ pH} + 0.197 (E^0_{Ag/AgCl}) \quad (2)$$

Further, the charge transfer resistance and junction capacitance of the photoelectrodes were studied through Nyquist plot and Mott-Schottky plot. Mott-Schottky experiment was carried out within the potential range of -1.0V to 0.6V vs Ag/AgCl at 1000 Hz frequency using ac RMS amplitude of 10 mV. Incident photon to current conversion efficiency (IPCE) and absorbed photon to current conversion efficiency (APCE) was calculated according to the equations within the wavelength range of 350–700 nm.

$$IPCE = \frac{I_{ph}}{P_{in}} \times \frac{1240}{\lambda} \times 100\% \quad (3)$$

$$APCE = \frac{IPCE}{1 - 10^{-A_\lambda}} \times 100\% \quad (4)$$

where, P_{in} is incident power density (W cm⁻²), I_{ph} is output photocurrent density (A cm⁻²), λ is wavelength (nm) and A_λ is the absorbance of the photoanode at any particular wavelength (λ).

4. Results and discussion

4.1. Structural and morphological analysis

The crystalline structures of as synthesized materials have been explored by powder XRD. Fig. 1b illustrates the XRD patterns of Ag-AgVO₃, MoS₂ and MoS₂/Ag-AgVO₃. The strong peaks at 2θ values of 25°, 27.5°, 28.32°, 29.8°, 31.58°, 32.14°, 32.95°, 34.97°, 39.5° and 40.5° can be assigned to the diffraction plans of (220), (310), (22-1), (-311), (221), (-131), (002), (311), (131) and (420) for AgVO₃ which confirms the monoclinic α-phase of AgVO₃ with space group C2/c [JCPDS No. 15-50645] [47]. The diffraction peaks at 2θ values of 38.1° and 44.3° are represent the presence of (111) and (200) diffraction planes of Ag NPs [JCPDF card 04-0783] [47]. The characteristic (100), (103), (105) and (110) peaks of MoS₂ indicate the hexagonal phase of MoS₂ [JCPDS no. 37-1492] [48]. After heterostructure formation, (220), (310), (22-1), (-131), (311), (400) and (420) remains unchanged, whereas a new diffraction peak comes at 31.75° which may be the combined peak of (221) and (-131) located at 31.58° and 32.14° for pure Ag-AgVO₃.

The morphology and the elemental analysis of the synthesized materials have been studied by FESEM and TEM. Fig. S1 shows the FESEM images of MoS₂ powders before and after probe sonication. It can be clearly observed that thin layers of MoS₂ nanosheets are formed after 4 h probe sonication from MoS₂ powder (Fig. S1b). On the other hand, Ag NPs decorated 1D AgVO₃ nanorods with a size of 200 nm in width and more than 6 μm in length have been obtained through co-precipitation method at room temperature (Fig. S1c). TEM image of Ag-AgVO₃ further reveals that very small Ag NPs are formed on the surface of AgVO₃ nanorods (Fig. 2a). Additionally, the high resolution TEM (HRTEM) identifies two set of different lattice fringes. The lattice fringe -0.28 nm matches well with the (-131) plane of α-AgVO₃ NPs (Fig. 2b) [30]. Meanwhile, the lattice spacing

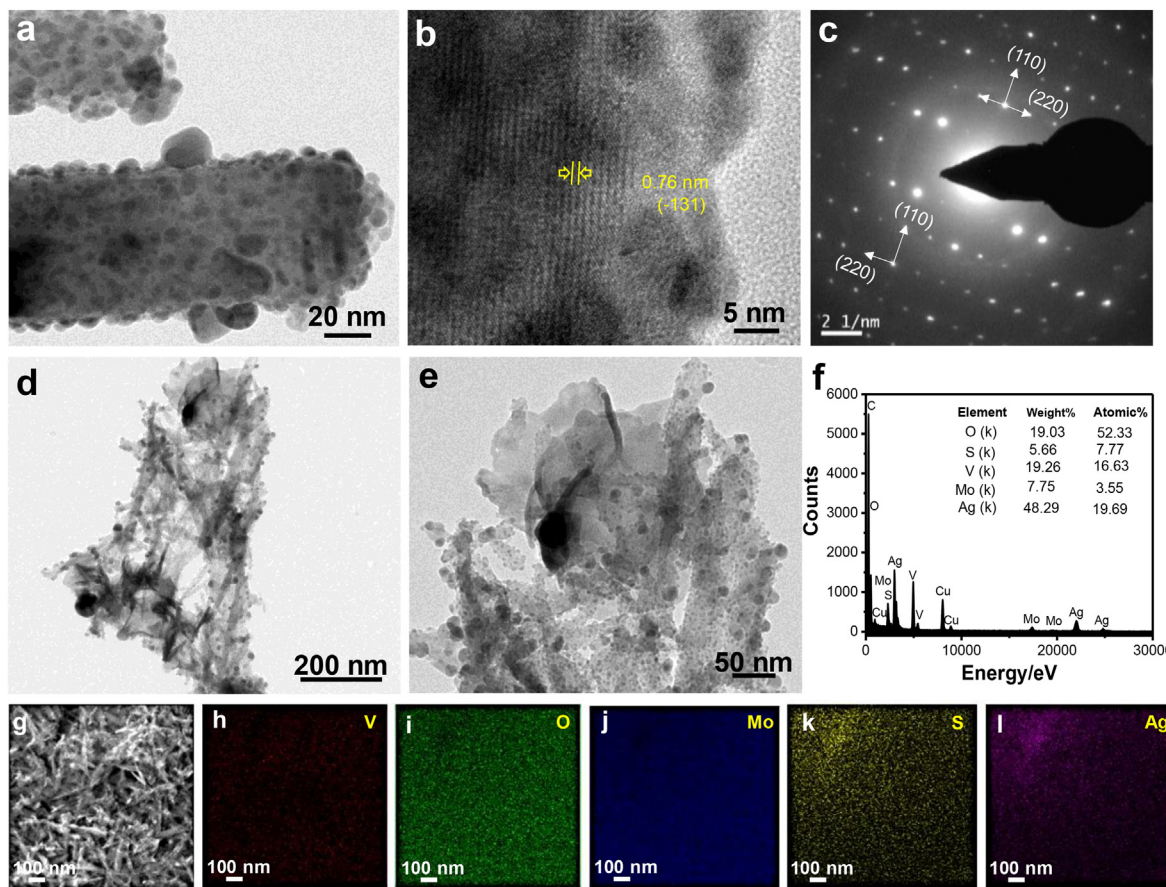


Fig. 2. (a) TEM image, (b) HRTEM image and (c) SAED pattern of Ag–AgVO₃ synthesized at room temperature. (d) Low and (e) High magnification TEM images and (f) EDX spectrum of MoS₂/Ag–AgVO₃ heterostructures. (g) FESEM image of MoS₂/Ag–AgVO₃ and corresponding energy-dispersive X-ray spectroscopy (EDS) elemental mapping for (h) V, (i) O, (j) Mo, (k) S and (l) Ag.

of ~ 0.236 nm corresponds to the (111) plane of metal Ag (Fig. S2) [49]. Moreover, the corresponding selected area electron diffraction (SAED) pattern supports the single crystallinity of each individual AgVO₃ nanorod in which the diffraction spots with d-values of 0.35 nm and 0.73 nm assigned to the (220) and (110) planes of the α -AgVO₃ (Fig. 2c) [49]. The TEM images (Fig. 2d and e) of heterostructures exhibit an interconnected architecture, consisting of thin layers of stacked 2D MoS₂ nanosheets and AgVO₃ nanorods. Further, the magnified TEM image of the heterostructures shows that Ag NPs decorated AgVO₃ nanorods are dispersed on the surface of MoS₂ nanosheets, implies an assembly between nanorods and nanosheets through an electron mediator. However, the energy-dispersive X-ray (EDX) spectrum illustrates the chemical composition of MoS₂/Ag–AgVO₃ heterostructures which composed of Ag, V, O, Mo and S (Fig. 2f). The atomic ratio of Mo and S is 1:2 calculated from EDX. However, the atomic ratio of Ag, V and O is about 1.18:1:3, which is close to the stoichiometric ratio of AgVO₃ (1:1:3). As Ag NPs are also formed, total atomic weight is slightly greater for Ag. Thus, heterostructuring of MoS₂ and AgVO₃ does not change the stoichiometric ratio of individual MoS₂ and AgVO₃. Fig. 2g–l represents the FESEM image of MoS₂/Ag–AgVO₃ and the corresponding energy-dispersive X-ray spectroscopy (EDS) elemental mapping for V, O, Mo, S and Ag which further confirm the successful formation of MoS₂/Ag–AgVO₃ heterostructures.

To elucidate the surface chemical compositions and oxidation state of the constituent elements of MoS₂/Ag–AgVO₃ heterostructures, XPS analysis has been carried out. Fig. 3a represents the

XPS survey spectra of Ag–AgVO₃, MoS₂ and MoS₂/Ag–AgVO₃ heterostructures where peaks at binding energy 159.5, 229.7, 364.2, 515.6, 528.6 and 571.3 eV correspond to S, Mo, Ag, V and O respectively, supporting the formation of heterostructures. Fig. 3b–f illustrates the magnified XPS spectra of Ag 3d, V 2p, O 1s, S 2p and Mo 3d regions. The core level Ag 3d spectra display a doublet signal of Ag⁺ 3d_{5/2} and Ag⁺ 3d_{3/2} at binding energies of 367.9 eV and 373.9 eV respectively. Notably, a strong peak at 368.4 eV has been observed after fitting which is ascribed to the presence of Ag⁰ state [50]. In addition, the heterostructure formation with MoS₂ leads to a shift of the Ag 3d peaks toward the higher binding energy with a value of ~ 0.38 eV (Fig. S3). Peak shifting indicates a possibility of sharing electrons with neighboring atoms in terms of asymmetry in the bond arrangements, which creates an extra pressure on the electrons. So, slightly high binding energy is required for ejection of electrons compared to base material during the excitation process. Moreover, the shifting towards high binding energy implies a band bending which results a charge redistribution at the interface as well as indicates the decrease of electron density in the Ag⁺ cation, which implies an electron transfer from the AgVO₃ to MoS₂ [50]. As shown in Fig. 3c, V 2p signal represents two peaks at 516.4 eV and 523.9 eV are attributed to the binding energies of V⁵⁺ 2p_{5/2} and V⁵⁺ 2p_{3/2} [51]. Hence, the XPS spectrum of O 1s shows two peaks at 529.9 eV and 531.6 eV which could be assigned to the binding energies of V–O bond and surface adsorbed oxygen respectively (Fig. 3d) [52]. The strong peaks located at binding energies of 232.7 eV and 229.4 eV are ascribed to Mo 3d_{3/2}

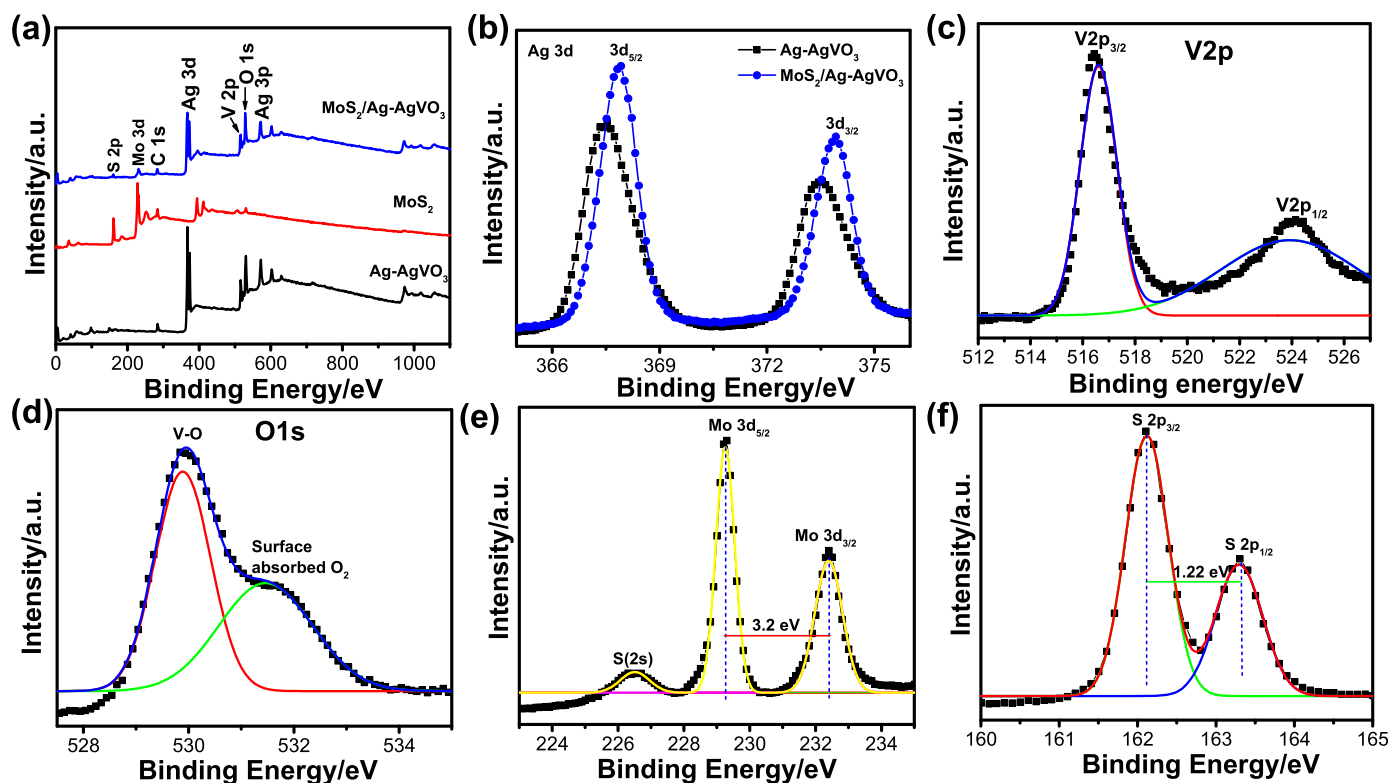


Fig. 3. (a) The XPS spectra of the Ag–AgVO₃, bare MoS₂ and MoS₂/Ag–AgVO₃ heterostructures. (b–f) Magnified XPS spectra for Ag 3d, V 2p, O 1s, Mo 3d and S 2p of MoS₂/Ag–AgVO₃ heterostructures. Here the scattered and solid lines represent the experimental and fitted data.

and Mo 3d_{5/2} respectively, in which the spin–orbit separation of 3.2 eV suggests Mo⁴⁺ state of Mo [53]. In addition, the characteristic peaks obtained at 161.9 eV and 163.1 eV (separated by 1.22 eV) correspond to S 2p_{3/2} and S 2p_{1/2} respectively, confirming S²⁻ state of S within the MoS₂/Ag–AgVO₃ heterostructures [54]. Moreover, the peak intensity of Ag 3d, Mo 3d and S2p peaks have been increased after heterostructures formation, indicating electrons are diffused towards the surface (Fig. S3) as the intensity of peak is directly depends on the number of electron in the respective chemical state [54]. Thus, XPS spectra suggest the co-existence of MoS₂, AgVO₃ and heterostructure formation.

The chemical structures of the heterostructures and the interactions between MoS₂ and AgVO₃ have been further studied by FT-IR and Raman analysis. The Ag–AgVO₃ shows characteristic peaks at 3456, 1641, 1383, 1113, 928, 775, 635 and 509 cm⁻¹ (Fig. 4a). The peaks at 3456 cm⁻¹ correspond to O–H stretching vibration and bending vibration of physisorbed water molecules and 1641 cm⁻¹ correspond to surface hydroxyl groups [50]. A peak at 928 cm⁻¹ arises due to the symmetric stretching vibrations of VO₃ whereas, additional peaks at 775 and 635 cm⁻¹ are assigned to the antisymmetric stretching vibrations of VO₃ [55]. The symmetric stretching mode of V–O–V units are confirmed by the presence of FTIR peak at 509 cm⁻¹ as reported earlier [59]. New vibration peaks appear at 1107 cm⁻¹ and 621 cm⁻¹ in heterostructures, which are attributed to the characteristic peaks of MoS₂ [56]. Furthermore, the as-prepared materials have been characterized by the Raman spectroscopy. Fig. 4b shows the Raman peaks of Ag–AgVO₃, bare MoS₂ and MoS₂/Ag–AgVO₃ heterostructures. The characteristic peaks of Ag–AgVO₃ at 919, 867, 809, 624, 526, 332 and 213 cm⁻¹ which are well matched with the previously reported literatures (Fig. 4b) [51]. The Raman peaks at 919 and 867 cm⁻¹ correspond to V=O stretching vibration and peaks at 624 and 526 cm⁻¹ are

attributed to the V–O–V stretching vibration. Further, peak at 809 cm⁻¹ is originated from the V–O–Ag stretching vibration [51]. However, the MoS₂ exhibits characteristic Raman peaks at 380 and 407 cm⁻¹ corresponds to in-plane E_{2g} mode and the out-of-plane A_{1g} mode respectively which are consistent with Raman results of monolayer MoS₂ in the reported literature. The inplane E_{2g} mode originates due to opposite vibration of two S atoms with respect to the Mo atom and the A_{1g} mode arises due to the out-of-plane vibration of S atoms [57]. In heterostructures, both Raman peaks of MoS₂ and AgVO₃ are present whereas, a blue shift has been observed for V–O–V bands which suggests the bond length becomes weaker due to presence of a covalent bond between MoS₂ and AgVO₃ [57]. Moreover, this result again confirms the heterostructures formation between AgVO₃ and MoS₂.

4.2. Optical absorption properties

To investigate the influence of heterostructure formation on the optical absorption, UV–Vis diffuse reflectance spectra (DRS) have been studied. Fig. 4c illustrates the UV–Vis absorption spectra of Ag–AgVO₃, bare MoS₂ and MoS₂/Ag–AgVO₃ heterostructures. The bare MoS₂ and Ag–AgVO₃ exhibits absorption both in the UV and visible regions. Interestingly, after heterostructure formation absorption intensities of MoS₂/Ag–AgVO₃ increase at each wavelength and the absorption edge shifts to near IR region compared to individual elements. Thus, presence of Ag NPs remarkably enhance the absorption of light by virtue of SPR effect which induce a local electromagnetic field at the interfaces of the semiconductors. As a result, electron-hole pair formation and separation ability at the interfaces increases, which would be helpful to achieve efficient photocatalytic activity under visible light. Further, by using the Kubelka–Munk [(αhν)² vs photon energy (hν)] plot (Eq. (5)) band

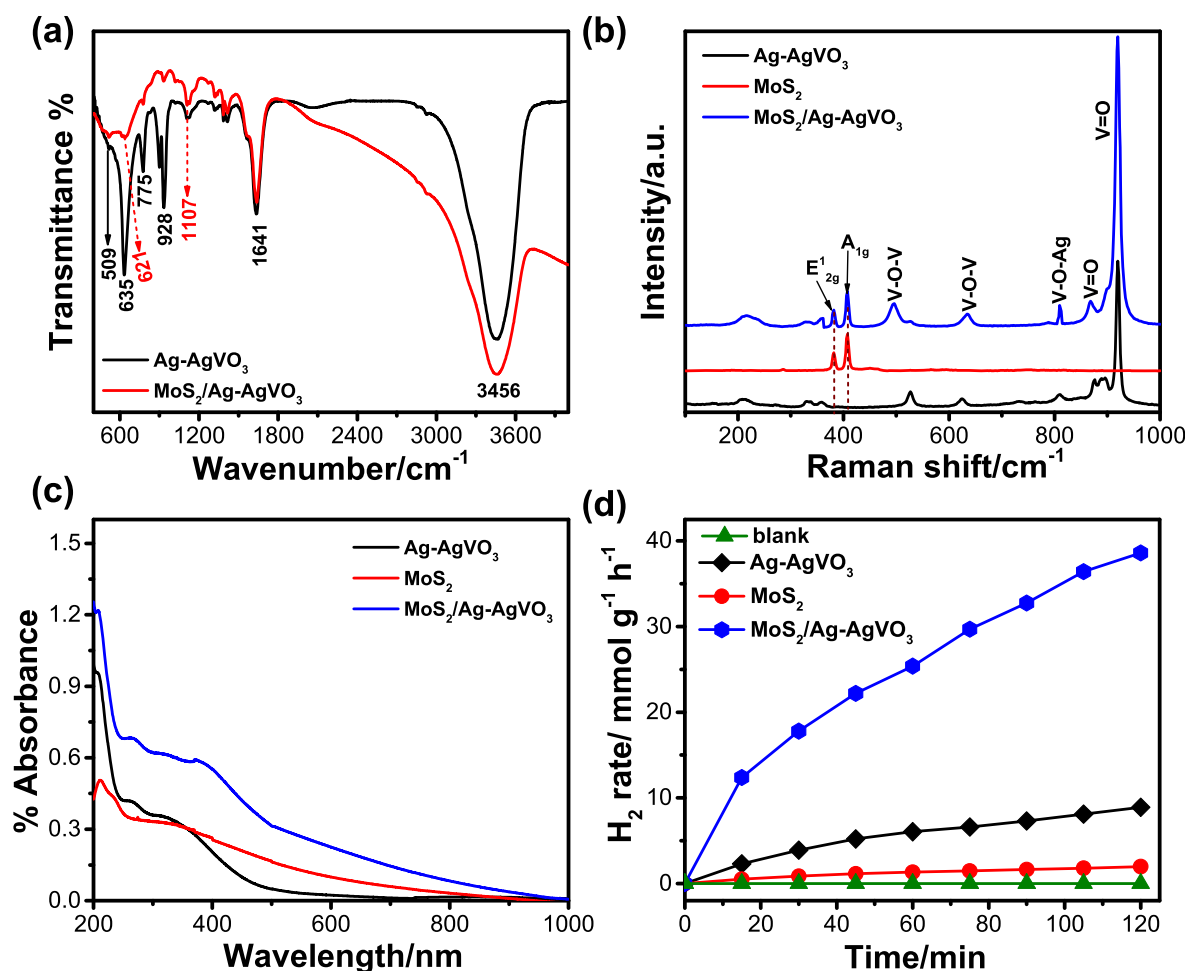


Fig. 4. (a) FTIR spectra, (b) Raman spectra, (c) Diffuse reflectance spectra of Ag–AgVO₃, bare MoS₂ and MoS₂/Ag–AgVO₃ heterostructures and (d) photocatalytic hydrogen generation without light and catalyst (green line), in presence of Ag–AgVO₃ (black line), bare MoS₂ (red line) and MoS₂/Ag–AgVO₃ heterostructures (blue line) after 120 min of visible light irradiation. (For interpretation of the references to colour in this figure legend, the reader is referred to the Web version of this article.)

gaps of MoS₂ and Ag–AgVO₃ have been calculated.

$$\alpha h\nu = A(h\nu - E_g)^{n/2} \quad (5)$$

where, α is the absorption coefficient, ν is the light frequency, A is the proportionality constant, and E_g is the band gap of the material (Fig. S4). The calculated E_g of the MoS₂ and Ag–AgVO₃ are 2.3eV and 2.8 eV respectively.

4.3. Photocatalytic activity

Visible light driven photocatalytic activity of MoS₂, Ag–AgVO₃ and MoS₂/Ag–AgVO₃ have been performed for H₂ generation through water reduction at pH 7 in presence of methanol as hole scavenging agent as it reacts with the photogenerated holes usually faster than water, leads to excess electron in the medium for H₂ generation [58]. Fig. 4d shows the photocatalytic H₂ generation of Ag–AgVO₃, bare MoS₂ and MoS₂/Ag–AgVO₃ heterostructures through water reduction, where no generation of H₂ gas is observed without light and catalyst. The pure MoS₂ shows low H₂ generation of ~1.9 mmol g⁻¹ after 2 h continuous visible light irradiation due to the fast recombination of photogenerated charge carriers and low carrier density. In contrast, an increase in H₂ generation have been observed for Ag–AgVO₃ (~8.9 mmol g⁻¹), which may be attributed

due to the presence of Ag NPs on the surface of 1D AgVO₃ because of SPR effect and high carrier density at the catalyst surface. However, MoS₂/Ag–AgVO₃ heterostructure exhibits highest H₂ generation which reaches ~38.6 mmol g⁻¹ in 120 mins because of fast electron transfer between the MoS₂ and AgVO₃ through bridged Ag NPs. Interestingly, the H₂ generation rate increases linearly with time for heterostructures, indicating that a strong driving force has been maintained by the catalyst for water reduction over the examined period. Further, to understand the role of sacrificial agent in H₂ generation, a set of experiments have been carried out by varying the volume % of methanol. Fig. S5 a demonstrates the effect of methanol (volume %) on the H₂ generation as sacrificial agent. Photocatalytic H₂ generation increase with the increase of methanol up to 25 vol % because of fast capturing the photogenerated holes which hinder the rapid recombination rate of charge carriers, and then goes to decrease due to back reaction and photocorrosion. Fig. S5b presents the calculated AQY% for the catalysts, where MoS₂/Ag–AgVO₃ heterostructures exhibits highest photocatalytic H₂ generation efficiency of 13.8% followed by Ag–AgVO₃ (3.2%) and bare MoS₂ (0.7%). Thus, heterostructure formation improve the H₂ generation rate as well as AQY% which indicate that efficient electron-hole generation and separation processes may be happened at the interfaces of the heterostructured catalyst.

4.4. Photoelectrochemical (PEC) properties

To gain deeper insights into the photogenerated charge separation and transport process in the photocatalytic reactions, electrochemical measurements have been conducted further by preparing electrodes of as synthesized materials on FTO glass by doctor-blade method. Cyclic voltammetry (CV) has been carried out to study the electrochemical properties of the as prepared electrodes of MoS_2 , Ag-AgVO_3 and $\text{MoS}_2/\text{Ag-AgVO}_3$ using 0.5 M Na_2SO_4 -phosphate buffer solution (pH 7) as electrolyte and Ag/AgCl electrode as reference electrode at a scan rate of 10 mV s^{-1} (Fig. 5a). In the cathodic polarization process, two peaks have been observed for Ag-AgVO_3 at $\sim -0.31 \text{ V}$ and $\sim -0.59 \text{ V}$ vs Ag/AgCl with current density of $\sim -69 \mu\text{A cm}^{-2}$ and $\sim -336 \mu\text{A cm}^{-2}$, which corresponds to the initial reduction of Ag^+ to Ag^0 and V^{5+} to V^{4+} respectively. Similarly, two characteristic peaks have been appeared in the anodic scan at $\sim 0.27 \text{ V}$ and $\sim 0.12 \text{ V}$ vs Ag/AgCl , which are in well agreement with the previously reported literatures [59,60]. On the other hand, no prominent cathodic peak is present in MoS_2 electrode, but a broad peak is observed around $\sim -0.8 \text{ V}$ vs Ag/AgCl . However, the CV of the $\text{MoS}_2/\text{Ag-AgVO}_3$ electrode shows a single peak at $\sim -0.45 \text{ V}$ vs Ag/AgCl in cathodic scan with current density of $\sim -519 \mu\text{A cm}^{-2}$. This large current density of heterostructures demonstrate an enhanced electron transfer rate through the interfaces [50]. Further, linear sweep voltammetry (LSV) have been studied under chopped light illumination of 100 mW cm^{-2} (Fig. 5b). The bare MoS_2 photoanode shows low current density in the full potential range, because of its poor ability of charge separation, which leads to the fast recombination of photoinduced electron-hole pairs. However, an enhanced current density has been obtained for Ag-AgVO_3 and $\text{MoS}_2/\text{Ag-AgVO}_3$ electrodes and it reaches maximum value of $\sim 80 \mu\text{A cm}^{-2}$ at 0.8 V vs Ag/AgCl for

$\text{MoS}_2/\text{Ag-AgVO}_3$ heterostructures. This result demonstrates that presence of Ag NPs significantly improves visible-light absorption by plasmonic effect and efficiently separates the photoinduced electrons and holes by making electron migration bridge between two semiconductors, leading to a remarkable enhancement in PEC water splitting. Transient photocurrent measurements through chronoamperometry (CA) and electrochemical impedance spectroscopy (EIS) have been performed further to gain insight into the carrier separation and transport efficiency of the photoanodes. It can be clearly observed that the current density increases for $\text{MoS}_2/\text{Ag-AgVO}_3$ heterostructure ($\sim 64 \mu\text{A cm}^{-2}$) compared to bare MoS_2 ($\sim 25 \mu\text{A cm}^{-2}$) and Ag-AgVO_3 ($\sim 35 \mu\text{A cm}^{-2}$) after 500 sec and remains almost constant with time (Fig. 5c). Therefore, it can be concluded that heterojunction formation can promote the charge separation and suppress the recombination of photogenerated electron-holes. Fig. 5d represents the Nyquist diagram of as prepared electrodes, where the radius of each arc is associated with the charge transfer resistance (R_{ct}) at the electrode electrolyte interface. A single semicircle has been obtained for both MoS_2 and Ag-AgVO_3 electrodes, whereas a distorted semicircle has been observed for $\text{MoS}_2/\text{Ag-AgVO}_3$ heterostructures. This may results due to the increase of electron diffusion to the catalyst surface [61].

The straight line in the lower frequency region arises due to more diffusion process of the electrolyte. The diameter presents the R_{ct} over the electrode-electrolyte interface. As shown in Fig. 5d the diameter of heterostructures ($0.46 \text{ k}\Omega$) is considerably smaller than that of bare MoS_2 ($1.6 \text{ k}\Omega$) and Ag-AgVO_3 ($1.5 \text{ k}\Omega$), suggests that heterostructures provide facile access for charge carrier interpolation during the water splitting process. Thus, all electrochemical investigations demonstrate that, heterostructure formation between MoS_2 and Ag-AgVO_3 accelerates the interfacial transfer and separation of photogenerated charges which results high activity in

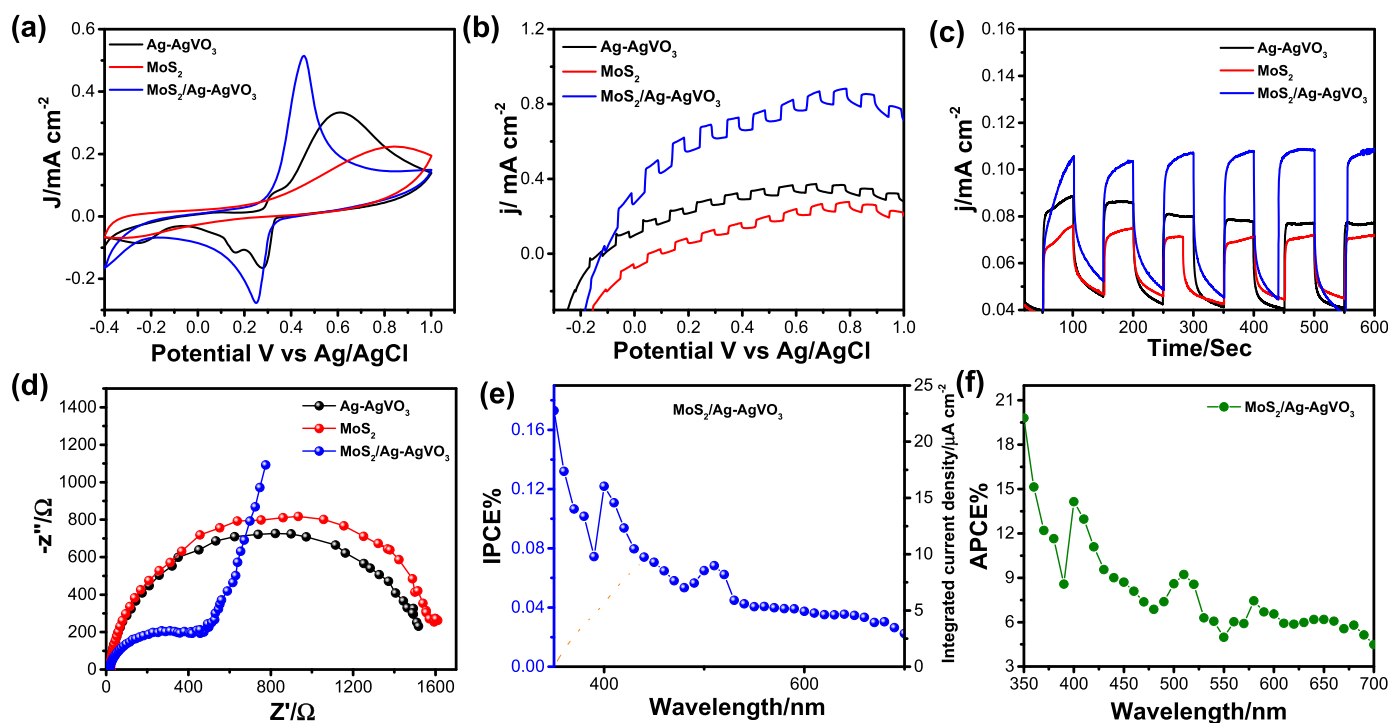


Fig. 5. (a) Cyclic voltammogram (CV) of prepared electrodes in presence of 0.1 M Na_2SO_4 -phosphate buffer solution (pH 7) as electrolyte at a scan rate of 10 mV s^{-1} . (b) linear sweep voltammetry (LSV) and (c) chronoamperometry (CA) under chopped light illumination of 100 mW cm^{-2} of as prepared electrodes in presence of 0.1 M Na_2SO_4 -phosphate buffer solution at a scan rate of 10 mV s^{-1} . (d) Nyquist plots of Ag-AgVO_3 , bare MoS_2 and $\text{MoS}_2/\text{Ag-AgVO}_3$ heterostructures recorded at 0.1 V vs Ag/AgCl under light illumination. (e) Calculated incident photon to current conversion efficiency (IPCE%) and corresponding integrated current density (product of the IPCE spectrum with the AM 1.5G photon flux), (f) Absorbed photon to current conversion efficiency (APCE%) of $\text{MoS}_2/\text{Ag-AgVO}_3$ photoanode within the wavelength range 350–700 nm.

photocatalytic H_2 generation. Moreover, the quantum efficiency of the $MoS_2/Ag-AgVO_3$ heterostructure has been studied in details by calculating incident photon to current conversion efficiency (IPCE) and absorbed photon to current conversion efficiency (APCE) from the action spectra through CA measurements within the wavelength range of 350–700 nm [62]. Fig. 5e represents the IPCE vs wavelength plot where two distinct enhanced regions are observed at 400 nm and 510 nm with efficiency of 0.12% and 0.06% respectively. The integrated current density of the $MoS_2/Ag-AgVO_3$ photoanode reaches to $21 \mu A cm^{-2}$ which well consistent with the photo current density calculated from LSV curve. The APCE plot represents the similar trend like IPCE with two enhanced region at visible region (Fig. 5f). Thus, heterostructure formation is beneficial to enhance the light absorption, charge separation and surface catalytic reactions which consequently enhance the incident photon to current conversion efficiency.

4.5. Possible photocatalytic mechanism

The separation and recombination processes of photoinduced charge carriers of the as-prepared samples have been further examined by the Photoluminescence (PL) spectra. Generally, the PL emission are originated from the recombination of electron hole pairs in a semiconductor. The low PL intensity presents low recombination of photo induces electron hole pairs, thereby high photocatalytic performance [63]. Fig. 6a shows the PL spectra of $Ag-AgVO_3$ and $MoS_2/Ag-AgVO_3$ heterostructures upon excitation

at 340 nm. The band to band recombination and distortion in the [O–Ag–O] and [O–V–O] bonds in $AgVO_3$ lattice are mainly responsible for PL emissions. In the PL spectra a pronounced maximum at 467 nm has been observed which corresponds to band to band recombination of photoinduced charge carriers. Additionally, a peak at 450 nm comes due to distortions in the tetrahedral $[VO_4]$ clusters [64]. In addition, a weak emission peak has also been presented at 560 nm, indicates an ordered structure of $AgVO_3$. However, the PL emission peak intensity has been decreased after heterostructure formation with MoS_2 without effecting the spectral position of the peaks, suggesting improve charge separation and transfer ability of heterostructures. Furthermore, to understand the ultrafast charge transfer processes associated at the interface between MoS_2 and $AgVO_3$, picosecond resolved time correlated single photon counting (TCSPC) of the materials have been recorded. Fig. 6b shows the decay curve of $Ag-AgVO_3$ which is properly fitted with a double exponential with average lifetime of ~ 1.30 ns. However, the average decay time for MoS_2 (~ 0.71 ns) is lower than $Ag-AgVO_3$, which has an ultrafast component of ~ 25 ps (21.3%). The average decay time decreases from 0.71 ns to 0.36 ns after heterostructure formation between MoS_2 and $Ag-AgVO_3$ (Table 1). Interestingly, the contribution of the fast component of $MoS_2/Ag-AgVO_3$ heterostructure has been increased to nearly 40% from 21.3% compared to bare MoS_2 . This result clearly indicated that, electron transfer occurs from $AgVO_3$ to MoS_2 after heterostructure formation and reduce the recombination rate which is well consistent with the PL data (Fig. 6a). Similar behaviour was observed by

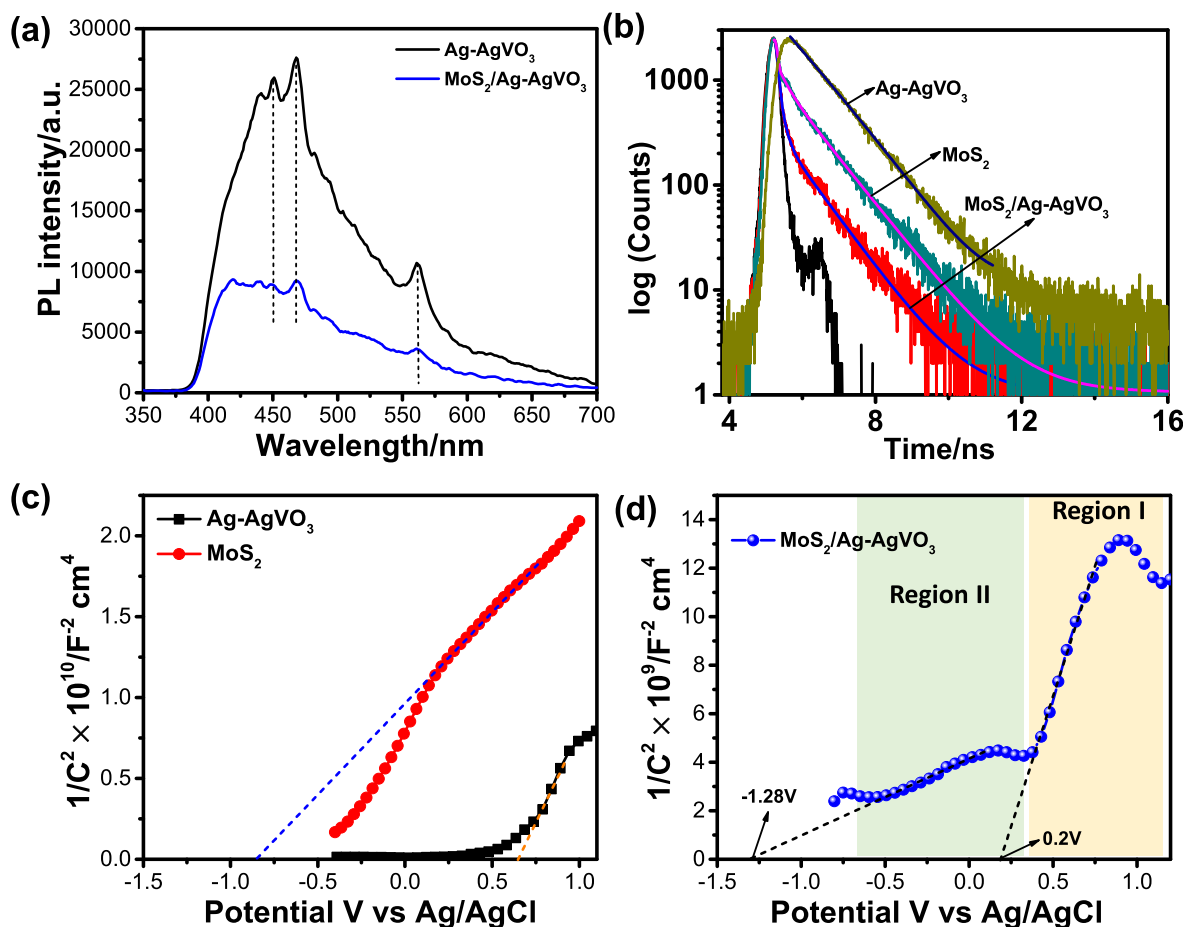


Fig. 6. (a) Photoluminescence (PL) spectra of $Ag-AgVO_3$ and $MoS_2/Ag-AgVO_3$ heterostructures upon excitation at 340 nm. (b) The picosecond-resolved TCSPC spectra of as prepared materials upon excitation at 375 nm. Mott-Schottky plots of (c) $Ag-AgVO_3$, bare MoS_2 and (d) the $MoS_2/Ag-AgVO_3$ heterostructures in the presence of 0.1 M Na_2SO_4 electrolytes (pH 7) using an AC frequency of 1000 Hz. The intercept of the plot (at $1/C^2 = 0$) has been used to determine the flat band potential (E_{fb}) of the photoelectrodes.

Table 1

Decay parameters of Ag–AgVO₃, MoS₂ and MoS₂/Ag–AgVO₃ heterostructures with Excitation wavelength, E_{ex} = 375 nm and Emmission wavelength, E_{em} = 450 nm.

| sample | τ_1 (a ₁ %) ns | τ_2 (a ₂ %) ns | τ_3 (a ₃ %) ns | τ_{avg} (ns) |
|--|--------------------------------|--------------------------------|--------------------------------|-------------------|
| Ag–AgVO ₃ | 1.31 (55.6) | 1.30 (44.4) | | 1.30 |
| MoS ₂ | 0.26 (10.5) | 0.99 (68.2) | 0.025 (21.3) | 0.71 |
| MoS ₂ /Ag–AgVO ₃ | 0.13 (26.4) | 0.91 (34.2) | 0.051 (39.4) | 0.36 |

Table 2

Electrochemical parameters calculated from Mott-Schottky plots for prepared electrodes.

| Catalyst | E _{fb} in V vs Ag/AgCl | CB in V vs NHE | VB in V vs NHE | E _g in eV |
|----------------------|---------------------------------|----------------|----------------|----------------------|
| Ag–AgVO ₃ | 0.65 | 1.06 | 3.86 | 2.8 |
| MoS ₂ | −0.83 | −0.42 | 1.88 | 2.3 |

Sardar et al. [65] in case of PDPB-ZnO heterostructure due to electron transfer from the conjugated polymer nanofibers to the ZnO nanoparticles.

Finally, Mott-Schottky (M – S) experiment of as prepared electrodes has been carried out to find out the band edge potentials of constituent semiconductors as they play crucial role in determining the transfer route of the charge carriers. Fig. 6c shows the M – S plot of Ag–AgVO₃ and bare MoS₂ electrodes in the presence of 0.5 M Na₂SO₄ electrolytes (pH 7) using an AC frequency of 1000 Hz, where the positive slopes confirm the n-type behavior of the materials.

The flat band potentials (E_{fb}) of the electrodes have been determined by taking an intercept of the plot (at 1/C² = 0) using the following equation [66].

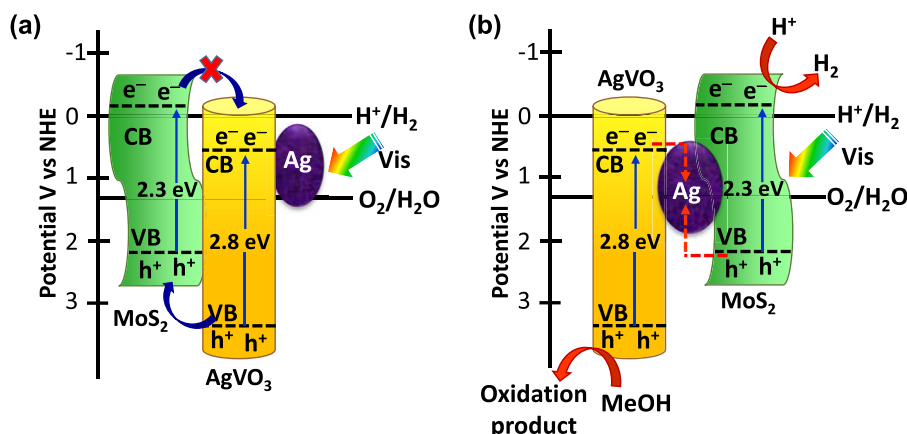
$$\frac{1}{C_{sc}^2} = \frac{2}{eN_A\epsilon\epsilon_0} \left(E - E_{fb} - \frac{KT}{E} \right) \quad (6)$$

where, C_{sc} is the space charge capacitance (in F cm^{−2}), e is electronic charge in C, ε is the dielectric constant of the semiconductors, ε₀ is the permittivity of free space, N_A is the charge carrier density in cm^{−3}, E_{fb} is the flat band potential in V, K is the Boltzmann constant and T is the temperature in K.

Notably, a negative shift in the flat band potential (E_{fb}) has been observed for MoS₂ (−0.83V vs Ag/AgCl) compare to Ag–AgVO₃ (0.65V vs Ag/AgCl). As the E_{fb} is near to the CB for n-type semiconductor, thus the positions of CB are 0.45V and −1.03 V (vs Ag/AgCl, CB = E_{fb} − 0.2 V) [67,68], therefore they are 1.06 V and −0.42 V vs NHE (Normal Hydrogen Electrode) for Ag–AgVO₃ and bare MoS₂

electrodes respectively (Fig. 6c). So, the VB positions of Ag–AgVO₃ and bare MoS₂ electrodes would be 3.86 V and 1.88 V vs NHE respectively (Table 2) which corresponds to the results of UV–Vis DRS analysis. After heterostructure formation, a couple of slopes have been observed. When the applied potential is more positive (Region I), the space–charge region of the thin-film is depleted and the capacitance of the working electrode is similar to that of the AgVO₃ electrode. The linear fit of this region gives flat band (E_{fb}) potential of 0.2V vs Ag/AgCl, which is more negative than the Ag/AgVO₃ (0.65 V vs Ag/AgCl). When the applied potential goes to negative (Region II), dramatic increase in the capacitance has been observed which arise from the space charge region of MoS₂/Ag–AgVO₃ junction. The E_{fb} of this region (−1.28V vs Ag/AgCl) is also more negative than the MoS₂ (−0.83V vs Ag/AgCl). However, the linear regions are separated by a shoulder at about 0.15 V vs Ag/AgCl, indicates the formation of MoS₂/Ag–AgVO₃ interface [69].

Based on the experimental results, it can be proposed that the improved photocatalytic activity achieves due to the enhancement of light absorption capacity as well as efficient charge separation of photogenerated electron hole pairs. Generally, the charge transfer mechanism of heterostructures follow type-II heterojunction pathway, where the CB electrons (more negative potential) of one semiconductor transfer to the CB of another semiconductor and the VB holes (more positive potential) transfer to the relatively low positive potential VB of another semiconductor. Consequently, electrons and holes may accumulated in CB and VB of two different semiconductors respectively [70,71]. Hence, in the present system, the photogenerated CBelectron of MoS₂ may preferably transfer to the CB of AgVO₃ due to more negative CB potential of MoS₂ and the holes in the VB of AgVO₃ would simultaneously transfer to the VB of MoS₂. However, the CB potential of AgVO₃ (+1.06 V vs NHE) is more positive than the potential required for the water reduction (0 V vs NHE, H⁺/H₂), therefore the electrons in the CB of AgVO₃ cannot reduce the water into H₂ [72]. So, this type-II heterojunction charge-transfer mechanism may not be possible for MoS₂/Ag–AgVO₃ heterostructures (Scheme 1a). Consequently, a plausible Z-scheme charge-transfer mechanism for the MoS₂/Ag–AgVO₃ heterostructures can be proposed in Scheme 1b. Under visible light illumination, the photo excited electrons on the CB of AgVO₃ easily transfer into the Ag NPs because the CB edge is more negative than the Fermi level of the metallic Ag NPs. At the same time, the holes on the VB of MoS₂ may migrate into the metal AgNPs, as the valence band of MoS₂ is more positive than the Fermi level of metallic Ag. Meanwhile, Ag NPs also absorb visible light and generate photo-excited electron and a hole due to the SPR effect and dipolar character of metallic Ag. The plasmon-induced electrons of Ag



Scheme 1. Proposed (a) Type II heterostructure and (b) Z-scheme mechanism of MoS₂/Ag–AgVO₃ heterostructures for photocatalytic H₂ generation under visible light irradiation.

nanoparticles can be transported to the CB of MoS₂ because of electronic oscillation with upshifted energy states which is greater than the CB of the neighboring semiconductor [73,74]. Therefore, enrichment of photo excited electrons occurs on the CB of MoS₂ with a more negative potential than of water reduction (0 V vs NHE) and accumulation of holes take place on the valence band of AgVO₃ with a more positive potential, greater than water oxidation potential (1.23 V vs NHE). This synergistic charge transfer process through Z-scheme bridge made by Ag NPs remarkably enhance the separation of photogenerated charge carriers and reduce the rapid recombination on the surface of individual AgVO₃ and MoS₂. Additionally, metallic Ag NPs enhance the catalytic performance towards H₂ generation through SPR effect of a resonant collective oscillation of photoinduced electrons over Ag NPs which extend the absorption up to visible region. However, the existence of Ag–AgVO₃ nanocrystals on the surfaces of the MoS₂ nanosheets form an uniquely hierarchical nanostructure, which provides a high surface area and a large number of interfaces between the Ag–AgVO₃ and MoS₂. The high surface areas and interfaces provide numerous active sites for the photocatalytic reactions. Consequently, it can be concluded that the enhanced photocatalytic performance of MoS₂/Ag–AgVO₃ heterostructures mainly ascribed to the efficient separation of charge carriers according to the Ag-promoted Z-scheme mechanism.

5. Conclusion

In summary, Z-scheme heterostructures has been developed with Ag NPs decorated 1D AgVO₃ nanorods by facile coprecipitation method on MoS₂ nanosheet at room temperature. As synthesized materials then used as photocatalyst in photocatalytic H₂ generation by water reduction in presence of methanol as hole scavenger. The introduction of metallic Ag NPs between AgVO₃ and MoS₂ enhance the light absorption capacity in visible region by virtue of surface plasmonic resonance effect. Moreover, it develops the Z-scheme bridge mechanism between AgVO₃ and MoS₂ to drive the efficient separation of photoinduced charge carriers. In addition, the well-matched band positions of AgVO₃ and MoS₂ composite conforms the Z-scheme charge transfer mechanism with a higher reducing capability, leading to the enhancement of photocatalytic H₂ generation under visible light illumination. MoS₂/Ag–AgVO₃ Z-scheme heterostructures show four fold and twenty fold enhanced H₂ generation compared to Ag–AgVO₃ and bare MoS₂ respectively. Moreover, MoS₂/Ag–AgVO₃ Z-scheme heterostructures significantly improve the catalytic activity towards water oxidation by enhancing the photoelectrochemical current density and long-term stability under visible light irradiation. Thus, this work represents a paradigm of the all-solid-state Z-scheme photocatalyst having the advantages of enhanced visible light harvesting, efficient charge separation and transfer, low photocorrosion and provides a possible way to develop more AgVO₃ based Z-scheme photocatalysts with useful properties for environmental and energy applications.

Declaration of competing interest

The authors declare that they have no known competing financial interests or personal relationships that could have appeared to influence the work reported in this paper.

None.

CRediT authorship contribution statement

Susmita Bera: Conceptualization, Methodology, Formal analysis, Investigation, Data curation, Writing - original draft. **Srabanti**

Ghosh: Conceptualization, Validation, Visualization, Supervision, Writing - review & editing. **Rajendra N. Basu:** Supervision, Visualization, Writing - review & editing.

Acknowledgements

The authors acknowledge Director, CSIR-CGCRI for his kind permission to publish the work. One of the authors (SB) is thankful to Department of Science & Technology (DST), India, for providing INSPIRE fellowship award. The authors also wish to thank Dr. Soumyadip Rakshit of IIT Bombay for his help in TCSPC study.

Appendix A. Supplementary data

Supplementary data to this article can be found online at <https://doi.org/10.1016/j.jallcom.2020.154527>.

References

- [1] A.J. Bard, M.A. Fox, Artificial photosynthesis: solar splitting of water to hydrogen and oxygen, *Acc. Chem. Res.* 28 (1995) 141–145.
- [2] K. Sivula, R. Krol, Semiconducting materials for photoelectrochemical energy conversion, *Nat. Rev. Mater.* 1 (2016) 1–15.
- [3] K. Maeda, Photocatalytic water splitting using semiconductor particles: history and recent developments, *J. Photochem. Photobiol. C Photochem. Rev.* 12 (2011) 237–268.
- [4] D. Kong, Y. Zheng, M. Kobielski, Y. Wang, Z. Bai, W. Macyk, X. Wang, J. Tang, Recent advances in visible light-driven water oxidation and reduction in suspension systems, *Mater. Today* 21 (2018) 897–924.
- [5] S.J.A. Moniz, S. Ghosh (Eds.), *Visible-Light-Active Photocatalysis: Nanostructured Catalyst Design, Mechanisms and Applications*, Wiley-VCH Verlag GmbH & Co. KGaA, Germany, 2018, ISBN 978-3-527-34293-8 (Chapter 8).
- [6] X. Chen, S. Shen, L. Guo, S.S. Mao, Semiconductor-based photocatalytic hydrogen generation, *Chem. Rev.* 110 (2010) 6503–6570.
- [7] R.R. Hao, G.H. Wang, H. Tang, L.L. Sun, C. Xu, D.Y. Han, Template-free preparation of macro/mesoporous g-C₃N₄/TiO₂ heterojunction photocatalysts with enhanced visible light photocatalytic activity, *Appl. Catal., B* 187 (2016) 47–58.
- [8] J. Chen, M. Wang, J. Han, R. Guo, TiO₂ nanosheet/NiO nanorod hierarchical nanostructures: p-n heterojunctions towards efficient photocatalysis, *J. Colloid Interface Sci.* 562 (2020) 313–321.
- [9] T. Hisatomi, K. Domen, Introductory lecture: sunlight-driven water splitting and carbon dioxide reduction by heterogeneous semiconductor systems as key processes in artificial photosynthesis, *Faraday Discuss* 198 (2017) 11–35.
- [10] K. Sivula, R. Krol, Semiconducting materials for photoelectrochemical energy conversion, *Nat. Rev. Mater.* 1 (2016) 1–15.
- [11] J. Low, J. Yu, M. Jaroniec, S. Wageh, A.A. Al-Ghamdi, Heterojunction photocatalysts, *Adv. Mater.* 29 (2017) 1601694–1601714.
- [12] K. Afroz, M. Moniruddin, N. Bakranov, S. Kudaibergenov, N.A. Nuraje, A heterojunction strategy to improve the visible light sensitive water splitting performance of photocatalytic materials, *J. Mater. Chem. B* (2018) 21696–21718.
- [13] H. Li, W. Tu, Y. Zhou, Z. Zou, Z-scheme photocatalytic systems for promoting photocatalytic performance: recent progress and future challenges, *Adv. Sci.* 3 (2016) 1500389–1500392.
- [14] K. Qi, B. Cheng, J. Yu, W. Ho, A review on TiO₂-based Z-scheme Photocatalysts, *Chin. J. Catal.* 38 (2017) 1936–1955.
- [15] Q. Xu, L. Zhang, J. Yu, S. Wageh, A.A. Al-Ghamdi, M. Jaroniec, Direct Z-scheme photocatalysts: principles, synthesis, and applications, *Mater. Today Off.* 21 (2018) 1042–1063.
- [16] J. Low, C. Jiang, B. Cheng, S. Wageh, A.A. Al-Ghamdi, J. Yu, A review of direct Z-scheme photocatalysts, *Small Methods* 1 (2017) 1700080–1700101.
- [17] S. Yu, S.Y. Lee, J. Yeo, J.W. Han, J. Yi, Kinetic and mechanistic insights into the all-solid-state Z-schematic system, *J. Phys. Chem. C* 118 (2014) 29583–29590.
- [18] A.J. Bard, Photoelectrochemistry and heterogeneous photo-catalysis at semiconductors, *J. Photochem.* 10 (1979) 59–75.
- [19] H. Tada, T. Mitsui, T. Kiyonaga, T. Akita, K. Tanaka, All-solid-state Z-scheme in CdS–Au–TiO₂ three-component nanojunction system, *Nat. Mater.* 5 (2006) 782–786.
- [20] Y. Sasaki, A. Iwase, H. Kato, A. Kudo, The effect of Co-catalyst for Z-scheme photocatalysis systems with an Fe³⁺/Fe²⁺ electron mediator on overall water splitting under visible light irradiation, *J. Catal.* 259 (2008) 133–137.
- [21] A. Iwase, Y.H. Ng, Y. Ishiguro, A. Kudo, R. Amal, Reduced graphene oxide as a solid-state electron mediator in Z-scheme photocatalytic water splitting under visible light, *J. Am. Chem. Soc.* 133 (2011) 11054–11057.
- [22] X. Chen, Y. Dai, X. Wang, Methods and mechanism for improvement of photocatalytic activity and stability of Ag₃PO₄: a review, *J. Alloys Compd.* 649 (2015) 910–932.

- [23] J. Chen, X. Xiao, Y. Wang, M. Lu, X. Zeng, Novel AgI/BiOBr/reduced graphene oxide Z-scheme photocatalytic system for efficient degradation of tetracycline, *J. Alloys Compd.* 800 (2019) 88–98.
- [24] H. Li, H. Yu, X. Quan, S. Chen, Y. Zhang, Uncovering the key role of the Fermi level of the electron mediator in a Z-scheme photocatalyst by detecting the charge transfer process of WO₃-metal-g-C₃N₄ (metal = Cu, Ag, Au), *ACS Appl. Mater. Interfaces* 8 (2016) 2111–2119.
- [25] Y. He, L. Zhang, B. Teng, M. Fan, New application of Z-scheme Ag₃PO₄/g-C₃N₄ composite in converting CO₂ to fuel, *Environ. Sci. Technol.* 49 (2015) 649–656.
- [26] J. Hou, Z. Wang, C. Yang, W. Zhou, S. Jiao, H. Zhu, Hierarchically plasmonic Z-scheme photocatalyst of Ag/AgCl nanocrystals decorated mesoporous single-crystalline metastable Bi₂O₃/TiO₂ nanosheets, *J. Phys. Chem. C* 117 (2013) 5132–5141.
- [27] R. Wang, L. Cao, Facile synthesis of a novel visible-light-driven AgVO₃/BiVO₄ heterojunction photocatalyst and mechanism insight, *J. Alloys Compd.* 722 (2017) 445–451.
- [28] A. Beltrán, L. Gracia, J. Andrés, E. Longo, First-Principles study on polymorphs of AgVO₃: assessing to structural stabilities and pressure-induced transitions, *J. Phys. Chem. C* 121 (2017) 27624–27642.
- [29] B. Liu, L. Mu, X. Han, J. Zhang, H. Shi, Highly efficient visible-light-driven photocatalytic activity of g-C₃N₄@Ag/AgVO₃ composites for dye degradation and bacterial inactivation, *J. Photochem. Photobiol. Chem.* 380 (2019) 111866–111871.
- [30] X. Wang, J. Yang, S. Ma, D. Zhao, J. Dai, D. Zhang, In situ fabrication of AgI/AgVO₃ nanoribbon composites with enhanced visible photocatalytic activity for redox reactions, *Catal. Sci. Technol.* 6 (2016) 243–253.
- [31] F. Wu, X. Li, W. Liu, S. Zhang, Highly enhanced photocatalytic degradation of methylene blue under the indirect all-solid-state Z-scheme g-C₃N₄-RGO-TiO₂-Nanoheterojunctions, *Appl. Surf. Sci.* 405 (2017) 60–70.
- [32] X. Wang, S. Li, Y. Ma, H. Yu, J. Yu, H₂WO₄-H₂O/Ag/AgCl composite nanoplates: a plasmonic Z-scheme visible-light photocatalyst, *J. Phys. Chem. C* 115 (2011) 14648–14655.
- [33] F. Chen, Q. Yang, X. Li, G. Zeng, D. Wang, C. Niu, J. Zhao, H. An, T. Xie, Y. Deng, Hierarchical assembly of graphene-bridged Ag₃PO₄/Ag/BiVO₄ (040) Z-scheme photocatalyst: an efficient, sustainable and heterogeneous catalyst with enhanced visible-light photoactivity towards tetracycline degradation under visible light irradiation, *Appl. Catal., B* 200 (2017) 330–342.
- [34] Y. Liu, H. Zhang, J. Ke, J. Zhang, W. Tian, X. Xu, X. Duan, H. Sun, M.O. Tade, S. Wang, OD (MoS₂)/2D (g-C₃N₄) heterojunctions in Z-scheme for enhanced photocatalytic and electrochemical hydrogen evolution, *Appl. Catal., B* 228 (2018) 64–74.
- [35] H.J. Yun, H. Lee, N.D. Kim, D.M. Lee, S. Yu, J. Yi, A combination of two visible-light responsive photocatalysts for achieving the Z-scheme in the solid state, *ACS Nano* 5 (2011) 4084–4090.
- [36] R. Kobayashi, S. Tanigawa, T. Takashima, B. Ohtani, H. Irie, Silver-inserted heterojunction photocatalysts for Z-scheme overall pure-water splitting under visible-light irradiation, *J. Phys. Chem. C* 118 (2014) 22450–22456.
- [37] R.Q. Ye, H.B. Fang, Y.-Z. Zheng, N. Li, Y. Wang, X. Tao, Fabrication of CoTiO₃/g-C₃N₄ hybrid photocatalysts with enhanced H₂ evolution: Z-scheme photocatalytic mechanism insight, *ACS Appl. Mater. Interfaces* 8 (2016) 13879–13889.
- [38] A. Bafaqeer, M. Tahir, A.A. Khan, N.A.S. Amin, Indirect Z-scheme Assembly of 2D ZnV₂O₆/RGO/g-C₃N₄ Nanosheets with RGO/pCN as solid-state electron mediators toward Visible Light-enhanced CO₂ reduction, *Ind. Eng. Chem. Res.* 58 (2019) 208612–208624.
- [39] S.-Y. Yu, L.-P. Mei, Y.-T. Xu, T.-Y. Xue, G.-C. Fan, D.-M. Han, G. Chen, W.-W. Zhao, Liposome-mediated in situ formation of AgI/Ag/BiOI Z-scheme heterojunction on foamed nickel electrode: a proof-of-concept study for cathodic liposomal photoelectrochemical bioanalysis, *Bioanalysis. Anal. Chem.* 91 (2019) 3800–3804.
- [40] A.H. Khan, S. Ghosh, B. Pradhan, A. Dalui, L.K. Shrestha, S. Acharya, K. Ariga, Two-dimensional (2D) nanomaterials towards electrochemical nano-architectonics in energy-related applications, *Bull. Chem. Soc. Jpn.* 90 (2017) 627–648.
- [41] A. Radisavljevic, J. Radenovic, V. Brivio, A.K. Giacometti, Single-layer MoS₂ transistors, *Nat. Nanotechnol.* 6 (2011) 147–150.
- [42] D. Lu, Q. Wang, K.K. Kondamareddy, A. Wang, H. Hao, Q. Wu, Efficiently visible-light-induced photoactivity of MoS₂ nanoflowers/chromic oxide/protonated titanatenanoflakes edge-on ternary heterostructures for production of hydrogen, *J. Alloys Compd.* 761 (2018) 31–40.
- [43] K.F. Mak, C. Lee, J. Hone, J. Shan, T.F. Heinz, Atomically thin MoS₂: a new direct-gap semiconductor, *Phys. Rev. Lett.* 105 (2010) 136805–136809.
- [44] D. Lu, H. Wang, X. Zhao, K.K. Kondamareddy, J. Ding, C. Li, P. Fang, Highly efficient visible-light-induced photoactivity of Z-scheme g-C₃N₄/Ag/MoS₂ ternary photocatalysts for organic pollutant degradation and production of hydrogen, *ACS Sustain. Chem. Eng.* 5 (2017) 1436–1445.
- [45] M.J. Islam, D.A. Reddy, N.S. Han, J. Choi, J.K. Song, T.K. Kim, An oxygen-vacancy rich 3D novel hierarchical MoS₂/BiOI/AgI ternary nanocomposite: enhanced photocatalytic activity through photogenerated electron shuttling in a Z-scheme manner, *Phys. Chem. Chem. Phys.* 18 (2016) 24984–24993.
- [46] W.K. Jo, T. Adinaveen, J.J. Vijaya, N.C.S. Selvam, Synthesis of MoS₂ nanosheet supported Z-scheme TiO₂/g-C₃N₄ photocatalysts for the enhanced photocatalytic degradation of organic water pollutants, *RSC Adv.* 6 (2016) 10487–10497.
- [47] R.C. Oliveira, C.C. Foggi, M.M. Teixeira, M.D.P. Silva, M. Assis, E.M. Francisco, B.N.A.S. Pimentel, P.F.S. Pereira, C.E. Vergani, A.L. Machado, J. Andres, L. Gracia, E. Longo, Mechanism of antibacterial activity via morphology change of α-AgVO₃: theoretical and experimental insights, *ACS Appl. Mater. Interfaces* 9 (2017) 11472–11481.
- [48] Q. Pang, Y. Zhao, X. Bian, Y. Ju, X. Wang, Y. Wei, B. Liu, F. Du, C. Wang, G. Chen, Hybrid graphene@MoS₂@TiO₂ microspheres for use as a high performance negative electrode material for lithium ion batteries, *J. Mater. Chem.* 5 (2017) 3667–3674.
- [49] Y. Sang, L. Kuai, C. Chen, Z. Fang, B. Geng, Fabrication of a visible-light-driven Plasmonic Photocatalyst of AgVO₃@AgBr@Ag Nano belt Heterostructures, *ACS Appl. Mater. Interfaces* 6 (2014) 5061–5068.
- [50] S. Zhang, J. Li, X. Wang, Y. Huang, M. Zeng, J. Xu, Rationally designed 1D Ag@AgVO₃ nanowire/graphene/protonated g-C₃N₄ nanosheet heterojunctions for enhanced photocatalysis via electrostatic self-assembly and photochemical reduction methods, *J. Mater. Chem.* 3 (2015) 10119–10126.
- [51] X. Kong, Z. Guo, C. Zeng, J. Huang, L. Cao, L. Li, L. Yin, P. Wen, Q. Feng, Z. Xu, Soft chemical in situ synthesis, formation mechanism and electrochemical performances of 1D bead-like AgVO₃ nanoarchitectures, *J. Mater. Chem.* 3 (2015) 18127–18135.
- [52] J.-M. Song, Y.-Z. Lin, H.-B. Yao, F.-J. Fan, X.-G. Li, S.-H. Yu, Superlong β-AgVO₃ nanoribbons: high-yield synthesis by a pyridine-assisted solution approach, their stability, electrical and electrochemical properties, *ACS Nano* 3 (2009) 653–660.
- [53] R.S. Devan, V.P. Thakare, V.V. Antad, P.R. Chikate, R.T. Khare, M.A. More, R.S. Dhayal, S.I. Patil, Y.-R. Ma, L. Schmidt-Mende, Nano-heteroarchitectures of two-dimensional MoS₂@One-dimensional brookite TiO₂ Nanorods: prominent electron emitters for displays, *ACS Omega* 2 (2017) 2925–2934.
- [54] S. Bera, S. Ghosh, R.N. Basu, Fabrication of Bi₂S₃/ZnO heterostructures: an excellent photocatalyst for visible-light-driven hydrogen generation and photoelectrochemical properties, *New J. Chem.* 42 (2018) 541–554.
- [55] V. Sivakumar, R. Suresh, K. Giribabu, V. Narayanan, AgVO₃ nanorods: synthesis, characterization and visible light photocatalytic activity, *Solid State Sci.* 39 (2015) 34–39.
- [56] T. Zhu, L. Huang, Y. Song, Z. Chen, H. Ji, Y. Li, Y. Xu, Q. Zhang, H. Xu, H. Li, Modification of Ag₃VO₄ with graphene-like MoS₂ for enhanced visible-light photocatalytic property and stability, *New J. Chem.* 40 (2016) 2168–2177.
- [57] J. Zhao, Z. Zhang, S. Yang, H. Zheng, Y. Li, Facile synthesis of MoS₂ nanosheet-silver nanoparticles composite for surface enhanced Raman scattering and electrochemical activity, *J. Alloys Compd.* 559 (2013) 87–91.
- [58] W. Zhen, W. Jiao, Y. Wu, H. Jing, G. Lu, The role of interlayer metallic copper for visible photocatalytic hydrogen generation over Cu/Cu₂O/Cu/TiO₂ catalyst, *Catal. Sci. Technol.* 7 (2017) 5028–5037.
- [59] D. McNulty, Q. Ramasse, C. O'Dwyer, The structural conversion from α-AgVO₃ to β-AgVO₃: Ag nanoparticle decorated nanowires with application as cathode materials for Li-ion batteries, *Nanoscale* 8 (2016) 16266–16275.
- [60] S. Zhang, W. Li, C. Li, J. Chen, Characterization, and electrochemical properties of Ag₂V₄O₁₁ and AgVO₃ 1-D nano/microstructures, *J. Phys. Chem. B* 110 (2006) 24855–24863.
- [61] S. Ghosh, S.R. Keshri, R.N. Basu, Enhanced solar hydrogen generation using Cu–Cu₂O integrated polypyrrole nanofibers as heterostructured catalysts, *Int. J. Hydrogen Energy* (2020), <https://doi.org/10.1016/j.ijhydene.2019.12.118>.
- [62] P.P. Patel, P.J. Hanumantha, O.I. Velikokhatnyi, M.K. Datta, D. Hong, B. Gattu, J.A. Poston, A. Manivannan, P.N. Kumta, Nitrogen and cobalt co-doped zinc oxide nanowires—Viable photoanodes for hydrogen generation via photoelectrochemical water splitting, *J. Power Sources* 299 (2015) 11–24.
- [63] L. Jiang, K. Wang, X. Wu, G. Zhang, S. Yin, Amorphous bimetallic cobalt nickel sulfide cocatalysts for significantly boosting photocatalytic hydrogen evolution performance of graphitic carbon nitride: efficient interfacial charge transfer, *ACS Appl. Mater. Interfaces* 11 (2019) 26898–26908.
- [64] M.T. Fabbro, C. Saliby, L.R. Rios, F.A.L. Porta, L. Gracia, M.S. Li, J. Andrés, L.P.S. Santos, E. Longo, Identifying and rationalizing the morphological, structural, and optical properties of β-Ag₂MoO₄ microcrystals, and the formation process of Ag nanoparticles on their surfaces: combining experimental data and first-principles calculations, *Sci. Technol. Adv. Mater.* 16 (2015), 065002–065012.
- [65] S. Sardar, P. Kar, H. Remita, B. Liu, P. Lemmens, S.K. Pal, S. Ghosh, Enhanced charge separation and FRET at heterojunctions between semiconductor nanoparticles and conducting polymer nanofibers for efficient solar light harvesting, *Sci. Rep.* 5 (2015) 17313–17327.
- [66] S. Ghosh, H. Remita, R.N. Basu, Visible-light-induced reduction of Cr(VI) by PDPB-ZnO nanohybrids and its photo-electrochemical response, *Appl. Catal., B* 239 (2018) 362–372.
- [67] P. Chen, P. Xing, Z. Chen, X. Hu, H. Lin, L. Zhao, Y. He, In-situ synthesis of AgNbO₃/g-C₃N₄ photocatalyst via microwave heating method for efficiently photocatalytic H₂ generation, *J. Colloid Interface Sci.* 534 (2019) 163–171.
- [68] S. Bera, S. Ghosh, S. Shyamal, C. Bhattacharya, R.N. Basu, Photocatalytic hydrogen generation using gold decorated BiFeO₃ heterostructures as an efficient catalyst under visible light irradiation, *Sol. Energy Mater. Sol. Cells* 194 (2019) 195–206.
- [69] Z. Mazouz, L. Beji, J. Meddeb, H.B. Ouada, Electrochemical characteristics of the n⁺-type GaAs substrate in HCl electrolyte and the morphology of the obtained structure, *Arabian J. Chem.* 4 (2011) 473–479.
- [70] K. Wang, Y. Li, J. Li, G. Zhang, Boosting interfacial charge separation of Ba₅Nb₄O₁₅/g-C₃N₄ photocatalysts by 2D/2D nanojunction towards efficient

- visible-light driven H₂ generation, *Appl. Catal., B* 263 (2020) 117730–117740.
- [71] S. Ghosh, A.K. Mallik, R.N. Basu, Enhanced photocatalytic activity and photo-response of poly(3,4-ethylenedioxythiophene) nanofibers decorated with gold nanoparticle under visible light, *Sol. Energy* 159 (2018) 548–560.
- [72] H. Liu, H. Zhou, X. Liu, H. Li, C. Ren, X. Li, W. Li, Z. Lian, M. Zhang, Engineering design of hierarchical g-C₃N₄@Bi/BiOBr ternary heterojunction with Z-scheme system for efficient visible-light photocatalytic performance, *J. Alloys Compd.* 798 (2019) 741–749.
- [73] L. Jiang, J. Li, K. Wang, G. Zhang, Y. Li, X. Wu, Low boiling point solvent mediated strategy to synthesize functionalized monolayer carbon nitride for superior photocatalytic hydrogen evolution, *Appl. Catal. B* 260 (2020) 118181, <https://doi.org/10.1016/j.apcatb.2019.118181>.
- [74] J. Hu, L. Wang, P. Zhang, C. Liang, G. Shao, Construction of solid-state Z-scheme carbon-modified TiO₂/WO₃ nanofibers with enhanced photocatalytic hydrogen production, *J. Power Sources* 328 (2016) 28–36.

Assemble of Bi-doped TiO₂ onto 2D MoS₂: an efficient p–n heterojunction for photocatalytic H₂ generation under visible light

Susmita Bera, Ankita Kumari¹, Srabanti Ghosh* and Rajendra N Basu* 

Energy Materials & Devices Division, (Formerly Fuel Cell & Battery Division) CSIR—Central Glass and Ceramic Research Institute, 196, Raja S. C. Mullick Road, Kolkata-700032, India

E-mail: ghosh.srabanti@gmail.com, srabanti@cgcri.res.in, mbasu@cgcri.res.in and rajenasu54@gmail.com

Received 23 September 2020, revised 12 January 2021

Accepted for publication 29 January 2021

Published 15 February 2021



CrossMark

Abstract

Fabrication of noble-metal-free, efficient and stable hybrid photocatalyst is essential to address the rapidly growing energy crisis and environmental pollution. Here, MoS₂ has been used as the co-catalyst on Bi-doped TiO₂ to form a novel heterostructure to increase the utilization of the photogenerated charge carriers for improving photocatalytic H₂ evolution activity through water reduction. Significantly increased photocatalytic H₂ generation has been achieved on the optimized MoS₂/Bi-TiO₂ nanocomposite ($\sim 512 \mu\text{mol g}^{-1}$) after 4 h of visible light illumination, which is nine times higher than that of the pristine TiO₂ ($\sim 57 \mu\text{mol g}^{-1}$). The measurements of photocurrent, charge transfer resistance and photo-stability of MoS₂/Bi-TiO₂ photoanode imply that charge separation efficiency has been improved in comparison to the pure MoS₂ and TiO₂ photoanodes. Further, the Mott–Schottky study confirmed that a p–n heterojunction has been formed between n-type MoS₂ and p-type Bi-doped TiO₂, which provides a potential gradient to increase charge separation and transfer efficiency. On the basis of these experimental results, this enhanced photocatalytic activity of MoS₂/Bi-TiO₂ heterostructures could be ascribed to the significant visible light absorption and the efficient charge carrier separation. Thus, this work demonstrates the effect of p–n junction for achieving high H₂ evolution activity and photoelectrochemical water oxidation under visible light illumination.

Supplementary material for this article is available [online](#)

Keywords: Bi-doped TiO₂, p–n heterojunction, photocatalytic activity, water splitting, interfacial charge transfer

(Some figures may appear in colour only in the online journal)

1. Introduction

The ongoing concerns regarding environmental pollution and energy crisis have stimulated current research to explore

sustainable and clean energy sources [1–3]. In this respect, sunlight-driven water splitting using particular photocatalyst has attracted significant attention as a green approach for large-scale production of renewable solar hydrogen, which in turn a promising alternative as renewable energy because of zero carbon emission and high energy density [4–10]. The steps in photocatalytic water splitting are absorption of photons by the catalyst, leading to the formation of

¹ Present address: School of Energy Science & Engineering, Indian Institute of Technology-Kharagpur.

* Authors to whom any correspondence should be addressed.

photogenerated electrons and photoinduced holes, then migration of excited charge carriers towards the surface where oxidation and reduction reactions take place [4, 6]. Thus, several parameters such as the ability to absorb a wide range of the solar spectrum, efficient charge transfer and oxidation/reduction are very crucial to improve the overall efficiency. Therefore, the focus of the current research is the development of novel photocatalysts which can possess a high light-harvesting efficiency along with improved charge migration.

Semiconductors are widely used as photocatalysts to harvest solar energy directly and convert it into chemical energy which could be useful for organic pollutant removal, water reduction to generate H₂, CO₂ reduction etc [10–13]. TiO₂ has been considered as the most efficient photocatalyst because of its high oxidizing ability, however, the limited absorption in the UV region and slow charge transfer rate results in low hydrogen conversion efficiency and quantum efficiency. Moreover, the fast recombination rate of electrons and holes due to the high density of the trap state reduces the oxidation ability of TiO₂ [14]. To overcome this drawback and to extend its spectral response to visible light, different methods have been followed, including metal and non-metal doping [12, 15, 16], coupling of TiO₂ with other semiconductor materials [17, 18], polymers [19, 20], graphene [21], dye sensitization [22], Schottky junctions with metals such as Au, Ag, Pt, Bi, Cu [23, 24], crystal facet engineering etc. Doping is considered as an effective route to extend the light absorption towards longer wavelengths by introducing additional energy states within the valence band (VB) and conduction band (CB) of the TiO₂. These additional states can inhibit the electrons–holes recombination by trapping the excited carriers [25]. In this way, more charge carriers could be successfully diffused to the surface of the photocatalyst and facilitate the charge separation.

In particular, doping of Bi³⁺ into semiconductor photocatalysts may influence the luminescence efficiency by reducing the photo-induced electron-hole recombination, which further improves the catalytic performance [26–30]. Additionally, oxygen vacancy can be generated at the intermediate level that may trap electrons to form the active radicals. Very recently, Li *et al* [31] showed that doping of Bi³⁺ into ZnWO₄ semiconductor enhanced the photocatalytic activity for NO removal due to the formation of oxygen vacancy. These oxygen vacancies increase the oxygen molecule adsorption at the semiconductor surface to generate superoxide radicals (O₂⁻). Wu *et al* [28] also reported that the optimal doping of Bi (1.0 mol%, both Bi³⁺ and Bi⁰ state exists in the ratio of 3:1) into TiO₂ lattice enhanced the photocatalytic H₂ generation and Rhodamine B decolorization. On the other hand, semimetal Bi⁰ can also exhibit a direct surface plasmonic resonance effect like novel metals (Au, Pd, Ag, Pt), that enhances the light absorption up to the visible region [28]. Thus, Bi⁰ has been considered as one of the promising candidates to increase visible light-harvesting and photocatalytic activity. For example, Lv *et al* [32] fabricated Bi–Bi₂MoO₆/CdS-DETA all-solid-state Z-scheme heterostructures which exhibited high H₂ generation through water splitting due to surface plasmonic resonance effect of Bi

nanoparticles. Bi promoted a novel Z-Scheme Bi–BiOCl/AgCl heterojunction has been developed by Du *et al* [33], which showed five times enhanced H₂ generation rate compared to bare BiOCl under visible light due to improved electron–hole transfer and separation through Bi. Moreover, Bi-nanoparticles can form a Schottky barrier when attached with other semiconductors and provide an internal electric field to accelerate the charge separation efficiency. Recently, Hao *et al* [34] demonstrated that the presence of Bi⁰ on the surface of Bi-doped (in Bi³⁺ state) TiO₂ formed M–S junction, which promoted the light-harvesting and the charge transfer ability. Magnussion *et al* [35] also developed a Schottky barrier between Bi nanoparticles and ZnO through photoelectron spectroscopy under ultrahigh-vacuum conditions. It is clear that Bi doping either in Bi⁰ state or Bi³⁺ state into the semiconductor band structure could lead a positive impact to improve the solar light absorption ability for longer wavelengths. However, the efficiency of the photocatalytic reaction may control by the oxidation state of the Bi which plays a key role in band gap engineering. Thus, mechanistic understanding of the valence state of metal dopants in photocatalytic reactions is of significant importance.

Beyond conventional semiconductors, transition metal dichalcogenide materials, consisting of single or few-atom thick covalently bonded lattices have attracted immense interest in photocatalysis due to some unique properties, such as optical, electrical, photonic, mechanical, catalytic etc which are originated from two-dimensional (2D) layered structure [36, 37]. Among transition-metal dichalcogenides, single or few layers of molybdenum disulfide (MoS₂) found to be very attractive in terms of physical, electrochemical properties and mainly applied in diverse areas; for examples photovoltaics [38], energy storage [39, 40], supercapacitors [41], biosensors [42] and photocatalytic H₂ generation [43–47]. Bulk MoS₂ is an indirect bandgap semiconductor (bandgap ~ 1.2 eV) and showed indirect to direct band gap transition for monolayer MoS₂ (~1.9 eV) due to the quantum confinement effects [48, 49]. Interestingly, the coordination of the Mo atom and its d-electrons have a crucial role in determining the electronic structure of MoS₂, makes it an important candidate for photocatalysis. Moreover, the dangling bonds and unsaturated coordination of MoS₂ edges offer opportunities for surface-active applications [50–53]. MoS₂ can fabricate a van der Waals heterostructure by vertically stacked with other semiconductors, which overcomes the weakness of single 2D layered material and extend its electronic and optoelectronic properties by introducing new physics at the interface. For example, n-type monolayer MoS₂ developed a p–n junction with type-II band alignment after stacking on p-type WSe₂ [54]. Ceballos *et al* [55] showed ultrafast charge separation and long-lived interlayer excitons in out-of-plane MoS₂-MoSe₂ heterostructure. Recently, Li *et al* [44] fabricated (MoS₂-TiO₂)/Au ternary component hybrid materials that enhance the photoelectrochemical (PEC) current density under visible light. Moreover, MoS₂ has been reported as an efficient electrocatalyst for H₂ evolution reaction through water splitting, owing to the nanosized edge defects which are preferential for H₂ adsorption [45–47].

Thus, few-layered MoS₂ nanosheets may serve as co-catalyst for improving the efficiency of H₂ evolution.

Herein, a heterostructure has been developed by assembling of Bi modified TiO₂ nanoparticles on the surface MoS₂ nanosheets by chemical method. Introduction of Bi into the TiO₂ crystal reduces the band gap of TiO₂ and makes it suitable for visible light absorption whereas, the presence of MoS₂ in the heterostructures enhances the H₂ generation activity by water reduction. The fast interfacial charge transfer efficiency of MoS₂/Bi-TiO₂ heterostructures have been explained by PEC analysis. A possible p–n junction charge transfer mechanism has been proposed by analyzing the energy-band structure of the component elements.

2. Experimental section

2.1. Chemicals

Bulk molybdenum sulfide (MoS₂) powder, Bi(NO₃)₃·5H₂O, polyvinylpyrrolidone (PVP), TiO₂ powder and ethanol (C₂H₅OH), methanol (CH₃OH) were procured from Sigma Aldrich, USA. All the chemicals had been used as received. Ultrapure water was used as a solvent (18.2 MΩ cm).

2.2. Preparation of the MoS₂ nanosheets

Few layers of MoS₂ nanosheets were synthesized by surfactant assisted exfoliation method followed by the similar method developed by Wang *et al* [56] with some modification. MoS₂ powder (0.4 g) and 0.5 g of PVP as stabilizer were dispersed in 200 ml of deionized water and stirred vigorously for 30 min at 70 °C. Then, the solution was bath sonicated for 1 h and then probe sonicated for 4 h at 50 kHz frequency. Finally, washing and centrifugation were done at 10 000 rpm for five times using water, ethanol and then dried in an oven at 60 °C [45].

2.3. Preparation of the Bi-modified TiO₂ nanoparticles

A series of Bi-doped TiO₂ (Bi-TiO₂) having different molar concentrations of Bi(NO₃)₃·5H₂O, (1–10 mM) was prepared by a facile chemical reduction method. At first, 50 mg TiO₂ was dispersed in 50 ml deionized water by stirring for 30 min. After that, the certain amount of Bi(NO₃)₃·5H₂O was added and stirred for another 15 min. At the same time, a 10 ml NaBH₄ (3–30 mM) solution was prepared which was added dropwise into the above solution and stirred for 10 min. The amount of Bi(NO₃)₃·5H₂O and the NaBH₄ were taken in a 1:3 molar ratio. Next, the sample was collected by centrifugation with water, ethanol and dried overnight in an oven (60 °C).

2.4. Preparation of the MoS₂/Bi-TiO₂ heterostructures

At first, 50 mg ultrasonicated MoS₂ was dispersed in 50 ml of deionized water and stirred for 30 min. Then 10 weight % of Bi-doped TiO₂ (using 2 mM of Bi) was added into the mixture with continuous vigorous stirring at room temperature for

24 h in dark condition. The concentration of Bi-doped TiO₂ is varied from 1, 5, 10 to 20 weight % and leveled as MBT-1, MBT-5, MBT-10 and MBT-20. The final solution was centrifuged at 12 000 rpm for several times. After drying the precipitate at 60 °C for overnight, MoS₂/Bi-TiO₂ composites were ready for photocatalytic application.

2.5. Characterization of materials

The morphology, size and analysis of elements were studied by FESEM (Carl-Zeiss, LEO. 430i, Sigma) and TEM (Tecnai G², 30ST). Phase purity of the synthesized materials was confirmed by XRD within 20°–80° (2θ range) at 40 kV and 40 mA. A Cu Kα radiation was used in Philips X'Pert, The Netherlands to obtain the x-ray beam. Raman spectra of the synthesized material were studied by Jobin Yvon HR800 instrument to get the idea of the number of layers, phases and defects in the MoS₂, as well as the crystallinity, phase composition of the TiO₂. A 540 nm laser beam had been employed on the sample surface. Further, the valence of the elements was confirmed by XPS spectroscopy using PHI 5000 spectrophotometer, Versa Probe II. The optical properties of the materials were studied by Shimadzu, UV-3600 spectrophotometer and photocatalytic H₂ evolution rate were determined by online gas chromatography through the YL Instrument, 6500GC system. The thermal stability of the materials was investigated using thermogravimetric analysis (TGA, NETZSCH, STA 449 F3, Jupiter). The test was carried out in air with a heating rate of 10 °C min⁻¹ from room temperature to 800 °C. The Bi content in the TiO₂ was determined by a Spectro Ciros Vision inductively coupled plasma atomic emission spectroscopy (ICP-AES) instrument, Spectro GmbH, Germany.

2.6. Measurement of photocatalytic activity

Online gas chromatography was employed to measure the H₂ generation rate quantitatively. Water-methanol Ar saturated solution of 50 ml (25 volume % methanol) having 25 mg catalyst had been taken in a closed reactor. H₂ generation was measured under continuous light illumination of 100 mW cm⁻² from a Xe-arc lamp (250 W). PEC properties of the materials were measured by galvanostat-potentiostat (Autolab, PGSTAT302N, The Netherlands). A Pt wire, saturated Ag/AgCl electrode and a thin film of as prepared material on FTO were used as a counter electrode, a reference electrode and a working electrode respectively. The linear sweep voltammogram (LSV) of the prepared photoanodes were taken in presence of 0.1 M Na₂SO₄ phosphate buffer (pH 7) within the potential of –0.4 to 1 V versus Ag/AgCl at a scan rate 10 mV s⁻¹ under light illumination. Chronoamperometry (CA) was employed to check the stability and light sensitivity of the prepared photoanodes at 0.26 V versus Ag/AgCl under chopping condition. The obtained potentials were converted into reference hydrogen electrode (RHE) by following the equation (1)

$$E_{\text{RHE}} = E_{\text{Ag/AgCl}} + 0.059 \text{ pH} + 0.197 E_{\text{Ag/AgCl}}^0 \quad (1)$$

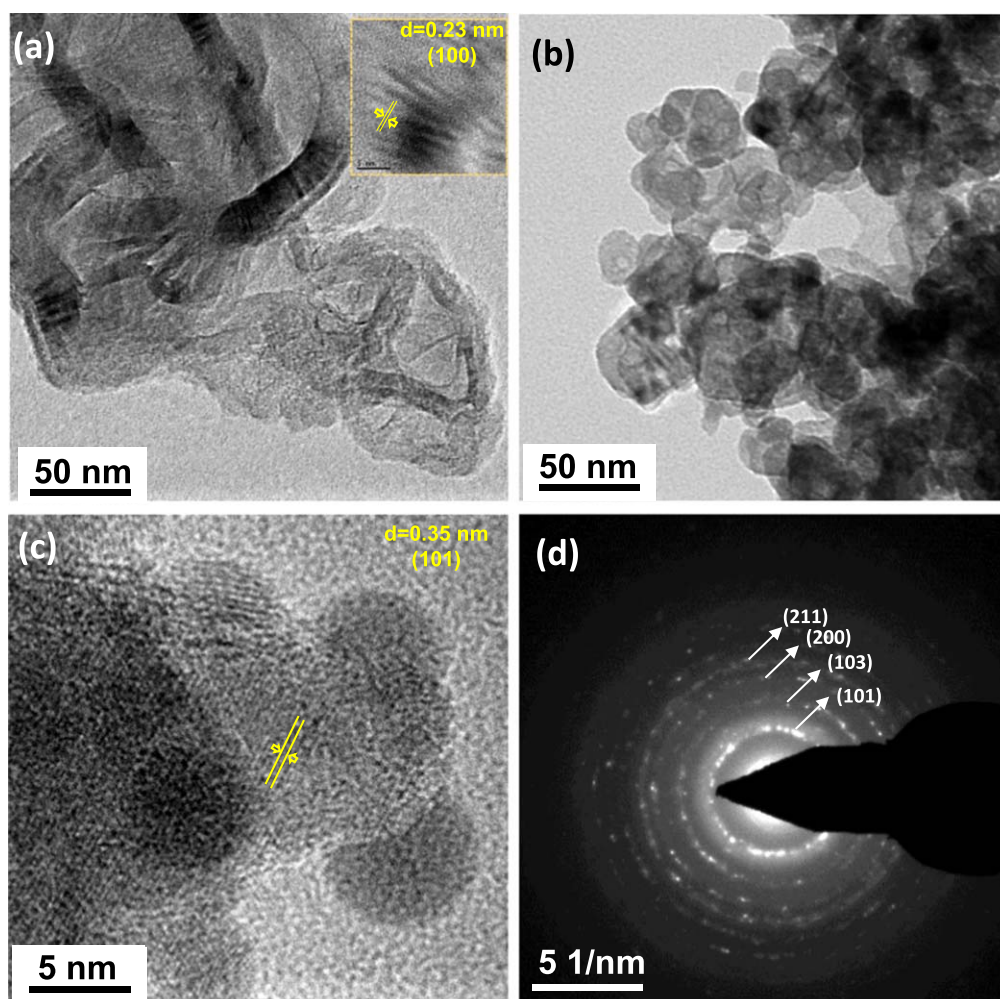


Figure 1. TEM images of (a) MoS₂ nanosheet, (b) Bi modified TiO₂ (using 2 mM Bi), (c) high resolution (HRTEM) and (d) selected area electron diffraction pattern of Bi modified TiO₂ (using 2 mM Bi).

Next, junction capacitance and the charge transfer resistance of the photoelectrodes were measured through M–S (potential range -1.0 to 1.5 V versus Ag/AgCl, frequency \rightarrow 1000 Hz, ac voltage \rightarrow 10 mV) and Nyquist experiments.

3. Results and discussion

The morphology and microstructural properties of the MoS₂ and the composites have been studied by TEM and high resolution TEM (HRTEM). Figure 1 shows the TEM image of MoS₂ nanosheets, which consists of multiple layers that are highly crystalline. The HRTEM identifies lattice fringe of 0.23 nm (inset of figure 1(a)) corresponding to the (100) hexagonal facets of MoS₂ [44]. Figures 1(b) and (c) present TEM and HRTEM images of TiO₂ nanoparticles after Bi modification, where the crystal fringe of 0.35 nm identifies the (101) planes of TiO₂ in anatase phase [47]. Moreover, the polycrystalline nature of TiO₂ nanoparticles has been confirmed by the selected area electron diffraction pattern (SAED) (figure 1(d)).

Figure 2(a) shows the TEM image of MoS₂/Bi-TiO₂ composite (10 weight% Bi-TiO₂ (2 mM Bi) loaded MoS₂), where average \sim 40 nm spherical Bi modified TiO₂ nanoparticles are formed on the surface of MoS₂ nanosheets after 24 h slow stirring.

The HRTEM image shows the clear lattice fringes which are perfectly aligning across the entire surface (figure 2(b)), reveals the single-crystallinity of MoS₂ nanosheet. The lattice fringes of \sim 0.27 nm can be indexed to (100) planes of hexagonal MoS₂ [45]. The corresponding SAED pattern shows an ordered array of bright spots, represents the single crystallinity of MoS₂ along with the rings correspond to polycrystalline TiO₂ (figure 2(c)). The energy-dispersive x-ray (EDX) spectrum illustrates the chemical composition of MoS₂/Bi-TiO₂ heterostructures which composed of Mo, O, Bi, Ti and S (figure 2(d)).

The XRD pattern of TiO₂ nanoparticles match very well with the JCPDS No. 21-1272, can be indexed to the anatase phase (figure 3(a)) [44]. After Bi modification (using 1 and 2 mM Bi), no shifting or extra significant diffraction peaks of Bi species have been observed, indicating the doping of Bi does not affect the crystal structure of TiO₂ at low

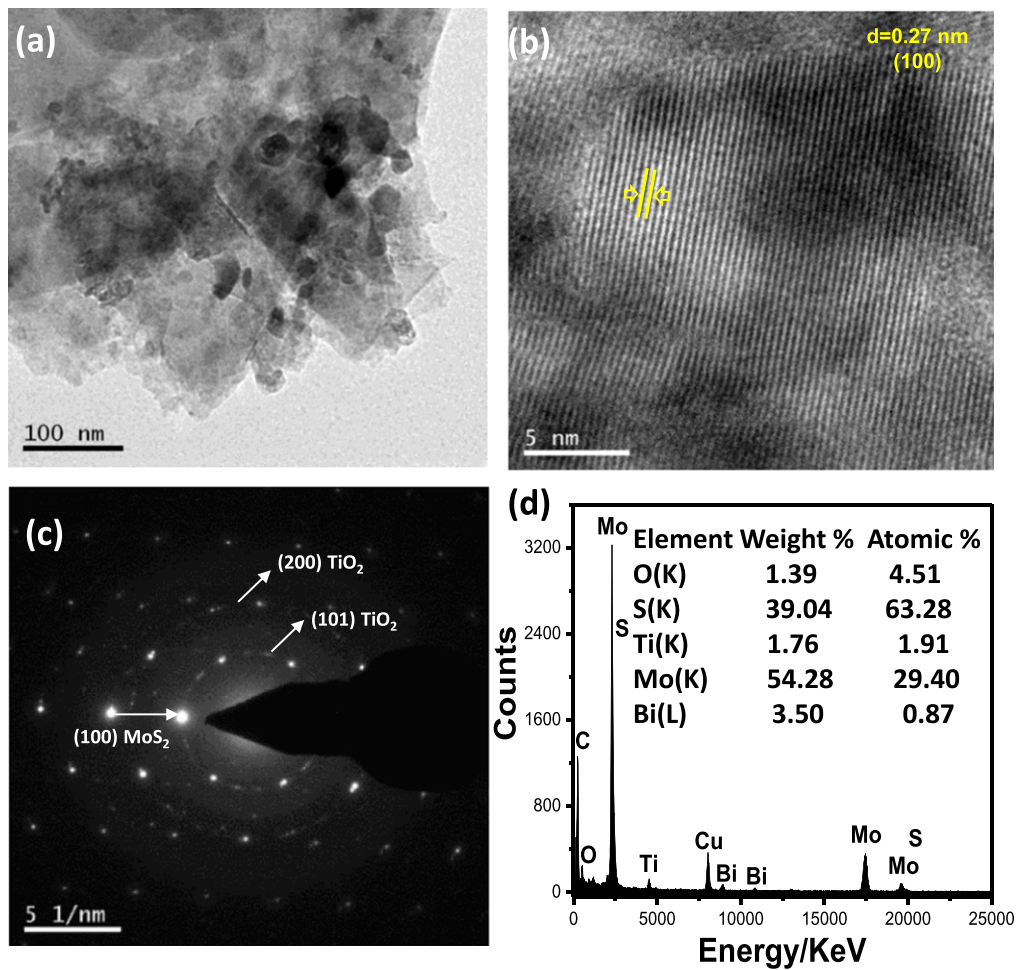


Figure 2. (a) TEM image, (b) HRTEM image, (c) SAED pattern and EDX spectrum of MoS₂/Bi-TiO₂ (MBT-10) heterostructures.

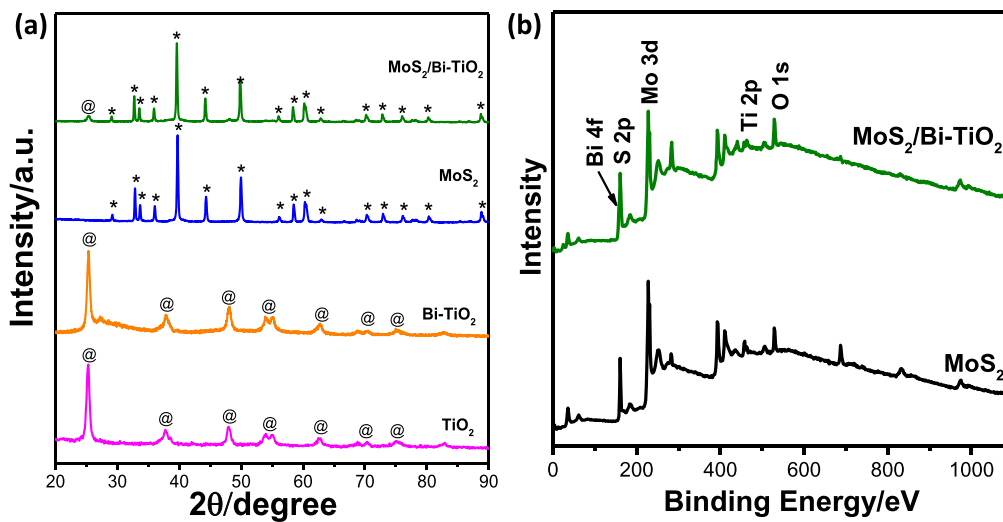


Figure 3. (a) XRD pattern of TiO₂, Bi-doped TiO₂ (using 2 mM Bi), MoS₂ and MoS₂/Bi-TiO₂ (MBT-10) heterostructures. (b) The surface survey XPS spectra of the MoS₂/Bi-TiO₂ (MBT-10) heterostructures and the bare MoS₂.

concentration. However, at higher loading concentration (using 3 and 5 mM Bi), prominent diffraction peaks of metallic Bi arises (figure S1 (available online at stacks.iop.org/NANO/32/195402/mmedia)). Therefore, 2 mM Bi concentration has been fixed for doping. On the other hand,

the XRD pattern of the MoS₂ indicates the hexagonal phase of MoS₂ (JCPDS no. 37-1492) [49]. However, the XRD pattern of MoS₂/Bi-TiO₂ shows mainly MoS₂ peaks along with (101) diffraction peaks of anatase TiO₂ (figure 3(a)). This result demonstrates the heterostructure formation and co-

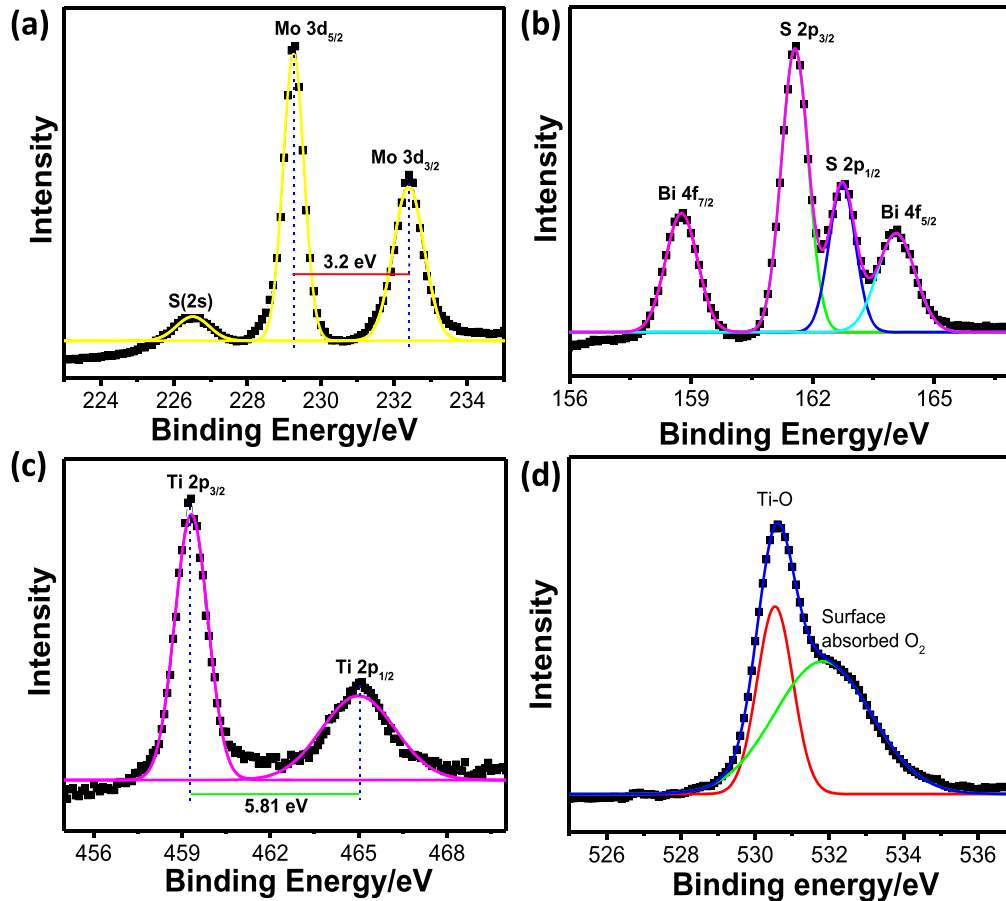


Figure 4. (a) Magnified XPS spectra for Mo 3d, Bi 4f, S 2p, Ti 2p and O 1s of MoS₂/Bi-TiO₂ (MBT-10) heterostructures. The scattered lines represent the experimental data and solid lines for fitted data.

existence of MoS₂ and TiO₂ in the composite sample. Further, the quantity of Bi concentration in Bi-TiO₂ samples has been calculated from the thermogravimetric analysis and the ICP-AES. With increase the loading concentration, the stability of the TiO₂ has been improved (figure S2). The wt% of Bi calculated from TG and ICP-AES are summarized in table S1.

XPS analysis has been studied further to analyze the surface chemical composition and valance state of the components (figure 3(b)). The XPS survey spectra confirm that the sample is composed of Mo, S, Ti, Bi and O. The peaks at ~229.4 eV and ~232.7 eV having spin-orbit separation of ~3.2 eV are ascribed to Mo 3d_{5/2} and Mo 3d_{3/2} state respectively, indicating Mo⁴⁺ state of Mo [45]. The characteristic peaks corresponding to S 2p_{1/2} and S 2p_{3/2} in MoS₂/Bi-TiO₂ composite are located at ~163.1 eV and ~161.9 eV respectively. The peaks are separated by ~1.22 eV which confirms the S²⁻ of S (figure 4(b)) [45]. The XPS peaks at ~164.5 eV (Bi 4f_{5/2}) and ~159.2 eV (Bi 4f_{7/2}) indicate the Bi³⁺ state of Bi [57]. Moreover, the binding energies of ~464.3 eV and ~458.8 eV correspond to the Ti 2p_{1/2} and Ti 2p_{3/2} confirms that Ti present in Ti⁴⁺ state within the heterostructures (figure 4(c)) [44]. The fitted O 1s spectrum shows two peaks (figure 4(d)), one for the lattice oxygen (at 530.2 eV) and another for surface hydroxyl oxygen (at ~531.7 eV) [46].

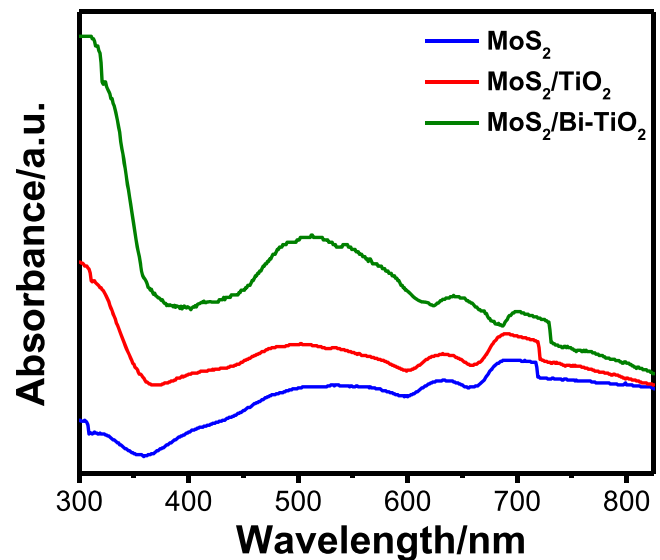


Figure 5. UV-vis absorption spectra of bare MoS₂, MoS₂/TiO₂ and MoS₂/Bi-TiO₂ (MBT-10) heterostructures.

The optical absorbance of MoS₂, TiO₂, MoS₂/TiO₂ and MoS₂/Bi-TiO₂ heterostructures has been measured by UV-visible spectroscopy from 300 to 900 nm wavelength at room temperature which shows three distinct absorption peaks (figure 5). The doublet peak at ~629 and ~685 nm with

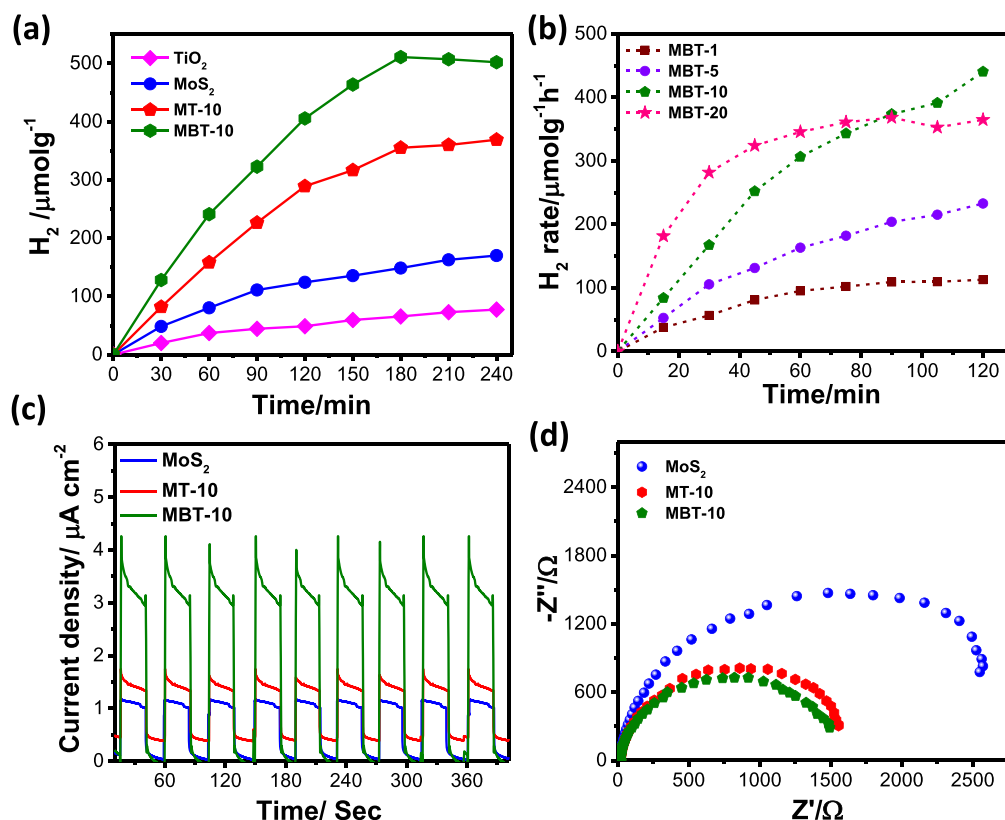


Figure 6. (a) Photocatalytic H₂ generation in presence of MoS₂, MoS₂/TiO₂-10 (MT-10) and MoS₂/Bi-TiO₂ heterostructures (MBT-10) after 240 min of visible light irradiation. (b) Effect of Bi-TiO₂ loading on MoS₂ for photocatalytic H₂ generation. (c) Transient photocurrent spectra of MoS₂, MoS₂/TiO₂ and MoS₂/Bi-TiO₂ heterostructure-modified ITO electrodes at a bias of 0.26 V versus Ag/AgCl reference electrode in presence of 0.1 M Na₂SO₄ buffer solution (suppress photogenerated holes and drive photogenerated electrons to reduce protons to H₂). (d) Nyquist plots of the electrodes at potential 0.1 V versus Ag/AgCl under continuous light illumination.

splitting energy ~ 0.16 eV is well consistent with the ideal value for MoS₂ (0.15 eV, theoretically calculated) [58]. The peaks arise due to the direct electronic transition at the K point of the first Brillouin zone. However, the energy difference between two peaks arises from the spin-orbit coupling of the VB [59]. A broad peak at 400–600 nm has been observed which originates from the interband transition between occupied and unoccupied Mo 3d orbitals in the K-point of the first Brillouin zone [60]. In comparison to the pure MoS₂, the peak positions of MoS₂/Bi-TiO₂ are slightly red shifted because of the interaction between two components, indicating a decrease in the bandgap.

Further, the band gap of the materials was calculated by extrapolating the tangent of Kubelka–Munk $(\alpha h\nu)^2$ versus $h\nu$ plot. Here ' α ' is the absorption coefficient and ' $h\nu$ ' is photon energy [61]. Initially, the calculated band gap for Bi-TiO₂ was ~ 2.5 eV which is lowered from the pure TiO₂ (3.21 eV) and further significantly lowered after the formation of heterostructure with MoS₂ (~ 1.74 eV) (figure S3). The doping of Bi ions is mainly responsible for the band gap reduction of TiO₂, because of the formation of intermediate energy levels between the top of the Bi³⁺ 6s band and the bottom of the Ti⁴⁺ 3d band [28, 29]. However, Bi³⁺ 6s level is located above the VB of TiO₂ [30]. Thus, it can be concluded that incorporation of Bi-content effectively narrowing the band gap of TiO₂ and make it active for visible light absorption.

The photocatalytic activity of the as synthesized materials has been studied by measuring the amount of H₂ generation through water reduction under visible light illumination. For this experiment, 25 volume % of methanol has been taken as hole scavenger as it can react with the photo-induced holes usually faster compared to water, leaving excess photogenerated electrons in the electrolyte for reduction reactions. Clearly, after heterostructure formation with MoS₂, the photocatalytic activity of TiO₂ has been enhanced. The MoS₂/TiO₂ (10% loading of TiO₂, (MT-10) heterostructures) shows six and three-fold enhanced H₂ generation (~ 367 $\mu\text{mol g}^{-1}$) compared to pristine TiO₂ (57 $\mu\text{mol g}^{-1}$) and bare MoS₂ (~ 130 $\mu\text{mol g}^{-1}$) respectively. However, the heterostructure composed of MoS₂ and Bi-doped TiO₂ shows the highest H₂ generation of ~ 512 $\mu\text{mol g}^{-1}$ in 4 h of visible light illumination, which may be attributed to the enhanced light absorption by Bi-doped TiO₂ and availability of active sites for hydrogen evolution (figure 6(a)) [62]. Moreover, MoS₂/Bi-TiO₂ heterostructures displayed a linear evolution of H₂ for the entire period (figure S4).

Further, the effect of Bi-TiO₂ loading on MoS₂ has been studied. It has been clearly shown from figure 6(b) that with the increase of the Bi-TiO₂ loading (1–20 wt%), H₂ generation rate has been increased up to a certain concentration because of the increment of active sites on the MoS₂ surface for water reduction. Further increase in loading concentration

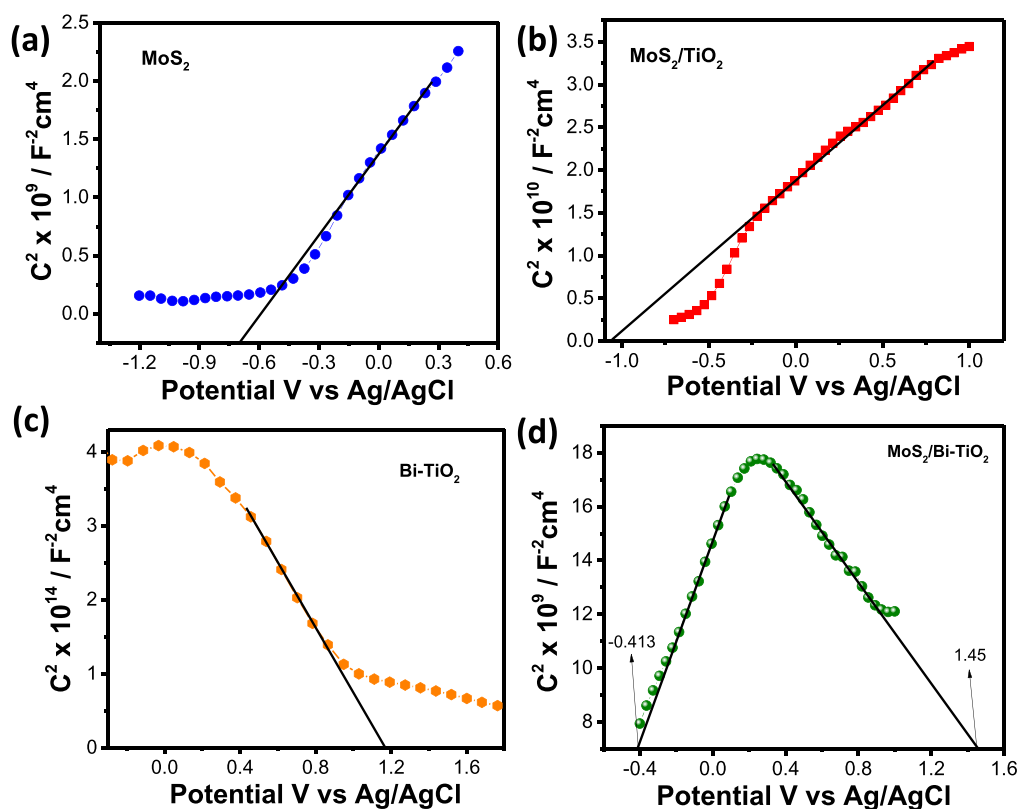
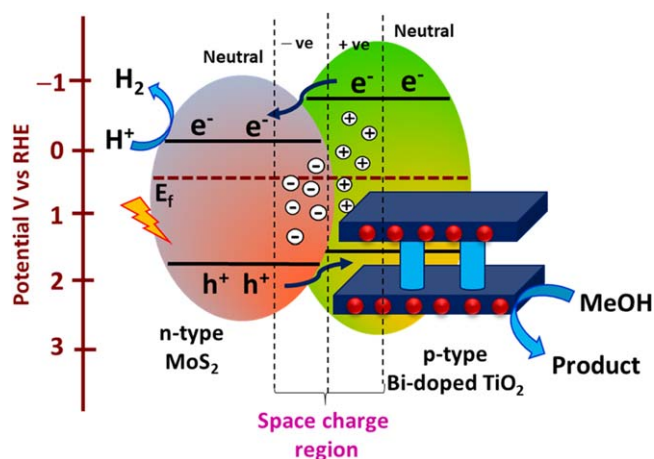


Figure 7. Mott–Schottky plots of (a) bare MoS₂, (b) MoS₂/TiO₂ (MT-10), (c) Bi-doped TiO₂ and (d) MoS₂/Bi-TiO₂ (MBT-10) heterostructures. The experiment was carried out in Na₂SO₄ solution (0.1 M) under 1000 Hz AC frequency. Flatband (E_{fb}) of photoelectrodes have been calculated from the intercept of the plots at $1/C^2 = 0$.



Scheme 1. Schematic illustration of the charge transfer in MoS₂/Bi-TiO₂ p–n heterojunction.

falling down the photocatalytic activity, which may happen because of excessive loading of Bi-doped TiO₂ on the MoS₂, leads to aggregation of Bi-TiO₂ nanoparticles. Moreover, the effect of Bi-doping on TiO₂ for the photocatalytic H₂ generation has been studied (figure S5). With the increase of Bi-content, the H₂ generation rate has been improved due to the presence of additional electronic states between the VB and CB of TiO₂. Consequently, the probability of electron-hole recombination may be reduced which enhances the catalytic activity. On the other hand, solution pH has a crucial role in

controlling the photocatalytic activity of the catalyst. At neutral pH (pH 7) MBT-10 showed the highest activity (figure S6).

The transient photocurrent responses of MoS₂, MoS₂/TiO₂ and MoS₂/Bi-TiO₂ heterostructures have been recorded for several on-off cycles under illumination. The MBT-10 heterostructure (10 wt% loading of Bi-TiO₂ on MoS₂) exhibits the highest photocurrent density of $\sim 3.6 \mu\text{A cm}^{-2}$, which is 3.2 fold of bare MoS₂ ($\sim 1.2 \mu\text{A cm}^{-2}$) (figure 6(c)). Thus, transient photocurrent results are well consistent with the H₂ generation and further supports that the existence of MoS₂ and Bi-doped TiO₂ in the heterostructures could result in high active sites for oxidation-reduction reactions. Furthermore, the charge carrier separation efficiency of MoS₂/Bi-TiO₂ has been studied by impedance spectroscopy. As shown in figure 6(d), a smaller semicircular arc has been obtained for MBT-10 compared to MT-10 and bare MoS₂ electrodes, indicating that the heterostructure formation with Bi-doped TiO₂ reduces the charge-transfer resistance at the electrode-electrolyte interface [53]. Further detailed electrochemical study has been carried out for MBT heterostructures with different loading of Bi-TiO₂. It can be clearly observed that 10 wt% loading exhibits the smallest charge transfer resistance among all materials. However, at higher loading (20 wt%), charge transfer resistance at the electrode-electrolyte interface has been increased (figure S7(a)). A similar trend has been observed in LSV and CA measurements of MoS₂/Bi-TiO₂ heterostructures at various

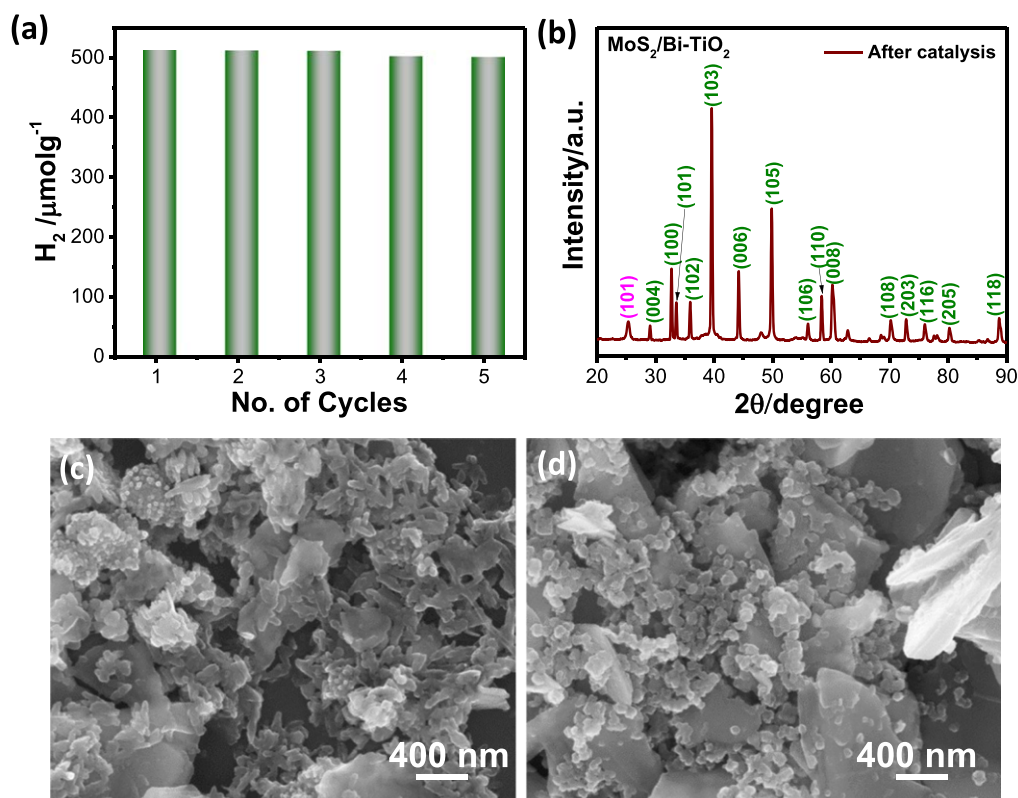


Figure 8. (a) Recycling test of MoS₂/Bi-TiO₂ for photocatalytic H₂ generation. (b) XRD pattern of MoS₂/Bi-TiO₂ catalyst after photocatalytic H₂ generation. The FESEM micrographs of the MoS₂/Bi-TiO₂ (b) before and (c) after the catalytic reaction.

loading of Bi-doped TiO₂ (figures S7(b) and (c)). Therefore, it can be concluded that 10 wt% loading of Bi-TiO₂ on the MoS₂ surface is the optimal condition which offers minimum resistance with a significant amount of available catalytic active sites. At higher loading concentration, photo-current density has been decreased due to the surface agglomeration.

For better understanding the enhanced catalytic activity of MoS₂/Bi-TiO₂ heterostructures, the Mott–Schottky study has been further carried out. Figures 7(a)–(d) shows the Mott–Schottky plots of bare MoS₂, MoS₂/TiO₂ (MT-10), Bi-doped TiO₂ (using 2 mM Bi) and MoS₂/Bi-TiO₂ (MBT-10) heterostructures. The positive slopes in the linear regions confirm the n-type conductivity of MoS₂ and MoS₂/TiO₂ (figures 7(a) and (b)). Flatband (E_{fb}) potentials have been obtained by calculating the intersection of the linear fit to the $1/C^2$ measurements with the x -axis, which is -0.69 V (versus Ag/AgCl) for bare MoS₂ and -1.06 V (versus Ag/AgCl) for MoS₂/TiO₂. The negative shift of E_{fb} reveals that heterostructure formation with TiO₂ accelerates the charge transferring and catalyzes the reduction reactions for H₂ generation [45].

The E_{fb} potentials could be near to the CB edges ($CB = E_{fb} - 0.2$ V) for the n-type conductors [61]. Thus, the CB potentials of MoS₂ is -0.28 V after converting the potential versus RHE scale by following the equation (1). As a consequence, the VB potentials have been calculated using the optical bandgap, which is 1.63 V (versus RHE) for MoS₂. However, the Bi doping in the TiO₂ lattice changes the conductivity of TiO₂ and shows p-type conductivity with E_{fb}

potential of 1.16 V (versus Ag/AgCl). As Bi³⁺ replaces the Ti⁴⁺ so an extra hole remains in the crystal which plays a crucial role as the free carrier in conductivity. The VB and CB potentials of Bi-doped TiO₂ are 1.57 and -1.28 V versus RHE respectively. As expected, MoS₂/Bi-TiO₂ heterostructure shows both p-type and n-type conductivity for the presence of n-type MoS₂ and p-type Bi-doped TiO₂, i.e. a p–n junction may be formed at the interface between two semiconductors. As a result, enhanced electron–hole transfer efficiency has been achieved through the junction due to the presence of an internal electric field.

Before light illumination on the MoS₂/Bi-TiO₂ heterostructure, the electrons of MoS₂ near the junction try to diffuse into the p-type Bi-doped TiO₂, leaving the holes. Similarly, the holes on the p-type Bi-doped TiO₂ near the junction tend to diffuse into the n-type MoS₂, leaving negatively charged electrons. This diffusion of electrons and holes will be continued until the Fermi level equilibrium of the system is achieved, which results in a space charge region on both sides of the junction interface and creates an internal electric field. Now, when this equilibrium system is irradiated by light energy (greater than the work function energy of the constituent semiconductors) then both the semiconductors will be excited and produce excitons (excited electrons and holes). The photo-generated electrons of p-type Bi-doped TiO₂ will transfer to the CB of the n-type MoS₂ and the holes of MoS₂ will transfer to the VB of the Bi-doped TiO₂ by the influence of the internal electric field (Scheme 1). In this way, a special separation of electrons and holes will occur which

can reduce the formation of electron–hole pairs [63]. Consequently, the excited electrons accumulated on the CB of MoS₂ which have higher negative potential compared to the water reduction potential (0 V versus RHE). These electrons can easily reduce the water and generate H₂ from H⁺. Simultaneously, oxidation of the water molecules takes place by the accumulated holes on the VB of Bi-doped TiO₂ which are highly positive and can oxidize the water.

Figure 8(a) implies that the MoS₂/Bi-TiO₂ heterostructure can be reused at least three times for H₂ generation. To check the structural stability, XRD and FESEM of MoS₂/Bi-TiO₂ heterostructure have been studied before and after catalysis. All the characteristic peaks are present after catalytic reaction and no other extra peak has been observed (figure 8(b)). As shown in figures 8(c) and (d), a similar kind of morphology has been observed after 2 h of photocatalytic H₂ generation. Therefore, it can be concluded that the heterostructure is stable under light illumination and photocatalytic reactions, represent a green way for solar light-harvesting applications.

4. Conclusion

A p–n junction of MoS₂/Bi-TiO₂ heterostructure was developed for visible light-sensitive water splitting. The introduction of Bi into the TiO₂ crystal leads to more efficient light absorption by hybridized VB. The photo-excited electrons in the CB of Bi-modified TiO₂ transferred to MoS₂ and holes of MoS₂ transfer to the VB of Bi-TiO₂ through the junction between them. The p–n junction provides an internal driving force to accelerate the charge separation. As a result, four-fold enhanced H₂ generation rate achieved for MoS₂/Bi-TiO₂ p–n junction compared to bare MoS₂. Moreover, the MoS₂/Bi-TiO₂ heterostructure shows superior catalytic activity in PEC measurements because of low charge transfer resistance at the electrode-electrolyte interfaces. This study provides an efficient p–n junction for solar energy harvesting applications.

Data availability statement

The data that support the findings of this study are available upon reasonable request from the authors.

ORCID iDs

Rajendra N Basu  <https://orcid.org/0000-0002-0585-9354>

References

- [1] Bard A J and Fox M A 1995 Artificial photosynthesis: solar splitting of water to hydrogen and oxygen *Acc. Chem. Res.* **28** 141–5
- [2] Kim J H, Hansora D, Sharma P, Jang J-W and Lee J S 2019 Toward practical solar hydrogen production—an artificial photosynthetic leaf-to-farm challenge *Chem. Soc. Rev.* **48** 1908–71
- [3] Hisatomi T, Kubota J and Domen K 2014 Recent advances in semiconductors for photocatalytic and photoelectrochemical water splitting *Chem. Soc. Rev.* **43** 7520–35
- [4] Wang Q and Domen K 2020 Particulate photocatalysts for light-driven water splitting: mechanisms, challenges, and design strategies *Chem. Rev.* **120** 919–85
- [5] Pinaud B A et al 2013 Technical and economic feasibility of centralized facilities for solar hydrogen production via photocatalysis and photoelectrochemistry *Energy Environ. Sci.* **6** 1983–2002
- [6] Ghosh S (ed) 2018 *Visible-Light-Active Photocatalysis: Nanostructured Catalyst Design, Mechanisms and Applications* (Germany: Wiley-VCH Verlag GmbH & Co. KGaA) ch 8
- [7] Wang Z, Li C and Domen K 2019 Recent developments in heterogeneous photocatalysts for solar-driven overall water splitting *Chem. Soc. Rev.* **48** 2109–25
- [8] Jian J, Jiang G, Krol R, Wei B and Wang H 2018 Recent advances in rational engineering of multinary semiconductors for photoelectrochemical hydrogen generation *Nano Energy* **51** 457–80
- [9] Ghosh S, Thandavarayan M and Basu R N 2016 Nanostructured conducting polymers for energy applications: towards a sustainable platform *Nanoscale* **8** 6921–47
- [10] Sivula K and Krol R 2016 Semiconducting materials for photoelectrochemical energy conversion *Nat. Rev. Mater.* **1** 1–15
- [11] Yuan X, Floresyona D, Aubert P H, Bui T T, Remita S, Ghosh S, Brisset F, Goubard F and Remita H 2019 Photocatalytic degradation of organic pollutant with polypyrrole nanostructures under UV and visible light *Appl. Catal. B* **242** 284–92
- [12] Gu I, Sayed M, Shah N S, Khan J A, Polychronopoulou K, Iqbal J and Rehman F 2020 Solar light responsive bismuth doped titania with Ti³⁺ for efficient photocatalytic degradation of flumequine: synergistic role of peroxymonosulfate *Chem. Eng. J.* **384** 123255–72
- [13] Ghosh S, Remita H and Basu R N 2018 Visible-light-induced reduction of Cr (VI) by PDPB-ZnO nanohybrids and its photo-electrochemical response *Appl. Catal. B* **239** 362–72
- [14] Hernandez-Alonso M D, Fresno F, Suarez S and Coronado J M 2009 Development of alternative photocatalysts to TiO₂: challenges and opportunities *Energy Environ. Sci.* **2** 1231–57
- [15] Wang F, Wong R J, Ho J H, Jiang Y and Amal R 2017 Sensitization of Pt/TiO₂ using plasmonic Au nanoparticles for hydrogen evolution under visible-light irradiation *ACS Appl. Mater. Interfaces* **9** 30575–81
- [16] Kouamé N A, Alaoui O T, Herissan A, Larios E, José-Yacaman M, Etcheberry A, Colbeau-Justina C and Remita H 2015 Visible light-induced photocatalytic activity of modified titanium (IV) oxide with zero-valent bismuth clusters *New J. Chem.* **39** 2316–22
- [17] Chen Y, Chuang C-H, Qin Z, Shen S, Doane T and Burd C 2017 Electron-transfer dependent photocatalytic hydrogen generation over cross-linked CdSe/TiO₂ type-II heterostructure *Nanotechnology* **28** 084002–6
- [18] Kubakaddi S B, Chirakkara S, Hosamani G and Shivaprasad S M 2018 Nanostructured p-TiO₂/n-GaN heterostructure as a potential photoelectrode for efficient charge separation *Nanotechnology* **29** 50LT02–7
- [19] Zhao Y, Zeng Q, Feng T, Xia C, Liu C, Yang F, Zhang K and Yang B 2019 Carbonized polymer dots/TiO₂ photonic crystal heterostructures with enhanced light harvesting and

- charge separation for efficient and stable photocatalysis *Mater. Chem. Front.* **3** 2659–67
- [20] Wang X, Jiang S, Huo X, Xia R, Muhire E and Gao M 2018 Facile preparation of a TiO₂ quantum dot/graphitic carbon nitride heterojunction with highly efficient photocatalytic activity *Nanotechnology* **29** 205702–5
- [21] Wang K, Endo-Kimura M, Belchi R, Zhang D, Habert A, Bouclé J, Ohtani B, Kowalska E and Herlin-Boime N 2019 Carbon/graphene-modified titania with enhanced photocatalytic activity under UV and Vis irradiation *Materials* **12** 4158–64
- [22] Bach U, Lupo D, Comte P, Moser J E, Weissörtel F, Salbeck J, Spreitzer H and Grätzel M 1998 Solid-state dye-sensitized mesoporous TiO₂ solar cells with high photon-to-electron conversion efficiencies *Nature* **395** 583–5
- [23] Mendez-Medrano M G, Kowalska E, Lehoux A, Herissan A, Ohtani B, Rau S, Colbeau-Justin C, Rodríguez-Lopez J L and Remita H 2016 Surface modification of TiO₂ with Au nanoclusters for efficient water treatment and hydrogen generation under visible light *J. Phys. Chem. C* **120** 25010–22
- [24] Nischk M, Mazierski P, Wei Z, Siuzdak K, Kouame N A, Kowalska E, Remita H and Zaleska-Medynska A 2016 Enhanced photocatalytic, electrochemical and photoelectrochemical properties of TiO₂ nanotubes arrays modified with Cu, AgCu and Bi nanoparticles obtained via radiolytic reduction *Appl. Surf. Sci.* **387** 89–102
- [25] Ji T H, Yang F, Lv Y Y, Zhou J Y and Sun J Y 2009 Synthesis and visible-light photocatalytic activity of Bi-doped TiO₂ nanobelts *Mater. Lett.* **63** 2044–8
- [26] Murcia-López S, Hidalgo M C and Navío J A 2011 Synthesis, characterization and photocatalytic activity of Bi-doped TiO₂ photocatalysts under simulated solar irradiation *Appl. Catal. A* **404** 59–67
- [27] Reddy P A K, Srinivas B, Kala P, Kumari V D and Subrahmanyam M 2011 Preparation and characterization of Bi-doped TiO₂ and its solar photocatalytic activity for the degradation of isoproturon herbicide *Mater. Res. Bull.* **46** 1766–71
- [28] Wu Y Q, Lu G X and Li S B 2009 The doping effect of Bi on TiO₂ for photocatalytic hydrogen generation and photodecolorization of rhodamine B *J. Phys. Chem. C* **113** 9950–5
- [29] Xu J J, Chen M D and Fu D G 2011 Study on highly visible light active Bi-doped TiO₂ composite hollow sphere *Appl. Surf. Sci.* **257** 7381–4
- [30] Hu Y, Cao Y T, Wang P X, Li D Z, Chen W, He Y H, Fu X Z, Shao Y and Zheng Y 2012 A new perspective for effect of Bi on the photocatalytic activity of Bi-doped TiO₂ *Appl. Catal. B* **125** 294–301
- [31] Li S, Chang L, Peng J, Gao J, Lu J, Zhang F, Zhu G and Hojamberdiev M 2020 Bi⁰ nanoparticle loaded on Bi³⁺-doped ZnWO₄ nanorods with oxygen vacancies for enhanced photocatalytic NO removal *J. Alloys Compd.* **818** 152837–46
- [32] Lv J, Zhang J, Liu J, Li Z, Dai K and Liang C 2018 Bi SPR-Promoted Z-Scheme Bi₂MoO₆/CdS-Diethylenetriamine composite with effectively enhanced visible light photocatalytic hydrogen evolution activity and stability *ACS Sustain. Chem. Eng.* **6** 696–706
- [33] Du M, Zhang S, Xing Z, Li Z, Yin J, Zou J, Zhu Q and Zhou W 2019 All-Solid Z Scheme Bi–BiOCl/AgCl heterojunction microspheres for improved electron–hole separation and enhanced visible light driven photocatalytic performance *Langmuir* **35** 7887–95
- [34] Hao W, Teng F, Liu Z, Yang Z, Liu Z and Gu W 2019 Synergistic effect of Mott–Schottky junction with oxygen defect and dramatically improved charge transfer and separation of Bi@Bi-doped TiO₂ *Sol. Energy Mater. Sol. Cells* **203** 110198–206
- [35] Magnusson K O and Wiklund S 1994 Interface formation of Bi on ceramic ZnO: a simple model varistor grain boundary *J. Appl. Phys.* **76** 7405–9
- [36] Liu Y, Duan X, Huang Y and Duan X 2018 Two-dimensional transistors beyond graphene and TMDCs *Chem. Soc. Rev.* **47** 6388–409
- [37] Lu Q, Yu Y, Ma Q, Chen B and Zgang H 2016 2D transition-metal-dichalcogenide-nanosheet-based composites for photocatalytic and electrocatalytic hydrogen evolution reactions *Adv. Mater.* **28** 1917–33
- [38] Wi S, Kim H, Chen M, Nam H, Guo L J, Meyhofer E and Liang X 2014 Enhancement of photovoltaic response in multilayer MoS₂ induced by plasma doping *ACS Nano* **8** 5270–81
- [39] Pang Q, Zhao Y, Bian X, Ju Y, Wang X, Wei Y, Liu B, Du F, Wang C and Chen G 2017 Hybrid graphene@MoS₂@TiO₂ microspheres for use as a high performance negative electrode material for lithium ion batteries *J. Mater. Chem. A* **5** 3667–74
- [40] Stephenson T, Li Z, Olsen B and Mitlin D 2014 Lithium ion battery applications of molybdenum disulfide (MoS₂) nanocomposites *Energy Environ. Sci.* **7** 209–31
- [41] Wang T, Chen S, Pang H, Xue H and Yu Y 2016 MoS₂-Based nanocomposites for electrochemical energy storage *Adv. Sci.* **4** 1600289–315
- [42] Sarkar D, Liu W, Xie X, Anselmo A C, Mitragotri S and Banerjee K 2014 MoS₂ field-effect transistor for next-generation label-free biosensors *ACS Nano* **8** 3992–4003
- [43] Guo L, Yang Z, Marcus K, Li Z, Luo B, Zhou L, Wang X, Du Y and Yang Y 2018 MoS₂/TiO₂ heterostructures as nonmetal plasmonic photocatalysts for highly efficient hydrogen evolution *Energy Environ. Sci.* **11** 106–14
- [44] Li Y-Y, Wang J-H, Luo Z-J, Chen K, Cheng Z-Q, Ma L, Ding S-J, Zhou L and Wang Q-Q 2017 Plasmon-enhanced photoelectrochemical current and hydrogen production of (MoS₂-TiO₂)/Au hybrids *Sci. Rep.* **7** 7178–216
- [45] Bera S, Ghos S and Basu R N 2020 Silver as solid-state electron mediator in MoS₂/Ag–AgVO₃ Z-Scheme heterostructures for photocatalytic H₂ generation *J. Alloys Compd.* **830** 154527–39
- [46] Zong X, Yan H, Wu G, Ma G, Wen F, Wang L and Li C 2008 Enhancement of photocatalytic H₂ evolution on CdS by loading MoS₂ as cocatalyst under visible light irradiation *J. Am. Chem. Soc.* **130** 7176–7
- [47] Xiang Q, Yu J and Jaroniec M 2012 Synergetic effect of MoS₂ and graphene as co-catalysts for enhanced photocatalytic H₂ production activity of TiO₂ nanoparticles *J. Am. Chem. Soc.* **134** 6575–8
- [48] Xiong W, Xia C, Du J, Wang T, Peng Y, Wei Z and Li J 2017 Band engineering of MoS₂/Stanene heterostructure: strain and electrostatic gating *Nanotechnology* **28** 195702–10
- [49] Mak K F, Lee C, Hone J, Shan J and Heinz T F 2010 Atomically thin MoS₂: a new direct-gap semiconductor *Phys. Rev. Lett.* **105** 136805–8
- [50] Li Y, Hong H, Xue X, Zhang Z and Tian H 2019 MoS₂ as cocatalyst for improving photocatalytic performance of Bi₂MoO₆ *ChemistrySelect* **4** 5222–7
- [51] Samadi M, Sarikhani N, Zirak M, Zhang H, Zhang H-L and Moshfegh A Z 2018 Group 6 transition metal dichalcogenide nanomaterials: synthesis, applications and future perspectives *Nanoscale Horiz.* **3** 90–204
- [52] Zhang G, Liu H, Qu J and Li J 2016 Two-dimensional layered MoS₂: rational design, properties and electrochemical applications *Energy Environ. Sci.* **9** 1190–209
- [53] Wang H, Li C, Fang P, Zhang Z and Zhang J Z 2018 Synthesis, properties, and optoelectronic applications of two-

- dimensional MoS₂ and MoS₂-based heterostructures *Chem. Soc. Rev.* **47** 6101–27
- [54] Cheng R, Li D, Zhou H, Wang C, Yin A, Jiang S, Liu Y, Chen Y, Huang Y and Duan X 2014 Electroluminescence and photocurrent generation from atomically sharp WSe₂/MoS₂ heterojunction p–n diodes *Nano Lett.* **14** 5590–7
- [55] Ceballos F, Bellus M Z, Chiu H-Y and Zhao H 2014 Ultrafast charge separation and indirect exciton formation in a MoS₂-MoSe₂ van der waals heterostructure *ACS Nano* **8** 12717–24
- [56] Wang X, Chen S, Zhang M, Huang Y, Feng S and Zhao D 2017 MoS₂ quantum dots modified Ag/polyaniline composites with enhanced photogenerated carrier separation for highly efficient visible light photocatalytic H₂ evolution performance *Catal. Sci. Technol.* **7** 3531–8
- [57] Bera S, Ghosh S, Shyamal S, Bhattacharya C and Basu R N 2019 Photocatalytic hydrogen generation using gold decorated BiFeO₃ heterostructures as an efficient catalyst under visible light irradiation *Sol. Energy Mater. Sol. Cells* **194** 195–206
- [58] Zhu Z Y, Cheng Y C and Schwingenschlögl U 2011 Giant spin–orbit-induced spin splitting in two-dimensional transition-metal dichalcogenide semiconductors *Phys. Rev. B* **84** 153402–7
- [59] Umrao S, Jeon J, Jeon S M, Choi Y J and Lee S 2017 A homogeneous atomic layer MoS₂(1–x)Se_{2x} alloy prepared by low-pressure chemical vapor deposition, and its properties *Nanoscale* **9** 594–603
- [60] Ahmad R, Srivastava R, Yadav S, Singh D, Gupta G, Chand S and Sapra S 2017 Functionalized molybdenum disulphide nanosheets for 0D-2D hybrid nanostructure: photoinduced charge transfer and enhanced photoresponse *J. Phys. Chem. Lett.* **8** 1729–38
- [61] Zhao Y-F, Yang Z-Y, Zhang Y-X, Jing L, Guo X, Ke Z, Hu P, Wang G, Yan Y-M and Sun K-N 2014 Cu₂O decorated with cocatalyst MoS₂ for solar hydrogen production with enhanced efficiency under visible light *J. Phys. Chem. C* **118** 14238–45
- [62] Ghosh S, Keshri S R, Bera S and Basu R N 2019 Enhanced solar hydrogen generation using Cu-Cu₂O integrated polypyrrole nanofibers as heterostructured catalysts *Int. J. Hydrog. Energy* **45** 6159–73
- [63] Chen Y, Crittenden J C, Hackney S, Sutter L and Hand D W 2005 Preparation of a novel TiO₂-based p–n junction nanotube photocatalyst *Environ. Sci. Technol.* **39** 1201–9

Band Edge Engineering of BiOX/CuFe₂O₄ Heterostructures for Efficient Water Splitting

Susmita Bera, Srabanti Ghosh,* T. Maiyalagan, and Rajendra N. Basu

Cite This: *ACS Appl. Energy Mater.* 2022, 5, 3821–3833

Read Online

ACCESS |

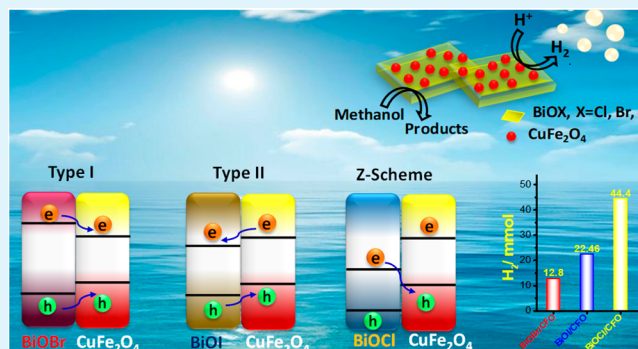
Metrics & More

Article Recommendations

Supporting Information

ABSTRACT: Layered bismuth oxyhalides (BiOX, X = Cl, Br, and I) are promising visible light-responsive photocatalysts but suffer from inadequate electron transportation from the bulk to the surface. Construction of heterostructures has been considered as a convenient approach to improve the spatial charge carrier separation and enhance the efficiencies of the surface-reactive charges for catalysis. Here, a series of heterostructures has been successfully designed for n-type bismuth oxyhalides and p-type spinel ferrites CuFe₂O₄ (CFO) by a facile and generalized protocol *via* the hydrothermal method followed by the co-precipitation method. The heterostructure introduces built-in electric field at the interface that facilitates vectorial charge transfer, which demonstrated significantly improved visible light-driven photocatalytic activity toward H₂ generation without using any noble metal co-catalyst. A conventional type-I and type-II charge transfer mechanism has been followed for BiOBr/CFO and BiOI/CFO heterostructures, respectively, which may effectively lower charge transfer resistance compared to that for bare BiOBr and BiOI, suggesting facile charge transfer. Remarkably, a direct Z-scheme BiOCl/CFO heterostructure has been formed between BiOCl and CFO with an intimate interfacial contact, which demonstrated 5.7 times higher H₂ generation activity than pure BiOCl and two fold improved catalytic efficiency compared to type-II BiOI/CFO heterostructures under visible light. Very low resistance in electrochemical impedance spectra confirmed the superiority of the direct Z-scheme in promoting the charge separation and transfer and increase in carrier density. Moreover, the optimal space charge layer width and the redox potentials have been achieved for BiOCl/CFO through the engineering of band edge potentials, which reduces the fast recombination rate. This work offers a paradigm for the design of highly engineered BiOX-based heterostructures with tuned band structures for efficient photocatalytic water splitting.

KEYWORDS: BiOX (X = Cl, Br, and I), band gap engineering, heterostructure, direct Z-scheme, water splitting, H₂ generation, photoelectrochemical properties



1. INTRODUCTION

Solar energy conversion to generate renewable fuel H₂ through water splitting by developing sustainable, low-cost, and efficient photocatalysts, provides a potential approach to meet the global energy demand.^{1–4} On account of the photocatalyst development, various metal oxides (such as TiO₂, ZnO, Fe₂O₃, Cu₂O, WO₃, and BiVO₄), hydroxides, chalcogenides (like MoS₂, MoSe₂, WS₂, and WSe₂), MXenes, black phosphorus, and organic semiconductors such as conjugated polymers, graphitic carbon nitrides, graphene, metal organic frameworks, covalent organic frameworks, and so forth are fabricated and studied for water splitting over the past decades.^{5–10} However, the efficiency is still not significant for the large-scale application as most of these photocatalysts suffer from fast charge carrier recombination and low absorption in the visible region, which accounts for 53% of the total solar spectrum. Therefore, it is required to exploit

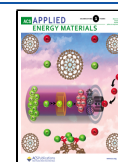
efficient catalysts with high photocatalytic activity and stability under visible light.

In this regard, bismuth oxyhalides (BiOX, X = Cl, Br, and I), a new family of photocatalysts, have attracted intense interest in various photocatalytic applications due to their layered structure, which is composed of [Bi₂O₂]⁺ slabs interleaved with double halogen atoms [X][−] with an open crystalline nature. The van der Waals force within the halide layers and the covalent bond between [Bi₂O₂]⁺ and [X][−] make the intrinsic structure of BiOX very stable.^{11,12} Besides, the open crystalline structure benefits a large space for the polarization of atoms

Received: January 26, 2022

Accepted: February 24, 2022

Published: March 9, 2022



and induces a static electric field perpendicular to the $[\text{Bi}_2\text{O}_2]^+$ slabs, which further accelerates the charge separation along the (001) direction.¹³ In addition, BiOX generates facile O-vacancies during photocatalysis under UV light due to low-energy Bi–O bonds present on the surface.^{14–16} As an example, Sun *et al.*¹⁷ experimentally demonstrated the enhanced photocatalytic activity of BiOCl nanosheets towards organic pollutant rhodamine B degradation because of O defects generated on the exposed (001) surface under UV light. Furthermore, Zhang¹⁸ showed selective transfer of photogenerated electrons to the (001) surface of BiOCl as a vacancy state lying below the CB, which acts as trapping state. On the other hand, BiOX shows an indirect transition band gap, that is, electrons have to travel a certain *k*-spacing to be emitted to the VB; thus, electron–hole recombination is low compared to that in direct-band gap semiconductors.¹⁴ However, the wide band gap of BiOCl (2.4–3.4 eV) limits its photocatalytic activity under visible light, and owing to positive conduction band minima (CBM), BiOCl is improper for water splitting, CO₂ reduction, and N₂ fixation. Thus, photocatalytic activity is confined only for organic pollutant degradation under UV light.^{14,19} Although, BiOBr (2.3–2.9 eV) could absorb visible light, the large band gap still restricts its effective performance, while the relatively smaller band gap of BiOI (1.8–2.1 eV) suffers from the fast recombination of electrons and holes.^{17,18} Thus, coupling of secondary semiconductors with BiOBr and BiOI may improve the photocatalytic performance under visible light. As an example, binary and ternary heterojunctions have been fabricated with BiOBr, such as SnWO₄/BiOBr,²⁰ N-CQDs/OV-BiOBr,²¹ Ag/AgBr/BiOBr,²² and BiOBr/ZnO/BiOI,²³ to increase the visible light-driven photocatalytic activity toward organic pollutant degradation. Significant efforts have been made on BiOI *via* heterostructure formation with other semiconductors, like CdS,²⁴ CuI,²⁵ and g-C₃N₄²⁶ to prolong the lifetime of the excited charge carriers by lowering the fast recombination rate. However, these BiOI-based heterostructures are tested mainly for organic dye degradation, and very limited reports on photocatalytic H₂ generation are present, up to date. Meanwhile, some literature studies demonstrated BiOI as an O₂ evolving catalyst through photocatalytic and photoelectrochemical (PEC) water oxidation, although the efficiency is still too low for large-scale application.^{27,28} This stimulates our interest to design BiOX-based efficient catalysts, which can have strong redox potentials to drive the water splitting reactions along with minimal recombination, high charge separation, and visible light absorption capabilities. In this regard, the direct Z-scheme heterostructure, which consists of a reductive semiconductor with a highly negative CB and another oxidative semiconductor having highly positive VB, is gaining intense research interest as it offers strong redox capability to drive catalytic reactions.^{4,29} Apart from this, this Z-scheme system benefits an internal potential gradient and spatial charge separation *via* recombination of low-energy electrons and holes within the body.⁴

Recently, considerable attention has been paid to the narrow-band gap spinel ferrites (MFe₂O₄, M = Co, Ni, Mn, Cu, and Zn) in photocatalysis due to the various chemical compositions, multiple oxidation states, environmental compatibility, stability, easy synthesis, and low cost. In addition, the available large number of active sites is a potential factor of spinel ferrites for the catalytic reactions.³⁰ Matsumoto³¹ reported that the electrical conductivity and surface electro-

chemical reactivity of spinel ferrites are much higher compared to those of corresponding single-component iron oxides due to the improved electron transport process *via* different metal cations. The magnetic properties of spinel ferrites would be helpful for the removal of catalysts from the reaction medium using a magnet. As an outstanding member of the spinel ferrite family, CuFe₂O₄, with a band gap of 1.65 eV and strong visible light response, has received more attention in PEC water splitting both as a photoanode³² and photocathode.^{33,34} The chemical stability at high temperature and the phase transition of CuFe₂O₄ (CFO) give rise to interesting electrical and magnetic properties. However, it suffers from a low surface area, irregular morphology, and limited catalytic activity due to fast charge carrier recombination. Besides, single-semiconductor CFO is unable to evolve O₂ through water oxidation because of low VB potential. At the same time, the large difference between CB potential and water reduction potential leads to poor activity in photocatalytic H₂ generation. There have been reports on modification of CFO to overcome the aforesaid issues.^{35–38} For example, Hussain *et al.*³⁵ fabricated the Fe₂O₃/CFO composite to modulate the charge separation by developing a Z-shaped path for enhanced water oxidation and reduction. A type-II heterostructure was developed by Cheng *et al.*³⁶ between CFO and g-C₃N₄, which exhibited photocatalytic H₂ generation in presence of the Pt (3 wt %) co-catalyst and triethanolamine (10 vol %) sacrificial electron donor under visible light. Very recently, Das and co-workers³⁷ fabricated p–n junctions of CFO/NiAl LDH and demonstrated an enhanced photocatalytic H₂ generation rate compared to that of bare LDH and CFO, which is associated with the increased trapping sites due to multiple oxidation states of charge carriers that effectively prolong the lifetimes. However, the H₂ generation rates of these heterostructures are very low. In particular, the highly negative CB potential, the p-type conductivity, and the narrow band gap of CFO fascinate us to couple with BiOX to develop Z-scheme heterostructures. To the best of our knowledge, BiOX/CFO heterostructures are not prepared and tested for photocatalytic H₂ generation.

In this work, heterostructures are fabricated between n-type BiOX and p-type CFO by the facile hydrothermal method followed by the co-precipitation method. Depending on the position of the VB and CB of BiOX, three types of heterostructures (type-I, type-II, and Z-scheme) are formed. The new band edge position with respect to the redox potentials for both H₂ and O₂ evolution is suitable for efficient water splitting. The Z-scheme heterostructure showed significantly high catalytic efficiency in photocatalytic H₂ generation through water reduction and PEC water oxidation under visible light. Moreover, possible charge transfer mechanisms of the as-prepared heterostructures have been proposed to explain the catalytic reactions.

2. EXPERIMENTAL SECTION

2.1. Chemicals. Bismuth nitrate pentahydrate $\text{Bi}(\text{NO}_3)_3 \cdot 5\text{H}_2\text{O}$, potassium iodide (KI), sodium chloride (NaCl), potassium bromide (KBr), mannitol, methanol, and ethanol were obtained from Merck chemicals. Deionized (DI) water, 18.2 MΩ cm (Millipore System), was used as solvent.

2.2. Synthesis of BiOX (X = Cl, Br, and I). The BiOCl, BiOBr, and BiOI were synthesized by the one-step hydrothermal method.³⁵ To prepare BiOCl, 0.5 M $\text{Bi}(\text{NO}_3)_3 \cdot 5\text{H}_2\text{O}$ was dissolved in 20 mL of 0.1 M mannitol solution under magnetic stirring for 20 min. Then, 10 mL of 0.5 M KCl solution was added dropwise to the Bi solution under vigorous stirring. The solution color changed to white, which

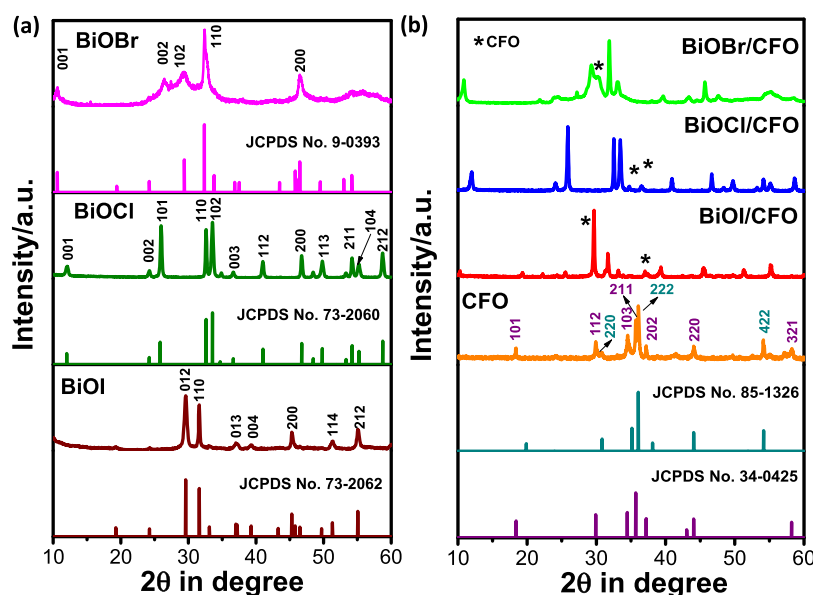


Figure 1. XRD pattern of (a) bare semiconductors BiOI, BiOCl, and BiOBr with the standard XRD patterns, (b) CuFe_2O_4 (CFO) nanoparticles with standard XRD patterns, BiOI/CFO, BiOCl/CFO, and BiOBr/CFO heterostructures.

was then transferred into a 50 mL-capacity stainless-steel autoclave and heated to 150 °C for 3 h. After cooling down, the sample was collected and washed with DI water and ethanol several times. The final white precipitate was dried in an oven at 60 °C overnight. The BiOBr and BiOI were also prepared by a similar method using KBr and KI as Br and I source, respectively.

2.3. Synthesis of BiOX/CFO Heterostructures. BiOX/CFO heterostructures were synthesized by the facile co-precipitation method. At first, 30 mg of BiOX was mixed in 30 mL of DI water by 10 min ultrasonication. At the same time, 0.57 g of $\text{Cu}(\text{NO}_3)_2 \cdot 6\text{H}_2\text{O}$ and 1.92 g of $\text{Fe}(\text{NO}_3)_3 \cdot 9\text{H}_2\text{O}$ were dissolved in 30 mL of DI water. After that, the mixed solution was added dropwise to the BiOX solution and mixed for 15 min to yield a homogeneous mixture. The whole mixture was then refluxed at 75 °C under stirring for another 30 min. After cooling down, the solid precipitate was collected by centrifugation with DI water and ethanol several times and then dried in an oven at 75 °C for overnight.

2.4. Characterizations. Powder X-ray diffraction (XRD) of the as-synthesized materials was performed using a Philips X'Pert system. To analysis size and morphology of the bare semiconductors and heterostructures, field emission scanning electron microscopy (FESEM) was employed using Carl-Zeiss, Sigma (LEO. 430i). Transmission electron microscopy (TEM) was used to further study the crystalline properties by employing Tecnai G² 30ST, FEI. Formation of heterostructures and the oxidation states were investigated by X-ray photoelectron spectroscopy (XPS). A PHI 5000 Versa Probe II spectrophotometer was used to conduct this experiment. Here, the charge correction was performed by considering C 1s (284.5 eV) spectra as a standard. Furthermore, the thermal stability of the as-prepared heterostructures was studied using a NETZSCH, STA 449 F3 Jupiter instrument through thermogravimetric analysis. The Fourier transform infrared (FTIR) spectra and Raman spectra were collected using a JASCO FTIR-6300 spectrometer and a Jobin Yvon HR800 confocal Raman system (540 nm laser beam). Room-temperature UV–visible absorption spectra of the bare semiconductors and the heterostructures were taken using a Cary 5000 UV–vis–NIR spectrophotometer.

2.5. PEC Measurements. The PEC properties of pure BiOX, CFO, and the heterostructures were studied by preparing thin films on FTO-coated glass slides (2 cm × 2 cm) by the spin coating method at 4000 rpm for 1 min. Catalyst solutions were prepared at a concentration of 2 mg/mL in ethanol, and 100 μL was used for preparing each thin film layer. Total three layers were coated on the FTO slides and dried at 200 °C for 2 h. A three-electrode quartz cell

containing 0.1 M Na_2SO_4 (~pH 7) electrolyte, a Pt wire, and KCl saturated Ag/AgCl as counter and reference electrodes, respectively, was used as the PEC cell, and the measurements were performed using a galvanostat–potentiostat (PGSTAT302 N, Autolab, The Netherlands) under a 35 W xenon lamp. The current density was recorded between the applied potential ranges of –0.4 to 1 V versus Ag/AgCl at a 50 mV s^{-1} scan rate through linear sweep voltammetry (LSV). Furthermore, photocurrent density and the stability were checked *via* chopped chronoamperometry (CA) at an applied potential of 0.6 V versus Ag/AgCl. The electrochemical impedance spectra were measured in an AC frequency range of 100 kHz to 0.1 Hz with 0.1 V amplitude to calculate the charge transfer resistance at electrode–electrolyte interfaces. Junction capacitance of the electrodes was recorded at 1000 Hz frequency *via* the Mott–Schottky (M–S) study for determining the flat band potentials and free charge carrier density. The Nernst equation was employed to convert the potentials ($E_{\text{Ag/AgCl}}$) to the normal hydrogen electrode scale (E_{RHE}), as follows

$$E_{\text{RHE}} = E_{\text{Ag/AgCl}} + 0.059 \times \text{pH} + 0.197 \quad (1)$$

2.6. Photocatalytic H₂ Generation. Photocatalytic H₂ generation of the as-synthesized materials was tested through water reduction in a closed quartz cell containing 30 mL of solution with a catalyst concentration of 1 mg/mL under visible light irradiation (250 W xenon lamp) through online gas chromatography (GC) using 25 vol % methanol as a sacrificial agent. The solution was argon-purged for 15 min before the experiment. The area under the Gaussian peak in GC gives the amount of H₂ evolved. The apparent quantum yield (AQY) of H₂ generation has been calculated further using the following equation

$$\text{AQY} \% = \frac{2 \times \text{moles of H}_2 \text{ produced}}{\text{no. of incident photons}} \times 100 \quad (2)$$

3. RESULTS AND DISCUSSION

3.1. Structural Analysis. The phase composition and crystalline structure of bare semiconductors and the prepared heterostructures have been investigated using a powder X-ray diffractometer. Figure 1a,b shows the XRD pattern of bare semiconductors BiOI, BiOCl, BiOBr, and CuFe_2O_4 (CFO) nanoparticles and BiOI/CFO, BiOCl/CFO, and BiOBr/CFO heterostructures. In the case of BiOI, the diffraction peaks at

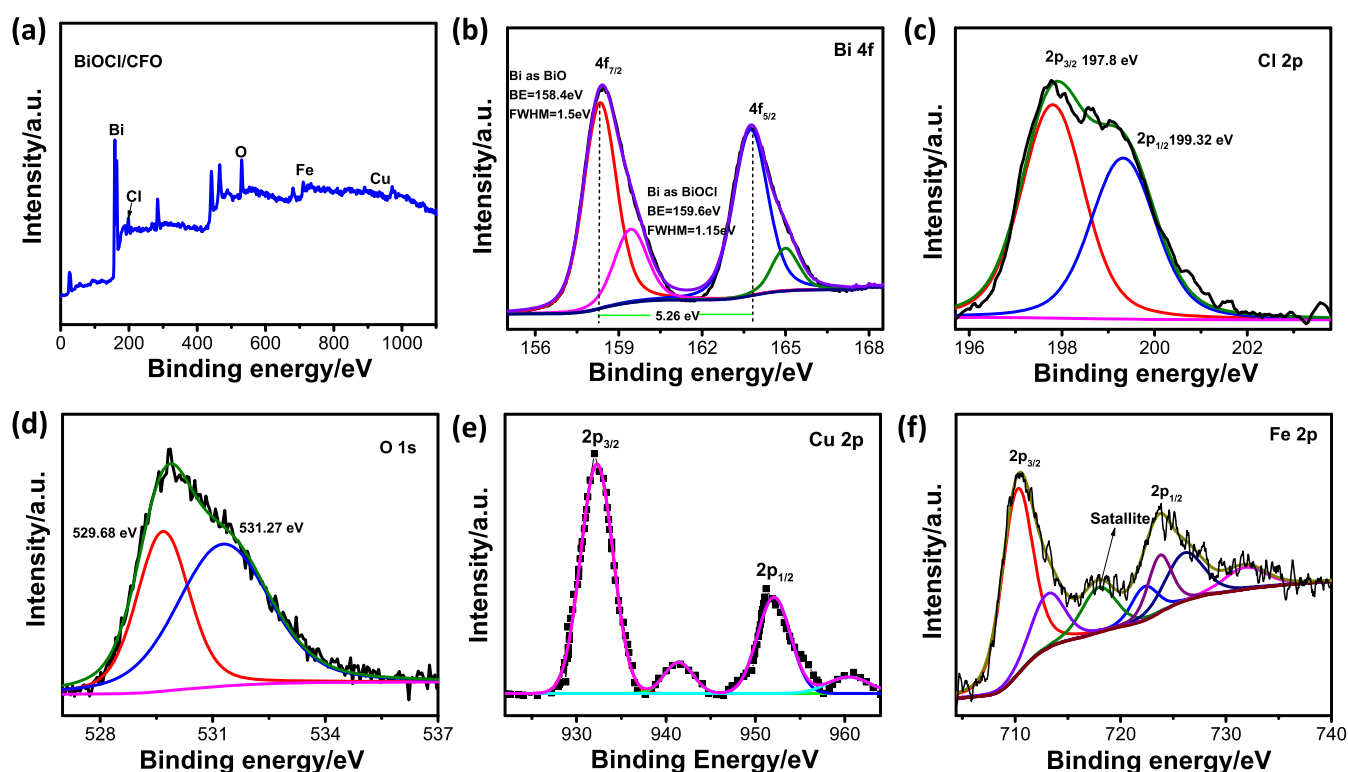


Figure 2. (a) Surface survey XPS spectra of BiOCl/CFO heterostructures. High-resolution XPS spectra of (b) Bi 4f, (c) Cl 2p, (d) O 1s, (e) Cu 2p, and (f) Fe 2p of BiOCl/CFO heterostructures.

2θ of 29.53, 31.53, 36.96, 39.31, 45.29, 51.27, and 55.08° related to (012), (110), (013), (004), (200), (114), and (212) planes, respectively, clearly indicate the tetragonal phase of BiOI (JCPDS no. 73-2062).³⁸ The diffraction peaks at 2θ of 12.12, 24.25, 26.04, 32.67, 33.56, 36.61, 41.08, 46.81, 49.86, 54.34, 55.23, and 58.81° indexed to (001), (002), (101), (110), (102), (003), (112), (200), (113), (211), and (104), (212) planes, respectively, indicate the tetragonal BiOCl (JCPDS no. 73-2060).³⁹ The XRD pattern of BiOBr exhibits five characteristic peaks of (001), (002), (102), (110), and (200) at 2θ of 10.51, 26.27, 29.35, 32.43, and 46.56°, respectively, which are well-matched with the tetragonal phase of BiOBr (JCPDS no. 9-0393).⁴⁰ Interestingly, the presence of the (001) peak for BiOCl and BiOBr strongly reveals the [X–Bi–O–Bi–O–X] stacking structure along the c-axis.³⁹ The characteristic peaks at 2θ of 18.36, 29.89, 34.42, 35.69, 37.14, 44.03, and 58.16° corresponding to (101), (112), (103), (211), (202), (220), and (321) planes, respectively, confirm the tetragonal spinal structure of CuFe₂O₄ (JCPDS no. 34-0425).³⁶ However, three characteristic peaks of (220), (222), and (422) which are marked by green at 2θ values 30.8, 36.05, and 54.17°, respectively, represent the cubic phase of CuFe₂O₄ (JCPDS no. 85-1326).⁴¹ After heterostructure formation, no shifting of the BiOX peaks has been observed and the characteristic peaks of CFO are present (marked by “*”), implying the successful heterostructure formation between BiOX and CFO (Figure 1b).

XPS analysis was performed to study the surface and sub-surface chemical states of heterostructure samples. The surface survey scan spectra of BiOCl/CFO confirm the presence of Bi, Cl, O, Fe, and Cu in heterostructures (Figure 2a). In Bi 4f spectra, two peaks at binding energies of ~163.75 and ~158.41 eV might be assigned to Bi 4f_{5/2} and Bi 4f_{7/2}, respectively,

which are further fitted properly (Figure 2b).⁴² The characteristic Bi 4f_{7/2} peak can be fitted with two peaks located at binding energies of ~158.4 eV and ~159.62 eV, corresponding to Bi=O and O=Bi–Cl bonds. Similar results have been obtained for BiOBr/CFO heterostructures (Figure S1). However, the Bi 4f_{7/2} of BiOI/CFO has been fitted with single peaks located at a binding energy of 158.54 eV (Figure S2). Now, it is well known that the Bi 4f_{7/2} located at a binding energy between 157.2 and 158.1 eV corresponds to the metallic Bi⁰ state (Bi–Bi), whereas peak position at 158.4 ± 0.4 and 158.8 ± 0.3 eV indicates presence of Bi(OH)₃, (Bi–OH), and BiOOH (O=Bi–OH) states.^{43–45} Therefore, it can be concluded that the surface is mainly composed of Bi(OH)₃, that is, the Bi³⁺ state for all the heterostructures, which is further verified by the obtained O/Bi atomic ratio. In addition, a binding energy difference of ~5.3 eV between Bi 4f_{7/2} and Bi 4f_{5/2} strongly supports the presence of the Bi³⁺ state.⁴⁶ The Cl 2p spectrum has been fitted into two peaks at ~197.8 and ~199.32 eV binding energies belonging to Cl 2p_{3/2} and Cl 2p_{1/2}, respectively, confirming the Cl[–] state in the heterostructure (Figure 2c), which is well-consistent with the reported literature.^{47–49} The O 1s spectrum of BiOCl/CFO heterostructures is fitted into two peaks, one located at ~529.83 eV corresponding to lattice oxygen atoms which are chemically bonded and another at ~531.59 eV related to adsorbed oxygen (Figure 2d).⁴² The Cu 2p spectrum shows two main peaks at ~932.36 eV (Cu 2p_{3/2}) and ~951.97 eV (Cu 2p_{1/2}) with two satellite peaks at ~941.3 eV and ~961.06 eV, which are well-consistent with the Cu²⁺ state (Figure 2e).⁵⁰ The Fe 2p peaks located at binding energies of ~710.28 eV and ~723.83 eV correspond to Fe 2p_{3/2} and Fe 2p_{1/2}, respectively, arising from the spin–orbital interaction (Figure 2f).⁵⁷ Due to different d-orbital electron configurations, Fe 2p

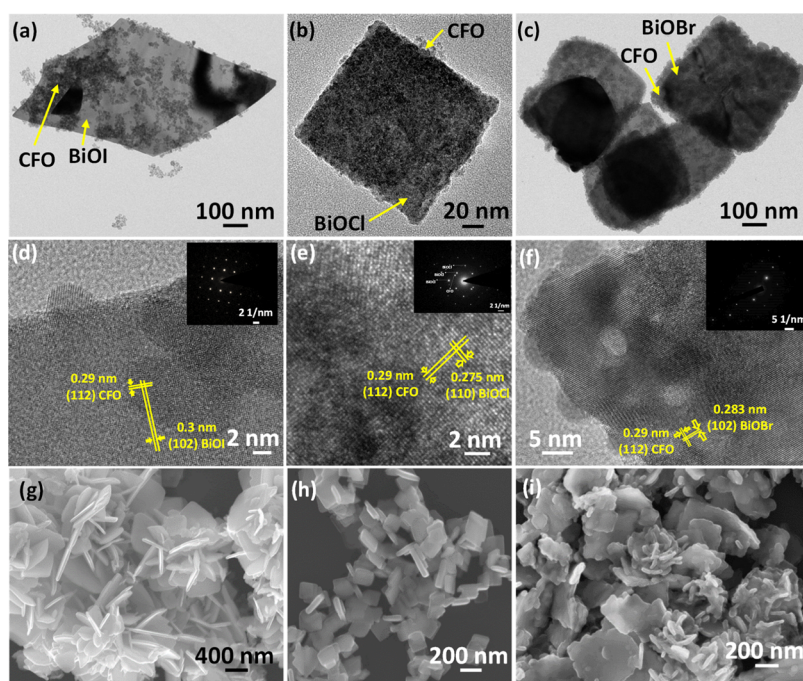


Figure 3. TEM image of (a) BiOI/CFO, (b) BiOCl/CFO, and (c) BiOBr/CFO. HRTEM images of (d) BiOI/CFO, (e) BiOCl/CFO, and (f) BiOBr/CFO heterostructures. Insets: corresponding SAED patterns. FESEM images of bare semiconductors (g) BiOI, (h) BiOCl, and (i) BiOBr.

and Fe 3p generally exhibit a satellite peak at 6 or 8 eV above their $2p_{3/2}$ principal peaks, respectively. Here, a satellite peak at ~ 718.09 eV has been found about 7.8 eV above the Fe $2p_{3/2}$ peak, which could be considered as the characteristic peak of the Fe^{3+} state. The XPS spectra of BiOI/CFO and BiOBr/CFO are presented in Figures S1 and S2, which reveal that Bi, I, Br, Cu, Fe, and O are present. Furthermore, the Bi 4f core-level XPS spectra of bare BiOX ($X = \text{Cl}, \text{Br}, \text{and I}$) and BiOX/CFO heterostructures have been investigated, where a shifting of the peaks toward lower binding energy is observed after heterostructure formation (Figure S3). Peak shifting indicates a possibility of sharing electrons with neighboring atoms in terms of asymmetry in the bond arrangements. Moreover, the shifting toward lower binding energy implies a band bending, which results in a charge redistribution at the interface and indicates the increase in electron density on BiOX.⁶⁰

Furthermore, TG analysis of bare semiconductors and heterostructures are studied to check the thermal stability of the as-prepared materials. As shown in Figure S4, formation of heterostructures between BiOX and CFO enhances the thermal stability of the materials. The Raman and FTIR analysis of the prepared materials has been carried out further to analyze the chemical structures. Figure S5a represents the Raman spectra of bare CFO and BiOCl and BiOCl/CFO heterostructures. The two prominent Raman peaks have been observed for BiOCl, centered at ~ 142.74 and ~ 198.52 cm^{-1} , which well agreed with A_{1g} and E_g internal Bi–Cl stretching modes, respectively.⁵¹ In the case of CFO, three characteristic peaks at 213, 274, and 472 cm^{-1} are assigned to spinel copper ferrite.⁵² After heterostructure formation, the prominent Bi–Cl A_{1g} and E_g stretching modes with the CFO vibration peaks have been observed, which strongly reveals the heterostructure formation. Figure S5b shows the FTIR spectra of BiOCl and CFO and BiOCl/CFO heterostructures, where the characteristic band around ~ 1623 cm^{-1} confirms the O–H bending vibrations. The absorption band at ~ 528 cm^{-1} corresponds to

the symmetrical vibrations of the Bi–O stretching mode. Moreover, the absorption peaks at ~ 1400 cm^{-1} might be assigned as the asymmetric stretching vibration of the Bi–Cl band.⁵² For CFO, the absorption band in the range of 330–350 cm^{-1} arises due to stretching vibrations of octahedral metal–oxygen bonding and at ~ 580 cm^{-1} for tetrahedral metal–oxygen bonding.⁵³ However, the strong CFO absorption band is absent in BiOCl/CFO, which might be a result of strong interaction between BiOCl and CFO.

3.2. Morphology. The morphology and structure of heterostructures were analyzed by FESEM and TEM. Figure 3a–c illustrates the TEM image of BiOI/CuFe₂O₄, BiOCl/CuFe₂O₄, and BiOBr/CuFe₂O₄ heterostructures, respectively. It has been clearly observed that all the pure bismuth oxyhalides possess nanosheet-like morphology. The average size of BiOX nanosheets are ~ 450 , ~ 110 , and ~ 300 nm for BiOI, BiOCl, and BiOBr, respectively. Moreover, all the BiOX nanosheets are fully covered with the small CFO nanoparticles. High-resolution TEM (HRTEM) images of the BiOX/CFO heterostructures clearly exhibit good crystallinity with clear lattice fringes. Figure 3d represents the cross-fringes of (102) and (112) planes of BiOI and CFO having the d-spacings of 0.3 and 0.29 nm, respectively.⁵⁴ Two sets of lattice fringes having the interplanar spacings of ~ 0.275 and ~ 0.29 nm are related to (110) and (112) planes of BiOCl and CFO, respectively (Figure 3e).¹⁷ At the same time, two sets of bright spots are presented in the selected area electron diffraction pattern (SAED), which also confirm the heterostructure formation between BiOCl and CFO (inset of Figure 3e). The HRTEM images of BiOBr/CFO display presence of both crystal planes (102) and (112) having d-spacings of 0.283 and 0.29 nm corresponding to BiOBr and CFO, respectively (Figure 3f).³⁷ The spot pattern in the SEAD pattern clearly indicates the single-crystalline nature of BiOBr nanosheets. Furthermore, FESEM images of the bare BiOX semiconductors have been presented in Figure 3g–i, where

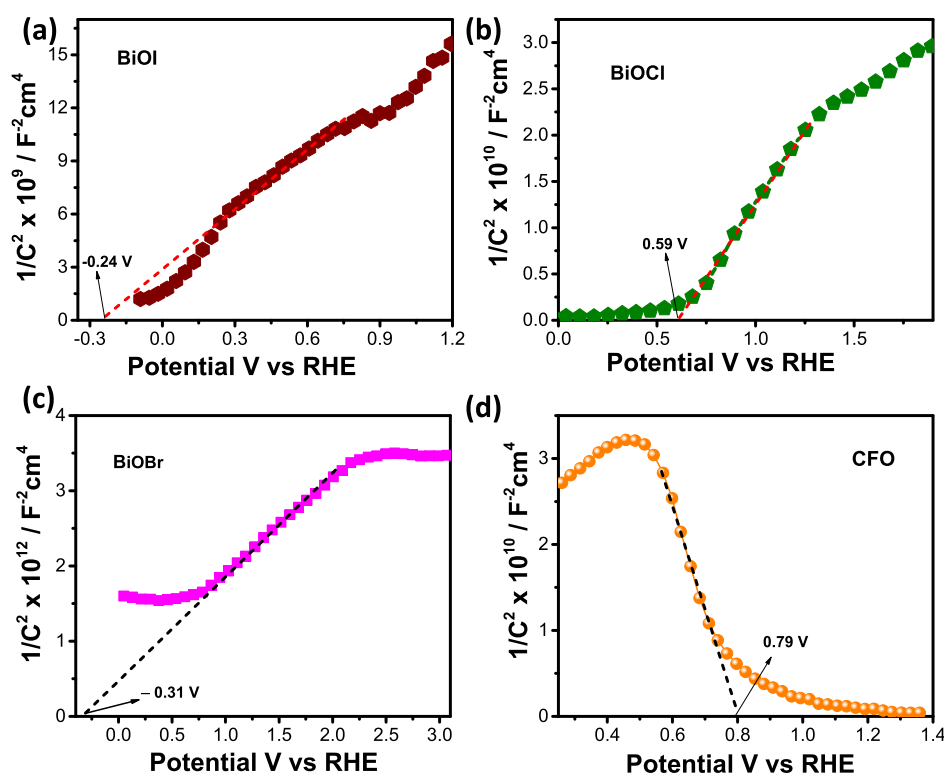


Figure 4. M–S plots of pure semiconductors (a) BiOI, (b) BiOCl, (c) BiOBr, and (d) CFO.

nanosheet-like morphology is also observed for BiOI, BiOCl, and BiOBr, which is consistent with TEM images. However, BiOI and BiOBr exhibited a trend to form assembled structures, whereas BiOCl showed uniform square-like nanosheets. The TEM image of the bare CFO has been shown in Figure S6; on average, ~13 nm CFO spherical nanoparticles are formed. The O/Bi and Bi/X atomic ratios have been calculated further from the TEM–EDX image for the bare BiOX (X = Cl, Br, and I) to have the insightful information about types of material formed (Figure S7a–c). The values of the O/Bi atomic ratio are 1.16, 1.02, and 1.77 for BiOCl, BiOBr, and BiOI, respectively. The atomic ratios of Bi/X (X = Cl, Br, and I) are 1.03, 2.16, and 1.11 in the case of BiOCl, BiOBr, and BiOI, respectively, which are well-consistent with the reported literature and confirm the formation of BiOX.⁵⁵ Furthermore, the FESEM–EDX image of the BiOCl/CFO heterostructure has been investigated, where the Bi/Cl atomic ratio is 1.07, nearly equal to that of the bare BiOCl (Figure S7d). Therefore, it can be confirmed that heterostructure formation does not change the atomic ratio of the elements.

3.3. Electrochemical Properties. Besides the structural characterization, intrinsic electronic properties like band gap, band edge position, free carrier density, space charge layer width have a significant role in optimizing the photocatalytic activity. To further address the relative band structure of BiOX and CFO samples under study, the flat-band potential (E_{fb}) is measured using the electrochemical method in 0.1 M NaSO₄ solution (pH 7) and the M–S plots are shown in Figure 4. The M–S plots of all the BiOX samples show a positive slope, which is typical for n-type semiconductors and associated with the O vacancy in the crystal lattice originated from the high oxygen density in the (001) facet. The E_{fb} is located at –0.86, –0.017, and –0.92 V versus Ag/AgCl for BiOI, BiOCl, and BiOBr, respectively. The E_{fb} values are obtained as –0.24, 0.59,

and –0.31 V versus RHE by using the Nernst equation (eq 1). It is generally accepted that the E_{fb} of n-type semiconductors is located just below the CBM, and for BiOX, the difference between CBM and E_{fb} is around 0.3 V.⁴² Therefore, the CB is at –0.54, 0.29, and –0.61 V versus RHE for BiOI, BiOCl, and BiOBr, respectively ($CB = E_{fb} - 0.3$ V). The VB was estimated to be at 1.22, 2.52, and 2.32 V for BiOI, BiOCl, and BiOBr, respectively, using their band gaps, calculated from the UV–vis spectra ($VB - CB = E_g$). However, bare CFO shows a negative slope, that is, p-type conductivity and the E_{fb} at 0.18 V versus Ag/AgCl, thereby 0.79 V versus RHE. As the E_{fb} of p-type semiconductors lies just above the valence band maxima (VBM), thus the VB and CB would be at 1.09 and –0.56 V versus RHE, respectively. The calculated E_{fb} , CB, VB potentials are presented in the Table 1. The M–S plot of the bare BiOX

Table 1. Calculated Flat Band Potentials (E_{fb}), Position of the VB and CB Potentials, and Band Gaps of the as-Synthesized Materials

| material | type of material | E_{fb} (V) vs RHE | CB (V) vs RHE | VB (V) vs RHE | E_g eV |
|----------------------------------|------------------|---------------------|---------------|---------------|----------|
| BiOI | n-type | –0.24 | –0.54 | 1.22 | 1.76 |
| BiOCl | n-type | 0.59 | 0.29 | 2.52 | 2.23 |
| BiOBr | n-type | –0.31 | –0.61 | 2.32 | 2.63 |
| CuFe ₂ O ₄ | P-type | 0.79 | –0.56 | 1.09 | 1.65 |

(X = Cl, Br, and I) at three different frequencies are shown in Figure S8, where a frequency-independent nature has been observed, indicating that the flat band potential of the materials are frequency-independent.

Depending on the position of the VB and CB of BiOX and CFO, plausible charge transfer band diagrams have been schematically presented in Scheme 1. It has been clearly observed that the band alignments of BiOBr with CFO are

Scheme 1. Band Alignments of (a) BiOI/CFO, (b) BiOBr/CFO, and (c) BiOCl/CFO Heterostructures

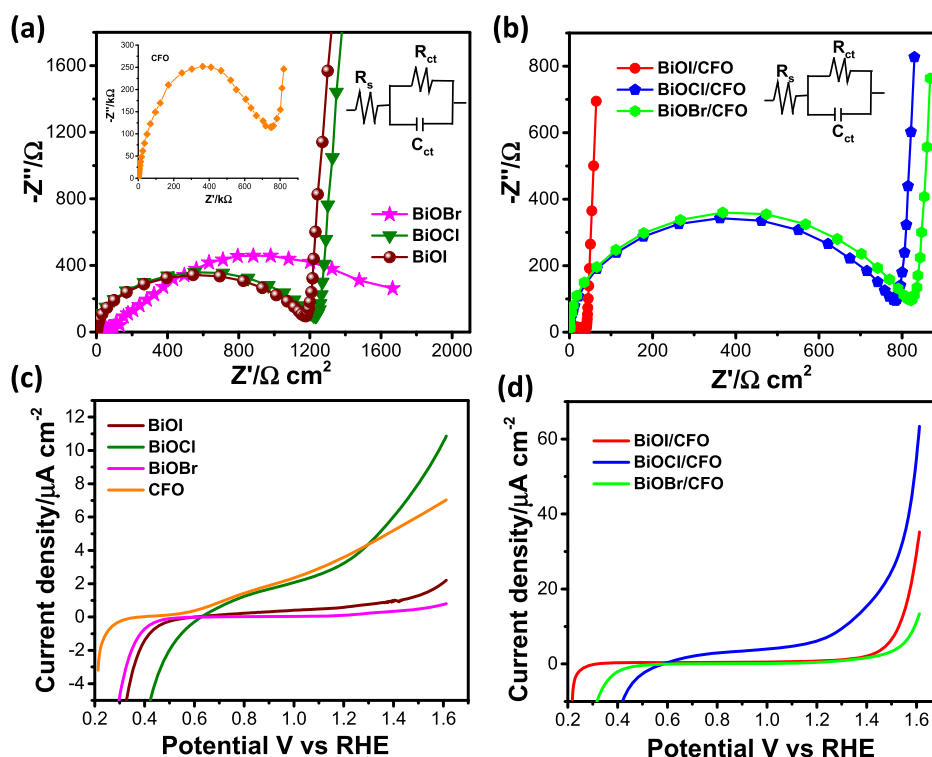
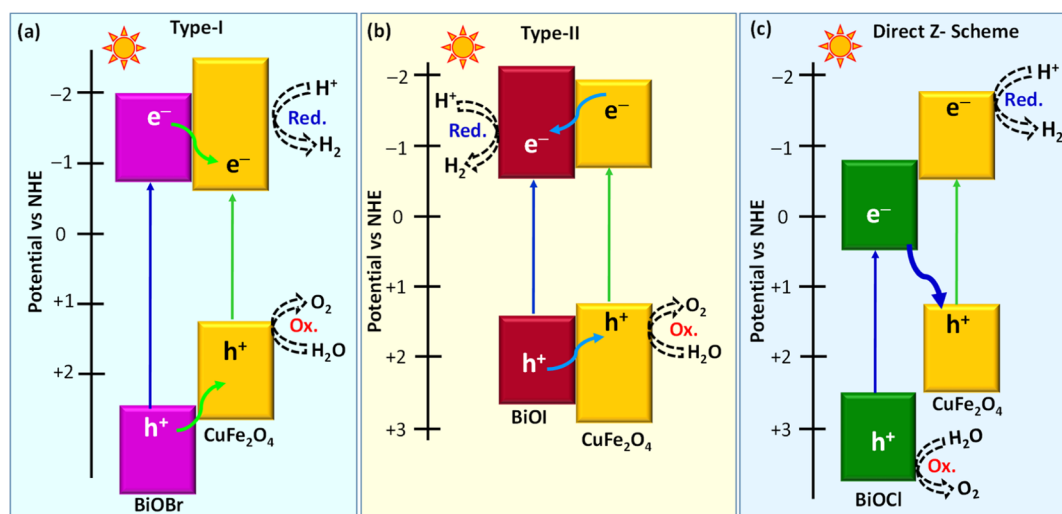


Figure 5. Impedance spectra of (a) bare BiOI, BiOCl, and BiOBr; inset: bare CFO and (b) BiOI/CFO, BiOCl/CFO, and BiOBr/CFO heterostructures. The equivalent circuit parameters are shown in the inset of (a,b). LSV curves of (c) bare semiconductors BiOI, BiOCl, BiOBr, and CFO and (d) BiOI/CFO, BiOCl/CFO, and BiOBr/CFO heterostructures under continuous light illumination (35 W xenon lamp) in 0.1 M Na_2SO_4 electrolyte.

well-matched with the conventional type-I heterostructure. The CBM and VBM of BiOBr both have higher potential than CFO (Scheme 1a). Thus, in presence of light energy, photo-generated electrons and holes of BiOBr will migrate to the CB and VB of CFO, respectively, due to lower potential of CFO. Thus, special charge separation of electrons and holes may not be possible in this system; rather, the recombination rate will be increased, which reduces the number of excited carriers for water splitting.

On the other hand, the CBM of both BiOI and CFO are negative and CFO has higher potential than BiOI, whereas the VBM of BiOI are located at higher potential compared to

those of CFO (Scheme 1b). Thus, in presence of light energy, photo-generated electrons of CFO will migrate to the CB of BiOI and the photoinduced holes will follow the opposite direction (BiOI to the VB of CFO) due to lower potential of CFO. In this way, the charge separation will happen in two different semiconductors, and the water oxidation and reduction occur by the CB electrons of BiOI and VB holes of CFO, respectively. Meanwhile, in BiOCl/CFO heterostructures, the difference between CBM of BiOCl and CFO is large enough and the electrons of BiOCl lie at positive potential, which is insufficient for the water reduction reaction (Scheme 1c). At the same time, holes of CFO will not oxidize

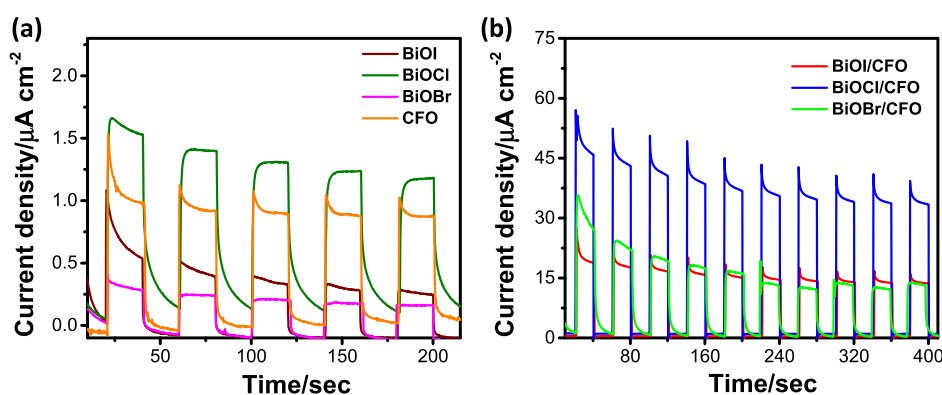


Figure 6. Transient photocurrent spectra of (a) bare semiconductors CFO, BiOI, BiOCl, and BiOBr and (b) BiOI/CFO, BiOCl/CFO, and BiOBr/CFO heterostructures under chopped light conditions, measured by chronoamperometry at a fixed potential of 0.6 V vs Ag/AgCl.

the water molecules due to a low positive potential of 0.99 V versus RHE. Thus, these electrons will try to recombine with the VB holes of CFO to form electron–hole pairs. Thereby, spatial charge separation occurs between BiOCl and CFO by accumulating highly negative excited electrons in the CB of CFO and photoinduced holes in the VB of BiOCl with enough potentials for water splitting. Thus, BiOCl/CFO offers optimized redox ability with a low charge carrier recombination rate and minimal energy loss due to backward reactions.⁵⁶

Furthermore, the junction capacitance of the as-prepared heterostructures have been studied through M-S measurement, where a “V”-shaped nature is observed for all the heterostructures, confirming the presence of n-type BiOX and p-type CFO (Figure S9). The carrier concentrations of the bare semiconductors and the heterostructures have been calculated using following equation

$$\frac{1}{C^2} = \frac{2}{eN_d e \epsilon_0} \left(E - E_{fb} - \frac{KT}{e} \right) \quad (3)$$

where C is space charge capacitance at the junction interface ($F\text{ cm}^{-2}$), E_{fb} is flat-band potential (V), N_d is free charge carrier density (cm^{-3}), e is the charge on electrons (C), ϵ is dielectric constant of the semiconductors, ϵ_0 is permittivity of free space, K is the Boltzmann constant, and T is temperature (K). The calculated N_d values are tabulated in Table S1, where BiOCl/CFO shows 2.5 times and 7 times higher carrier concentration compared to BiOI/CFO and BiOBr/CFO, respectively. Thus, the Z-scheme heterostructure is more effective to promote the catalytic redox reactions. Space charge layer width is also an important parameter to optimize the charge transfer efficiency of a photocatalyst. The space charge layer width (W_{sc}) has been calculated further using the following equation

$$W_{sc} = \sqrt{\left(\frac{2\epsilon\epsilon_0 V_s}{eN_d} \right)} \quad (4)$$

where V_s is the applied potential. The variation of space charge layer width with the applied potential for bare BiOX and the heterostructures has been shown in Figure S10, where a drift-assisted transport in the space charge region is evident at lower potentials. After heterostructure formation, the W_{sc} decreases for each BiOX, indicating efficient charge transfer through the electrode–electrolyte interface *via* band bending due to presence of an internal potential gradient at the junction interface.⁵⁷ More interestingly, the Z-scheme heterostructure

exhibited the lowest W_{sc} , which is indicative of high catalytic efficiency.

To investigate the better charge transfer efficiency of the prepared heterostructures at the electrode–electrolyte interface, electrochemical impedance measurement has been performed in presence of light. Figure 5a represents the Nyquist plots of the bare BiOX and the CFO, where much higher resistance has been obtained for bare CFO ($\sim 639\text{ k}\Omega$, inset of Figure 5a). Among the BiOX, BiOBr shows a single semicircular arc with a charge transfer resistance of $\sim 1749\ \Omega$, whereas BiOCl and BiOI exhibit a semicircle in high-frequency region, a small Warburg line in intermediate-frequency region, and almost a vertical line in the low-frequency region. The semicircular part corresponds to the electron transfer between redox species and the electrode *via* surface states or reaction intermediates, and the steep region arises due to the diffusion of redox species, indicating the capacitive nature of the electrode.

Interestingly, the smaller semicircle radius of the Nyquist plots has been noticed after heterostructure formation between BiOX and CFO, signifying the improved electron–hole transfer than that of component semiconductors. However, direct Z-scheme BiOCl/CFO exhibits the smallest charge transfer resistance ($\sim 41.08\ \Omega$) compared to BiOI/CFO ($\sim 766.4\ \Omega$) and BiOBr/CFO ($\sim 819.7\ \Omega$), which means that fast interfacial charge transfer occurs in the Z-scheme system resulting in the effective separation of electron–hole pairs (Figure 5b). In other words, the Z-scheme heterostructure significantly improves the electrical conductivity at the interface in presence of light, which may be useful for water splitting reactions. All the Nyquist spectra were further fitted with the Randles-equivalent circuit model *via* Z-View software, and the fitted parameters are tabulated in the Table S2, and the plots are represented in Figure S11. To further explore the catalytic properties of the as-synthesized materials, a series of electrochemical and optical measurements has been conducted. Figures 5c,d and S12 exhibit the LSV curves of bare semiconductors and the heterostructures in 0.1 M Na_2SO_4 aqueous solution under continuous visible light illumination using a 35 W xenon lamp as a light source. Clearly, heterostructure formation effectively enhances the current density compared to their component semiconductor current density, which might be attributed to the synergetic effects of low charge transfer resistance, high charge carrier concentration, and efficient charge separation through the interfaces. In addition, the CFO nanoparticles may serve as effective

active sites to promote the redox reactions for H_2 generation by accumulating the photogenerated electrons, which is further verified by the transient photocurrent measurement. The photo-stability of the anodes has been determined by measuring transient photocurrent density through CA. The BiOCl exhibited the highest photocurrent density compared to other BiOX semiconductors, which is consistent with the LSV result (Figure 6a). As expected, the Z-scheme BiOCl/CFO heterostructures shows remarkably increased photocurrent density compared to type-II heterostructures, implying that the direct Z-scheme system is more efficient in the water oxidation reaction (Figure 6b). The theoretical PEC H_2 generation for the Z-scheme BiOCl/CFO heterostructure was further calculated from the chronoamperometry spectra by determining the charge (Q) passed through the photoanode. The charge has been determined by integrating the current over the time, and the moles of H_2 are equal to $Q/2F$, where F is the Faraday constant ($F = 96,500$).⁶¹ The estimated PEC H_2 generation for the BiOCl/CFO heterostructure reaches 0.05 μmol at 450 s (Figure S13).

In order to get more details about quantum efficiency of the Z-scheme heterostructures, incident photon-to-current conversion efficiency (IPCE) has been calculated from the action spectrums through CA measurement within the visible region (400–750 nm). The Z-scheme BiOCl/CFO heterostructure has very low efficiency in the wavelength region of >600 nm, whereas it shows prominent enhanced efficiency in the range of <600 nm and maximum at 450 nm (~25%) (Figure S14). The enhanced activity within the range of 450–750 nm could possibly be achieved by effective visible light absorption and electron–hole separation, which is in accordance with the consequence of electrochemical impedance measurements.

3.4. UV–vis Absorption and Band Gap Calculation.

Furthermore, the optical absorption of bare semiconductors and the heterostructures are studied by diffuse reflectance spectroscopy (DRS) to investigate the influence of heterostructures on light absorption. Figure 7 represents the DRS

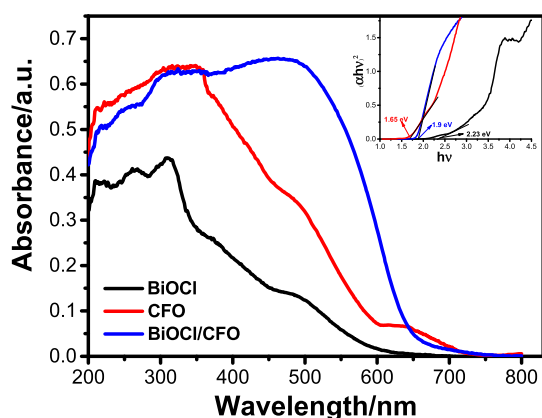


Figure 7. DRS of BiOCl, BiOCl/CFO, and bare CFO. Inset: Kubelka–Munk $[(\alpha h\nu)^2 \text{ vs photon energy } (h\nu)]$ plots of CFO, BiOCl, and BiOCl/CFO.

spectra of bare CFO and BiOCl and BiOCl/CFO heterostructures. BiOCl has strong absorption in the UV and visible region, which significantly boosted up after heterostructure formation with CFO at each wavelength. Interestingly, a prominent absorption hump has been observed within the wavelength range of 380–550 nm, which may have arisen due

to strong interaction between BiOCl and CFO, which is well-consistent with the IPCE result. Therefore, it can be concluded that improved light absorption in this region enhances the photon to current conversion efficiency of the Z-scheme heterostructure. Furthermore, the absorption spectra of BiOI, BiOBr, BiOI/CFO, and BiOBr/CFO are studied and shown in Figure S15, where prominent enhancement is observed in intensity and in the absorption edge for heterostructures compared to bare BiOX. A classical Kubelka–Munk $[(\alpha h\nu)^2 \text{ vs photon energy } (h\nu)]$ equation has been used to calculate the band gap of the materials (inset of Figures 7 and S16). It is widely accepted that the BiOX and CFO follow indirect and direct transition, respectively. Thus, the calculated indirect band gaps are 1.76, 2.23, and 2.63 eV for BiOI, BiOCl, and BiOBr, respectively, and the direct band gap is 1.65 eV for CFO, well matched with the previously reported literature.¹² The calculated band gap of BiOCl nanosheets is 2.2 eV, which reduces to 1.9 eV after CFO nanoparticle deposition on the surface. The band gap reduction may be attributed to formation of a heterostructure between BiOCl and CFO, which further facilitates the photon absorption, photogenerated charge carrier generation, and separation.

3.5. Photocatalytic H_2 Generation. The photocatalytic activity of BiOX and the heterostructures was measured through H_2 generation from water under visible light illumination. The time course of hydrogen generation has been measured under continuous visible light illumination (250 W Xe lamp) and in presence of 25 vol % methanol as a sacrificial agent (Figure 8). Here, catalysts (1 mg/mL concentration) are dispersed in water medium under light illumination without any external potential. BiOI exhibits the highest H_2 generation (~18.45 mmol) among the BiOX due to a more negative CB, which provides high reduction potential. However, the H_2 generation of CFO is very low (~4.2 mmol) because of fast recombination of the excited charge carriers, owing to a narrow band gap. Interestingly, the H_2 generation has been significantly increased after heterostructure formation in a steady manner, which validates the aforesaid estimated reasons of high conductivity, large number of active sites, and efficient charge separation. Under visible light, BiOCl/CFO exhibits the highest mass specific activity (~22.2 mmol h^{-1}), followed by BiOI/CFO (~12.5 mmol h^{-1}), and then BiOBr/CFO (~6.5 mmol h^{-1}), consistent with their ability to absorb the visible light (Figure 8b). For comparison, a mixed sample of BiOCl and CFO (at equal mass ratio) was prepared and the photocatalytic H_2 generation was tested, where eight times lower activity was obtained than that of BiOCl/CFO heterostructures under similar reaction conditions. This result clearly confirms the intimate contact between BiOCl and CFO after heterostructure formation, which facilitates the charge separation and transfer through the junction. Furthermore, the H_2 generation data of all the bare BiOX ($X = \text{Cl, Br, and I}$) and CuFe_2O_4 as well as heterostructures are linearly fitted (Figure S17a,b), and the fitted parameters are represented in Table S3. The H_2 generation of bare BiOX and CFO is roughly linear and may be associated with fast recombination. Additionally, the H_2 generation increases up to a certain time and then becomes saturated due to presence of a limited sacrificial agent in the reaction system. However, Z-scheme BiOCl/CFO and type-II BiOI/CFO exhibit linear H_2 generation for the entire time period because of efficient charge separation and transfer to the surface of the catalyst. On the other hand, roughly linear trend has been observed for type-I BiOBr heterostructures as

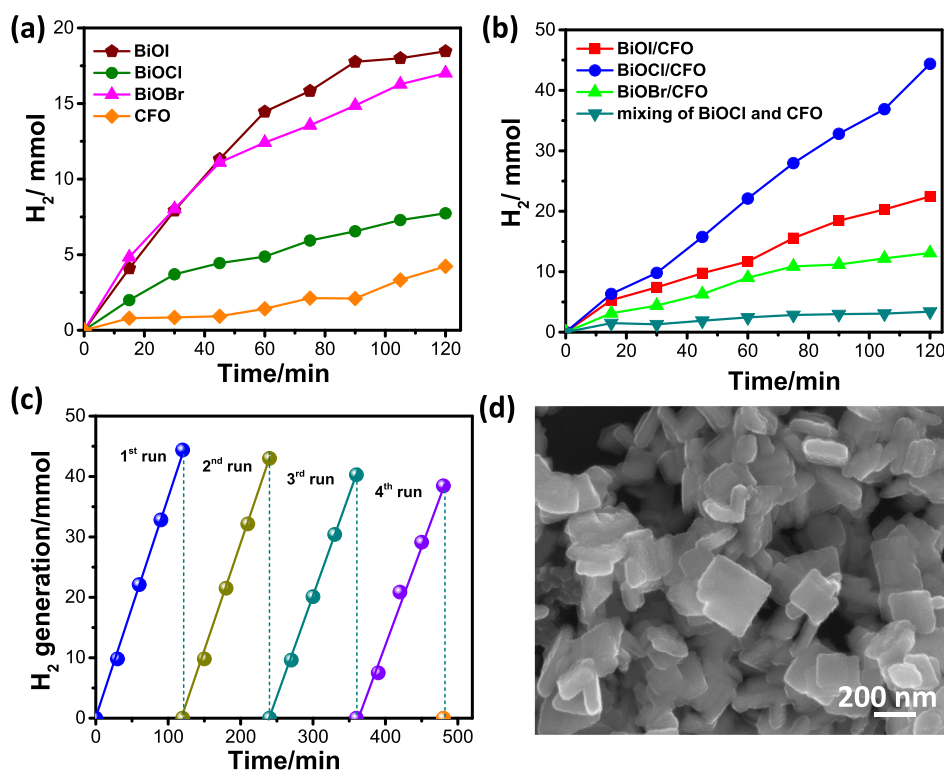


Figure 8. Photocatalytic hydrogen generation in the presence of (a) bare BiOX (X = Cl, Br, and I) and CFO and (b) BiOX/CFO (X = Cl, Br, and I) heterostructures for 2 h under visible light from an aqueous solution containing 25 vol % methanol as a sacrificial agent at pH 7, (c) recycling test of the BiOCl/CFO heterostructure for H₂ generation, and (d) FESEM image of BiOCl/CFO after the catalytic reaction of H₂ generation under visible light.

the photogenerated charge carriers accumulate on the CFO, which may increase the electron–hole recombination rate, thereby reducing the number of free electrons for water reduction. Figure S18 presents the calculated AQY % for the catalysts (calculated using eq 2), where BiOCl/CFO heterostructures exhibit the highest photocatalytic H₂ generation efficiency of 9.9% followed by BiOI/CFO (5%) and BiOBr/CFO (4%). Thus, direct Z-scheme heterostructure formation improves the H₂ generation rate and AQY %, which can be described on the basis of the charge transfer process. The effect of sacrificial agents (commonly used alcohol and aldehydes) in H₂ generation has been investigated (Figure S19a). The redox potential of a sacrificial hole scavenger for H₂ generation should be more negative than that of the valence band of a semiconductor so that it can consume the holes and suppress the recombination of photogenerated electrons.⁵⁸ Notably, methanol shows the highest H₂ generation (~44.4 mmol) compared to ethanol (~38.5 mmol), formaldehyde (34.1 mmol), 2-propanol (~24.8 mmol), and ethylene glycol (~18.7 mmol), suggesting that the length of the carbon chain is inversely proportional to water reduction ability. However, the oxidation potential and permittivity of sacrificial agents play a potential role in H₂ generation as they act as electron donors to consume the holes. According to Gouy–Chapman theory, surface charge density is proportional to the dielectric constant of the solvent.⁵⁷ As shown in Table S4, the oxidation potential of methanol is lower than that of ethanol, 2-propanol, and ethylene glycol but the permittivity is higher than that of ethanol and 2-propanol. Although, the permittivity of ethylene glycol is much higher compared to that of other solvents, the higher oxidation potential (1.54 eV, which is higher than water oxidation potential 1.23 eV) lowers its activity as it is poorly

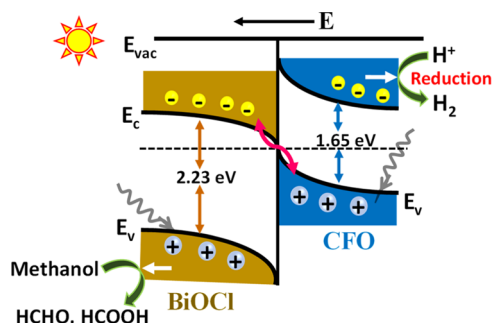
oxidized. Therefore, methanol is considered as a preferable sacrificial agent in photocatalytic hydrogen generation, having lower oxidation potential and considerable permittivity. The effect of the sacrificial donor/solvent ratio in photocatalytic H₂ generation has been investigated for the BiOCl/CFO heterostructure (Figure S19b). The volume % of methanol has been varied from 5 to 50%, where the amount of H₂ generation increases with the increase in methanol concentration up to a certain percentage and then decreases. The 25 and 30 vol % shows almost similar results; however, the amount of H₂ generation decreases when 50 vol % is used. Methanol generally acts as a hole scavenger, that is, it reacts with photoinduced holes faster than water and reduces the probability of electron–hole recombination. Therefore, an optimized percentage may boost the catalytic reactions in a forward direction. The higher concentration of methanol may generate higher amount of reactant products, which further leads to sluggish reaction rate kinetics due to an unwanted backward reaction.

In addition to its remarkable photocatalytic activity, the BiOCl/CFO heterostructure exhibits very good stability as a photocatalyst. As shown in Figure 8c, no noticeable decrease in the activity for photocatalytic hydrogen production can be observed in the cycling tests (a minimal 14% loss after the fourth run), indicating that the as-prepared heterostructure may effectively restrain photocorrosion under visible light and possess stable photocatalytic H₂ generation activity. Moreover, no obvious structural modification can be observed for the BiOCl/CFO heterostructure even after photocatalytic reactions (Figure 8d). Therefore, the remarkable catalytic activity and stability make the heterostructure a promising photo-

catalyst for hydrogen production from water splitting under visible light.

3.6. Proposed Mechanism for H₂ Generation. Conceptually, when two semiconductors come in contact with each other, a junction is created, which in turn facilitates electron transfer from the higher energy level to the lower energy level to achieve equilibrium. At equilibrium, bands of the material bend according to their Fermi level position and try to line up with the Fermi level (Scheme 2). Under light irradiation,

Scheme 2. Schematic Illustration of the Charge Transfer Process and the Photocatalytic H₂ Generation of the Novel Z-Scheme BiOCl/CFO Heterostructure under Visible Light Irradiation



photoinduced electrons and holes are generated both in BiOCl and CFO. As the CB of BiOCl is located near the VB of CFO, thus low-energy electrons of BiOCl may directly recombine with the holes of CFO by leaving excited electrons on the CB of CFO as shown in Scheme 2. Due to upward band bending, CB electrons of CFO may not transfer from CFO to BiOCl and may flow away from the junction. These electrons can easily reduce the water molecules to H₂ (H⁺/H₂, 0 V vs RHE) due to strong redox capability (−0.65 V). At the same time, photoinduced holes are consumed by the scavenger methanol and reduce the recombination rate as holes react faster with methanol than water. Thus, the direct Z-scheme photocatalytic system may effectively lower the backward reactions and enhance the amount of H₂ generation under visible light. On the other hand, the high-energy photogenerated electron and holes are migrated to the BiOI/CFO and BiOBr/CFO type-II and type-I heterostructures and lose their redox ability for water splitting, resulting in lower H₂ generation compared to the Z-scheme photocatalytic system (Scheme 1). The H₂ production rate of some reported CFO- and BiOX-based materials and patent photocatalysts⁵⁹ are listed in Table S5 to compare the photocatalytic activity, where very high photocatalytic activity has been achieved for the developed Z-scheme BiOCl/CFO heterostructures. Therefore, it can be concluded that the position of the energy bands has a strong role in controlling the electron hole transfer and formation of different types of heterostructures.

4. CONCLUSIONS

In summary, we developed three types of heterostructures (direct Z-scheme, type-I, and type-II) between n-type layered oxyhalides (BiOX) and p-type CuFe₂O₄ as photocatalysts for water splitting. The highest activity was achieved over the BiOCl/CFO photocatalyst, with a H₂ production rate of 22.2 mmol h^{−1}, compared to BiOI/CFO and BiOBr/CFO heterostructures, highlighting the intense promoting effect of

direct Z-scheme charge transfer mechanism. The self-induced internal field gradient of BiOCl along with the intimate contact between BiOCl and CFO accelerates the charge separation efficiency and extends the visible light absorption at longer wavelengths. Additionally, the highly dispersed O 2p band of BiOX helps in narrowing the band gaps and enhancing stability against water oxidation. The electrochemical measurements confirmed that the synergetic effects of high carrier concentration, low charge transfer resistance, and sufficient redox potentials resulted in the highest photocatalytic activity of BiOCl/CFO toward H₂ generation. Hence, the present study strongly suggests that fine and extensive regulation of band edge energies has a key role in controlling the charge separation efficiency, which in turn influences the photocatalytic activity. These band edge-engineered nanostructures are promising for efficient and stable H₂ generation through water reduction under visible light.

■ ASSOCIATED CONTENT

Supporting Information

The Supporting Information is available free of charge at <https://pubs.acs.org/doi/10.1021/acsaem.2c00296>.

XPS, TG curves, Raman spectra, and FTIR of BiOCl/CFO, BiOBr/CFO, and BiOI/CFO heterostructures; TEM image of CuFe₂O₄ nanoparticles; TEM-EDX of BiOX (X = Cl, Br, and I) and BiOCl/CFO heterostructures; M-S plots; space charge layer width versus applied potential; fitted Nyquist plots of BiOX and BiOX/CFO heterostructures; LSV curves of BiOX/CFO heterostructures under dark and light illumination; chopped CA spectra; PEC and IPCE spectra of the BiOCl/CFO heterostructure; UV-vis absorption and Kubelka-Munk plots of BiOI, BiOBr, BiOI/CFO, and BiOBr/CFO; fitted H₂ generation; AQY of bare BiOX, CFO, and BiOX/CFO heterostructures; effects of different sacrificial hole scavengers and sacrificial donor/solvent ratios in photocatalytic H₂ generation for BiOCl/CFO heterostructures; tables of calculated charge carrier concentrations, fitting parameters of linearly fitted photocatalytic H₂ generation, permittivity, and oxidation potential of the sacrificial agents; and comparison of photocatalytic applications of CFO- and BiOX-based materials (PDF)

■ AUTHOR INFORMATION

Corresponding Author

Srabanti Ghosh – Energy Materials & Devices Division, CSIR—Central Glass and Ceramic Research Institute, Kolkata 700032, India; Academy of Scientific & Innovative Research (AcSIR), Ghaziabad 201 002, India; orcid.org/0000-0002-0739-2831; Email: srabanti@cgcri.res.in, ghosh.srabanti@gmail.com

Authors

Susmita Bera – Energy Materials & Devices Division, CSIR—Central Glass and Ceramic Research Institute, Kolkata 700032, India

T. Maiyalagan – Department of Chemistry, SRM Institute of Science and Technology, Kattankulathur 603203, India; orcid.org/0000-0003-3528-3824

Rajendra N. Basu – Fuel Cell & Battery Division, CSIR—Central Glass and Ceramic Research Institute, Kolkata

700032, India; Present Address: School of Advanced Materials, Green Energy and Sensor Systems, Indian Institute of Engineering Science & Technology, Howrah, West Bengal, India

Complete contact information is available at:
<https://pubs.acs.org/10.1021/acsaem.2c00296>

Notes

The authors declare no competing financial interest.

ACKNOWLEDGMENTS

The authors acknowledge the Director, CSIR-CGCRI, for her kind permission to publish this work. One of the authors (S.B.) is thankful to the Department of Science and Technology (DST), India, for providing the INSPIRE fellowship award. We acknowledge the financial support from the Science and Engineering Research Board (SERB) through the “SERB-POWER Grant” (project no. SPG/2020/000720).

REFERENCES

- (1) Protti, S.; Fagnoni, M. The sunny side of chemistry: green synthesis by solar light. *Photochem. Photobiol. Sci.* **2009**, *8*, 1499–1516.
- (2) Wang, Q.; Hisatomi, T.; Jia, Q.; Tokudome, H.; Zhong, M.; Wang, C.; Pan, Z.; Takata, T.; Nakabayashi, M.; Shibata, N.; Li, Y.; Sharp, I. D.; Kudo, A.; Yamada, T.; Domen, K. Scalable water splitting on particulate photocatalyst sheets with a solar-to-hydrogen energy conversion efficiency exceeding 1%. *Nat. Mater.* **2016**, *15*, 611.
- (3) Ravelli, D.; Protti, S.; Fagnoni, M.; Albin, A. Visible Light Photocatalysis. A Green Choice? *Curr. Org. Chem.* **2013**, *17*, 2366–2373.
- (4) *Heterostructured Photocatalysts for Solar Energy Conversion*; Ghosh, S., Ed.; Elsevier Inc., 2020, ISBN: 9780128200735.
- (5) Jing, L.; Zhou, W.; Tian, G.; Fu, H. Surface tuning for oxide-based nanomaterials as efficient photocatalysts. *Chem. Soc. Rev.* **2013**, *42*, 9509–9549.
- (6) Prasad, C.; Yang, X.; Liu, Q.; Tang, H.; Rammohan, A.; Zulfikar, S.; Zyryanov, G. V.; Shah, S. Recent advances in MXenes supported semiconductors based photocatalysts: Properties, synthesis and photocatalytic applications. *J. Ind. Eng. Chem.* **2020**, *85*, 1–33.
- (7) Floresyona, D.; Goubard, F.; Aubert, P.-H.; Lampre, I.; Mathurin, J.; Dazzi, A.; Ghosh, S.; Beauvier, P.; Brisset, F.; Remita, S.; Ramos, L.; Remita, H. Highly active poly(3-hexylthiophene) nanostructures for photocatalysis under solar light. *Appl. Catal., B* **2017**, *209*, 23–32.
- (8) Djara, R.; Lacour, M.-A.; Merzouki, A.; Cambedouzou, J.; Cornu, D.; Tingry, S.; Holade, Y. Iridium and Ruthenium Modified Polyaniline Polymer Leads to Nanostructured Electrocatalysts with High Performance Regarding Water Splitting. *Polymers* **2021**, *13*, 190.
- (9) Xiang, Q.; Cheng, B.; Yu, J. Graphene-Based Photocatalysts for Solar-Fuel Generation. *Angew. Chem., Int. Ed.* **2015**, *54*, 11350–11366.
- (10) Colson, J. W.; Woll, A. R.; Mukherjee, A.; Levendorf, M. P.; Spittler, E. L.; Shields, V. B.; Spencer, M. G.; Park, J.; Dichtel, W. R. Oriented 2D covalent organic framework thin films on single-layer graphene. *Science* **2011**, *332*, 228–231.
- (11) Li, J.; Yu, Y.; Zhang, L. Bismuth oxyhalide nanomaterials: layered structures meet photocatalysis. *Nanoscale* **2014**, *6*, 8473–8488.
- (12) Shojja, S.; Yangjeh, A. H.; Mousavi, M.; Ghosh, S.; Maiyalagan, T. Carbon dots and Bi₄O₅Br₂ adhered on TiO₂ nanoparticles: Impressively boosted photocatalytic efficiency for removal of pollutants under visible light. *Sep. Purif. Technol.* **2020**, *250*, 117179.
- (13) Shi, M.; Li, G.; Li, J.; Jin, X.; Tao, X.; Zeng, B.; Pidko, E. A.; Li, R.; Li, C. Intrinsic Facet-dependent Reactivity of Well-defined BiOBr Nanosheets on Photocatalytic Water Splitting. *Angew. Chem., Int. Ed.* **2020**, *59*, 6590–6595.
- (14) Li, H.; Li, J.; Ai, Z.; Jia, F.; Zhang, L. Oxygen Vacancy-Mediated Photocatalysis of BiOCl: Reactivity, Selectivity, and Perspectives. *Angew. Chem., Int. Ed.* **2018**, *57*, 122–138.
- (15) Zhang, X.; Zhang, Y.; Feng, Z.; Zhao, J.; Yang, Z.; Wang, X.; Wang, W. Self-accelerating photocharge separation in BiOBr ultrathin nanosheets for boosting photoreversible color switching. *Chem. Eng. J.* **2022**, *428*, 131235.
- (16) Zhou, Q.; Huang, W.; Xu, C.; Liu, X.; Yang, K.; Li, D.; Hou, Y.; Dionysiou, D. D. Novel hierarchical carbon quantum dots-decorated BiOCl nanosheet/carbonized eggshell membrane composites for improved removal of organic contaminants from water via synergistic adsorption and photocatalysis. *Chem. Eng. J.* **2021**, *420*, 129582.
- (17) Sun, J.; Li, X.; Zhao, Q.; Liu, B. Ultrathin nanoflake-assembled hierarchical BiOBr microflower with highly exposed {001} facets for efficient photocatalytic degradation of gaseous ortho-dichlorobenzene. *Appl. Catal., B* **2021**, *281*, 119478.
- (18) Zhang, L.; Wang, W.; Sun, S.; Jiang, D.; Gao, E. Selective transport of electron and hole among {0 0 1} and {1 1 0} facets of BiOCl for pure water splitting. *Appl. Catal., B* **2015**, *162*, 470–474.
- (19) Cao, J.; Li, J.; Chu, W.; Cen, W. Facile synthesis of Mn-doped BiOCl for metronidazole photodegradation: Optimization, degradation pathway, and mechanism. *Chem. Eng. J.* **2020**, *400*, 125813.
- (20) Chowdhury, A. P.; Shambharkar, B. H. Fabrication and characterization of BiOBr-SnWO₄ heterojunction nanocomposites with boosted photodegradation capability. *Chem. Eng. J. Adv.* **2020**, *4*, 100040.
- (21) Yu, H.; Huang, J.; Jiang, L.; Shi, Y.; Yi, K.; Zhang, W.; Zhang, J.; Chen, H.; Yuan, X. Enhanced photocatalytic tetracycline degradation using N-CQDs/OV-BiOBr composites: Unraveling the complementary effects between N-CQDs and oxygen vacancy. *Chem. Eng. J.* **2020**, *402*, 126187.
- (22) Ye, L.; Liu, J.; Gong, C.; Tian, L.; Peng, T.; Zan, L. Insights into the interfacial carrier behaviour of copper ferrite (CuFe₂O₄) photoanodes for solar water oxidation. *ACS Catal.* **2012**, *2*, 1677–1683.
- (23) Zarezadeh, S.; Habibi-Yangjeh, A.; Mousavi, M.; Ghosh, S. Synthesis of novel p-n-p BiOBr/ZnO/BiOI heterostructures and their efficient photocatalytic performances in removals of dye pollutants under visible light. *J. Photochem. Photobiol., A* **2020**, *389*, 112247.
- (24) Song, C.; Feng, Y.; Shi, W.; Liu, C. Fabrication and mechanism of a novel direct solid-state Z-scheme photocatalyst CdS/BiOI under visible light. *CrystEngComm* **2016**, *18*, 7796–7804.
- (25) Sun, M.; Hu, J.; Zhai, C.; Zhu, M.; Pan, J. CuI as Hole-Transport Channel for Enhancing Photoelectrocatalytic Activity by Constructing CuI/BiOI Heterojunction. *ACS Appl. Mater. Interfaces* **2017**, *9*, 13223–13230.
- (26) Hu, L.; He, H.; Xia, D.; Huang, Y.; Xu, J.; Li, H.; He, C.; Yang, W.; Shu, D.; Wong, P. K. Highly Efficient Performance and Conversion Pathway of Photocatalytic CH₃SH Oxidation on Self-Stabilized Indirect Z-Scheme g-C₃N₄/I³⁻-BiOI. *ACS Appl. Mater. Interfaces* **2018**, *10*, 18693–18708.
- (27) Chen, T.-H.; Yoshida, M.; Tsunekawa, S.; Wu, J.-H.; Lin, K.-Y. A.; Hu, C. Development of BiOI as an effective photocatalyst for oxygen evolution reaction under simulated solar irradiation. *Catal. Sci. Technol.* **2020**, *10*, 3223–3231.
- (28) Alam, K. M.; Kumar, P.; Kar, P.; Thakur, U. K.; Zeng, S.; Cui, K.; Shankar, K. Enhanced charge separation in g-C₃N₄-BiOI heterostructures for visible light driven photoelectrochemical water splitting. *Nanoscale Adv.* **2019**, *1*, 1460–1471.
- (29) Wang, Q.; Hisatomi, T.; Suzuki, Y.; Pan, Z.; Seo, J.; Katayama, M.; Minegishi, T.; Nishiyama, H.; Takata, T.; Seki, K.; Kudo, A.; Yamada, T.; Domen, K. Particulate photocatalyst sheets based on carbon conductor layer for efficient Z-scheme pure-water splitting at ambient pressure. *J. Am. Chem. Soc.* **2017**, *139*, 1675–1683.
- (30) VN, A.; Rastogi, S.; Rastogi, P. K.; S, T.; S, V.; Shaji, S.; V, R. R.; Garza-Navarro, M. A.; Thomas, S.; Narayanan, T. N.; Anantharaman, M. R. Engineering nanostructured spinel ferrites by

co-substitution for total water electrolysis by preferential exposure of metal cations on the surface. *Sustain. Energy Fuels* **2020**, *4*, 3915–3925.

(31) Matsumoto, Y. Energy Positions of Oxide Semiconductors and Photocatalysis with Iron Complex Oxides. *J. Solid State Chem.* **1996**, *126*, 227–234.

(32) Liu, Y.; Le Formal, F.; Boudoire, F.; Yao, L.; Sivula, K.; Guijarro, N. Insights into the interfacial carrier behaviour of copper ferrite (CuFe_2O_4) photoanodes for solar water oxidation. *J. Mater. Chem. A* **2019**, *7*, 1669–1677.

(33) Matsumoto, Y.; Omae, M.; Sugiyama, K.; Sato, E. New photocathode materials for hydrogen evolution: calcium iron oxide (CaFe_2O_4) and strontium iron oxide ($\text{Sr}_7\text{Fe}_{10}\text{O}_{22}$). *J. Phys. Chem.* **1987**, *91*, 577–581.

(34) Park, S.; Baek, J. H.; Zhang, L.; Lee, J. M.; Stone, K. H.; Cho, I. S.; Guo, J.; Jung, H. S.; Zheng, X. Rapid Flame-Annealed CuFe_2O_4 as Efficient Photocathode for Photoelectrochemical Hydrogen Production. *ACS Sustainable Chem. Eng.* **2019**, *7*, 5867–5874.

(35) Hussain, S.; Hussain, S.; Waleed, A.; Tavakoli, M. M.; Wang, Z.; Yang, S.; Fan, Z.; Nadeem, M. A. Fabrication of $\text{CuFe}_2\text{O}_4/\alpha\text{-Fe}_2\text{O}_3$ Composite Thin Films on FTO Coated Glass and 3-D Nanospine Structures for Efficient Photoelectrochemical Water Splitting. *ACS Appl. Mater. Interfaces* **2016**, *8*, 35315–35322.

(36) Cheng, R.; Fan, X.; Wang, M.; Li, M.; Tian, J.; Zhang, L. Facile construction of $\text{CuFe}_2\text{O}_4/g\text{-C}_3\text{N}_4$ photocatalyst for enhanced visible-light hydrogen evolution. *RSC Adv.* **2016**, *6*, 18990–18995.

(37) Das, S.; Patnaik, S.; Parida, K. Dynamic charge transfer through Fermi level equilibration in the p- $\text{CuFe}_2\text{O}_4/n\text{-NiAl}$ LDH interface towards photocatalytic application. *Catal. Sci. Technol.* **2020**, *10*, 6285–6298.

(38) Li, G.; Qin, F.; Wang, R.; Xiao, S.; Sun, H.; Chen, R. BiOX (X = Cl, Br, I) nanostructures: Mannitol-mediated microwave synthesis, visible light photocatalytic performance, and Cr(VI) removal capacity. *J. Colloid Interface Sci.* **2013**, *409*, 43–51.

(39) Tang, W.; Zhang, Y.; Guo, H.; Liu, Y. Heterogeneous activation of peroxymonosulfate for bisphenol AF degradation with $\text{BiOI}_{0.5}\text{Cl}_{0.5}$. *RSC Adv.* **2019**, *9*, 14060–14071.

(40) Lv, J.; Hu, Q.; Cao, C.; Zhao, Y. Modulation of valence band maximum edge and photocatalytic activity of BiOX by incorporation of halides. *Chemosphere* **2018**, *191*, 427–437.

(41) Chen, S.-M.; Umamaheswari, R.; Mani, G.; Chen, T.-W.; Ali, M. A.; MA, A.-H. F.; Elshikh, M. S.; Farah, M. A. Hierarchically structured CuFe_2O_4 ND@RGO composite for the detection of oxidative stress biomarker in biological fluids. *Ing. Chem. Front.* **2018**, *5*, 944–950.

(42) Bhachu, D. S.; Moniz, S. J. A.; Sathasivam, S.; Scanlon, D. O.; Walsh, A.; Bawaked, S. M.; Mokhtar, M.; Obaid, A. Y.; Parkin, I. P.; Tang, J.; Carmalt, C. J. Bismuth oxyhalides: synthesis, structure and photoelectrochemical activity. *Chem. Sci.* **2016**, *7*, 4832–4841.

(43) Morandi, P.; Flaud, V.; Tingry, S.; Cornu, D.; Holade, Y. Tartaric acid regulated the advanced synthesis of bismuth-based materials with tunable performance towards the electrocatalytic production of hydrogen peroxide. *J. Mater. Chem. A* **2020**, *8*, 18840–18855.

(44) Zalineeva, A.; Serov, A.; Padilla, M.; Martinez, U.; Artyushkova, K.; Baranton, S.; Coutanceau, C.; Atanassov, P. B. Self-Supported Pd_xBi Catalysts for the Electrooxidation of Glycerol in Alkaline Media. *J. Am. Chem. Soc.* **2014**, *136*, 3937–3945.

(45) Casella, I. G.; Contursi, M. Characterization of bismuth adatom-modified palladium electrodes: The electrocatalytic oxidation of aliphatic aldehydes in alkaline solutions. *Electrochim. Acta* **2006**, *52*, 649–657.

(46) Bera, S.; Ghosh, S.; Basu, R. N. Fabrication of $\text{Bi}_2\text{S}_3/\text{ZnO}$ heterostructures: an excellent photocatalyst for visible-light-driven hydrogen generation and photoelectrochemical properties. *New J. Chem.* **2018**, *42*, 541–554.

(47) Guo, M.; Zhou, Z.; Yan, S.; Zhou, P.; Miao, F.; Liang, S.; Wang, J.; Cui, X. $\text{Bi}_2\text{WO}_6\text{-BiOCl}$ heterostructure with enhanced photo-

catalytic activity for efficient degradation of oxytetracycline. *Sci. Rep.* **2020**, *10*, 18401–18415.

(48) Hu, J.; Fan, W.; Ye, W.; Huang, C.; Qiu, X. Insights into the photosensitivity activity of BiOCl under visible light irradiation. *Appl. Catal., B* **2014**, *158–159*, 182–189.

(49) Di, J.; Xia, J.; Yin, S.; Xu, H.; Xu, L.; Xu, Y.; He, M.; Li, H. One-pot solvothermal synthesis of Cu-modified BiOCl via a Cu-containing ionic liquid and its visible-light photocatalytic properties. *RSC Adv.* **2014**, *4*, 14281–14290.

(50) Ghosh, S.; Keshri, S. R.; Bera, S.; Basu, R. N. Enhanced solar hydrogen generation using Cu-Cu₂O integrated polypyrrole nanofibers as heterostructured catalysts. *Int. J. Hydrogen Energy* **2020**, *45*, 6159–6173.

(51) Chatterjee, B. K.; Bhattacharjee, K.; Dey, A.; Ghosh, C. K.; Chattopadhyay, K. K. Influence of spherical assembly of copper ferrite nanoparticles on magnetic properties: orientation of magnetic easy axis. *Dalton Trans.* **2014**, *43*, 7930–7944.

(52) Li, L.; Zhang, M.; Zhao, Z.; Sun, B.; Zhang, X. Visible/near-IR-light-driven TNFePc/BiOCl organic-inorganic heterostructures with enhanced photocatalytic activity. *Dalton Trans.* **2016**, *45*, 9497–9505.

(53) Waldron, R. D. Infrared spectra of ferrites. *Phys. Rev.* **1955**, *99*, 1727.

(54) Li, T. B.; Chen, G.; Zhou, C.; Shen, Z. Y.; Jin, R. C.; Sun, J. X. New photocatalyst BiOCl/BiOI composites with highly enhanced visible light photocatalytic performances. *Dalton Trans.* **2011**, *40*, 6751–6758.

(55) Chang, X.; Wang, S.; Qi, Q.; Gondal, M. A.; Rashid, S. G.; Gao, S.; Yang, D.; Shen, K.; Xu, Q.; Wang, P. Insights into the growth of bismuth nanoparticles on 2D structured BiOCl photocatalysts: an in situ TEM investigation. *Dalton Trans.* **2015**, *44*, 15888–15896.

(56) Kumar, S.; Yadav, N.; Kumar, P.; Ganguli, A. K. Design and Comparative Studies of Z-Scheme and Type II Based Heterostructures of $\text{NaNbO}_3/\text{CuInS}_2/\text{In}_2\text{S}_3$ for Efficient Photoelectrochemical Applications. *Inorg. Chem.* **2018**, *57*, 15112–15122.

(57) Bera, S.; Ghosh, S.; Shyamal, S.; Bhattacharya, C.; Basu, R. N. Photocatalytic hydrogen generation using gold decorated BiFeO₃ heterostructures as an efficient catalyst under visible light irradiation. *Sol. Energy Mater. Sol. Cells* **2019**, *194*, 195–206.

(58) Wang, M.; Shen, S.; Li, L.; Tang, Z.; Yang, J. Effects of sacrificial reagents on photocatalytic hydrogen evolution over different photocatalysts. *J. Mater. Sci.* **2017**, *52*, 5155–5164.

(59) Protti, S.; Albini, A.; Serpone, N. Photocatalytic generation of solar fuels from the reduction of H₂O and CO₂: a look at the patent literature. *Phys. Chem. Chem. Phys.* **2014**, *16*, 19790–19827.

(60) Zhang, S.; Li, J.; Wang, X.; Huang, Y.; Zeng, M.; Xu, J. Rationally designed 1D Ag@AgVO₃ nanowire/graphene/protonated g-C₃N₄ nanosheet heterojunctions for enhanced photocatalysis via electrostatic self-assembly and photochemical reduction methods. *J. Mater. Chem.* **2015**, *3*, 10119–10126.

(61) Morales-Guio, C. G.; Tilley, S. D.; Vrubel, H.; Grätzel, M.; Hu, X. Hydrogen evolution from a copper(I) oxide photocathode coated with an amorphous molybdenum sulphide catalyst. *Nat. Commun.* **2014**, *5*, 3059–3066.